


# Chronically silencing cortical projection neurons leads to neuroanatomical and motor degeneration

**by**

**Marissa Hope Mueller**

***A dissertation submitted in partial fulfilment of the requirements for the degree of Doctor of Philosophy (Physiology, Anatomy and Genetics)***

**Balliol College**

**University of Oxford**

**2026**

**TIABTTEOM**

Marissa H. Mueller

marissa.mueller@balliol.ox.ac.uk

ORCiD: https://orcid.org/0000-0002-9729-8311

© Marissa H. Mueller 2026

# Abstract

**Background:** The cerebral cortex is exceptionally complex. Computational capacities enabled by cytoarchitectural diversity are established during neurodevelopment which, if dysfunctional, can lead to neurological and psychiatric disorders. Neurons in deep cortical layers 5-6 (L5-6) are of particular interest, presenting as substrates where prenatal insults may provoke postnatal deficits. Studies using mouse-models show that L6b cells—which resemble human white-matter-interstitial-neurons (WMINs)—are remnants of the neurodevelopmentally-critical subplate; subplate axons pioneer corticofugal pathways which L5 axons later descend and dominate. Through adulthood, subplate-remnant abnormalities are associated with diseases of cortical hyperexcitability, yet anatomical and morphometric ramifications are incompletely characterised. Dysfunctional L5-projections can lead to neuromotor degeneration, however pathophysiological trajectories remain unknown. **Hypotheses:** Genetically-targeting mouse L5-6b cells elicits widespread neuroanatomical and functional changes. Particularly, L6-'augmentation' may yield neuron hypertrophy resembling that of WMINs in postmortem tissues from human autism and epilepsy patients, while L5-'silencing' may spur progressive neuromotor decline supporting top-down theories of motor neuron degeneration. Investigations across functional, histological, and neuroimaging methods may derive complimentary network insights exceeding those which any technique would provide in isolation. **Methods:** I developed and validated a novel mouse home-cage-monitoring system (*SnackerTracker-TracKIT*) and computational enhancements for a whole-brain cell analysis pipeline (r-QUINT) to enhance behavioural and anatomical outputs, respectively. r-QUINT described ramifications of genetic L6-'silencing'/'augmentation', and a longitudinal study featuring behavioural, anatomical, and multimodal MRI experiments characterised consequences of L5-'silencing'. **Results:** Chapter-3 introduces the *SnackerTracker* device and *TracKIT* analysis platform. Chapter-4 describes r-QUINT refinements, which reveal changes following L6b perturbations, while morphometric comparisons support L6b-WMIN analogy. Chapter-5 presents convergent evidence of neuromotor deterioration upon L5-silencing, where pathological trajectories resemble those of upper-motor-neuron diseases. Neuroimaging predicts—and histology validates—where and when deficits emerge. **Conclusions:** This thesis presents methodological developments and multimodal analyses which characterise effects of silencing deep-layer cortical neurons, thereby enhancing knowledge surrounding associated disease-relevant networks.

# Acknowledgements

## Statement regarding the use of AI

Any use of generative AI complies with the University of Oxford's Policy for using Generative AI in Research (v1.0, https://www.ox.ac.uk/research/support/governance-and-committees/research-policies/policy-for-using-generative-ai-in) and corresponding Medical Sciences Division regulations (https://www.medsci.ox.ac.uk/for-staff/opportunities-and-updates/research-and-innovation-committee-guidance-on-the-use-of-artificial-intelligence-tools-in-your-research). In this thesis, AI tools (i.e., ChatGPT) were employed during software development for: visual elements and .mlapp formatting in TracKIT; .swc trace rotation (**A.10.9**); creation and visual presentation of resulting graphs in polar plot scripts (**A.10.10**); kurtosis filtering (**A.10.17**); MGE filtering (**A.10.18**); .Rmd processing (**A.10.19**), and translating code written by others into programming languages with which I am familiar for personal learning (non-substantive use). Scripts are otherwise my original work. Both ChatGPT and Google's AI search mode assisted in suggesting relevant manuscripts for literature reviews. In no instance was AI—particularly generative AI—used for text ideation, generation, or editing. The written and visual content of this thesis is my own.

## Statement of previous acceptance

The concept of the *SnackerTracker*, its preliminary prototype, and rudimentary benchtop testing were introduced in my previous MSc in Neuroscience dissertation (University of Oxford). No other part of my thesis has been accepted or is currently being submitted for any degree, diploma, certificate or other qualification in this University or elsewhere. Published content included in this text constitutes my original contribution to any published manuscript.

## Resulting publications

**Mueller, M. H.**; Greene, G.; Mellor-Davis, E.; Yuan, R.; Kyne, R. S.; Lavda, M.; Oh, J.; Ho, T. T. B.; Blachowiak, K.; Platt, M.; et al. MRI, histology, and behaviour data reveals neuromotor degeneration upon cortical layer 5 silencing. *Hum Brain Mapp,* 2026, (2), 6436. DOI: 10.5281/zenodo.20817055.

**Mueller, M. H.**; Tir, S.; Pothecary, C.; Meijer, E.; Brown, L.; Foster, K.; Vyazovskiy, V.; Peirson, S.; Molnár, Z. The SnackerTracker: A novel home-cage monitoring device for measuring food-intake and food-seeking behaviour in mice. *Wellcome Open Res,* 2025, 10 (172). DOI: 10.12688/wellcomeopenres.23850.1.

Vadisiute, A.; Szabo, F.; Luchanskaya, S.; Drevenakova, V.; Messore, F.; Ugwudike, A.; Greene, G.; **Mueller, M.**; et al. Deletion of Snap25 disrupts glial remodelling in aging mouse brain. *iScience,* 2026, 29 (7). DOI: 10.1016/j.isci.2026.116478.

Molnár, Z.; Kim, Y.; Kronman, F. N.; **Mueller, M. H.**; Price, D. J. Chapter 23 - brain development. In Kaufman's atlas of mouse development supplement, Morriss-Kay, G., Srinivas, S. Eds.; *Academic Press*, 2025, (2), 371-390. DOI: 10.1016/C2023-0-00224-2

Meijer, E. J.; **Mueller, M.**; Krone, L. B.; Yamagata, T.; Hoerder-Suabedissen, A.; Wilcox, S.; Alfonsa, H.; et al. Cortical layer 6b mediates state-dependent changes in brain activity and effects of orexin on waking and sleep. *eLife*, 2025, 14. DOI: 10.7554/eLife.106992.2.

Messore, F.; Narayanan Therpurakal, R.; Dufour, J.; Hoerder-Suabedissen, A.; Guidi, L.; Korrell, K.; **Mueller, M.**; et al. An orexin-sensitive subpopulation of layer 6 neurons regulates cortical excitability and anxiety behaviour. *Transl Psychiatry,* 2025, 15 (1), 147. DOI: 10.1038/s41398-025-03350-2.

Vadisiute, A.; Meijer, E.; Therpurakal, R. N.; **Mueller, M.**; Szabó, F.; Messore, F.; Jursenas, A.; Bredemeyer, O.; Krone, L. B.; Mann, E.; et al. Glial cells undergo rapid changes following acute chemogenetic manipulation of cortical layer 5 projection neurons. *Commun Biol,* 2024, 7 (1), 1286, Research article. DOI: 10.1038/s42003-024-06994-w.

## Software and protocol deposits

**Mueller, M.**; Zolnik, T.; Molnar, Z. Polar Plotting. 1 ed.; *Zenodo*: 2026. DOI: 10.5281/zenodo.20287397.

**Mueller, M.**; Tir, S.; Pothecary, C.; Meijer, E.; Brown, L.; Foster, K.; Vyazovskiy, V.; Peirson, S.; Molnar, Z. SnackerTracker. *protocols.io* 2025, Workflow. DOI: 10.17504/protocols.io.rm7vzke8rvx1/v1.

**Mueller, M.**; Vyazovskiy, V.; Molnar, Z.; Peirson, S. TracKIT. 2 ed.; *Zenodo*: 2025. DOI: 10.5281/zenodo.14632999.

**Mueller, M.**; Vadisiute, A.; Molnar, Z. ImARef. 2 ed.; *Zenodo*, 2024. DOI: 10.5281/zenodo.14933978.

## Statement of authorship and contribution

All experimental and intellectual results and rationale in this thesis are my own. Exceptions and contributions from others (including in the above publications) are as follows.

*Work assisted or conducted by others:*

Dr. Elise Meijer supported *SnackerTracker* development and coined its name (**2.2.2**). Dr. Anna Hoerder-Suabedissen managed breeding and genotyping throughout L6 and L5 studies (**2.1.2**), provided technical expertise throughout histology experiments (**5.3**), and advised the use of the CAMP scoring system (**2.4.3**, **5.1.2**). Dr. Florina Szabó performed PV-VVA histology for experimental pilot r-QUINT DREADD experiments and PTEN-augmented interneuron evaluations (**4.2.1**-**4.2.3**, **4.3.4**), assisted with SDCM parameter optimisation (**A.6.2**), and provided a copy of her thesis from which I derived results for methodological comparison (**4.1.4**, **4.3.4**). Dr. Tim Zolnik and Dr. Britta Eickholt from Charité Universitätsmedizin Berlin provided all PTEN brains for subsequent processing in Oxford (**2.1.1**, **2.1.2**, **4.1.4**, **4.3**). Dr. Tim Zolnik provided human and mouse neuron image stacks for morphometric and polar plot analyses (**2.3.5.1**, **2.3.5.5**, **4.4**) and stimulating discussions surrounding network explanations, including publications referenced in-text (**4.4.5**, **4.5.4**). Dr. Ed Drydale assisted with SDCM acquisition optimisation and pilot Arivis pipeline development at Oxford's Centre for Human Genetics Cellular Imaging Core (**2.3.3, 4.1.3**). Dr. Mohamed Tachrount developed MRI scanning sequences employed throughout STAMINA experiments (**2.5.1.3**, **2.5.2.3**, **5.2**). Dr. Cristiana Tisca offered generous technical expertise in MRI *ex vivo* sample preparation (**2.5.2**), data pre-processing (**2.5.3**), and co-registration (particularly diffusion and QSM) (**2.5.4**). Ms. Ruoqi Yuan (MSc student) performed blinded behavioural analyses of L5-silenced mice, including of images, traces, and videos I acquired in hindlimb clasp, ledge walk, CatWalk, and nesting assessments (**2.4.3**-**2.4.4**, **5.1.2**, **5.1.4**-**5.1.5**). Ms. Jade Oh, Ms. Tien Ho, Dr. Myrto Lavda, Dr. Cristiana Tisca, Dr. Mark Platt, Ms. Kamila Blachowiak, Dr. Ioana Grigoras, Dr. Mohamed Tachrount, Dr. Yingshi

Feng, and Dr. Elizabeth de Guzman sporadically queued overnight *ex vivo* scanning (**2.5.2.2**). Ms. Ritika Mukherji conducted hamster *SnackerTracker* recordings with my assistance (**2.2.5**, **3.3.5**). Ms. Eden Mellor-Davis (Crankstart Internship Programme), Ms. Laura Rihova, and Ms. Gretchen Greene assisted with L5-silenced histological experiments (**5.3.1**-**5.3.4**) and testing the spinal scaffolds I developed (**A.5.4**). Mr. Reuben Kyne performed spatial transcriptomic analyses of *Rbp4*-Cre cells using open-source datasets to assess intratelencephalic/extratelencephalic projection coverage (**Figure 4B**). Ms. Lieselotte Schlopp (FHS student) and Ms. Gretchen Greene conducted experiments using Rbp4-Cre internal organs, including but not limited to the results noted in **5.3.5**. Mr. Adriano dos Santos assisted with DLE experiments and provided PIR data (**A.9.3**). Ms. Sri Chava and Dr. Maciej Kliszczak conducted all SSFM imaging using core facilities at the Oxford Centre for Human Genetics' Cellular Imaging Core (**5.3.1**-**5.3.4**). Dr. Linus Milinski and Dr. Anna Hoerder-Suabedissen provided Fezf2 tissues (**5.5.4**). Mr. Mohamed Abuelem has now conducted follow-up electrophysiological testing of *Rbp4*-Cre tissues (**5.5.4**). Dr. Elizabeth de Guzman is conducting fMRI analyses (**2.5.3.5**, **5.5.3**). Staff from the University of Oxford's Biological Sciences Building—particularly Ms. Jessica Law, Ms. Chloe Cotton, and Ms. Debbie Cobley—provided support and advice in animal welfare monitoring (**2.1.2**).

*Software development contributions:*

In addition to the use of AI when developing software in across projects in this thesis (**Statement regarding the use of AI**), I adapted and incorporated elements of original scripts created by the following individuals into my own: Dr. Joshua Hrisko and Mr. Karl Söderby (for operational *SnackerTracker* code https://makersportal.com/blog/2019/5/12/arduino-weighing-scale-with-load-cell-and-hx711 and https://docs.arduino.cc/tutorials/mkr-mem-shield/mkr-mem-shield-data-logger, **A.10.1**); Dr. Cristiana Tisca (for MRI pre-processing and co-registration, **A.10.13**-**A.10.16**); and Prof. Jason Lerch (for MRI pre-processing, registration, and analyses, **A.10.11**-**A.10.12**, **A.10.19**).

## Statement of support

Appreciation must be extended to supervisors and colleagues who supported me in experimental planning, in resource provision (also see **Funding**), and in my technical training.

Experiments were guided by my primary supervisors—Prof. Zoltán Molnár, Prof. Stuart Peirson, and Prof. Vladyslav Vyazovskiy—throughout the past four years. Senior postdoctoral scientist Dr. Anna Hoerder-Suabedissen and junior research fellow Dr. Auguste Vadisiute offered technical expertise and advice which extended through multimodal elements of STAMINA upon its initiation (**1.5.5**). This capstone-like project recruited the driving force of the Oxford Centre for Integrative Neuroimaging's Preclinical Imaging Group led by Prof. Jason Lerch who, after examining my transfer of status, joined STAMINA planning meetings to advise neuroimaging directions. Dr. Kamila Szulc-Lerch and Prof. Kevin Talbot further advocated for more extensive behavioural testing and histology all of which was incorporated into the study design (**Figure 4**).

Many thanks must be extended to the following group leaders for their generous provision of resources which enabled the projects described in this thesis: Prof. Zoltán Molnár, Prof. Stuart Peirson, and Prof. Vladyslav Vyazovskiy for their supply of animal model-systems (**2.1.1**-**2.1.3**); Prof. Zoltán Molnár, Prof. Stuart Peirson, Prof. Vladyslav Vyazovskiy, Dr. Sean Smart, Prof. Heidi Johansen-Berg, and Prof. Jason Lerch for employment under personal project licenses (**2.1.1**); Prof. Zoltán Molnár and Prof. Jason Lerch for use of wet-lab space (**2.3.2**); Prof. Stuart Peirson and Prof. Vladyslav Vyazovskiy for use of soldering rooms and benchtop testing space (**2.2.1**, **2.2.2**); Prof. Armin Lak, Prof. Stuart Peirson, Prof. Jason Lerch, and Dr. Sean Smart for simultaneous use of Ultimaker 3D printers to enable timely *SnackerTracker* construction for STAMINA (**2.2.1**, **5.1.1**); Dr. Keiran Foster and Oxford's Department of Physics Electronics Workshop for partnership in future contracted *SnackerTracker* provision (**3.5.2**); Prof. David Bannerman for use of the CatWalk system and grip-strength testing setup (**5.1.4**, **5.1.5**); and Prof. Jason Lerch for use of neuroimaging facilities and coverage of associated costs (**5.2**).

Across project aspects, exceptional technical training was provided to me by the generosity of experienced colleagues and mentors: Dr. Bashir Ahmed in the use of QuPath software (**2.3.4.3**); Dr. Florina Szabó, Dr. Auguste Vadisiute, and Dr. Anna Hoerder-Suabedissen in histology (**2.3.2**); Dr. James Bancroft and Dr. Ed Drydale in SDCM imaging and Arivis analyses (**Figure 16**); Dr. Carina Pothecary in the use of LTCs, LDRs, STAMINA cage setups, and Ultimaker 3D printing (**2.1.2**, **2.2.1**); Dr. Ma'ayan Semo in VCT configuration and AnyMaze operation (**2.4.2**); Dr. Selma Tir in DVC setups (**2.2.3**); Dr. Ioana Grigoras in CatWalk and grip-strength testing (**2.4.4**-**2.4.5**); Dr. Mohamed Tachrount, Dr. Sean Smart, Dr. Myrto Lavda, Dr. Antoine Cherix, and Dr. Clemence Ligneul throughout *in vivo* MRI scanning (**2.5.1**); Ms. Ritika Mukherji in thermography (**2.4.1**); Dr. Cristiana Tisca, Dr. Sean Smart, and Dr. Mohamed Tachrount in *ex vivo* MRI scanning (**2.5.2**); Prof. Jason Lerch, Dr. Cristiana Tisca, Dr. Myrto Lavda, and Ms. Jade Oh in MRI pre-processing (**2.5.3**); Dr. Cristiana Tisca in MRI co-registration, including the provision of foundational scripts and feedback following my adaptations (**2.5.4**); Prof. Jason Lerch throughout MRI analyses, also including the provision of foundational scripts and feedback following my adaptations (**2.5.5**); and Prof. Zoltan Molnár in DiI tracing (**5.5.4**, **A.8.6**).

## Funding

This DPhil was funded by the Rhodes Scholarship (Rhodes Trust), the Clarendon Scholarship (University of Oxford), and Goodger and Schorstein Scholarship (University of Oxford). Fees for the Wellcome Centre for Integrative Neuroimaging's Graduate MRI Programme were paid for by Balliol College. The following agencies supported this research: Wellcome Trust (227093, Prof. Stuart Peirson); Medical Research Council (MR/W029073/1, Prof. Zoltán Molnár); Biotechnology and Biological Sciences Research Council (BB/X008711/1 and BB/X002357/1, Prof. Vladyslav Vyazovskiy and Prof. Stuart Peirson, respectively); and Einstein Stiftung (Prof. Zoltán Molnár). The Centre for Integrative Neuroimaging was supported by core funding from the Wellcome Trust (203139/Z/16/Z and 203139/A/16/Z).

## Special thanks

Thank you to Prof. Zoltán Molnár, my primary supervisor, for your unwavering support and care both personally and professionally. I am grateful for your enthusiasm across all aspects of this work, for your encouragement through difficulties, and for enabling me to pursue ideas and drive research directions. You trusted my judgement when I did not, established collaborations to ensure that help and training was available wherever needed, and ensured that every opportunity was afforded to explore parallel interests in industry, remote work, and teaching. During a lecture you once said that you aspire to be like Santiago Ramón y Cajal, in excellence in science and in education; I and innumerable others say the same of you.

Thank you to Prof. Vladyslav Vyazovskiy and Prof. Stuart Peirson, my secondary supervisors, for challenging me to grow as an independent thinker and person. Your dedication to scientific rigor and your clear passion for discovery is inspiring. Your mentorship, patience, and guidance throughout my studies—including advice to simply sleep—is ever appreciated. Thank you for never failing to make time for meetings amidst demanding schedules. Your passion for research in sleep and circadian biology is abundantly contagious; I have never left a meeting with questions unanswered. I am fortunate and forever grateful for your constructive criticism, which strengthened all aspects of this project, and your continued support.

Thank you to Prof. Jason Lerch who has become an unofficial supervisor since the transfer of status. You welcomed me into your lab and immediately made me feel as though I was a valued member of your team. It has been a privilege to begin to work alongside and learn from members of the Preclinical Imaging Group. You foster an environment which is constantly intellectually stimulating, challenging, and empowering. The humility and genius with which you craft and execute ideas is inspiring. I aspire to your example, feel privileged for the opportunity to join OxCIN post-DPhil, and have so much to look forward to learning.

Thank you to Dr. Anna Hoerder-Suabedissen, who originally characterised the layer 5 model and drove its study. Moreover, I am grateful for your continuous advice through experimental planning and execution, for your fierce professional and personal support, and for your strong leadership. I only aim for your standard of scientific excellence and character.

Thank you to Prof. Jonathan Bard, my Balliol advisor, for your steady mentorship, guidance, and kindness. Your lifelong dedication to science shines in every conversation.

Thank you to Dr. Sean Smart, Dr. Bashir Ahmed, Dr. Ma'ayan Semo, Dr. Carina Pothecary, Dr. Mohamed Tachrount, Ms. Kamila Blachowiak, Dr. James Bancroft, and Dr. Ed Drydale for your technical expertise and constant kindness. Your support of my work and the work of others is entirely indispensable. Appreciation is not conveyed as often as it is due.

Thank you to our collaborators from Charité Universitätsmedizin led by Prof. Britta Eickholt—and particularly Dr. Tim Zolnik—for many insightful and stimulating conversations, and for hosting the Molnár group in Berlin. I greatly value our scientific discussions and hope these continue for years to come.

Dr. Auguste Vadisiute—you have been an anchor as a colleague and as a friend. Dr. Iona Thomas-Wright—thank you for the many adventures past and yet to come.

Research is not undertaken alone; I am incredibly fortunate to have been surrounded by individuals with whom countless discussions and adventures have made this journey enriching and enjoyable. Thank you particularly to Ms. Gretchen Greene, Mr. Mohamed Abuelem, Dr. Myrto Lavda, Ms. Jade Oh, Dr. Cristiana Tisca, and last but certainly not least Ms. Ritika Mukherji. Your selflessness, constant willingness to help others, and altruism makes working with you a joy and privilege. I will never forget the pizzas, games, and many laughs.

To Ms. Laura Rihova, Ms. Eden Mellor-Davis, Ms. Lieselotte Schlopp, and Ms. Ruoqi Yuan who dove into the layer-5 study and contributed instrumentally—thank you for your technical talent, constancy amidst the craziness, and keen initiative.

Thank you to Dr. Elise Meijer, Dr. Linus Milinsky, Dr. José Prius Mengual, Dr. Laura Steel, Dr. Selma Tir, Dr. Fernando Messore, Dr. Florina Szabó, Dr. Ioana Grigoras, and Dr. Sara Bandiera for providing advice, training, and collaborative support. You set high standards in our labs by example and help others meet theirs in turn.

Thank you to Dr. Frey-Law and Dr. Breyan Neyland, my undergraduate mentors, who inspired me to pursue research and the Rhodes Scholarship. This would not have been possible without you. Thank you for your constant and ongoing support.

To my given and chosen family who have supported me throughout this thesis and beyond. Thank you to dearest Ed and Elnora, Rick and Nicole, Lynn and Jeff (homemade maple syrup has fuelled these final stages of thesis-writing), Matt and Michelle, Lucille, Jay and Marcy (and Nicole to complete our quad squad), Randy and Mary-Lyn, Tim and Lynette (and Campbelle, for your thoughtful texts 'just because'), Michelle and Eric, Jennifer and Craig, and Rob and Frankie—I am forever grateful for your formative influence in my life. To Peggy's memory; may ALS someday be no more.

To Justine and to Matt—no matter the distance, you are always my little bud, and your big sis is always so proud. During the Oxford interview, I was asked who I looked up to, and I said you (only in height, of course).

To Eldon and Adeline, whose humble strength, constant hope, and warm character continues to guide and ground me. To Jutta, for your unwavering interest in my work and travels, and moreover for your example of resilience and grace to which I aspire. To Rolf, whose lessons, laughs, and legacy live on.

To Krista and Peter, whose steady love, quiet sacrifices, and enduring belief have shaped every step of this journey and remain the foundation on which all I do is built. TIABTTEOM.

To Andrew, whose love, wit, steadfast support, understated understanding, and enduring presence have profoundly impacted both this work and its author.

## Preface

Shortly after moving to the UK and beginning Oxford's MSc in Neuroscience programme, I applied to the DPhil in Physiology, Anatomy, and Genetics. I proposed extending my Trinity term MSc project with the Molnár lab—3D printing the cerebral cortex—for another three years. It had been my goal to apply to this project for over a year and a half, wherein I changed my undergraduate biomedical engineering elective focus area from musculoskeletal biomechanics to stem cells and regenerative medicine. I was interviewed, accepted, and elated.

On the first day of my Trinity term rotation, we decided to pursue to a different project—the transition to sleep research was intimidating yet proved wholly stimulating and enjoyable. I studied whether chronic manipulations to cortical layer 6b influenced the effects of orexin (a wake-promoting neurohormone). This employed the dopamine receptor 1a (*Drd1a*-Cre) mouse line, which possesses *Snap25* mutations such that Cre-expressing cells throughout cortical layer 6 are functionally 'silenced'. We predicted that, if *Drd1a* cells influence orexin networks, *Drd1a*-silenced mice should not exhibit increased wakefulness upon orexin injection.

After finishing the MSc and beginning the DPhil, I was to expand upon the work completed by 1) considering cortex-mediated orexigenic effects on feeding behaviour (as orexin is known to promote both wakefulness and feeding), and 2) characterising whole-brain neuroanatomical changes due to L6-silencing. I began developing a device to monitor mouse home-cage feeding and activity called the *SnackerTracker*. However, just as it began functioning reliably, breeding complications and maternal cannibalism devastated the *Drd1a*-Cre line.

A colony reset was initiated. With hopes that mice may be available within two years' time, I decided to continue developing neuroanatomical analysis software (for use on tissues from a different *Drd1a*-augmented line in the meantime from collaborators in Berlin) and the *SnackerTracker* (for use once *Drd1a*-silenced mice again became available). As work progressed, I sought to acquire *in vivo* pilot data to test *SnackerTracker* efficacy using surplus wild-type mice

and others with known circadian disturbances (cryptochrome 1/2 double-knockouts). As pilots began, I learned that other surplus mice from the Vyazovskiy lab resembled those of the *Drd1a*-Cre line; retinol binding protein 4 (*Rbp4*-Cre) mice featured genetically manipulated cells expressed in cortical layer 5, as opposed to 6b, with the same *Snap25* 'silencing' mutation. *Rbp4*-Cre-silencing had been shown to elicit sleep disturbances; thus, the *SnackerTracker* should be able to detect increased activity as a proxy for increased wakefulness in L5-silenced animals. I acquired these mice and initiated another small pilot experiment.

Unexpectedly, I observed similar activity patterns in layer 5-silenced mice compared to controls, however layer 5-silenced mice appeared to eat constantly throughout their subjective day and night. I initially suspected *SnackerTracker* malfunction, however I observed the same patterns in every mouse tested. With time, I noticed that some began to develop signs of motor deficits including an odd-looking 'hindlimb clasp'. All layer 5-silenced animals acquired this phenotype with age, which I learned had been noted previously but never fully characterised. Could progressive fine motor deterioration be impeding these animals' ability to feed, explaining the odd *SnackerTracker* patterns? This precipitated the final chapter of my thesis, which evaluates the effects of cortical layer 5-silencing on neuromotor degeneration. I initiated a comprehensive multimodal investigation integrating behavioural assays, *in vivo* and *ex vivo* MRI, and immunohistology to characterise anatomical and physiological trajectories of motor decline.

My DPhil has been one of calibration and recalibration. Through topical pivots, I acquired a wide range of skills driven by necessity and fostered by colleagues, supervisors, friends, and family. Through pragmatic pivots, both personally and in practice, I decided to forego medical school (which I had deferred to study at Oxford) and fully pursue science. I find profound fulfilment in generating and chasing ideas, developing new methods, and teaching others. What a privilege it is to have pursued through a DPhil—and to now choose in a career—this endless pursuit and dissemination of knowledge.

# Table of contents


**Title** ---- 1
**Dedication** ---- 3
**Copyright** ---- 4
**Abstract** ---- 5
**Acknowledgements** ---- 6
**Statement regarding the use of AI** ---- 6
**Statement of previous acceptance** ---- 6
**Resulting publications** ---- 7
**Software and protocol deposits** ---- 7
**Statement of authorship and contribution** ---- 8
**Statement of support** ---- 10
**Funding** ---- 11
**Special thanks** ---- 12
**Preface** ---- 15
**Table of contents** ---- 17
**List of abbreviations** ---- 23
**List of figures** ---- 25
**List of tables** ---- 26
**Chapter 1: Introduction** ---- 27
**1.1 Development of the brain and cortical layers** ---- 27
***1.1.1 Modelling the cortex*** ---- ***27***
***1.1.2 Organogenesis and lamination*** ---- ***27***
***1.1.3 Establishment of projections and their refinement*** ---- ***28***
***1.1.4 Cell diversity*** ---- ***29***
***1.1.5 Regional heterogeneity*** ---- ***30***
**1.2 Layer 6b: emerging roles of early remnants** ---- 32
***1.2.1 Targeting the subplate*** ---- ***32***
***1.2.2 Cell augmentation*** ---- ***32***
***1.2.3 Cell silencing*** ---- ***33***
***1.2.4 Orexin*** ---- ***34***
***1.2.5 Sleep and feeding behaviour*** ---- ***35***
**1.3 Layer 5: established roles and emerging effects** ---- 36
***1.3.1 Targeting layer 5*** ---- ***36***
***1.3.2 Silencing and anatomy of cortical projection neuron subtypes*** ---- ***37***
***1.3.3 Physiology and behaviour*** ---- ***38***
***1.3.4 Motor neurons and pathways*** ---- ***38***
***1.3.5 Diseases involving motor degeneration*** ---- ***41***
**1.4 Current states and directions** ---- 41
***1.4.1 Measuring animal activity and feeding*** ---- ***41***
***1.4.2 Behavioural data analysis*** ---- ***43***
***1.4.3 Neuroanatomical quantification*** ---- ***45***
***1.4.4 Layer 6 networks and translatability*** ---- ***45***
***1.4.5 Layer 5 and top-down motor neuron degeneration*** ---- ***46***
**1.5 Aims and hypotheses** ---- 48
***1.5.1 The SnackerTracker: measuring feeding and activity behaviour*** ---- ***48***
***1.5.2 TracKIT: analysing behavioural data*** ---- ***50***
***1.5.3 r-QUINT: neuroanatomical analysis pipeline refinement*** ---- ***51***

***1.5.4 L6b manipulations: effects of silencing and augmentation ----------53***
***1.5.5 L5-silencing: project STAMINA investigates motor degeneration ---------53***
**Chapter 2: Methods ----------56**
**2.1 Animal models, experiments, and statistics summary ----------56**
***2.1.1 Compliance ----------56***
***2.1.2 Breeding and maintenance----------56***
***2.1.3 Experimental and genetic conditions----------57***
***2.1.4 Replicates and metadata ----------60***
***2.1.5 Statistical conventions and software ----------63***
**2.2 *SnackerTracker* development and validation ----------64**
***2.2.1 Construction ----------64***
***2.2.2 Preliminary benchtop and in vivo testing ----------64***
***2.2.3 Studies in clock-deficient mice----------65***
***2.2.4 Dim light in the evening----------65***
***2.2.5 Hamsters ----------65***
**2.3 Histological characterisations ----------65**
***2.3.1 Biological targets ----------65***
***2.3.2 Tissue preparation and immunohistochemistry ----------66***
***2.3.3 Image acquisition and visualisation ----------69***
***2.3.4 QUINT image analysis ----------69***
*2.3.4.1 Pre-processing----------69*
*2.3.4.2 Atlas mapping ----------69*
*2.3.4.3 Feature extraction ----------70*
*2.3.4.4 Data registration----------70*
*2.3.4.5 Output tagging, re-formatting, and analyses----------70*
***2.3.5 Morphometrics ----------70***
*2.3.5.1 Image acquisition----------70*
*2.3.5.2 Pre-processing----------71*
*2.3.5.3 Neurite tracing ----------71*
*2.3.5.4 Soma characterisation----------71*
*2.3.5.5 Analyses and visualisation----------72*
**2.4 Motor-associated behavioural testing----------73**
***2.4.1 Home cage monitoring ----------73***
***2.4.2 Visual cliff test ----------73***
***2.4.3 Continuous assessment of motor phenotypes----------73***
***2.4.4 CatWalk----------73***
***2.4.5 Grip test----------74***
**2.5 Neuroimaging----------74**
***2.5.1 In vivo MRI acquisition ----------74***
*2.5.1.1 Animal preparation ----------74*
*2.5.1.2 In vivo scanning setup ----------74*
*2.5.1.3 In vivo scan protocol ----------75*
***2.5.2 Ex vivo MRI acquisition----------76***
*2.5.2.1 Sample preparation ----------76*
*2.5.2.2 Ex vivo scanning setup----------76*
*2.5.2.3 Ex vivo scan protocol----------77*
***2.5.3 Image processing----------78***
*2.5.3.1 Analysis tools and ecosystem ----------78*
*2.5.3.2 Anatomical T1W and T2W----------78*
*2.5.3.3 Diffusion ----------79*

*2.5.3.4 Quantitative susceptibility mapping ---- 80*
*2.5.3.5 Functional MRI ---- 81*
***2.5.4 Co-registration ---- 81***
*2.5.4.1 T2W masking ---- 81*
*2.5.4.2 DWI masking ---- 82*
*2.5.4.3 QSM masking ---- 83*
*2.5.4.4 DWI to T2W ---- 83*
*2.5.4.5 QSM to T2W ---- 84*
***2.5.5 Data analyses ---- 84***
*2.5.5.1 Script overview ---- 84*
*2.5.5.2 Configuration ---- 85*
*2.5.5.3 Statistics ---- 85*
*2.5.5.4 Regional analyses ---- 86*
*2.5.5.5 Voxelwise processing ---- 86*
**Chapter 3: Results – *SnackerTracker* and *TracKIT* development and validation for feeding and activity measurement ---- 87**
**3.1 SnackerTracker development and validation ---- 88**
***3.1.1 SnackerTracker overview and design ---- 88***
***3.1.2 Chassis hardware ---- 90***
***3.1.3 Electronics hardware ---- 90***
***3.1.4 Operational software ---- 92***
***3.1.5 Validation ---- 92***
**3.2 TracKIT development ---- 93**
***3.2.1 TracKIT overview and design ---- 93***
***3.2.2 Processing steps ---- 95***
***3.2.3 Present and possible output metrics ---- 97***
***3.2.4 Food intake vs food-seeking behaviour ---- 98***
***3.2.5 Parameter usage ---- 98***
**3.3 Preliminary applications and biological insights ---- 99**
***3.3.1 DVC correlation ---- 99***
***3.3.2 Activity and feeding behaviour ---- 101***
***3.3.3 Circadian and ultradian rhythms ---- 104***
***3.3.4 PIR combination and effects of DLE ---- 107***
***3.3.5 Seasonal hamster feeding and video recordings ---- 109***
**3.4 SnackerTracker and TracKIT design considerations ---- 110**
***3.4.1 Hardware limitations ---- 110***
***3.4.2 Software limitations ---- 112***
***3.4.3 Device longevity ---- 113***
***3.4.4 In vivo complications ---- 113***
***3.4.5 Genotype-phenotype confounds ---- 114***
**3.5 Indications and future directions ---- 115**
***3.5.1 Parsing and advancing behavioural HCM ---- 115***
***3.5.2 Contracted provision ---- 115***
***3.5.3 Improving animal welfare ---- 116***
***3.5.4 Drug-delivery and pharmacological applications ---- 116***
***3.5.5 Future SnackerTracker-TracKIT directions and customisability ---- 117***
**Chapter 4: Results – Layer 6b silencing and augmentation yields anatomical changes revealed by analysis pipeline refinement ---- 119**
**4.1 QUINT pipeline improvements and initial validations ---- 120**
***4.1.1 Overview and adaptations ---- 120***

*4.1.2 Image acquisition, pre-processing, and segmentation ---- 122*
*4.1.3 Morphometric tagging and multiplexing ---- 124*
*4.1.4 Workflow testing and validation ---- 126*
*4.1.5 Pipeline limitations ---- 128*
**4.2 Experimental DREADD application ---- 129**
*4.2.1 DREADDs ---- 129*
*4.2.2 Excitatory DREADDs ---- 131*
*4.2.3 Inhibitory DREADDs ---- 131*
*4.2.4 Timeline considerations ---- 134*
*4.2.5 Biological indications ---- 134*
**4.3 *Drd1a* neurons upon cell augmentation and silencing ---- 135**
*4.3.1 Layer 6 boundaries and quality control ---- 135*
*4.3.2 Drd1a and CPLX3 characterisation ---- 137*
*4.3.3 Drd1a subpopulations via CPLX3 colocalisation ---- 141*
*4.3.4 Interneurons and perineuronal nets ---- 143*
*4.3.5 Genotype trends and indications ---- 146*
**4.4 Morphometric analogousness ---- 149**
*4.4.1 Polar plot distinctions ---- 149*
*4.4.2 Human and mouse branch overview ---- 151*
*4.4.3 Neurite characteristics ---- 152*
*4.4.4 Soma morphometrics ---- 153*
*4.4.5 Inter-species subtype differences ---- 155*
**4.5 Indications and future directions ---- 157**
*4.5.1 QUINT pipeline refinements ---- 157*
*4.5.2 Layer 6-silencing and orexin ---- 160*
*4.5.3 Receptor expression insights ---- 164*
*4.5.4 Layer 6-augmentation and mTOR ---- 166*
*4.5.5 Evolutionarily preserved morphometrics and networks ---- 168*
**Chapter 5: Results – L5-silencing leads to progressive anatomical and motor degeneration as revealed by multimodal datasets ---- 169**
**5.1 Behaviour ---- 170**
*5.1.1 Physical features and feeding behaviour ---- 170*
*5.1.2 Continuous assessment of motor phenotypes ---- 179*
*5.1.3 Visual cliff test ---- 180*
*5.1.4 Grip strength and nesting ---- 182*
*5.1.5 CatWalk ---- 182*
**5.2 MRI ---- 185**
*5.2.1 In vivo T1W anatomical scans ---- 185*
*5.2.2 In vivo DTI and resting state fMRI ---- 190*
*5.2.3 Ex vivo T2W anatomical scans ---- 190*
*5.2.4 Ex vivo DTI ---- 193*
*5.2.5 Ex vivo QSM ---- 204*
**5.3 Histology ---- 207**
*5.3.1 Rbp4-Cre characterisation ---- 207*
*5.3.2 Motor neurons ---- 209*
*5.3.3 Myelination and protein aggregates ---- 216*
*5.3.4 Glial cells and interneurons ---- 218*
*5.3.5 Peripheral expression ---- 227*
**5.4 Multimodal insight ---- 228**
*5.4.1 Experimental strategy ---- 228*

*5.4.2 Model characterisation* ---- *229*
*5.4.3 Local degeneration* ---- *234*
*5.4.4 Downstream degeneration* ---- *237*
*5.4.5 A note out of interest* ---- *237*
**5.5 Indications and future directions** ---- **238**
*5.5.1 Motor neuron degeneration* ---- *238*
*5.5.2 The seemingly contradictory notion of hyperexcitability* ---- *240*
*5.5.3 Limitations and ongoing analyses* ---- *241*
*5.5.4 Future experiments* ---- *243*
*5.5.5 MRI-histology insights* ---- *245*
**Conclusions** ---- **246**
**Behavioural home-cage monitoring** ---- **246**
**Layer 6b: Characterising subplate remnant neuroanatomy** ---- **246**
**Layer 5: Multimodal methods reveal progressive neuromotor degeneration** ---- **247**
**Appendices** ---- **249**
**A.1 Genetic strategies and mechanisms** ---- **249**
*A.1.1 PTEN mechanisms* ---- *249*
*A.1.2 Snap25 mechanisms* ---- *250*
*A.1.3 DREADD mechanisms* ---- *251*
**A.2 Statistics** ---- **251**
**A.3 SnackerTracker development** ---- **252**
*A.3.1 Bill of materials* ---- *252*
*A.3.2 Ultimaker Cura print settings* ---- *253*
*A.3.3 Chassis schematics* ---- *254*
*A.3.4 Electronics schematics* ---- *258*
*A.3.5 Component assembly* ---- *259*
*A.3.6 SnackerTracker calibration* ---- *260*
*A.3.7 Preliminary test details* ---- *261*
*A.3.8 Preliminary test results* ---- *263*
*A.3.9 Software variables* ---- *265*
*A.3.10 Representative output file* ---- *268*
**A.4 SnackerTracker setups** ---- **269**
*A.4.1 SnackerTrackers in digitally ventilated cages* ---- *269*
*A.4.2 SnackerTrackers and passive infrared monitoring* ---- *270*
*A.4.3 SnackerTrackers in Faraday LTCs with hamsters* ---- *270*
*A.4.4 SnackerTracker feeding behaviour* ---- *271*
*A.4.5 SnackerTracker feeding behaviour* ---- *271*
**A.5 Tissue processing** ---- **272**
*A.5.1 Protein targets* ---- *272*
*A.5.2 Expected protein expression* ---- *275*
*A.5.3 Vibratome slicing* ---- *276*
*A.5.4 Spinal scaffolds* ---- *276*
*A.5.5 Immunohistochemistry specifications* ---- *277*
*A.5.6 Sample immunohistochemistry optimisations* ---- *278*
*A.5.7 Sample initial immunohistochemistry combinations* ---- *281*
*A.5.8 r-QUINT of regions of interest* ---- *282*
*A.5.9 Orexin receptor in situ hybridisation* ---- *284*
**A.6 Imaging and analyses** ---- **285**
*A.6.1 Microscopy cost estimation* ---- *285*
*A.6.2 Microscopy specifications* ---- *286*

*A.6.3 QuPath cell detection parameters* ---- *286*
*A.6.4 Nutil brain region definitions* ---- *287*
*A.6.5 Ex vivo MRI sample preparation* ---- *288*
**A.7 Quality control** ---- **289**
*A.7.1 Morphometrics – trace projections* ---- *289*
*A.7.2 Effects of out-of-skull sample inclusion* ---- *290*
*A.7.3 T2W nonuniformity corrections* ---- *290*
*A.7.4 Ex vivo DWI pre-processing* ---- *290*
*A.7.5 Ex vivo QSM pre-processing* ---- *291*
*A.7.6 MGE masking* ---- *291*
*A.7.7 MGE-T2W co-registration* ---- *291*
**A.8 Histology supplements** ---- **292**
*A.8.1 Excitatory DREADD subcortical PV/VVA co-expression and densities* -- *292*
*A.8.2 Inhibitory DREADD subcortical PV/VVA co-expression and densities* --- *293*
*A.8.3 Excitatory DREADD cortical PV/VVA co-expression and VVA densities* *294*
*A.8.4 Inhibitory DREADD cortical PV/VVA co-expression and VVA densities* - *295*
*A.8.5 Fezf2 Histology* ---- *297*
*A.8.6 Exploratory DiI tracing setup* ---- *303*
**A.9 Behaviour supplements** ---- **303**
*A.9.1 CRY-deficiency: disaggregated by sex* ---- *303*
*A.9.2 CRY-deficiency: individual SnackerTracker recordings* ---- *304*
*A.9.3 DLE: PIR data* ---- *306*
*A.9.4 STAMINA: SnackerTracker results disaggregated by sex* ---- *307*
*A.9.5 STAMINA: CAMP results disaggregated by sex* ---- *308*
*A.9.6 STAMINA: VCT results disaggregated by sex* ---- *309*
*A.9.7 STAMINA: Grip strength and nesting disaggregated by sex* ---- *309*
*A.9.8 STAMINA: CatWalk results disaggregated by sex* ---- *310*
**A.10 Original software** ---- **311**
*A.10.1 Arduino software development – Editor and IoT* ---- *311*
*A.10.2 MATLAB – TracKIT* ---- *311*
*A.10.3 ImageJ – r-QUINT pre-processing* ---- *311*
*A.10.4 Groovy – r-QUINT downsampling and segmentation* ---- *311*
*A.10.5 Groovy – r-QUINT object classifiers* ---- *311*
*A.10.6 ImageJ – conversions* ---- *311*
*A.10.7 MATLAB – r-QUINT reformatting and soma integration* ---- *311*
*A.10.8 ImageJ – Z-stack modification* ---- *311*
*A.10.9 ImageJ – Trace rotation* ---- *311*
*A.10.10 MATLAB – Neurite morphometrics* ---- *311*
*A.10.11 Bash – File conversions* ---- *312*
*A.10.12 CLI – pydpiper pipelines* ---- *312*
*A.10.13 Bash – T2W pre-processing* ---- *312*
*A.10.14 Bash – QSM orientation corrections* ---- *312*
*A.10.15 Bash – Mask generation* ---- *312*
*A.10.16 Bash – Registrations* ---- *312*
*A.10.17 Python – kurtosis filtering* ---- *312*
*A.10.18 Bash – MGE filtering* ---- *312*
*A.10.19 R – MRI analyses* ---- *312*
**Bibliography** ---- **313**

# List of abbreviations

ALS: amyotrophic lateral sclerosis ..... 41
ANOVA: analysis of variance ..... 63
AP: anteroposterior ..... 28
CAMP: continuous assessments of motor phenotypes ..... 53
CD68: Cluster of differentiation 68 ..... 232
CHAT: choline acetyltransferase ..... 39
cKO: conditional knockout ..... 33
CNO: clozapine-N-oxide ..... 52
$Cre^{ER}$: inducible Cre via estrogen receptor attachment ..... 68
CRY: cryptochrome ..... 50
CST: corticospinal tract ..... 29
CTGF: connective tissue growth factor ..... 46
CTIP2: COUP-TF-interacting protein 2 ..... 36
CTRL: control (animal or condition) ..... 33
DAPI: 4',6-diamidino-2-phenylindole ..... 67
DLE: dim light in the evening ..... 50
DORA: Dual orexin receptor antagonist ..... 162
Drd1a: dopamine receptor 1a ..... 32
DREADDs: designer receptors exclusively activated by designer drugs ..... 51
DVC: digitally ventilated cage ..... 56
DWI: diffusion weighted imaging ..... 53
EEG: electroencephalography ..... 38
EMG: electromyography ..... 38
FA: fractional anisotropy ..... 80
FDR: false discovery rate ..... 85
FED3: Feeding Experimentation Device 3 ..... 42
FEZF2: Fez family zinc finger 2 ..... 36
FISO: isotropic volume fraction ..... 80
fMRI: functional magnetic resonance imaging ..... 53
FOTN: first-order thalamic nuclei ..... 29
FTD: frontotemporal dementia ..... 41
GABA: γ-aminobutyric acid ..... 29
GAM: general additive model ..... 85
GFAP: glial fibrillary acidic protein ..... 30
GUI: graphical user interface ..... 69
HCM: home cage monitoring ..... 41
HOTN: higher-order thalamic nuclei ..... 29
IBA1: ionized calcium-binding adaptor molecule 1 ..... 37
ICVF: intracellular volume fraction ..... 80
IHC: immunohistochemistry ..... 53
IoT: Internet of things ..... 92
L1-6: layers 1-6 ..... 27
LDR: light-dependent resistor ..... 92
LMNs: lower motoneurons ..... 38
LSFM: light sheet fluorescence microscopy ..... 157
lsq: least-squares ..... 63

LTC: light-tight chamber ..... 56
M1: primary motor cortex ..... 30
MBP: myelin binding protein ..... 37
MD: mean diffusivity ..... 80
mEPSCs: spontaneous miniature excitatory postsynaptic currents ..... 240
MGE: multigradient echo ..... 54
MRI: magnetic resonance imaging ..... 53
mTOR: mechanistic target of rapamycin ..... 33
$N_E/N_T$: number of experimental or technical replicates ..... 57
NEUN: neuronal nuclei ..... 45
NF-H: neurofilament heavy peptide ..... 36
NODDI: Neurite Orientation Dispersion and Density Imaging ..... 80
OD: orientation dispersion ..... 80
ORX: orexin ..... 34
ORXA: orexin isoform A ..... 34
ORXB: orexin isoform B ..... 34
ORXR1: orexin receptor subtype 1 ..... 34
ORXR2: orexin receptor subtype 2 ..... 34
PBS: phosphate buffer saline ..... 66
PFA: paraformaldehyde ..... 66
PFC: prefrontal cortex ..... 30
PIRs: passive infrared sensors ..... 65
PSCM: point scanning confocal microscope ..... 70
PTEN: phosphatase and tensin homolog ..... 33
PV: parvalbumin ..... 37
QSM: quantitative susceptibility mapping ..... 54
Rbp4: retinol binding protein 4 ..... 36
RFP: red fluorescent protein ..... 33
ROI: regions of interest ..... 45
RSA: retrosplenial area ..... 30
S1: primary somatosensory cortex ..... 30
S100β: S100 calcium-binding protein β ..... 273
SATB2: special AT-rich sequence-binding protein 2 ..... 36
SDCM: spinning disk confocal microscopy ..... 69
SMI32: Sternberger Monoclonals Incorporated 32 ..... 36
Snap25: synaptosomal-associated protein 25kDa ..... 33
SNARE: soluble N-ethylmaleimide-sensitive fusion attachment protein receptor ..... 33
SSFM: slice scanning fluorescence microscopy ..... 69
STAMINA: SnackerTracker And MRI Investigation of Neuroanatomy and Activity ..... 53
STPT: serial two-photon tomography ..... 126
T1W: T1-weighted ..... 53
T2W: T2-weighted ..... 54
TBR1: T-box brain 1 ..... 32
TDP-43: TAR DNA binding protein-43 ..... 41
UMNs: upper motoneurons ..... 38
VCT: visual cliff test ..... 55
VVA: vicia villosa agglutinin ..... 37
WMINs: white matter interstitial neurons ..... 28
WT: wild-type ..... 50

# List of figures

Figure 1. Cortical development and deep-layer projections in mice and humans. ..... 31
Figure 2. Major descending motor pathways in the mouse central nervous system. ..... 40
Figure 3. Illustrates the A) original QUINT pipeline[220] and B) proposed refinements. ..... 52
Figure 4. Summarises STAMINA study design. ..... 55
Figure 5. L5-6 Cre-expression and genetic conditions. ..... 57
Figure 6. *SnackerTracker* design and operation. ..... 88
Figure 7. *SnackerTracker* chassis 3D modelling and materialisation. ..... 90
Figure 8. Illustrates *SnackerTracker* electronics. ..... 91
Figure 9. Illustrates the *SnackerTracker* IoT GUI. ..... 93
Figure 10. *TracKIT* GUI. ..... 94
Figure 11. *SnackerTracker*-DVC alignment. ..... 100
Figure 12. CTRL and CRY-deficient mouse behaviour differs across light conditions. ..... 102
Figure 13. Animal feeding periodicity and intensity differs across lighting conditions. ..... 105
Figure 14. *SnackerTrackers* reveal changes in activity and food intake with DLE. ..... 108
Figure 15. Hamster *SnackerTracker* data under summer and winter photoperiods. ..... 110
Figure 16. Progression of sample sections through the revised QUINT pipeline[32]. ..... 121
Figure 17. Compares SDCM and SSFM image quality. ..... 122
Figure 18. r-QUINT segmentation accuracy. ..... 124
Figure 19. Illustrates 3D soma and neurite morphometric feature extraction using Arivis. ..... 125
Figure 20. r-QUINT validation. ..... 127
Figure 21. Illustrates *Drd1a*-Cre$^{+}$ densities and CPLX3 colocalisation. ..... 128
Figure 22. DREADD r-QUINT subcortical analyses. ..... 130
Figure 23. PV/VVA cortical densities differ upon excitatory DREADD activation. ..... 132
Figure 24. PV/VVA cortical densities differ upon inhibitory DREADD activation. ..... 133
Figure 25. *Drd1a*/TBR1/CPLX3 co-staining discriminates cortical L6 cell subtypes. ..... 136
Figure 26. Cortical *Drd1a*-Cre neuron proportions and heterogeneity. ..... 137
Figure 27. *Drd1a*/CPLX3 characterisation following L6 silencing and augmentation. ..... 140
Figure 28. *Drd1a*/CPLX3 subtype characterisation upon L6 silencing/augmentation. ..... 142
Figure 29. PV/VVA characterisations upon L6-augmentation. ..... 144
Figure 30. r-QUINT vs PSCM PV/VVA analyses upon L6-augmentation. ..... 145
Figure 31. Polar plot method comparison. ..... 150
Figure 32. Interspecies comparison of subplate-remnant cell subtypes. ..... 151
Figure 33. Compares dendrite features of human WMIN and mouse L6b neuron subtypes. ..... 153
Figure 34. Illustrates L6b soma characteristics. ..... 154
Figure 35. Schematic of a future experiment proposal. ..... 164
Figure 36. *Rbp4*-Cre animal data. ..... 170
Figure 37. Daily feeding behaviour and food intake in L5 CTRL and cKO mice. ..... 171
Figure 38. Sample female L5-CTRL/cKO *SnackerTracker* traces. ..... 172
Figure 39. Sample male L5-CTRL/cKO *SnackerTracker* traces. ..... 173
Figure 40. The second pilot corroborates motor-related changes upon L5-cKO. ..... 175
Figure 41. STAMINA L5-cKO and CTRL mouse body weights over time. ..... 176
Figure 42. STAMINA *SnackerTracker* results. ..... 178
Figure 43. STAMINA CAMP results reveal motor deterioration in L5-cKO mice. ..... 180
Figure 44. Summarises STAMINA VCT results. ..... 181
Figure 45. STAMINA results following grip strength and nesting tests. ..... 182
Figure 46. STAMINA CatWalk gait evaluations reveal motor deficits in L5-cKO mice. ..... 184
Figure 47. T1W *in vivo* MRI overview. ..... 186
Figure 48. T1W *in vivo* MRI maps. ..... 187

Figure 49. Volumetric ROI analysis following T1W *in vivo* MRI in L5-cKO vs CTRL mice. ..... 189
Figure 50. T2W *ex vivo* MRI reveals volumetric differences upon L5-cKO. ..... 191
Figure 51. Volumetric ROI analysis following T2W *ex vivo* MRI in L5-cKO vs CTRL mice. ..... 192
Figure 52. *Ex vivo* DWI regional analyses reveal brain-wide changes upon L5-cKO. ..... 196
Figure 53. *Ex vivo* DWI voxelwise analyses. ..... 197
Figure 54. *Ex vivo* FA analyses. ..... 198
Figure 55. *Ex vivo* MD analyses. ..... 199
Figure 56. *Ex vivo* MK analyses. ..... 200
Figure 57. *Ex vivo* OD analyses. ..... 201
Figure 58. *Ex vivo* ICVF analyses. ..... 202
Figure 59. *Ex vivo* FISO analyses. ..... 203
Figure 60. *Ex vivo* QSM analyses. ..... 206
Figure 61. *Rbp4*-Cre$^{+}$ expression in the brain and spinal cord. ..... 208
Figure 62. *Rbp4*-Cre/NEUN/SMI32 degeneration in cortical ROIs at 21wks. ..... 210
Figure 63. *Rbp4*-Cre/NEUN/SMI32 degeneration in motor projection tracts at 21wks. ..... 211
Figure 64. *Rbp4*-Cre/NEUN/SMI32 non-L5 expression at 21wks. ..... 212
Figure 65. *Rbp4*-Cre/CHAT/SMI32 expression and colocalisation in the brainstem at 21wks. 214
Figure 66. *Rbp4*-Cre/CHAT/SMI32 expression and colocalisation in the spinal cord at 21wks. 215
Figure 67. *Rbp4*-Cre$^{+}$/MBP/AT8 expression in motor-related projection tracts at 21wks. ..... 217
Figure 68. *Rbp4*-Cre/MBP/AT8 expression and colocalisation in the spinal cord at 21wks. .... 218
Figure 69. *Rbp4*-Cre$^{+}$ degeneration is accompanied by glial infiltration upon L5-cKO. ..... 220
Figure 70. *Rbp4*-Cre$^{+}$ tract degeneration prompts microglia and astrocyte infiltration. ..... 221
Figure 71. Changes in glial expression emerge in the spinal cord at 21wks. ..... 222
Figure 72. Cortical heterogeneity in microglial infiltration emerges upon L5-cKO. ..... 223
Figure 73. No obvious changes in cortical PV/VVA expression emerge at 21wks. ..... 224
Figure 74. No obvious changes in PV/VVA emerge in motor tracts upon *Snap25*-cKO. ..... 225
Figure 75. Illustrates *Rbp4*-Cre/PV/VVA expression in the spinal cord at 21wks. ..... 226
Figure 76. *Rbp4*-Cre$^{+}$ expression emerges in peripheral organs at ~21wks. ..... 227
Figure 77. Illustrates STAMINA's multimodal experimental strategy. ..... 228
Figure 78. *Rbp4*-Cre$^{+}$::*Snap25*$^{fl/fl}$ model characterisation. ..... 230
Figure 79. Exploratory insudeum griseum (IG) and fasciola cinerea (FC) illustration. ..... 238

# List of tables

Table 1. Lists and describes major descending motor-related white matter tracts in mice. ..... 39
Table 2. Features and limitations of HCM tools measuring mouse feeding. ..... 42
Table 3. Summary of software tools for behavioural data analysis. ..... 44
Table 4. Criteria and constraints influencing *SnackerTracker* development. ..... 49
Table 5. Experimental/pilot cohorts used to assess *SnackerTracker* function. ..... 50
Table 6. Summarises criteria and constraints influencing *TracKIT* design and development. ..... 51
Table 7. Predicted ramifications of Rbp5-Cre-driven *Snap25*-cKO. ..... 54
Table 8. Study conditions and expected outputs across experiments in this thesis. ..... 58
Table 9. Lists experimental genotypes and parental crosses where applicable. ..... 59
Table 10. Lists animal replicate information for each experiment in this thesis. ..... 60
Table 11. Lists statistical tests across experiments. ..... 63
Table 12. Lists the tissues dissected for each driver line. ..... 68
Table 13. Summarises IHC combinations in this thesis. ..... 68
Table 14. SnackerTracker prototypes. ..... 89
Table 15. Lists and describes the major steps involved in *TracKIT* data processing. ..... 95
Table 16. *TracKIT* output metrics. ..... 97
Table 17. Summarises comparisons between mouse and human L6b neurons. ..... 168

# Introduction

## 1.1 Development of the brain and cortical layers

### *1.1.1 Modelling the cortex*

The human brain is infinitely complex. The cerebral cortex is particularly esoteric as the seat of basic and higher functions including movement and attention. Many neurological and psychiatric conditions have neurodevelopmental origins whether symptoms manifest prenatally or later in adulthood. Studying the relevance of cortical development to diseased states requires the use of animal models as *in silico* and *in situ* alternatives cannot yet recapitulate the hallmark cytoarchitecture of cortical layers 1-6 (L1-6). Significant bioengineering advances have enabled human induced pluripotent neural stem cell-derived systems to exhibit upper- and lower-layer neurons in sliced neocortical organoids[1] and cell-seeded droplet-based scaffolds compatible with *in vivo* xenotransplantation[2]. However, culture methods fail to integrate combinations of endogenous hormonal signalling, vascular networks, endothelial cell scaffolding, adaptive immune function, and bidirectional long-range connections with intra- and sub-cerebral structures during early tissue development which are critical for protracted cortical lamination and maturation. The mouse is one of the phylogenetically lowest-order species which possesses a six-layered cortex (**Figure 1A**), and has thus been extensively employed in scientific research. Vast libraries of mouse-specific genetic engineering tools are available which enable researchers to characterise consequences of targeted cell manipulations. This notion underpins my thesis, which studies the effects of genetically manipulating deep-layer cortical projection neurons—namely, L5-6b—to explore their relevance to developmentally-linked neuropathologies.

### *1.1.2 Organogenesis and lamination*

Brain morphogenesis follows an integrated series of steps, many of which rely on deep-layer cortical projection neurons in mice and humans[3]. Following neural induction, neurulation,

and proliferation, dorsoventral and anteroposterior (AP) chemical gradients establish primary brain divisions. The forebrain divides into diencephalic and telencephalic vesicles which enlarge to caudally envelop the early brainstem. This establishes the longitudinal fissure and primordial cortical hemispheres. Asymmetric proliferation proceeds perpendicular to lateral ventricular surfaces in the germinal ventricular zone; inner daughter cells retain progenitor characteristics while outer daughter cells migrate and further differentiate. These immature earliest-generated cortical neurons form the preplate, which is separated from the prolific ventricular zone below by tangentially oriented fibres of the intermediate zone. As preplate maturation proceeds, laminar subdivisions emerge in germinal and postmitotic compartments. The ventricular zone divides to yield the subventricular zone between intermediate and ventricular zones, with the intermediate zone above forming early white matter tracts. The preplate splits into the marginal zone, which predates L1, and the innermost subplate which gives rise to the cortical plate predating L2-6. Subplate neurons themselves undergo continued maturation and eventually precipitate white matter interstitial neurons (WMINs) in humans and L6b in mice (**Figure 1A**)[4, 5]. Cortical neurons settle in an inside-first-outside-last manner such that earlier-born cells reside in deep layers and later-born cells progressively reside in outer layers[6].

### *1.1.3 Establishment of projections and their refinement*

During preplate establishment, the cortex both projects subcortically and receives area-specific thalamic innervation[7]. These projections are refined by intrinsic and extrinsic factors during later stages. Intrinsic signals include graded molecular and gene expression patterns which establish coordinates for cortical arealisation and connectivity[8-10]. Differences across the pallial-subpallial boundary guide axon pathfinding from extrinsic subcortical structures such that afferents influence developing circuitry[7, 11]. Projections from thalamic axons initially transmit spontaneous activity to the cortex but later convey sensory information from the environment which impacts the size and identity of cortical areas[12, 13]. All cortical areas are connected to the

thalamus, yet specific thalamic nuclei project to specific cortical areas. Sensory first-order thalamic nuclei (FOTN) include the dorsolateral geniculate and ventral posteromedial nucleus, which project to primary visual and somatosensory areas, respectively. Thalamocortical axons form the primordial internal capsule, which facilitates reciprocal innervation between cortical regions and higher-order thalamic nuclei (HOTN)[7, 11]. L5 extratelencephalic axons are the first to innervate subcortical targets via the internal capsule, thereby pioneering corticothalamic and corticospinal tracts (CST). Thalamocortical-corticothalamic connectivity is facilitated via thalamic projections to the subplate, which is the largest cortical structure during early development[5, 14, 15]. Subplate neurons transiently innervate L4—the primary target of sensory thalamic afferents in the adult brain—establishing an indirect thalamocortical pathway while fostering thalamus-L4 pathway maturation[16-19]. Shortly before birth in both mice and humans, thalamic axons begin to detach from the subplate which in turn rewires to form intratelencephalic branches and cortical plate synapses[12, 20]. Apoptotic processes result in up to ~80% subplate neuron loss during the first postnatal week in carnivores and primates; superfluous connections are pruned, including most to L4, lending to dramatic activity-dependent pathway refinement[5, 14, 15, 21-23]. Plasticity continues through adolescence, and to a lesser extent through adulthood[24], resulting in profound complexity across the mature cortex (**Figure 1B-C**).

### *1.1.4 Cell diversity*

Newly generated cells migrate from sites of origin to generate diverse neuronal and glial subtypes across the cortex[6, 25-28]. Mature neurons are classified as excitatory or inhibitory, which typically feature glutamatergic or γ-aminobutyric acid (GABA) neurotransmitters, respectively. Excitatory neurons are generally pyramidal, though some can be nonpyramidal, while inhibitory cells (including most interneurons) are usually nonpyramidal[29]. Fated pyramidal neurons migrate from the ventricular zone into the preplate along guiding radial glia cells[30] such that cells proceed past those born earlier to reach final cortical positions. This establishes “cortical columns” where

cells derived from the same progenitor settle above their sites of origin with slight horizontal dispersion to accommodate increasing cortical surface area[6, 31]. Mature pyramidal cells feature intracortical and extracortical projections, while nonpyramidal cells predominantly project locally and have distinct origins—mouse interneurons arise from lateral and medial ganglionic eminences and migrate laterally into the preplate[25]. Microglia are derived from mesodermal progenitors, migrate into neuroepithelial tissue, and adopt roles from immune surveillance to synaptic pruning and phagocytosis. Macroglia, including astrocytes and oligodendrocytes, are derived from later-stage neuroectodermal radial glia. Oligodendrocytes are typically associated with axon myelination, and glial fibrillary acidic protein (GFAP)-expressing astrocytes with synaptic regulation and reactive gliosis, yet both adopt diverse roles in metabolism, immunity, and neural plasticity. Glial cells are heterogeneous and dynamic with maturation, adopting their form and function according to homeostatic demands.

### *1.1.5 Regional heterogeneity*

Mature neuron subtypes and projections differ with cortical depth and topography to enable diverse functions[26]. Most layers feature a ~4:1 pyramidal to nonpyramidal cell ratio, save L1 which lacks excitatory soma. However, laminar patterns and relative cell proportions are not uniform: the primary motor cortex (M1), prefrontal cortex (PFC), and retrosplenial areas (RSAs) feature indistinguishable L2-3 and lack L4; the entorhinal cortex features a clear L2/3 boundary but still lacks L4; the primary somatosensory cortex (S1) features L4 barrel fields corresponding to whisker inputs yet obscures L2-3; and cortical thickness generally decreases posteriorly. **Figure 1B** highlights cytoarchitectural diversity in the mature cortex, while **Figure 1C** summarises key thalamocortical-corticothalamic, intratelencephalic, and extratelencephalic L5-6b networks of present interest (**1.2-1.3**). This complexity, compounded by topology and depth, establishes different cell proportions and populations contributing to distinct cortical circuits capable of performing wide-ranging computational functions.

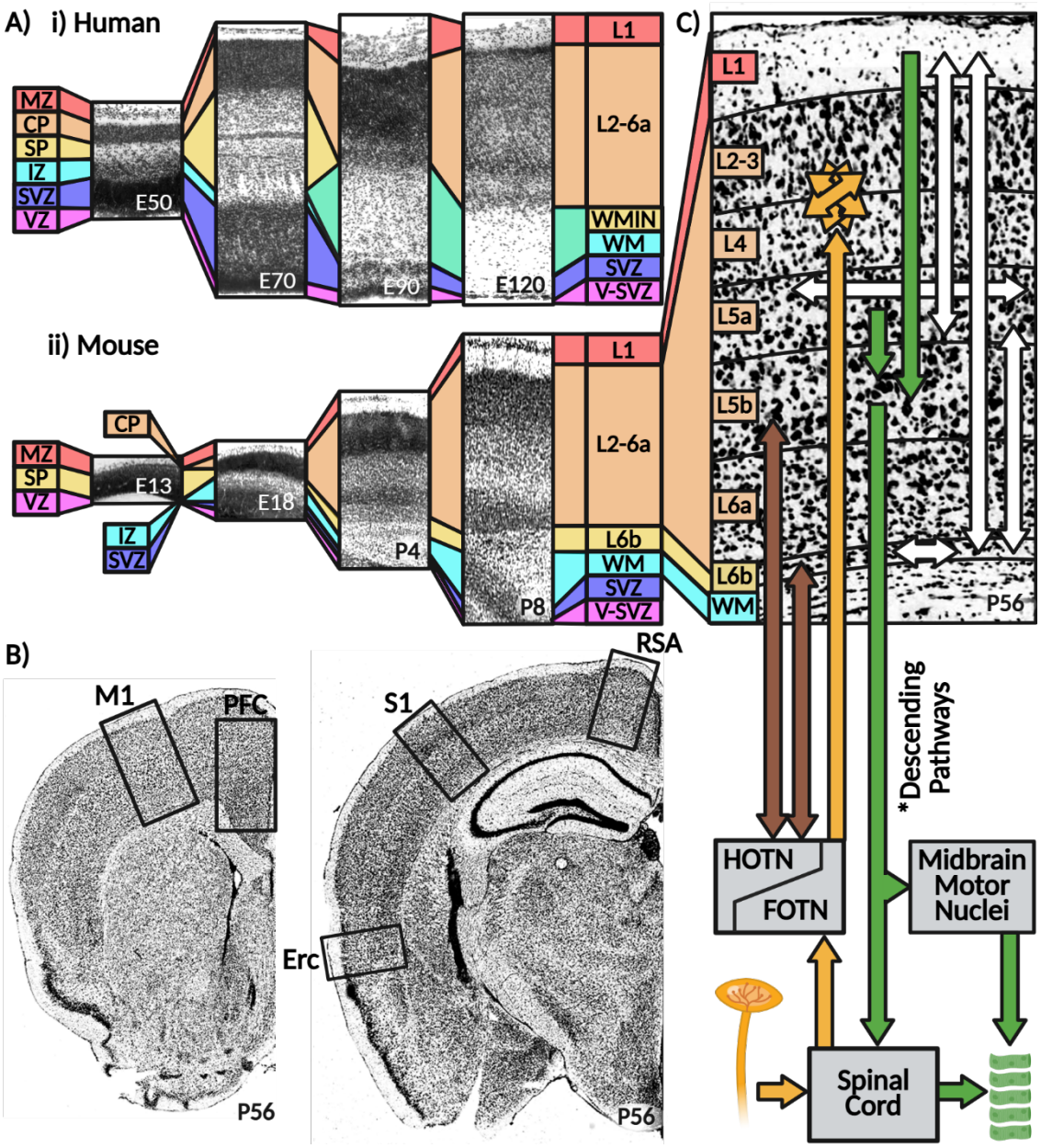


**Figure 1.** Cortical development and deep-layer projections in mice and humans. Developmental trajectories of critical structures in the i) human and ii) mouse cortex are traced from primordial to mature states. Both mature cortices possess six layers, yet the fate of subplate remnants differ: in humans, these become scattered through the white matter as WMINs, while in mice these settle as a thin compact band of L6b cells at the base of the cortex. B) The mature cortex is highly heterogeneous; M1/PFC are thicker than RSA/S1/entorhinal (Erc) cortical areas, while some regions possess unique motifs like the granular barrel field in S1 L4. C) Details cortical layers and projections of interest (S1, non-barrel field): yellow=ascending pathways from peripheral sensory cells via FOTN to L4 for signal dissemination; brown=L5-6b corticothalamic-thalamocortical loops; white=interlayer/intralayer processing; and green=descending motor pathways which elicit muscle contraction. *Associated tracts are elaborated upon in **Figure 2**. The schematic in A) was inspired by Hoerder-Suabedissen et al. (2015)[5], while B-C) were created using open-source Allen Brain Atlas images[32]. MZ=marginal zone; CP=cortical plate; SP=subplate; IZ=intermediate zone; (V-) SVZ= (ventricular-) subventricular zone; and VZ=ventricular zone.

## 1.2 Layer 6b: emerging roles of early remnants

### *1.2.1 Targeting the subplate*

Subplate cell remnants have been historically deemed "functionally insignificant" through adulthood[33], yet a growing body of evidence indicates otherwise[5, 15, 27, 33-37]. Roles of L6b have been studied using dopamine receptor 1a (*Drd1a*) genetic targeting in mice[4, 35, 38, 39]; while over 30 *Drd1a*-Cre lines have been produced, the MMRRC variant (**Table 9**)[40] is unique as $Cre^+$ soma are localised to L6a-b with little subcortical expression[4]. Diversity within L6 is well-established in this line[41-43], where T-box brain 1 (TBR1, L6)[44, 45] and complexin-3 (CPLX3, L6b)[35, 44, 46, 47] antibodies can be used to immunohistochemically target subtypes. Critically, *Drd1a*-Cre neurons exhibit intertelencephalic and corticothalamic-thalamocortical projections, presenting as a developmentally persistent node capable of integrating and refining local and long-range communications[4, 48-50]. This is relevant to human disease as both mouse and human subplate cells exhibit enriched gene expression patterns associated with susceptibility to autism and schizophrenia[33]. It is possible that, in cases of environmental or genetic insult during critical periods, abnormal apoptotic processes may yield increased or decreased remnant cell prevalence, activity, and widespread network connectivity[35, 51]. Whether this underlies or exacerbates neurodevelopmentally-linked neurological or psychiatric conditions of cortical hyperexcitability (e.g., autism and epilepsy, see **1.2.2**), hypoexcitability (e.g., narcolepsy, see **1.2.3**-**1.2.5**), or aspects of both (e.g., schizophrenia, see **1.2.2**-**1.2.3**)[35, 51] warrants investigation.

### *1.2.2 Cell augmentation*

Abnormal WMIN distributions have been described in several neurological and psychiatric diseases. While both increased and decreased densities have been reported in postmortem samples from schizophrenia patients[34, 52], increased WMIN prevalence, hypertrophy, and activity have been documented in the brains of patients diagnosed with drug-

resistant epilepsy and autism[53-55]. <1% of individuals suffer from epileptic seizures, yet this proportion rises to ≥46% in autistic individuals, suggesting that comorbid disease presentations may share underlying features like cortical hyperexcitability[56-60]. Pathological subplate growth (or decreased senescence) has been linked to the dysregulation of phosphatase and tensin homolog (PTEN) whose transcribing gene exhibits missense mutations in autistic and epileptic WMINs[61, 62]. PTEN negatively regulates the mechanistic target of rapamycin (mTOR) pathway[35, 36] whose overactivation in subplate cells may underly increased cell proliferation and decreased postnatal apoptosis (**A.1.1**)[33-35, 53, 63, 64]. I reason that mTOR disinhibition in L6b neurons may promote cell longevity or hypertrophy (including of thalamocortical signals to L4), radial migration[65], and pathological cortical excitability or sensory sensitivity[35, 56, 66]. Interestingly, genetically modified mouse lines which exploited PTEN conditional knockout (cKO) strategies to model autism-associated phenotypes simultaneously yielded mice prone to seizures and neuron hyperexcitability relative to controls (CTRLs)[67-71]. Both autism- and epilepsy-associated PTEN mutations have been identified, are expressed in subplate neurons, and are linked to increased white matter density and hypertrophy[55, 69, 72, 73]. Therefore, in this thesis, I selected a mouse model featuring *Drd1a*-Cre-dependent 'augmentation' via PTEN truncation (**2.1.3**) to study the effects of what I predict will be increased subplate neuron persistence and hypertrophy.

### *1.2.3 Cell silencing*

In contrast, decreased L6b driving or modulatory influences over corticothalamic-thalamocortical networks may be relevant to other neurological conditions including but not limited to schizophrenia and narcolepsy (see **1.2.4**-**1.2.5**)[41, 48, 49, 74-76]. To study this, I employed mice featuring *Drd1a*-Cre-driven synaptosomal-associated protein 25kDa (*Snap25*) cKO and stop-floxed Ai14 red fluorescent protein (RFP) reporter expression[4, 75, 77-79]. SNAP25 is a member of the soluble N-ethylmaleimide-sensitive fusion attachment protein receptor (SNARE) complex which facilitates presynaptic vesicle fusion and $Ca^{2+}$-dependent neurotransmission (**A.1.2**)[40, 80-

[82]. Cre-expression initiates at birth without altering axon targeting or cortical layering, resulting in cells which postnatally appear normal yet cannot communicate with downstream targets via regulated synaptic vesicle release[80, 83, 84]. SNAP25 mutations have been independently linked to cortical hyposensitivity (including disinhibition) and WMIN hypotrophy in schizophrenia[35, 85, 86], which contrasts hypersensitivity and WMIN hypertrophy in autism and epilepsy[87-90]. Functionally 'silencing' L6a-b cell subtypes via *Drd1a*-Cre-driven *Snap25* truncation compliments augmentation via PTEN truncation in investigating roles of subplate remnants[4, 77].

### *1.2.4 Orexin*

L6 neurons have been posited to regulate brain state control[48, 78, 91, 92] conceivably due to unique responsivity[93-95] to the neuropeptide orexin (ORX[96], also called hypocretin[97]). ORX is associated with increased feeding[96-99] and wakefulness[95, 99-105], while decreased ORX levels have been linked to anorexia[106-108] and remain diagnostic criteria for narcolepsy[51, 109-111]. ORX-producing neurons in the lateral hypothalamic area are innervated by cortical and subcortical structures[112, 113] which signal prepro-ORX generation and cleavage into ORX isoform A (ORXA) or B (ORXB)[93, 96, 97]. ORXA exhibits greater molecular stability and binds preferentially to ORX receptor subtype 1 (ORXR1), while ORXA/B bind to ORX receptor subtype 2 (ORXR2) with near-equal affinity[96]. ORXR1-2 are expressed throughout cortical and subcortical structures, however cortical ORXR2 is localised to L6a-b and ORXR1 to L6b[93-95, 100]. Single-cell patch-clamp recordings show L6b depolarisation upon ORXA and ORXB administration, some L6a depolarisation with ORXB, and no response to either isoform in more-pial layers[48, 98]. Non-*Drd1a*-Cre$^+$ neurons do not respond to ORX, while 79% of *Drd1a*-Cre$^+$ neurons respond strongly[48, 78], supporting *Drd1a*-Cre suitability in studying ORX-L6b relations. Interestingly, L6a-b neurons reciprocally innervate lateral hypothalamic ORX-producing neurons which also bypass FOTN and project HOTN[48, 74]. This conceivable functional interrelation between L6b cells and ORX networks motivated me to investigate how *Drd1a*-Cre perturbation may alter anatomical networks and feeding behaviour.

### *1.2.5 Sleep and feeding behaviour*

Increasing evidence indicates that the cortex may actively orchestrate sleep and feeding behaviour[75, 114-116]. ORXR-expressing L6b neurons may facilitate feed-forward cortical activation which, given vast intratelencephalic-extratelencephalic and corticothalamic-thalamocortical connections[74], renders L6b a putative substrate for integrating and refining bottom-up sensory information with top-down signals. As ORX promotes wakefulness and feeding in mice[95, 96, 99], *Drd1a*-silencing should thwart both. However, recent work showed that *Drd1a*-silenced animals counterintuitively exhibited increased and more-fragmented sleep compared to CTRLs upon ORXA administration[75]. This could be explained by ORXR expression in a subset of *Drd1a*-Cre neurons related to network inhibition[48] or increased activation of non-*Drd1a* ORXR-expressing neurons by compensatory mechanisms. Irrespectively, more extensive characterisations of $Cre^+$ cell densities and distributions are warranted, as is the development of better tools to simultaneously measure sleep and feeding behaviour. It makes sense that these functions might be related; a sleeping animal will not tend to eat, and a hungry animal will not tend to sleep. The only known study to date which investigated the role of L6b on ORX-mediated feeding remains unpublished due to confounded data. Following *Drd1a*-silencing and ORXA/ORXB/saline injection, food intake was manually measured as automated systems were incompatible with physiological sleep recordings in Faraday chambers; pellets were weighed, placed into cages, and retrieved twice daily such that mass differences proxied food consumption[75]. However, this physically disrupted animals by both awakening them and conceivably inducing stress, either of which could have impacted feeding. Moreover, crude discrete measurements at only two timepoints each day could not detail precisely when and at what rate animals were eating. This motivated me to conceptualise how a better means of non-invasively and continuously measuring feeding alongside sleep might be possible, and in a manner which was compatible with individually ventilated cage systems within electrically insulated chambers.

## 1.3 Layer 5: established roles and emerging effects

### *1.3.1 Targeting layer 5*

Like L6b, L5 features diverse cell subtypes[117-123]. In L5a, pyramidal and non-pyramidal intratelencephalic neurons possess smaller and more-pial soma while larger extratelencephalic pyramidal soma primarily reside in L5b[118, 124]. Intratelencephalic subtypes are distinguishable by antibodies targeting special AT-rich sequence-binding protein 2 (SATB2)[44, 125, 126] and COUP-TF-interacting protein 2 (CTIP2)[44, 118, 119], while extratelencephalic neurons express Fez family zinc finger 2 (FEZF2)[125, 127] and neurofilament heavy peptides (NF-H, recognised by Sternberger Monoclonals Inc. 32, SMI32)[118]. Both subtypes possess apical dendrites extending to L1, yet with distinct properties[120]. Intratelencephalic dendrites are thinner, branch less[124, 128, 129], and can adapt action potential frequencies[124, 128, 130]. Extratelencephalic neurons fire non-adaptive high-frequency "bursts" where axons receive both "bottom-up" inputs (originating peripherally) from FOTN and "top-down" inputs (originating cranially) from the cortex and HOTN[117, 124, 128-136]. Intratelencephalic pyramidal neurons also receive top-down inputs and reciprocally innervate thalamic/cortical afferents, yet projections to L5b are unilateral. This suggests that L5 facilitates widespread signal processing and eventual relay towards L5b extratelencephalic neurons, which comprise nearly all cortical outputs (**Figure 1C**)[117, 129, 132, 133, 137-140]. Using a similar genetic strategy as in L6 (**1.2.3**), roles of L5 cells can be explored via retinol binding protein 4 (*Rbp4*)-Cre-driven *Snap25*-cKO[39, 40, 64]. *Rbp4*-Cre labels ~15% of L5 neurons, with some expression in the hippocampus and cerebellum[77], which uniquely include L5b pyramidal tract neurons compared to pan-glutamatergic drivers[141-143]. *Rbp4*-Cre L5b corticothalamic axons bypass FOTN, form hypertrophic HOTN synapses with unique finger-like protrusions, and project extensively to corticostriatal and pallidal regions[77, 120, 144, 145]. While this *Rbp4*-Cre line was originally created to study neurodevelopmental activity-dependent effects of such L5 projections[77, 79, 145, 146], in this thesis I investigate their persisting roles through adulthood upon *Snap25*-cKO[114, 147].

### *1.3.2 Silencing and anatomy of cortical projection neuron subtypes*

Neuroanatomical effects of L5-silencing have been studied during early postnatal stages and to a lesser extent through adulthood[77, 79, 145-147]. *Rbp4*-Cre *Snap25*-cKO neurons initially exhibit normal axon projections and synaptogenesis, yet deficits in myelination, synapse maintenance, and cell integrity emerge with time[77, 79, 80, 83, 145-147]. L5 *Rbp4*-Cre degeneration progresses from axon punctation to cell dissolution, where resulting cellular debris features broad-spectrum-fluorescence[77]. By postnatal day 18, cKO thalamocortical axons are thinner than heterozygote CTRLs and lack specialised polysynaptic hypertrophic boutons with dendritic excrescences[77, 145]. Myelin binding protein (MBP, a marker for mature myelin) quantifications probing axon integrity showed no differences in the striatal at postnatal day 8 or 2wks[79]. Striatal and M1 oligodendrocyte expression was unaffected at postnatal day 8, 2wks, and 3wks, yet trends emerged towards reduced g-ratios in the dorsal-CST and node of Ranvier lengths in the corpus callosum[79]. Smaller g-ratios yet unchanged axon diameters indicate increased myelination, yet the dorsal-CST exhibited indistinguishably dense tract innervation by *Rbp4*-Cre and non-*Rbp4*-Cre axons. Therefore, whether increased myelination occurs in *Rbp4*-Cre cKO or CTRL axons by compensatory mechanisms cannot be concluded[77, 79]. Similarly, whether decreased callosal node of Ranvier lengths counter cKO axon hypoexcitability by reducing firing thresholds or provoking failure where nodes are excessively close remains unknown[148, 149]. In the cortex, increased ionized calcium-binding adaptor molecule 1 (IBA1) microglial densities emerge with age (i.e., after 8 months)[77], and the prevalence of parvalbumin (PV)-expressing GABAergic interneurons and vicia villosa agglutinin (VVA) perineuronal nets shifts in select cortical regions and layers[146]. However, such quantifications to date have not extended past 12wks of age. Further analyses across a broader range of cortical/subcortical targets and neuronal/glial cell types in older mice are warranted given the emergence of early differences before the onset of more pronounced anatomical and behavioural deficits[77, 114, 150, 151].

### *1.3.3 Physiology and behaviour*

Several studies have revealed behavioural changes upon L5-cKO[77, 114]. No differences have been reported pre-weaning, yet cKO animals thereafter exhibit less weight gain relative to CTRLs which is indistinguishable at 2wks, minor at 12wks, and significant by 30wks[77]. This was replicated in a study which investigated effects of *Rbp4*-Cre-driven *Snap25*-cKO on sleep and wakefulness[114] on the premise that, like L6b, L5 may integrate widespread thalamocortical-intratelencephalic inputs and exact widespread brain-state control[117, 118, 120, 137, 139]. Sleep-wake states exist across a continuum which ranges ranging from deep sleep to conscious wakefulness, all of which are commonly quantified using cortical electroencephalography (EEG) and electromyography (EMG) readouts[75, 114]. However, few studies previously considered an active role for the cortex in sleep-wake control which evidence has since supported[75, 114, 152-154]. *Rbp4*-Cre-driven *Snap25*-cKO yielded increased wakefulness compared to CTRLs, alongside decreased slow-wave activity rebound following sleep deprivation, suggesting a role for L5 in propagating slow-wave activity, non-rapid eye movement sleep, and cortical synchronisation[114]. However, studies were only conducted in cKO mice at ~12wks[114], which is prior to reports of cell degeneration and motor deficits[77]. In the seminal investigation of *Rbp4*-Cre *Snap25*-cKO, Hoerder-Suabedissen et al. briefly report that 16 of 21 cKO mice aged >30wks exhibited an abnormal "hindlimb clasp" when suspended by the tail[77]. However, no practical or underlying mechanistic rationale to explain this motor abnormality has yet been proposed.

### *1.3.4 Motor neurons and pathways*

While L5 neurons are broadly associated with processing information and generating motor-preparatory signals, L5b pyramidal tract neurons target nuclei associated with movement execution via descending motor pathways (**Figure 2**)[120, 155-159]. Motor neurons can be classified as upper motoneurons (UMNs), whose soma reside in the cortex (e.g., L5b cells, which are analogous to human Betz cells), or lower motoneurons (LMNs), whose soma reside in the

brainstem or spinal cord and express choline acetyltransferase (CHAT)[160-162]. UMN axons traverse the internal capsule, decussate, and synapse with pontine, medullary, or spinal cord LMNs and interneurons. LMNs innervate and induce the contraction of peripheral muscles, while interneurons either arrest or enable contraction by inhibition or disinhibition, respectively[158, 163]. Major descending tracts in mice are homologous to those in humans yet assume different ipsilateral/contralateral paths (**Table 1, Figure 2**)[121-123, 158, 159, 164-167]. Spinal cord targets are precisely organised in dorsal/ventral horn Rexed laminae across cervical, thoracic, and lumbar segments per tract and pathway (**Figure 2**)[159, 167]. It remains unknown as to whether changes in UMNs, LMNs, or other cell subtypes associated with *Rbp4*-Cre projections precede behaviourally observable motor deficits in L5-silenced mice. However, like EEG/EMG sleep readouts, neuroanatomical changes in the cortex have been historically considered symptomatic—not causal—across a range of conditions involving motor dysfunction[159-161].

**Table 1.** Lists and describes major descending motor-related white matter tracts in mice.

| Tract name | Tract path |
|---|---|
| Dorsal, lateral, and ventral CSTs | Descends from L5b through the internal capsule, cerebral peduncles, medullary pyramids, and spinal cord dorsal, lateral, or ventral funiculi to control skilled voluntary movements[168]. |
| Rubrospinal tracts | Originate in the red nucleus[159] and traverse the brainstem and lateral spinal cord to control distal limb flexors[167, 169, 170]. |
| Reticulospinal tracts | Originate from pontine reticular nuclei and medullary nuclei and traverse ventral and lateral funiculi to control muscle contraction, tone, and reflexivity[171-174]. |
| Vestibulospinal tracts | Originate in vestibular brainstem nuclei and traverse ventrolateral funiculi to maintain muscle tone and coordination[163, 171, 172, 175]. |
| Hypothalamic pathways | Originate in periventricular and lateral hypothalamic areas, target intermediary pontine relay nuclei, and join reticulospinal tracts to facilitate motivated locomotion (e.g., feeding and safety-seeking behaviour)[176]. |
| Fastigial pathways | Originate in fastigial nuclei and join both reticular and ventral spinal tracts to coordinate bilateral limb movements[177]. |
| Cerebellar pathways | Originate in interposed and dentate cerebellar nuclei and relay information to M1 for skilled motor preparation and refinement[177, 178]. Additional sensory feedback to M1 is provided via the medial lemnicus. |

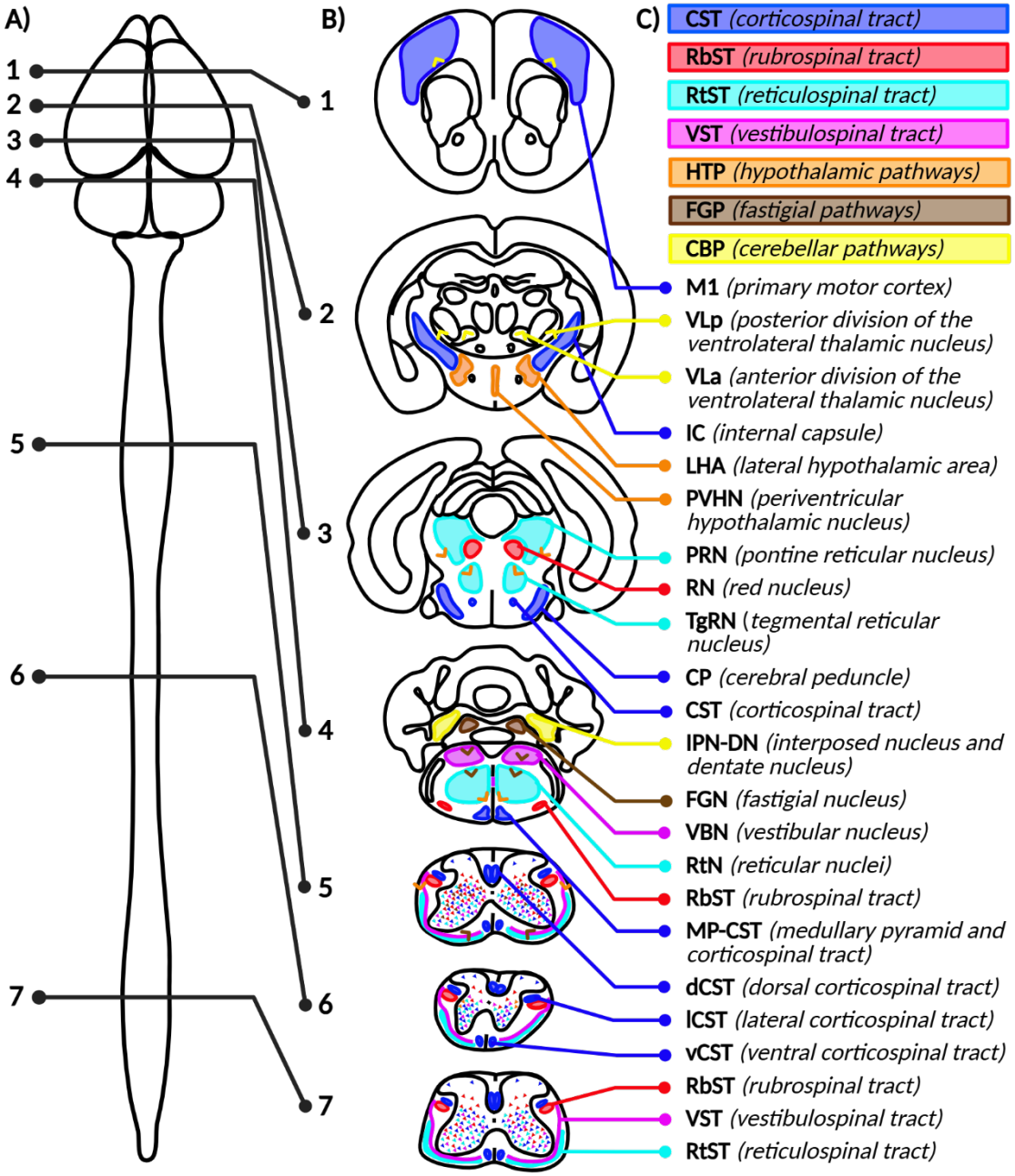


**Figure 2.** Major descending motor pathways in the mouse central nervous system. A) I sketched a crude representation of the mouse brain and spinal cord, where the location of selected slices used for illustration in B) are indicated at the following AP levels: 1=prefrontal; 2=hippocampal; 3=midbrain; 4=cerebellar; 5=cervical spinal cord; 6=thoracic spinal cord; and 7=lumbar spinal cord. I colour-coded major tracts and minor pathways according to the legend in C). White matter regions or nuclei belonging to each are labelled beneath, while arrows differentiate relay nuclei (e.g., the vestibulospinal tract initiates in vestibular nuclei, yet vestibular nuclei are also relay centres in fastigial pathways). Small triangles in spinal cord sections indicate the AP level and Rexed laminae where each tract/pathway terminates. Illustrations were created manually yet informed using Allen Brain Atlas brain and spinal cord maps[32, 179].

### *1.3.5 Diseases involving motor degeneration*

Numerous diseases involving UMN or LMN degeneration lack causal explanations. Some of the most common human disorders where L5 extratelencephalic neurons have been implicated—and which can be compared to features of *Rbp4*-Cre anatomical/behavioural decline[77]—include: Huntington's disease, which is associated with impaired corticostriatal communications and L5a thinning[180, 181]; Parkinson's disease, where multiple mouse models exhibit impaired intratelencephalic, thalamocortical, and corticostriatal tract deficits[182-186]; frontotemporal dementia (FTD), which affects L5b von Economo neurons in the frontal cortex[187, 188]; and motor neuron diseases like primary lateral sclerosis which affects UMNs (including L5b Betz cells but not LMNs)[189] and amyotrophic lateral sclerosis (ALS, where both LMNs and UMNs eventually degenerate)[190-194]. Shared features across each include neurodegeneration and protein aggregation—namely huntingtin in Huntington's disease, α-synuclein in Parkinson's disease[182-186], and TAR DNA binding protein 43 (commonly termed TDP-43) and hyperphosphorylated tau (recognised by the antibody AT8) in both FTD[187, 188] and ALS[191, 193]—where L5b cells may be a common substrate. Large L5b neurons have high metabolic/structural demands, rendering them particularly vulnerable to "the Bermuda triangle" of insults underlying neurodegeneration: oxidative modifications, mitochondrial dysfunction, and impaired protein degradation[182, 185, 189, 194, 195]. Yet, whether L5b neuron degeneration presents as a disease origin or symptom—and by which underlying mechanisms—remains hotly contested, perhaps most notably in ALS[196] which I will discuss further (**1.4.5**).

## 1.4 Current states and directions

### *1.4.1 Measuring animal activity and feeding*

Developing and automating home cage monitoring (HCM) has become an emerging field of practical scientific interest, where integrating quantifications of rodent food-intake remains

non-trivial. Accurately measuring laboratory rodent food-intake is important as researchers commonly control or modify the type, amount, and timing of feeding to observe effects across experimental conditions (as I propose doing following *Drd1a*-Cre manipulations)[197, 198]. Unsurprisingly, the past 10 years have produced numerous HCM methods capable of automatically quantifying animal feeding including sophisticated whole-cage monitoring suites, cage integrations, and video-based systems (**Table 2**)[197-204]. All possess unique advantages yet are practically limited in either possessing a problematic animal-food interface, failing to directly measure food intake (only feeding behaviour as a proxy), or proving incompatible with elements of current home-cage setups—namely, simultaneous EEG/EMG recordings (**Table 2**), which are indispensable for my proposed L6-ORX-sleep investigations[75, 197-201, 203-205].

**Table 2.** Features and limitations of HCM tools measuring mouse feeding. Green=full HCM suites; blue=cage integrations; purple=video-based systems; BW=body weight; and RW=running wheel. See www.cost-teatime.org/about/technologies/ for an extended and updated list.

| System (Developer) | Beneficial and Limiting Features |
|---|---|
| Promethion Cages (Sable Systems)[199] | ✓ Sophisticated monitoring across many outputs (e.g., food/water intake, RW, metabolism, video/motion tracking, BW); remote monitoring; traditional food presentation. **X** Expensive; proprietary hardware and software; cannot accommodate simultaneous measurement of sleep and feeding behaviour. |
| CLAMS (Columbus Instruments)[200] | |
| CageView (Tactile Robotics Ltd.)[203] | ✓ Less expensive than HCM suites; many outputs (e.g., food/water intake, video/motion tracking) modular; traditional food presentation. **X** More expensive than the FED3; proprietary hardware and software; cannot accommodate simultaneous measurement of sleep and feeding behaviour. |
| Feeding Experimentation Device (FED3, NIH)[201] | ✓ Inexpensive; modular (easy to simply place within common home-cage setups); open-source hardware and analysis software. **X** Animals must be trained to press a lever, which may alter feeding behaviour or confound experiments[206]; pellet-jamming restricts food access and introduces welfare concerns; pellets are prone to crumble; cannot accommodate simultaneous measurement of sleep and feeding behaviour. |
| PhenoTyper (Noldus Information Technology)[197] | ✓ Video tracking; modular additions including automated food dispensers, water lickometers, and integrations for optogenetics and telemetry; remote monitoring. **X** Expensive; only measures dispensed food and animal-food interactions; AI video analyses are prone to failure if obstructed by cage enrichment; proprietary hardware and software; cannot accommodate simultaneous measurement of sleep and feeding behaviour. |
| Integrated DeepLabCut (Mathis Lab)[204] | ✓ Free analysis software integrated with video tracking; open-source; remote monitoring; traditional cage-hopper food presentation; can accommodate simultaneous measurement of sleep and feeding behaviour. **X** Indirect measure of animal interactions with food; automated video analyses are prone to failure if obstructed by cage bedding or enrichment. |

### *1.4.2 Behavioural data analysis*

Many software packages have been produced to analyse HCM data; however, each are limited in application, warranting the development of a more robust open-source platform which can process data from acquisition systems with transparency and consistency. **Table 3** details some available and currently-maintained software tools which have been developed and applied to mouse behaviour analysis, including the present capacity of each to generate desirable activity- and circadian-related output metrics relevant to current or future analyses. Different tools are more-or-less suited to generating different metrics, yet none excel universally. BioDare2 produces excellent period decompositions yet cannot discriminate behavioural data[207]. Integrated DeepLabCut-Bonsai systems generate real-time activity and event data, however cannot discern periodicities, bouts, or feeding[204, 208]. COMPASS and Nestbox scripts achieve all the above, yet still do not accept feeding data[205, 209, 210]. HCM suites with dedicated software like PhenoMaster and TSE analytics are perhaps the most well-suited to generate feeding outputs, however underlying algorithms are proprietary and only work with expensive compatible hardware systems (e.g., in 2021, I received a quote for ~450,000.00 USD for the purchase and installation of a 16-cage system). Analysis methods which do exist are not used consistently across behavioural and circadian studies, varying significantly both between international research groups and even within individual laboratories[205, 210-212]. That is, different platforms and unique software specifications even within the same platform can drastically alter results and confound inter-study comparisons[213]. No known universal open-source platform currently accepts time-series feeding and activity data from non-proprietary input sources, which will be necessary if I wish to analyse data from any novel device capable of measuring food intake and feeding behaviour in genetically modified mice (i.e., *Drd1a*-Cre-driven *Snap25*-cKO in the first instance).

**Table 3.** Summary of software tools for behavioural data analysis. Blue=proprietary, green=open source; yellow=circadian-related metric; purple=activity-related metric; orange=both circadian- and activity-related; LD=light-dark; f=frequency; t=time; BP=blood pressure; BT=body temperature; CRL=Circadian Rhythm Laboratory; FI=food intake; HR=heart rate; PIR=passive infrared monitoring; RER=respiratory exchange ratio; RFID=radio frequency identification; RW=running wheel; T=periodicity; and WI=water intake.

| Software Name (Release Date, Developer) | Data Type(s) | Output Metric | | | | | | | | | | | | | | | |
|---|---|---|---|---|---|---|---|---|---|---|---|---|---|---|---|---|---|
| | | Raw time-course | Actograms | Activity counts and t | Activity rates | Bout analysis | Time active/inactive | LD discrimination | LD integration | Average T | T decompositions | Phase shifts | Event marking (f, t) | Latency to event | Interdaily stability | Region breakdown | Social interaction |
| COMPASS (2016, Peirson Lab)[205, 209] | PIR | ✓ | ✓ | ✓ | ✓ | ✓ | ✓ | ✓ | X | ✓ | ✓ | ✓ | ✓ | X | ✓ | X | X |
| Nestbox scripts (2024, Oxford Univ.)[210] | RW, PIR | ✓ | ✓ | ✓ | ✓ | ✓ | ✓ | ✓ | X | ✓ | ✓ | ✓ | ✓ | X | ✓ | X | X |
| DeepLabCut (2018, Mathis Lab)[204] | Pose estimation | ✓ | X | X | X | X | X | X | X | X | X | X | X | X | X | ✓ | X |
| Bonsai (2015-2020, NeuroGEARS)[208] | Real-time I/O (i.e., with DeepLabCut) | ✓ | X | ✓ | ✓ | X | ✓ | ✓ | X | X | X | X | ✓ | ✓ | X | ✓ | X |
| ActogramJ (2011, Yoshii Lab)[214] | Time series (PIR, RW, video etc.) | ✓ | ✓ | X | ✓ | X | X | ✓ | X | ✓ | X | ✓ | ✓ | X | X | X | X |
| easyClock (2025, Ja Lab)[215] | Time series (PIR, RW, BT etc.) | ✓ | ✓ | ✓ | ✓ | ✓ | ✓ | ✓ | X | ✓ | ✓ | ✓ | ✓ | X | ✓ | X | X |
| BioDare 2 (2014, Millar Lab)[207] | Time series (PIR, RW, video etc.) | ✓ | ✓ | X | X | X | X | ✓ | X | ✓ | ✓ | ✓ | X | X | X | X | X |
| Kronos (2023, Cryan Lab)[216] | Time series (PIR, RW, video etc.) | ✓ | ✓ | ✓ | ✓ | ✓ | ✓ | ✓ | X | ✓ | ✓ | ✓ | ✓ | X | X | X | X |
| MouseVUER (2024, Dennis Lab)[217] | Video tracking | ✓ | X | ✓ | ✓ | ✓ | ✓ | ✓ | X | X | X | X | ✓ | ✓ | ✓ | ✓ | X |
| Live Mouse Tracker (2019, Inst. Past.)[218] | Video tracking, RFID | ✓ | X | ✓ | ✓ | ✓ | ✓ | ✓ | X | X | X | X | ✓ | ✓ | X | ✓ | ✓ |
| SimBA (2020, Golden Lab)[219] | Behavioural classification | ✓ | X | X | X | X | X | X | X | X | X | X | ✓ | ✓ | X | X | ✓ |
| ClockLab (1990s, Actimetrics) | Activity (RW, PIR) | ✓ | ✓ | ✓ | ✓ | ✓ | ✓ | ✓ | X | ✓ | ✓ | ✓ | ✓ | X | ✓ | X | X |
| EthoVision XT (2001, Noldus) | Video tracking | ✓ | X | ✓ | ✓ | ✓ | ✓ | ✓ | X | X | X | X | ✓ | ✓ | X | ✓ | ✓ |
| Any-maze (1999, Stoelting) | Video tracking | ✓ | X | ✓ | ✓ | ✓ | ✓ | ✓ | X | X | X | X | ✓ | ✓ | X | ✓ | ✓ |
| PhenoMaster (2000s, TSE) | HCM (video, FI, WI, $O_2$, $CO_2$, RER) | ✓ | ✓ | ✓ | ✓ | ✓ | ✓ | ✓ | X | X | X | X | ✓ | ✓ | ✓ | ✓ | ✓ |
| DAMS (2005, TriKinetics) | Beam break | ✓ | ✓ | ✓ | ✓ | ✓ | ✓ | ✓ | X | ✓ | X | X | X | X | ✓ | X | X |
| DSI Ponemah (1980s, DSI) | Telemetry (BT, HR, EEG/EMG, BP) | ✓ | ✓ | ✓ | ✓ | X | ✓ | ✓ | X | ✓ | ✓ | X | ✓ | X | ✓ | X | X |
| BioDAQ (2010, Research Diets) | FI, WI | ✓ | X | ✓ | ✓ | ✓ | ✓ | ✓ | ✓ | X | X | X | ✓ | ✓ | X | X | X |

### *1.4.3 Neuroanatomical quantification*

Quantifying anatomical changes due to genetic manipulations both within L5-6b and in projection regions of interest (ROIs) can be achieved on several levels. The Molnár laboratory previously assessed distributions of GABAergic interneurons in these same mouse models using conventional anatomical methods[146]. However, these approaches are limited in surveilling only a small fraction of pre-selected brain ROIs. This motivated me to conceptualise a way to upscale present experiments to encompass whole-brain quantifications, where ROIs would remain pre-defined for statistical analyses yet *post hoc* assessments of any definable ROI would become possible. To this aim, the QUINT pipeline[220] employs 2D imaging and 3D reconstruction[220] in a three-step workflow: 1) atlas mapping, where histological slices are registered using QuickNII[221]; 2) feature segmentation, where cells are detected using ilastik[222] (though tools like ImageJ[223] are also compatible); and 3) data registration, where segmentations and atlas maps are combined to register detected features to brain regions in 3D space using Nutil[224]. However, the pipeline only accommodates single-fluorophore detections, cannot regionalise morphometric data[220, 222], and does not produce statistical results alongside easily interpretable graphs. Pipeline refinement is therefore needed for compatibility with L5-6b subpopulation characterisation.

### *1.4.4 Layer 6 networks and translatability*

Given the critical role of the subplate during neurodevelopment and evidence implicating its importance beyond, further work is needed to: 1) better-characterise the cortical distribution of L6b subtypes under unperturbed, augmented, and silenced states; and 2) address the incompletely evidenced notion that *Drd1a*$^+$ L6b neurons are analogous to human WMINs[4, 5]. 18±7% of S1 L6b neurons stained for neuronal nuclei (NEUN) are labelled by *Drd1a*-Cre at postnatal day 8, of which 31±8% co-expressing CPLX3 can be deemed "subplate remnants"[4, 46]. *Drd1a*$^+$/CPLX3$^-$ cells include but cannot be definitively classified as "non-subplate remnants" as, though a significant subpopulation, CPLX3 is only expressed in 43±9% of S1 L6b neurons at

postnatal day 8[47]. Quantifications in older mice showed 24±4% S1 L6b NEUN$^+$/*Drd1a*$^+$ expression in 5wk brains[4] and 40±2% at 7-14wks[47]. However, NEUN$^+$/*Drd1a*$^+$/CPLX3$^+$ colocalisation has not been evaluated in older mice—only at 5wks with connective tissue growth factor (CTGF)[48, 50], another subplate marker having ~90% overlap with *Cplx3*[82, 225]—nor have similar data been acquired across cortical regions. This is important to characterise as, in cases of subplate dysfunction, one cannot predict functional ramifications if cells are differentially expressed and if infarcts are regionally localised[49, 50]; knowledge gleaned from experiments conducted in S1[42, 48, 50] are not necessarily translatable pan-cortically (**1.1.5**)[226]. Interpreting the results of studies employing *Drd1a*-Cre mouse lines and their relevance to human conditions[4, 48, 50, 75, 77, 78] relies on the assumption that *Drd1a*-expressing cells are analogous to WMINs. L6b neurons and WMINs both exhibit extensive prenatal proliferation, postnatal apoptosis yet persisting thalamocortical projections, and similar gene expression patterns[3-5, 15, 27, 35, 42, 50, 227-231]. Fusiform, multipolar, inverted pyramidal, and polymorphic WMINs have been observed in primates and humans[227, 228] while mouse L6b neurons assume multipolar, neurogliaform, and pyramidal subtypes[42, 50, 229]. This informs heterogeneity in WMIN/L6b morphological profiles[48, 50], where no comparisons between ORX-sensitive subtypes have yet been conducted to evaluate similarity.

### *1.4.5 Layer 5 and top-down motor neuron degeneration*

Consider ALS as a prototypical motor neurodegenerative condition where L5b cells are etiologically implicated. Theories of disease onset and progression are classified as 'bottom-up/dying-back' (i.e., originating in peripheral LMNs), 'top-down/dying-forward' (i.e., originating in cerebral UMNs), or 'independent' (i.e., both top-down and bottom-up)[160-162, 190-192, 196, 232-236]. The latter could be supported by evidence of motor deficits following L5-silencing[77]. The dying-back hypothesis proposes that ALS originates in peripheral LMNs, where abnormal cytoskeletal transport[161, 237] or infarct to the neuromuscular junction triggers degeneration and retrograde disease propagation to the spinal cord and brain[160, 191, 235, 238, 239]. If muscle cells fail to secrete

neurotrophic or myogenic factors to afferent innervations (i.e., decreased positive feedback), axons retract and compound activity-dependent muscle/neuron atrophy[234, 235, 239-242]. Toxic ligands released from damaged muscles can be endocytosed by afferent synapses, undergo active transport to LMN soma, and catalyse a degenerative spiral if compensatory innervation attempts from other LMNs are plagued by vulnerable neuromuscular junction environments[234, 239, 240]. Degeneration is thought to then spread to UMNs via retrograde propagation, resulting in dysfunctional LMN-UMN synapses[161, 234, 238, 239]. The dying-forward hypothesis posits that L5b Betz cells incipiently exhibit pathological aggregation of proteins like TDP-43—a shared pattern in ALS and FTD—which spread to directly-targeted LMNs (e.g., α-motoneurons) and provoke degeneration[162, 187, 190, 191, 196, 238, 243]. Anterograde degeneration may be initiated and perpetuated by UMN glutamatergic excitotoxicity across cortical regions[160, 187, 190-192, 196, 232, 244]—including but not limited to M1 in ALS and the PFC in FTD[192, 194]—where soluble cytotoxic proteins propagate to monosynaptic subcortical targets via prion-like axoplasmic transport[162, 233, 236, 238, 243]. Protein phosphorylation, ubiquination, and cytoplasmic aggregation in α-motoneurons then ultimately leads to LMN degeneration[194, 236, 238, 243, 245]. Interestingly, extraocular and pelvic sphincter motor nuclei constitute the only LMNs which are not directly innervated by UMNs and which do not degenerate in ALS (supporting top-down theories)[196, 233, 246]. The motor deficits reported upon L5-silencing by no means render this an "ALS mouse model"[77]; however, *Rbp4*-Cre-driven *Snap25*-cKO may feature yet-uncharacterised neuroanatomical and behavioural deficits which resemble observations in widely-used genetic mouse lines featuring mutations in genes linked to ALS including *SOD1*, *FUS*, *TARDBP*, and *C9ORF72*[160, 193, 196, 234-237, 239, 243, 245, 247, 248]. Interestingly, all exhibit UMN-LMN synapse dysfunction[194, 234] and both *SOD1* and *FUS* have been specifically linked to decreased SNAP25 expression[234]. Motor function in L5-silenced mice may decline further with age[77, 192, 194]; therefore, a more comprehensive characterisation[232] of this model will inform pathophysiological trajectories of neuromotor decline and disease-relevance.

## 1.5 Aims and hypotheses

### *1.5.1 The SnackerTracker: measuring feeding and activity behaviour*

The first results chapter (3) describes the development and validation of a novel animal home-cage monitoring system—the *SnackerTracker*—to ultimately quantify food intake and feeding behaviour[211] in mice upon *Drd1a*-Cre-driven *Snap25*-cKO. Given significant overlap between DRD1A and ORXR expression in L6, and in positing that L6 cells act as a cortical node in ORX networks, I hypothesised that *Drd1a*-Cre-driven *Snap25*-cKO should thwart feeding- and wake-promoting effects of ORX . The *SnackerTracker* is uniquely capable of measuring this, thus its development was warranted; to my knowledge, no current system can continuously measure food-intake while remaining compatible with EEG/EMG sleep studies (**Table 2**)[75]. While this *Drd1a*-Cre-feeding study could not be conducted due to breeding complications (**Preface**), *SnackerTracker* development, validation, and application in other contexts proceeded. Device design criteria and constraints are listed in **Table 4**. Development involved computer-aided design and 3D printing, electronics assembly, construction, software production, and testing. I then conducted *in vivo* compatibility and validation tests using surplus C57BL/6J and *Rbp4*-Cre *Snap25*-cKO mice; as *Rbp4*-silencing yields increased wakefulness and sleep-fragmentation[114], I reasoned that the *SnackerTracker* should reveal more frequent feeding behaviour. I assessed the *SnackerTracker's* ability to detect changes in *three key feeding behaviour parameters* using distinct experimental/pilot cohorts (**Table 5**): genetically modifying the mouse circadian clock should alter behavioural *patterns/rhythmicity*; altering the intensity and timing of dark-onset should *phase-shift* feeding behaviour; and mimicking seasonal lighting conditions should alter the absolute *quantity* of food consumption in animals maintained under summer vs winter photoperiods. A validated means of measuring of animal food intake and feeding behaviour could provide novel insights into circadian, metabolic, or motor phenotypes, rendering the *SnackerTracker* a valuable tool in present and future research applications.

**Table 4.** Criteria and constraints influencing *SnackerTracker* development. Requirements are classified as follows: green = primary (mandatory, without which the device would not be viable and novel); blue = secondary (ideal, though not essential for device functionality; and purple = tertiary (extra, which would simply improve the system).

| Design Criteria or Constraint | Description |
|---|---|
| Satisfy UK and Oxford BSB animal home cage size requirements and restrictions | The *SnackerTracker* must satisfy the most conservative legal requirements of European Union Directive 2010/63. Animal home-cages must provide at least 330cm² floor area in total and 60cm² per animal. The most restrictive cage area and height in commonly used enclosures is 435cm² and 12cm, respectively. The *SnackerTracker* therefore cannot have an aerial footprint greater than 105cm² or a vertical height exceeding 12cm. |
| Biocompatible | The chassis must consist of biocompatible materials to avoid physical (i.e., sharp edges or restrictive spaces) or chemical (i.e., non-toxic) harm to animals. |
| Faultless electronics | Electrically active components must be inaccessible to animals, wired correctly, and insulated to prevent short-circuits or exposed connections. |
| Avoid heat generation | The device cannot produce excessive heat which may harm animals, confound behaviour, interfere with thermographic recording, or damage the device itself. |
| Noiseless | Operation cannot generate excessive noise, could cause animals stress. 'Noise' includes all frequencies within animals' hearing range (i.e., 1-100kHz for mice). |
| Accurate data recording | Devices must be calibrated to known weights and validated to ensure accurate measurement over time (i.e., no drift). |
| Continuous data recording | Measurements must be registered continuously to reveal patterns of animal-device interactions and food intake. |
| Accurate real-time alignment | Both absolute (i.e., that a second is indeed a second) and relative accuracy (i.e., aligning with the date/time at which recordings took place) must be validated. |
| Local data storage | Data must be reliably stored to integrated hardware for later retrieval. |
| Robust data collection and processing | Data collection and processing must be validated across a range of experimental setups to ensure that both hardware and software elements are robust and compatible in diverse settings. |
| Cost-effective | A similar system (i.e., the FED3)[201] is listed at €475 with material costs totalling €205. Costs should be minimised and ideally not exceed this (£180). |
| Mimics standard food presentation | The device should mimic the way in which food is currently presented to mice (i.e., from a food hopper above the floor) to avoid confounding comparisons between past and future works and to prevent pellets from spoiling. |
| Wireless operation | This would make devices compatible with individually ventilated cages (i.e., no need for external power cabling) if battery life is sufficient (e.g., 24 hours). |
| Event-marking | Switches could be incorporated to mark experimentally relevant events which would be denoted in data outputs for qualitative or quantitative consideration. |
| Easy operation | The device must be easy to use experimentally (e.g., seamless software upload, calibration, cage insertion, data extraction, and data processing). |
| Intuitive interface | Both operational and analysis software must have an intuitive interface for user-operation. Code should include thorough error-checking. |
| Ease of analysis | Analysis software must be properly annotated and available open-source. |
| Wireless control and monitoring | The device could enable researchers to remotely control device operation and to remotely monitor outputs for quality control and animal surveillance. |
| Cloud-based data storage | Data could be stored remotely (e.g., cloud-based, in addition to local SD card storage) to improve ease of data extraction. |
| Cage enrichment | The device may enrich the animal home-cage environment. |
| Additional peripheral integrations | Easy-to-incorporate additional peripheral integrations include auditory sensors, speakers, thermographic cameras, passive infrared sensors, LED lights, optogenetic probes, or thermal leads. |

**Table 5.** Experimental/pilot cohorts used to assess *SnackerTracker* function. Hypotheses for each application are indicated in **bold**.

| Test number | Description |
|---|---|
| **1: testing feeding patterns and rhythmicity** | This employed CTRL wild-type (WT, C57BL/6J) mice and circadian clock-deficient mice (i.e., cryptochrome (CRY) 1 and 2 double-knockout, *Cry1*$^{-/-}$*;Cry2*$^{-/-}$ (**Table 9**), also termed "CRY-deficient")[249], both under conditions of controlled 12hr:12hr light-dark cycles and constant-darkness. Mice are nocturnal; they are active and feed during dark phases with a peak at dark onset, then are inactive with bouts of spontaneous activity during light phases[250]. The circadian clock maintains regular physiological behaviour without environmental cues (e.g., light-dark cycles) such that activity patterns persist under constant conditions (e.g., constant-darkness)[251]. WT CTRL animals should therefore exhibit rhythmic behavioural patterns under both light-dark cycles and constant darkness. In contrast, while CRY-deficient animals exhibit normal rhythms in light-dark conditions due to light-dependent negative masking, behaviour becomes arrhythmic under constant darkness with irregular bouts of activity throughout a 24h period[249, 252]. **The *SnackerTracker* should be able to detect this expected shift to behavioural arrhythmicity in CRY-deficient animals in constant-darkness and reveal whether the pattern and quantity of feeding changes.** |
| **2: testing for phase-shifted feeding behaviour** | Genetically-WT mice which were or were not exposed to dim light in the evening (DLE). Standard home cages employ 12h:12h light-dark cycles, while DLE introduces a 'natural' transitionary period of low-intensity illumination at dark-onset to simulate dusk or artificial lighting[253]. This experiment tests whether the *SnackerTracker* can identify feeding differences in mice housed with DLE. Given that DLE can phase-shift locomotive onsets and peripheral molecular clock rhythms[253], and that dim light through the night can shift the timing of activity[254] and food intake[255], **I predict that the intensity of WT mouse activity and feeding may exhibit later peak-onset in the evening under conditions of DLE.** |
| **3: testing for changes in the quantity of food intake** | "Summer" and "winter" hamsters maintained in home-cage conditions mimicking seasonal light-cycle changes. Hamsters are typically heavier and are expected to eat more in the summer than in the winter[256, 257]. Therefore, under otherwise controlled conditions, **the *SnackerTracker* should be able to detect periodic variations in hamster feeding behaviour; hamsters maintained under summer photoperiods should consume more food than those maintained under winter photoperiods**. |

### *1.5.2 TracKIT: analysing behavioural data*

Chapter 3 also describes the design and development of the *TracKIT* analysis platform, which was created alongside the *SnackerTracker* for data processing[258]. I detail criteria and constraints in **Table 6**, where programme design should prioritise future inter-system operability such that *TrackIT* can accept any time-series data and generate a range of experimental outputs.

**Table 6.** Summarises criteria and constraints influencing *TracKIT* design and development. Green = primary (mandatory, without which the programme would not be viable and novel); blue = secondary (ideal but not essential); and purple = tertiary (extra, simply to improve functionality). Refer to **Table 3** to compare these criteria to features of existing platforms.

| Design Criteria | Description |
|---|---|
| Open-source | Scripts should be created, annotated, and shared using open-source tools (e.g., R) and distribution platforms (e.g., Zenodo and GitHub). |
| Inputs | The platform should be capable of accepting time-series data from a range of HCM systems and data types (e.g., food-intake, activity, and temperature). |
| Outputs | Automatically-generated outputs should include: Raw and derivative time-course plots; total feeding/activity; feeding/activity totals in the light phase vs in the dark phase; light-dark integration (i.e., checking specified light-dark cycles against raw inputs from LDRs; average and decomposed periodicities; and phase shifts. |
| Analysis features | Analysis bouts should be customisable. The programme should be executable using standard operating systems (e.g., Windows or iOS). |
| Outputs | Further outputs include time active/feeding; event-marking; and interdaily stability[259]. |
| Analysis features | The platform should feature an intuitive user interface. It should be capable of analysing technical/experimental replicates for integrated statistical processing. |
| Outputs | Sociability could be considered an interactive factor in cases of group-housing. |
| Analysis features | The GUI should be visually appealing and accommodate extended recording durations. |

### *1.5.3 r-QUINT: neuroanatomical analysis pipeline refinement*

The second results chapter (4) first describes anatomical pipeline refinements to enable whole-brain cell density and morphology analyses following L5-6b manipulations (**Figure 3**)[260]. I predicted that altering the activity of cortical projection neurons in a chronic (genetic) or acute (chemogenetic) fashion would alter cell densities and distributions. Evaluating this required an imaging and analysis method capable of quantifying the prevalence and soma size of cells featuring multiple fluorophore combinations across the brain. I therefore aimed to develop a refined (r-QUINT) pipeline to 1) enable multiplexed signal detection and segmentation; 2) statistically process atlas-registered outputs; and 3) incorporate morphometric analyses. To validate pipeline refinements, I analysed adult WT PV/VVA cell expression patterns using r-QUINT for comparison to recently published data, hypothesising that cell densities across atlas-defined ROIs should be similar across methods[261, 262]. I then quantified and compared PV/VVA densities between mice with L5 *Rbp4*-Cre-driven expression of excitatory or inhibitory designer receptors exclusively activated by designer drugs (DREADDs) subjected to saline injection (CTRL)

or chemogenetic clozapine-N-oxide (CNO) actuation[263-268] to fully test pipeline performance in available experimental tissues. I predicted that no monumental differences should emerge in PV interneurons following acute perturbations, but that subtle compensatory VVA perineuronal net reorganisation across projection layers 2-6 may emerge. This "acute" *Rbp4*-Cre DREADD activation/inhibition in adult mice contrasts "chronic" silencing via *Snap25* truncation, which initiates at birth and continues throughout the life of the experimental animal[77]. Analysing the effects of chronic silencing remains the focus of this thesis following pipeline validation.

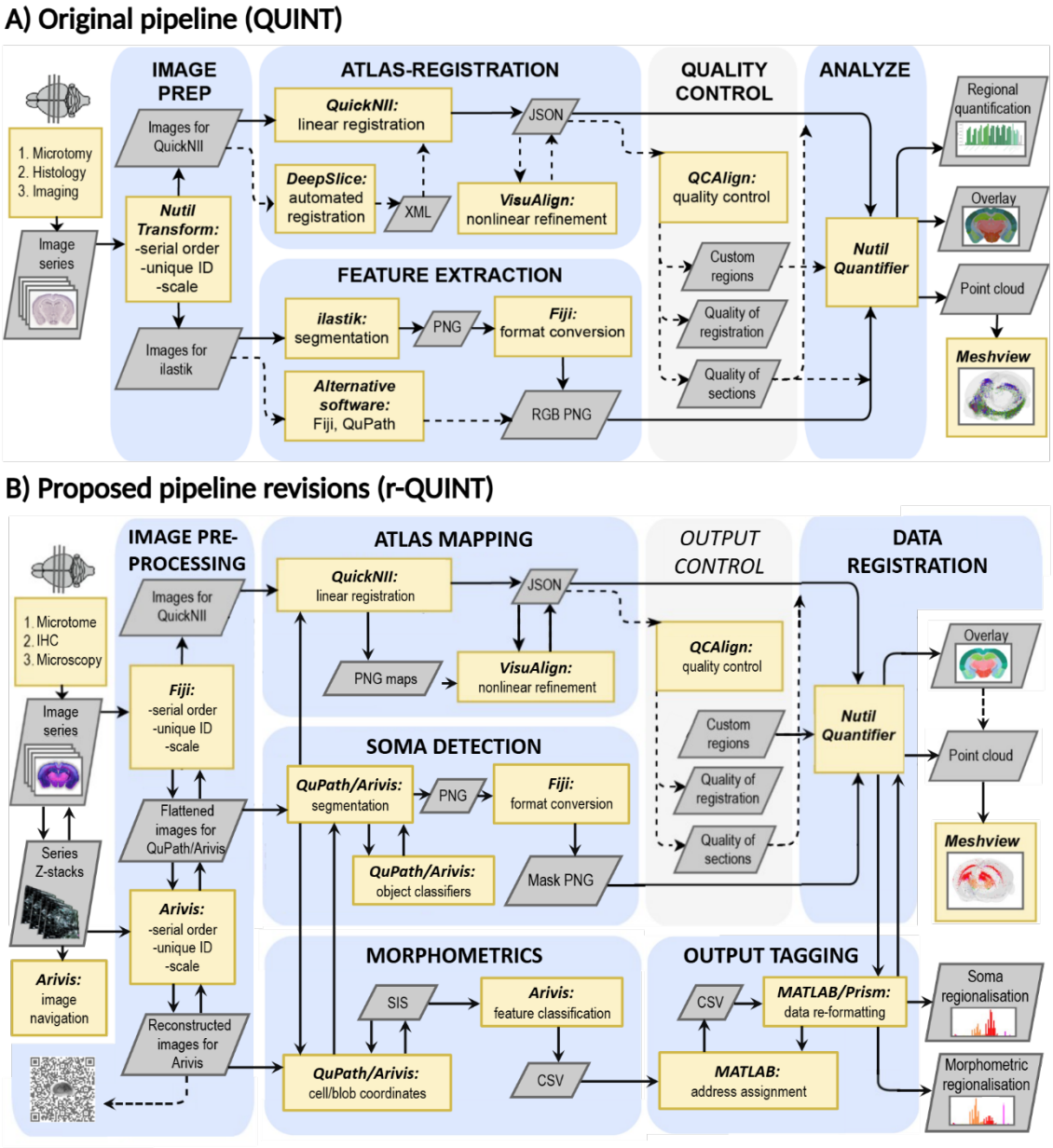


**Figure 3.** Illustrates the A) original QUINT pipeline[220] and B) proposed refinements.

### *1.5.4 L6b manipulations: effects of silencing and augmentation*

Chapter 4 thereafter 1) characterises cell densities and distributions following *Drd1a*-Cre manipulations, particularly *Drd1a*$^+$/CPLX3$^+$ colocalisation which may indicate distinct ORX-sensitive L1-projecting subcircuitry[48, 50, 82], and 2) morphologically evaluates analogy between mouse L6b *Drd1a*-Cre cells and human WMINs[269, 270]. r-QUINT analyses brain-wide PV-VVA signatures following L6-augmentation, then L6 subtypes (i.e., *Drd1a*-Cre$^+$ cells in L6a-b ±CPLX3 in L6b) upon chronic L6-augmentation/silencing via PTEN/*Snap25*-cKO. I expected little change in PV/VVA following PTEN-cKO, yet increased Cre$^+$ densities and hypertrophy (particularly CPLX3$^+$ subtypes)[67, 271]. I predicted no changes in *Drd1a*-Cre$^+$ densities upon *Snap25*-cKO in line with prior work[4, 77, 83], and that L6b *Drd1a*$^+$ cells and human WMINs would exhibit similar morphological soma and neurite features[4, 5]. Given the capacity of subplate neurons to elicit widespread functional consequences, I aimed to characterise cortical heterogeneity in *Drd1a*-Cre neurons (including upon genetic silencing/augmentation) and evaluate L6b/WMIN analogy to probe roles of subplate remnants through adulthood. This will inform the relevance of the subplate across a range of human neurological and psychiatric disorders[5, 33-35, 37, 48, 49, 75, 77, 78].

### *1.5.5 L5-silencing: project STAMINA investigates motor degeneration*

The third results chapter (5) reports and characterises progressive neuromotor deficits upon chronically silencing *Rbp4*-Cre neurons in mice[272]. This involved the design and execution of a comprehensive multimodal investigation—***S****nacker****T****racker* **a**nd **M**RI **I**nvestigation of **N**euroanatomy and **A**ctivity (STAMINA)—integrating behavioural assays, *in vivo* and *ex vivo* magnetic resonance imaging (MRI), and immunohistochemistry (IHC) to capture whole-brain changes over time (**Figure 4**). I longitudinally quantified and compared behavioural measures including continuous assessments of motor phenotypes (CAMP)[273], gait[274, 275], and grip strength to *in vivo* T1-weighted (T1W) anatomical MRI, diffusion weighted imaging (DWI), and functional MRI (fMRI) to evaluate correlation or lack thereof at three main time points: 4-7wks, after the

first signs of neurodegeneration emerge yet before motor deficits[77]; 11-14wks, the age of *Rbp4*-Cre mice used in physiological studies; and 18-21wks, when motor deficits are expected[77, 114]. At 18-21wks, I obtained *ex vivo* T2-weighted (T2W) anatomical, DWI, and multigradient echo (MGE) scans for quantitative susceptibility mapping (QSM) followed by immunohistochemistry to yield convergent evidence supporting or disputing degenerative hypotheses (**Table 7**). That is, I conducted longitudinal behavioural tests and *in vivo* MRI aim to complimentarily identify *when* and *where* anatomical and functional deficits emerge, then *ex vivo* MRI and histology to provide higher-resolution insights into underlying neuroanatomical network- and cellular-level effects. Effects of *Rbp4*-Cre-driven *Snap25*-cKO have not been systematically characterised in the context of neuromotor deficits[77]; therefore, I aim to determine the spatiotemporal progression of anatomical and functional degeneration following L5-silencing and the conceivable roles of *Rbp4*-Cre neuron subpopulations and *Snap25* truncation in motor dysfunction.

**Table 7.** Predicted ramifications of Rbp5-Cre-driven *Snap25*-cKO. These are expected to augment with time.

| **Trend** | **Domain** | | |
|---|---|---|---|
| | **Behavioural** | **Neuroimaging (MRI)** | **Histology (IHC)** |
| **Increasing** | Amount and irregularity of *SnackerTracker*[211]-TracKIT activity and feeding; kyphosis; and gait irregularity. | Neurite dispersion and mean diffusivity in L5 motor areas which precede or accompany behavioural deficits. | Tau accumulation in *Rbp4*$^+$ soma and axons; microglia and astrocytes near *Rbp4*$^+$ soma, tracts, and downstream targets; and subsequent LMN degeneration. All may correspond with MRI and trajectories of behavioural decline. |
| **Decreasing** | Body weight; nesting behaviour; CAMP scores; grip strength; gait fluency and speed; and overall activity in the visual cliff test (but not visual acuity). | T1W-T2W volumes, kurtosis, intracellular volume fractions, and magnetic susceptibility in L5, followed by fractional anisotropy in projection tracts (e.g., CST, **Figure 2**). All may precede or accompany trajectories of behavioural deficits. | The integrity or density of: L5 *Rbp4*$^+$/NEUN$^+$ cells (i.e., those also SMI32$^+$); LMN in midbrain motor nuclei (save oculomotor and pelvic sphincter nuclei) and anterior horn Rexed laminae VII-IX across the spinal cord; and myelination in L5 projection tracts. All may correspond with MRI and trajectories of behavioural decline. |

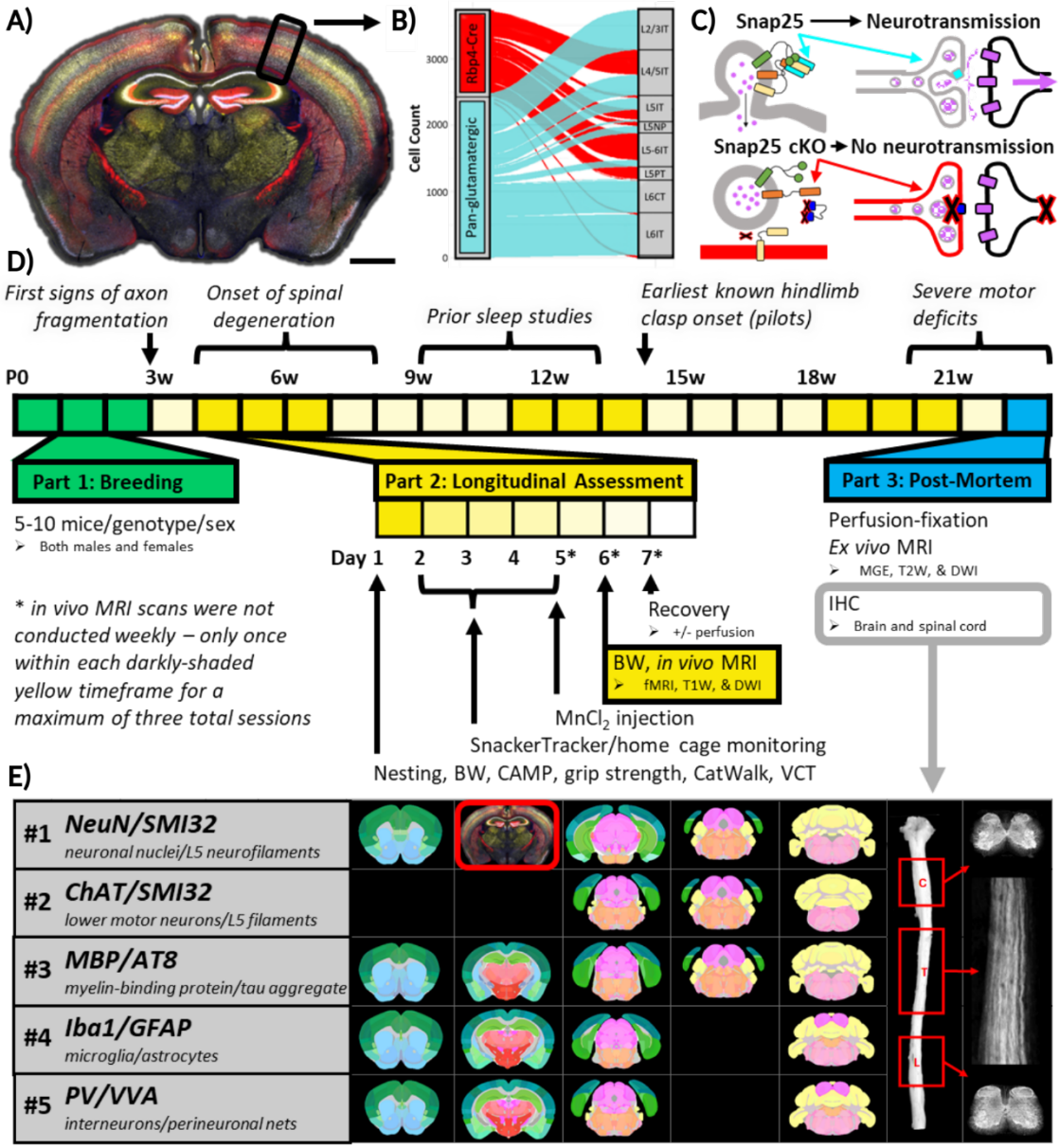


**Figure 4.** Summarises STAMINA study design. This includes the A-C) genetic model and D-E) longitudinal strategy. A) Illustrates coronal *Rbp4*-Cre expression (*Rbp4*-Cre=red, DAPI=blue, NEUN=white, SMI32=yellow). B) Describes L5 projections, highlighting *Rbp4*-Cre L5 pyramidal tract selectivity compared to pan-glutamatergic drivers from Allan Brain Atlas open-source datasets[143]. C) *Rbp4*-Cre neurons in cKO animals cannot communicate with downstream target neurons due to *Snap25* truncation (**A.1.2**). D) Depicts the longitudinal experiment conducted: green=breeding strategy; yellow=repeated measures of nesting behaviour, body weight, CAMP, grip strength, gait (CatWalk), the visual cliff test (VCT), home cage activity and feeding (*SnackerTracker*), and $MnCl_2$ injection preceding *in vivo* MRI (T1W, DWI, and fMRI); and blue = perfusion-fixation for *ex vivo* MRI (T2W, DWI, and MGE/QSM) followed by brain and spinal cord IHC. E) IHC involves five stain combinations (#1-5, each also including DAPI and *Rbp4*-Cre-RFP) and strategically selected brain and spinal cord sections for each[32, 77, 179]. The red box highlights a sample stain output corresponding to the enlarged image in A). Chapter 2 subsections provide detailed descriptions of each study component. IT=intratelencephalic; NP=non-pyramidal; PT=pyramidal tract; CT=corticothalamic; and BW=body weight.

# Chapter 2: Methods

## 2.1 Animal models, experiments, and statistics summary

### *2.1.1 Compliance*

All UK-based studies comply with the UK Animals (Scientific Procedures) Act (1986), Oxford's Policy on the Use of Animals in Scientific Research, and the ARRIVE guidelines 2.0[276]. Procedures were approved by Oxford's Animal Welfare and Ethical Review Board and performed under valid Study Plans (SP384827), personal licenses (PIL-I84222165), and project licenses (PPL-PP0546018, PPL-P828B64BC, PPL-PP0911346, PPL-PP9610226, PPL-PP6154904, and PPL-P78348294). Work conducted at Charité Universitätsmedizin Berlin, including mouse tissue collection for PTEN studies and human tissue collection for morphometric analyses, were approved by local ethics committees (EA2/111/14, EA2/064/22, EA4/206/20, and EA2/086/20). Human data were anonymised for the purpose of this thesis and provided as blinded image stacks; further details (including subject metadata) will be provided in the resulting publication.

### *2.1.2 Breeding and maintenance*

I conducted animal experiments in Oxford at the Biological Sciences Building. Facilities maintained specific pathogen free conditions as monitored via serology, parasitology, and bacteriology reports from Surrey Diagnostics Ltd. (Cranleigh, SRY, UK). No animals with records of previous regulated procedures were used. Genotyping was conducted by Transnetyx (Cordova, TN, USA) using probes designed for each gene. Details regarding forward/reverse primer and reporter sequences are commercially sensitive, however gene names for reference or future inquiry include: *Snap25*-9 FL; *Snap25*-9 WT; Cre; Rosa WT; and Rosa-Ai-LSL FL. All mice were bred on a C57BL/6J background and singly-housed in standard open-top-cages under 12:12h light-dark conditions within light-tight chambers (LTCs), save CRY-deficient mice (**2.1.3**)[249] which were housed in digitally ventilated cages (DVCs) under either 12:12h cycles or

constant darkness via Leddy lighting (Tecniplast, Buguggiate, VA, Italy)[277]. Djungarian hamsters (*Phodopus sungorus*) were singly housed in open-top-cages within Faraday LTCs, where LEDs established 16:8h light-dark cycles for 'summer' photoperiods and 8:16h light-dark cycles for 'winter' photoperiods. Animals were provided *ad libitum* food and water and underwent daily welfare monitoring. Mice featuring PTEN mutations were bred and maintained at Charité Universitätsmedizin Berlin; brains were dissected before transport to Oxford for histology.

### *2.1.3 Experimental and genetic conditions*

**Figure 5** illustrates L5-6b manipulations, while **Table 8**-**Table 9** summarise genetic models used in this thesis. **A.2** lists animal metadata including age, body weight, and the number of experimental and technical replicates ($N_E/N_T$) throughout. I used both male and female mice, unless otherwise indicated, with age- and sex-matched littermate CTRLs where possible.

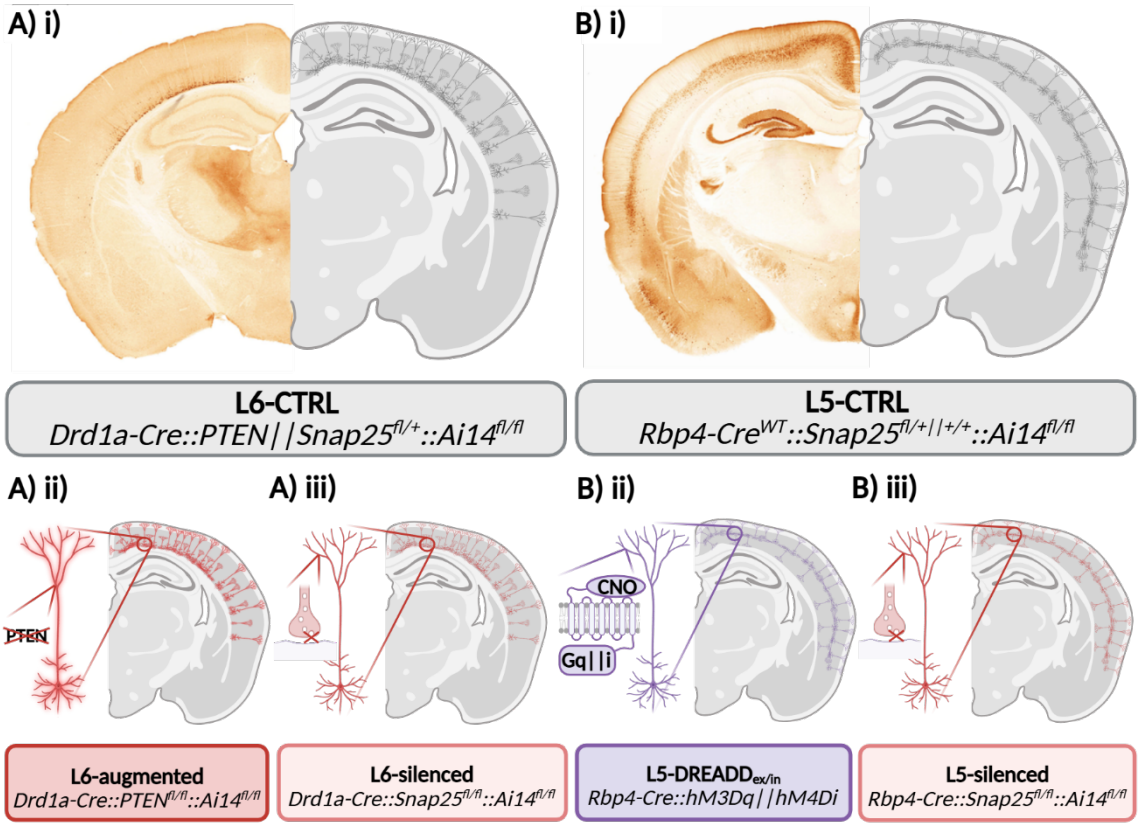


**Figure 5.** L5-6 Cre-expression and genetic conditions. Expected A) *Drd1a*-Cre (ID=65835) and B) *Rbp4*-Cre (ID=67801) expression is shown via i) GENSAT X-gal staining[278]. Mutations involve A) ii) PTEN manipulation (**A.1.1**), A-B) iii) *Snap25* truncation (**A.1.2**), and B) ii) DREADD activation/silencing (**A.1.3**). See **Table 9** for genotype details. ex=excitatory; in=inhibitory.

**Table 8.** Study conditions and expected outputs across experiments in this thesis. All involve mature adult male and female mice unless otherwise noted for STAMINA experiments. Relevant underlying mechanistic explanations and study metadata are indexed accordingly. LD=standard 12:12hr light-dark conditions; DD=constant darkness. See ***Table 9** for genotype details, and ****Table 10** for sample metadata per experimental condition.

| Experiment Details | Genotype* | Condition** | Primary Outputs |
|---|---|---|---|
| ***SnackerTracker* validation and *TracKIT* development:** Test whether the device can identify changes in food intake and feeding behaviour (**1.5.1**); datasets are also used to develop *TracKIT* (**1.5.2, 3.2**) | CRY-WT (CTRL) | LD | **Food intake** (i.e., the mass of food consumed) **and feeding behaviour** (i.e., interactions with the feeding device which do not necessarily involve food consumption) |
| | | DD | |
| | CRY-deficient[249] | LD | |
| | | DD | |
| | WT C57BL/6J | LD | |
| | | DLE | |
| | WT hamster | Summer | |
| | | Winter | |
| **r-QUINT validation:** Test whether QUINT revisions are accurate and can identify changes in cell densities or distributions following acute genetic manipulations (**1.5.3, 4.2**) | *Drd1a*-Cre$^{WT}$ CTRLs | N/A | ***Drd1a* and PV/VVA densities and distributions** for comparison to published datasets[261, 262] and across experimental conditions. DREADD activation/inhibition was confirmed via cFos immunostaining |
| | Excitatory DREADDs (**A.1.3**) | CNO [10mg/kg] | |
| | | Saline | |
| | Inhibitory DREADDs (**A.1.3**) | CNO [1mg/kg] | |
| | | Saline | |
| **L6 subtype characterisation:** Analyse pan-cortical *Drd1a* subtype densities and distributions under augmented, silenced, and CTRL states (**1.5.4**, **4.3**) | *Drd1a*-PTEN-cKO (L6-augmented) (**1.2.2**) | N/A | **PV/VVA and *Drd1a*/CPLX3 densities and distributions** (including colocalisation) |
| | *Drd1a*-PTEN-CTRL | | |
| | *Drd1a-Snap25*-cKO (L6-silenced) (**1.2.3**) | | ***Drd1a*/CPLX3 densities and distributions** (including colocalisation analyses) |
| | *Drd1a-Snap25*-CTRL | | |
| **L6b morphometrics:** Evaluate mouse L6b vs human WMIN analogousness (**1.5.4, 4.4**) | *Drd1a*-CTRL | N/A | **Neurite traces and soma characteristics** (including branch analyses) |
| **STAMINA:** Characterise effects of L5-silencing on neuromotor degeneration in a longitudinal multimodal study involving behavioural, neuroimaging, and histology data (**1.5.5, 5.1-5**) | *Rbp4-Snap25*-cKO (L5-silenced) (**1.2.3**) | 4-7wks; 11-14wks; 18-21wks | **Behavioural capacity** (food intake and feeding activity, nesting, visual acuity, motor performance, gait, and grip strength); **MRI signatures** (*in vivo* T1W, DWI, and fMRI followed by *ex vivo* T2W, DWI, and MGE/QSM); and **cell densities and distributions** (*Drd1a* with NEUN/SMI32, CHAT/SMI32, MBP/AT8, IBA1/GFAP, and PV/VVA) |
| | *Rbp4-Snap25*-CTRL | 4-7wks; 11-14wks; 18-21wks | |
| **L5 subtype comparison:** Characterise L5-silencing via tamoxifen Cre estrogen receptor induction in *Fezf2* drivers to compare to *Rbp4* results (**1.5.5, A.8.5**) | *Fezf2-Snap25*-cKO (L5-silenced via Cre-induction) | 4wks and 8wks post-tamoxifen | **Cell densities and distributions** (*Drd1a* with NEUN/SMI32, CHAT/SMI32, MBP/AT8, IBA1/GFAP, and PV/VVA, all including colocalisations) |
| | *Fezf2-Snap25*-CTRL (not silenced via Cre-induction) | 4wks and 8wks post-tamoxifen | |

**Table 9.** Lists experimental genotypes and parental crosses where applicable. All mice were bred on a C57BL/6J background. PTEN-cKO and PTEN-CTRL brains were provided by Dr. Britta Eickholt. *Rbp4*-Cre males cannot be used for breeding due to brief germline Cre-expression and global off-target effects. *Rbp4*-Cre::*Snap25*$^{fl/fl}$ females cannot be used for breeding due to detrimental maternal behaviour (e.g., late time to first litter, and dams drag pups out of the nest to die).

| Target | Modification (name) | Genotype | Parental cross (supplier) | |
|---|---|---|---|---|
| ***Rbp4 (L5)*** | Acute L5 activation (excitatory DREADDs) | *Rbp4*-Cre$^{+}$::hM3Dq | ♀ | Tg(*Rbp4*-cre)KL100Gsat/Mmucd (***Rbp4*-Cre driver**; GENSAT, No: *Rbp4*_KL100) |
| | | | ♂ | B6.129-Gt(ROSA)26Sor$^{tm1(CAG-CHRM4*,-mCitrine)Ute}$/J (**hM3Dq**; Jackson Lab., No: 026219) |
| | Acute L5 inhibition (inhibitory DREADDs) | *Rbp4*-Cre$^{+}$::hM4Di | ♀ | Tg(*Rbp4*-cre)KL100Gsat/Mmucd (***Rbp4*-Cre driver**; GENSAT, No: *Rbp4*_KL100) |
| | | | ♂ | B6N;129-Tg(CAG-CHR3*, mCitrine)1Ute/J (**hM4Di**; Jackson Lab., No: 026220) |
| | L5 driver-line control (CTRL DREADD ) | *Rbp4*-Cre$^{+}$::Ai14$^{fl/fl}$ | ♀ | Tg(*Rbp4*-cre)KL100Gsat/Mmucd (***Rbp4*-Cre driver**; GENSAT, No: *Rbp4*_KL100) × B6;129S6-Gt(ROSA)26Sor$^{tm14(CAG-tdTomato)Hze}$/J (**Ai14/Ai14**; Jackson Lab., No. 007908) |
| | | | ♂ | B6;129S6-Gt(ROSA)26Sor$^{tm14(CAG-tdTomato)Hze}$/J (**Ai14/Ai14**; Jackson Lab., No. 007908) |
| | Chronic L5 silenced (L5/*Rbp4*-silenced/cKO) | *Rbp4*-Cre$^{+}$::*Snap25*$^{fl\|+}$::Ai14$^{fl/fl}$ | ♀ | [Tg(*Rbp4*-cre)KL100Gsat/Mmucd (***Rbp4*-Cre driver**; GENSAT, No: *Rbp4*_KL100) × B6-*Snap25*$^{tm3mcw}$ (***Snap25*$^{fl/+}$**, from Dr. Michael C. Wilson)] × B6;129S6-Gt(ROSA)26Sor$^{tm14(CAG-tdTomato)Hze}$/J (**Ai14**; Jackson Lab., No. 007908) |
| | Chronic L5-heterozygote control (L5/*Rbp4*-CTRL) | *Rbp4*-Cre$^{+}$::*Snap25*$^{fl/+}$::Ai14$^{fl/fl}$ | | |
| | Chronic L5 Cre$^{WT}$ control (L5/*Rbp4*-CTRL) | *Rbp4*-Cre$^{-}$::*Snap25*$^{fl/fl\|+}$::Ai14$^{fl/fl}$ | ♂ | B6-*Snap25*$^{tm3mcw}$ (***Snap25*$^{fl/fl}$**, from Dr. Michael C. Wilson)] × B6;129S6-Gt(ROSA)26Sor$^{tm14(CAG-tdTomato)Hze}$/J (**Ai14/Ai14**; Jackson Lab., No. 007908) |
| ***Drd1a (L6)*** | Chronic L6 silenced (L6/*Drd1a*-silenced/*Snap25*-cKO) | *Drd1a*-Cre$^{+}$::*Snap25*$^{fl/fl}$::Ai14$^{fl/fl}$ | ♀ | [Tg(*Drd1a*-cre)FK164Gsat/Mmucd (***Drd1a*-Cre driver**; MMRRC, No: 30781) × B6-*Snap25*$^{tm3mcw}$ (***Snap25*$^{fl/fl}$**, from Dr. Michael C. Wilson)] × B6;129S6-Gt(ROSA)26Sor$^{tm14(CAG-tdTomato)Hze}$/J (**Ai14**; The Jackson Laboratory, No. 007908) |
| | Chronic L6 *Snap25* heterozygous and Cre$^{WT}$ CTRL (L6/*Drd1a Snap25*-CTRL,) | *Drd1a*-Cre$^{+/WT}$::*Snap25*$^{fl/+}$::Ai14$^{fl/fl}$ | ♂ | B6-*Snap25*$^{tm3mcw}$ (***Snap25*$^{fl/fl}$**, from Dr. Michael C. Wilson)] × B6;129S6-Gt(ROSA)26Sor$^{tm14(CAG-tdTomato)Hze}$/J (**Ai14/Ai14**; Jackson Lab., No. 007908) |
| | Chronic L6 augmented ('L6/*Drd1a*-augmented/PTEN-cKO') | *Drd1a*-Cre$^{+}$::PTEN$^{fl/fl}$::Ai14$^{fl/fl}$ | ♀ | [Tg(*Drd1a*-cre)FK164Gsat/Mmucd (***Drd1a*-Cre driver**; MMRRC, No: 30781) × B6.129S4-Pten$^{tm1hwu}$/J (**PTEN$^{fl/fl}$**; The Jackson Laboratory, No. 006440)] × B6;129S6-Gt(ROSA)26Sor$^{tm14(CAG-tdTomato)Hze}$/J (**Ai14**; Jackson Lab., No. 007908) |
| | Chronic L6 PTEN het control ('L6/*Drd1a*-control/PTEN-CTRL') | *Drd1a*-Cre$^{+}$::PTEN$^{fl/+}$::Ai14$^{fl/fl}$ | ♂ | B6.129S4-Pten$^{tm1hwu}$/J (**PTEN$^{fl/fl}$**; The Jackson Laboratory, No. 006440) × B6;129S6-Gt(ROSA)26Sor$^{tm14(CAG-tdTomato)Hze}$/J (**Ai14/Ai14**; Jackson Lab., No. 007908) |
| ***CRY*** | Disrupted circadian clock ('CRY-deficient') | *Cry1*$^{tm1Jhjh/tm1Jhjj}$;*Cry2*$^{tm1Jhjh/tm1Jhjj}$ | ♀ | *Cry1*$^{tm1Jhjh/tm1Jhjj}$;*Cry2*$^{tm1Jhjh/tm1Jhjj}$ |
| | | | ♂ | *Cry1*$^{tm1Jhjh/tm1Jhjj}$;*Cry2*$^{tm1Jhjh/tm1Jhjj}$ |
| | Intact circadian clock ('CRY-WT/CTRL') | C57BL/6J | ♀ | C57BL/6J |
| | | | ♂ | C57BL/6J |
| ***N/A*** | Altered photoperiods ('summer' or winter' hamsters) | WT | Djungarian hamsters (Phodopus sungorus) are from the breeding colony of Dr. Herwig at Ulm University who are descendants of animals caught near Omsk, Western Siberia[257] | |

### *2.1.4 Replicates and metadata*

**Table 10** lists replicate metadata across experiments in this thesis. Statistical test details are provided in **2.1.5**, and results in **A.2**. See **2.2-2.5** for experiment-specific information.

**Table 10.** Lists animal replicate information for each experiment in this thesis. See ***Table 8** for study details and ****Table 9** for genotype information. N in brackets indicate those kept following quality control checks. *Single neurons=$N_E$, though multiple neurons were often recorded from the same subject. In the age column, the maximum number of within-subject measurements are indicated in brackets. **Awaiting provision by collaborators. †Data for **Figure 41**-**46** (chapter 5 behaviour) are binned by age for comparison to longitudinal plots and to show how many mice proceeded through each week of the longitudinal study (many being introduced at intermediate ages, and some being culled <21wks). ‡Depicts the total number of animals employed within the three timeframes outlined in **Figure 4** for **Figure 47**-**49** (chapter 5 *in vivo* neuroimaging), **Figure 50**-**60** (chapter 5 *ex vivo* neuroimaging), and **Figure 61**-**76** (chapter 5 histology, where $N_T$ indicates the number of replicate slices per AP level and stain combination in **Figure 4**). Note that L5-CTRLs include both *Rbp4* heterozygote CTRLs and *Rbp4*-$Cre^{WT}$-CTRLs for behavioural and neuroimaging experiments, yet only heterozygote CTRLs for histology as RFP expression is required for *Rbp4*-Cre quantifications. Also note that histology and *ex vivo* neuroimaging cohorts are not identical; some brains were not scanned *ex vivo* and proceeded directly to histology. Complete STAMINA metadata are provided in **A.2**. N/A=not applicable; M=male; F=female; Ch=chapter; !=sensitive; ×=insensitive; Pyr=pyramidal; NPyr=non-pyramidal.

| Ch | Figure | Condition | $N_E$ | $N_T$ | Age (wks) |
|---|---|---|---|---|---|
| 3 | Figure 11-13 | light-dark/CRY-WT, F | 3 | N/A | Adult (>10) |
| | | light-dark/CRY-deficient, F | 3 | N/A | Adult (>10) |
| | | constant-darnkess/CRY-WT, F | 3 | N/A | Adult (>10) |
| | | constant-darkness/CRY-deficient, F | 3 | N/A | Adult (>10) |
| | | light-dark/CRY-WT, M | 3 | N/A | Adult (>10) |
| | | light-dark/CRY-deficient, M | 3 | N/A | Adult (>10) |
| | | constant-darkness/CRY-WT, M | 3 | N/A | Adult (>10) |
| | | constant-darkness/CRY-deficient, M | 3 | N/A | Adult (>10) |
| | Figure 14 | CTRL, M (C57BL/6J) | 3 (2) | N/A | Adult (>10) |
| | | CTRL, F (C57BL/6J) | 3 | N/A | Adult (>10) |
| | | DLE, M (C57BL/6J) | 2 (1) | N/A | Adult (>10) |
| | | DLE, F (C57BL/6J) | 3 | N/A | Adult (>10) |
| | Figure 15 | Summer (WT hamster), M | 1 | N/A | Adult |
| | | Winter (WT hamster), M | 1 | N/A | Adult |
| 4 | Figure 20A-C | r-QUINT, PTEN-CTRL, M | 2 | 4 | 10.9±0.7 |
| | | r-QUINT, PTEN-CTRL, F | 1 | 4 | 10.9±0.7 |
| | Figure 20A-B | qBrain, PV-Cre;GFP, M | 5 | 270/50µm | Adult (>10) |
| | | qBrain, PV-Cre;GFP, F | 5 | 270/50µm | Adult (>10) |
| | Figure 20C, Figure 30 | ImageJ, PTEN-CTRL, M | 3 | 3 | 10.9±0.7 |
| | | ImageJ, PTEN-CTRL, F | 1 | 3 | 10.9±0.7 |
| | Figure 21 | PTEN-CTRL, M | 2 | 4 | 10.9±0.7 |
| | | PTEN-CTRL, F | 1 | 4 | 10.9±0.7 |
| | Figure 22-23 | Excitatory DREADD, CNO [10mg/kg] | 3 | 3 | Adult (~7) |
| | | Inhibitory DREADD, Saline | 3 | 3 | Adult (~7) |

| | | | | | |
|---|---|---|---|---|---|
| | **Figure 22**, **Figure 24** | Inhibitory DREADD, CNO [1mg/kg] | 2 | 3 | Adult (~7) |
| | | Inhibitory DREADD, Saline | 2 | 3 | Adult (~7) |
| | **Figure 25** | L6-*Snap25*-CTRL, M | 3 | 3 | 11±0.48 |
| | **Figure 25-29** | L6-*Snap25*-cKO, M | 5 | 3 | 10.6±0.39 |
| | **Figure 25-30** | L6-PTEN-CTRL, M | 2 | 4 | 10.9±0.7 |
| | | L6-PTEN-CTRL, F | 1 | 4 | 10.9±0.7 |
| | | L6-PTEN-cKO, M | 2 | 4 | 10.9±0.7 |
| | | L6-PTEN-cKO, F | 1 | 4 | 10.9±0.7 |
| | **Figure 31-34** | Mouse *Drd1a*-Cre+ ORX-! Pyr | 7 | ≤4* | NA** |
| | | Mouse *Drd1a*-Cre+ ORX-× Pyr | 1 | 1 | NA** |
| | | Mouse *Drd1a*-Cre+ ORX-! NPyr | 2 | 1 | NA** |
| | | Mouse *Drd1a*-Cre+ ORX-× NPyr | 0 | 0 | NA** |
| | | Human ORX-! Pyr | 26 | ≤6* | NA** |
| | | Human ORX-× Pyr | 7 | 1 | NA** |
| | | Human ORX-! NPyr | 7 | 1 | NA** |
| | | Human ORX-× NPyr | 11 | ≤4* | NA** |
| **5** | **Figure 36A,C** | Prior, *Rbp4*-Cre$^{WT}$-CTRL, M | 8 | N/A | 12.2±0.8 |
| | | Prior, *Rbp4*-Cre$^{+}$-CTRL, M | 5 | N/A | 14.8±1.7 |
| | | Prior, *Rbp4*-Cre$^{+}$-cKO, M | 12 | N/A | 12.9±0.8 |
| | **Figure 36B,D, Figure 37-39** | Pilot, *Rbp4*-Cre$^{WT}$-CTRL, M | 10 (3) | N/A | 19.2±1.14 |
| | | Pilot, *Rbp4*-Cre$^{WT}$-CTRL, F | 2 | N/A | 18.5±1.50 |
| | | Pilot, *Rbp4*-Cre$^{+}$-CTRL, M | 3 (2) | N/A | 19.0±0.9 |
| | | Pilot, *Rbp4*-Cre$^{+}$-CTRL, F | 2 (0) | N/A | 34.0±0.0 |
| | | Pilot, *Rbp4*-Cre$^{+}$-cKO, M | 2 (1) | N/A | 20.0±0.5 |
| | | Pilot, *Rbp4*-Cre$^{+}$-cKO, F | 3 (2) | N/A | 21.0±1.9 |
| | **Figure 40** | L5-CTRL, 11-13wks, M | 1 | N/A | 12.6±0.0 |
| | | L5-CTRL, 11-13wks, F | 2 | N/A | 13.5±0.1 |
| | | L5-CTRL, 14-16wks, M | 6 (4) | N/A | 14.7±0.2 |
| | | L5-CTRL, 14-16wks, F | 2 | N/A | 14.4±0.4 |
| | | L5-CTRL, 17-19wks, M | 6 (5) | N/A | 17.9±0.4 |
| | | L5-CTRL, 17-19wks, F | 9 (5) | N/A | 17.8±0.4 |
| | | L5-CTRL, 20-22wks, M | 5 | N/A | 20.5±0.4 |
| | | L5-CTRL, 20-22wks, F | 5 | N/A | 20.9±0.4 |
| | | L5-cKO, 11-13wks, M | 2 | N/A | 12.9±0.3 |
| | | L5-cKO, 11-13wks, F | 4 (3) | N/A | 12.3±0.4 |
| | | L5-cKO, 14-16wks, M | 2 (1) | N/A | 14.1±0.2 |
| | | L5-cKO, 14-16wks, F | 2 (1) | N/A | 14.1±0.2 |
| | | L5-cKO, 17-19wks, M | 4 (3) | N/A | 18.2±0.4 |
| | | L5-cKO, 17-19wks, F | 5 | N/A | 18.4±0.2 |
| | | L5-cKO, 20-22wks, M | 5 | N/A | 20.4±0.2 |
| | | L5-cKO, 20-22wks, F | 6 | N/A | 20.3±0.3 |
| | **Figure 41-46†** | 3wks (CTRL-M/CTRL-F/cKO-M/cKO-F) | 5/2/1/3 | N/A | 3.0-3.9 |
| | | 4wks (CTRL-M/CTRL-F/cKO-M/cKO-F) | 5/2/1/3 | N/A | 4.0-4.9 |
| | | 5wks (CTRL-M/CTRL-F/cKO-M/cKO-F) | 4/4/1/2 | N/A | 5.0-5.9 |
| | | 6wks (CTRL-M/CTRL-F/cKO-M/cKO-F) | 4/4/1/2 | N/A | 6.0-6.9 |
| | | 7wks (CTRL-M/CTRL-F/cKO-M/cKO-F) | 4/4/1/2 | N/A | 7.0-7.9 |
| | | 8wks (CTRL-M/CTRL-F/cKO-M/cKO-F) | 8/7/4/3 | N/A | 8.0-8.9 |
| | | 9wks (CTRL-M/CTRL-F/cKO-M/cKO-F) | 8/7/3/3 | N/A | 9.0-9.9 |

| | | | | | |
|---|---|---|---|---|---|
| | | 10wks (CTRL-M/CTRL-F/cKO-M/cKO-F) | 8/8/4/3 | N/A | 10.0-10.9 |
| | | 11wks (CTRL-M/CTRL-F/cKO-M/cKO-F) | 8/8/4/3 | N/A | 11.0-11.9 |
| | | 12wks (CTRL-M/CTRL-F/cKO-M/cKO-F) | 7/8/4/3 | N/A | 12.0-12.9 |
| | | 13wks (CTRL-M/CTRL-F/cKO-M/cKO-F) | 7/7/4/3 | N/A | 13.0-13.9 |
| | | 14wks (CTRL-M/CTRL-F/cKO-M/cKO-F) | 6/6/4/2 | N/A | 14.0-14.9 |
| | | 15wks (CTRL-M/CTRL-F/cKO-M/cKO-F) | 6/5/4/1 | N/A | 15.0-15.9 |
| | | 16wks (CTRL-M/CTRL-F/cKO-M/cKO-F) | 6/5/4/2 | N/A | 16.0-16.9 |
| | | 17wks (CTRL-M/CTRL-F/cKO-M/cKO-F) | 6/3/4/2 | N/A | 17.0-17.9 |
| | | 18wks (CTRL-M/CTRL-F/cKO-M/cKO-F) | 4/3/5/2 | N/A | 18.0-18.9 |
| | | 19wks (CTRL-M/CTRL-F/cKO-M/cKO-F) | 4/1/5/2 | N/A | 19.0-19.9 |
| | | 20wks (CTRL-M/CTRL-F/cKO-M/cKO-F) | 4/1/5/2 | N/A | 20.0-20.9 |
| | | 21wks (CTRL-M/CTRL-F/cKO-M/cKO-F) | 4/1/5/1 | N/A | 21.0-21.9 |
| | **Figure 47-49‡** | 4-7wks, CTRL-M | 4 | N/A | 5.0±0.5 |
| | | 4-7wks, CTRL-F | 3 | N/A | 5.5±0.6 |
| | | 4-7wks, cKO-M | 1 | N/A | 6.1±0.0 |
| | | 4-7wks, cKO-F | 2 | N/A | 5.1±0.8 |
| | | 11-14wks, CTRL-M | 7 | N/A | 13.5±0.3 |
| | | 11-14wks, CTRL-F | 8 (7) | N/A | 13.4±0.4 |
| | | 11-14wks, cKO-M | 4 (3) | N/A | 13.4±0.6 |
| | | 11-14wks, cKO-F | 3 | N/A | 13.6±0.5 |
| | | 18-21wks, CTRL-M | 6 (5) | N/A | 19.8±0.8 |
| | | 18-21wks, CTRL-F | 3 | N/A | 19.3±1.1 |
| | | 18-21wks, cKO-M | 5 | N/A | 20.9±0.4 |
| | | 18-21wks, cKO-F | 2 | N/A | 19.9±1.5 |
| | **Figure 50-60‡** | 4-7wks, CTRL-M | 1 (0) | N/A | 4.3±0.0 |
| | | 4-7wks, CTRL-F | 0 | N/A | 0.0±0.0 |
| | | 4-7wks, cKO-M | 1 (0) | N/A | 4.3±0.0 |
| | | 4-7wks, cKO-F | 1 (0) | N/A | 4.3±0.0 |
| | | 11-14wks, CTRL-M | 2 | N/A | 12.6±1.2 |
| | | 11-14wks, CTRL-F | 3 | N/A | 13.5±0.2 |
| | | 11-14wks, cKO-M | 0 | N/A | 0.0±0.0 |
| | | 11-14wks, cKO-F | 2 | N/A | 13.5±0.3 |
| | | 18-21wks, CTRL-M | 5 | N/A | 20.3±1.8 |
| | | 18-21wks, CTRL-F | 5 (4) | N/A | 18.3±1.9 |
| | | 18-21wks, cKO-M | 5 (4) | N/A | 21.4±0.6 |
| | | 18-21wks, cKO-F | 2 | N/A | 20.8±0.9 |
| | **Figure 61-76‡** | 4-7wks, CTRL-M | 6 (0) | 2 | 5.4±0.7 |
| | | 4-7wks, CTRL-F | 1 (0) | 2 | 4.0±0.0 |
| | | 4-7wks, cKO-M | 2 (0) | 2 | 5.8±1.5 |
| | | 4-7wks, cKO-F | 5 (0) | 2 | 6.1±0.8 |
| | | 11-14wks, CTRL-M | 2 (0) | 2 | 12.6±0.9 |
| | | 11-14wks, CTRL-F | 3 (0) | 2 | 13.5±0.1 |
| | | 11-14wks, cKO-M | 0 (0) | 0 | 0.0±0.0 |
| | | 11-14wks, cKO-F | 3 (0) | 2 | 13.5±0.1 |
| | | 18-21wks, CTRL-M | 8 (1) | 2 | 20.1±0.7 |
| | | 18-21wks, CTRL-F | 7 (0) | 2 | 20.7±0.7 |
| | | 18-21wks, cKO-M | 7 (1) | 2 | 20.6±0.7 |
| | | 18-21wks, cKO-F | 6 (0) | 2 | 21.4±0.8 |

### *2.1.5 Statistical conventions and software*

**2.2-2.5** provide test-specific details, yet the below conventions apply throughout. T-values are reported as $t_{(df)}$ for t-tests and F-values as $F_{(DFn,DFd)}$ for regressions and analyses of variance (ANOVA). Significance is defined as $p<\alpha=0.05$, and power as $(1-\beta)=0.8$. Effect sizes (d) are deemed very small (≤0.2), small (0.2-0.5), moderate (0.5-0.8), or large (>0.8). I report data as mean ($\bar{x}$) ± standard error ($\sigma_M$). I used G*Power (v3.1.9.7)[279] for *a priori* and *post hoc* power calculations. GraphPad Prism (v10.2, Dotmatics Ltd., Bishop's Stortford, HRT, UK) generated all statistical results save *SnackerTracker* effect sizes (**2.2**) which I analysed via MATLAB (R2024b, v9.13, The MathWorks Inc., Natick, MA, USA) and neuroimaging outputs (**2.5**) via R (v.4.3.2) (**2.5.5**). $r^2$ quantified spread following least-squares (lsq) linear regression constrained at Y=0. I tested the significance of Pearson's correlations against null hypotheses of X=Y. Two-way and three-way ANOVA employed corrections for multiple comparisons using the Šidák method, the Holm-Šidák method, or by controlling false discovery rate using the two-stage step-up of Benjamini, Krieger and Yekutieli. **Table 11** lists methods employed per figure in this thesis, save for neuroimaging experiments (see **2.5.5** and **A.10.19**). I checked Gaussian distributions using QQ plots and Shapiro-Wilk normality tests, and variance by homoscedasticity plots.

**Table 11.** Lists statistical tests across experiments. BKY=two-stage setup procedure of Benjamini, Krieger, and Yekutieli; SM=Šidák method; and HSM=Holm-Šidák method.

| **Test** | **Comparisons** | **Figures** |
|---|---|---|
| Pearson's correlation | - | Figure 11 |
| Student's t-test | - | Figure 12, Figure 14 |
| Cohen's d | - | Figure 23B,E,H |
| Regression | - | Figure 20A-B |
| Two-way ANOVA | SM | Figure 20C, Figure 36 |
| Two-way ANOVA | HSM | Figure 21B,D, Figure 37E-N |
| Two-way ANOVA | BKY | Figure 22E-H, Figure 23B,E,H, Figure 24B,E,H, Figure 25E,F, Figure 26C, Figure 27, Figure 28, Figure 29, Figure 30 |
| Three-way ANOVA | - | Figure 21B,D, Figure 22E-H, Figure 23A,D,G, Figure 24A,D,G, Figure 37 |
| Three-way ANOVA | SM | Figure 13, Figure 33, Figure 34 |
| Repeated measures three-way ANOVA | BKY | Figure 41, Figure 42I-N, Figure 43A-E, Figure 44, Figure 45A-B, Figure 46A-D, L-M |

## 2.2 *SnackerTracker* development and validation

### *2.2.1 Construction*

*SnackerTracker* construction is described in protocols.io[280], in the manuscript[211], and in **A.3** which provides: the bill of materials (**A.3.1**); optimised Ultimaker S3 3D printer (v5.1.0, Ultimaker BV, Utrecht, NL) (**A.3.2**); chassis objects and schematics I created using TinkerCAD (v2022, AutoDesk Inc., San Francisco, USA), mesh-corrected using MeshLab (v2022.02, ISTI-CNR, Pisa, IT), visualised using BabylonJS (v5.3.0, BabylonJS, San Diego, USA), animated using Maya (v2024.1, AutoDesk, San Francisco, USA), and sketched using FreeCAD (v0.21.1) (**A.3.3**); and electronics schematics I created using CircuitDiagram (v2023, https://www.circuit-diagram.org/) (**A.3.4**). I trimmed and buffered chassis elements with acetone upon print completion. See **A.3.5** for device assembly details and videos. I developed operational software using the Arduino Editor and Integrated Development Environment (v2.0, Arduino, BCMI, Redmond, USA) (**A.10.1**). The project is available via the Arduino Project Hub: https://projecthub.arduino.cc/marissamueller/snackertracker-d86bf3.

### *2.2.2 Preliminary benchtop and in vivo testing*

I conducted benchtop and *in vivo* tests to evaluate device performance for: 1) calibration accuracy (**A.3.6**); 2) drift[281]; 3) timing; 4) LDR function; 5) combined operation; and 6) *in vivo* compatibility including i) accuracy, ii) whether the manner of food presentation impacts feeding behaviour (e.g., cage floor vs suspended from *SnackerTrackers*), and iii) crumbling (**A.3.7**). I cropped recordings from 6) iii) surplus L5-silenced mice (**Preface**) to 48hrs such that 2×24-hour periods could be analysed further (chapter 5). This isolated time in the light phase, dark phase, or at dark/light-onset (i.e., the first three hours after lights turned ‘off’ or ‘on’). I excluded datasets if recordings terminated early due to battery failure, if data failed to read to the microSD card, or if raw traces exhibited significant chipping artifacts (**3.1**).

### *2.2.3 Studies in clock-deficient mice*

I introduced *SnackerTrackers* to CRY-deficient and CRY-WT mice singly housed in DVCs to test whether the *SnackerTracker* could identify changes in feeding behaviour (see **A.4.1** for experimental setups and **1.5.1** for expected results). After >1 day of habituation, I collected 2×48-hour recordings per animal: one under 12:12h conditions, and the other under constant darkness. I recorded the difference between the mass of the *SnackerTracker* with food before and after recordings. DVCs recorded activity across floor regions divided into a 3×4 grid. Upon analyses, I grouped regions to represent whole-cage or mid-cage areas where *SnackerTrackers* were placed. I began and ended recordings after morning welfare inspections. I cropped 48hr recordings to 24hr timelines, beginning at dark-onset where applicable, and thereafter reported outputs in Zeitgeber time for light-dark conditions or circadian time (CT) for constant darkness.

### *2.2.4 Dim light in the evening*

I introduced *SnackerTrackers* to WT mice in open-top-cages in one of two LTCs. Both were set to 12:12h cycles, yet one stimulated DLE with 3h of dim light after 'dark-onset' (**1.5.1**). Passive infrared sensors (PIRs) and *SnackerTrackers* measured activity and feeding (**A.4.2**)[205].

### *2.2.5 Hamsters*

I introduced *SnackerTrackers* to fully adapted Djungarian hamsters maintained under short and long photoperiods (**1.5.1**)[257]. LTCs under both lighting cycles (**2.1.1**, **A.4.3**) were each equipped with 1080P USB IR Night Vision Waterproof Dome Cameras (ELP, Shenzhen, GD, CN) to qualitatively assess whether *SnackerTracker*-recorded feeding behaviour reflected reality[282].

## 2.3 Histological characterisations

### *2.3.1 Biological targets*

I explored expected protein expression patterns, mutations, and pharmacological agents of interest using GeneCards[283], MalaCards[284], and UniProt[285]. Single-cell RNA-sequencing

data from the Allan Brain Atlas was analysed using the Seurat R package (v5.0.0)[142] to compare projections in *Rbp4*-Cre vs pan-glutamatergic lines (Scl17a7-IRES2-Cre/wt;Ai14(RCL-tdT)/wt). That is, *Rbp4*-Cre labels glutamatergic neurons which preferentially target L5 pyramidal tract neurons and bypasses more-pial intratelencephalic neurons (**Figure 4B**)[143]. Expected expression patterns of *Drd1a*/*Rbp4*/*Fezf2* Cre-drivers (**A.5.1**) informed network rationalisation, histological experiment planning, and analyses. **A.5.2** compares mouse/human RNA profiles of cortical layer markers and proteins of interest. Notably, *Rbp4*/*Drd1a* transcriptomics do not match *Rbp4*- and *Drd1a*-Cre profiles[4, 40, 77, 278], so I used GENSAT to predict driver-line expression.

### *2.3.2 Tissue preparation and immunohistochemistry*

Adult mice were anesthetised and culled by intraperitoneal pentobarbital overdose (XVD135, Animalcare, Nether Poppleton, UK) followed by exsanguination and perfusion fixation using 0.01M phosphate buffered saline (PBS, P4417/Sigma-Aldrich, Darmstadt, DE) and 4% paraformaldehyde (PFA diluted in PBS, F8775/Sigma-Aldrich). Tissues were dissected (**Table 12**), post-fixed for 24h in PFA, then stored in 0.01M PBS with 0.05% sodium azide (S2002-25G/Sigma-Aldrich) at 4°C. Brains were embedded in 4.5% agarose, cut 50µm coronally using a vibrating microtome (VT1000S/Leica, Wetzlar, DE), and placed into 24-well plates for storage (**A.5.3**). Spinal cords were processed similarly yet embedded with custom 3D-printed scaffolds which dissolved as encompassing agarose gelatinised. This enabled me to process ≤9 sections simultaneously, expediting slicing 9-fold (**A.5.3**, **A.5.4**). Other organs underwent 30µm cryostat slicing (Jung CM3000/Leica) to evaluate off-target expression[286]. Brain and spinal cord sections at pre-specified AP positions (**Table 13**) were placed in 24-well plates with 500µL/well. I conducted IHC washes/incubations at room temperature on a rotating shaker, beginning with 3×10min washes in 0.01M PBS. For IBA1/GFAP IHC (**Table 13-6**), I incubated sections in PBS with 0.1M glycine (299294/Sigma-Aldrich) for 20min. This quenched aldehydes by neutralising PFA residues and minimising background noise as IBA1/GFAP contrast was otherwise poor. I

followed aldehyde-quenching with a 5min PBS rinse before blocking via 2hrs incubation in Triton™ X-100 (85111/Thermo Scientific™, Waltham, USA) and either normal donkey serum (D9663/Sigma-Aldrich) or normal goat serum (ab7481/Abcam, Cambridge, UK) diluted in PBS. PV/VVA (**Table** 13-**1**) blocking also included 0.15M NaCl and 0.1mM $CaCl_2$ to optimise lectin binding. I then incubated sections with primary antibodies in block solution for 30hrs at 4°C. Thereafter, I washed sections 3×10min in PBS, incubated with secondary antibodies in block solution for 2hrs, washed 3×10min in PBS, incubated with 1:1000 4',6-diamidino-2-phenylindole (DAPI, D1306/Invitrogen, Carlsbad, USA) in PBS for 30min, and finally washed 2×10min in PBS. I mounted tissues with coverslips using 60µL ProLong™ Glass (P36984/Invitrogen) per slide. Across experiments, $N_E$=brains from different mice, and $N_T$=replicate slices from within the same brain. **A.5.5** provides optimised antibody details, concentrations, and incubation times per stain combination. Optimisations were necessary as perfusion and storage of *Rbp4*-Cre *Snap25*-cKO tissues differed from **2.3.1** and followed *ex vivo* MRI protocols (**2.5.2.1**-**2.5.2.2**). Therefore, both previously established (**Table 13-1/2/6**) and yet-untried (**Table 13-1/2/6**) formulae required testing. I conducted optimisations with/without aldehyde quenching and heat-induced epitope retrieval. Epitope retrieval restores fixation-masked antigenicity using heated buffers; I warmed 0.01M pH 6.0 sodium citrate (71402/Sigma-Aldrich) in PBS to 60-65°C, poured solutions into small glass vials, then transferred sections into each vial. I placed glass vials in heated water baths upon shakers, covered with tin foil for protection against light and buffer evaporation, and left them to incubate for 30mins at 60-65°C. This should have been conducted in a designed-for-purpose incubation chamber. I then removed glass vials from water baths and allowed them to cool for 25mins. I returned tissues to 24-well plates and washed 3×5 min before proceeding with blocking and primary incubation. I provide sample optimisation panels in **A.5.6**, finalised protocols in **A.5.5**, initial pilots in **A.5.7**, and target information in **A.5.1** which includes colocalisation descriptions.

**Table 12.** Lists the tissues dissected for each driver line. $Cre^{ER}$=genetically modified estrogen receptor linked to render Cre inducible upon tamoxifen injection.

| Driver Line | Tissues Dissected |
|---|---|
| *Drd1a*-Cre | Brain |
| *Rbp4*-Cre | Brain, spinal cord, liver, pancreas, duodenum, small intestine, and eyes |
| *Fezf2*-$Cre^{ER}$ | Brain and spinal cord |

**Table 13.** Summarises IHC combinations in this thesis. Target, product, and protocols details are provided in **A.5.1** and **A.5.5**. $N_T$=2 for each slice indicated. C=cervical; T =thoracic; and L=lumbar.

| Line | | Target | Slices: Brain | Slices: Spinal Cord |
|---|---|---|---|---|
| *Rbp4* DREADDs | 1 | PV<br>VVA<br>DAPI<br>*Rbp4* | | |
| *Drd1a* PTEN cKO | 1 | PV<br>VVA<br>DAPI<br>*Drd1a* | | |
| | 2 | CPLX3<br>TBR1<br>DAPI<br>*Drd1a* | | |
| *Drd1a Snap25*-cKO | 2 | CPLX3<br>TBR1<br>DAPI<br>*Drd1a* | | |
| *Rbp4*-Cre and *Fezf2*-$Cre^{ER}$ *Snap25*-cKO (Driver=*Rbp4*\|\|*Fezf2*) | 3 | NEUN<br>SMI-32<br>DAPI<br>Driver | | |
| | 4 | CHAT<br>SMI-32<br>DAPI<br>Driver | | |
| | 5 | Mbp<br>AT8<br>DAPI<br>Driver | | |
| | 6 | IBA1<br>GFAP<br>DAPI<br>Driver | | |
| | 1 | PV<br>VVA<br>DAPI<br>Driver | | |

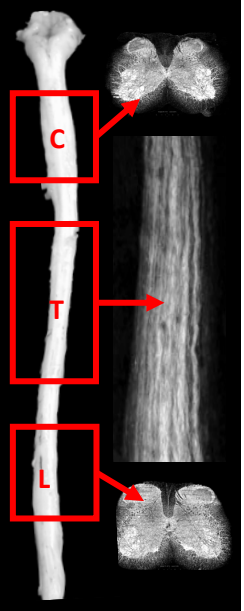

### *2.3.3 Image acquisition and visualisation*

I acquired images with 20X objectives and spinning disk confocal microscopes (SDCM, Olympus SpinSR SoRa, Tokyo, JP) in chapter 4), while chapter 5 involved slice scanning fluorescence microscopy (SSFM, VS200/Evident, Tokyo, JP). cellSens (v4.1.1/Evident) software applied high-density maps for both, yet SSFM employed the VS200 graphical user interface (GUI) (v4.1.2). SDCM and SSCM details following costings (**A.6.1**) and optimisations (**A.6.2**). I visualised outputs using Arivis (for coronal viewing, pilots, and video creation), ImageJ (for ROI extraction and scale bars in *Drd1a* experiments), and Biorender (for all figures) (https://BioRender.com).

### *2.3.4 QUINT image analysis*

#### *2.3.4.1 Pre-processing*

I pre-processed raw .vsi files using a custom Fiji/ImageJ (2.9.0v1.54b) .ijm script (**A.10.3**). This involved importing coronal sections with split channels at a downsampled factor of 4 (Series 3) then applying maximum-intensity z-stack projections, auto-thresholding, and background subtraction. Channels were colourimetrically reassigned, merged, and saved as composite .tiffs.

#### *2.3.4.2 Atlas mapping*

I imported composite .tiffs into QuPath (v0.4.2)[287] where a Groovy script (**A.10.4**) and ImageJ macro (**A.10.6**) exported and converted full-coronal sections as RGB .pngs with 8X-downsampling (yielding a total downsampling factor of 32 given initial 4X-downsampling in **2.3.4.1**) for QuickNII compatibility (RRID:SCR_016854)[221]. For each animal, $N_T$ sections were imported to FileBuilder[221] and merged to .xmls for section alignment and atlas registration in QuickNII (2017 CCFv3)[288]. QuickNII outputted .json anchoring files which I imported into VisuAlign (v0.8 RRID:SCR_017978) for nonlinear refinement. I manually confirmed QuickNII and VisuAlign registrations for each individual section. VisuAlign produced aligned .jsons and .flat atlas brain maps—the combined product of *Atlas Mapping* (**Figure 3**).

### *2.3.4.3 Feature extraction*

Using pre-processed .tiffs from **2.3.4.1**, Groovy scripts from **2.3.4.2** (**A.10.4**-**A.10.5**) detected cells (**A.6.3**-**A.6.4**) and outputted .svg segmentations, all of which I examined manually for accuracy and parameter-readjustment if needed. Multiplexed analyses considered PV/VVA, CPLX3/TBR1, NEUN/SMI-32, NEUN/CHAT, and MBP/AT8 with RFP drivers (**Table 13**). A Fiji/ImageJ .ijm script (**A.10.6**) converted .svgs to binary masks (creating outlines around adjacent detections), inverted pixels, and outputted RGB .pngs[224]. I explored morphometrics in *Drd1a*-Cre PTEN-cKO samples using Arivis (Vision4D/v4.1.2/Arivis AG, Rostock, DE).

### *2.3.4.4 Data registration*

I imported cell detection .pngs, VisuAlign .json files, and VisuAlign .flat maps into Nutil[224]. I defined brain ROIs (**A.5.8**) using a custom Excel sheet (**A.6.4**)[224] and piped these to the Quantifier with masks[220]. The Quantifier generated 3D point cloud .jsons and .csv reports. I visualised .jsons using MeshView (ABA Mouse CCFv3 2017, RRID:SCR_017222).

### *2.3.4.5 Output tagging, re-formatting, and analyses*

A custom MATLAB script reformatted Nutil reports, which tagged morphometrics upon regionalisation (**A.10.7**). I imported outputs to Prism for graphing and analyses. In addition to **A.2**, the two-stage step-up method of Benjamini, Krieger and Yekutieli returned intermediate data which the MATLAB script used to extract pairwise comparisons. Using pooled $\sigma_M$ under assumptions of equal variance, these employed independent samples Student's t-tests and effect size calculations (Cohen's d)[289] for heat map generation.

## *2.3.5 Morphometrics*

### *2.3.5.1 Image acquisition*

Following electrophysiological studies, imaging was conducted by collaborators at Charité - Universitätsmedizin Berlin using a point scanning confocal microscope (PSCM)

(DMi6000B-CS/Leica) to image whole-cells (20X/0.75 oil immersion objective, x-y-z voxel resolution=0.379×0.379×2.00µm$^3$/vx, x-y frame size=2048×2048px). .vsis were acquired using excitation wavelengths of 405nm (UV Diode 405, band=406-458), 488nm (Vis OPSL 488, band≈512-563), 552nm (OPSL 552, band≈579-623), and 638nm (Vis Diode 638, band≈660-673). Adjacent z-stacks were imaged if the maximum x-y frame size could not encompass all branches. Raw .vsis were sent to me for pre-processing and analyses (**2.3.5.2**-**2.3.5.5**).

### *2.3.5.2 Pre-processing*

Neuron pre-processing involved contrast-adjustments, rotations, and cropping. Large cells which could not be contained within a single frame required merging; I padded and truncated adjacent .vsi z-stacks using ImageJ macros (**A.10.8**), then manually expanded canvases and translated images to ensure x/y alignment. I merged and converted resulting images to greyscale .tiffs. I rotated those featuring pyramidal cells such that apical dendrites pointed upwards (**A.10.9**). I saved final .tiffs for subsequent feature extraction and analyses.

### *2.3.5.3 Neurite tracing*

I traced neurites using Image J's semi-automated Simple Neurite Tracer[290]. I saved resulting traces as both .swcs and .traces, and used the reconstruction plotter to export 2D projections as .pngs for visualisation (**A.7.1**). .trace analyses returned branch contraction, length, complexity, convex hull size, and Sholl indices for further processing (**2.3.5.5**). I produced Sholl plots illustrating the number of branch intersections across concentric circles at increasing distances from soma using Sholl Analysis tools (radius step size=2, default normaliser/decay).

### *2.3.5.4 Soma characterisation*

Traced neurons underwent pre-processing, segmentation, and feature-extraction for soma analyses. Images were cropped, converted to 8-bit architecture, and denoised by contrast (windowing≈200-255) and threshold (windowing≈250-255) adjustment. I binarized and filled

thresholded outputs. I segmented images using the *3DSuite-3D Manager* (windowing=128-255) and feature extractions via *3D Measure*. I documented soma volumes, surface areas, compactness, sphericity, and ellipsoid features for further processing.

### *2.3.5.5 Analyses and visualisation*

Analyses involved custom MATLAB scripts (**A.10.10**). These generated group $\bar{x}$, $\sigma_M$, and $N_E$ data for neuron type (pyramidal/nonpyramidal), sensitivity to ORX (sensitive/insensitive); and species (human/mouse) then used .swcs to generate polar plots. I converted cartesian coordinates into polar coordinates relative to soma loci and averaged pixels to generate representative data (**Equation 1**) in 10° bins. Bins represent pixels in one of three manners: 1) by total pixel count, where bins represent branch density; 2) by total pixel distance from the soma, where bins represent arborisation strength; or 3) by average pixel distances, wherein bins indicate how far branches typically terminate from the soma (see **4.4** for more details). I processed datasets independently using each option. I converted select .tiffs and .pngs into .jpegs for stylistic editing in PhotoScapeX (v4.2.1/MOOII Tech, Seoul, KR) and animation using HitFilm Express (v21.1.2.0/FXhome Ltd., Norwich, UK).

$$\partial x_{px} = x_{px} - x_{soma}(+360°) \text{ and } \partial y_{px} = y_{px} - y_{soma}\ (+360°)^{*}$$

$$\theta_{px} = tan^{-1}\left(\frac{\partial y_{px}}{\partial x_{px}}\right)$$

$$d_{px} = \sqrt{\partial {x_{px}}^2 + \partial {y_{px}}^2}$$

$$1)\ V_{bin} = \sum {N_{px}}_{\theta bin};\ 2)\ V_{bin} = \sum {d_{px}}_{\theta bin};\ 3)\ V_{bin} = \sum \frac{d_{px}}{{N_{px}}_{\theta bin}}$$

**Equation 1.** Cartesian to polar coordinate conversion. *360° were added to any negative x- or y-pixel (px) differential ($\partial x_{px}$ and $\partial y_{px}$, respectively), which represents the same angle in the polar coordinate reference frame, to ensure that all values were between 0-360° for subsequent averaging. Values for polar plot bins ($V_{bin}$) can be represented by 1) total pixel counts ($N_{px}$), 2) total pixel distances from the soma ($d_{px}$), or 3) average pixel distances from the soma.

## 2.4 Motor-associated behavioural testing

### *2.4.1 Home cage monitoring*

STAMINA HCM involved *SnackerTracker* measurements, infrared video recordings, and nesting assessments. During *SnackerTracker* optimisations, data from the *Rbp4*-Cre *Snap25*-cKO cohort used to evaluate crumbling and weight loss (**2.2.2**) underwent further quantifications (**5.1.1**). Weekly, I collected seven-day *SnackerTracker* recordings (**1.5.5**, **A.2**), truncated these to five-day traces, and analysed each using *TracKIT* (**A.10.2**). During weekly device resets, I recorded body masses and photographed nests for scoring[291] by a blinded researcher using ImageJ's *Blind Analysis Tools*[223, 292]. At 18-21wks, thermographic recordings additionally monitored body positions/temperatures using Xi 80° Spot Finder Infrared Cameras (Optris, Berlin, BE, DE)[282]. I did not analyse thermography data due to time constraints.

### *2.4.2 Visual cliff test*

Throughout STAMINA, I subjected mice to the VCT using a custom setup and standard procedures[293]. I placed animals in the flat zone and allowed them to freely roam for 5mins. Video recordings were scored using ANY-maze (v7.32, Stoelting, Dublin, IE) for time in the flat-zone, drop-zone, and edge-zone via body tracking rather than head- or tail-derived metrics.

### *2.4.3 Continuous assessment of motor phenotypes*

I conducted CAMP scoring, albeit unblinded, according to predefined criteria[273]. I assigned and summed scores of 0-3 across 4 domains: hindlimb clasping; ledge-walking; gait; and kyphosis. I captured and later anonymised videos so that each could be scored by a blinded researcher using ImageJ's *Blind Analysis Tools*[223, 292].

### *2.4.4 CatWalk*

I subjected L5-silenced and CTRL mice to weekly CatWalk tests (Noldus, Wageningen, NL) throughout STAMINA[294]. Following one week of training and habituation, I placed mice at

one end of the CatWalk platform across which they scurried to return to their home-cage. A compliant run required: minimum duration=0.5s; maximum duration=5.0s; maximum speed variation=60%; and minimum number of compliant runs=$N_T$=3. I averaged successful runs to return weekly metrics per animal ($N_T$) using CatWalkXT v.10.6.608 (RRID:SCR_021262)[274, 275].

### *2.4.5 Grip test*

I tested L5-silenced and CTRL mouse grip strengths weekly during STAMINA using a grip strength meter (San Diego Instruments) according to standard protocols[295]. I obtained and averaged $N_T$=3 measures from each animal per weekly session.

## 2.5 Neuroimaging

### *2.5.1 In vivo MRI acquisition*

#### *2.5.1.1 Animal preparation*

*In vivo* neuroimaging for STAMINA (**1.5.5**) involved acquiring >3 manganese-enhanced MRI scans per L5-silenced and CTRL mouse (i.e., at 4-7wks, 11-14wks, and 18-21wks). While all mice were subjected to the same combination of behavioural tests, *ex vivo* MRI, and histological examination as chronologically detailed in **Figure 4**, only some underwent *in vivo* neuroimaging as listed in **Table 10**. That is, I subjected all mice to tests in the same sequence, along the same timeline, and in the order deemed least to most aversive (i.e., in vivo MRI always following any prior motor or home-cage monitoring). 24hrs prior to *in vivo* scans, I interperitoneally injected mice with 300 mM $MnCl_2 \cdot 4H_2O$ (0.01$\dot{3}$mL/g )[296] (M3634-100G/Sigma-Aldrich) in saline (1300101/Animalcare) for contrast gain before returning them to their home cage.

#### *2.5.1.2 In vivo scanning setup*

Scanning involved anaesthetic induction with 4% isoflurane (30135687/BSB), which I reduced to 0.3-1.6% following 0.1mg/mL medetomidine in saline (30313785/BMS) bolus injection (0.2mg/kg body weight) via subcutaneous catheterisation, and continuous infusion

thereafter (0.4mg/kg/hr). This maintained a target breathing rate of 100-160 breaths/min for fMRI BOLD imaging[297]. I applied Viscotears (21190800/Novartis, Basel, CH) to prevent eye dehydration, and maintained body temperatures around ~36-37°C using a custom blanket and heated cradle with cheek clamps. Scans lasted ≈2hrs45mins, after which I reapplied Viscotears via a subcutaneous 5mg/mL atipamezole bolus (10mg/kg body weight) (30313774/BMS) for recovery[297, 298]. I returned mice to heated home-cages and monitored them until normal behaviours returned (e.g., locomotion, inquisition, eating, and drinking). Post-scan daily welfare checks included mash removal and weighing to monitor recovery.

### *2.5.1.3 In vivo scan protocol*

I acquired *in vivo* T1W, DWI, and resting-state fMRI scans using a Bruker 7-Tesla scanner (BioSpec 70/20 USR) equipped with a 4-channel receive-only cryoprobe and Paravision 360 (v3.5, Bruker BioSpin, Billerica, USA). 2×MGE anatomical T1W acquisitions involved: repetition time=60ms; echo time=3.28ms; inter-echo spacing=4.23ms; number of echoes=3; flip angle=30°; field of view=1.64×1.2×1.35mm; and isotropic resolution=75µm. ×3 2D spin-echo echo planar imaging datasets were acquired for DWI: 1) 1 volume at b=0mm$^2$/s using blip-down reverse-phase encoding; 2) 32 volumes at b=1,000mm$^2$/s with b=0mm$^2$/s volumes interlaced in the same blip-up phase-encoding direction (i.e., 1×b=0 mm$^2$/s, 15×b=1,000mm$^2$/s, repeated twice); and 3) 64 blip-up volumes at b=2,000mm$^2$/s with b=0mm$^2$/s volumes interspersed similarly. For each: repetition time=7500ms; echo time=26ms; pulse width=0.27ms; pulse separation=13.1ms; flip angle=90°; field of view=1.4×1.4×1.75mm; and isotropic resolution=175µm. Resting-state fMRI gradient-echo echo-planar imaging acquisitions involved: 8 volumes for a quality control snapshot followed by 600 volumes for data collection; repetition time=1500ms; echo time=15ms; flip angle=55°; field of view=1.5×1.08×1.6mm; and x-y resolution=100µm. I securely transferred scans to centralised University compute clusters for processing (**2.5.3**).

### *2.5.2 Ex vivo MRI acquisition*

#### *2.5.2.1 Sample preparation*

Mice were anesthetised and culled by intraperitoneal pentobarbital overdose followed by exsanguination and perfusion fixation using 0.01M PBS (20012027/Gibco, Waltham, USA), heparin anticoagulent (30170145/Wockhardt, Mumbai, IN), and 2mM Gadovist (gadolinium) contrast agent (30351004/Bayer, Leverkusen, DE) for the first flush, and PBS, Gadovist, and 16% PFA diluted to 4% (15710/Electron Microscope Services, Hatfield, USA) for the second flush. I kept the brain within the skull upon dissection—removing extraneous skin and muscle, jaws, and zygomatic bones—and post-fixed the skull alongside other extracted tissues (**Table 12**) for 24h in PFA with Gadovist at 4°C. I transferred samples to glass vials containing PBS, Gadovist, and sodium azide and stored each for 2-6mo at 4°C before proceeding to scan *ex vivo*[299].

#### *2.5.2.2 Ex vivo scanning setup*

Upon removing skulls from storage, I padded each with KimWipes (34120/Kimberly-Clark, Irving, USA), and rinsed surfaces with Fluorinert (FC-770/3M, Minnesota, USA). I anchored skulls to custom-3D-printed plinths, which I then inserted into a 15mL Falcon tube filled with Fluorinert (**A.6.5**, **Appx-Figure 23A**). I erroneously dissected some of my first brains from the skull out of habit, and therefore devised creative means of plinth-affixation; I ventrally glued brains to surgical tape, adhered the tape to plinths, and padded and inserted plinths into Falcon tubes to maintain a ≈0.5-1mm gap between the dorsal cortical surface and tube interior (**A.6.5**, **Appx-Figure 23B-C**). After positioning custom bubble-traps at the mouth of each tube and loosely tightening caps, I secured tubes within a vacuum pump to remove intracranial bubbles via negative pressurisation (**A.6.5**, **Appx-Figure 23D**). Once de-bubbled, I tightened caps and stored tubes upright at 4°C. Both when bubble-checking and overnight scanning, I secured tubes secured within custom cradles such that air was constrained within bubble-traps and the dorsal

surface of skulls faced upwards[300]. I performed tuning and matching to adjust for frequency wobble and impedance drift, respectively, after which localiser scans confirmed satisfactory sample alignment. After configuring initial settings and running multi-slice localisers, I adjusted fields of view as required to ensure sample coverage. Bubble-checking involved ≈6min MGE T2W acquisitions which I inspected for quality control. If bubbles persisted, I iteratively re-vaccuumed and re-checked until quality-compromising bubbles were satisfactorily removed. I excluded *ex vivo* samples if representative T2 values exceeded 10% tolerance of the mean cohort value (i.e., $\bar{x}$=27.1, range=24.4-29.8) or if T2 maps exhibited contrast inversion artifacts[299, 300]. Samples fit for inclusion proceeded to overnight scanning.

### *2.5.2.3 Ex vivo scan protocol*

*Ex vivo* MRI employed a Bruker 7-Tesla scanner equipped with Paravision 360 and a 2-channel receive-only cryoprobe. Initial scans included 2D and multi-slice localisers, T2 maps, and b0 maps. I acquired 2×T2W 3D fast-spin-echo rapid acquisition with relaxation enhancement sequences: echo-train length=6; repetition time=350ms; echo spacing=12ms; effective echo time=36ms; flip angle=180°; field of view=2.4×0.96×1.2mm; and isotropic resolution=60µm[300]. 3×segmented echo-planar imaging acquisitions for DWI involved: 1) 1 blip-down volume at b=0mm$^2$/s; 2) 32 blip-up volumes at b=2,500mm$^2$/s with b=0mm$^2$/s volumes interspersed (i.e., 1×b=0 mm$^2$/s, 15×b=2,500mm$^2$/s, repeated twice); and 3) 32 blip-up volumes at b=10,000mm$^2$/s with similar b=0mm$^2$/s placing[300]. Each employed: 12 segments; echo time=30ms; repetition time=400ms; pulse width=6.7ms; pulse separation=13.5ms; flip angle=90°; field of view=2.4×0.96×1.2mm; and isotropic resolution=100µm[300]. 2×MGE acquisitions each featured repetition time=68ms, echo time=3ms, inter-echo spacing=3ms, echo-train length=20, 1 repetition, flip angle=20°, field of view=2.4×0.96×1.2mm, and isotropic resolution=100µm. This yielded a total acquisition time of≈11.5hrs. I reconstructed complex real and imaginary MGE data before cluster transfer for image processing and analyses[300].

### *2.5.3 Image processing*

#### *2.5.3.1 Analysis tools and ecosystem*

I analysed MRI data using Oxford's cluster computing ecosystem. The biomedical research computing cluster housed T1W/T2W processing (**2.5.3.2**, **2.5.4**) and RStudio (.Rmd) analyses (v4.3.2/Posit, Boston, USA) (**2.5.5**), while the open on-demand and Jalapeno cluster processed DWI and QSM (**2.5.3.3**-**2.5.3.4**), including via FSL (v6.0.7.18, FMRIB, Oxford, UK)[301] and FSLeyes (v1.16.2) for analyses and visualisation, before import to the biomedical research computing cluster for registration and analyses (**2.5.4-2.5.5**). Preprocessing employed the Linux command line interface with Python, Java, MATLAB, and bash elements as required.

#### *2.5.3.2 Anatomical T1W and T2W*

I processed T1W/T2W data using advanced normalisation tools and Mouse Imaging Centre Build Model infrastructure[302-304]. T1W.dcm file preparation involved a custom script (**A.10.11**) which converted .dcms to .nii files (*dcm2niix*), averaged .niis in 3D (*AverageImages* using default voxelwise normalisation), denoised outputs (*DenoiseImage* using the default Rican noise model, patch radius=1, and search radius=2 without downsampling), then converted resulting volumes to .mnc format (*nii2mnc*). I transferred .mncs to the cluster for use in the *pydpiper* pipeline[305], which 1) generated a *makeflow* file, 2) fixed a time allocation variable, and 3) used the *makeflow* file to run *pydpiper* via a terminal multiplexer session within a singularity environment (**A.10.12**). Using 3D-averaged .mncs from all samples (none of which were excluded following quality control checks), *pydpiper* generated 'standard-space' volumes following rigid-body lsq-6, affine lsq-12, and nonlinear transformations. lsq-6 transformations align individual volumes in space and orientation using three translations and three rotations along x/y/z axes. Lsq-12-parameter (12 degrees of freedom) transforms additionally adjust for brain size and warping by incorporating three scaling and three shearing transformations in x/y/z

planes. This accounts for overall differences in brain volumes across samples, which is critical in longitudinal datasets including both young mice with inherently smaller brains (>4wks) and older mature mice with larger brains (<21wks). Nonlinear warping corrects for local differences between individual and averaged samples, which is furthermore relevant in accounting for structural differences which may emerge due to genotype, age, or simple inter-individual variability. For each modality, *pydpiper* generated the matrix transforms (.xfm files) by which individual 'native-space' samples could be registered to standard-space volumes. I converted T2W images to .niis before transfer to the cluster for denoising, averaging, .mnc conversion using a custom script (**A.10.11**). I then executed *pydpiper* (**A.10.12**). Quality checks revealed notably warped standard-space volumes with dorsal signal loss (**A.7.2**, **A.7.3**), where I excluded all N=2 out-of-skull samples due to tissue damage. Repeated *pydpiper* execution improved warping, yet dorsal signal loss persisted. This was ameliorated using nonuniformity corrections (*nu_correct*, tested with combinations of iterations=50/100/150/200/250/300 and distance=2.0/1.5/1.0mm where I found iterations=200 and distance=2.0mm to be optimal). I re-ran *pydpiper* using nonuniformity-corrected .mncs, which recovered dorsal signal (**A.7.3**).

### *2.5.3.3 Diffusion*

DWI processing employed both established pipelines and custom modifications across a ten-step workflow involving: 1) orientation corrections to align scanner-outputted orientations with pipeline processes; 2) mask generation to specify brain volumes; 3) Gibbs ringing corrections to remove oscillatory artifacts near high-contrast tissue boundaries, which occur due to high-frequency data truncation during finite k-space sampling[306, 307]; 4) *topup* corrections for susceptibility-induced distortions due to magnetic field inhomogeneities near air-tissue interfaces using the blip-down b=0s/mm$^2$ volume and the first b=0s/mm$^2$ volume of the b=2,500s/mm$^2$ shell[308]; 5) orientation re-adjustments, 6) Eddy corrections to align volumes and correct for drift and distortions which occur during rapid gradient-switching[308, 309]; 7) *dtifit*, which

outputs maps of diffusion tensor eigenvectors, diffusion tensor eigenvalues, fractional anisotropy (FA), mean diffusivity (MD), and diffusion kurtosis which estimates non-Gaussian diffusion as a proxy for tissue complexity; 8) Neurite Orientation Dispersion and Density Imaging (NODDI)[310] using FSL's *cuDIMOT* (v12.6.0) and cluster parallelisation[311] to generate intracellular volume fraction (ICVF), isotropic volume fraction (FISO), and orientation dispersion (OD) parametric maps; 9) FSL's *bedpostx* via *cuDIMOT* to output voxelwise ball-and-stick measures of fibre orientations for probabilistic tractography; and 10) resampling outputted volumes to T2W standard-space for co-registration (**2.5.4**)[300, 312]. *Ex vivo* data processing involved .nii conversion, then DWI pipeline execution (incorporating steps 1-7 above) using input files from each individual sample and *run_dki_bothshells*[300, 312]. *cuDIMOT* thereafter generated NODDI outputs using a previously optimised axial diffusivity value of $0.47\times10^{-3}mm^2/s$ prior to *bedpostx*. I evaluated resulting maps–including intermediate Gibbs- and Eddy-corrected volumes–for quality control (**A.7.4**). I excluded N=2 out-of-skull and N=3 in-skull acquisitions due to tissue damage or poor T2 contrast. I extracted and averaged the four interspersed $b=0mm^2/s$ volumes from Gibbs/*topup*/Eddy-corrected files using FSL's *fslroi* and *fslmaths* commands, respectively. I transferred resulting averaged-b0, *dtifit*, and NODDI volumes to the cluster for .mnc conversion, T2W co-registration (**2.5.4.2**, **2.5.4.4**), and .Rmd analyses (**2.5.5**).

### *2.5.3.4 Quantitative susceptibility mapping*

I processed MGE images using a QSM and R2*/T2* pipeline which involved three steps: 1) preparation (prep_data_qsm_r2s.sh), 2) execution (qsm_pipeline_data_prepped.sh), and 3) susceptibility referencing (reference_QSM_output.sh)[300, 313]. The pipeline requires high-fidelity brain masks as inputs due to the integrity of QSM outputs being particularly vulnerable to effects of non-brain voxels (**A.7.6**). Thus, in contrast to anatomical and DWI protocols (**2.5.3.2**-**2.5.3.3**), I conducted masking (**2.5.4.3**) prior to QSM and R2*/T2* processing which then proceeded as follows[300, 313]. 1) Data preparation involved pre-processing volumes, checking for quality control,

and correcting orientations. I co-registered and averaged magnitude and complex data before Gibbs corrections[306, 307]. I visualised raw, registered, averaged, and Gibbs-corrected volumes via FSLeyes and excluded N=2 out-of-skull and N=3 in-skull samples again due to tissue damage or poor T2 contrast (**A.7.5**). N=6 samples were incorrectly orientated, conceivably due to inconsistent acquisition settings, and thus required custom transformations (**A.7.7**) across all prep_data_qsm_r2s.sh outputs (i.e., raw magnitude data from both repetitions, averaged and Gibbs-corrected volumes, and raw and resampled volumes from real and imaginary components across both channels and repetitions). 2) QSM and R2*/T2* pipeline execution then involved coil-combining complex data (*MCPC_3D*)[314], estimating field maps, correcting for background signal, and inverting dipoles for QSM followed by Gibbs-corrected magnitude data-fitting for R2*/T2*[300, 313-316]. 3) Susceptibility maps required referencing wherein the mean value across brain-masked-voxels was calculated and subtracted from constituent voxels[300, 313]. I visualised resulting susceptibility, R2*, and T2* volumes for quality control (**A.7.5**) and converted these to .mncs for subsequent co-registration (**2.5.4.5**) and analyses (**2.5.5**).

#### *2.5.3.5 Functional MRI*

Ongoing fMRI analysis efforts employ the RABIES pipeline[317], which corrects for motion and susceptibility distortions before registration, segmentation, and processing in R. Further analyses are being actively pursued, yet are beyond the scope of this thesis (**5.5.3**).

### *2.5.4 Co-registration*

#### *2.5.4.1 T2W masking*

T2W standard-space served as the target framework to which I co-registered other *ex vivo* acquisitions. Two unsuccessful attempts preceded a third successful masking strategy. After my first attempt with T2W, DWI, and MGE volumes failed (i.e., advancing directly to **2.5.4.4**-**2.5.4.5**), I examined individual samples and noticed that those with the greatest extracranial

signals exhibited the most warping. As non-brain signals confound registrations, I decided to mask DWI and MGE volumes (**2.5.4.2**-**2.5.4.3**) for a second attempt (still using the same unmasked T2W volumes). This improved registrations, yet not satisfactorily. I then multiplied T2W lsq-6 standard-space volumes by corresponding masks (*minccalc*), then inverted *pydpiper*-outputted native-to-standard .xfms (*xfminvert*) and applied these to lsq-6 standard-space masks (*mincresample*) using a custom script (**A.10.15**). I then subjected native-space masks to voxelwise multiplication with T2W volumes to generate masked native-space samples. My third registration attempt–using masked DWI and MGE source-volumes with masked T2W target-volumes–yielded multimodal registrations of acceptable quality (**2.5.4.4**-**2.5.4.5**, **A.7.7**). I then piped T2W *pydpiper* outputs into RStudio for analyses (**2.5.5**).

### *2.5.4.2 DWI masking*

I used averaged-b0 volumes to generate masks for *dtifit* and NODDI outputs (**2.5.3.3**) before T2W standard-space co-registration. My first unsuccessful attempt to do so involved running *pydpiper* on averaged-b0s, then transforming standard-space atlases into native-space by inverting .xfms and resampling. I converted outputs to .niis (*mnc2nii*), binarised each (*fslmaths -bin*), then iteratively dilated (*fslmaths -dilM*) and eroded (*fslmaths -ero*) masks to exclude extracranial signals. However, after lengthy attempts, many samples remained poorly represented masks. My second successful attempt involved applying nonuniformity corrections (*nu_correct* with iterations=200 and distance=2mm) to averaged-b0 volumes and *pydpiper* execution (**A.10.12**). The outputted nonlinear standard-space volume underwent voxelwise multiplication by its respective mask to generate a masked standard-space averaged-b0 volume. I used a custom script (**A.10.15**) to generate native-space masks for each sample by inverting native-to-nonlinear .xfms, copying and resampling the nonlinear standard-space mask into native space, then multiplying these by nonuniformity-corrected averaged-b0 native-space volumes. I manually confirmed mask quality before proceeding to registrations (**2.5.4.4**).

### *2.5.4.3 QSM masking*

Like DWI, QSM masking entailed unsuccessful attempts following QSM and R2*/T2* pipeline protocols[300, 313] before acceptable masks employed a modified strategy. My initial efforts used reg_magnitude_for_brain_mask.sh[300, 313] and FSL's *fslroi* to register magnitude data from the sixth echo of the first repetition. I needed to correct orientations (*orient_corr*)[300, 313], yet mis-orientated samples required further transformations (prep_data_qsm_r2s.sh) (**2.5.3.4**, **A.10.15**). Upon transfer to BMRC and .mnc conversion, I piped orientated volumes through *pydpiper* (**A.10.12**). I resampled the resulting lsq-6 standard-space atlas to native space for each sample using corresponding .xfms, then binarised and transformed volumes to .niis (*fslmaths -bin*). As with DWI, I applied iterative dilations (*fslmaths -dilM*), erosions (*fslmaths -ero*), and quality control checks, yet brain volume coverage again proved poor (**A.7.6**). My second attempt involved copying nonlinearly-transformed masks extracted from nu-corrected averaged-b0 *pydpiper* outputs for .nii conversion. These masks improved brain coverage, however those from mis-orientated samples appeared to be mis-aligned in 3D space (**A.7.6**) and caused QSM and R2*/T2* pipelines to fail (**2.5.3.4**). I translated and rotated masks from these samples in FSL before transfer to BMRC, .mnc conversion, and averaged-b0-space resampling to correct metadata corruption. I converted resulting masks to .niis for visualisation, where all then sufficiently covered brain volumes (**A.7.6**) for input to the QSM and R2*/T2* pipeline (**2.5.3.4**).

### *2.5.4.4 DWI to T2W*

I used a custom script to register masked volumes to T2W standard-space (**A.10.16**). This involved generating and concatenating (*xfmconcat*) rigid (lsq-6) and affine (lsq-12) T2W→DWI .xfms, inverting this to produce DWI→T2W affine .xfms, concatenating with T2W affine→nonlinear .xfms (from T2W *pydpiper* outputs) to produce DWI native-space→T2W standard-space transforms, then applying.xfms to native-space DWI volumes. Quality control checks confirmed registrations following .nii conversion. I included additional filtering (*minccalc*)

for voxelwise analyses (**2.5.5**) to negate values which were null (invalid for logarithms) or >2 ($e^2$≈7.4-fold increases deemed non-biological). Kurtosis outputs required filtering where values >30 or <0 were considered non-biological and omitted (**A.10.17**) prior to .Rmd analyses (**2.5.5**).

#### *2.5.4.5 QSM to T2W*

I co-registered pipeline outputs (X, R2*, and T2*) (**2.5.3.4**) to T2W standard-space using a custom script (**A.10.16**). I translated MGE images to overlap with masked T2W standard-space volumes for compatibility with advanced normalisation tools (*minc_modify_header* and *mincresample*) (**A.7.7**). I inverted and concatenated T2W *pydpiper*-outputted native→lsq-6 .xfms (*xfmconcat*) with native→nonlinear .xfms to generate lsq-6→nonlinear transforms. I applied inverted ( nonlinear→lsq-6) transforms to resample nonlinear standard-space T2W masks into lsq-6 standard-space. I multiplied resulting masks by *pydpiper*-outputted lsq-6 maps to generate masked lsq-6 standard-space volumes, which served as T2W targets for MGE co-registration (**A.10.16**). Additional filtering negated null and non-biological voxels using custom scripts (**A.10.18**) before .nii conversion visualisation for quality control (**A.7.7**). I piped registered and filtered MGE outputs into the .Rmd script for further analyses (**2.5.5**).

### *2.5.5 Data analyses*

#### *2.5.5.1 Script overview*

I employed the same .Rmd script for *in vivo* and *ex vivo* neuroimaging analyses (**A.10.19**) which involves four steps: 1) configuration, where required tools, analysis specifications, and data are loaded; 2) statistical processing, where several models are built, evaluated to optimise parameterisation, then executed regionally and voxelwise; 3) regional analyses, which generate hierarchical trees, ROI plots, and statistical outputs; and 4) voxelwise analyses, which generates brain maps for qualitative evaluation. I processed *in vivo* T1W and co-registered *ex vivo* T2W,

DWI, and MGE as described in **2.5.5.2**-**2.5.5.5**. *In vivo* DWI, resting-state fMRI, and *ex vivo* tractography analyses are beyond the scope of this thesis and remain active future directions.

### *2.5.5.2 Configuration*

Script execution required access to 31 libraries (**A.10.19**) which I first imported for programme initialisation. Editable parameters provided for customisation include: cohort type (i.e., *in vivo* or *ex vivo*); fixed effects (i.e., whether to solely consider effects of genotype or age×genotype interactions); random effects for *in vivo* datasets (i.e., none, the individual baseline/intercept, or the baseline and growth trajectory); total brain volume covariance (with/without); sample type for *ex vivo* analyses (i.e., depending on skull inclusion and age); centred age for analyses (e.g., 21wks); data type (i.e., compatible across anatomical, FA, MD, MK, OD, ICVF, FISO, X, R2*, and T2* outputs); outlier handling (i.e., to keep or omit outliers defined as $\pm 2.5\sigma_M$); statistical model assessment (i.e., Akaike information criterion or Bayesian information criterion); statistical model application (i.e., best-fit or pre-specified); and visualisation preferences. I used this script to import and organise pipeline data volumes and cohort metadata into data structures for navigation and analyses.

### *2.5.5.3 Statistics*

I constructed, optimised, and applied statistical models across neuroimaging datasets. Linear formulae involved combinations of fixed effects (i.e., sex, genotype, optionally age, and optionally total brain volume) and random effects for longitudinal *in vivo* datasets only (i.e., none, the Y-intercept only for baselines, or both the Y-intercept and the slope for growth trajectories). I produced general additive models (GAM) with and without total brain volume covariance. Linear models employed standard regressions using ordinary lsq for *ex vivo* datasets, mixed-effects regressions for *in vivo* datasets, and estimated marginal means to generate age contrasts across modalities. I controlled for false discovery rates (FDR) using the Benjamini-Hochberg method. Functions for both linear and GAM formulae extracted fit statistics (i.e., t-, p-

, and FDR-adjusted q-values) for overall effects of genotype, genotype effects centred at 4, 12, and 21wks, age×genotype interactions, and sex effects. I applied functions to each model per ROI (**2.5.5.4**), calculated model fits, and applied optimal parameters accordingly (**2.5.5.2**).

### *2.5.5.4 Regional analyses*

I segmented *in vivo* acquisitions using the Dorr-Steadman-Ullman 90µm atlas[302, 318, 319], and *ex vivo* acquisitions using the Dorr-Steadman-Ullmann-Richards-Qiu-Egan 40µm atlas[302, 318-321]. Segmentations from both[304] were labelled using Allen Brain CCFv3 hierarchical definitions[32]. I incorporated outputs from the pre-specified or best-fit statistical model into data frames (**2.5.5.3**), averaged across hemispheres via hierarchical tree pruning, then summed outputs across all regions to generate whole-brain data. Anatomical analyses projected volumetric changes across samples belonging to each experimental condition as anatomical heat-maps onto 2D slices extracted from standard-space volumes (**2.5.5.2**). I similarly processed *ex vivo* DWI and MGE outputs using the same scripts and T2W co-registration (**2.5.4.4**-**2.5.4.5**). I plotted volumetric, DWI, and MGE data for pre-specified ROIs with age-dependent trendlines and statistics. Both *in vivo* and *ex vivo*, bed nucleus of the stria terminalis (BNST) volumetric plots tested whether male volumes were greater than female volumes (with no age-sex interaction) as a standard means of quality control.

### *2.5.5.5 Voxelwise processing*

I employed the pre-specified or best-fit linear model for voxelwise calculations as significant computational requirements rendered GAMs incompatible. I replaced ROIs with the logarithm of the Jacobian matrix determinant to compare individual voxels to standard-space representations. I selected the full determinant over the nonlinear counterpart to account for rigid and affine effects–not solely local nonlinear differences independent to overall brain shape and size. 3D arrays were populated with t-, p-, and q-values accordingly for visualisation.

# Chapter 3: Results – *SnackerTracker* and *TracKIT* development and validation for feeding and activity measurement

This chapter describes *SnackerTracker*/*TracKIT* development and application as a novel open-source hardware/software platform capable of continuously monitoring rodent food intake. *SnackerTracker* invention was necessary as, to my knowledge, no other home-cage measurement system can quantify feeding behaviour without compromising the parallel sleep recordings required for L6-ORX experiments: EEG/EMG leads are incompatible with commercial whole-cage systems (**Table 2**, **Table 4**); video-based options merely predict *when* feeding is occurring rather than *how much*; and manual measurements inevitably awaken and cause stress to animals (**1.4.1**, **1.5.1**). I created *TracKIT* to analyse *SnackerTracker* data, yet it proved more broadly valuable as a software tool which can accept any time-series data and generate a range of outputs relevant to circadian and home-cage behavioural monitoring (**1.4.2**, **1.5.2**). Through iterative design processes (**3.1.1**-**3.1.4**, **3.2**), I validated *SnackerTracker* and *TracKIT* systems using both benchtop testing (**3.1.5**) and a series of three *in vivo* experiments (**Table 5**):

- **3.3.1-3.3.3** – I predict that the *SnackerTracker* will detect changes in the *pattern* of feeding behaviour in CRY-deficient mice housed in constant-darkness.
- **3.3.4** – DLE home-cage lighting conditions should delay the onset and peak of feeding behaviour, and *SnackerTrackers* should be able to identify this *phase shift*.
- **3.3.5** – Hamsters maintained in summer and winter photoperiods eat more and less food, respectively. I predict that *SnackerTrackers* will identify differences in the *quantity* of food intake and prove compatible with this alternative rodent species.

Ultimately, a cost-effective and adaptable system which continuously monitors the amount and timing of food intake and feeding behaviour—without confounding simultaneous sleep recordings—will both enable investigations into the effects of L5-6b perturbations and contribute to the field of laboratory animal home-cage monitoring (**3.4**-**3.5**).

## 3.1 SnackerTracker development and validation

### *3.1.1 SnackerTracker overview and design*

The *SnackerTracker* is a novel animal home-cage monitoring system which measures animal food intake, feeding activity, and ambient lighting[211]. **Figure 6** depicts its design and operation following prototype development (**Table 14**) according to requirements detailed in **1.5.1**. Major design components include the frame (chassis) (**3.1.2**), electronics (**3.1.3**), and operational software (**3.1.4**). I 3D-printed each of prototypes V1-10 for benchtop testing to confirm device operation and accuracy; I introduced V3, V5, V6, and V8 *in vivo* for a limited time (<3hrs) under constant supervision, then used V9 for longer *in vivo* validations (**3.1.5**). The need to analyse *SnackerTracker* data prompted me to develop of the *TracKIT* platform (**3.2**), which I then used to analyse data from V9-10 which collected data parallel to DVCs, PIR systems, and video recordings (**3.3**). Each *SnackerTracker* of the final V10 design cost ≈£120 at the time of writing. I made hardware and software resources available via open-source platforms[211, 258, 277, 280, 322-324], rendering the *SnackerTracker* a system which researchers can freely download, build, and customise according to future study requirements. I provide detailed construction and operation instructions via online repositories to promote transparency and accessibility[211].

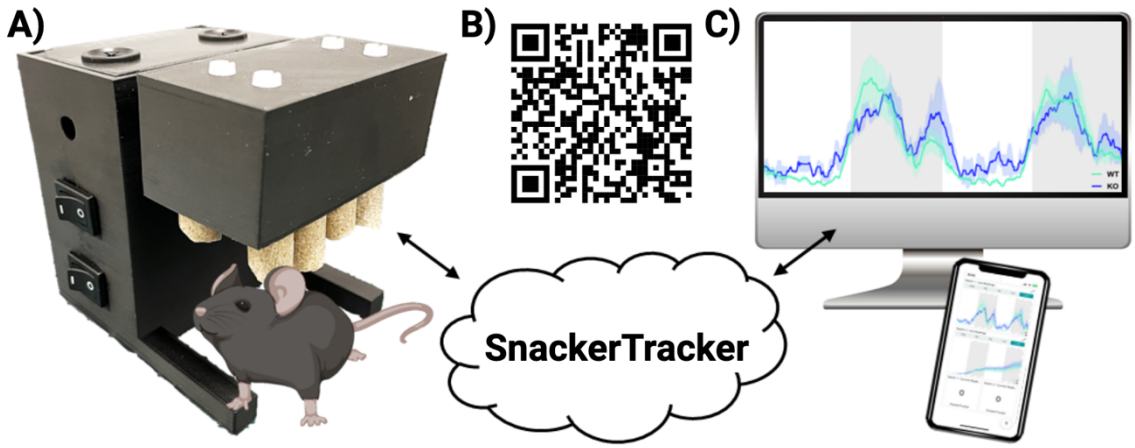


**Figure 6.** *SnackerTracker* design and operation. Illustrates A) the final prototype with a roughly-to-scale cartoon mouse, a B) QR link to a *SnackerTracker* overview video[277], and C) data analysis and cloud-based capabilities including remote monitoring and operation.

**Table 14.** SnackerTracker prototypes. Illustrates the 10 prototype iterations (V1-10) contributing to the final *SnackerTracker* design (green). I created all 3D models using TinkerCAD.

| V# | Features | Image | V# | Features | Image |
|---|---|---|---|---|---|
| V1 | Large; cage interface fixed to the chassis body; circular openings; Arduino Uno R3 microcontroller | 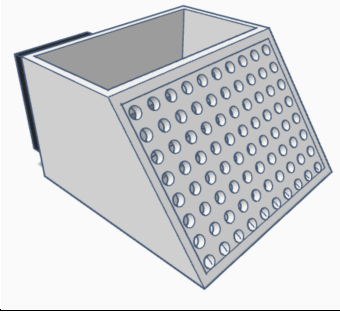 | V6 | Slanted design; integrated electronics; stacked protoboard; case covering; removable food holder; printable with or without cage interface; toggle switches | 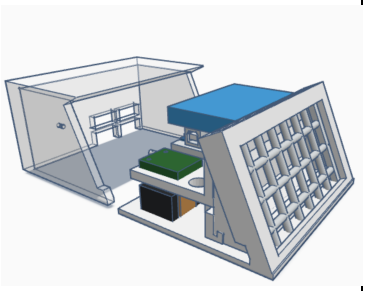 |
| V2 | Removeable cage with bars; can be printed with a cage or as a frame (to later affix chicken wire); wired switch | 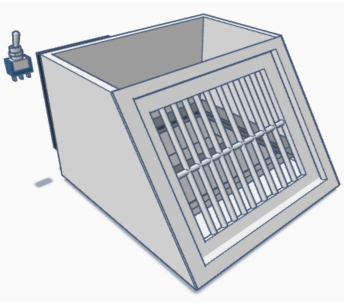 | V7 | Compatible with HCM legal size requirements, (smaller); hanging cage; optimised for MKR Wi-Fi 1010 integration; case covering; with or without cage interface | 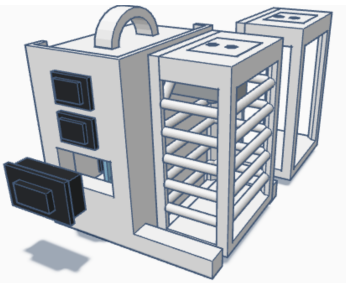 |
| V3 | Smaller; vertical interface with openings on vertical and horizontal chassis faces; no proposed electronics interface | 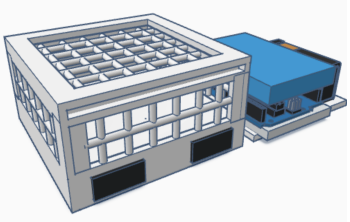 | V8 | Hanging cage; stacked MEM and MKR Wi-Fi 1010 microchips and optimised electronics accordingly, including SD card alignment; case covering; hanging pellets | 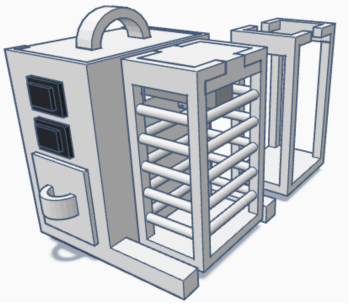 |
| V4 | Excludes 3D-printed bars such that chicken wire can be affixed | 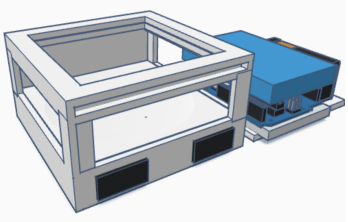 | V9 | Hanging pellets; covered plug-ins for input wiring (e.g., USB power); re-designed electronics configuration; LDR inclusion on the top of the food holder | 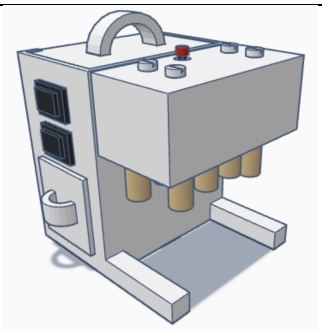 |
| V5 | Features a climbing ramp and only a vertical cage interface; not optimised for electronics; printable with or without cage | 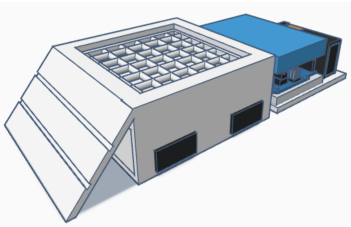 | V10 | Optimised wiring; grommets for inputs; reorientated LDR; smooth chassis edges; increased number of suspended pellets (9→12) | 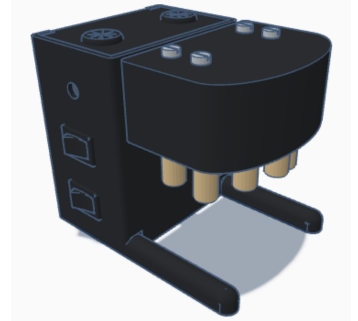 |

### *3.1.2 Chassis hardware*

**Figure 7** depicts chassis development via *SnackerTracker* 3D modelling through component isolation, print assembly, and final product materialisation. See **A.3.1** for the BOM, **A.3.2** for 3D printing settings, and **A.3.3** for technical chassis drawings (V9).

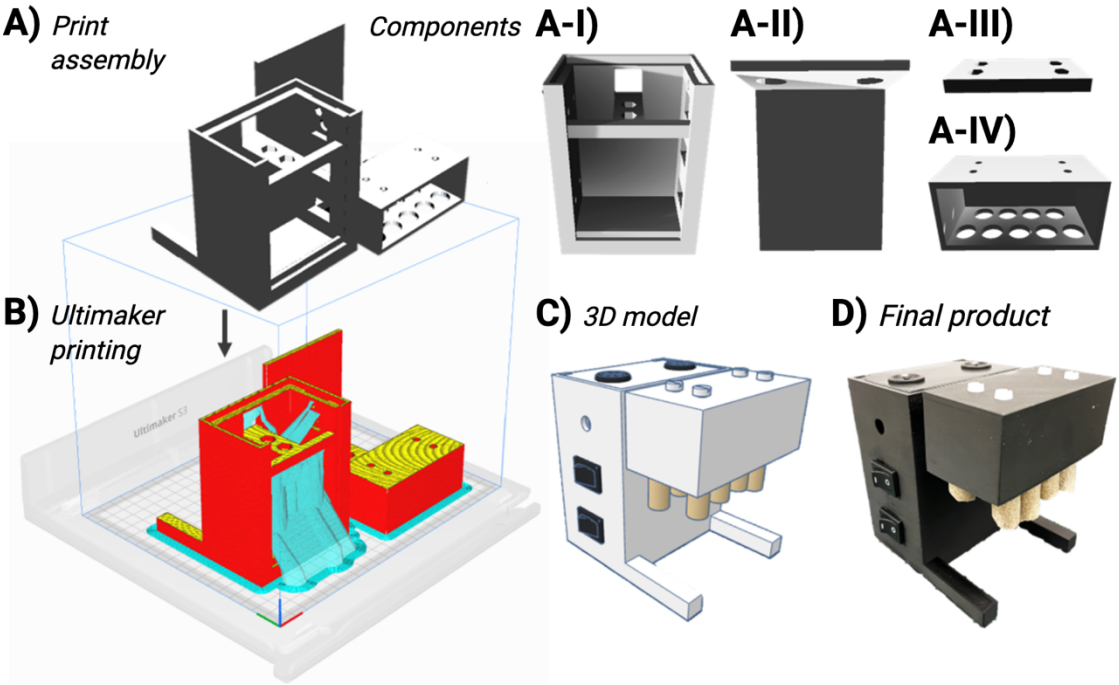


**Figure 7.** *SnackerTracker* chassis 3D modelling and materialisation. A) Four constituent elements were rendered: I) main body; II) case cover; III) mount plate; and IV) food holder. B) Shows the Cura print configuration (red=outer chassis wall; yellow=top surface; cyan=supports). C) This transformed the *SnackerTracker* TinkerCAD model into the D) final assembled device. See **A.3.3** for schematics and **A.3.5** for videos of 3D printing and construction.

### *3.1.3 Electronics hardware*

**Figure 8** illustrates electronic elements, component connectivity, and where all the above are mounted within the chassis. See **A.3.4** for electronics schematics which, alongside **A.3.3**, can be provided to electronics workshops for contracted assembly. **A.3.5** provides detailed descriptions of chassis and electronics assembly, including QR links to videos providing a step-by-step demonstration of how to build and use a *SnackerTracker*. Note that the make and model of individual electronic components may vary in future applications, and additional elements can be integrated via the Arduino MEM shield according to study requirements.

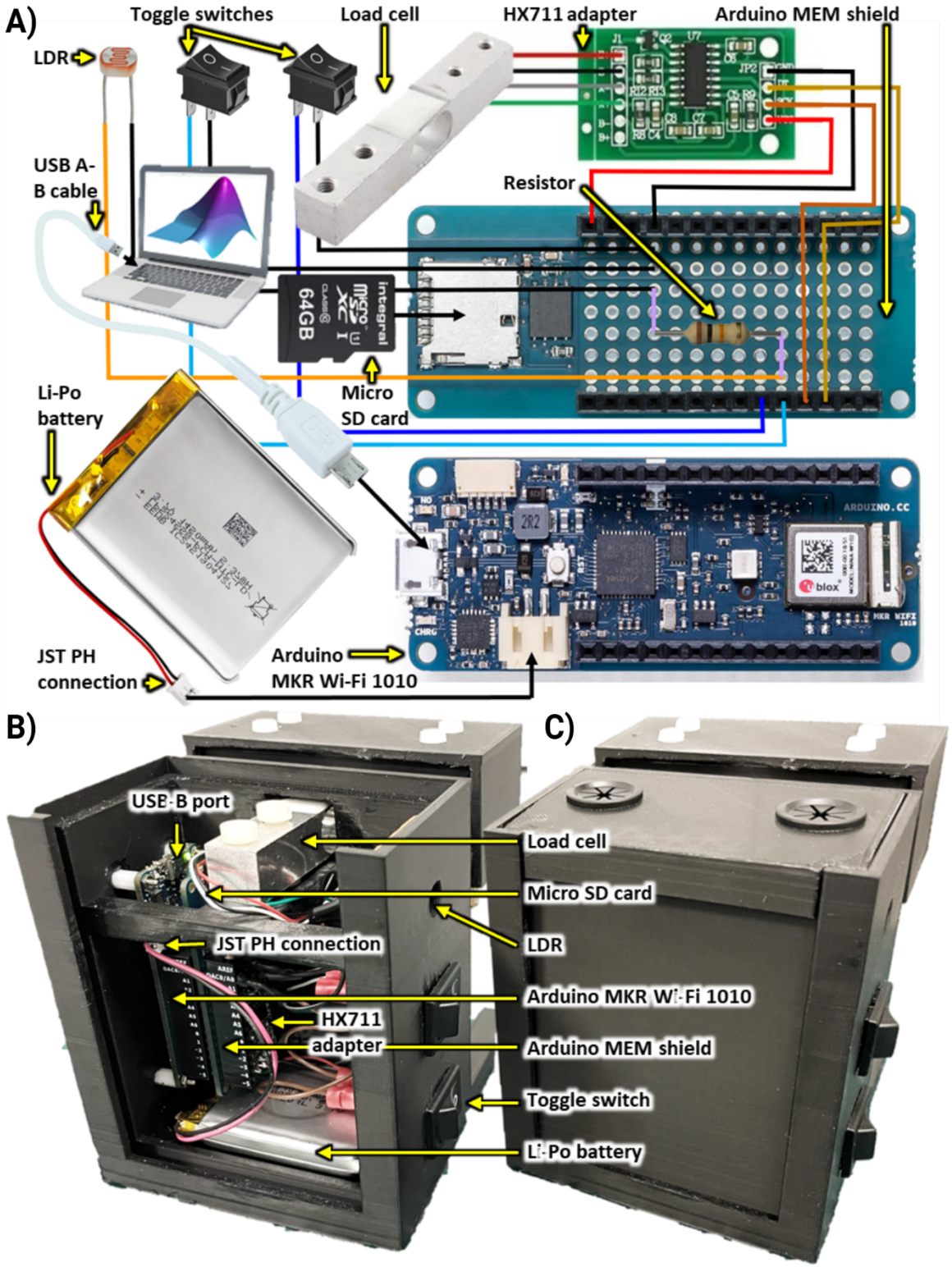


**Figure 8.** Illustrates *SnackerTracker* electronics. A) Graphical representations depict element connectivity, while B-C) show components mounted within the chassis both B) without and C) with the case cover. Refer to **A.3.3** and **A.3.4** for chassis and circuit schematics, respectively, and **A.3.5** for construction tutorial videos.

### *3.1.4 Operational software*

On-chip software controls *SnackerTracker* operation (**A.10.1**). Once downloaded, the script executes a *setup* function for device initialisation and *loop* function for data recording. Initialisation mandates calibration (**A.3.6**) via USB connection to a local computer, online access to the Editor, and Create Agent installation (v1.2.6, Arduino)–a background application which enables computer-chip communications. After *setup* calibration and *loop* initiation, the USB cable can be optionally disconnected for wireless recording. Automatic USB-to-lithium polymer battery power-switching enables USB-supplied *SnackerTracker* operation and battery charging when connected, and battery operation otherwise. Wi-Fi connection to the Arduino Internet of Things (IoT) platform enables real-time data monitoring from networked systems via the IoT Remote App (v1.6.0) (**Figure 9**). *Loop* records data at a tuneable frequency (e.g., 1Hz) until power is lost (e.g., disconnect the USB and battery to stop recordings). The SD card can then be removed for data processing.

### *3.1.5 Validation*

**A.3.7** describes preliminary validation tests which I conducted to assess device function before *in vivo* application. I provide results in **A.3.8**, which confirmed *SnackerTracker* 1) calibration accuracy, 2) measurement consistency, 3) time-sensitivity, 4) light-dependent resistor (LDR) functionality, 5) combined operability, and 6) *in vivo* compatibility. *In vivo* compatibility tests showed adequate i) correlation to manual daily food measurements, ii) food accession modality (i.e., finding no use-prohibitive difference between cage-floor/hopper vs *SnackerTracker* presentation), and iii) extended recording duration fidelity with minimal pellet crumbling. Further analyses of datasets from 6) iii), which employed surplus L5-silenced mice (**Preface**), motivated the STAMINA study and are accordingly detailed in chapter 5. I deemed *SnackerTracker* performance sufficient to proceed to full-cohort *in vivo* experiments (**3.3**); however, this required a suitable data analysis programme (**3.2**).

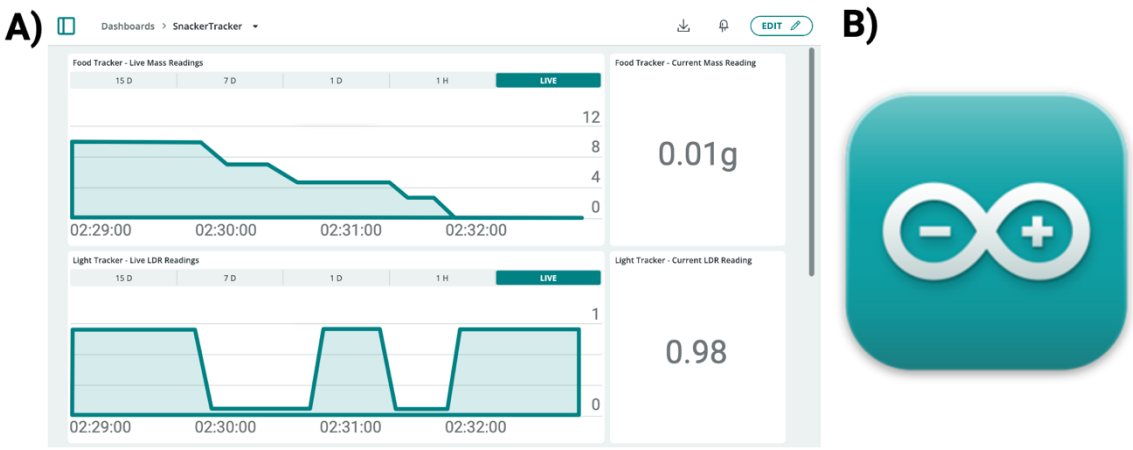


**Figure 9.** Illustrates the *SnackerTracker* IoT GUI. A) The data collection dashboard enables remote real-time monitoring and, with development, operational control. B) The dashboard can be visualised on any connected device via the iOS- and Android-compatible mobile app.

## 3.2 TracKIT development

### *3.2.1 TracKIT overview and design*

*TracKIT* is a MATLAB app (.mlapp) which accepts time-series data, filters traces, and returns a range of summary metrics relevant to animal home-cage and circadian monitoring. I optimised its use for *SnackerTracker* analyses, yet it is compatible with other file types including but not limited to those from DVCs (**3.3.1**-**3.3.3**), PIRs, and thermographic cameras (all of which I've successfully tested). The platform relies on code I developed using MATLAB (**A.10.2**); yet, it operates as a standalone open-source application if users download the free MATLAB Runtime compiler (R2022b, v9.13). *TracKIT* analysed all pilot data and STAMINA outputs (**5.1**). It features a GUI (**Figure 10A**) where users provide input files, processing parameters, and output specifications (**Figure 10B**). As such, users are not required to interact with a CLI or coding environment. *TracKIT* pre-processes files in five steps, each of which I explain in **3.2.2** (**Figure 10I-V**). I ensured that intermediate processing stages are displayed (**Figure 10D**) so a user can confirm data quality before adjusting parameters or exporting results (**Figure 10C**). I have made *TracKIT* available on GitHub (**https://github.com/marhmue/2024_SnackerTracker_Code**), Figshare[148], and Zenodo[86].

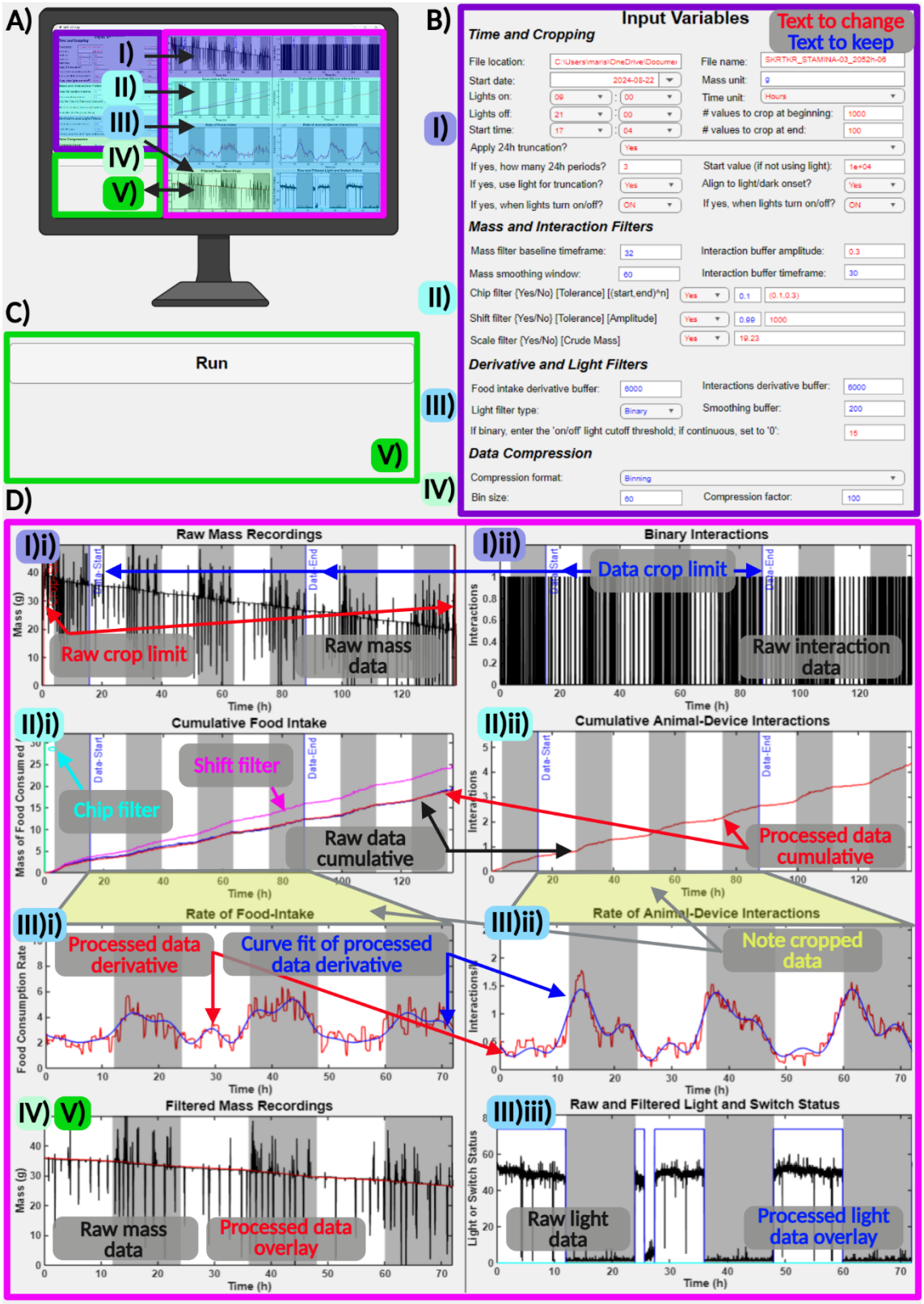


**Figure 10.** *TracKIT* GUI. The A) GUI features a B-C) parameter-input and D) processing panel. Parameter sets and corresponding processing steps I-V)–colour-coded by location in A) and magnified for dissection in B-D)–are elaborated upon in **3.2.2** and **3.2.5**. I describe the distinction between food-intake and animal-device interactions ("feeding behaviour") in **3.2.4**.

### *3.2.2 Processing steps*

Data processing involves five major steps (**Figure 10I-V**) where key variables–denoted here in [square brackets] and detailed further in **A.3.9**–are extracted from user inputs and used to curate input files. I detail these steps in **Table 15**.

**Table 15.** Lists and describes the major steps involved in *TracKIT* data processing.

| Step # | Description |
|---|---|
| **I) Metadata and cropping** (**Figure 10BI**) | After pointing *TracKIT* to input files [skrtkrFileLocation], indicating desired output units for mass (typically grams) [massUnit] and time (typically hours for present applications) [timeFormat], and specifying both the time at which recordings start [startDate, timeStart] and the expected light schedule (i.e., when lights turn 'on' and 'off') [timeLightOn, timeLightOff], the user must define how raw data (**Figure 10DIi**) is to be cropped. This involves both initial truncation (i.e., specifying the number of values to remove from subsequent analyses at the beginning and end of recordings, indicated in red as the "raw crop limit" in **Figure 10DIi**) [truncateStart, truncateEnd, startPoint, endPoint] and duration specification: If 24h truncation is selected [do24HTruncation], user must indicate how many consecutive 24h periods are desired for analyses [howMany24H] such that the file is cropped accordingly; otherwise, data will be processed until the terminal raw crop limit. The user must then indicate the desired start value according to 1) the defined light schedule such that processed data will begin at the first instance of lights turning 'on' or 'off' after the initial raw crop limit [lightFor24HCrop, lightFor24HCropONOFF], or 2) a custom value [do24HStart], where the user can still specify whether outputs should be aligned to begin at light or dark onset (in which case any data before the start value translocates to the end of the dataset) [alignLight]. Irrespective of how defined, the determined start and end value constitute the "data crop limit" in **Figure 10DIi-ii**. These cropping methods provide comprehensive control over the duration and form of data to be extracted from *SnackerTracker* output files for further processing. |
| **II) Filtering** (**Figure 10BII**)*:* | Filters identify 'spikes' in raw data traces to discern both the amount of food removed from the hopper and the incidence of animal-device interactions (distinguished in **3.2.4**). The mass filter baseline timeframe [setTime, optimised during development at 32] determines the number of initial mass values (beginning at the raw crop limit) which are averaged and overwritten. The interaction buffer timeframe [measureSpan, mandatorily >setTime] then defines the number of prior measurements against which each upcoming raw value is evaluated, beginning at the index setTime+1. If the difference between the upcoming raw value and any preceding within the interaction buffer timeframe exceeds the interaction buffer amplitude [bufferHere, optimised at 30, which acts as a band pass filter], the raw value is both removed from the raw trace and assigned a value of 1 in a separate binary array to denote an animal-device interaction (**Figure 10BIii**, an actogram). Once the entire file is traversed, null values are overwritten upon linearly interpolating flanking data points. Resulting traces then undergo moving-average smoothing using the number of data points specified by the mass smoothing window [window, optimised at 60]. A shift filter can then be applied in cases where data following prior measurements may increase (e.g., if bedding, nesting material, or mice lie atop the food hopper); the amplitude [shiftFilter] determines the upcoming timeframe over which each data point is assessed, and the tolerance [shiftTolerance, optimised at 0.99] defines the percentage of values therein which must be equal to |

| | |
|---|---|
| | or less than the indexed value. Otherwise, the indexed value is assigned to that of the directly preceding data point, and all following data are shifted by the same margin accordingly. A 'chip' filter can be optionally applied in extreme cases of this [doChipFilter]; if large 'chips' are observed in raw traces (resembling an upright or inverted top hat), users can specify bounding indices [chipStartTime, chipEndTime] within which values will be designated as null if they exceed the specified tolerance [chipMass, optimised at 0.1] and interpolated as with the prior band pass filter. The scale filter [doScale] performs an additional quality control check against the expected total mass difference between initial and final data points (i.e., if acquired before and after recordings) [crudeMass]. A warning flag is relayed if this difference exceeds 5% of the crude mass, which indicates that equipment or calibration errors may have compromised the present recording. After filtering, the resulting mass trace is inverted; the difference between all values and the initial mass is reported for each index of a new array to represent cumulative food intake at any given time point (**Figure 10DIIi**) rather than the mass of food removed from the hopper. In another new array, total interaction counts are calculated by summing all prior binary values to represent cumulative animal-device interactions at any given time point (**Figure 10DIIii**). |
| **III) Derivations, fitting, and light filtering (Figure 10BIII)** | Cumulative food intake and animal-device interaction traces are derived to return time rates-of-change (**Figure 10DIIIi-ii**). The food intake derivative buffer [fooddervBuffer, optimised at 6000] and interactions derivative buffer [intdervBuffer, optimised at 6000] define the number of points across which slopes are calculated. Curves are then fit to derivative timelines using MATLAB's Curve Fitting toolbox (v3.8) and the Sum of Sine regression model. This employs a nonlinear lsq method using the Trust-Region algorithm and default constraints to generate a standard curve according to $\sum_{i=1}^{j} a_i \sin(b_i x + c_i)$. Extracted parameters of interest include primary (j=1) waveform displacement ($d$=$a_1$), angular frequency ($\omega$=$b_1$), phase shift ($\varphi$=$c_1$), and goodness of fit ($r^2$). Amplitude and frequency data are transformed to return curve intensity ($A$=2*$d$) and period $\left(\tau = \frac{1}{f} = \frac{2\pi}{\omega}\right)$. $X^2$ periodograms are generated yet are not shown in the GUI. Raw light recordings are then subjected to a smoothing buffer [smoothLightWindow, optimised at 200] as in II) and processed to either retain smoothed light readings, or to undergo binarisation according to the specified light filter type [lightFilterType, optimally at 'Binary']. If binarisation is selected, smoothed values greater and less than the light cutoff threshold [lightCutoff] are assigned values of 1 and 0, respectively (**Figure 10DIIIiii**). |
| **IV) Data compression (Figure 10BIV)** | User can compress outputs to reduce file size or standardise units (**Figure 10DIV**) by defining a compression format [doFileCompression, optimally at 'Binning']: if 'binning' is selected, the specified bin size [binDuration, optimised at 60] must be defined wherein the mean of data within the time-range are deposited; if 'averaged' is selected, the specified compression factor 'n' [compressionSecondsFactor, optimised at 100] rather simply extracts and outputs every '$n^{th}$' value; and no further processing occurs if compression is not specified. Binning flexibility is advantageous for parallel data alignment (e.g., as in **3.3.1**, where DVCs outputs bins per minute). |
| **V) Quality checks, output evaluation, and export (Figure 10BV)** | Outputs of steps I-V) are provided for the user to visualise and check for quality control (**Figure 10D**). The processed mass trace is overlaid with the raw trace to assess accuracy (**Figure 10DV**) [finaliseOutput]. If unsatisfactory, the user can repeat steps I-V) and iteratively adjust cropping, filtering, derivation, smoothing, and compression specifications (see **3.2.5** for parameter notes). Once deemed acceptable, *TracKIT* creates an output folder containing 1) a screenshot of the GUI as in **Figure 10A**, 2) a .csv summary and metadata file, 3) a .csv file containing raw and processed data, and optionally 4) a .csv file containing compressed data if specified in step IV). I provide sample output .csv files in **A.3.10**. .csvs can then be imported into other programs (e.g., Prism) for graphical and statistical analysis. |

### *3.2.3 Present and possible output metrics*

*TracKIT* generates a unique combination of output traces and summary metrics (**Table 16**, which can be directly compared to rows representing other presently-available analysis methods in **Table 3)**. Activity-related metrics include daily activity, light/dark phase activity, activity in hourly bins, daily bouts, light/dark phase bouts, and hourly bouts, where bouts are definable if bin-compression is specified in *TracKIT* processing step IV) (**Table 15**). Circadian-related metrics include Sum of Sine- or $X^2$- periods ($\tau$), strengths of periodic components ($A$), and phase angles of entrainment ($\varphi$).

**Table 16.** *TracKIT* output metrics. These can be compared to **Table 3**. A green 'X' indicates outputs which are not presently generated by *TracKIT* but could be easily incorporated in future versions. A red 'X' indicates outputs which the *SnackerTracker* cannot produce, thus *TracKIT* has not been developed to accommodate. LD=light-dark; yellow=circadian-related; purple=activity-related; and orange=both circadian- and activity-related.

| **Software Name (Release Date, Developer)** | **Data Type(s)** | **Output Metric** | | | | | | | | | | | | | | |
|---|---|---|---|---|---|---|---|---|---|---|---|---|---|---|---|---|
| | | Raw time-course | Actograms | Activity counts and t | Activity rates | Bout analysis | Time active/inactive | LD discrimination | LD integration | Average T | T decompositions | Phase shifts | Event marking (f, t) | Latency to event | Interdaily stability | Region breakdown | Social interaction |
| TracKIT (2026, present thesis) | Food intake and food-seeking behaviour | ✓ | ✓ | ✓ | ✓ | ✓ | ✓ | ✓ | ✓ | ✓ | ✓ | ✓ | X | X | X | ✓ | X |

Future *TracKIT* versions could easily return additional circadian metrics. Active phases (the time between activity onset and offset within a cycle) and rest phases (the time between rest onset and offset within a cycle) could be extracted by 1) employing bout-based compression, 2) specifying a threshold above/below which bouts would be classified as 'activity' or 'rest' in a separate array, and 3) calculating activity or rest durations represented by adjacent supra- or sub-threshold bouts, respectively. Peak activity and rest onsets could be extracted as the midpoint of the largest activity or rest bout upon integration (after weighting and summing bouts according to contributing bin values). Time to peak activity or rest onsets could then be

calculated relative to dark or light onset, respectively. For longer recordings, interdaily stability could be determined according to **Equation 2**[325]. I have already developed code to integrate event-marking according to *SnackerTracker* switch status. Additional specifications detailing how switch data is to influence processing should be incorporated into future *TracKIT* versions.

**Equation 2.** Interdaily stability calculation. IS=interdaily stability; n=total number of data points (e.g., 10,080 for 7 days of per-minute data); p=number of data points per day (e.g., 1,440 for per-minute data); $\bar{x}$=data mean across all days; $\bar{x}_h$=data mean per hour averaged across all days; $x_i$=individual data points in the time series being analysed[325].

$$IS = \frac{n \sum_{h=1}^{p} (\bar{x}_h - \bar{x})^2}{p \sum_{i=1}^{n} (x_i - \bar{x})^2}$$

### *3.2.4 Food intake vs food-seeking behaviour*

Critically, this script mathematically discriminates absolute food-intake from animal-device interactions operationally termed "food-seeking behaviour". That is, food-intake and derived rates represent food calculated as being removed from the *SnackerTracker* food holder, which is assumed to represent food being consumed by an animal (**3.4.4**, **3.1.5**, **A.3.8**). Animal-device interactions (see processing step III in **3.2.2**) distinctly represent cases where an animal may interact with yet not necessarily eat from the food holder. I instituted this after observing that some animals seemed exceptionally interested in poking, pressing against, or climbing atop *SnackerTrackers*. Conceivably, more-intense animal-device interactions or "food-seeking behaviour" may distinguish animals which are more active, or animals which may be attempting yet failing to eat due to conceivable motor impairment. See **3.5.3** for welfare implications, and **5.1.1** for the present experimental relevance of this in L5-silenced mice.

### *3.2.5 Parameter usage*

Time series analyses are notoriously inconsistent across behavioural rodent work in the field of circadian biology[205, 210-212], which emphasises the need to understand and report how data are processed[213]. If *TracKIT* parameters including but not limited to bin size, smoothing

filters, and derivative buffers vary (**A.3.9**), outputs change notably. *TracKIT* introduces capacity for error during cropping and filtering; translocation should never be specified as it yields inaccurate results (and was only created to accommodate shorter datasets acquired during pilot testing and validation), and the subjective chip filter skews results if used incorrectly (thus all chip filters are automatically documented, **A.3.10**). Analyses should therefore be conducted blindly whenever possible. *TracKIT* is advantageous in that it can accept a wide range of input data types, return a wide range of activity and circadian metrics (**3.2.3**), and document which parameters were employed per trace analysis (**3.2.2**). However, this does not rectify larger issues: little standardisation and enforcement exists to guide how time-series data should be processed and reported for inter-study comparisons[213].

## 3.3 Preliminary applications and biological insights

### *3.3.1 DVC correlation*

I first employed *SnackerTrackers* experimentally to evaluate differences in food-intake and feeding-behaviour between CRY-deficient and CTRL mice housed within DVCs under either 12:12hr light-dark conditions or constant darkness (**1.5.1**, **A.4.1**). This served as *in vivo* device validation against an established means of home-cage activity monitoring, demonstrated *TracKIT* useability in analysing DVC data, and provided biological insights described in **3.3.2**-**3.3.3**. Overall, *SnackerTracker* outputs resembled DVC whole- and mid-cage data across both cumulative and derived traces (**Figure 11A-B**). Good correlations emerged between acquisition methods for both total feeding and activity (Pearson's $0.982<r<0.997$, **Figure 11C**) and rates of food-intake and animal-device interactions (Pearson's $0.72<r<0.85$, **Figure 11D**). As anticipated, correlations were the greatest between *SnackerTracker*-derived animal-device interactions (here termed "activity") and DVC-derived mid-cage data, which is where *SnackerTrackers* were physically located. This demonstrates *SnackerTracker* compatibility with use in standard cages, and validity compared to DVC monitoring.

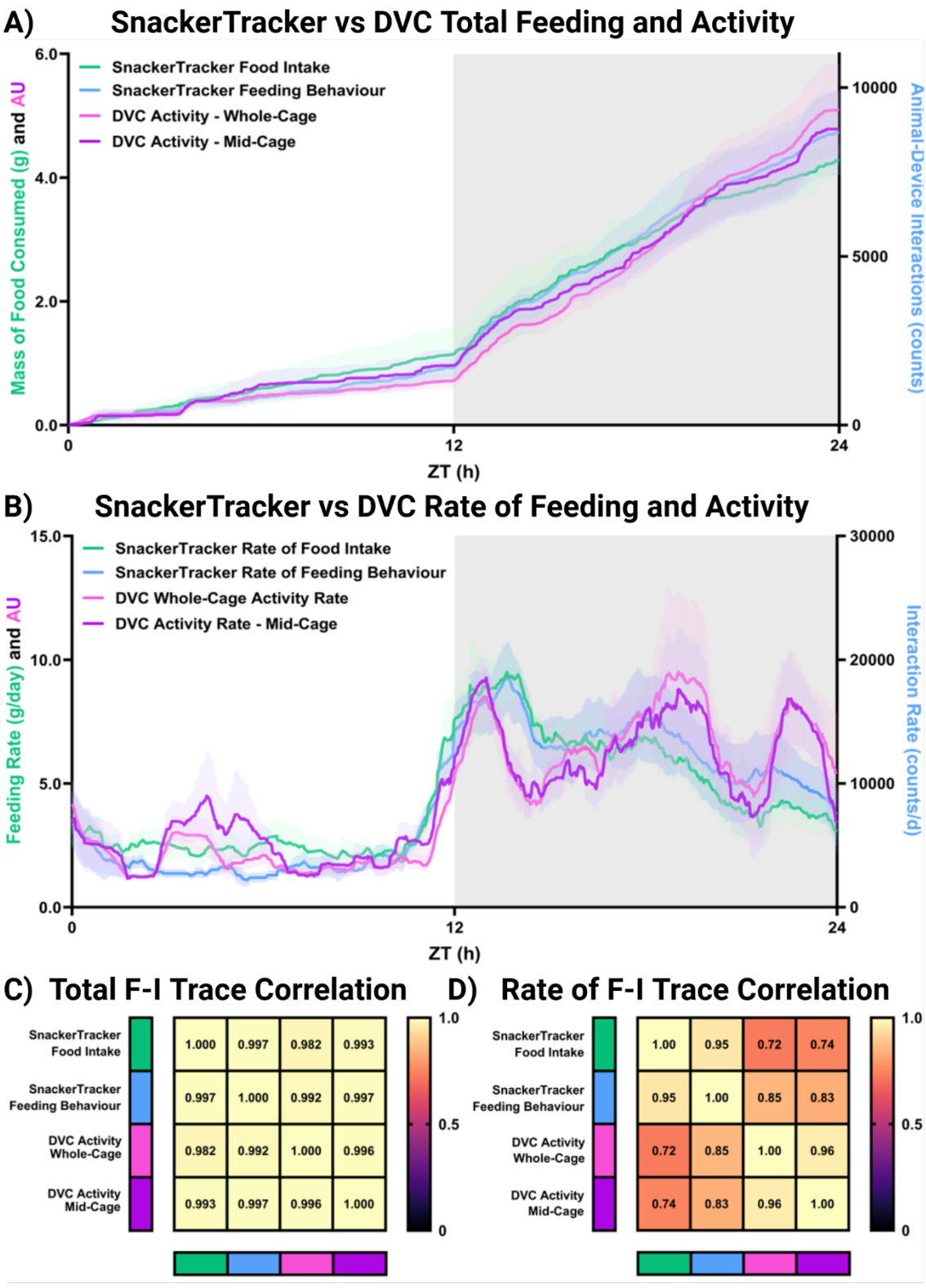


**Figure 11.** *SnackerTracker*-DVC alignment. Includes *SnackerTracker* food intake, *SnackerTracker* feeding behaviour, whole-cage DVC activity, and mid-cage DVC activity (see **A.4.1**). Daily traces for WT animals are shown as A) total food intake or activity and B) derivative rates. Pearson's r correlation matrices evaluate agreement between the time-course of each recording method for C) cumulative and D) derivative plots corresponding to A) and B), respectively. ZT=Zeitgeber time. $N_E$=6 per condition. See **Table 10**-**Table 11** and **A.2** for replicate and statistical details.

### *3.3.2 Activity and feeding behaviour*

I predicted that CRY-deficient mice would exhibit arrhythmic patterns of food intake and feeding behaviour when housed in constant-darkness–in contrast to diurnal rhythmicity under 12:12hr light-dark conditions and in CTRLs under all lighting conditions–and that *SnackerTrackers* would be able to detect these subtleties. I analysed genotype differences across *SnackerTracker* output metrics after confirming that no adverse welfare effects emerged. CTRL mice weighed significantly more than CRY-deficient mice (27.3±1.82g vs 22.7±1.2g, $t_{(16)}$=2.317, p=0.043), and no weight-loss differences before/after (proximity) *SnackerTracker* recordings emerged in CTRL or CRY-deficient male and female mice (proximity: $F_{(1,16)}$=0.0232, p=0.8807; proximity×genotype: $F_{(1,16)}$=0.0232, p=0.8807; proximity×sex: $F_{(1,16)}$=0.2093, p=0.6535). **Figure 12** compares *SnackerTracker* animal feeding behaviour and food-intake across genotypes and light conditions. I include both male and female data in **Figure 12**, show sex-disaggregated traces in **A.9.1**, and provided individual traces in **A.9.2**. Rates of animal-device interactions and food-intake are greater during the dark-phase as expected (**Figure 12A-B** for activity, **Figure 12C-D** for feeding). Visually, this is reflected as an increase in rates of activity and feeding in the dark-phase of **Figure 12E** and **Figure 12F**, respectively. In 12:12hr conditions, while overall animal-device interactions appear similar in CTRL and CRY-deficient mice (**Figure 12I**, $t_{(20)}$=0.0025, p>0.999), CRY-deficient animals show increased activity during the light-phase (**Figure 12A**, $t_{(20)}$=3.174, p=0.0099). CRY-deficient mice eat less compared to CTRLs in 12:12hr conditions (**Figure 12K**, $t_{(20)}$=3.466, p=0.0061), particularly in the dark-phase (**Figure 12D**, $t_{(20)}$=3.983, p=0.0044) despite no difference during the light-phase (**Figure 12C**, $t_{(20)}$=0.4931, p=0.9973). Total animal-device interaction rates do not differ between light conditions (**Figure 12I-J**, light condition×genotype: $F_{(1,20)}$=0.3733, p=0.5481). However, decreased feeding in CRY-deficient mice under 12:12hr light cycles is not reflected in constant-darkness; no genotype difference emerges in the absence of external light cues (**Figure 12K-L**, light condition×genotype: $F_{(1,20)}$=0.1842, p=0.1898).

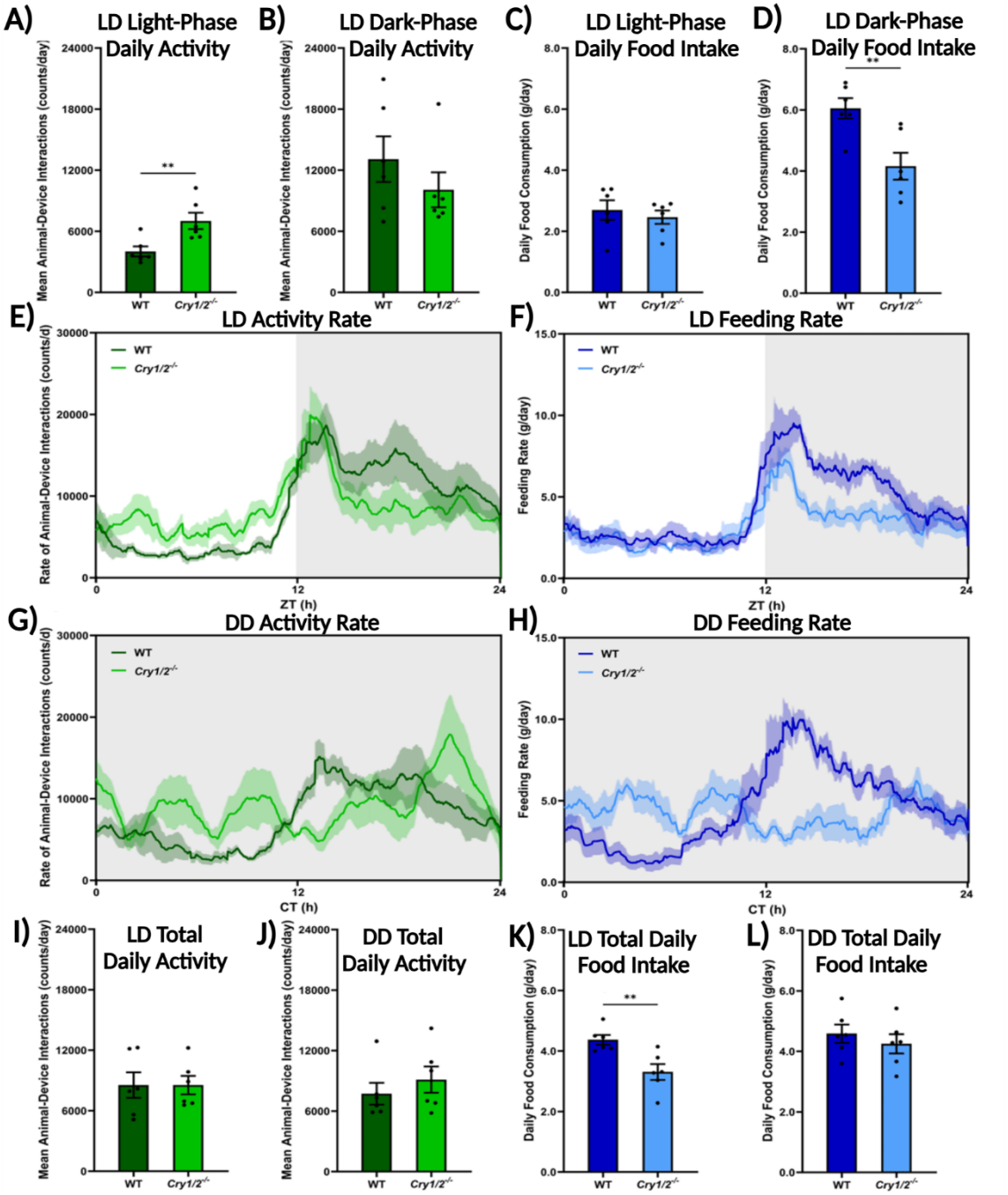


**Figure 12.** CTRL and CRY-deficient mouse behaviour differs across light conditions. Under 12:12h light-dark (LD) cycles, CRY-deficient animals (*Cry1/2*$^{-/-}$) are A) more active in the light-phase compared to CTRLs, yet no difference emerges in the B) dark-phase. C) Light-phase feeding does not differ between CTRL and CRY-deficient mice while D) CRY-deficient mice eat less during the dark-phase. 24h LD E) activity and F) food-intake timelines illustrate these differences, which are not conserved in constant-darkness (DD). For both G) activity and H) feeding, CTRL mice exhibit a similar pattern as in E-F) while CRY-deficient mice exhibit shorter ~5hr bouts. While patterns differ, 24h activity totals for I) LD (E-integral) and J) DD (G-integral) do not differ by genotype. Conversely, K) CRY-deficient mice eat less than CTRLs in LD (F-integral), yet I) CRY-deficient feeding increases to resemble that of CTRLs in DD (H-integral). I provide sex-disaggregated data in **A.9.1**, and individual animal traces in **A.9.2**. **=p<0.01, ZT=Zeitgeber time. $N_E$=6 for both WT and CRY-deficient groups. See **Table 10**-**Table 11** and **A.2** for replicate and statistical details.

Characterising feeding behaviour and food intake in mice with disrupted biological rhythms can complement prior studies and inform future investigations relevant to sleep and circadian disorders. While genotype differences in total activity do not emerge in 12:12hr conditions, decreased CRY-deficient dark-phase food-intake relative to CTRLs may either be due to smaller CRY-deficient mice requiring less food, or CRY-deficient mice weighing less due to reduced food intake. Prior work has shown that, under 12:12hr conditions, CRY-deficient mice weigh 10–20% less than control animals[326, 327], exhibit perturbed lipid metabolism[328], and rapidly gain weight when exposed to high fat diets[327], rendering this a popular model used to study the role of circadian disturbance in obesity and metabolic syndrome[327, 329, 330]. However, my results suggest that decreased CRY-deficient feeding is restored to CTRL levels in constant-darkness ($p=0.4585$). This indicates that the extent to which circadian disruption influences metabolism or weight change may be tuneable by environmental lighting, which in turn may confound the interpretation of interventions to circadian dysregulation (e.g., altered diets[327, 331-333], drug administration[334-336], or scheduled feeding). Activity differences across lighting conditions have been previously studied in CRY-deficient mice[337, 338] and others with disrupted circadian rhythms upon Period 1 and 2 double-knockout ($Per1^{-/-}$,$Per2^{-/-}$)[339-341], Bmal1 knockout ($Bmal1^{-/-}$)[342-344], and CLOCK mutation[345-347]; however, parallel feeding patterns have not yet been explored. This is surprising as rhythmic expression of some hepatic enzymes associated with feeding persist even in the absence of an intact circadian clock, which influences global clock gene transcription[340, 348-350]. If true, feeding signals are capable of intrinsically driving behaviour in cases of circadian disruption and absent external cues. This could explain why, while CTRL animals maintained daily rhythms in constant-darkness as in LD, CRY-deficient animals exhibited irregular bouts of activity in constant-darkness (**3.3.3**). Overall, my findings align with and expand upon previous literature, demonstrating that *SnackerTrackers* can identify differences in the patterns of CRY-deficient vs CTRL mouse food intake and feeding behaviour.

### *3.3.3 Circadian and ultradian rhythms*

**Figure 13** compares the periodicity and intensity of food intake and feeding behaviour across genotype, sex, and light conditions (i.e., light-dark vs constant-darkness). CRY-deficient feeding periodicity decreases in constant-darkness ($\bar{x}$=24.00h in light-dark conditions vs $\bar{x}$=21.55h in constant-darkness for CTRLs, yet $\bar{x}$=19.90h in light-dark conditions vs $\bar{x}$=10.80h in constant-darkness for CRY-deficient mice), with a significant influence due to light condition ($F_{(1,8)}$=7.344, p=0.0267) and genotype ($F_{(1,8)}$=11.51, p=0.0095) but not sex ($F_{(1,8)}$=3.061, p=0.1183, **Figure 13A**). Similarly, **Figure 13B** shows that CRY-deficient food intake periodicity decreases in constant-darkness ($\bar{x}$=22.52h in light-dark conditions vs $\bar{x}$=22.27h in constant-darkness for CTRLs, yet $\bar{x}$=23.31h in light-dark conditions vs $\bar{x}$=12.76h in constant-darkness for CRY-deficient mice), with a significant effect of light condition ($F_{(1,8)}$=11.03, p=0.0105), genotype ($F_{(1,8)}$=7.934, p=0.0226), and the light condition×genotype interaction ($F_{(1,8)}$=11.07, p=0.0104) but not sex ($F_{(1,8)}$=2.449, p=0.1562). Female mice feed more intensely (i.e., greater feeding amplitudes) (sex: $F_{(1,8)}$=21.82, p=0.0016, **Figure 13C**) across light conditions and genotypes (genotype: $F_{(1,8)}$=1.710, p=0.2273; light condition: $F_{(1,8)}$=0.05525, p=0.8201). **Figure 13D** shows decreased CRY-deficient feeding intensity compared to CTRLs ($F_{(1,8)}$=39.07, p=0.0002) in all mice (sex: $F_{(1,8)}$=0.07726, p=0.7881) across lighting conditions (light condition: $F_{(1,8)}$=1.980, p=0.1971).

Plainly, CTRL mice exhibit similar activity and feeding patterns across lighting conditions while CRY-deficient mice do not. Rather, CRY-deficient mice exhibit rhythmic behaviours in light-dark conditions yet present with <24h ultradian rhythms in activity and feeding rates in constant-darkness (τ≈10.80h and τ≈12.76h, respectively). This may occur due to underlying feeding-driven rhythms (**3.3.2**) or dopaminergic ultradian oscillations which promote alertness and prominently influence behavioural patterns in voles[351]. Ultradian rhythms are independent of the canonical circadian clock as they persist following SCN lesion[352], with dopamine levels continuing to increase and decrease with activity[337]. Therefore, dopaminergic oscillations are a

candidate driver of daily rhythms in CRY-deficient mice across lighting conditions, where removing circadian-like effects of external light cues in constant-darkness conceivably unmasks underlying ultradian influences.

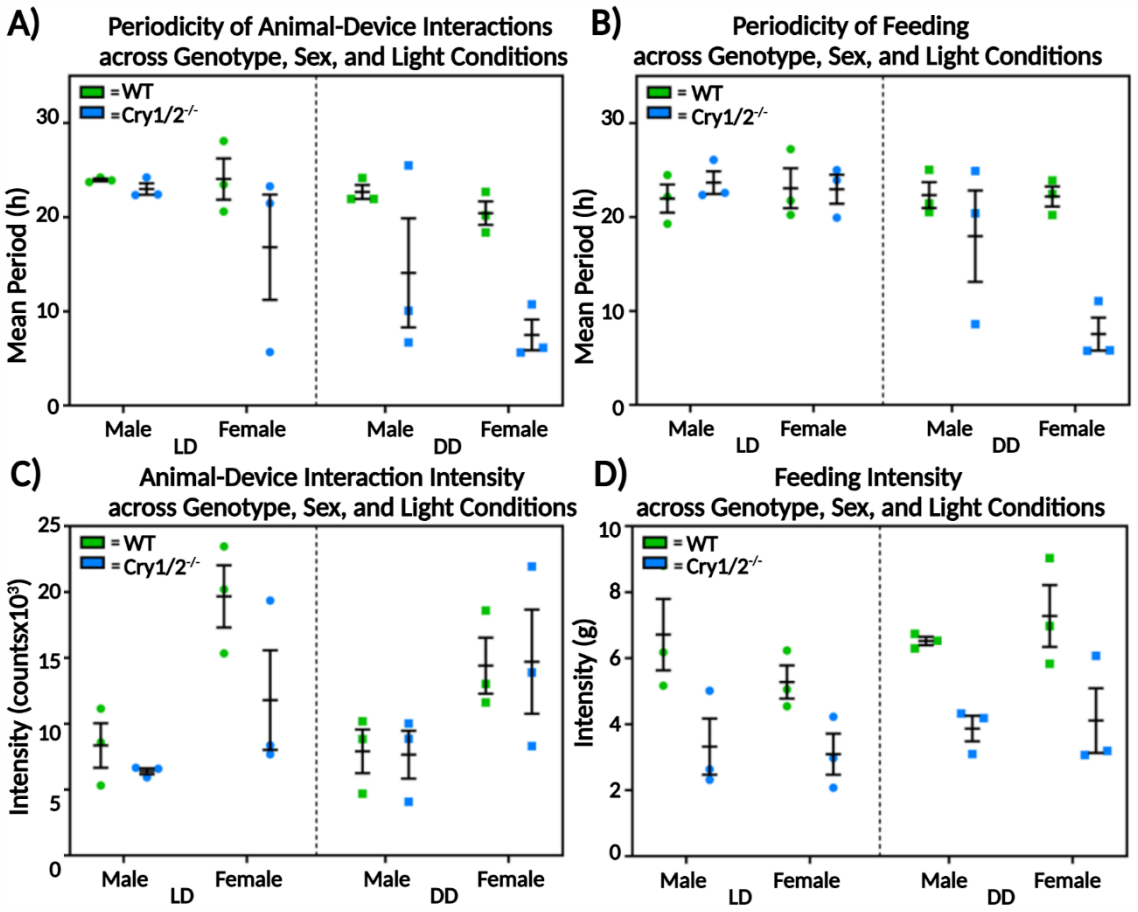


**Figure 13.** Animal feeding periodicity and intensity differs across lighting conditions. A) The period of animal-device interactions is shorter in CRY-deficient mice (*Cry1*$^{-/-}$,*Cry2*$^{-/-}$) compared to CTRL mice, which is more pronounced in constant-darkness (DD) compared to 12:12hr light-dark cycles (LD). B) Similarly, feeding periodicity decreases for CRY-deficient mice in constant-darkness in both male and female mice (i.e., a significant effect of light condition and genotype, including their interaction, but not sex though the trend appears more prominent in females). C) Female mice show more intense animal-device interactions than males across genotypes and lighting conditions. D) Both male and F CRY-deficient mice exhibit decreased feeding intensities compared to CTRLs under 12:12hr conditions and constant-darkness. $N_E$=6 for both WT and CRY-deficient cohorts. See **Table 10**-**Table 11** and **A.2** for replicate and statistical details.

Upon examining individual datasets (**A.9.2**), I observed ultradian feeding bouts in constant-darkness in all CRY-deficient mice, yet these appear shorter and more prominent in females (τ≈7.54h, *A*≈15,000 counts/d for females vs τ≈17.0h, *A*≈7,500 counts/d for males). Such

sex differences are not obvious in combined timelines even after sex-disaggregation (**Figure 12**, **A.9.1**). More intense female vs male interactions have been previously reported in longitudinal actogram experiments[353], and the presently observed τ≈17.0h in male CRY-deficient mice closely resembles that of published running-wheel activity timelines calculated to have an average period of ≈17h (where no female data was collected)[337]. Differences between males and females in this study could be due to random variability, true sex-differences, or both. Contrary to historical arguments to only include male mice in experiments due to oestrous cycle-induced variability in females every ≈4-5d, male mice have interestingly been shown to exhibit more extreme daily body temperature and activity fluctuation[354]. Nevertheless, daily temperature oscillations during the female oestrus phase–particularly in the dark phase–suggests that oestrogen enhances fluctuation[355]. When oestrogen levels peak, female mice exhibit increased locomotor activity and body temperature oscillations[355], which may be associated with cyclically elevated metabolic demands. Mouse temperature, feeding, and activity timelines have been shown to closely correlate when aligned and compared[356-359]. Therefore, presently observed female feeding and activity data having shorter periods and more prominent amplitudes might have occurred due to higher levels of circulating oestrogen in female mice. This could particularly explain sex-differences in constant-darkness due to a combination of both unmasked underlying rhythms in the absence of external light cues and increased oestrogen-related temperature oscillations in darkness[355]. This does not preclude—but rather compliments—dopaminergic ultradian conjectures as oestrogen can increase dopamine levels, the number of dopamine receptors, and the affinity of dopamine transporters in the brain[360]. Sex-differences in observed activity bouts could be driven by a range of physiological factors related to interactions between oestrogen and dopamine oscillation, altered body temperatures, appetite, or metabolic needs, yet is more likely attributable to a combination of all the above. Together, this provides evidence of–and possible explanations for–sex-dependent ultradian rhythms in CRY-deficient mice.

### *3.3.4 PIR combination and effects of DLE*

I introduced *SnackerTrackers* to WT mice under 12:12h light-dark cycles or 12:12h light-dark cycles with 3h of DLE at dark-onset for three reasons: 1) to visualise light-traces and confirm DLE; 2) to determine whether DLE alters amounts or patterns of food intake and feeding behaviour; and 3) to evaluate agreement between *SnackerTracker* and PIR recordings. *SnackerTracker* measurements indeed show strict 12:12h 'on'/'off' LDR traces under light-dark conditions (**Figure 14A,C**) and decreased light intensity after dark-onset with DLE (**Figure 14B,D**). However, LDR data also shows that DLE lasts longer than the expected 3hr window (**Figure 14Bi**), and that ≈3h of dim light unexpectedly occurs after light-onset where lights gradually turn 'on' rather than switching abruptly (**Figure 14Bii-iii**). This highlights the importance confirming light conditions, particularly upon experimental manipulation, where actual traces may differ from what was intended. *SnackerTracker* data reveal no significant differences in total, light-phase, dark-phase, light-onset, or dark-onset feeding or activity under DLE or light-dark conditions (**Figure 14E-F,i-v**). However, PIR data indicated that total time asleep increased under DLE ($\bar{x}$=15.8±0.3 for DLE, $\bar{x}$=14.8±0.5 for standard 12:12hr conditions). DLE yielded no divergence from expected τ=24h fundamental periodicities under any condition (**Figure 14E-Fvi**), yet phase-advanced activity and feeding relative to 12:12hr conditions. This is obvious in **Figure 14A-D** (note **Figure 14Biv**), **Figure 14E-Fvii**, and in raw PIR data (**A.9.3**). No body weight differences emerged after recordings (before: 27.16±1.30 vs after: 27.54±1.19, p>0.05) in monitoring animal welfare. Prior studies have showed that dim light in the morning reduces activity, improves the transition to rest, and yields more-consolidated sleep[253, 254, 361]. This confounds interpretations of increased sleep and changes in feeding behaviour under DLE compared to standard 12:12hr conditions, where the presence of dim light in the morning preclude effects being concretely attributable to DLE. Irrespectively, and as hypothesised, phase-shifted activity patterns appear to emerge as detected by *SnackerTrackers* and corroborated by PIRs upon exposure to DLE.

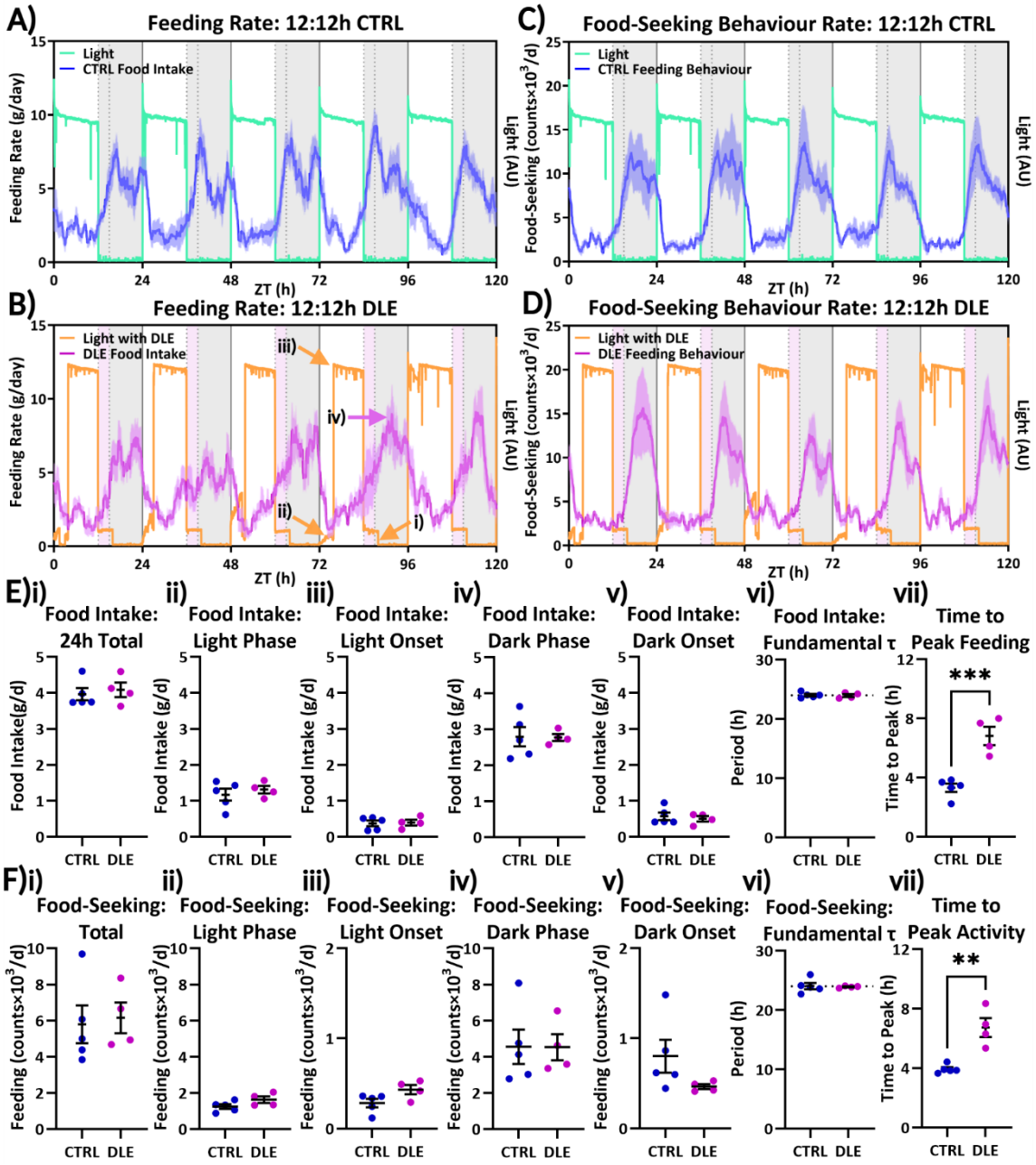


**Figure 14.** *SnackerTrackers* reveal changes in activity and food intake with DLE. Time-course data from 7d *SnackerTrackers* recordings illustrate mouse A-B) food-intake and C-D) food-seeking behaviour (animal-device interactions) under A,C) 12:12h light-dark CTRL ($N_E$=5) and B,D) 12:12h light-dark cycles with DLE ($N_E$=4). Region shaded in grey represent the scheduled dark-phase. Corresponding LDR recording of ambient cage lighting are overlaid, where A,C) abrupt light-dark transitions contrast B,D) i) DLE at dark-onset and ii-iii) dim light in the morning. No differences emerge for any extracted summary Ei-vi) food-intake or Fi-vi) food-seeking behavioural metric, including fundamental periodicities which do not differ from 24h daily rhythms as expected. However, the time to peak Evii) food-intake and Fvii) food-seeking behaviour increases under DLE, which can be visualised by comparing the proximity of peaks in blue traces in A,C) relative to dark-onset to those of magenta traces in B,D). The arrow in Biv) highlights this phase-shift. *=p<0.05, **=p<0.01, ***=p<0.001, ****=p<0.0001. ZT=Zeitgeber time. See **Table 10**-**Table 11** and **A.2** for replicate and statistical details.

### *3.3.5 Seasonal hamster feeding and video recordings*

I introduced *SnackerTrackers* to two male hamsters—one housed under a 'summer' photoperiod, and one under a 'winter' photoperiod—to 1) test whether devices are suitable for HCM in other rodent species, and 2) to assess whether *SnackerTrackers* can detect expectedly increased food intake in the summer photoperiod condition. **A.4.3** shows the cage setup with which *SnackerTrackers* proved compatible; hamsters ate throughout 7d recordings and did not lose weight (summer: 26.1g before vs 27.0g after; winter: 48.3g before vs 48.91g after). **Figure 15AIi** confirms expected light schedules in the summer condition; however, irregular lighting emerged in the winter condition (**Figure 15BIii**). This again stresses the importance of parallel LDR recordings as, otherwise, the difference between SnackerTracker-derived feeding patterns in summer/winter conditions (**Figure 15V-VI**) could have been interpreted as an effect of altered photoperiod rather than confounding light conditions. 'Winter' feeding and activity patterns in **Figure 15BV-VI** more closely resemble those of CRY-deficient mice in constant-darkness (**Figure 12G-H**), where what again appear to be shorter ≈5h ultradian rhythms could similarly be driven by feeding[340, 348-350]. The 'winter' hamster interacted more intensely with the *SnackerTracker* (**Figure 15V-VIi-ii**) and exhibited more feeding behaviour compared to the 'summer' hamster (**Figure 15III-IV**). This could be due to varied light exposure or increased body weight; however, I noticed that the 'summer' hamster was reported to eat an exceptionally small amount of food (<0.5g/d) which is not biologically sustainable (**Figure 15III**). I suspected that pellets may not have been entirely removed before *SnackerTracker* recordings began. I consulted parallel video recordings which showed that, indeed, the summer hamster had hidden a stash of small pellets deep within its bedding. As two food-sources were therefore present, *SnackerTracker* data in **Figure 15A** is invalid and does not truly represent total food intake and feeding behaviour. Here, *SnackerTracker* data identified this non-biological recording which, complimented by video recordings, revealed clear experimental error.

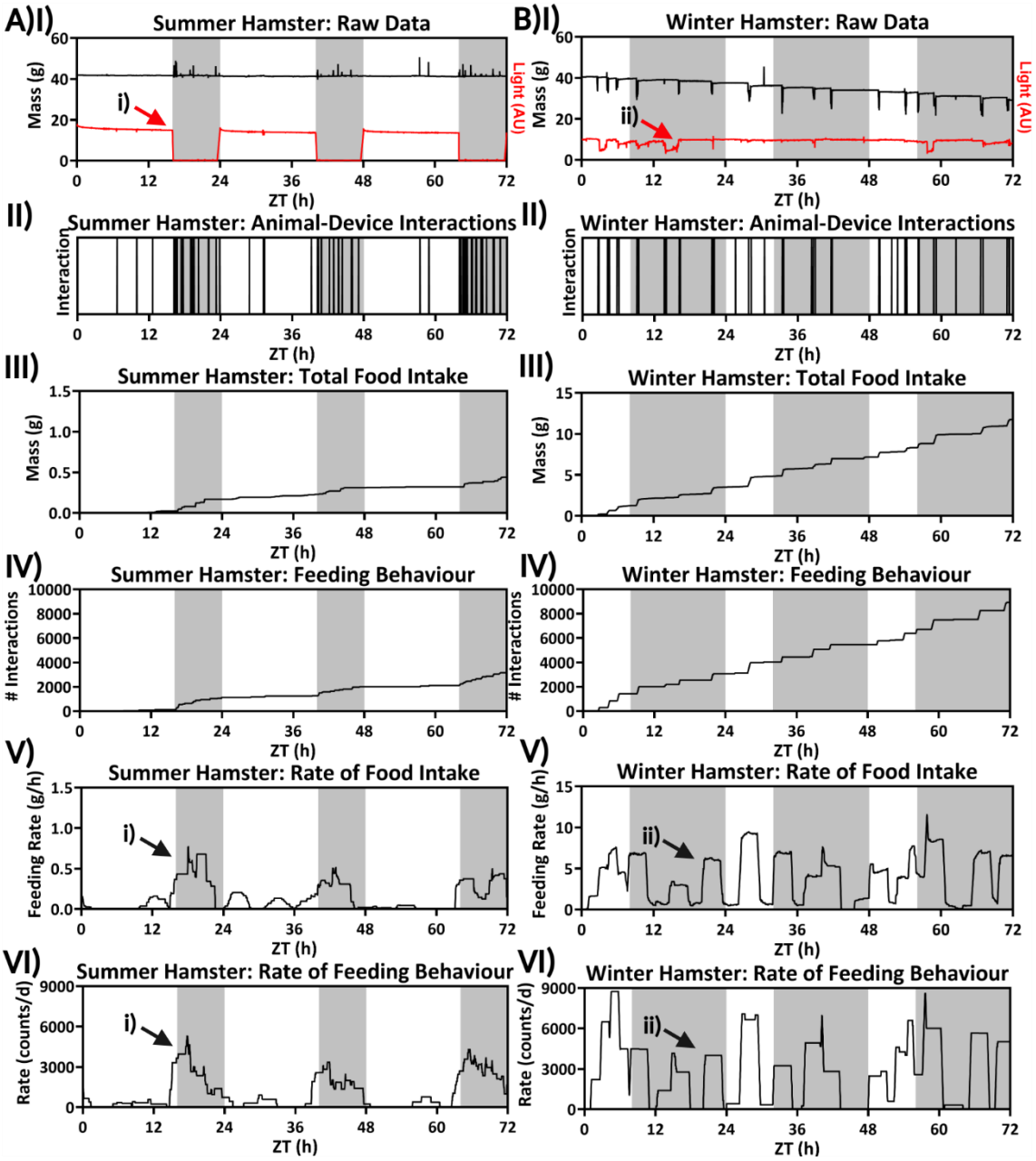


**Figure 15.** Hamster *SnackerTracker* data under summer and winter photoperiods. A) 'Summer' and B) 'winter' (protracted dark-phase) timelines include: I) raw mass and LDR data; II) animal-device interactions; III) total food intake; IV) total feeding behaviour; V) food-intake rates; and VI) feeding behaviour rates. BIi) Unexpectedly constant light in the 'winter' condition contrasts the AIi) 'summer' condition and may explain ultradian BVii) feeding and BVIii) activity patterns.

## 3.4 SnackerTracker and TracKIT design considerations

### *3.4.1 Hardware limitations*

Perhaps the most notable hardware limitations which emerged during *SnackerTracker* validations and preliminary applications included insufficient battery life and capacity for data

drift. Not-infrequently, battery failure via disconnection at the JST port or insufficient capacity to sustain longer recordings resulted in unsuccessful microSD logging (**3.1.4**) or early truncation, both of which led to data exclusion. To address this, I adapted my crimping technique to strengthen the JST connection and sourced alternative batteries with JST inserts. I have not encountered JST connection errors since. However, a limited battery life of ~2.5 days without IoT/Wi-Fi connectivity (which would increase current draw and decrease battery life further) remained problematic; batteries are required for wireless *SnackerTracker* operation, which is needed for compatibility within standard individually ventilated cages. As I anticipated needing to obtain >2.5d recordings, I adapted the case cover such that USB power could be supplied through a grommet aligned with the MKR 1010 port. I piloted USB-power-supplied recordings and collected continuous week-long recordings without issue (**A.4.4**). I describe the process of both wired and wireless data collection in protocols.io[280]. Although I did not observe data drift during testing (**2.2.2**), a lack thereof should not be assumed. Drift may onset with device wear and longer recording times (e.g., temperature and humidity fluctuations)[212] and should therefore be confirmed periodically (e.g., monthly if used frequently, otherwise before any set of recordings if unused for >1mo). Humidity fluctuations may introduce systematic error as pellets which absorb or lose ambient moisture will increase or decrease in weight, respectively. During this study, all mice were maintained in temperature- and humidity-controlled environments (20–24°C and 45–65% per UK regulations), which minimised the chance of this artifact occurring. However, even small differenced within this range could have a notable effect as elevated humidity can promote water retention, hinder pellet integrity, and accelerate food deterioration/crumbling. For any specific diet used for the first time, potential humidity confounds could be addressed by using an empty cage and weighing food at the start and end of a study to calibrate humidity effects. Future experiments should consider recording humidity to determine whether fluctuations capable of confounding results emerge.

### *3.4.2 Software limitations*

Further limitations surfaced in operational (**3.1.4**) and analysis (**3.2**) software. Despite successful IoT monitoring during benchtop testing (**3.1.4**-**3.1.5**), the IoT proved incompatible with university networks which I therefore chose not to use during *in vivo* recordings. A lack of IoT connection precludes remote monitoring, yet not local SD card data storage, so I solely used SD-logging thereafter. Future real-time data monitoring and remote-control could be achieved using alternative platforms (e.g., Node Red)[205, 209]. This would be an essential future direction if real-time feedback is necessary in future studies requiring experimental intervention according to animal activity, sleep, or feeding state. I designed *TracKIT* for *SnackerTracker* analyses, yet it can theoretically be used to process any time-series data as I demonstrated using DVC outputs (**3.3.1**). This is both a critical *TracKIT* platform feature and inherent limitation; underlying *TracKIT* scripts can be adapted to accommodate different input formats, yet the detailed structures of files from other HCM suites (e.g., Promethion[199] and CLAMS[200]), integrations (e.g., PhenoTyper[204]), and video-based systems (e.g., CageView[203]) are typically proprietary (**Table 2**). More sophisticated *TracKIT* processing algorithms should be considered and integrated to address confounds like humidity and data drift–for which calibration curves could be acquired and used to correct conceivable instances of either occurring–and to enable analyses of nuanced waveform features. Features like phase-space twist (i.e., degrees of amplitude-period co-modulation), waveform asymmetry (i.e., differences in the rate at which activity or feeding peaks rise and fall), and rhythm fragmentation indices (i.e., which quantify the variance explained by defined rhythms as compared to noise) may reveal insight into distinct circadian phenotypes[356] that currently cannot be detected by the Sum of Sine regression model presently employed. Whether for novel input file accommodation or computational advancement, I provide underlying scripts across multiple open-source platforms to encourage future community development.

### *3.4.3 Device longevity*

Additional challenges emerged related to device design and wear over time. Device longevity is a concern as mice naturally chew and scratch. Though damage was minimal after six months of use, printing or casting the chassis using more durable materials (e.g., aluminium) could preserve SnackerTracker integrity, though with increased cost. Surprisingly, I observed little to no device damage in any form during hamster pilot experiments (**3.3.5**). I proactively considered the possibility that urine may damage electronics, and circumvented this by bevelling the case cover design (**A.3.3**). When later testing USB power supply, one mouse chewed the wire at the grommet interface; wrapping the junction in electrical tape prevented further chewing, however this may not suffice if mice chew more aggressively. As with any recording device in the home cage, researchers should ensure that access to any wires or sensitive components is minimised and that devices are regularly inspected for damage.

### *3.4.4* **In vivo** *complications*

Additional *in vivo* limitations include incompatibility with social housing, capacity for error if pellets are removed but not ingested (i.e., 'crumbling' and 'cheekiness'), and 'chipping' phenomena. The current *SnackerTracker* design is solely suited to single-housing as one cannot otherwise discriminate which mouse would be removing pellet from the food holder at any given time. This could be circumvented if RFID or video-based tracking (e.g., AnyMaze) are combined with future *SnackerTracker* setups. Systematic error is likely present due to 'crumbling' if pellets are removed from the food holder but not imminently eaten (e.g., hoarded and later consumed). This was to proportionally little effect yet is not negligible; I sieved and weighed crumbs which accumulated daily amongst and under bedding material during *in vivo* pilot compatibility tests and estimated that this amounted to 0.219±0.016g/d (equivalent to <5% of animals' total food intake). Future studies should monitor and report crumbling as both an absolute mass and as a percentage of total food intake to account for natural differences between animals.

*SnackerTracker* hamster recordings introduce another crumbling-like source of possible error—which here I term 'cheekiness'–as hamsters can store food in their cheeks. Pellet masses reported as being removed from the *SnackerTracker* are typically assumed as being consumed but may be stored in the cheek for later digestion. Feeding patterns may then be misrepresented if cheek-filling and digestion occur at different times. 'Chipping' is another non-negligible issue as animals may sit, defecate, or place bedding atop the food holder. I therefore created the *TracKIT* 'chip filter' where, during processing step II, spikes can be manually identified, attenuated, and documented in output metadata to mitigate artifacts (**3.2.2, A.3.10**). *In vivo* complications are not unnavigable yet must be considered when conducting *SnackerTracker* experiments and interpreting results.

### *3.4.5 Genotype-phenotype confounds*

Any experimenter must also consider whether *SnackerTracker* food presentation (i.e., whether food is provided on the cage-floor or presented via a food-holder) influences feeding behaviour or food intake in genetically modified or ill animals. The final design presents food in a manner which resembles normal cages with food hoppers; any mouse line that struggles to access the food hopper in a normal cage should similarly struggle to access food from the *SnackerTracker*. Supplementing the cage floor with pellets or mash would render *SnackerTracker* recordings invalid, however *SnackerTracker* feeding would then resemble restricted feeding if no food supplements are provided (which should never occur unless experimentally planned and ethically approved). Similar considerations should be made when working with animals with anxiety phenotypes, as neophobic animals may eat less when presented with a novel food source. As such, alternative physiological and behavioural interpretations of *SnackerTracker* outputs should always be considered, and animals should be monitored closely during recordings (e.g., via body weight and general welfare documentation) especially when first exposed to this new feeding system.

## 3.5 Indications and future directions

### *3.5.1 Parsing and advancing behavioural HCM*

HCM has been integral to preclinical sleep and circadian research for decades; however, despite technological advancements, limitations related to behavioural specificity and analysis standardisation persist. Running wheels, video- tracking, beam-break sensors, PIRs, and DVCs quantify home cage behaviour, yet by different methods which can confound data collection and phenotype interpretation. Results from PIR and running-wheel data can drastically differ[362], and measuring activity using running wheels with EEG/EMG recordings independently affects sleep[363, 364]. Analyses can compound differences depending on which processing parameters are specified[213] and, critically, in how biological features of interest are extracted from raw data as exemplified in *SnackerTracker* measures of food intake vs food-seeking behaviour (**3.2.2**-**5.1.1**). Therefore, while quantifying home cage activity may proxy feeding behaviour, these measures are not interchangeable (**5.1.1**). Feeding should be measured using designed-for-purpose tools like the *SnackerTracker-TracKIT* platform, which is thus relevant in its capacity to provide targeted insight into the amount and pattern of animal food consumption.

### *3.5.2 Contracted provision*

*SnackerTracker* construction, modification, and implementation requires expertise in 3D printing, electronics, and coding. To cater for users who do not specialise in these techniques, I partnered with Oxford's Department of Physics Electronics design workshop and Dr. Keiran Foster (website: www.physics.ox.ac.uk/about-us/our-facilities-and-services/electronics-design-and-workshop; email: optec_enquiries@physics.ox.ac.uk). I provided their team with all construction details such that they can provide pre-assembled *SnackerTrackers* for a fee. At the time of the submission of this thesis, one *SnackerTracker* can be purchased for £250.00 and each additional device thereafter for £210.00 (including parts and labour).

### *3.5.3 Improving animal welfare*

The *SnackerTracker* also presents as a refinement to animal research. Documenting feeding patterns is informative when monitoring rodent welfare, particularly after surgical procedures to ensure normal recovery (reduced appetite will typically accompany sickness). More generally, incorporating *SnackerTracker* measurements into regular welfare assessments may identify abnormal feeding patterns or food intake as an early indication of disease or experimental complication. Particularly, prey species like mice may mask sickness behaviour as signs of weakness increase susceptibility to predation in nature. As increased levels of inflammatory cytokines during sickness may induce elevated body temperatures, decreased appetite, and significant metabolic changes[365], food intake measurements may identify illness before more overt behavioural signs like weight loss emerge. *SnackerTrackers* are furthermore non-invasive; researchers are not required to reach into cages to introduce or extract food, which minimises disruption to the home cage and stress to both animals and humans (**1.2.5**)[75]. LDR inclusion provides further welfare benefit as *SnackerTracker-TracKIT* identified unexpected cases where lights may have turned 'off' for several hours in **Figure 10DIIIiii** or remained nearly-constantly 'on' in **Figure 15BI**. Conditions of constant darkness or light can be detrimental to animal well-being[366, 367] and can profoundly influence activity (**3.3**); as such, any unexpected light cycle schedule deviation can confound sleep and circadian studies. Welfare checks can identify home cage light discrepancies or animal sickness at discrete times, yet additional continuous *SnackerTracker* recordings would provide complimentary insight into conceivable daily fluctuations and longitudinal trends across an animal's lifetime.

### *3.5.4 Drug-delivery and pharmacological applications*

*SnackerTrackers* could improve the accuracy of drug delivery via diet and improve preclinical pharmacological testing. Knowing how much drug-laden food an animal has eaten at any timepoint would enable precisely drug dosage calculations. In animal research, CNO and

tamoxifen are being increasingly used to elicit neuronal responses or trigger gene expression, respectively[147, 368]. CNO and tamoxifen are typically injected into mice or delivered via oral gavage, yet companies (e.g., Inotiv, Research Diets etc.) have begun producing drug-laced food pellets; tamoxifen is currently available, and CNO efforts are ongoing. Diet-based tamoxifen or CNO administration would be an immense welfare improvement, yet dosage amounts would be difficult to ascertain if food is provided *ad libetum*. Therefore, the *SnackerTracker* could be a valuable means of determining the mass of CNO/tamoxifen-laced food pellets consumed at any time–by knowing pellet drug concentrations, the amount of CNO or tamoxifen ingested could be calculated. *SnackerTracker* recordings would be relevant in using other pharmacological agents in research applications or preclinical drug development; precisely knowing when and how much food has been eaten could inform the efficacy of therapeutic candidates associated with diseases including but not limited to diabetes, digestive disruption, weight loss, eating disorders, and sleep disturbance[202, 348, 369-373]. If a researcher is using animal models to test a drug candidate, it is critical to characterise if and how feeding is influenced whether as an intended or unintended consequence. As I show throughout preliminary *in vivo* experiments (**3.3.4**, **3.5.1**), food-intake may not precisely correspond with activity or food-seeking behaviour, therefore a direct and dedicated means of measuring feeding is warranted[347, 374].

### *3.5.5 Future SnackerTracker-TracKIT directions and customisability*

The *SnackerTracker* and *TracKIT* platforms are novel in their open-source design and provision; I created both such that interaction with source files is not required for users with little programming experience, yet others capable of full-command can access underlying scripts, modify both the chassis and processing pipeline to suit individual experimental needs, and contribute to community improvement. In future applications, the *SnackerTracker* could be used in a range of home-cage setups, with additional animal species (e.g., voles and, if increased in size, possibly ferrets), and in combination with other monitoring systems according to study-

specific requirements. To follow-up on observed sex-differences in ultradian rhythms in CRY-deficient mice, feeding and activity data could be correlated to body temperatures over time to test the sex-dependency of feeding activity oscillations as a function of oestrous cycles and temperature profiles. This could be achieved by obtaining thermal data via implanted devices or non-invasive imaging[375], and activity via PIR or video recordings[205]. These parallel datasets could validate *SnackerTracker* recordings and provide additional insights into behaviours influencing data interpretation. I currently report *SnackerTracker* LDR measurements in arbitrary units; while this provides discrete 'on'/'off' insight, unitless metrics cannot discern absolute intensities or wavelengths. It may be difficult to incorporate more sophisticated light sensors into the existing *SnackerTracker* configurations; however, future experiments could easily involve placing open-top-cages with *SnackerTrackers* into LTCs equipped with spectrophotometers which quantify spectral distributions[210]. This would expand the scope of *SnackerTracker* application in experiments requiring precise light measurements (e.g., circadian photometry applications). For compatibility with studies involving head-mounted EEG/EMG leads, optogenetic implants, or multielectrode probes, the food holder could be redesigned such that pellets extend horizontally to prevent overhead wire-tangling. Future studies could use the *SnackerTracker* to evaluate food preferences by providing two or more devices in one cage, or by upgrading the design to possess two load cell-food hopper assemblies (with different food provided within each) for simultaneous self-contained measurement. Data could furthermore be used as an experimental outcome when comparing CRTL mice to those modelling a range of human diseases, for example decreased feeding following digestive disturbance using the dextran sodium sulphate colitis model[369], or increased feeding using models of Prader-Willi Syndrome[202]. Demand will drive future directions, which are wide in scope due to the adaptable design, low cost, and open-access provision of the *SnackerTracker* home-cage monitoring device and *TracKIT* analysis platform[211, 258, 280, 324, 376].

# Chapter 4: Results – Layer 6b silencing and augmentation yields anatomical changes revealed by analysis pipeline refinement

This chapter characterises whole-brain *Drd1a*-Cre cell densities and soma morphologies under chronically 'silenced' and 'augmented' conditions, then compares *Drd1a*-Cre cells and human WMINs to support or contest their analogy. While prior studies histologically document *Drd1a*-Cre$^{+}$ expression in select ROIs[4, 48, 50, 75, 77, 78], none capture conceivable network-level brain-wide effects (**1.2**). Means of whole-brain analyses are therefore necessary, yet to my knowledge none can yet 1) identify cells across fluorophore combinations, 2) atlas-map detections, and 3) incorporate soma size analyses. The QUINT pipeline accepts *single* fluorophore detections yet cannot accommodate *multiplexed* signals or soma integrations[220]. Therefore, I first describe computational improvements which render it (r-QUINT) suitable for present experiments (**4.1.1**-**4.1.3**). I then validate r-QUINT performance by comparing PV/VVA quantifications to recently published datasets, reasoning that densities should be similar across methods (**4.1.4**, **4.1.5**). To further test r-QUINT viability, I quantify PV/VVA expression in available L5 excitatory and inhibitory DREADD samples; I expected no differences to emerge in PV densities, yet that VVA may subtly vary to compensate acute L5 perturbation (**4.2**). I then use r-QUINT to histologically document changes in *Drd1a*-Cre subtype expression patterns upon chronic *Snap25*-cKO (I anticipated minimal genotype differences) and *PTEN*-cKO (I predicted increased cell prevalence and hypertrophy, particularly in CPLX3-expressing subtypes, resembling human conditions of altered WMIN morphology associated with PTEN dysfunction) (**4.3**). Finally, I compare single-neuron traces of mouse *Drd1a*-Cre cells and human WMINs, hypothesising that subtypes should bear morphometric resemblance across species according to ORX-sensitivity and pyramidal vs non-pyramidal characterisation (**4.4**). This will inform the notion of phylogenetically conserved roles of subplate remnants and the interpretation of results from studies employing the *Drd1a*-Cre mouse model when considering relevance to human conditions (**4.5**).

## 4.1 QUINT pipeline improvements and initial validations

### *4.1.1 Overview and adaptations*

Limitations of the QUINT workflow required computational refinements to enable pan-cortical analyses of cell densities, distributions, and morphologies across multiple fluorescently tagged proteins. As detailed schematically in **Figure 3**, methodologically in **2.3.4**, and pictorially in **Figure 16,** my refined pipeline involves: 1) pre-processing; 2) atlas mapping; 3) feature extraction; 4) data registration; and 5) output tagging. This improves 2D→3D analyses by enabling multiplexed morphometric integration and regionalisation. I describe methodological adaptations across steps 1-3) in **4.1.2**, particularly regarding image acquisition (i.e., SDCM and SSFM), standardised pre-processing (i.e., image format, channel colour assignment, contrast, pixel dimensions, and nomenclature), and segmentation (i.e., employing QuPath and Arivis as opposed to Ilastik or ImageJ). **4.1.3** details further adaptations across steps 3-5), which involve extracting multiplexed branch and soma morphometric features for integration with whole-brain quantifications. **4.1.4** provides preliminary validations of PV/VVA and *Drd1a* cell densities against previously published quantifications, while **4.1.5** describes present workflow limitations and promising future directions. Groovy and MATLAB scripts standardise image segmentation workflows, which I therefore have referenced in the appendices after having deposited each to open-source repositories (i.e., GitHub and Zenodo). Overall, I present alternative image acquisition and analysis methods which advance pipeline capabilities by enabling multiplexed analyses and morphometric integration. While I currently only incorporate soma volumes into r-QUINT analyses, results provide proof-of-concept for further development (i.e., to eventually tag other soma morphometric features and neurite characteristics) and stress the importance of standardisation in future applications.

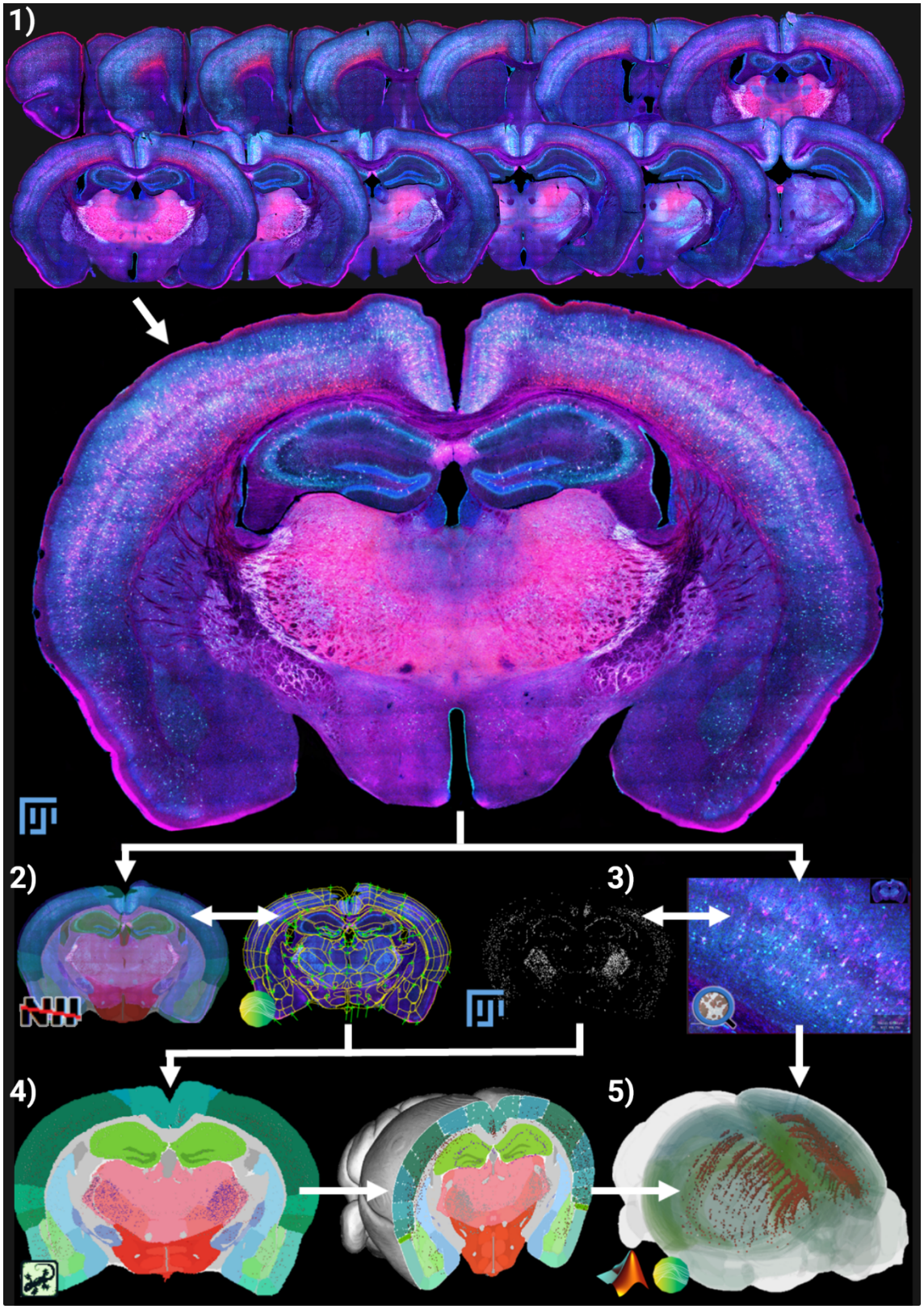


**Figure 16.** Progression of sample sections through the revised QUINT pipeline[32]. Steps and associated software include: 1) image pre-processing using Fiji/ImageJ; 2) atlas mapping via VisuAlign and QuickNII; 3) feature extraction (soma detection and morphometrics) using Fiji/ImageJ and QuPath; 4) registration using Nutil; and 5) output tagging via MATLAB and MeshView visualisation. Blue=DAPI, red=*Drd1a*, cyan=PV, and magenta =VVA.

### *4.1.2 Image acquisition, pre-processing, and segmentation*

Pipeline modifications encompassed standardised image acquisition, pre-processing, and segmentation adaptations to address microscopy artifacts and QUINT compatibility. I first considered which imaging modality to use as the pipeline originally employed SSFM[220]. SDCM significantly improved image quality (**Figure 17**) thereby warranted cost-benefit analyses (**A.6.1**). Costs included time, equipment usage fees, and image file size, while benefits included signal-to-noise ratio (SNR) and resolution. I initially selected SDCM for L6 studies due to an improved signal-to-nouse ratio suitable for morphometric analyses (**4.1.3**). However, I employed SSFM for L5 studies (chapter 5) given the larger number of sections across a greater number of fluorophore combinations and correspondingly prohibitive time, cost, and data storage requirements; I projected that SDCM for L5 studies would require ~511h of active scanning time, ~48.5TB of storage, and ~£24,500 in cost-recovery fees, while SSFM would require ~84.0h of automated scanning time, ~2.79TB, and ~£3,960 for an equivalent number of sections (**A.6.1**).

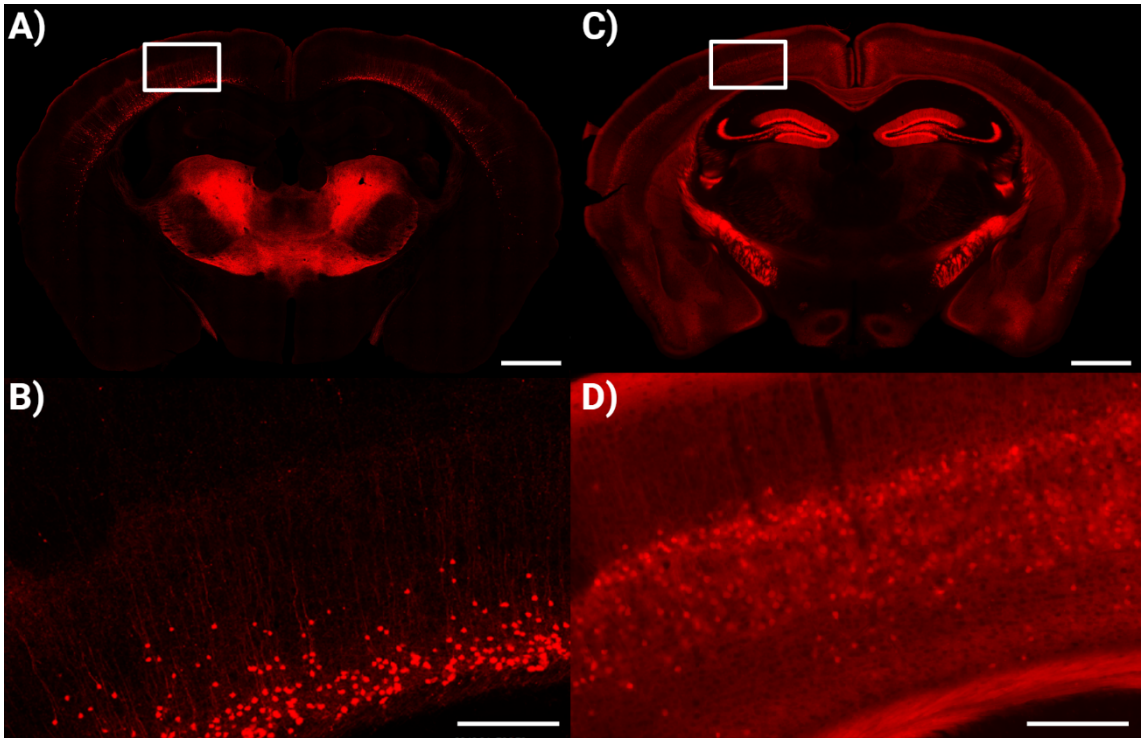


**Figure 17.** Compares SDCM and SSFM image quality. Pilot A-B) *Drd1a*-Cre$^{+}$ images from SDCM yielded superior SNR, yet C-D) *Rbp4*-Cre$^{+}$ images from SSFM were more time- and cost-effective. Rectangles in A,C) correspond to B,D), respectively. Scale bars: A,C)=1mm; B,D)=200µm.

Pre-processing employed custom ImageJ macros (**A.10.3, A.10.6**) which ensured that images were formatted as .tiffs, consistent across channel assignments, suitably contrasted, ≤10,000×10,000px, and named appropriately[220]. For image segmentation, QuPath substituted the use of Ilastik in the original QUINT *Feature Extraction* workflow (**Figure 3**); analysing exceptionally large full-coronal images proved incompatible with limited ImageJ RAM capacities, while QuPath employed a RAM-compatible multi-resolution method to break images into smaller tiles for processing followed by re-stitching. I therefore adapted QuPath Groovy segmentation scripts from a common scaffold (**A.10.4**) for each fluorophore combination. That is, I independently assessed signal intensity histogram distributions alongside combinations of cell detection parameters (**A.6.3**) and object classifiers to refine segmentation accuracy (i.e., circularity, area, and intensity via $\sigma_M$ cutoffs) (**A.10.5**). **Figure 18** illustrates sample segmentation and colocalisation fidelity. Proprietary programmes like Arivis could be alternatively employed where image pre-processing can be defined within segmentation pipelines (**4.1.3**); nevertheless, and in prioritising the use of open-source platforms wherever feasible, these ImageJ and QuPath scripts proved to be a viable workflow for standardised image pre-processing and segmentation. I used a third ImageJ macro (**A.10.6**) to mask segmentations. This involved additional processing where thin single-pixel outlines from QuPath detections were hyper-contrasted to ensure that each cell was distinguished from neighbours by a perimeter of at least one pixel. This is essential for Nutil quantifications yet inherently induces systematic error by underestimating soma areas by the area of perimeter-pixels omitted. Future computational adaptations could address this by incorporating **Equation 3** into **A.10.7**; assuming approximately circular soma, radii could be artificially increased by a value of 1 pixel (i.e., 0.325µm) then used to re-calculate areas.

**Equation 3.** Computational r-QUINT correction. Accounts for underestimated soma areas in r-QUINT due to perimeter hyper-contrasting. $v_c$=corrected volume; $v_o$=original volume; and δ=1px if volume units=px, or the equivalent width of one pixel (e.g., δ=0.325µm) if volume units=µm$^2$.

$$v_c = \pi\left(\sqrt{\frac{v_o}{\pi}} + \delta\right)^2$$

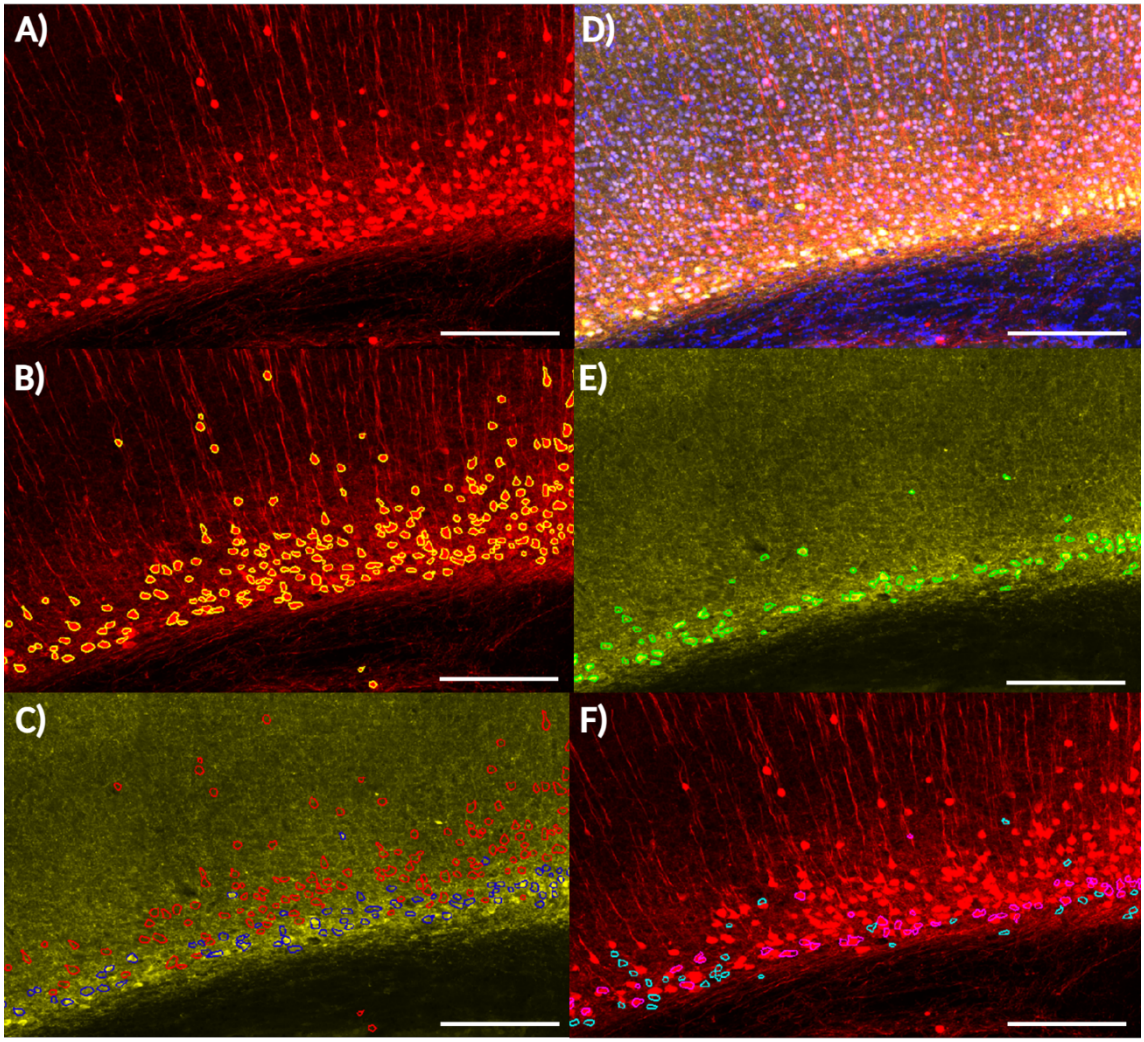


**Figure 18.** r-QUINT segmentation accuracy. A) *Drd1a*-Cre$^{+}$ cells are B) detected via QuPath object classification (*Drd1a*$^{+}$=yellow). Areas masked by *Drd1a* are evaluated for C) CPLX3 colocalisation (*Drd1a*$^{+}$/CPLX3$^{-}$=red; *Drd1a*$^{+}$/CPLX3$^{+}$=blue). Similarly, D) CPLX3$^{+}$ cells are E) detected (CPLX3$^{+}$=green) and tested for F) *Drd1a* overlay (CPLX3$^{+}$/*Drd1a*$^{-}$=cyan; CPLX3$^{+}$/*Drd1a*$^{+}$=magenta). While imperfect, segmentations across A-F) appear acceptable.

### *4.1.3Morphometric tagging and multiplexing*

I unsuccessfully attempted soma and neurite morphometric analyses using Arivis, then successfully turned to QuPath for r-QUINT data tagging and regionalisation. First, I used Arivis to pre-process and segment both soma and neurites (**Figure 19**). However, I was not satisfied with the quality of Arivis' automated neurite tracing which proved to be limited by imaging resolution. Arivis furthermore could not generate single-pixel perimeters around soma detections, thus proved incompatible with Nutil. So, I exclusively employed QuPath thereafter.

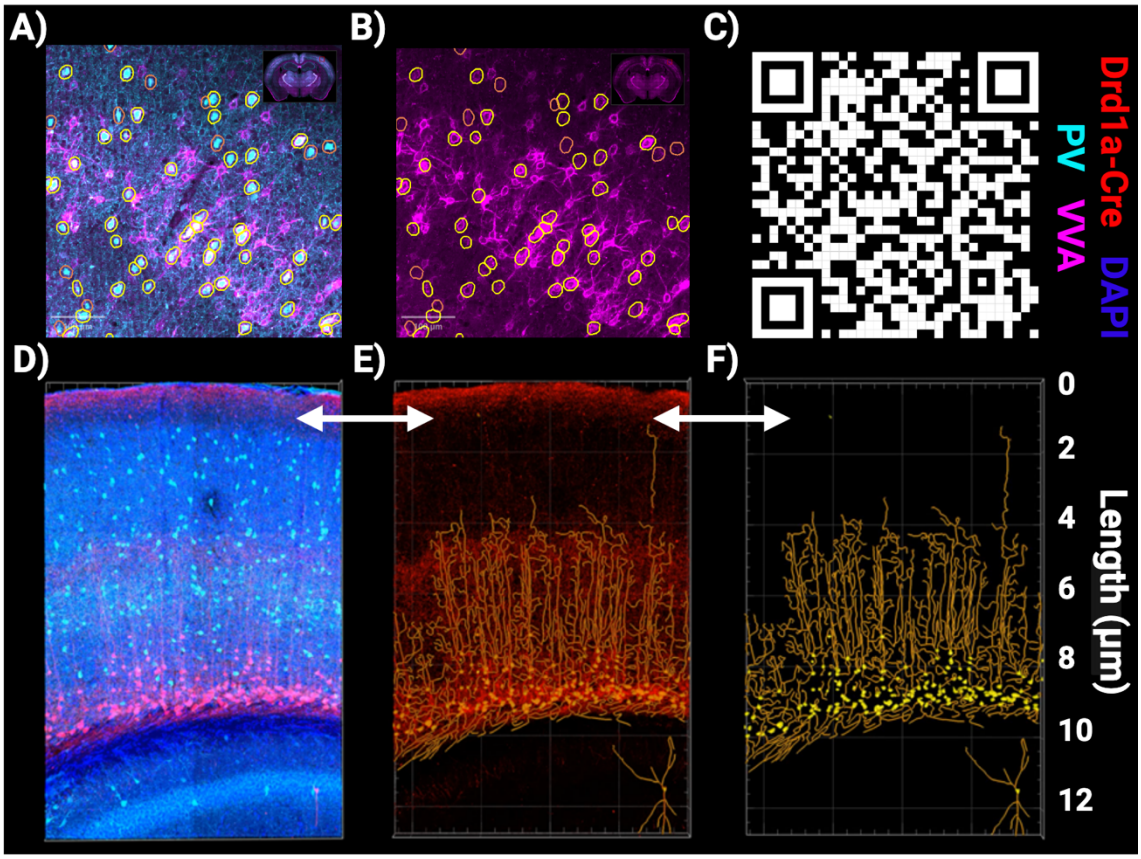


**Figure 19.** Illustrates 3D soma and neurite morphometric feature extraction using Arivis. This involves A) PV cell detection and B) VVA colocalisation ($PV^+/VVA^+$=yellow outline and $PV^+/VVA^-$ =orange outline). C) The QR-linked video[377] illustrates brain-wide *Drd1a* and PV cell segmentations upon r-QUINT processing, including D-F) sample *Drd1a*-$Cre^+$ neurite tracing in S1.

Following QuPath segmentations, I used multiplexed 'tagging' to assign x/y/z coordinate 'addresses' to detected cells in MATLAB (**A.10.7**). Nutil designates soma addresses to ROIs–conceptually, as one may assign a street address to a province–and outputs data tables containing labelled coordinates[224]. I capitalised upon this by linking morphometric feature extractions to seeding cell coordinate assignments/'addresses' via transient binary combination matrices following soma/neurite analyses. That is, I systematically deposit cell coordinates into matrix 'bins'–one bin per cell–such that rows correspond to identically-addressed cells in morphometric spreadsheets. These matrix data structures enable multiplexed analyses if multiple QuPath object classifications employ identical primary detections (e.g., $Cre^+$ soma) with various second detections (e.g., ±PV, then ±VVA). Using QuPath output tables, I add binary classifications to matrix bins detailing whether $Cre^+$ cells co-expresses or lack other signals.

Multiplexed fluorophore signatures are thereby detailed by $2^{(f-1)}$ binary values, where *f*=the number of signals considered. *f*≤3 for all L5-6 analyses where, for example, RFP/PV/VVA (*f*=3) involves $2^{(f-1)}$=4 combinations: $RFP^+/PV^+/VVA^+$, $RFP^+/PV^+/VVA^-$, $RFP^+/PV^-/VVA^+$, and $RFP^+/PV^-/VVA^-$. By this method, MATLAB scripts extract and link QuPath outputs–including cell densities and soma volumes–from any fluorophore combination in any atlas-defined ROI (**A.10.7**).

### *4.1.4 Workflow testing and validation*

To test r-QUINT accuracy, I analysed PV/VVA densities using SDCM sections from *Drd1a*-$Cre^+$ PTEN-CTRL brains for comparison to: 1) serial two-photon tomography (STPT) images analysed using qBrain[261]; and 2) PSCM images analysed via ImageJ[378]. 1) PV analyses of $N_E$=10 PV-IRES-Cre;GFP mice (B6;129P2-$Pvalb^{tm1(cre)Arbr/J}$, The Jackson Laboratory, No. 008069)[261] across 134 ROIs resembled data from $N_E$=3 r-QUINT/SDCM brains (**Figure 20A-B**, **A.2**). Units in **Figure 20A-B** represent the regional ratio of cells per ROI to those detected brain-wide; otherwise, r-QUINT quantifications from fewer SDCM sections would be systematically lower. In **Figure 20A**, the slope of the origin-constrained line-of-best-fit relating STPT/qBrain to SDCM/r-QUINT—y=(0.9880±0.0147)x—did not differ from the predicted value of 1 ($F_{(1,669)}$=2.575, p=0.1091, $r^2$=0.9593) (**A.2**), indicating fair alignment. However, this strong correlation is deceiving; if ROIs with large counts are omitted (i.e., excluding four whose SDCM PV-densities exceed 2.5$\sigma$), $r^2$=0.6774 and the slope of the line-of-best-fit (y=(0.9011±0.0368)x) differs significantly from 1 ($F_{(1,649)}$=27.95, p<0.0001) (**Figure 20B**). 2) PV SDCM-r-QUINT analyses of $N_E$=3 *Drd1a*-Cre PTEN-CTRL brains did not differ from PSCM-ImageJ analyses (method effect: $PV^+$ $F_{(1,25)}$=2.132, p=0.1567) across ROIs (**Figure 20C**, **A.2**). VVA differed significantly (method effect: $VVA^+$ $F_{(1,10)}$=41.27, p<0.0001; $PV^+/VVA^+$ $F_{(1,10)}$=19.47, p=0.0013; $PV^+/VVA^-$ $F_{(1,10)}$=30.00, p=0.0003) yet consistently (method×ROI: $VVA^+$ $F_{(1,10)}$=0.0009, p=0.9765; $PV^+/VVA^+$ $F_{(1,10)}$=3.503, p=0.0907; $PV^+/VVA^-$ $F_{(1,10)}$=3.108, p=0.1084), yielding identical conclusions upon extended analyses (see **4.3.4** and **A.2**). Collectively, these tests support r-QUINT validity.

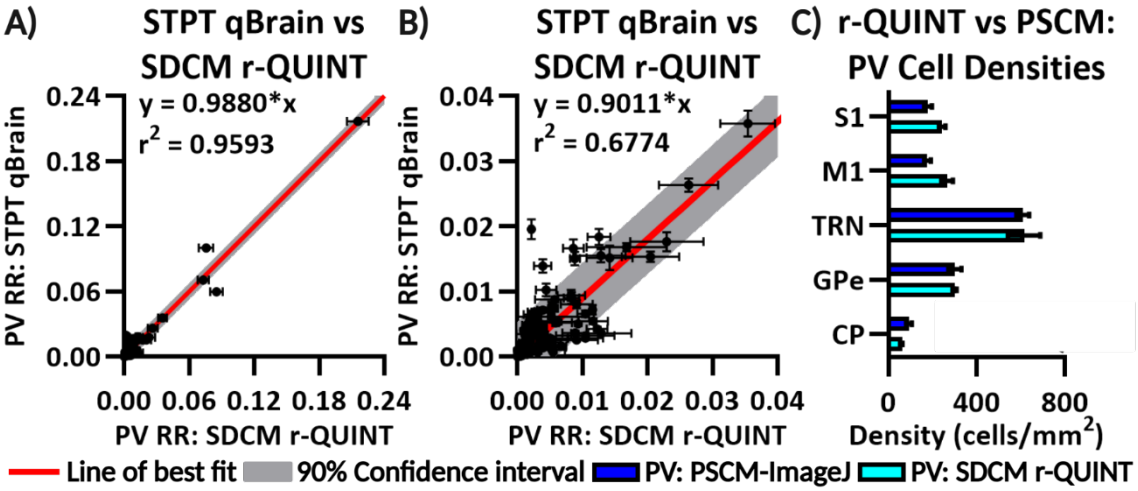


**Figure 20.** r-QUINT validation. r-QUINT/SDCM PV quantifications across ROIs (using $N_E$=3 PTEN-CTRL brains) correlate with qBrain analyses from STPT ($N_E$=10 PV-IRES-Cre;GFP brains)[261], both A) with and B) without omitting the four largest values. C) r-QUINT outputs resemble higher-resolution PSCM/ImageJ analyses ($N_E$=5 PTEN-CTRL brains) in select ROIs. RR=regional ratio (number of cells per ROI/number of cells brain-wide). See **Table 10**-**Table 11** and **A.2** for details.

I then conducted additional validations to assess *Drd1a*-Cre$^+$ subtype densities in pre-selected ROIs (extracted *post hoc* from r-QUINT) both to compare to results from published data (PSCM)[4] and for proof-of-concept laminar analyses. That is, I quantified Cre$^+$ cells from the same *Drd1a*-PTEN-CTRL driver as in **Figure 20** but rather tested the ability of r-QUINT to detect CPLX3 colocalisation before proceeding to *Drd1a* analyses across genetic conditions (**4.3**). In S1 L6b, r-QUINT yielded a *Drd1a* density of $9.55\times10^{-4}\pm5.98\times10^{-5}$cells/µm$^2$ with 49.5±4.8% *Drd1a*$^+$/CPLX3$^+$ colocalisation which resembles *Drd1a*=$5.4\times10^{-4}\pm9.3\times10^{-5}$cells/µm$^2$ with 31±8% *Drd1a*$^+$/CPLX3$^+$ from prior studies[4]. Within-order-of-magnitude differences are not unexpected as r-QUINT and literature estimates employed mice of different ages (76±5d and 35d, respectively). Then, in the PFC L6b, r-QUINT estimated *Drd1a*$^+$ densities of $9.22\times10^{-4}\pm7.14\times10^{-5}$ cells/µm$^2$ with 14.3±6.1% *Drd1a*$^+$/CPLX3$^+$[4, 78]. *Drd1a* densities were similar across cortical regions (region: $F_{(1,126)}$=0.5507, p=0.4594) and layers (layer×region: $F_{(6,126)}$=1.103, p=0.3646), yet *Drd1a*$^+$/CPLX3$^+$ colocalisation was notably less-prevalent in the PFC compared to S1 (region×colocalisation: $F_{(1,126)}$=33.94, p<0.0001) (**A.2**). **Figure 21** depicts r-QUINT quantifications across cortical regions and layers[78] as will be conducted for DREADD applications (**4.2**) and *Drd1a*-subset classifications (**4.3**).

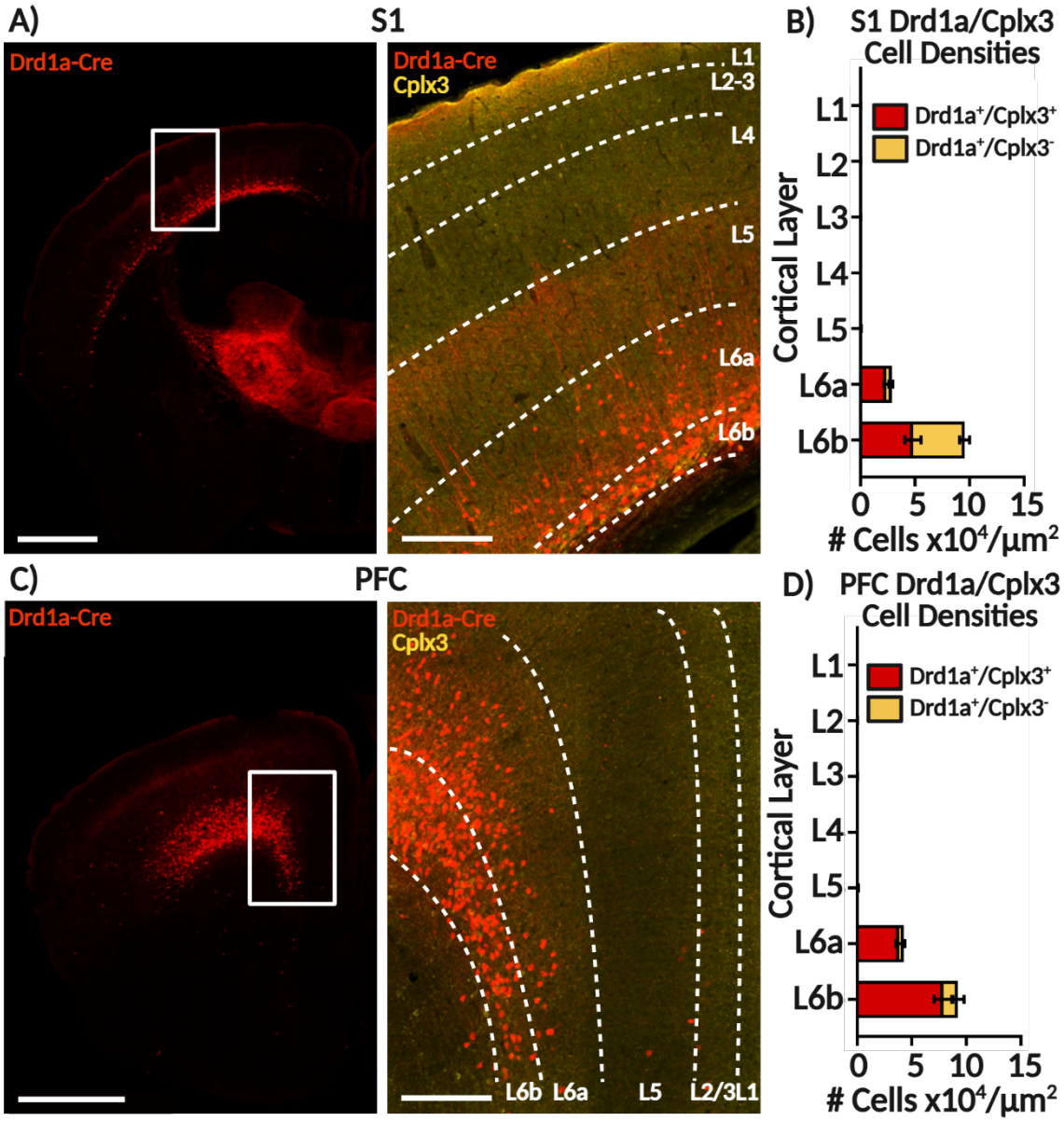


**Figure 21**. Illustrates *Drd1a*-Cre$^{+}$ densities and CPLX3 colocalisation. The A-B) S1 and C-D) PFC are shown. A,C) Rectangles in coronal hemisections are expanded and annotated across L1-6, which correspond to data in B) and D), respectively. Overall *Drd1a* densities are similar between regions, yet L6b CPLX3 colocalisation is greater in S1. Scale bars: A,C) hemisections=1mm; cortices=200µm. See **Table 10**-**Table 11** and **A.2** for replicate and statistical details.

### *4.1.5 Pipeline limitations*

Several limitations limit r-QUINT accuracy. Segmentation challenges remain, particularly in regions where cells are densely packed (e.g., dentate gyrus) and highly vulnerable to QuPath analysis parameters including signal intensity thresholds, watershed detection algorithms, and object classifications. I therefore manually checked all image segmentations for accuracy and

adjusted detection parameters as needed before proceeding with r-QUINT registrations. This was exceptionally time-consuming and counteracted both the intended time-saving and un-biasing benefits of 'semi-automated' analyses. The ability to analyse cell densities belonging to stained fluorophore combinations across ROIs and conditions introduces immense investigative capacities, yet at the expense of statistical power–corrections for multiple comparisons render many analyses statistically insignificant. A smaller number of ROIs and conditions can be pre-specified and extracted from r-QUINT analyses for proper statistical evaluation, while *post hoc* exploratory analysis thereafter can probe changes in regions which may not have otherwise been considered. Such exploratory assessments must be acknowledged as under-powered yet may prove useful in informing follow-up experiments.

## 4.2 Experimental DREADD application

### *4.2.1 DREADDs*

I then used r-QUINT to assess whether PV/VVA expression changed following acute genetic manipulation (**A.1.3**). **Figure 22A-D** shows sections from DREADD mice after saline or CNO injection following **i)** pre-processing, **ii)** mapping, and **iii)** segmentation. Analyses in pre-specified hippocampal and subcortical ROIs showed no significant differences in PV densities, yet subtle variation in VVA co-expression (**Figure 22E-H**, **A.8.1**-**A.8.2**). I expected no change in PV due to the acute nature of CNO action (i.e., effects emerge within minutes and last up to several hours) and PV protein stability[379, 380]. However, changes in VVA co-expression are conceivable due to the rapid plastic capacity of perineuronal nets to respond to L5 excitation or inhibition[147, 267, 381]. The zona incerta exhibited bidirectional changes in $PV^+/VVA^+$ upon CNO injection, with densities increasing and decreasing upon DREADD excitation and inhibition, respectively. More notable changes in PV/VVA densities and distributions may emerge and exacerbate with time[380] as, conceptually, PV cells could provide downstream homeostatic compensation for CNO-induced *Rbp4*-Cre excitation and inhibition.

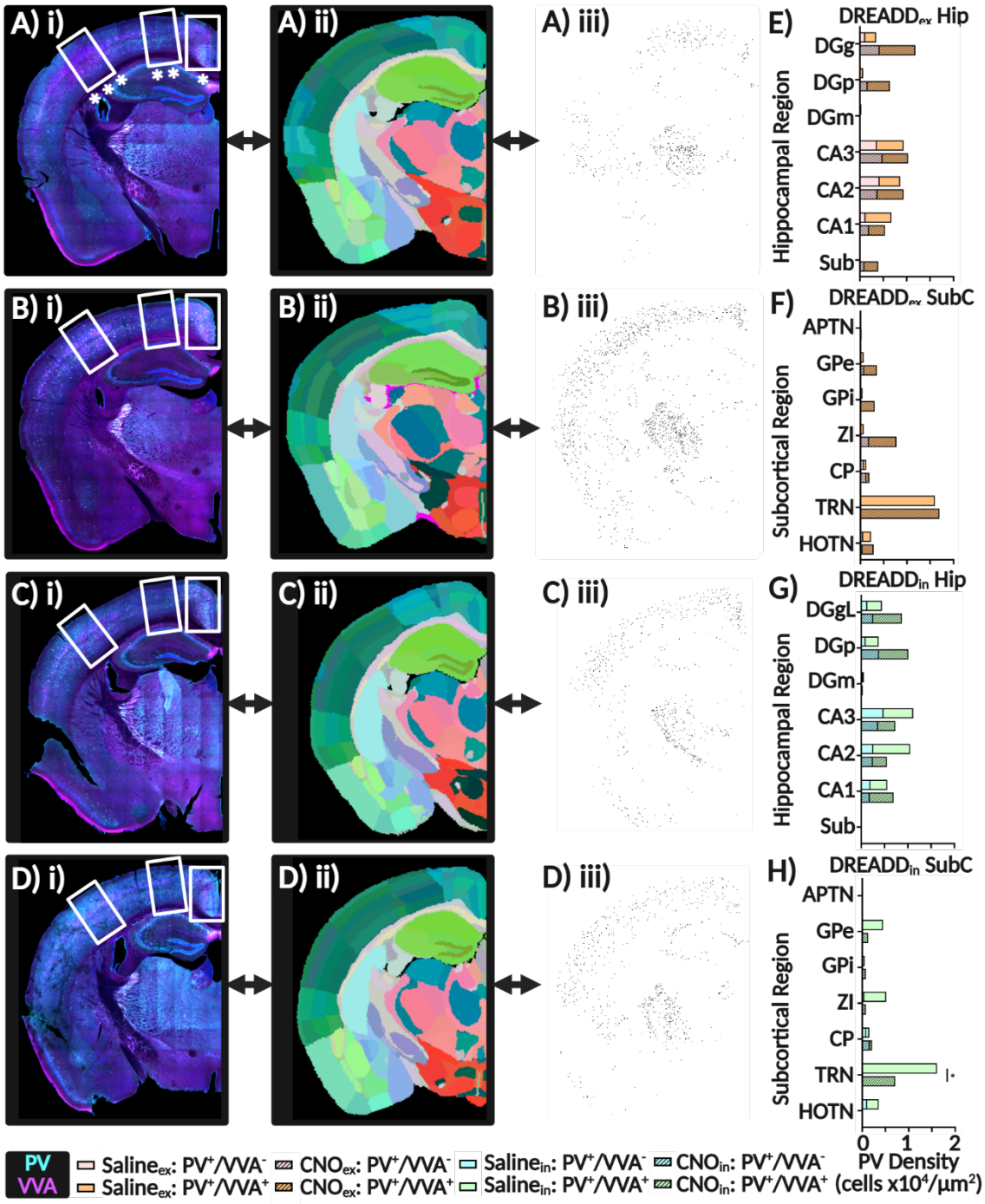


**Figure 22.** DREADD r-QUINT subcortical analyses. A-D) Shows the progression of representative coronal sections through r-QUINT i) pre-processing, ii) atlas-mapping, and iii) segmentation for mice with A-B) excitatory DREADDs and C-D) inhibitory DREADDs following A,C) saline and B,D) CNO administration. E-H) PV cell densities with and without VVA co-expression are shown for E-F) excitatory DREADD and G-H) inhibitory DREADD conditions in E,G) hippocampal (Hip) and F,H) subcortical (SubC) ROIs, where PV densities only differ in the TRN upon acute inhibition. Hemisection ROIs include the *RSA, **V1, and ***S1 as, for subsequent cortical analyses, those in A-B) i) correspond to zoomed images in **Figure 23** while those in C-D) i) correspond to zoomed images in **Figure 24**. *=p<0.05 following two-way ANOVA with corrections for multiple comparisons. See **Table 10**-**Table 11**, **A.2**, **A.8.1**, and **A.8.2** for replicate and statistical details.

### *4.2.2 Excitatory DREADDs*

I then considered effects of acute *Rbp4*-Cre excitation on PV/VVA expression in cortical ROIs. Analyses in the RSA, V1, and S1 showed no regional changes in PV densities or VVA co-expression upon CNO administration ($F_{(1,4)}$=2.613, p=0.1813) (**Figure 23**). I observed no changes between layers (RSA $F_{(1,4)}$=1.907, p=0.2394; V1 $F_{(1,4)}$=0.8506, p=0.4086; S1 $F_{(1,4)}$=5.841, p=0.073), yet subtle trends towards increased PV (particularly $PV^+/VVA^+$) within layers. Effect sizes were large in L5 across all regions (RSA d=1.263, p=0.233; V1 d=0.845, p=0.692; S1 d=1.860, p=0.022) yet only reached statistical significance in S1 L4-5 (**A.8.3, A.2**). This is consistent with subcortical trends (**Figure 22**), indicating compensation for increased L5 neuron activity via increased GABAergic network stability[379, 380] and circuit suppression. Despite increased $PV^+/VVA^+$ densities, VVA expression showed a trend towards decreasing across layers and cortical ROIs, with RSA exhibiting the most notable decreases in L5 (d=1.916, p=0.018) and L2-3 (d=2.142, p=0.006) (**A.8.3, A.2**). Collectively, this suggests perineuronal net re-distribution to favour $PV^+/VVA^+$ preservation or newfound co-expression, both of which are plausible given VVA dynamics (capable of responding to network alterations within minutes) and established roles of perineuronal nets in stabilising fast-spiking PV interneuron networks[381-383].

### *4.2.3 Inhibitory DREADDs*

Upon inhibitory DREADD actuation, I observed no change in PV densities across cortical ROIs ($F_{(1,2)}$=0.4246, p=0.5815) or layers (RSA $F_{(1,2)}$=0.04222, p=0.8562; V1 $F_{(1,2)}$=2.154, p=0.2799; S1 $F_{(1,2)}$=0.001787, p=0.9701) (**Figure 24**). However, a trend towards increased $PV^+/VVA^-$ densities and decreased or constant $PV^+/VVA^+$ densities emerged across ROIs. This was apparent especially in S1 where VVA co-expression decreased. Counterintuitively, VVA densities increased across layers in V1 ($F_{(1,14)}$=7.76, p=0.0146) and RSA ($F_{(1,14)}$=9.71, p=0.0076) yet were unchanged in S1 ($F_{(1,14)}$=2.50, p=0.1365) (**A.8.4, A.2**). As in **4.2.1**, this suggests more complex perineuronal net remodelling and emphasises the importance of considering cortical heterogeneity.

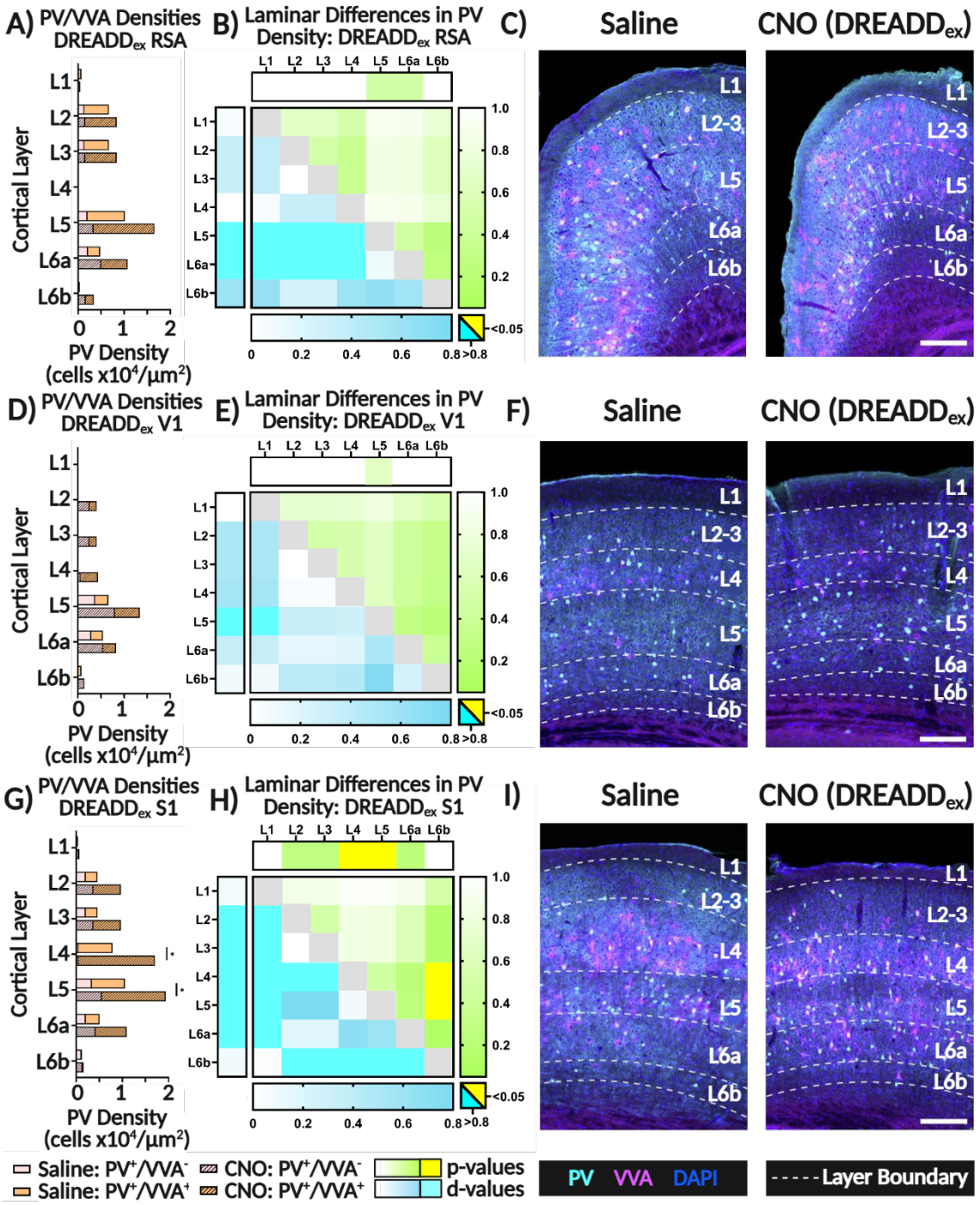


**Figure 23.** PV/VVA cortical densities differ upon excitatory DREADD activation. No changes in overall PV interneuron densities emerge across cortical ROIs, yet trends towards increased PV densities–particularly $PV^+/VVA^+$ subpopulations–are apparent in the A-C) RSA, D-F) V1, and G-I) V1. Heat maps in B,E,H) illustrate pairwise effects of CNO administration within and between cortical ROIs on PV densities; shades of blue/cyan indicate effect size as Cohen's d-values, and shades of green/yellow indicate statistical significance as p-values. Horizontal and vertical bars represent overall within-region/layer statistical significance and effect size, respectively. Sample images of the C) RSA, F) V1, and I) S1 correspond to **Figure 22Ai-Bi)**. Scale bars=100µm. *=$p$<0.05. See **Table 10**-**Table 11** and **A.2** for replicate and statistical details.

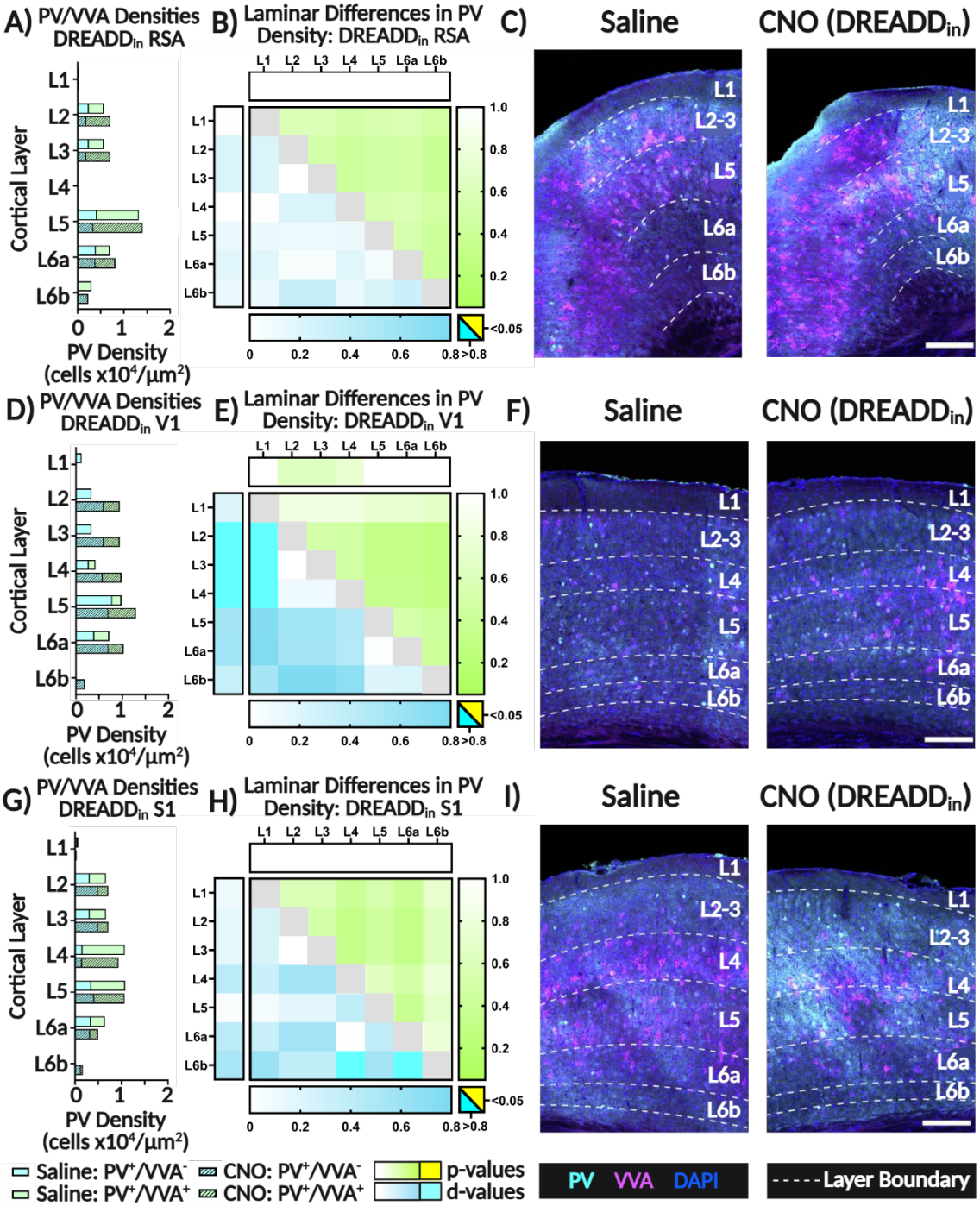


**Figure 24.** PV/VVA cortical densities differ upon inhibitory DREADD activation. No changes in overall PV interneurons densities emerge across cortical ROIs, yet trends towards an increased proportion of $PV^+/VVA^-$ emerge in the A-C) RSA, D-F) V1, and G-I) V1. Heat maps in B,E,H) illustrate pairwise effects of CNO administration on PV densities within and between cortical ROIs, where shades of blue/cyan indicate effect size as Cohen's d-values and shades of green/yellow indicate statistical significance as p-values. Horizontal and vertical bars represent overall within-region/layer statistical significance and effect size, respectively. Sample images of the C) RSA, F) V1, and I) S1 correspond to **Figure 22Ci-Di)**. Scale bars=100 µm. *=$p$<0.05. See **Table 10**-**Table 11** and **A.2** for replicate and statistical details.

### *4.2.4 Timeline considerations*

PV/VVA network changes due to chemogenetically activated or inhibited excitatory neurons have been observed in previous studies[381-383], however acute changes in PV cell densities are not biologically realistic and require alternative explanations. PV is a molecularly stable protein with a half-life of ~9-10 days and translation requiring at least 6hrs to reach detectable levels[379, 380, 384]. Therefore, trends towards increased or decreased PV cell densities after merely 90mins in this study are not likely[380]. PV exhibits a unique molecular structure which, unlike other calcium binding proteins, possesses three $Ca^{2+}$ binding domains[385]. PV is therefore vulnerable to conformational changes upon asymmetrical $Ca^{2+}$ association which can affect molecular kinetics and binding capacities[385]–including to antibodies. While the specific binding domain of the PV27 antibody is proprietary information, it is possible that PV calcium buffering upon CNO activation allosterically thwarts antibody binding.

### *4.2.5 Biological indications*

Collectively, these findings indicate rapid activity-dependent interactions between neuron networks, interneurons, and perineuronal nets[147]. Both acute and chronic changes in PV interneuron functionality and density, respectively, are thus plausible responses to CNO-induced L5 perturbation. Interneuron functionality can be regulated by perineuronal nets which structurally support synapses and network stability, yet upon degradation can re-open aspects of plasticity whether for increased access to cell surfaces and communicative capacity or for circuit destabilisation[381, 386]. Therefore, increased PV/VVA co-localisation upon excitatory DREADD activation may structurally support and facilitate interneuron networks–via VVA–as a rapid response to L5 hyperexcitability. Decreased PV/VVA co-localisation upon inhibitory DREADD activation may reflect compensatory PV disinhibition. Perineuronal nets therefore present as an acute means of modulating interneuron networks, which may be pharmacologically relevant in future investigations. Given that acute L5 excitation alters region-

and activity-dependent PV/VVA expression, chronically silenced *Rbp4*-Cre cells may exhibit similar effects which exacerbate over time, conceivably including changes in PV densities if analyses occur days or weeks after genetic perturbation[379, 380]. Results obtained using this *acute* model are therefore useful for comparison to *chronic* L5 manipulations (chapter 5)[146]. Overall, this pilot successfully demonstrated r-QUINT usage in a larger experimental dataset and yielded biological insights regarding effects of L5-DREADD manipulation[147].

## 4.3 *Drd1a* neurons upon cell augmentation and silencing

### *4.3.1 Layer 6 boundaries and quality control*

I then used r-QUINT to analyse effects of *Drd1a*-Cre perturbation (**Table 9**), which first required L6 boundary definitions and quality control checks. Deep cortical layers are difficult to discern using DAPI and *Drd1a*-Cre;Ai14 alone, I co-stained sections with CPLX3 and TBR1 to distinguish L6b/L6a and L6/L5, respectively (**Figure 25**). Accurate layer definitions are critical as densities in thin regions like L6b are particularly sensitive to area; this alone could explain why pilot L6b *Drd1a* and *Drd1a*$^{+}$/CPLX3$^{+}$ densities were greater than published values[4] even if actual counts were identical (**4.1.4**). I did not expect adult *Tbr1* cortical densities to differ across genetic conditions[44, 45], so used TBR1 quantifications to test whether r-QUINT returned similar densities as a validation check before proceeding to *Drd1a*/CPLX3 analyses (**4.3.2**-**4.3.3**). As expected, **Figure 25** shows no change in TBR1 density across cortical layers and genotypes ($F_{(3,70)}$=1.966, p=0.1270), yet a significant *post hoc* decrease in L5 relative to L6 as expected (L5-L6a, t=13.16, p<0.0001). TBR1 analyses across S1 layers revealed smaller soma areas in L4, which is expected in granule barrel regions (p<0.0001 across *post hoc* comparisons between L4 and all other layers, **A.2**). Accordingly, this yielded a significant layer effect ($F_{(6,70)}$=12.01, p<0.0001) and consistency across genotypes (layer×genotype: $F_{(18,70)}$=0.8200, p=0.6711). Together, CPLX3/TBR1 expression, TBR1 densities, and TBR1 soma analyses support r-QUINT validity, methodological consistency, and analysis quality assurance.

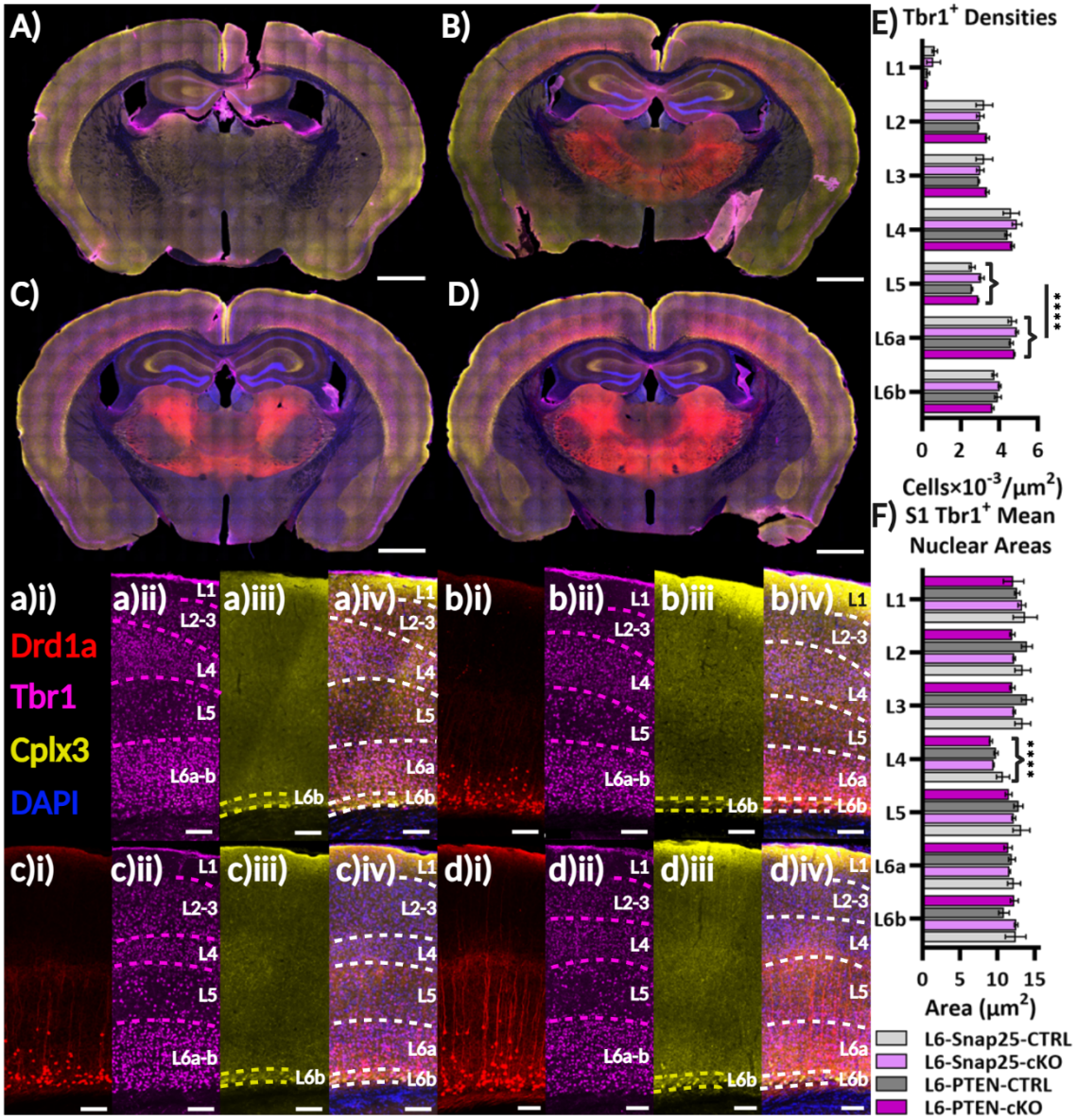


**Figure 25.** *Drd1a*/TBR1/CPLX3 co-staining discriminates cortical L6 cell subtypes. A-D) SDCM-acquired sections are shown for *Drd1a*-Cre driven A) *Snap25*-CTRL (note the lack of *Drd1a*-RFP expression), B) *Snap25*-cKO, C) PTEN-CTRL, and D) PTEN-cKO genetic conditions. Accordingly, a-d) depict i) *Drd1a*-TdTom, ii) TBR1, iii) CPLX3, and iv) merged signals in S1 where TBR1 and CPLX3 expression pattern distinguish L5-6 and L6a-L6b boundaries, respectively. I used these boundary definitions for r-QUINT analyses of TBR1 E) densities and F) soma areas. E) As expected, pan-cortical TBR1 densities are significantly greater in L6 than L5 which aids visual layer discrimination (****=p<0.0001 upon *post hoc* comparison). F) Taking S1 as a prototypical cortical region featuring the barrel cortex granule layer, r-QUINT revealed significantly smaller mean TBR1 soma areas in L4 compared to all other regions as expected (****=p<0.0001 upon *post hoc* comparisons). Together, E-F) provide r-QUINT quality assurance in detecting L5-6 density differences and decreased L4 soma sizes, respectively. Scale bars: A-D)=1mm; a-d)=100µm. See **Table 10**-**Table 11** and **A.2** for replicate and statistical details.

### *4.3.2 Drd1a and CPLX3 characterisation*

Overall, genotype did not influence *Drd1a*$^{+}$/NEUN$^{+}$ proportions pan-cortically or in individual ROIs (genotype: $F_{(2,35)}$=2.448, p=0.1012; genotype×region: $F_{(10,35)}$=2.006, p=0.0629) save M1 upon PTEN-cKO (L6-CTRL vs L6-augmented: p=0.0011) (**Figure 26**). ~28.4±2.64% NEUN$^{+}$ neurons were co-labelled with *Drd1a* in S1 L6b, which reflects published proportions (24±4%)[4].

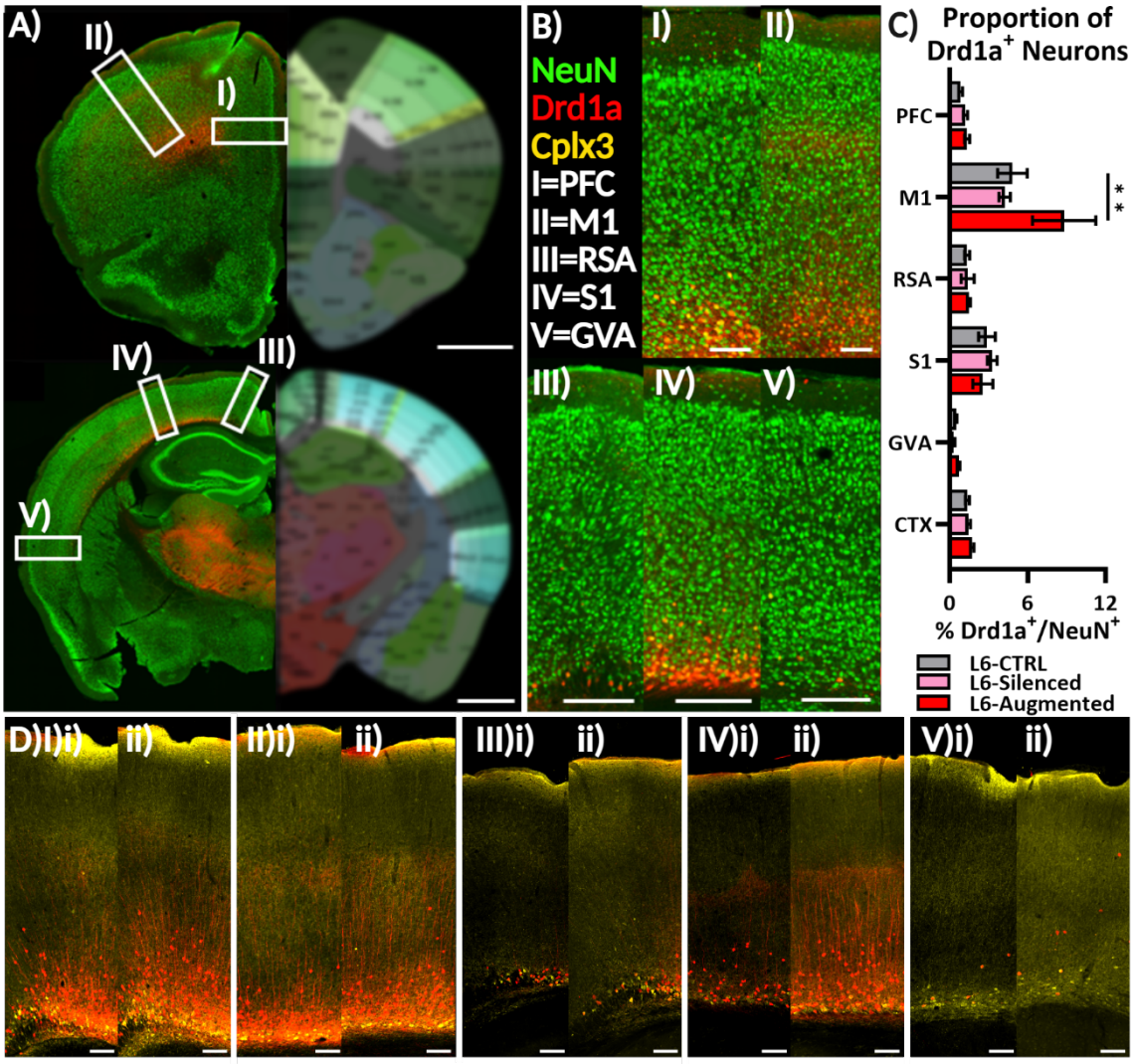


**Figure 26.** Cortical *Drd1a*-Cre neuron proportions and heterogeneity. A) Representative anterior and posterior L6-silenced sections are shown at the level of the PFC and S1, respectively. Left hemispheres with *Drd1a*-RFP and NEUN signal contain ROIs I-V) corresponding to BI-V). Right hemispheres contain atlas maps with ROIs I-V) illuminated across their areal definition in the selected 2D plane. C) Shows *Drd1a* prevalence as the % of total NEUN$^{+}$ neurons. D) Shows ROIs upon *Drd1a*/CPLX3 co-staining to highlight exacerbated *Drd1a* heterogeneity across i) PTEN-CTRL and ii) PTEN-cKO conditions. *Drd1a*$^{+}$ soma and apical dendrites appear larger upon ii) PTEN-cKO compared to i) *Snap25*-cKO. See **Figure 27** for regional and laminar *Drd1a*/CPLX3 quantifications, and **Figure 28.** for colocalisation analyses. **=p<0.01. Scale bars: A)=1mm; B)=200µm; D)=100µm. See **Table 10**-**Table 11** and **A.2** for replicate and statistical details.

*Drd1a*$^{+}$ densities varied across ROIs (region: $F_{(5,48)}$=61.55, p<0.0001) as in pilots (**4.1.4**) and were consistently influenced by genotype; *Snap25*-cKO and PTEN-cKO yielded trends towards increased and decreased densities respectively (genotype: $F_{(2,48)}$=6.737, p=0.0026; genotype×region: $F_{(10,48)}$=1.490, p=0.1723) (**Figure 27A**). The former aligns with prior reports in S1[92]. However, *Drd1a*$^{+}$ counts increased pan-cortically upon PTEN-cKO ($t_{(48)}$=3.714, p=0.0011) and decreased upon *Snap25*-cKO ($t_{(48)}$=3.226, p=0.0023), yet inconsistently across ROIs (region: $F_{(5,48)}$=370.5, p<0.0001; genotype: $F_{(2,48)}$=6.209, p=0.0040; region×genotype: $F_{(10,48)}$=4.610, p=0.0001) (**Figure 27B**). Increased pan-cortical *Drd1a*$^{+}$ cell counts yet unchanged densities upon PTEN-cKO may occur due to greater cortical volumes which maintain areal proportions and *Drd1a*$^{+}$/NEUN$^{+}$ colocalisation, while decreased volumes upon *Snap25*-cKO could explain the opposite effect. *Post hoc* calculations showed that L6-augmented cortical areas were indeed greater than CTRLs (≈%133±5.66, $t_{(8)}$=4.994, p=0.0021), while L6-silencing yielded smaller areas relative to CTRLs (≈%77.2±3.35, $t_{(8)}$=3.826, p=0.0050). *Drd1a*$^{+}$ soma areas consistently increased across ROIs upon PTEN-cKO while *Snap25*-cKO soma areas remained unchanged (region: $F_{(5,48)}$=19.18, p<0.0001; genotype: $F_{(2,48)}$=182.5, p<0.0001; region×genotype: $F_{(10,48)}$=0.6016, p=0.8045) (**Figure 27C**). *Drd1a*$^{+}$ neurons were most densely expressed in L6b (**Figure 27G**) yet were also prominent in L6a–particularly when counts were not visually abated by area (**Figure 27H**)–with little expression in L1-5. *Drd1a*-Cre therefore represents a L6 subset which overlaps with yet is not exclusive to L6b. Laminar *Drd1a*$^{+}$ densities differ across the cortex (layer: $F_{(3,48)}$=365.0, p<0.0001; region: $F_{(5,48)}$=35.51, p<0.0001; layer×region: $F_{(15,48)}$=17.65, p<0.0001) as do counts (layer: $F_{(3,40)}$=207.1, p<0.0001; region: $F_{(4,40)}$=118.2, p<0.0001; layer×region: $F_{(12,40)}$=57.57, p<0.0001) (**Figure 26**), stressing that the cortex is heterogeneous and that genetic consequences should not be assumed as ubiquitous throughout. Genotype effects were indeed inconsistent across ROIs; PTEN-cKO yielded decreased *Drd1a*$^{+}$ densities in L6b of M1, of S1, and pan-cortically, increased counts in L6a across ROIs, and a trend towards decreased counts in L6b.

*Snap25*-cKO yielded no change in densities or counts across ROIs and layers, save decreased counts in L6b RSA and increased counts in L6a S1 (**Figure 27G-H**).

In contrast to *Drd1a* heterogeneity (**Figure 27A**), CPLX3 cells were localised to L6b with similar densities across cortical ROIs (genotype: $F_{(2,54)}$=0.5889, p=0.5585; region: $F_{(5,54)}$=1.595, p=0.1771; genotype×region: $F_{(10,54)}$=0.5996, p=0.8071) (**Figure 27D**) and layers (layer×region: $F_{(15,48)}$=0.8820, p=0.5873). Counts only increased pan-cortically upon PTEN-cKO following *post hoc* tests ($t_{(48)}$=6.746, p<0.0001), remaining unchanged for *Snap25*-cKO ($t_{(48)}$=0.7421, p=0.4616) (**Figure 27E**). Notably, average CPLX3$^+$ soma areas did not significantly differ across genotypes or cortical ROIs (genotype: $F_{(2,48)}$=2.161, p=0.1262; region: $F_{(5,48)}$=1.705, p=0.1516; genotype×region: $F_{(10,48)}$=0.6162, p=0.7924) (**Figure 27F**, contrast with *Drd1a*$^+$ in **Figure 27C**). CPLX3$^+$ cells were present in L6a (**Figure 27I**)–more clearly when not normalised by area (**Figure 27J**) yet to a much lesser extent than *Drd1a*$^+$ (**Figure 27G-H**)–which indicates predominant yet not exclusive CPLX3-L6b localisation. If CPLX3 is to be deemed a 'true' L6b marker, expression in more-pial layers could be due to imperfect boundary definitions or a boundary which itself is not discrete; biologically, cortical layers are not likely definable by a physical line, but rather graded combinations of features including molecular expression and connectivity profiles. Laminar analyses are therefore approximations, not confident quantifications. Across ROIs and layers, genotype only affected CPLX3 densities in S1 L6b upon PTEN-cKO ($t_{(36)}$=3.839, p=0.0014) (**Figure 27I**). CPLX3$^+$ counts did not change in any ROI or layer upon *Snap25*-cKO, yet PTEN-cKO resulted in trends towards increased counts in L6a-b which reached statistical significance in L6a of M1 and pan-cortically (M1: $t_{(32)}$=2.996, p=0.0113; whole-cortex: $t_{(32)}$=3.231, p=0.0057) (**Figure 27J**). Given notable *Drd1a*$^+$ heterogeneity across cortical regions and layers which differ further with genetic perturbation—alongside comparatively consistent pan-cortical CPLX3$^+$ expression which differs more subtly upon PTEN-cKO—I next examined laminar and regional genotype differences across *Drd1a*-Cre subpopulations (**4.3.3**).

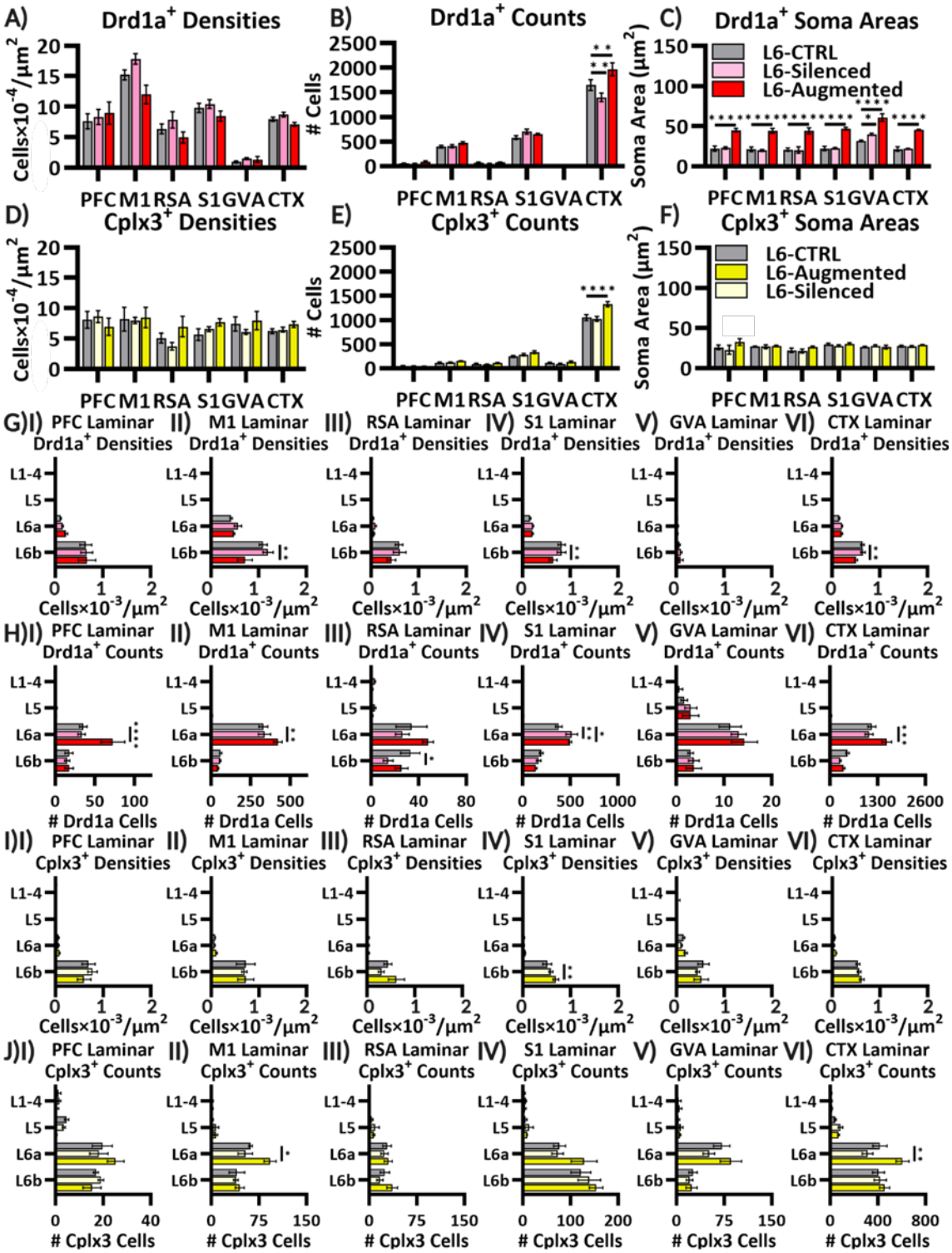


**Figure 27.** *Drd1a*/CPLX3 characterisation following L6 silencing and augmentation. Genotype effects on *Drd1a* neuron A) densities, B) counts, and C) soma areas are shown across cortical ROIs corresponding to I-V) in **Figure 26**, which are dissected into laminar densities and counts in G) and H), respectively. Similarly, effects of L6-silencing and L6-augmentation on regional CPLX3 D) densities, E) counts, and F) soma areas are extended laminarly for I) densities and J) counts. *=p<0.05, **=p<0.01, ***=p<0.001, and ****=p<0.0001 upon two-way ANOVA with corrections for multiple comparisons. See **Table 10**-**Table 11** and **A.2** for replicate and statistical details.

### *4.3.3 Drd1a subpopulations via CPLX3 colocalisation*

*Drd1a*/CPLX3 colocalisation dissected genotype effects on *Drd1a*$^+$ subtypes, revealing that laminar densities and distributions of cells lacking CPLX3 co-expression are more notably affected (**Figure 28.** ). No significant regional changes emerged upon PTEN-cKO or *Snap25*-cKO for *Drd1a*$^+$/CPLX3$^-$ or *Drd1a*$^+$/CPLX3$^+$; however, a trend towards increased densities and decreased counts upon *Snap25*-cKO contrasted decreased densities and increased counts upon PTEN-cKO, achieving statistical significance pan-cortically upon *post hoc* comparisons as in **4.3.3** (*Drd1a*$^+$/CPLX3$^-$ *Snap25*-cKO: $t_{(48)}$=2.185, p=0.0338; *Drd1a*$^+$/CPLX3$^-$ PTEN-cKO: $t_{(48)}$=3.391, p=0.0028; *Drd1a*$^+$/CPLX3$^+$ *Snap25*-cKO: $t_{(48)}$=5.681, p<0.0001; *Drd1a*$^+$/CPLX3$^+$ PTEN-cKO: $t_{(48)}$=3.945, p=0.0003) (**Figure 28. A-B,D-E**). L6-augmentation consistently increased soma areas across ROIs while no differences emerged upon L6-silencing for both *Drd1a*$^+$/CPLX3$^+$ (genotype: $F_{(2,48)}$=60.97, p<0.0001) and *Drd1a*$^+$/CPLX3$^-$ subtypes (genotype: $F_{(2,48)}$=233.2, p<0.0001) (**Figure 28. C,F**). Yet, overall CPLX3$^+$ soma areas did not increase upon PTEN-cKO, which is unintuitive given that *Drd1a*$^+$/CPLX3$^+$ proportions are not insignificant relative to total CPLX3$^+$ prevalence. This may be due to r-QUINT detection limits; CPLX3 and DRD1A are both membranous proteins, yet *Drd1a* signal was stronger and labelled larger soma areas than overlapping CPLX3 signal would have otherwise indicated. Therefore, *Drd1a* masking likely reveals increased areas (**Figure 26D**) which r-QUINT failed to identify from CPLX3 signal alone. Laminar examination showed that both cell subtypes are most prominently expressed in L6b, and L6a to a lesser extent, with L6b localisation favouring *Drd1a*$^+$/CPLX3$^+$ (**Figure 28. G-J**). No change emerged upon *Snap25*-cKO in any region, layer, or subpopulation, however PTEN-cKO yielded significant changes which differed according to cell subtype. *Drd1a*$^+$/CPLX3$^-$ densities decreased upon PTEN-cKO solely in L6b (M1, RSA, S1, and pan-cortically), while absolute counts did not differ in L6b yet increased in L6a (PFC, M1, S1, and pan-cortically) (**Figure 28. G-H**). In contrast, no differences emerged for *Drd1a*$^+$/CPLX3$^+$ save increased pan-cortical counts in L6a (**Figure 28. I-J**).

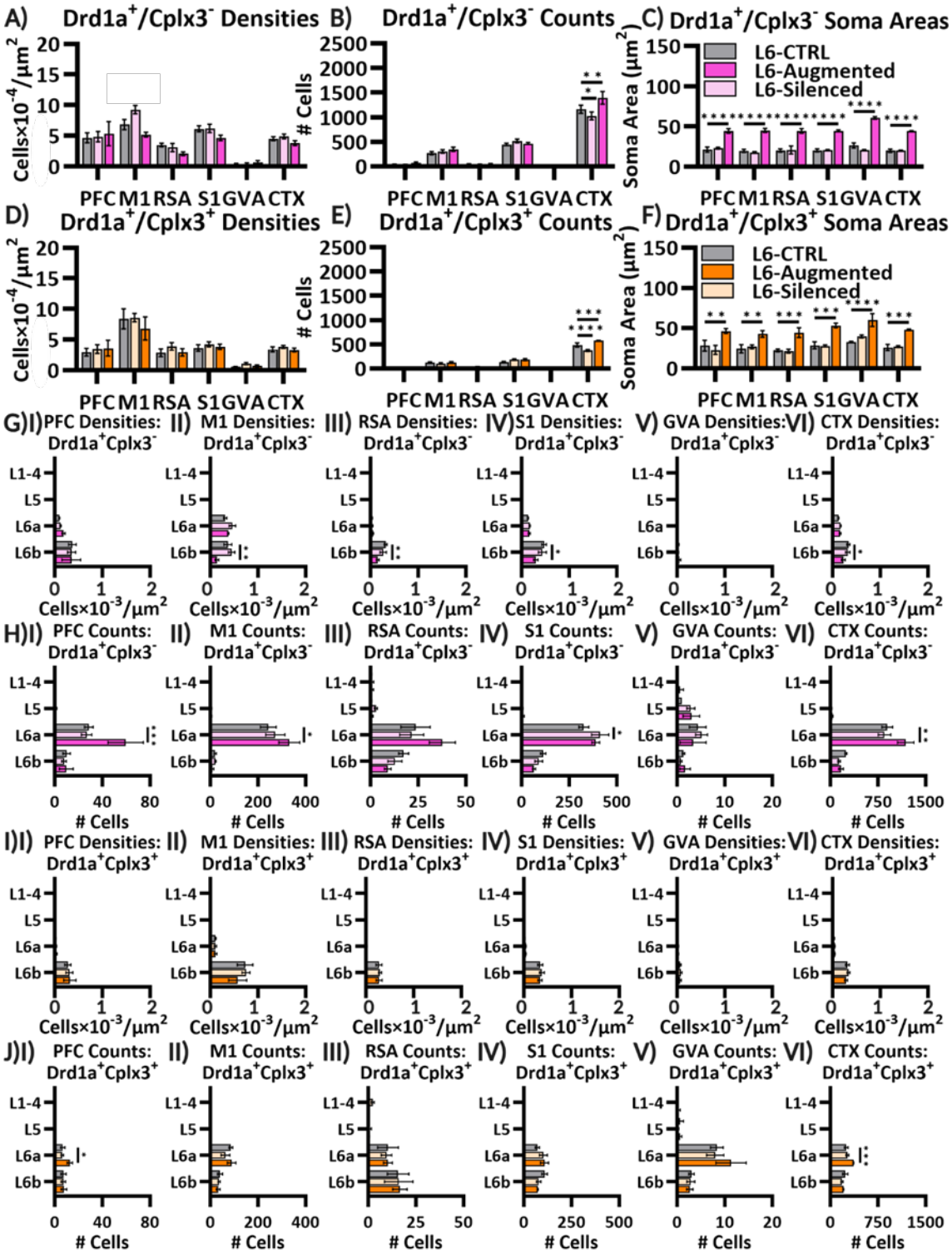


**Figure 28.** *Drd1a*/CPLX3 subtype characterisation upon L6 silencing/augmentation. Regional *Drd1a*$^{+}$/CPLX3$^{-}$ and *Drd1a*$^{+}$/CPLX3$^{+}$ cell A,D) densities, B,E) counts, and C,F) soma areas are shown following L6-silencing and L6-augmentation. Laminar genotype differences are expanded upon for *Drd1a*$^{+}$/CPLX3$^{-}$ and *Drd1a*$^{+}$/CPLX3$^{+}$ G,I) densities and H,J) counts, respectively, in: I) PFC, II) M1, III) RSA, IV) S1, V) GVA, and VI) pan-cortically (again corresponding to ROIs in **Figure 26**). *=p<0.05, **=p<0.01, ***=p<0.001, ****=p<0.0001. See **Table 10**-**Table 11** and **A.2** for replicate and statistical details.

### *4.3.4 Interneurons and perineuronal nets*

I finally evaluated effects of PTEN-cKO on PV and VVA across cortical ROIs and layers as in **4.1**-**4.2**. PV/VVA does not colocalise with *Drd1a*-Cre$^{+}$, thus their analyses examined broader global effects of genetic perturbation. ~30% of inputs to *Drd1a*$^{+}$ neurons arise from interneurons, and L6 neurons project to PV interneurons in L5-6; therefore, I predicted that L6-augmentation would yield subtle activity-dependent network-level differences in interneuron and perineuronal net prevalence[387]. Neither PV nor VVA soma areas differed upon PTEN-cKO (genotype: $F_{(1,48)}$=0.2364, p=0.6290), yet PV$^{+}$/VVA$^{+}$ soma were larger than those PV soma lacking VVA colocalisation (VVA coexpression: $F_{(1,48)}$=265.3, p<0.0001) (**Figure 29A-D**). Subtle changes emerged across PV/VVA densities and distributions (**Figure 29E-L**); PV did not differ upon PTEN-cKO in any ROI, yet a trend towards decreased densities emerged across regions (genotype: $F_{(1,24)}$=6.597, p=0.0169). Densities decreased pan-cortically in L4 ($t_{(24)}$=3.476, p=0.0117) where significance was only reflected in S1 ($t_{(24)}$=3.597, p=0.0087) (**Figure 29E,I**). Regional VVA densities did not differ upon PTEN-CKO across regions (genotype: $F_{(1,24)}$=2.028, p=0.1673) (**Figure 29F,J**). PTEN-cKO decreased PV$^{+}$/VVA$^{-}$ densities (genotype: $F_{(1,24)}$=9.079, p=0.0060), most notably in M1 ($t_{(24)}$=3.956, p=0.0035). Laminar dissection revealed pan-cortical decreases in L2-3 ($t_{(24)}$=3.810, p=0.0051), particularly in PFC ($t_{(24)}$=3.472, p=0.0118) and S1 ($t_{(24)}$=5.668, p<0.0001) (**Figure 29G,K**). In contrast, no regional PV$^{+}$/VVA$^{+}$ differences occurred upon PTEN-cKO (genotype: $F_{(1,24)}$=2.792, p=0.1078) yet decreases emerged pan-cortically in L4 ($t_{(24)}$=2.930, p=0.0431), specifically of S1 ($t_{(24)}$=3.638, p=0.0074) (**Figure 29H,L**). I conducted this work parallel to PCSM-ImageJ analyses in a smaller number of pre-defined ROIs, thus comparisons between methods expand upon methodological validations in **4.1.4** (**Figure 20C**). Results across methods are similar; overall conclusions are identical despite differences in absolute quantities (**Figure 30**). Soma area discrepancies were rectified upon applying the manual *post hoc* perimeter corrections (**Figure 30B,C**) I proposed in **4.1.2** (**Equation 3**). See **A.2** for *post hoc* comparisons.

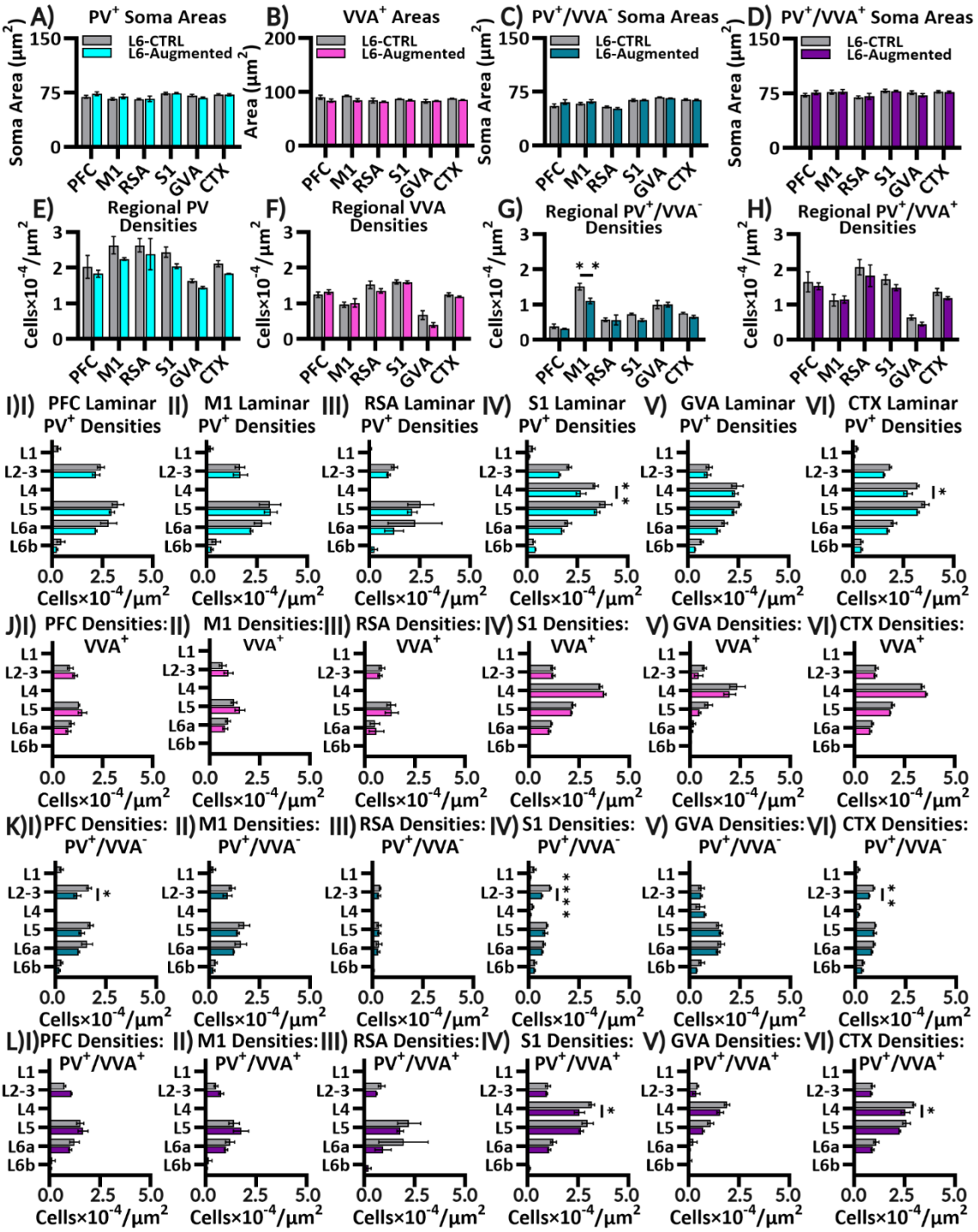


**Figure 29.** PV/VVA characterisations upon L6-augmentation. A-D) Cell soma areas do not differ upon *Drd1a*-Cre-driven PTEN-cKO across PV/VVA populations and subpopulations. However, PV cells lacking VVA are smaller than those co-expressing VVA. E-H) Total regional PV, VVA, and $PV^+/VVA^+$ densities do not differ significantly upon PTEN-cKO, yet $PV^+/VVA^-$ densities decrease across ROIs. Laminar examinations across I) PFC, II) M1, III) RSA, IV) S1, V) GVA, and VI) pan-cortical ROIs provide further insight into overall regional analyses for: E,I) PV; F,J) VVA; G,K)= $PV^+/VVA^-$, and H,L)= $PV^+/VVA^+$. *=p<0.05, **=p<0.01, ***=p<0.001, ****=p<0.0001. See **Table 10**-**Table 11** and **A.2** for replicate and statistical details.

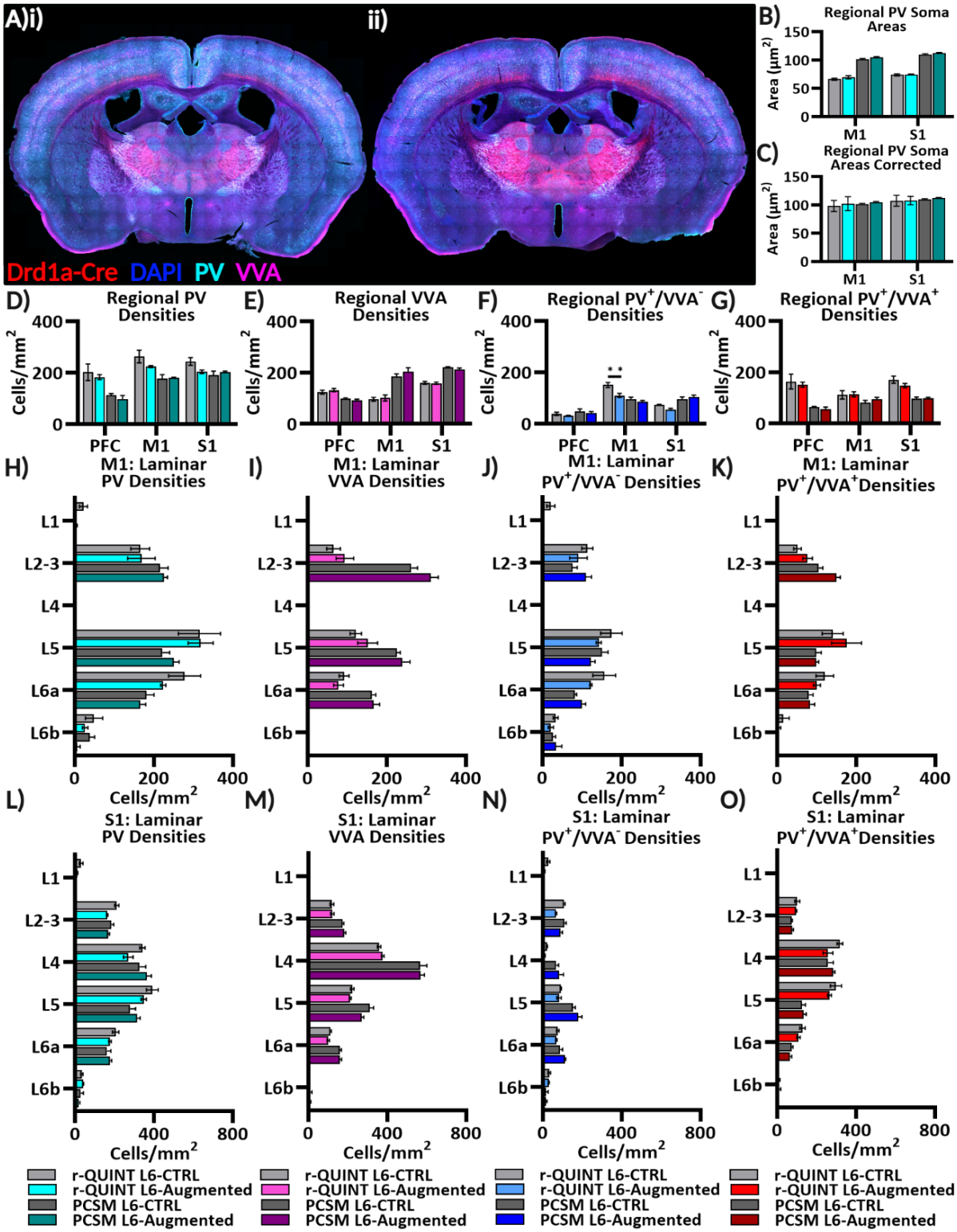


**Figure 30.** r-QUINT vs PSCM PV/VVA analyses upon L6-augmentation. A) Coronal SDCM images are shown for i) PTEN-CTRLs and ii) PTEN-cKOs. B) Absolute soma areas differ across methods yet are C) rectified upon application of **Equation 3** to r-QUINT outputs. In neither case does L6-augmentation yield significant changes. Neither method yielded regional or laminar differences in PV, VVA, or subpopulation analyses, save r-QUINT which indicated decreased $PV^+/VVA^-$ densities in M1 (this trend was reflected for PSCM yet did not achieve statistical significance). **=p<0.01. See **Table 10**-**Table 11** and **A.2** for replicate and statistical details.

### *4.3.5 Genotype trends and indications*

Together, r-QUINT analyses of laminar and regional *Drd1a*-Cre-expressing neurons (i.e., *Drd1a* and NEUN), subpopulations (i.e., with or without CPLX3 colocalisation), and non-*Drd1a*-expressing interneuron subtypes (i.e., PV and VVA) provide insights into the effects of genetic manipulations across the brain which largely reflect hypothesised ramifications. I expected minimal differences across cell subtypes and output metrics upon *Snap25*-cKO–conceivably decreased soma volumes and densities relative to CTRLs–while anticipating increased *Drd1a*$^{+}$ cell prevalence, hypertrophy, and overall brain volume upon PTEN-cKO[4, 33-35, 53, 63, 64]. I hypothesised that this may resemble human WMIN morphologies reported in cases of PTEN dysfunction, particularly in subplate-remnants co-expressing CPLX3. If any, I expected only subtle network-level changes in PV/VVA densities and distributions, the analysis of which doubled as r-QUINT validation against higher-resolution PSCM-ImageJ assessments in a subset of pre-defined cortical ROIs. The biological relevance of subtle PV/VVA differences will be briefly discussed in **4.5.1**, yet their inclusion remains primarily for the purpose of r-QUINT validation.

Little to no changes in *Drd1a*$^{+}$ soma areas, cell counts, densities, distributions, and proportions relative to total neuron counts emerged upon L6-silencing (**Figure 26**-**Figure 28**), which reflects and expands upon present knowledge. Previous literature reported no reduction in the total number of *Drd1a*$^{+}$ cells in S1 L6b of 8mo adult brains upon *Snap25*-cKO[4], which was replicated in present findings using 10-12wk adult brains alongside a lack of differences across other cortical ROIs. This was surprising as, over time, cells in which regulated synaptic vesicle release has been functionally abolished may either senesce due to network redundancy, thereby decreasing in density, or exhibit altered morphologies. I thought soma areas might therefore decrease subtly due to any combination of less activity-dependent growth during early postnatal development, less retrograde trophic support during maturation, or metabolic downregulation and decreased protein synthesis throughout adulthood. Qualitatively, full-coronal sections from

L6-silenced brains revealing *Drd1a*$^{+}$ expression and projections profiles appear similar compared to CTRLs (i.e., **Figure 25B** vs **Figure 25C**, respectively) as anticipated[4]. Present comparisons are flawed, however, as *Drd1a*$^{+}$ analyses were relative to PTEN-CTRLs–not strain-matched *Snap25*-heterozygotes or Cre-drivers without *Snap25*-floxed loci–due to the only available *Snap25*-CTRLs being Cre-WTs which inherently lack RFP. This is an active future direction from which data will be included for comparison to present findings. No change in CPLX3 densities, distributions, or soma areas upon L6-silencing reflects data published solely in S1 of adult mice[92]; however, present evaluations were conducted across multiple cortical ROIs which indicates CPLX3 consistency across regions and genotypes (**Figure 27**). Densities distinguished by *Drd1a*/CPLX3 colocalisation did not differ significantly upon L6-silencing, indicating a lack of compensatory subtype effects (i.e., no difference in *Drd1a*$^{+}$ soma areas alone could not preclude a lack of genotype differences if *Drd1a*$^{+}$/CPLX3$^{+}$ neurons increased in size while *Drd1a*$^{+}$/CPLX3$^{-}$ neurons decreased in size) (**Figure 28**). Despite only subtle anatomical changes in targeted *Drd1a*-Cre cells upon *Snap25*-cKO, physiological differences persist as shown in prior studies detailing effects on cortical excitability and anxiety[78], sleep[75], and feeding behaviour[75, 98] which will be discussed further (**4.5.2**).

In contrast, notable changes emerged upon PTEN-cKO. Soma areas increased across cortical ROIs (**Figure 27**) which aligns with expected effects of mTOR disinhibition (i.e., enhanced eIF4E-driven protein translation and S6-mediated cytoskeletal organisation, **A.1.1**). L6-augmented cells exhibited qualitatively exhibited increased apical dendrite thickness, arborisation, and signal intensity as shown in **Figure 26D**, particularly in S1 (**IV**), M1 (**II**), and the PFC (**I**) (**Figure 27B,H**). In full-coronal sections, downstream regions targeted by *Drd1a*$^{+}$ projections (e.g., HOTN) show greater RFP intensities upon PTEN-cKO (**Figure 25D**) compared to both PTEN-cKOs (**Figure 25C**) and Snap2-cKO (**Figure 25B**), indicating neurite hypertrophy and conceivably increased connectivity (including to L4[35, 56, 66], see **Figure 26DIVii**). Physiological

consequences should be investigated alongside detailed morphological analyses for comparison to the hyperactivity and hypertrophy observed in postmortem autistic and epileptic patient brains[53-55]. This could include single-cell *ex vivo* electrophysiological recordings to assess membrane properties, spike frequencies, and short-term synaptic plasticity. Hypothesised increases in cell counts due to greater cell proliferation or decreased postnatal apoptosis upon PTEN-cKO emerged across cortical ROIs, (**Figure 26G**), yet proportionally to neuron counts (i.e., consistent *Drd1a*/NEUN ratios, **Figure 26D**) and increased brain volumes, resulting in either maintained or slightly decreased densities upon regional (**Figure 26E**) and laminar (**Figure 27**) dissection. This reflects prior studies where neuron counts, soma and neurite size and complexity, and brain volumes increased upon PTEN-cKO in cortical neuron subpopulations (yet these subpopulations have never been previously restricted to deep layers)[68, 69, 388-391]. Regional heterogeneity upon PTEN-cKO may be due to either a smaller relative increase in *Drd1a*$^+$ counts or increased/maintained regional volumes. Differences were unsurprisingly most pronounced in M1 and S1 as these cortical ROIs exhibit the greatest total number of *Drd1a*-targeted cells. Despite no overall changes in CPLX3$^+$ soma areas and densities, with cell counts increasing proportionally to cortical area (**Figure 28C-E**), effects of PTEN-cKO differed across *Drd1a*$^+$ subtypes according to CPLX3 colocalisation. Contrary to hypotheses, increased densities and cell counts were more prominent in *Drd1a* cells lacking CPLX3. *Drd1a*$^+$/CPLX3$^+$ subtypes may exhibit greater network stability or resilience to effects of genotype, which is conceivable given that these subplate remnants preferentially survive into adulthood and exhibit precise projections to L1, L4, and HOTN capable of critically influencing TC-corticothalamic circuitry[231]. *Drd1a*$^+$ L6b and CPLX3 subplate remnant subpopulations are of particular interest given selective responsivity to ORX[48, 50, 98] and conceivably unique network effects. The relevance of this to human WMIN PTEN abnormalities and mTOR pathway dysfunction, diseases of cortical hyperexcitability, and corresponding avenues of pharmacological interest will be discussed further (**4.5.4**).

## 4.4 Morphometric analogousness

### *4.4.1 Polar plot distinctions*

I then conducted morphological analyses of human WMINs and mouse L6b neurons to evaluate analogy across species, including in subpopulations defined according to combinations of neuron type (i.e., pyramidal or non-pyramidal) and ORX-sensitivity (i.e., ORX-sensitive or ORX-insensitive). To this aim, I generated polar plots using a custom script (**A.10.10**) which represented overall neuron shape and size using one of three methods (#1-3). For each method, I operationally define plotted values within polar bins as representing: #1) "branch density"–the total number of neurite pixels in a "binarised" manner; #2) "arborisation strength"–the sum of all distances from the soma to each pixel in a "factorial" fashion; and #3) "neurite coverage"–the mean distance between the soma and each constituent pixel likening "averaging". **Figure 31** illustrates the results of group neurite analyses across conditions using each method solely for comparison, the biological relevance of which will be elaborated upon in **4.4.2**. The "binary" method #1 (**Figure 31A-B**) reveals the directions in which the greatest number of branches exist, however fails to distinguish relative distances from cell soma such that radial bins may drastically overrepresent a high concentration of proximal dendrites or underrepresent distal extensions. In contrast, while the "factorial" method #2 (**Figure 31C-D**) accounts for distance from the soma by summing distances, it may overrepresent distal neurites and drastically overshadow basal branches. The "averaging" method #3 (**Figure 31E-F**) appears to be the most widely used in previous morphometric studies[42, 392, 393]; while its units are intuitive and soma distances are incorporated into outputted plots, distal/apical dendrites can still be underrepresented if binned with highly prevalent proximal/basal dendrites. As polar plot representations of L6b neuron subtypes primarily aim to depict apical dendrites prominence, and that nuanced branch features will be quantitatively analysed in **4.4.3**, I chose to use method #2 for L6b/WMIN analyses.

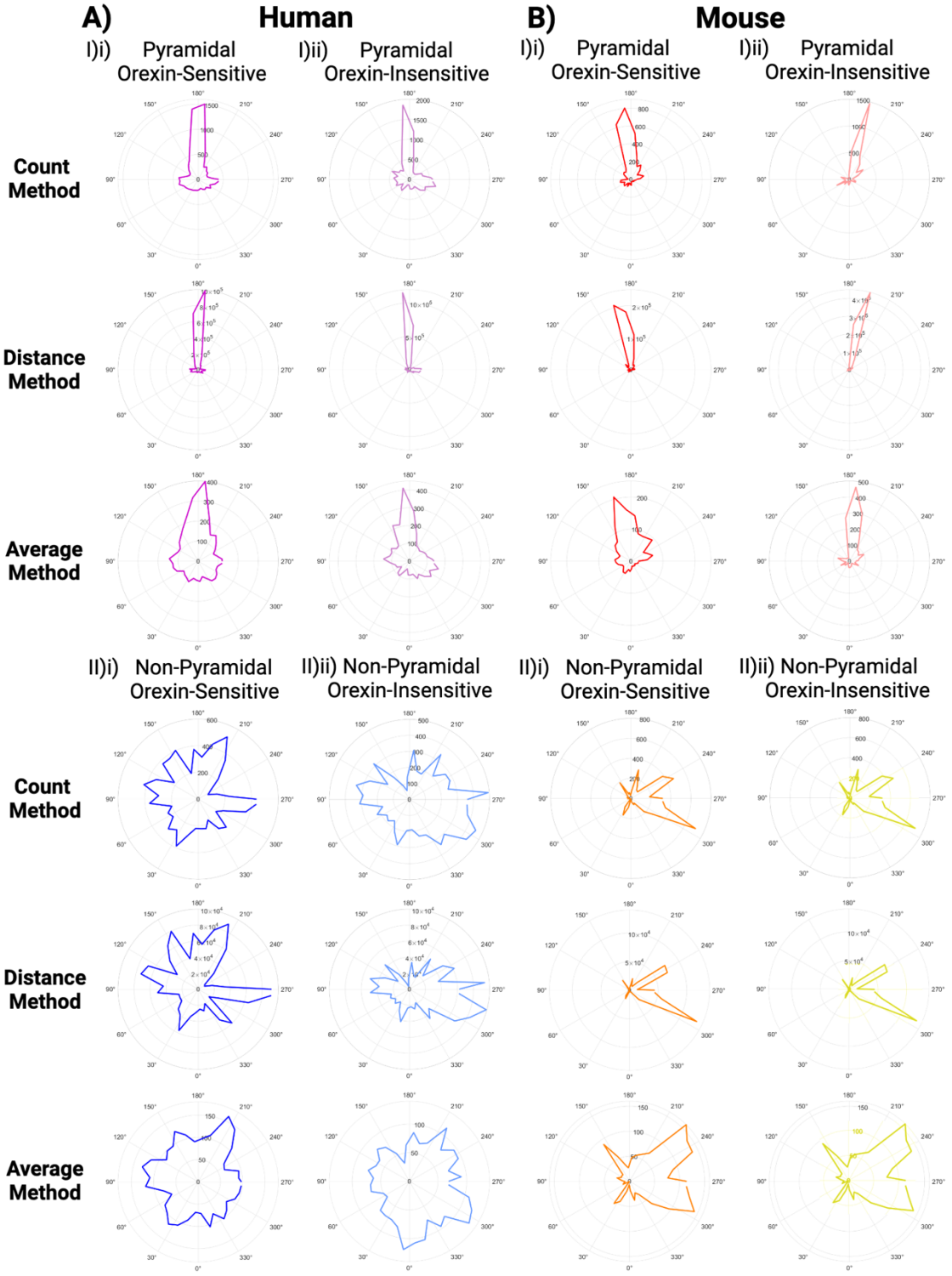


**Figure 31.** Polar plot method comparison. Similarities and difference emerge across plots of L6b A) human and B) mouse I) pyramidal and II) non-pyramidal i) ORX-sensitive or ii) ORX-insensitive neurons as obtained using the count, distance, or average method. The count method generates plots where all pixels contributing to 10° mins are weighted equally, and thus a balanced trace representation of both proximal and distal branches. The distance method strongly favours proximal voxels and therefore accentuates neurites which extend large distances from the soma (e.g., apical dendrites). The averaging method bolsters the influence of proximal branches, thus may reveal more detailed primary branch characteristics.

### *4.4.2 Human and mouse branch overview*

**Figure 32** illustrates representative single neurite traces of each subtype for qualitative inter-species comparison between human WMINs and mouse L6b cells. Traces and polar plots are not scaled identically as features of smaller mouse neurons would be indiscernible. Both human and mouse pyramidal neurons feature prominent apical dendrites and basal branches, neither of which differ in form with ORX-sensitivity. However, arborisation strength appears to increase in mouse and human ORX-sensitive cells as larger apical projections emerge in **Figure 32A)I)ii)** vs **A)I)i)** and **B)I)ii)** vs **B)I)i)**. In both species, non-pyramidal cells lack apical dendrites yet no differences emerge with ORX-sensitivity. Few $N_E$ currently contribute to mouse datasets; $N_E$=0 for non-pyramidal ORX-insensitive subtypes, thus **Figure 32B)II)ii)** is merely a placeholder. Additional neurons have been filled and will be analysed for eventual dataset inclusion.

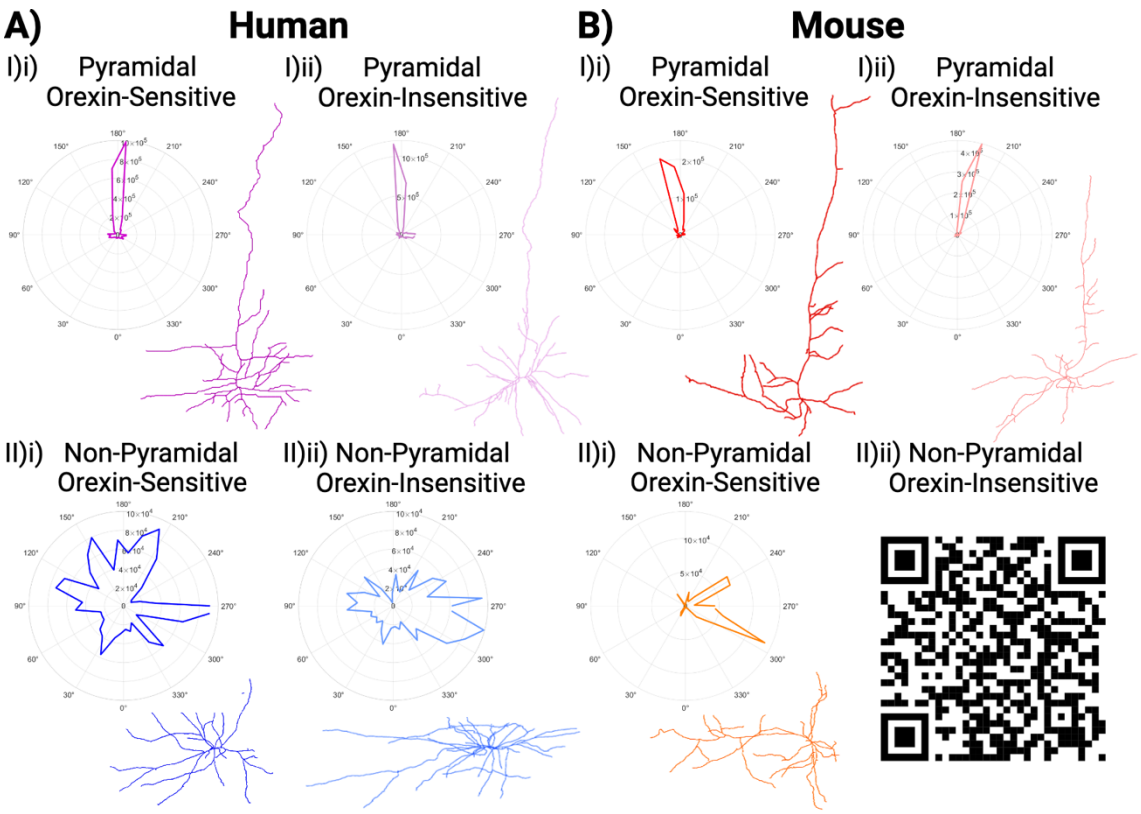


**Figure 32.** Interspecies comparison of subplate-remnant cell subtypes. Representative neuron traces and group polar plots are shown for A) human WMIN and B) mouse L6b I) pyramidal and II) non-pyramidal i) ORX-sensitive or ii) ORX-insensitive neurons. B)II)ii) No mouse non-pyramidal ORX-insensitive neurons have yet been analysed. The QR code links to a video illustrating the process of neurite tracing[394].

### *4.4.3 Neurite characteristics*

I then quantitatively compared human and mouse neuron subtypes. Sholl plots revealed no obvious differences between both human and mouse pyramidal vs non-pyramidal subtypes (**Figure 33A,C**), including according to ORX-sensitivity (**Figure 33B,D**), save longer tails for pyramidal apical dendrites which were more prominent in ORX-sensitive subtypes. This is consistent with polar plot indications (**Figure 32**). Sholl and single neurite trace feature extractions reveal no significant differences between either mouse or human ORX-sensitive and ORX-insensitive non-pyramidal neurons. Pyramidal vs non-pyramidal ORX-insensitive subtypes did not differ across any mouse or human neuron output; however, notable increases emerged in pyramidal ORX-sensitive neurons across metrics (**Figure 33**). Increased Sholl ramification indices indicate a greater number of concentric intersections relative to the number of primary dendrites (**Figure 32E**). Increased Sholl decay signifies a greater rate at which neurite densities decrease as distance from the soma increases (**Figure 32F**), while positive skewness indicates branching complexity being concentrated nearer soma (**Figure 32G**). Considered jointly, this suggests greater neurite complexity or growth specifically in basal regions of ORX-sensitive pyramidal neurons, yet not necessarily in the form of primary dendrites given increased Horton-Strahler bifurcation ratios (**Figure 32H**). Indeed, the total number of pyramidal ORX-sensitive branches increased (**Figure 32I**), which is specifically reflected in the number of basal dendrites (**Figure 32J**, calculated at a soma distance of 150/100µm for human/mouse data as determined *post hoc* from **Figure 31E-F**), but not primary dendrites (**Figure 32K**, calculated at a soma distance of 10-15µm from tracing seeds according to ellipsoid radii length predictions, **4.4.4**). Greater mean branch contraction values represent a greater ratio of Euclidian over total neurite path lengths, suggesting that ORX-sensitive pyramidal neurons are straighter or less-tortuous than other subtypes. **4.5.5** elaborates upon species differences or lack thereof, and **A.2** details all statistical summary and post hoc comparisons.

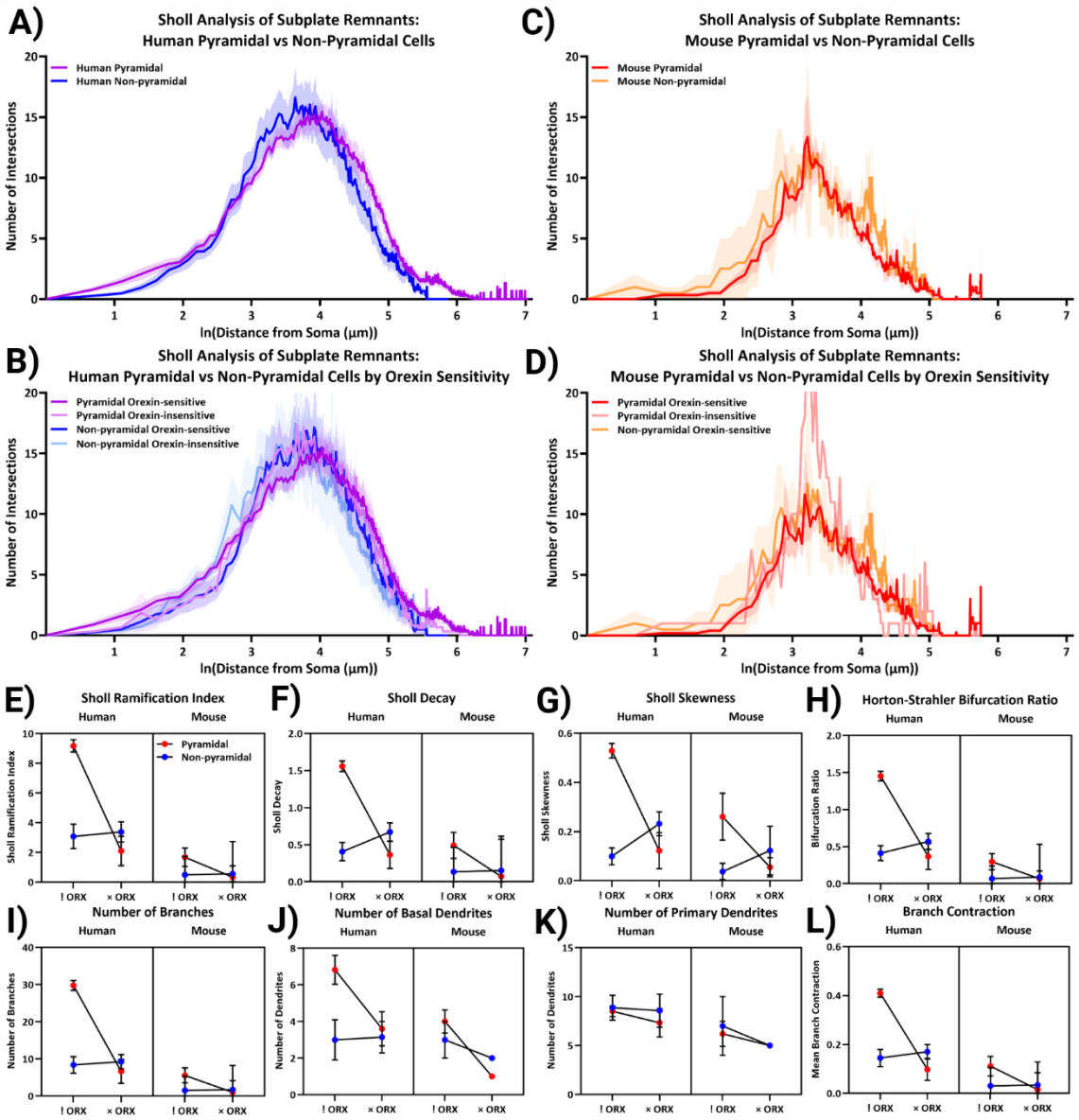


**Figure 33.** Compares dendrite features of human WMIN and mouse L6b neuron subtypes. A-B) Human and C-D) mouse Sholl plots illustrate A,C) pyramidal vs non-pyramidal subpopulations which I further dissect according to ORX-sensitivity in B,D). E-L) Highlights inter-species consistency across summary metrics from pyramidal and non-pyramidal ORX-sensitive (!) and ORX-insensitive (×) neurite trace analyses, including significant differences in pyramidal neurons according to ORX-sensitivity. See **Table 10**-**Table 11** and **A.2** for replicate and statistical details.

### *4.4.4 Soma morphometrics*

Soma analyses revealed identical patterns across summary metrics, including no change according to ORX-sensitivity in non-pyramidal neurons, significant differences in pyramidal ORX-sensitive cells, and inter-species consistency (**Figure 34**). Pyramidal ORX-sensitive cells exhibited

increased surface area, sphericity, and elongation, which suggests that cells are larger and more spherical while the aspect ratio of calculated representative ellipsoid is more protracted. This is geometrically conceivable if triangular-prism-like edges and vertices of pyramidal neurons recede as soma inflate in size along a preferential axis in ORX-sensitive neurons relative to ORX-insensitive cells (**Figure 34A-B**). Again, note that $N_E$ is very small and will increase when additional neurons are incorporated into present analyses.

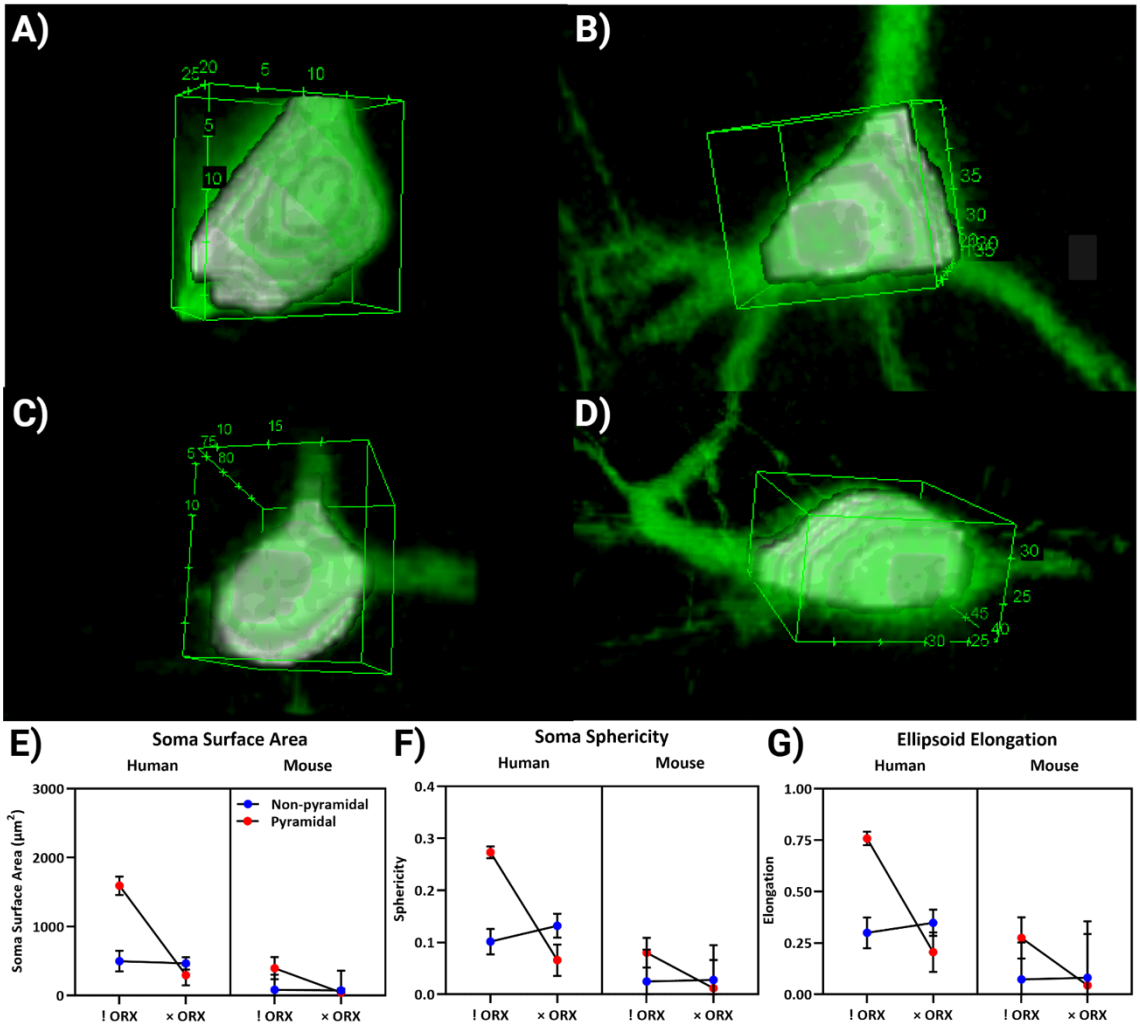


**Figure 34.** Illustrates L6b soma characteristics. A-D) Representative human neuron soma for each cell subtype: A) pyramidal and ORX-sensitive (!), B) pyramidal and ORX-insensitive (×), C) non-pyramidal and ORX-sensitive, and D) non-pyramidal and ORX-insensitive. Corresponding morphometric features extracted across both human and mouse neuron datasets include soma E) surface areas, F) sphericity, and G) elongation of the mathematically defined ellipsoid. A-D) Bounding boxes are shown in units=µm. See **Table 10**-**Table 11** and **A.2** for replicate and statistical details.

### *4.4.5 Inter-species subtype differences*

As indicated in previous literature and present results, cortical ORX-sensitivity is specific to L6b[98] yet sensitivity is not ubiquitous across all L6b cells[74, 395]. This emphasises the importance of further characterising subtype classifications, which here I parse according to pyramidal vs non-pyramidal cell type and ORX-sensitivity. In both human and mouse analyses, morphometric differences emerge only in ORX-sensitive pyramidal neurons compared to other subpopulations.

More prominent apical dendrite extensions in ORX-sensitive pyramidal neurons (**Figure 32**, **Figure 33A-D**) could be explained by distinct laminar projection profiles; ORX-sensitive pyramidal neurons may preferentially exhibit apical dendrite extensions to L1[396], while a greater proportion of ORX-insensitive neurons may terminate in lower layers. This could account for increased Sholl decay if considered in isolation yet would not explain increased Sholl skewness and basal branch counts which indicate increased proximal complexity that is not currently reflected in non-pyramidal ORX-sensitive vs ORX-insensitive subtypes. However, this lack of differences does not preclude the possibility of unique projections in non-pyramidal subtypes according to ORX-sensitivity–if present, they were indiscernible in morphometric analyses. However, if traces were accurate, my findings suggest a distinct ORX-sensitive pyramidal neuron subpopulation which is similarly present in human WMINs and mouse L6b neurons.

Proposed subtype-specific L1-projections relate to electrophysiological findings which describe L6b *Drd1a*$^{+}$ neurons which: project to L1, L6 interneurons, and L5 intratelencephalic and extratelencephalic neurons; receive extensive cortical inputs; lack primary thalamic inputs; feature efferent axons targeting HOTN; and elicit burst-firing in L5 (see **4.5.2**)[48, 50]. However, subclassifications of L6b ORX-sensitive *Drd1a*$^{+}$ neurons have previously been defined as largely *pyramidal* POm- and L5a-projecting neurons with long apical dendrites and predominantly *non-pyramidal* L1-projecting neurons[48] supposedly exhibiting large pial dendritic shafts resembling apical dendrites. My present results would be more consistent with these findings if: 1) there

were a greater proportion of ubiquitously-ORX-sensitive *pyramidal* L1-projecting and *non-pyramidal* L5/Pom-projecting subpopulations, which was not the case; or 2) if *pyramidal* L1-projecting and *non-pyramidal* L5/Pom-projecting subpopulations were proportionally sparse yet selectively ORX-sensitive. Alternatively, I may have erroneously characterised pyramidal vs non-pyramidal cells (classification can be difficult) or failed to trace non-pyramidal L1-projecting branches due to faint image signal. Cell types should be re-classified by a blinded colleague, and the layer in which distal neurites terminate should be confirmed. Traces should be re-visited, and expanded upon following deconvolution if necessary, to identify conceivably missed branches and optimise analyses.

Increased proximal branching in pyramidal ORX-sensitive subtypes aligns with increased basal dendrite complexity being a well-known characteristic of ORX-sensitive neurons[397]. ORX-sensitive L6b neurons receive extensive inputs from local and distant cortical sources[48, 50]; this is typically associated with more receptive dendrite fields, which can dynamically increase or decrease in branch number and complexity with increased or decreased synaptic inputs, respectively[398]. Increases observed in L6b ORX-sensitive pyramidal neurons may indicate greater capacity for more numerous or more frequent afferent signal consolidation before relay to L1 for further processing, to L5 for further intracortical or subcortical processing; or direct corticothalamic relay. Therefore, either statically or dynamically increased afferent inputs to ORX-sensitive pyramidal neurons could explain the observed interactive effect of ORX-sensitivity and cell type.

Together with previous literature, present findings suggest that subpopulations of L6b neurons exhibiting unique signal responsivity and projection selectivity may serve as a neurodevelopmentally-persistent ORX-sensitive network node capable of integrating and potentiating wake- or attention-promoting orexigenic effects. These effects and their conceivable consistency across species will be discussed further in **4.5.2** and **4.5.5**.

## 4.5 Indications and future directions

### *4.5.1 QUINT pipeline refinements*

Improved image analysis tools and methodological pipelines are essential to more completely characterise biological phenomena, to enable more targeted or complex investigative questions, and to provide novel anatomical insights. The QUINT pipeline presents unique advantages within the scope of whole-brain imaging and quantification methods, and the revisions I developed and employed significantly advance its analysis capabilities.

While manual cell counting or confirmation of detections in individual ROIs defined by targeted visual inspection may historically be deemed the 'gold-standard', QUINT presents the advantage of time in achieving similar quantifications by semi-automated detections, regionalisation, and atlas-mapping particularly when whole-brain analyses are desired. Manually counting tens of thousands of cells across multiple sections of multiple brains is simply not practical, and the likelihood of random human error on this scale cannot be ignored or necessarily deemed less than systematic errors due to automation. More advanced whole-brain imaging and analysis methods compared to QUINT-employed SDCM or SSFM could involve tissue clearance and light sheet fluorescence microscopy (LSFM)[399-402]. However, LSFM cell tagging is limited compared to slice histology; for the aims of this thesis, LSFM-suitable retroviruses did not exist, and L5-6b-specific antibodies were incompatible with clearance protocols[400-402]. LSFM requires immense costs across hardware usage, data storage, and computational processing domains, which rendered its use impractical for my present purposes.

Further improving the capabilities and usability of higher-throughput techniques like SDCM or SSFM with r-QUINT–which possess sufficient resolution for cell detections and soma characterisation yet are not prohibitively time- and cost-consuming–is therefore warranted. Present QUINT refinements enable fluorophore multiplexing and coarse soma analyses via QuPath and Groovy/MATLAB scripts yet lack more sophisticated soma and neurite

morphological analysis capacity. To this aim, future software adaptations could integrate Cellpose as a QuPath plugin for improved cell detections[403], Omnipose for complex neurite analyses which builds upon Cellpose architecture[404], or Arivis if cell-distinguishing perimeters could be established (**4.1.3**). Any of these would considerably expand current r-QUINT capabilities, therefore Cellpose/Omnipose integration is an active research direction. Other glial-specific neurite analyses scripts could be integrated and adapted for other cell types, including a currently unpublished algorithm which demonstrates considerable promise upon preliminary application[405]. Increased detections, resolutions, and nuanced feature extractions would require increasingly demanding computational resources exceeding those of typical computers which, if pursued, necessitates parcellation and cluster job submission with which QuPath and associated plugins are compatible. Several adaptations could additionally improve the r-QUINT user-interface. I created custom Excel sheets for Nutil piping which defined brain ROIs according to manual combinations of registerable Allen atlas-defined areas (**A.6.4**). While fully functional and adaptable for future applications, this sheet is cumbersome to navigate and edit. The default QUINT-provided spreadsheet could rather be used by Nutil, then customisations introduced by **A.6.4** could rather be incorporated within the initialisation section of the main MATLAB script (**A.10.7**) such that users can pre-select both *which* ROIs are to be analysed and *how* each ROI should be defined. The same MATLAB script should be refined such that it is usable open-source (e.g., as an MLAPP or Shiny app after translation to R). Both alternative GUIs would further improve user-friendliness. Rather than outputting spreadsheets containing data specifically formatted for copying-and-pasting into GraphPad Prism–another proprietary platform–a refined script should rather directly generate plots which are customisable via the GUI. Future pipeline improvements could accommodate 3D z-stack imaging and morphometrics analyses using the same data tagging technique (**4.1.3**, **A.10.7**). This could be a worthwhile future direction given that present 2D image analyses merely approximate 3D morphological

characteristics and are inherently limited. For example, a small 2D circle may represent the edge or tip of a much larger cell, or a large 2D circle acquired obliquely may overrepresent cell size,. 2D methods have been consistently shown to underestimate cell detections, yet to varying extents, and lack the spatial information needed for morphometric analyses[406-408]. Expanding the present r-QUINT pipeline to accommodate 3D images and analyses would require significantly increased imaging time, data storage capacity, and computational resources. However, the benefits of this and other prospective improvements may outweigh associated costs in future applications–increasingly so if costs decline as technologies continue to improve.

As with any methodological adaptation, meticulous validations are required and were conducted throughout **4.1**-**4.3**. r-QUINT accuracy was tested and largely supported relative to STPT-qBrain and PSCM-ImageJ PV quantifications (**Figure 20**, **4.1.4**), highlighting *Drd1a*$^{+}$ cortical heterogeneity (**4.1.4, A.2**) and the need for pan-cortical regional assessments when evaluating effects of genetic perturbation. Perhaps most notably, PV/VVA analyses upon L6-augmentation revealed identical findings relative to time- and cost-consuming PSCM-ImageJ analyses of a smaller number of ROIs, which in summary include: slightly increased PV soma areas in M1 and S1 upon PTEN-cKO; greater PV and VVA densities in M1 and S1 compared to PFC; and no overall regional or laminar density differences in M1 or S1 upon L6-augmentation save a trend towards decreased PV$^{+}$/VVA$^{-}$ densities in M1 (**Figure 30**). However, absolute values often differed between modalities, and to a greater extent for VVA and PV$^{+}$/VVA$^{+}$ than PV and PV$^{+}$/VVA$^{-}$. While this did not affect conclusions, it stresses that further refinement is needed across QuPath detection scripts which appear to exhibit a high false-negative rate in M1 and S1 compared to PCSM-ImageJ (**Figure 30E,G,I,K,M,O**). This suggests that the present r-QUINT pipeline may operate more reliably when analysing stronger signal from cytoplasmic antibodies like PV–for which automated cell quantifications are more accurate–emphasising the need for improved future detection software integration[403, 404].

Overall, if finer cell features including neurite characteristics, absolute soma area or volumes, and associated morphometrics are the primary desired research metric, targeted PSCM currently remains superior to r-QUINT. If higher-throughput and true whole-brain analysis is required, compatibility with LSFM should be considered. If desired outputs do not extend beyond coarse cell densities, counts, or soma areas or desired cell targets are incompatible with LSFM, r-QUINT with SDCM or SSFM may be ideal; r-QUINT accommodates broader IHC while maintaining relative time- and cost-efficiency, enables seamless *post hoc* analyses of any atlas-defined cortical or subcortical ROI, and boasts considerable capacity for future improvement. While both more targeted methods like PSCM-ImageJ and higher-throughput whole-brain techniques like LSFM exist, r-QUINT occupies a unique intermediary space in whole-brain histological analyses, and therefore present as a novel and worthwhile contribution to the field.

### *4.5.2 Layer 6-silencing and orexin*

A lack of gross histological differences upon *Drd1a*-Cre-driven *Snap25*-cKO must be considered conjunctly with the significant functional consequences previously reported[75, 78, 92]. Pharmacological interest warrants that further experiments expand upon present knowledge of the extent to which anatomical and physiological changes emerge, and consideration as to whether neurons may be therapeutically targetable.

Previous electrophysiological studies have provided insight into the roles of the same *Drd1a*-Cre subpopulation of present interest, including upon *Snap25*-cKO. *In vivo* EEG recordings following sleep deprivation and ORX-administration via showed that the total proportion of time spent awake and asleep following sleep deprivation were not altered[75]. However, upon power spectral density analyses, L6-silenced mice exhibited decreased theta-range (6-9Hz) cortical waveforms during wake and REM sleep and decreased total EEG power particularly during deep sleep, both of which indicate an impaired capacity for sleep-rebound following sleep deprivation[75]. ORXA administration increased wakefulness in both CTRL and cKO genotypes as

expected, however without anticipated attenuation upon *Snap25*-cKO, while ORXB administration attenuated theta-range oscillations in L6-silenced mice[75]. Independent findings from multielectrode array recordings and power spectra examination corroborate that ORX-sensitive L6b neuron delta-wave activation in the PFC is abolished upon *Drd1a*-Cre-driven *Snap25*-cKO[78]. However, analyses of higher frequencies were not provided due to statistically significant increases solely in the delta/theta-range following ORX application in *Drd1a*-Cre$^-$ slices despite increases across alpha, beta, and gamma bands. Effects due to *Snap25*-cKO at higher frequencies should be analysed *post hoc* as findings in the delta range are consistent with single-cell recordings which also show notable differences in the gamma-range[48]. *Drd1a*-driven channelrhodopsin expression and photoactivation yielded persistent cortical spiking, decreased slow-wave propensity (i.e., a 92±6% decrease in 5.2±0.4Hz high-delta/low-theta frequencies associated with cognitive slowing, light sleep, or meditation), and greater wake-like oscillations (i.e., a 3,863±1,265% increase in 102.0±3.0Hz high-gamma-range frequencies associated with intense cognition, selective attention, and information consolidation)[48]. *Drd1a* neurons were thus hypothesised to exert cortical control over higher-order processing[48].

These studies support the notion that *Drd1a* L6b subtypes may play a role in regulating levels of arousal or attention via ORX-gated thalamocortical-corticothalamic loops driving brain state control[74, 75]. Rather than acting as an 'on'/'off' switch, ORX-sensitive L6b neurons may instead "tune" input/output network gain in a feed-forward manner where: ORX-producing neurons reciprocally innervate L6a-b and HOTN belonging to corticothalamic-thalamocortical loops[48, 74]; ORX-producing neurons excite L6b and other brainstem arousal systems[154]; direct or indirect brainstem afferents contribute to thalamocortical relay for intracortical processing; and cortical L6b signal convergence physically manifests as an "integral arousal node"–integral in importance yet termed for what I propose is an additive and consolidatory function–to essentially calculate how awake or attentive an animal capable of higher-order processing must

be. While control over ORX-associated sleep and feeding functions are traditionally attributed to subcortical control centres[409, 410], cortical involvement and fine-tuning simply makes sense; consider cases of purposefully persevering through fatigue to meet late-night work deadlines or feeling hungry yet refraining from eating dessert because one wishes to eat healthier or lose weight. These are conscious decisions requiring higher-order cortical cognition where a range of input signals–including sleep pressure, stress, and metabolic demand–may be coordinated by L6b to determine and sustain degrees of arousal. This aligns with narcoleptic and anorexic phenotypes in cases of ORX-network disturbance where cognitive input may be impaired; dysfunctional WMIN/L6b integration and L1 projection for further cognitive processing may contribute to a decreased drive or capacity to intentionally remain awake or seek food.

ORXR-targeting has attracted pharmacological interest which may be informed by knowledge of targetable cortical neuron subtypes according to ORX-sensitivity. Dual-ORXR-antagonists (DORAs) have been FDA-approved to treat excessive feeding[411] and insomnia (e.g., suvorexant[412], lemborexant[413], and daridorexant[414]), and ORXR2-agonists are being developed as low ORXA is diagnostic criteria for type I narcolepsy[51, 414]; danavorexton[111], cleminorexton[415], firazorexton[416], and alixorexton[417] are undergoing clinical trials, and oveporexton[418] is due for priority FDA-review in 2026. To my knowledge, agonists have not yet been studied for treating anorexia despite evidence of low patient plasma ORXA levels[106-108]. Both dual- and ORXR1-agonists have not yet been developed, which may yield further specificity over disease-relevant ORX networks particularly where ORXA is implicated given ORXA-ORXR1 affinity. This is an important future direction as administration of DORAs, ORXR2-antagonists (e.g., seltorexant[419] and EMPA[420], which are undergoing preclinical trials), or ORXR2-agonists may elicit off-target effects in conceivable cases of ORXR1 mutation[421]. ORXR1-antagonists (e.g., ACT-335827[422] and SB-334867[421], which remain in preclinical development) or agonists (e.g., YNT-3708, a novel discovery in 2023)[110] may better-target phenotypes implicated by L6-augmentation or silencing,

respectively. These developments present both therapeutic potential and experimental promise in designing future studies to probe ORX ligand- and receptor-specific effects.

Future experiments should continue to study subplate remnant subpopulations. This could include probing yet-uncharacterised roles of ORX-sensitive cells in feeding behaviour, anxiety, and their interaction[78]. For example, a cohort of $N_E$=12 mice (3 for each combination of male and female *Drd1a*-cKOs/*Drd1a*-heterozygotes) maintained under a 12:12hr 03.00:15.00 light-dark cycle could be subjected to the experimental schedule propsed in **Figure 35**. In a crossover study design and following habituation, ICV-cannula-implanted mice could undergo ORXA, ORXB, or saline infusion at ~14.30 (~30mins before dark-onset), then return to home-cages for 48hr *SnackerTracker* recordings with 24h between consecutive acquisitions (**Figure 35A**). This could then be repeated, yet alongside anxiety tests (e.g., elevated-plus maze and open-field test) ~30-60mins after infusion–the time at which previous studies have shown anxiety-related effects or ORX-administration to emerge [423] and after which effects subside[75]–before similarly returning mice to home-cages for *SnackerTracker* recordings (**Figure 35B**). Conceivable differences in feeding behaviour, anxiety tests, and feeding behaviour with or without preceding anxiety tests could then be analysed across ORX-infusion and genetic conditions. I would expect ORX-administration to induce anxiety[78, 423] and feeding behaviour[98] which should diminish upon *Drd1a*-driven *Snap25*-cKO. It would be interesting to disentangle whether conceivable differences are specific to any ORX isoform. Further experiments could probe effects of *OrxR*-cKO rather than *Snap25*-cKO in *Drd1a*-specific subpopulations; *Drd1a*-Cre lines could be crossed with floxed *OrxR* constructs to investigate effects of deficient *OrxR1* (*Hcrtr1*$^{fl/fl}$ allele)[424] or *OrxR2* (*Hcrtr2*$^{fl/fl}$ allele)[425] transcripts in L6b subpopulations. Alternatively, to contrast chronic global L6-silencing, acute local *Drd1a*-Cre-driven DREADD manipulations (like those in **4.2**)[147] could be performed by crossing *Drd1a*-Cre with excitatory hM3Dq (B6N;129-Tg(CAG-CHR3*, mCitrine)1Ute/J, The Jackson Laboratory #026220) or inhibitory hM4Di alleles

(B6.129-Gt(ROSA)26Sortm1(CAG-CHRM4*,-mCitrine)Ute/J, The Jackson Laboratory #026219). CNO injection would enable investigations into regional effects of *Drd1a* perturbation, including but not limited to the PFC which evidence suggests may particularly influence ORX-related top-down control over arousal[78]. In cases of both global *Drd1a*-Cre-driven *OrxR*-cKO or local *Drd1a*-Cre-driven DREADD manipulation, ORXA and ORXB agonists could be applied as in prior studies[75, 426] to evaluate effects due to receptor abolition and region-specific augmentation or silencing, respectively. Neuroanatomical and behavioural characterisations of wakefulness, anxiety, and feeding phenotypes could thus be conducted across conditions to elucidate differences due to combinations of global vs regional and chronic vs acute *Drd1a*-Cre-driven perturbation.

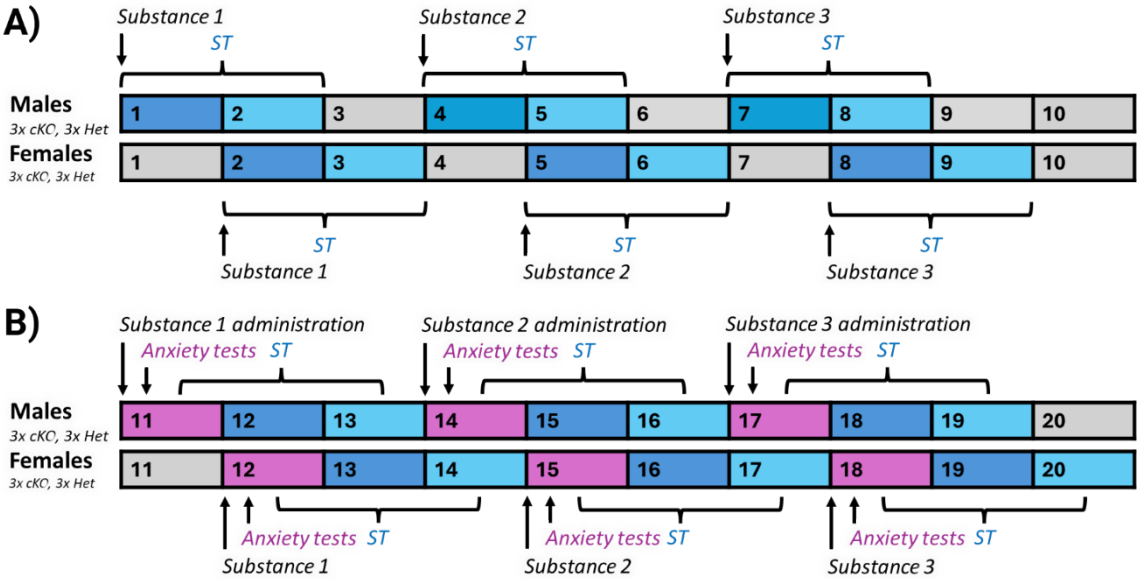


**Figure 35.** Schematic of a future experiment proposal. This behavioural study may probe effects of *Drd1a*$^{+}$ neurons on OR-mediated A) feeding behaviour and B) both feeding and anxiety. Substances 1-3 represent ORXA, ORXB, and saline in a randomised order. Numbers indicate experiment day. Blue=*SnackerTracker* (*ST*) recordings; purple=anxiety test (only within the first hour following substance administration, after which *SnackerTracker* recording commence); and grey=rest (i.e., no recording or substance administration for animal recovery).

### *4.5.3 Receptor expression insights*

Dissecting local ORX effects and isoform specificity would be particularly interesting in examining cortical and pericortical regions with high concentrations of ORXRs—namely, L6, the insudeum griseum, and fasciola cinerea. A seminal study which characterised *OrxR* expression

in the rat brain via *in situ* hybridisation indicated that *OrxR2* is present throughout L6, yet *OrxR1* appears more compactly expressed in deep layers (**A.5.9**)[93]. This contradicts electrophysiological studies claiming that cortical responses to ORX exclusively in L6b occur via ORXR2[98]. Bayer et al. arrived at this conclusion by comparing the depolarising action of ORXA with that of ORXB, observing no significant difference, and reasoning that effects were exacted via ORXR2s as ORXR2 exhibits equal affinity for ORXA and ORXB while ORXR1 preferentially binds to ORXA[96]. This would be a valid assumption if exclusively ORXR1s or ORXR2s could exist in L6b. However, both subtypes may exist; differences due to ORXR1 could be either attenuated (i.e., if ORXR1-expressing neurons are less-prevalent in L6b) or misrepresented (i.e., if ORXR1- expressing neurons were perchance not among the $N_E$=5 neurons selected for patch clamp recordings which, even if representative, were <10% powered to detect reported effects). Faint *OrxR1 in situ* hybridisation signal only in the deepest cortical layers is consistent with less-prevalent yet present L6b-*OrxR1* expression in prefrontal areas[93, 427]. Pericortically, the insudeum griseum and fasciola cinerea elicit particular interest due to striking *OrxR1* expression and in that the insudeum griseum is mislabelled as taenia tecta (TT)[93]. No known research efforts have since targeted *OrxR1*-specific insudeum griseum or fasciola cinerea effects, nor is much known about the function of either structure. Historically considered vestigial, the insudeum griseum has been postulated as a hippocampal subfield associated with the dentate gyrus via the fasciola cinerea[428]. Evidence suggests a neurodevelopmental role for the insudeum griseum in facilitating callosal white-matter axon guidance via dopaminergic inputs, where postnatal remnants persist as 'grey-matter tracts' tracing the midline of the corpus callosum[429-431]. Given speculated similarities in *OrxR1*-specific-expression, dopamine signalling, and historically vestigial classifications, it is plausible that the insudeum griseum may play a neurodevelopmentally similar role relative to callosal projections as the subplate does to cortical networks. In observing the appearance of the insudeum griseum and fasciola cinerea across

present SDCM scans, strikingly obvious and perhaps defining VVA signal is apparent (**Figure 16**, **Figure 22**, **Figure 30**, **Figure 79**). This could indicate that resident cells contribute to highly stable extracellular-matrix-shielded networks exhibiting restricted plastic capacity, synaptic inflexibility, protection from degradation and nonspecific signals, reduced membrane capacitance, and capacity for high-frequency firing. Further anatomical and electrophysiological characterisation of the insudeum griseum and fasciola cinerea should be conducted using existing datasets for exploratory analyses (**5.4.5**) to inform future directions–a worthwhile endeavour given what appears to be a rare opportunity to characterise a brain region which is phylogenetically conserved at least in mice and humans[432, 433] yet lacks a well-defined function.

### *4.5.4 Layer 6-augmentation and mTOR*

PTEN-cKO yields *Drd1a*$^+$ neuron hypertrophy and prevalence without altering projection targets, which is consistent with hypotheses. Extending upon **4.3.5**, increased *Drd1a*$^+$ counts in L6a relative to L6b (**Figure 27G**) may be simply explained by a greater number of *Drd1a*$^+$-targeted cells residing in the larger L6a. Unintuitively decreased L6b densities (**Figure 27G-H**) may be due to constant CPLX3 expression such that *Drd1a*$^+$ counts and cortical thickness increased, yet average CPLX3 signal did not, which assigned more *Drd1a*$^+$ neurons to L6a. Alternatively, both increased L6a counts and decreased L6b densities could be explained by increased pial migration upon mTOR disinhibition[65]. Greater differences in *Drd1a*$^+$ cells which lack CPLX3 co-expression could indicate resistance to genotype effects (**4.3.3**, **4.3.5**). CPLX3$^+$ subtypes may represent L1-projecting cells described morphometrically (**4.4**) and electrophysiologically[48], likening *Ctgf*$^+$ populations [48, 82, 225], as CPLX3 projections in **Figure 26D** appear to arborise in L1 but not L5 while *Drd1a* neurites are visible in both (also see **Figure 25**). If true, similar densities following PTEN-cKO suggests constant ORX-insensitive non-pyramidal L1-projecting CPLX3$^+$[82, 225] subpopulations which exhibit lower firing frequencies than *Drd1a*$^+$ neurons[48, 50]. Considered alongside morphometric consistency in non-pyramidal L6b subpopulations, yet increased complexity and

arborisation strength in pyramidal ORX-sensitive neurons (**4.4**), perhaps CPLX3-lacking L5/POm-projecting L6b subpopulations are more profoundly influenced by PTEN-cKO. Given the proposed role of L6b as an "integral arousal node", perhaps "integration" functions–including L1 projections–are less-affected by PTEN-cKO yet higher-frequency relay to L5 increases. Visually, this may be the case as more prominent apical dendrites appear to extend to L5 but not L1 upon PTEN-cKO in **Figure 25ci** vs **Figure 25di** and **Figure 26DIVi** vs **Figure 26DIViii**,.

Increased *Drd1a*$^{+}$ neuron prevalence and hypertrophy resemble human WMINs upon pathological PTEN mutation[55, 69], while increased L5/POm relay could relate to associated physiological consequences including cortical hyperexcitability and sensory sensitivity[35, 56, 66]. Increased WMIN densities are common to comorbid conditions of autism and epilepsy[55, 69, 72, 73], yet whether projections to L1 and/or L5 increase remains unknown. This could be tested in mouse L6-PTEN-cKO models using techniques like monosynaptic-CaMPARI-TTX/4APChR2 circuit mapping[48, 434, 435]. I would suspect patch clamp and local field potential recordings in *Drd1a*-Cre-driven PTEN-cKO neurons to yield decreased membrane resistances and increased action potential firing frequencies relative to CTRLs. After better characterising *Drd1a*$^{+}$ neuron phenotypes following PTEN-cKO, rescue could be attempted via mTOR inhibitor administration (**A.1.1**). Rapamycin and rapalogs ('first-generation' inhibitors) should be tested yet may not be optimally effective in rectifying effects of PTEN-cKO as rapamycin targets mTOR complex 1 (mTORC1)[61] and cannot entirely preclude upstream PTEN action via mTOR complex 2 (mTORC2). 'Second-generation' inhibitors (i.e., torin-1)[436] may be more potent due to simultaneous inhibition of mTORC1, mTORC2, and PIK3[61, 436]. Such follow-up investigations would inform whether attention should be directed towards mTOR inhibitor pharmacology for autism and epilepsy treatment. While first-generation inhibitors including rapamycin and everolimus have received FDA-approval for managing refractory focal seizures, proposed follow-up rescue experiments could test whether second-generation inhibitors should also be pursued.

### *4.5.5 Evolutionarily preserved morphometrics and networks*

Across neurite and soma analyses, human WMINs and mouse L6b neurons defined by cell type (i.e., pyramidal vs non-pyramidal) and ORX-sensitivity appear qualitatively similar, save differences due to scale (**Figure 32**, **Figure 34A-D**). However, present quantitative comparisons are limited by the low number of mouse neurons (**Figure 33**, **Figure 34E-G**). While current analyses identify no species differences due to cell type (species×type), ORX-sensitivity (species×ORX-sensitivity), or their interaction (species×type×ORX-sensitivity) (**Table 17**), this is not a sufficiently powered conclusion. Morphologies only provide some insight into whether cells are analogous. Previous studies report comparable L6b-WMIN molecular profiles[4, 5], and in original publications which define orexin/hypocretin[96, 97], human and rat homologs of *OrxR1* and *OrxR2* exhibit 94% and 95% similarity, respectively[98]. Present image stacks were obtained from biocytin-filled neurons following single-cell patch-clamp recordings, whose analyses will further inform subtype resemblance. Together, further morphometric analysis will complement genetic and physiological data to evaluate *Drd1a*-Cre/WMIN analogy and the notion of evolutionarily conserved yet incompletely characterised roles for ORX-sensitive subplate-remnant neurons.

**Table 17**. Summarises comparisons between mouse and human L6b neurons. Further details, are provided in **A.2**. Green=neurite analyses; blue=soma analyses. **ND**=no statistical difference.

| Output Metric | Reference | Species×Type | Species× ORX-sensitivity | Species×Type× ORX-sensitivity | Result |
|---|---|---|---|---|---|
| Sholl ramification index | **Figure 33E** | $F_{(1,55)}$=1.273, p=0.2641 | $F_{(1,55)}$=2.599, p=0.1127 | $F_{(1,55)}$=3.056, p=0.0860 | **ND** |
| Sholl decay | **Figure 33F** | $F_{(1,55)}$=0.7898, p=0.3780 | $F_{(1,55)}$=0.6870, p=0.4180 | $F_{(1,55)}$=2.591, p=0.1132 | **ND** |
| Sholl skewness | **Figure 33G** | $F_{(1,55)}$=0.4095, p=0.5249 | $F_{(1,55)}$=3.561, p=0.5531 | $F_{(1,55)}$=0.9310, p=0.3388 | **ND** |
| Horton-Strahler ratio | **Figure 33H** | $F_{(1,55)}$=1.418, p=0.2388 | $F_{(1,55)}$=1.825, p=0.1822 | $F_{(1,55)}$=3.531, p=0.0655 | **ND** |
| # Branches | **Figure 33I** | $F_{(1,55)}$=2.199, p=0.1438 | $F_{(1,55)}$=2.977, p=0.0901 | $F_{(1,55)}$=3.431, p=0.0694 | **ND** |
| # Basal dendrites | **Figure 33J** | $F_{(1,55)}$=0.4683, p=0.4971 | $F_{(1,55)}$=0.0217, p=0.8835 | $F_{(1,55)}$=0.0476, p=0.8282 | **ND** |
| # Primary dendrites | **Figure 33K** | $F_{(1,55)}$=0.0192, p=0.8904 | $F_{(1,55)}$=0.0868, p=0.7695 | $F_{(1,55)}$=0.0802, p=0.7782 | **ND** |
| Branch contraction | **Figure 33L** | $F_{(1,55)}$=0.7490, p=0.3905 | $F_{(1,55)}$=1.668, p=0.2020 | $F_{(1,55)}$=2.503, p=0.1194 | **ND** |
| Soma surface area | **Figure 34E** | $F_{(1,55)}$=0.5841, p=0.4480 | $F_{(1,55)}$=1.348, p=0.2506 | $F_{(1,55)}$=1.220, p=0.2743 | **ND** |
| Soma sphericity | **Figure 34F** | $F_{(1,55)}$=0.3811, p=0.5395 | $F_{(1,55)}$=1.074, p=0.3045 | $F_{(1,55)}$=2.389, p=0.1279 | **ND** |
| Ellipsiod elongation | **Figure 34G** | $F_{(1,55)}$=0.2096, p=0.6489 | $F_{(1,55)}$=0.7277, p=0.3973 | $F_{(1,55)}$=1.211, p=0.2760 | **ND** |

# Chapter 5: Results – L5-silencing leads to progressive anatomical and motor degeneration as revealed by multimodal datasets

This chapter maps the spatiotemporal progression of neuroanatomical and behavioural deterioration following *Rbp4*-Cre-driven *Snap25*-cKO, informing 1) the relevance of this mouse model to underlying mechanisms associated with motor neuron degeneration and 2) the ability of MRI to detect brain-wide changes upon cell-specific genetic manipulation. Upon identifying motor phenotypes in the L5-silenced mouse line (**Preface**, **5.1.1**), I proposed and executed a longitudinal study involving behavioural, neuroimaging, and histological experiments to systematically determine where and when signs of degeneration emerge (**1.5.5**). Throughout postnatal weeks 4-21, I tested the motor function of CTRL and L5-cKO mice (**5.1**) and conducted up to three interspersed *in vivo* MRI scans (i.e., volumetric, diffusion, and resting-state fMRI) (**5.2.1**, **5.2.2**). Following perfusion-fixation, I scanned brains *ex vivo* (i.e., volumetric, diffusion, and QSM) (**5.2.3**, **5.2.5**) then processed samples for immunolabelling (**Figure 4**) (**5.3**). I predicted that behavioural deficits would progressively emerge (i.e., irregular feeding and home-cage activity, hindlimb-clasping, decreased grip strength, and gait deficits), and that these would be accompanied by volumetric decreases in areas of *Rbp4*-Cre expression (i.e., projection tracts by 7wks, and soma by 16wks). In *Rbp4*-Cre projection tracts, I anticipated decreased FA with increased MD and susceptibility, while in areas of *Rbp4*-Cre soma expression I hypothesised decreased intracellular volume fractions and complexity with increased MD and neurite dispersion. I predicted this to reflect decreased L5 UMN (*Rbp4*-Cre$^{+}$/NEUN$^{+}$/SMI32$^{+}$) soma prevalence, *Rbp4*-Cre$^{+}$ axon integrity, and LMN CHAT expression alongside emergent tau aggregation, glial cell infiltration, and signs of interneuron or perineuronal net degradation in the brain and spinal cord (**Table 7**). Ultimately, I aim to characterises trajectories of motor degeneration in *Rbp4*-Cre mice upon *Snap25*-cKO and demonstrate methodological power in consolidating parallel neuroimaging, histological, and behavioural insights (**5.4**, **5.5**).

## 5.1 Behaviour

### *5.1.1 Physical features and feeding behaviour*

As detailed in the **Preface**, and **3.1.5**, I conducted pilot *SnackerTracker* validation tests 6iii) (**A.3.7**-**A.3.8**) using surplus ~18-20wk L5-silenced and CTRL mice to evaluate 1) whether significant crumbling emerged (**3.4.4**), and 2) whether *SnackerTrackers* were compatible with longer recording timeframes upon instituting the wired USB setup (**3.4.1**, **A.4.4**). Subtle changes in feeding patterns were not entirely unexpected; I reasoned that previously reported decreased body weight and sleep disturbances (i.e., increased wakefulness) in L5-silenced mice relative to CTRLs[77, 114], may correspond to decreased food intake and feeding behaviour. By extension, I argued that test 6iii) may also validate whether *SnackerTrackers* could detect expectedly decreased total feeding in L5-silenced mice.

Pilot results were unexpected. After confirming decreased body weights in L5-cKOs (**Figure 36**), *SnackerTracker* data showed that, while the pattern and amount of feeding behaviour appeared identical between groups (**Figure 37A-B**, **Figure 37E-I**), food intake appeared diurnal in CTRLs yet arrhythmic in L5-cKOs (**Figure 37C-D**). Surprisingly, despite lower body weights, L5-cKOs appeared to eat more than CTRLs, with increased food-intake during the light-phase/light-onset and decreased food-intake during the dark-phase/dark-onset (**Figure 37J-N**). This is consistent with a qualitative lack of regular diurnal fluctuation in the timeline trace of L5-cKOs compared to CTRLs (**Figure 37D**).

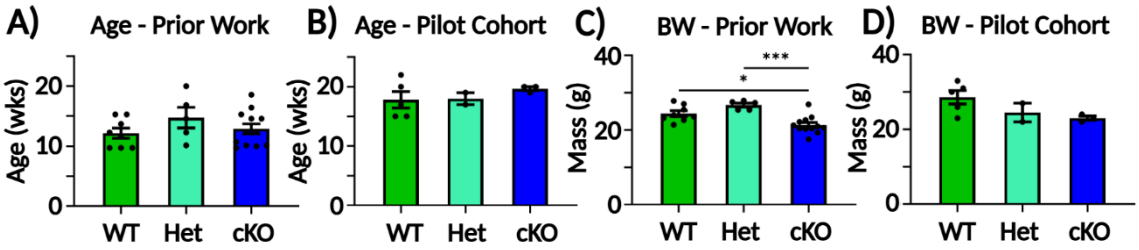


**Figure 36.** *Rbp4*-Cre animal data. Shows A-B) ages and C-D) body weights across L5-cKOs, heterozygote (Het) CTRLs, and WT CTRLs A,C) from prior work[114] and B,D) in the present pilot. *=p<0.05, ***=p<0.001. See **Table 10**-**Table 11** and **A.2** for replicate and statistical details.

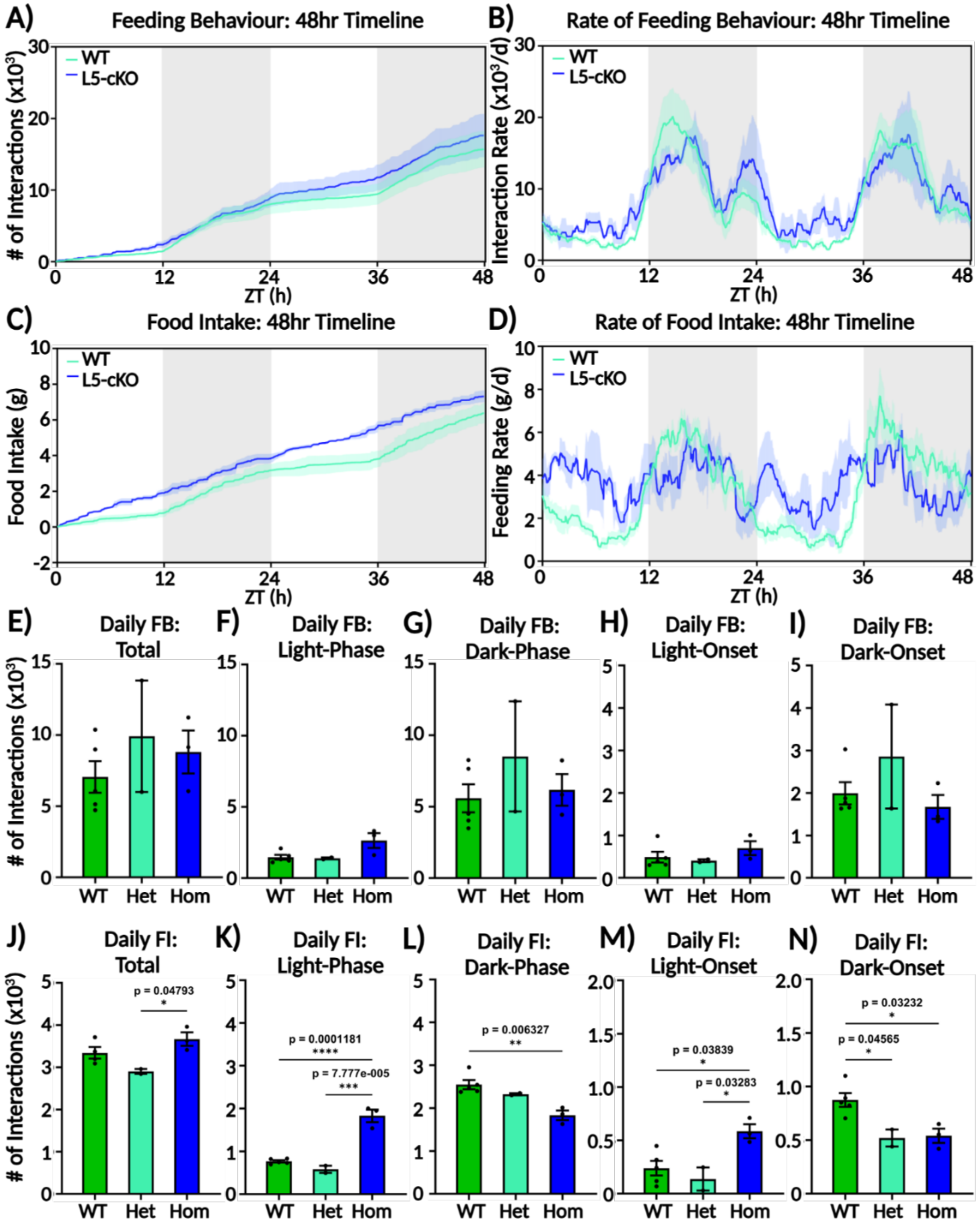


**Figure 37.** Daily feeding behaviour and food intake in L5 CTRL and cKO mice. 48hr A) cumulative and B) derivative rates of animal-device interactions ('feeding behaviour', FB) are shown with C) cumulative and D) rates of food intake (FI) for L5-cKO and both $Cre^{WT}$ and heterozygous (Het) CTRLs. Summary FB data show no significant differences between WT and Het CTRLs in daily totals, yet cKOs differ E) across 24hr periods, F) in the light-phase, G) at light-onset, H) in the dark-phase, and I) at dark-onset. Identical metrics are shown in J-N) for FI. Male and female data are combined, yet individual sample traces are provided in **Figure 39**-**Figure 38** due to a trend towards sex-differences (sex-disaggregated group data can be provided upon reasonable request. ZT=Zeitgeber time. See **Table 10**-**Table 11** and **A.2** for replicate and statistical details.

Sample individual traces from 1×M and 1×F CTRL and 1×M and 1×F cKO reflect this difference. Effects are more prominent in females (**Figure 38**) compared to males (**Figure 39**); the amplitude of feeding behaviour is greater, suggesting that female mice interact more intensely with *SnackerTrackers* as in **Figure 13C**, such that a more pronounced plateau in diurnal patterns becomes obvious (i.e., **Figure 38AV** vs **Figure 38BV** and **Figure 39AV** vs **Figure 39BV**).

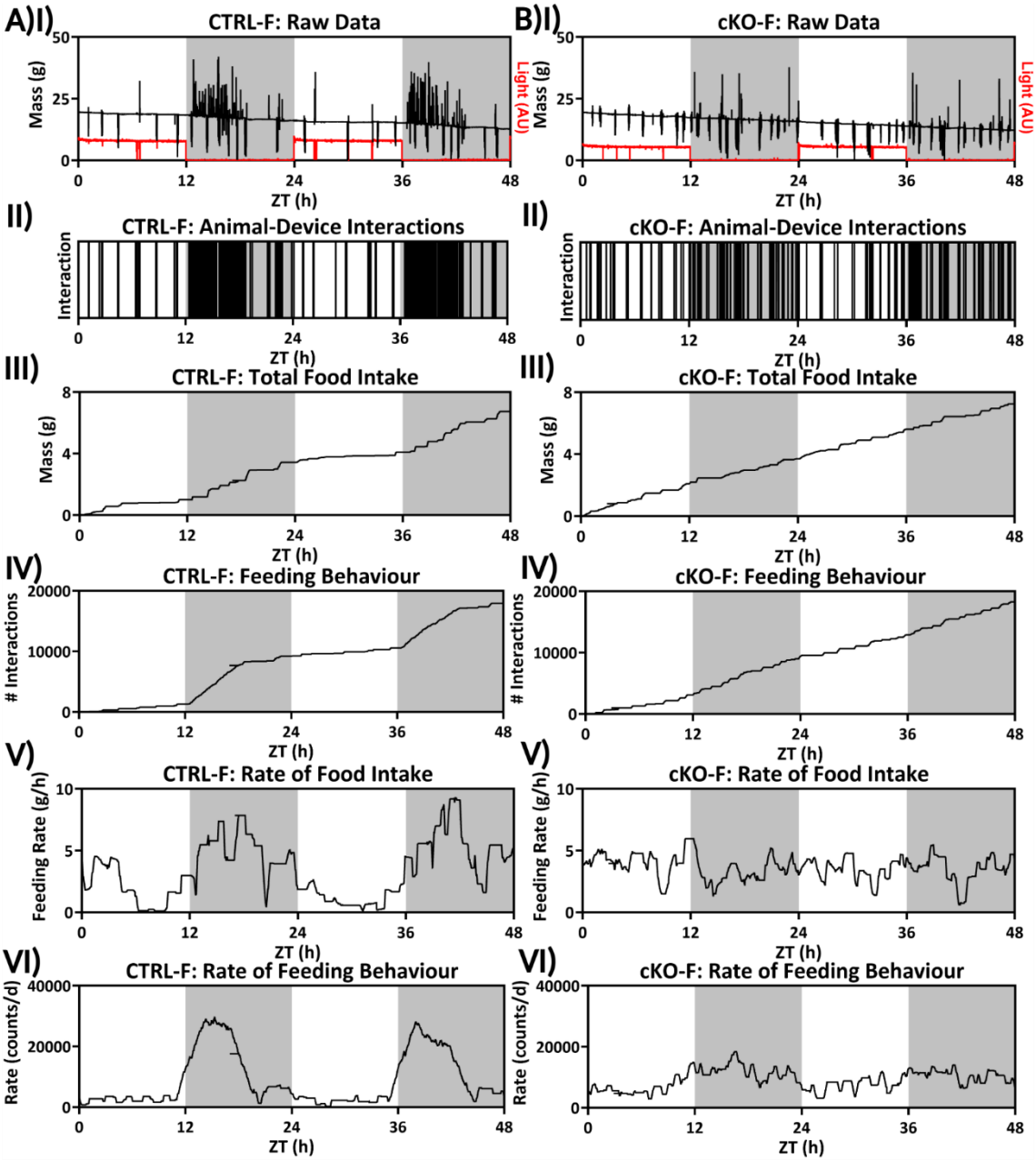


**Figure 38.** Sample female L5-CTRL/cKO *SnackerTracker* traces. A) CTRL and B) cKO timelines include I) raw mass and LDR data; II) extracted animal-device interactions; III) cumulative and V) derived food-intake; and IV) cumulative and VI) derived feeding behaviour. ZT=Zeitgeber time.

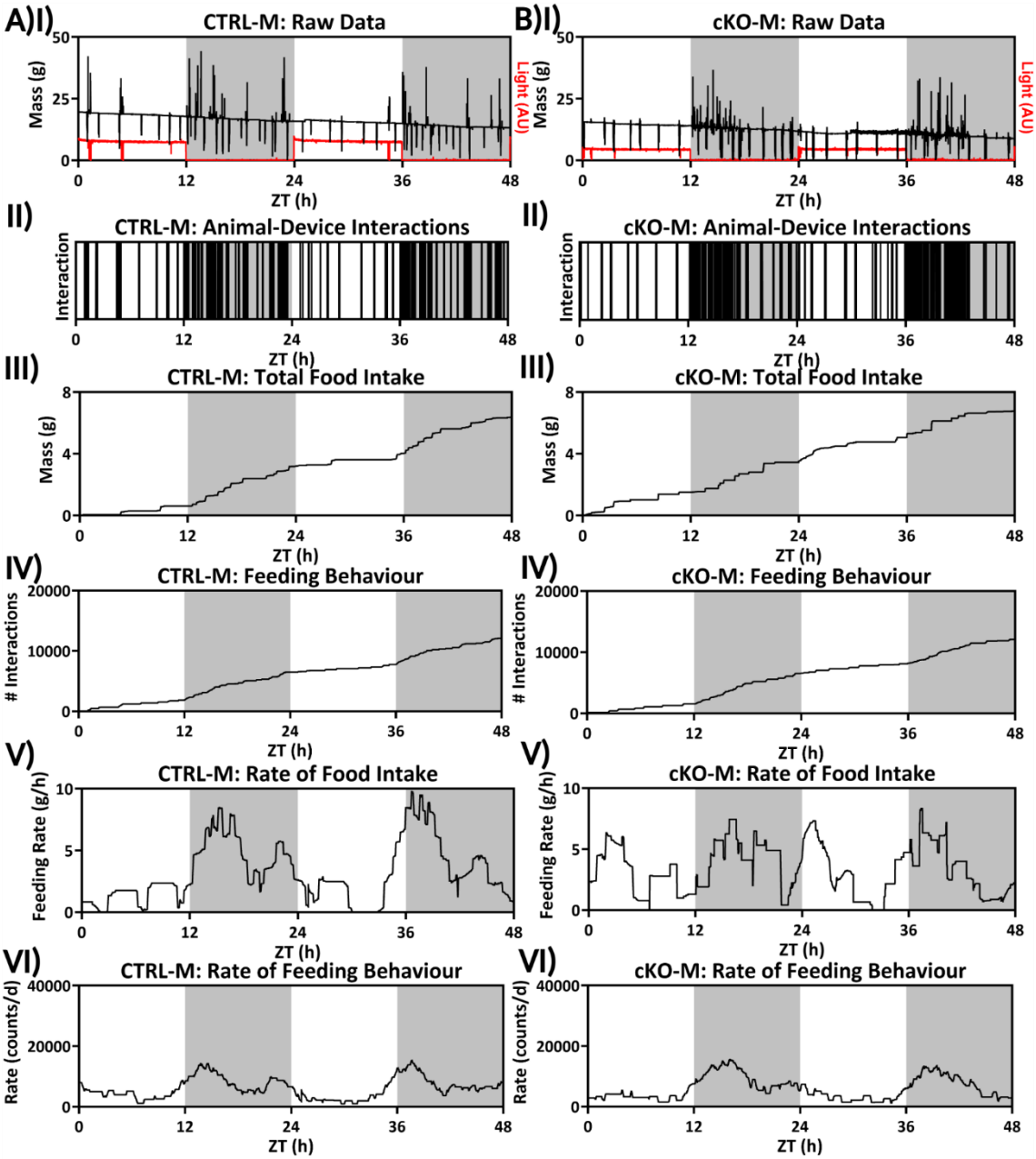


**Figure 39.** Sample male L5-CTRL/cKO *SnackerTracker* traces. A) CTRL and B) cKO timelines include I) raw mass and LDR data; II) animal-device interactions; III) cumulative and V) derived food-intake; and IV) cumulative and VI) derived food-seeking behaviour. ZT=Zeitgeber time.

Given the small $N_E$ in this initial test, I conducted a second pilot using additional surplus mice aged 13-22wks to assess 1) the consistency of feeding irregularities, and 2) whether effects only emerged at ~20wks; mice employed in prior sleep studies were younger (~13-15wks, **Figure 36**) and exhibited no apparent behavioural abnormalities[114]. Upon handling animals belonging to this second larger pilot cohort daily, I noticed that, with time, mice also appeared to exhibit

an unusual hindlimb clasp which I learned had been previously reported yet not characterised further[77]. I began qualitatively documenting whenever this hindlimb clasp emerged. After the final ~22wk timepoint, I downloaded and analysed data from all *SnackerTrackers*. Results in **Figure 40** show that, indeed, no differences between L5-cKO and CTRL mouse feeding behaviour or food intake present at ~13-15wks (**Figure 40A-B**). Only subtle signs of a hindlimb clasp in some L5-cKO mice were noticeable. However, the same irregular feeding pattern as in **Figure 37-Figure 39** emerged in L5-cKOs at ~20-22wks despite no change in food-seeking behaviour, alongside a pronounced hindlimb clasp in 8/10 animals (**Figure 40C-D**). I then thought that perhaps this feeding phenotype precipitated due to underlying motor deficits indicated by the hindlimb clasp, which may hinder animals' ability to physically reach and extract pellets from the food holder. I had collected *SnackerTracker* recordings weekly throughout the ~13-22wk timeframe, yet only initially analysed first and final timepoints, so I consulted my notes to see exactly which animals presented with a clasp and when. As a *post hoc* exploratory analysis, I extracted and combined viable traces across all animals and timepoints according to whether I had documented a clasp as present (**Figure 40G**) or absent (**Figure 40E**), then calculated the proportion of CTRL (**Figure 40F**) and L5-cKO mice (**Figure 40H**) exhibiting the phenotype. I predicted that more obvious differences in feeding patterns might emerge if the hindlimb clasp was responsible for feeding irregularities, which would suggest that differences in 'feeding behaviour' at ~20-22wks rather emerged as a consequence of motor deficits. Results in **Figure 40I-J** show that rates of animal-device interactions appeared identical between mice with and without the hindlimb clasp; however, as suspected, traces detailing food-intake rates from mice with the hindlimb clasp exhibit less-pronounced daily fluctuations than those of mice lacking the hindlimb clasp. Further *post hoc* Sum of Sine decompositions (**3.2.2**, step III) of individual traces consistently identified mice exhibiting the hindlimb clasp as having primary periods of the rate of food-intake which diverged from $\tau$=24h (**Figure 40K-L**).

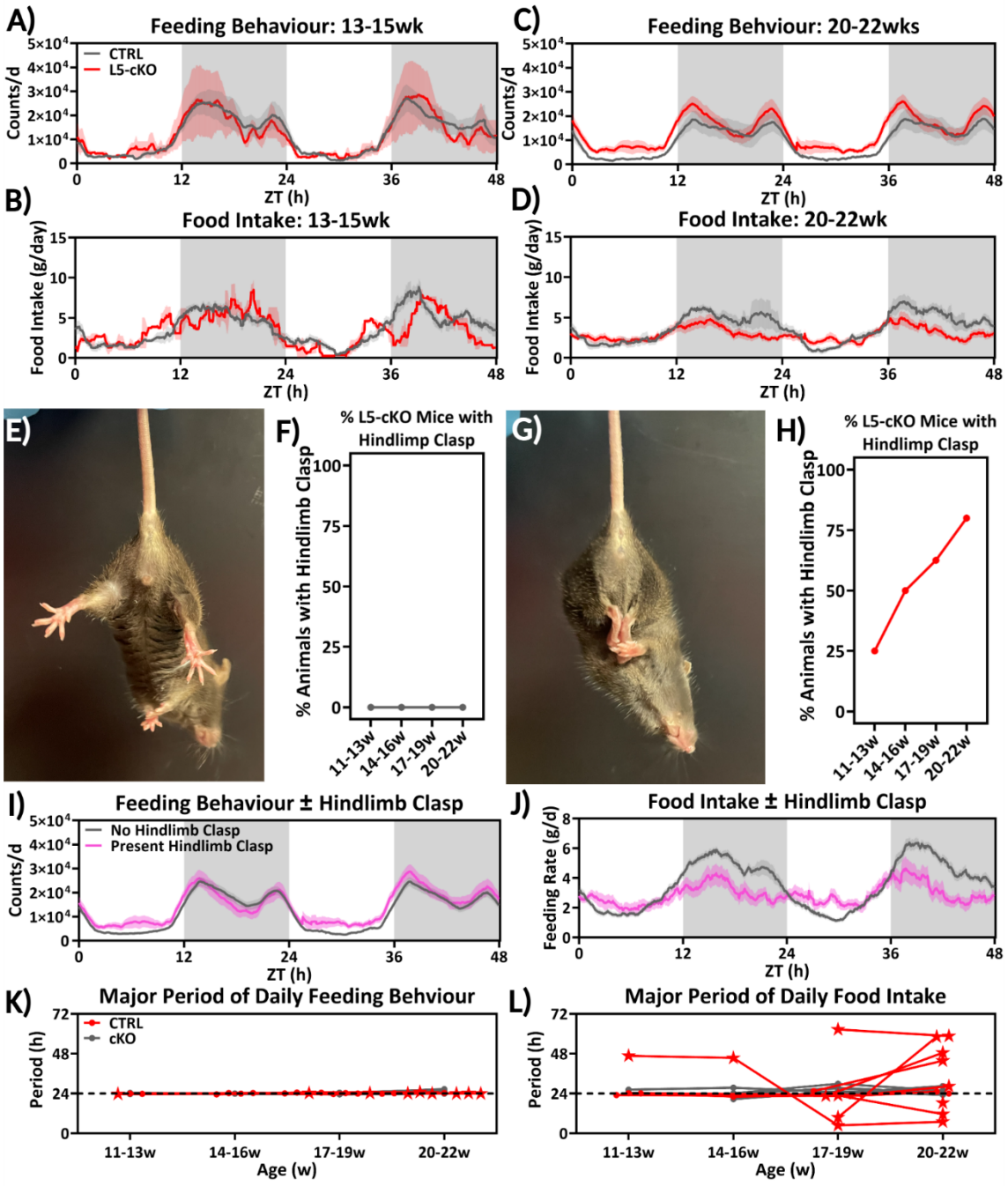


**Figure 40.** The second pilot corroborates motor-related changes upon L5-cKO. L5-cKO and CTRL A,C) feeding behaviour and B,D) food-intake are shown for mice aged A-B) ~13-15wks and C-D) ~20-22wks. The proportion of mice which E) do not develop the hindlimb clasp or G) exhibit a prominent clasping phenotype are shown for F) CTRL and H) L5-cKO mice over time I) Feeding behaviour and J) food intake traces are then disseminated according to whether recordings were obtained from mice possessing or lacking the hindlimb clasp phenotype. Period decompositions show K) no deviation from the expected primary periodicity of τ=24h for feeding behaviour in either CTRLs or L5-cKOs, yet L) notable deviation for food intake only in cKOs with time. K-L) Data from the same mouse are indicted with connected lines, and data from mice exhibiting the hindlimb clasp are marked with a ✶. ZT=Zeitgeber time. See **Table 10**-**Table 11** and **A.2** for replicate and statistical details.

This feeding phenotype–conceivably due to the emergence of a prominent hindlimb clasp arising from underlying motor deficits–motivated me to design, propose, and execute STAMINA (**1.5.5**, **Figure 4**). I will present and discuss the results throughout the remainder of this chapter. Behavioural characterisations involve more detailed food intake and feeding behaviour quantifications from younger ages (≥4wks) alongside systematic hindlimb-clasp documentation and broader CAMP scoring (**5.1.2**), VCT testing (**5.1.3**), grip strength assessment (**5.1.4**), and Catwalk gait evaluation (**5.1.5**).

**Figure 42** depicts body weight data from the complete STAMINA cohort. As expected, body weights increase in both genotypes over time, however to a consistently greater extent in CTRLs compared to L5-cKOs (genotype: $F_{(1,26)}$=33.38, p<0.0001; genotype×age: $F_{(18,200)}$=0.9373, p=0.5344). Female mice weighed consistently less than male mice (sex: $F_{(1,26)}$=97.64, p<0.0001), yet the effect of genotype did not differ by sex (genotype×sex: $F_{(1,26)}$=0.9625, p=0.3356) (**Figure 42A**). I therefore show results using combined data from both male and female mice here (**Figure 42B**) and in forthcoming behavioural plots, where no sex differences emerge unless otherwise stated. I provide sex-disseminated plots in **A.9**, and all corresponding statistics in **A.2**.

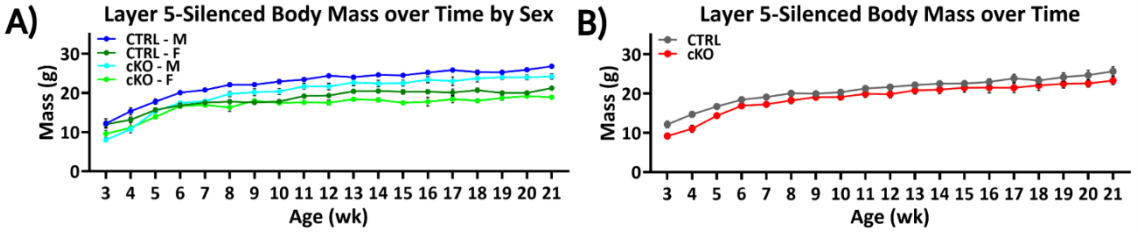


**Figure 41.** STAMINA L5-cKO and CTRL mouse body weights over time. L5-cKO mice weigh less than CTRLs, which is consistent over time A) in males and females and B) upon combining data from mice of both sexes. See **Table 10**-**Table 11** and **A.2** for replicate and statistical details.

**Figure 42** summarises *SnackerTracker* results following STAMINA cohort recordings, which are separated by sex in **A.9.4**. As in the second pilot (**Figure 40**), no difference in the pattern of food-seeking behaviour emerged at any age across trendlines and period decompositions (**Figure 42B,C,F,H**). However, L5-cKO mice exhibited increased total feeding

behaviour which is consistent over time (genotype: $F_{(1,26)}$=18.74, p=0.0002; genotype×age: $F_{(18,135)}$=33.38, p=0.8802) (**Figure 42J**), greater in females (sex: $F_{(1,26)}$=16.756, p=0.0152; genotype×sex: $F_{(1,26)}$= 0.0025, p=0.9608; genotype×sex×age: $F_{(18,135)}$=1.073, p=0.3862), and concentrated in the dark-phase (light-phase genotype: $F_{(1,26)}$=13.29, p=0.0012; light-phase genotype×age: $F_{(18,135)}$=1.144, p=0.3179; dark-phase genotype: $F_{(1,26)}$=15.40, p=0.0006; dark-phase genotype×age: $F_{(18,135)}$=0.5998, p=0.8948) (**Figure 42L,N**). This is consistent with the previous sleep study which reported intact circadian rhythms yet increased overall wakefulness particularly in the dark phase[114]. In contrast, no consistent difference in the food-intake of CTRL vs L5-cKO mice emerged over time across daily totals (genotype: $F_{(1,26)}$=2.405, p=0.1331; genotype×age: $F_{(18,1220)}$=0.9322, p=0.5419) (**Figure 42I**), in the light-phase (genotype: $F_{(1,26)}$=1.990, p=0.1702; genotype×age: $F_{(18,120)}$=1.452, p=0.1203) (**Figure 42K**), or in the dark-phase (genotype: $F_{(1,26)}$=0.1866, p=0.6693; genotype×age: $F_{(18,120)}$=1.1278, p=0.3352) (**Figure 42M**). Male mice ate more than females over time and across genotypes (sex: $F_{(1,26)}$=9.308, p=0.0052; age×sex: $F_{(18,120)}$=0.9396, p=0.5333; genotype×sex: $F_{(1,26)}$=0.0564, p=0.8142) (**A.9.4**). However, the pattern of food intake appeared to differ across genotypes. In young 3-4wk mice, feeding appears to be concentrated more closely around the time of dark-onset compared to CTRLs (**Figure 42A**). Yet, diurnal patterns appear equally prominent, are centred around τ=24h, and are indiscernible across genotypes (**Figure 42E**). In older 21wk mice, the pattern of food-intake in L5-cKOs appears less-prominent yet maintains some diurnality (**Figure 42C**). This is indinated by the red arrow in **Figure 42G**, where the expected period distribution is centred at τ=24h for both genotypes yet is of lower amplitude in L5-cKOs. As suggested following the second pilot (**Figure 40**), this subtle shift in feeding behaviour periodicities in L5-cKO mice may be conceivably due to deteriorating fine motor skills which are required to reach for food. Therefore, I proceeded to conduct and analyse targeted and systematic characterisations of related motor functions (**5.1.2-5.1.5**).

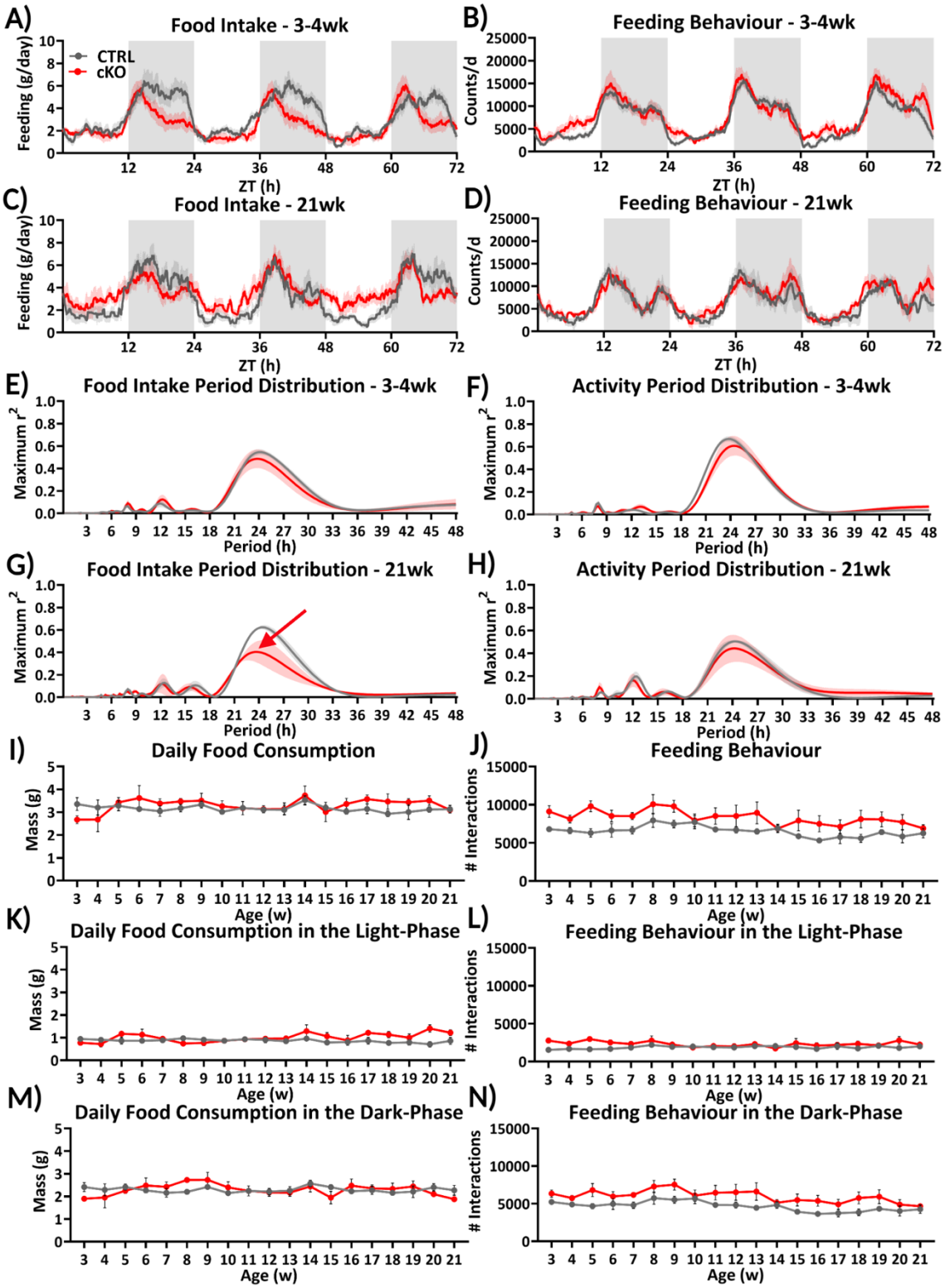


**Figure 42.** STAMINA *SnackerTracker* results. A,C) Food intake and B,D) feeding behaviour in L5-cKO vs CTRL mice are shown for A-B) 3-4wk and C-D) 21wk mice, with period decompositions in E-H) respectively. The red arrow in G) indicates a decreased amplitude around τ=24 in L5-cKO mice. Daily totals over time are shown for I) food intake in the K) light-phase and M) dark-phase, and J) feeding behaviour in the L) light-phase and N) dark-phase. See **A.9.4** for sex-disaggregated plots, and **Table 10**-**Table 11** and **A.2** for replicate and statistical details. ZT=Zeitgeber time.

### *5.1.2 Continuous assessment of motor phenotypes*

CAMP scoring[273] revealed the progressive emergence of significant motor deficits in L5-cKO mice over time. Note that, while I assigned unblinded CAMP scores to each mouse each week throughout STAMINA, blinded analyses of de-identified videos were conducted by another researcher several months later (**2.4.3**). CAMP trajectories and derived conclusions were identical in unblinded vs blinded analyses; the results of blinded analyses are shown in **Figure 43** and disseminated by sex in **A.9.5**. No genotype differences in CAMP scores emerged at the earliest 4wk timepoint, yet L5-cKO scores thereafter declined substantially (genotype: $F_{(1,26)}$= 305.2, p<0.0001; genotype×age: $F_{(18,200)}$=11.03, p<0.0001) (**Figure 43A**). The hindlimb clasp became increasingly prominent over time such that, by 21wks, L5-cKO mice became increasingly unable to extend their hindlimbs, often beginning subtly with one hindlimb or distal forelimb and hindlimb digits (genotype: $F_{(1,26)}$=228.6, p<0.0001; genotype×age: $F_{(18,200)}$=10.14, p<0.0001) (**Figure 43B**; particularly note the more subtle clasp in an 8-wk L5-cKO mouse compared to the pronounced clasp in a 21wk L5-cKO mouse in **Figure 43BIii** vs **Figure 43BIIii**). The ledge-walk revealed that L5-cKO mice became progressively unable to balance and walk along a narrow surface, which indicated deterioration in motor performance earlier and more prominently than the hindlimb clasp (genotype: $F_{(1,26)}$=178.8, p<0.0001; genotype×age: $F_{(18,200)}$=3.684, p<0.0001) (**Figure 43C**). Only some kyphosis was observed in L5-cKOs, though subtle differences may not have been documented due to my lack of knowledge and experience in identifying kyphotic posture (genotype: $F_{(1,26)}$=12.53, p=0.0015; genotype×age: $F_{(18,200)}$= 2.631, p=0.0005). Gait appeared slower and more unsteady in cKOs compared to CTRLs simply as observed in the home cage (genotype: $F_{(1,26)}$= 22.02, p<0.0001; genotype×age: $F_{(18,200)}$=1.588, p=0.0658). More nuanced differences in stride pattern, speed, and cadence appeared to emerge which could not be fully captured by scores of 0-3, therefore I relied on more sophisticated means of assessment for quantitative gait analyses (**5.1.5**).

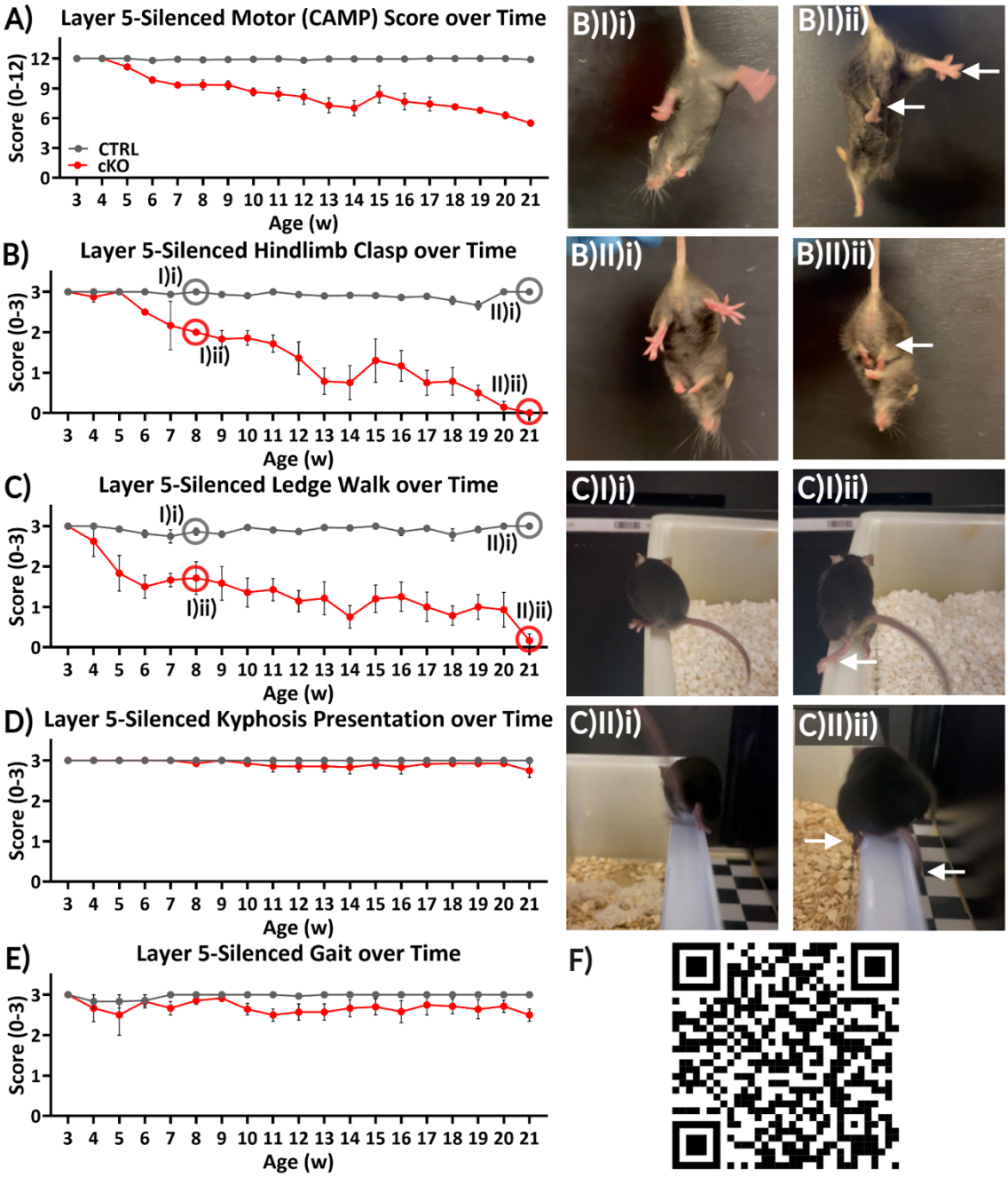


**Figure 43.** STAMINA CAMP results reveal motor deterioration in L5-cKO mice. **A)** Total CAMP scores encompass motor-associated assessments of B) the hindlimb clasp, C) the ledge-walk, D) kyphosis, and E) gait. I show representative images of i) CTRL and ii) L5-cKO mice at I) 8wks and II) 21wks for the B) hindlimb clasp and C) ledge-walk. Signs of motor deficits are indicated by white arrows, and corresponding videos can be viewed using the F) QR code provided[437]. Data are separated by sex in **A.9.5.** See **Table 10**-**Table 11** and **A.2** for replicate and statistical details.

### *5.1.3 Visual cliff test*

I conducted the VCT to test whether conceivable genotype differences emerged due to vision decline. RBP4 is a retinol binding protein responsible for transporting vitamin A (retinol)

to the eye, which may be critically disrupted if Cre is postnatally expressed off-target[438, 439]. I did not expect but nevertheless crudely tested for the possibility of vision deficits, assuming that increased time spent in the drop-zone (associated with risk or danger) or proportional flat/drop-zone time differing between L5-cKOs and CTRLs may indicate visual impairment. Admittedly, this same trend could present if L5-cKO mice were less risk-averse, which I would have followed-up upon if considerable genotype differences emerged. However, results shown in **Figure 44** (and separated by sex in **A.9.6**) reveal that L5-cKO mice only appear more prone to enter the edge-zone (genotype: $F_{(1,203)}=16.63$, $p<0.0001$; genotype×age: $F_{(18,203)}=0.8984$, $p=0.5812$) (**Figure 44D**); VCT outputs otherwise resemble CTRLs across time in the drop-zone (genotype: $F_{(1,203)}=0.6158$, $p=0.4335$; genotype×age: $F_{(18,203)}=0.7233$, $p=0.7850$) (**Figure 44A**), the flat-zone (genotype: $F_{(1,203)}=0.3340$, $p=0.5582$; genotype×age: $F_{(18,203)}=0.7498$, $p=0.7563$) (**Figure 44B**), and at the edge (genotype: $F_{(1,203)}=0.8016$, $p=0.3717$; genotype×age: $F_{(18,203)}=0.3737$, $p=0.9911$) (**Figure 44C**). The pattern of increased time in the drop-zone with age appears consistent across genotypes. Together with the fact that both CTRL and L5-cKO mice appeared responsive to light, handling, and *SnackerTrackers* upon food-holder refills, VCT results suggest that no obvious and severe vision deficits emerged.

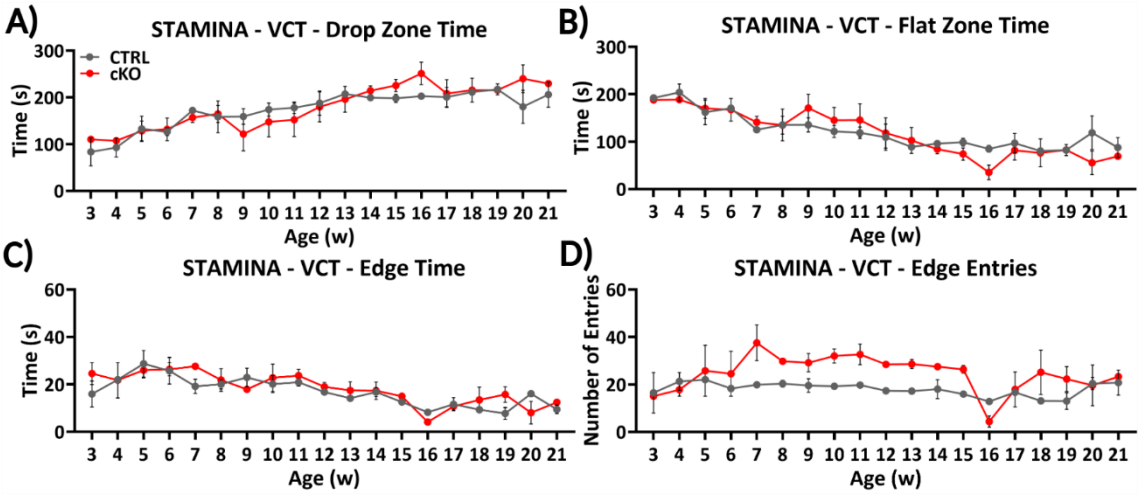


**Figure 44.** Summarises STAMINA VCT results. No obvious differences between L5-cKO and CTRL mice emerge in time spent in the A) drop-zone, B) flat-zone, or C) edge-zone, although L5-cKO mice appear to exhibit D) a greater number of edge entries. **See A.9.6 f**or sex-disaggregated plots, then **Table 10**-**Table 11** and **A.2** for replicate and statistical details.

### *5.1.4 Grip strength and nesting*

Grip testing similarly revealed that L5-cKO mice exhibit progressively decreased strength compared to CTRLs (**Figure 45**, **A.9.7**). CTRLs and L5-cKO mice performed similarly at younger ages (i.e., <10wks), and both showed increased grip strengths over time as expected of growing mice; however, the degree to which L5-cKOs improved was less than that of CTRLs (genotype: $F_{(1,22)}$=16.02, p=0.0006; genotype×age: $F_{(18,184)}$=0.7233, p=2.498) (**Figure 45A**). Results show that, overall, L5-cKO mice exhibit poor nesting-behaviour compared to CTRLs (genotype: $F_{(1,26)}$=148.6, p<0.0001; genotype×age: $F_{(18,191)}$=2.505, p=0.0011) (**Figure 45B**). Sample nest images are provided, where those corresponding to lower scores of 0-2 and higher scores of 3-4 are from L5-cKO and CTRL nests, respectively. This suggests that L5-cKO mice lack the fine motor skills needed to build more complex nests, which together with higher activity and distributed feeding patterns (**Figure 42**) may importantly confound previous reports of sleep disturbance[114].

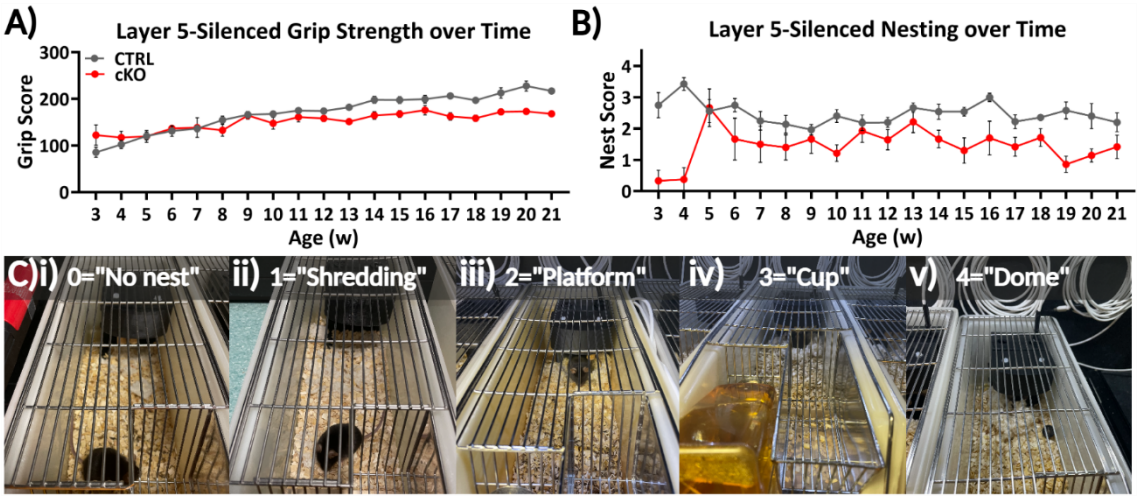


**Figure 45.** STAMINA results following grip strength and nesting tests. A) While initially indiscernible, L5-cKO mice exhibit weaker grip strength compared to CTRL mice over time. B) L5-cKO mice exhibit consistently poor nesting behaviour. See **A.9.7** for sex-disaggregated data, then **Table 10**-**Table 11** and **A.2** for replicate and statistical details.

### *5.1.5 CatWalk*

CatWalk tests enabled detailed examination of L5-cKO vs CTRL mouse gait, elaborating upon CAMP observations (**5.1.2**). Indeed, L5-cKO mice progressively exhibit gait deterioration

across several distinct yet complimentary outputs (**Figure 46**, **A.9.8**). Speed decreases over time where, although initially equivalent CTRLs, L5-cKO mice become relatively slower (genotype: $F_{(1,210)}$=278.6, p<0.0001; genotype×age: $F_{(18,210)}$=3.009, p<0.0001) (**Figure 46A**). Gait cadence–the frequency of steps taken traversing the CatWalk platform–also decreases in L5-cKOs (genotype: $F_{(1,210)}$=152.5, p<0.0001; genotype×age: $F_{(18,210)}$=0.4103, p=0.9848) (**Figure 46B**) which is not unexpected given that speed decreases. However, cadence differs notably across genotypes even at the youngest timepoints before differences in speed emerge. That is, before 6wks (see **A.2** for *post hoc* statistics), L5-cKO mice require fewer steps to traverse the same distance and may initially adopt longer strides to compensate for an early inability to move limbs at a higher frequency. Further subtle differences emerge as, at ~6wks, the step pattern of L5-cKO mice shifts to favour alternate (genotype: $F_{(1,210)}$=144.3, p<0.0001; genotype×age: $F_{(18,210)}$=1.011, p=0.4490) over cruciate step sequences (genotype: $F_{(1,210)}$=159.6, p<0.0001; genotype×age: $F_{(18,210)}$=0.9065, p=0.5713) (**Figure 46C-I,K**). Similarly, after ~6wks, a greater percentage of L5-cKO strides are taken with a three-paw base of support (genotype: $F_{(1,210)}$=58.20, p<0.0001; genotype×age: $F_{(18,210)}$=0.7926, p=0.7079) corresponding to decreased single-paw strides (genotype: $F_{(1,213)}$=31.91, p<0.0001; genotype×age: $F_{(18,213)}$=0.6730, p=0.8357) (**Figure 46L-M**). The alternate sequence is typically considered a more stable step pattern typical in healthy mice[275, 294] yet, combined with decreased speed and increased three-paw support over time, suggests that L5-cKO mice may gradually adopt a more cautious stereotypical gait strategy to mitigate increasing hindlimb rigidity and instability over time (i.e., as indicated by CAMP hindlimb-clasping and ledge-walking, **5.1.2**). Images of sample CatWalk runs are shown in **Figure 46N-Q** (I link corresponding videos in **Figure 46J**) where genotype differences are subtle at younger ages and more profound at older ages. Together, behavioural tests strongly indicate the progressive emergence of motor deficits in L5-cKO mice, prompting further functional and anatomical dissection of conceivable underlying networks (**5.2**-**5.3**).

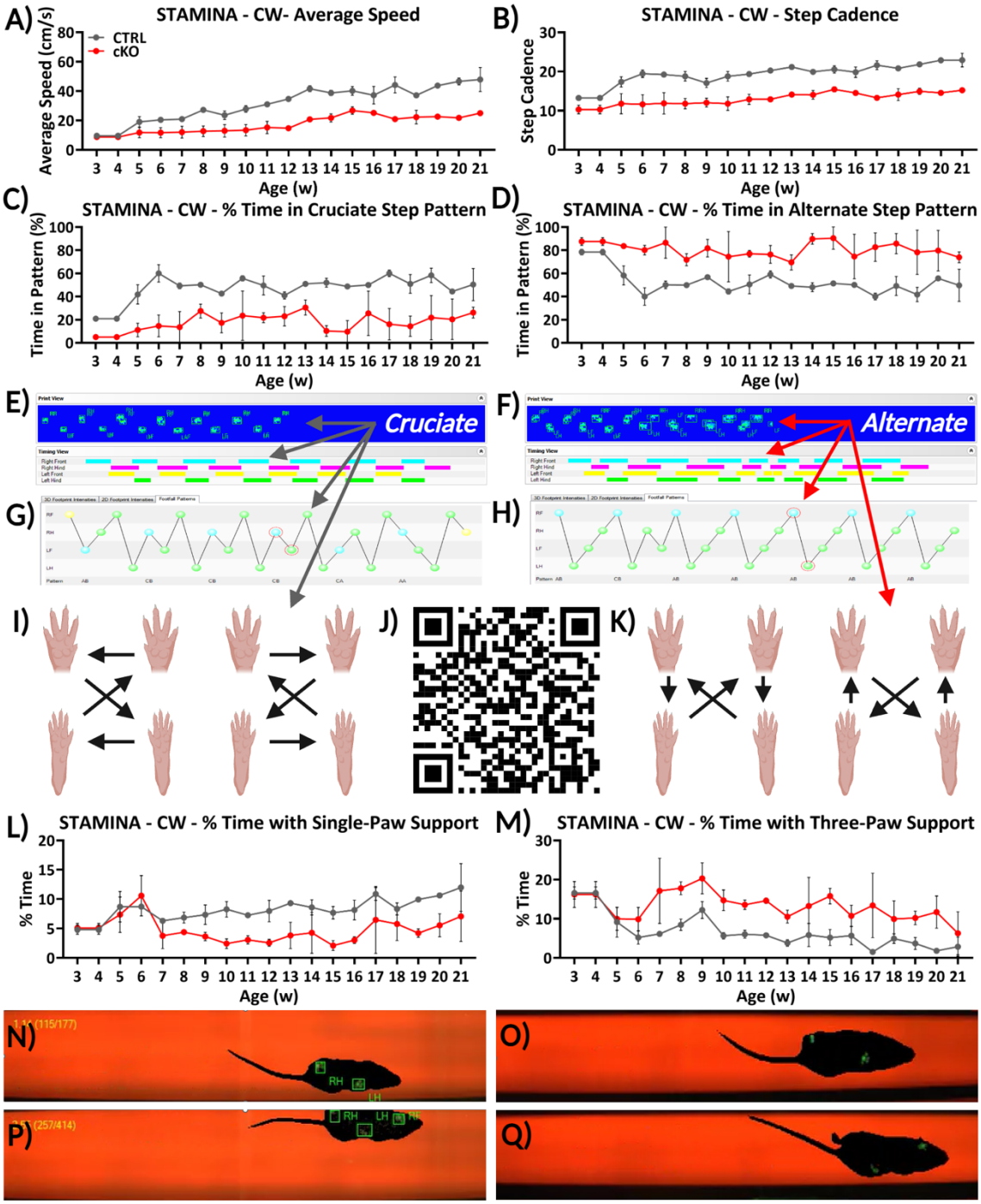


**Figure 46.** STAMINA CatWalk gait evaluations reveal motor deficits in L5-cKO mice. Summary metrics comparing L5-cKO vs CTRL gait features include A) average speed, B) step cadence, C) time in the cruciate step pattern, D) time in the alternate step pattern, L) time with single-paw support, and M) time spent with three-paw support. I illustrate E,G,I) cruciate and F,H,K) alternate step sequences, where a greater percentage of CTRL and L5-cKO strides are of the cruciate and alternate patterns, respectively. Images of representative CatWalk runs are shown for N) 8wk CTRL, O) 21wk CTRL, P) 8wk L5-cKO, and Q) 21wk L5-cKO mice. J) I provide corresponding videos via the QR code[437]. See **A.9.8** for sex-disaggregated data, then **Table 10**-**Table 11** and **A.2** for replicate and statistical details.

## 5.2 MRI

### *5.2.1 In vivo T1W anatomical scans*

Throughout STAMINA (**1.5.5**, **Figure 4**), I acquired repeated *in vivo* MRI scans from L5-cKO and CTRL mice across three timepoints–4-7wks, 11-14wks, and 18-21wks–to determine whether neuroimaging could detect predicted motor-related neurodegeneration in cortical and subcortical regions (**Figure 2**). If so, this could provide longitudinal insight into conceivable spatiotemporal patterns of deterioration. I will first describe results of T1W anatomical analyses, then *in vivo* DTI and fMRI in **5.2.2**., and finally *ex vivo* T2W, DTI, and QSM in **5.2.3**-**5.2.5**. As shown in **Figure 47**, *in vivo* T1W imaging quality-control checks confirmed that the bed nucleus of the stria terminalis is smaller in females compared to males (which is expected, and a common readout for overall scan fidelity, **Figure 47A**). More notably, L5-cKO mice exhibit smaller overall brain volumes (**Figure 47B**) which is not surprising given lower body weights (**Figure 41**). Brain maps in **Figure 47C** overlaid with t-statistics represent the difference between L5-cKO relative to CTRL volumes; I centred analyses at 21wks both to extract information at the age where I expected the largest genotype differences, and to enable more direct comparisons to *ex vivo* findings. T1W maps show regional decreases across nearly all areas, yet to various extents throughout the brain. In the hippocampus and amygdala, volumetric increases emerge, which is unexpected considering smaller whole-brain volumes. **Figure 47D** shows the same brain maps yet overlaid with t-statistics representing effects following total brain volume covariance. I show p-values in **Figure 47E**, and FDR-adjusted q-values in **Figure 47F**, to illustrate convergence of statistical significance after covariance (**Figure 47C**). I highlight this distinction as, in upcoming plots, I show regional and voxelwise maps with statistical representations of combinations of genotype, age, and sex differences as p-values. I provide maps with t-statistics and FDR-adjusted q-values, accompanied by regional graphs in **A.2** if not in the main text, then additional statistical tables and replicate values in **A.10.19** and **Table 10** respectively.

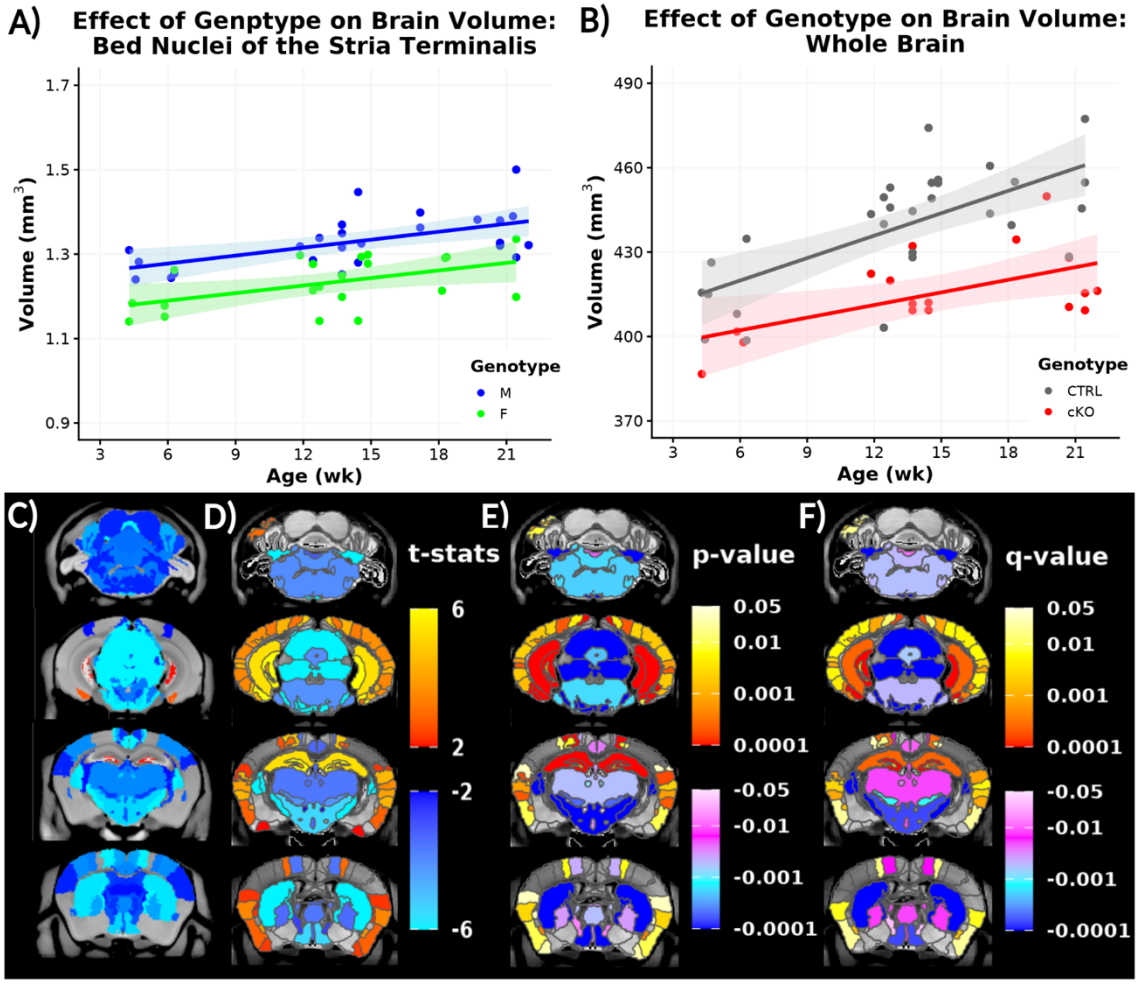


**Figure 47.** T1W *in vivo* MRI overview. Illustrates decreased total brain volumes in L5-cKO mice. A) volumes in the bed nucleus of the stria terminalis are consistently smaller in females; anything else would suggest poor scan quality. B) Decreases in L5-cKO vs CTRL brain volumes emerge over time. C-F) Heat maps show blue-purple=decreased or red-yellow=increased volumes in cKOs relative to CTRLs. C) T-statistic maps represent mostly decreasing volumetric changes before and D) after total brain volume covariance, then E) as p-values and F) as q-values following FDR-correction. I predominantly employ p-value brain maps in upcoming figures, with t-statistic and q-value equivalents in **A.2**. See **Table 10** and **A.2** further for replicate and statistical details.

With covariance, regional and voxelwise analyses reveal volumetric differences across genotypes at 21wk (**Figure 48**). Regional maps show that descending motor-related pathways through which L5 axons traverse exhibit volumetric reductions ( **Figure 48A,B,D,E**) in M1, CST, internal capsule, cerebral peduncles, medial lemniscus, thalamus, motor-associated nuclei, pallidum, pontine reticular nuclei, rubrospinal tract, fastigial nuclei, and interposed and dentate nuclei (**Figure 49**). While regional maps enable ROI analyses, voxelwise plots better-represent raw data which may otherwise appear obsolete if diluted by averaging across atlas-defined

regions. Further, the Dorr-Steadman-Ullman atlas (**2.5.5.4**) does not distinguish cortical layers or HOTN from FOTN. **Figure 48C,F** shows that, while some differences in the thalamus are indicated regionally, voxelwise maps show that differences converge in HOTN—nuclei to which *Rbp4*-Cre corticothalamic axons are known to selectively project (**1.3.1**)[77, 120, 144, 145].

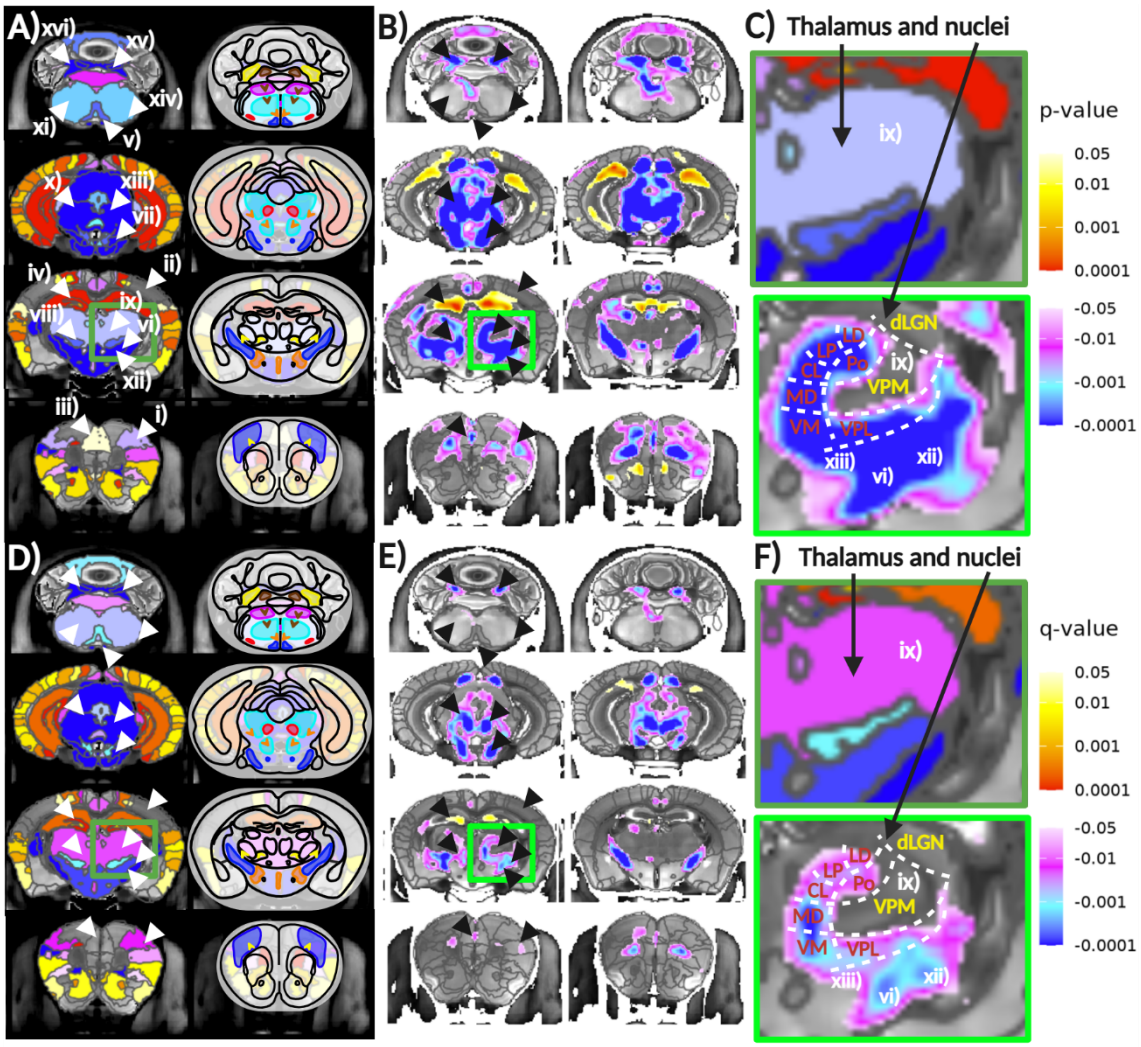


**Figure 48.** T1W *in vivo* MRI maps. Volumetric differences emerge across ROIs upon L5-cKO. A-C) P-values and D-F) q-values represent increases (yellow-red) and decreases (purple-blue) due to genotype at 21wks. I overlay A,D) sketches from **Figure 2** to reference motor-related ROIs: M1; ii) S1; iii) PFC; iv) dentate gyrus; v) CST; vi) internal capsule; vii) cerebral peduncles; viii) medial lemniscus; ix) thalamus; x) midbrain and xi) medullar motor-related nuclei; xii) pallidum; xiii) pontine reticular nuclei; xiv) rubrospinal tract; xv) fastigial nuclei; and xvi) interposed and dentate nuclei. Arrows indicate these ROIs in B,D,E). I analysed images A,D) regionally and B,E) voxelwise, where C,F) voxelwise data studies ROIs lacking atlas definition: dLGN=dorsolateral geniculate; VPM=ventral posteromedial; Po=posterior; LD=lateral dorsal; LP=lateral posterior; CL=centrolateral; MD=mediodorsal; VM=ventromedial; and VPL=ventral posterolateral. FOTN=yellow, HOTN=red. See **Table 10** and **A.2** for replicate and statistical details.

Where **Figure 48** illustrates effects due to genotype at 21wks–where behavioural phenotypes emerge most prominently–**Figure 49** reveals age-related trends both via regional maps of interpolated effects at 4wks, 12wks, and 21wks (**Figure 49A**), and via graphs detailing measurements in pre-selected motor-related ROIs over time (**Figure 49B**). Graphs are useful to visualise effects related to **Figure 48**, **Figure 49A**, and genotype×age effects for comparison to behavioural trends (**5.1**, **5.4**). **Figure 49B** shows that, indeed, genotype×age differences emerge in M1, S1, and PFC where L5-cKO volumes decline over time (**Figure 49i-iii**) while in the CST (including the internal capsule and cerebral peduncles) L5-cKO volumes fail to increase to the same extent as CTRLs (**Figure 49Bv-vii**). This indicates selective volumetric decline in the tracts traversed and regions targeted by *Rbp4*-Cre$^{+}$ axons. Downstream deterioration may be due to axon degeneration (previously indicated[77] and analysed in **5.3.1**) or activity-dependent effects, both of which I will discuss further (**5.4**-**5.5**). Yet, T1W data also indicates volumetric increases in regions of high *Rbp4*-Cre expression (e.g., throughout the cortex and hippocampus). I did not expect this, as I rather thought volumes may decrease with L5-degeneration[77]. However, increased volumes could conceivably result from compensatory neuroinflammatory responses (e.g., microglial or astrocytes infiltration which I explore in **5.3.4**), intracellular edema preceding apoptosis (considered in **5.2.4**), or extracellular edema (also considered in **5.2.4**). Interestingly, the only other region to increase in volume–even before total brain volume covariance–was the subventricular zone (**A.2**). The subventricular zone is a neural stem cell niche which persists through adulthood and can respond to damage by upregulating progenitor proliferation[440, 441]. In cases of motor degeneration, subventricular zone cells have been shown to differentiate into astrocytes rather than neurons, contributing to glial scar formation yet limiting functional neuron re-integration. Increased volumes in the hippocampus and some cortical ROIs emerged, yet could neither be resolved laminarly due to atlas limitations or voxelwise due to *in vivo* resolution limits. Higher-resolution *ex vivo* scans and histology then proceeded (**5.2.3**-**5.2.5**).

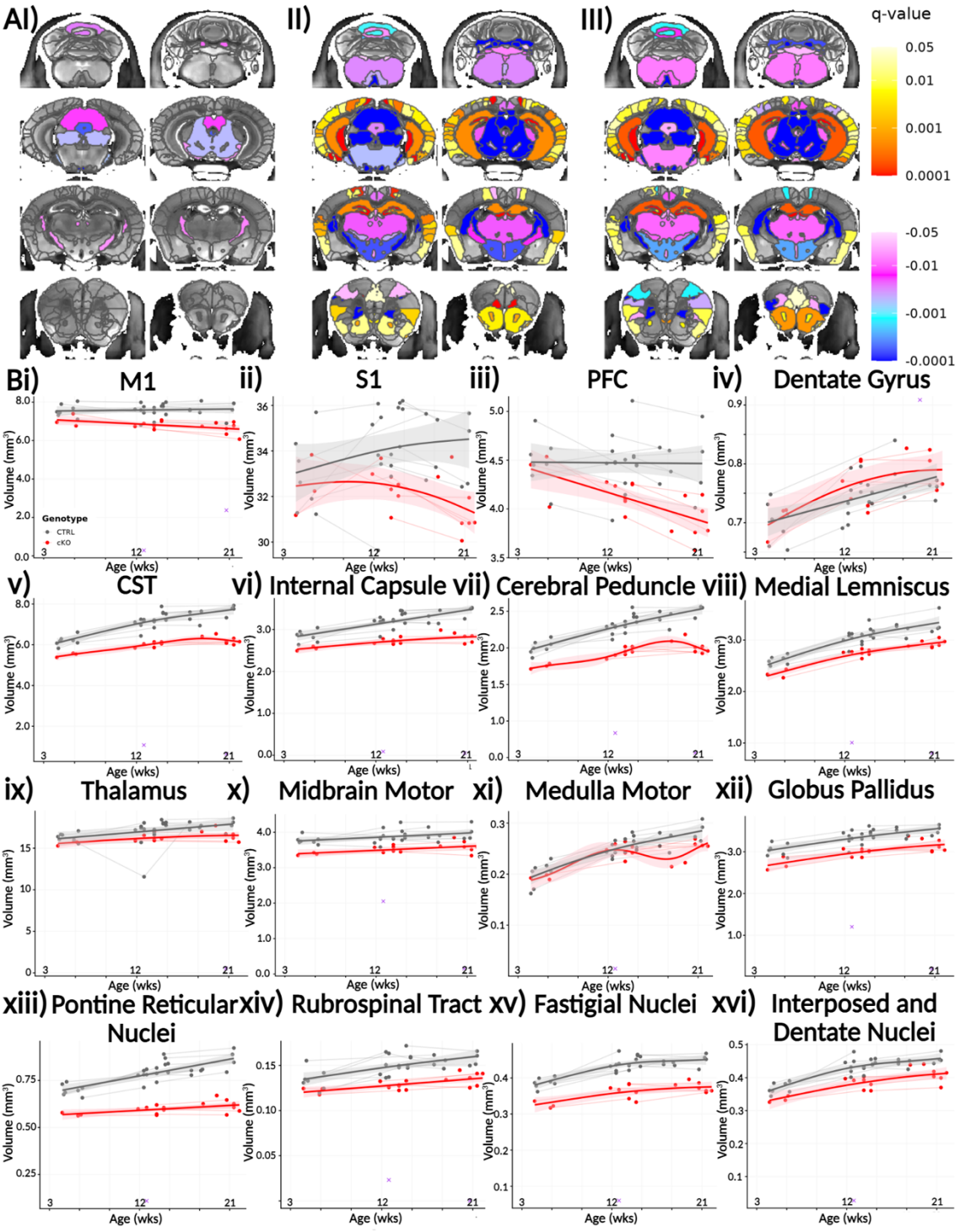


**Figure 49.** Volumetric ROI analysis following T1W *in vivo* MRI in L5-cKO vs CTRL mice. A) Illustrates interpolated volumetric differences at I) 4wks, II) 12wks, and III) 21wks. B) ROIs belonging to i-iv) cortical and hippocampal ROIs housing *Rbp4*-Cre$^{+}$ soma; v-viii) *Rbp4*-Cre$^{+}$ axon projection tracts (**5.3.1**); ix-xii) motor-related subcortical targets, and xiii-xvi) motor-related medullar and cerebellar targets correspond to those in **Figure 48**. Connected points represent data from the same mouse. See **Table 10** and **A.2** for replicate and statistical details.

### *5.2.2 In vivo DTI and resting state fMRI*

To briefly note before proceeding to *ex vivo* MRI results: I acquired *in vivo* DTI and resting-state fMRI scans yet have not fully analysed these due to time constraints. I describe planned future analyses in **5.5.3**, which broadly includes DWI (as in **5.2.4**) to inform the time-trajectory of differences which emerge *ex vivo* (albeit at lower resolution), diffusion tractography to test regional connectivity or lack thereof, and RABIES-based BOLD signal evaluation to evaluate conceivable changes in functional networks over time.

### *5.2.3 Ex vivo T2W anatomical scans*

Following perfusion-fixation, dissection, and solely in-skull sample preparation (**2.5.2.1**), higher-resolution *ex vivo* MRI scans (75$\mu m^3$/vx) largely replicate *in vivo* findings (60$\mu m^3$/vx) centred at 21wks (**Figure 50**). Similar patterns of volumetric changes emerge, yet to less-significant extents; FDR corrections render nearly all voxels sub-threshold (**Figure 50A-B,D-E**). Despite attempts to achieve volumetric laminar discrimination by averaging 2×T2W 3D fast-spin-echo acquisitions, *ex vivo* voxelwise maps did not reveal layer-specific changes, if existent, across coronal, horizontal, or sagittal planes (**Figure 50B,E,G**). Voxelwise horizontal and sagittal maps further indicate decreased volumes in motor trigeminal nuclei (**Figure 50G**) which I analyse accordingly in **5.3.2**. *Ex vivo* thalamic dissections resemble *in vivo* observations where volumetric decreases appear highly localised to HOTN yet are diluted when averaged across the atlas-defined thalamus (**Figure 50C,F**) [302, 318-321]. Analyses over time are considerably underpowered due to a limited $N_E$ at younger ages (none currently <8wks). Nevertheless, age-related trends and regional graphs are illustrated in **Figure 51**, and ill-powered statistical reports throughout **A.2**. Incorporating additional replicate data from 4-7wk brains remains an active future direction (see **5.5.3**).

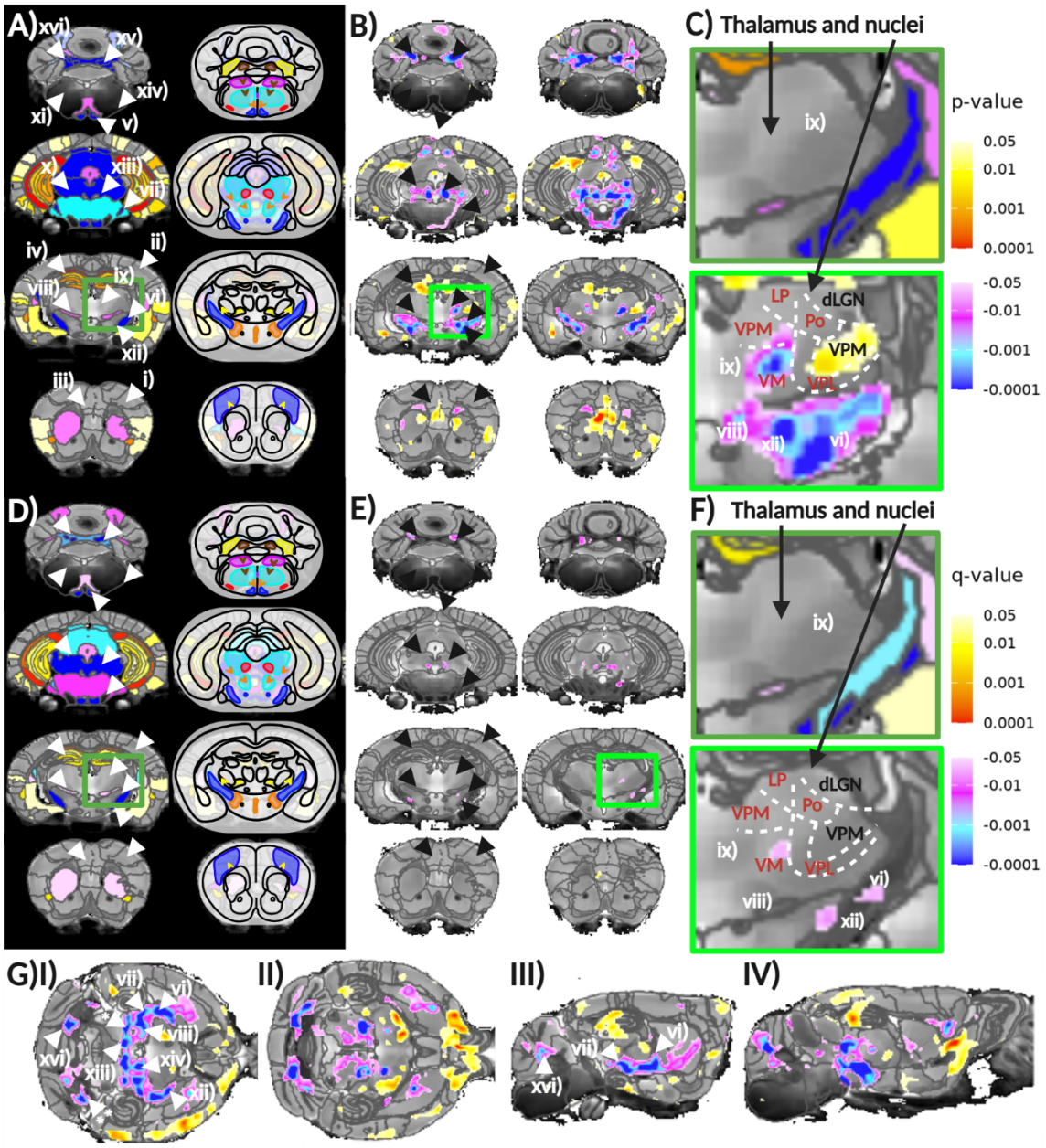


**Figure 50.** T2W *ex vivo* MRI reveals volumetric differences upon L5-cKO. These resemble *in vivo* results (**Figure 48**), yet are comparatively tapered and more clearly confined to motor-related ROIs. Heat maps of A-C,G) p-values and D-F) q-values represent volumetric increases (yellow-red) and decreases (purple-blue) due to genotype at 21wks across A,D) regional and B,E,G) voxelwise analyses. A,D) Overlaid sketches from **Figure 2** reference ROIs corresponding to data in **Figure 51**: i) M1; ii) S1; iii) PFC; iv) hippocampal dentate gyrus; v) CST; vi) internal capsule; vii) cerebral peduncles; viii) medial lemniscus; ix) thalamus; x) midbrain and xi) medullar motor-related nuclei; xii) globus pallidus; xiii) pontine reticular nuclei; xiv) rubrospinal tract; xv) fastigial nuclei; and xvi) interposed and dentate nuclei. G) Voxelwise I-II) horizontal and III-IV) sagittal maps illustrate localised patterns. *=motor trigeminal nucleus; **=cerebellar peduncles. C,F) Voxelwise data enable sub-regional evaluation of smaller areas (i.e., thalamic nuclei) which otherwise lack regional discrimination: dLGN=dorsolateral geniculate; Po=posterior; LP=lateral posterior; VPM=ventral posteromedial; VM=ventromedial; and VPL=ventral posterolateral. FOTN=black, HOTN=red. See **Table 10** and **A.2** for replicate and statistical details.

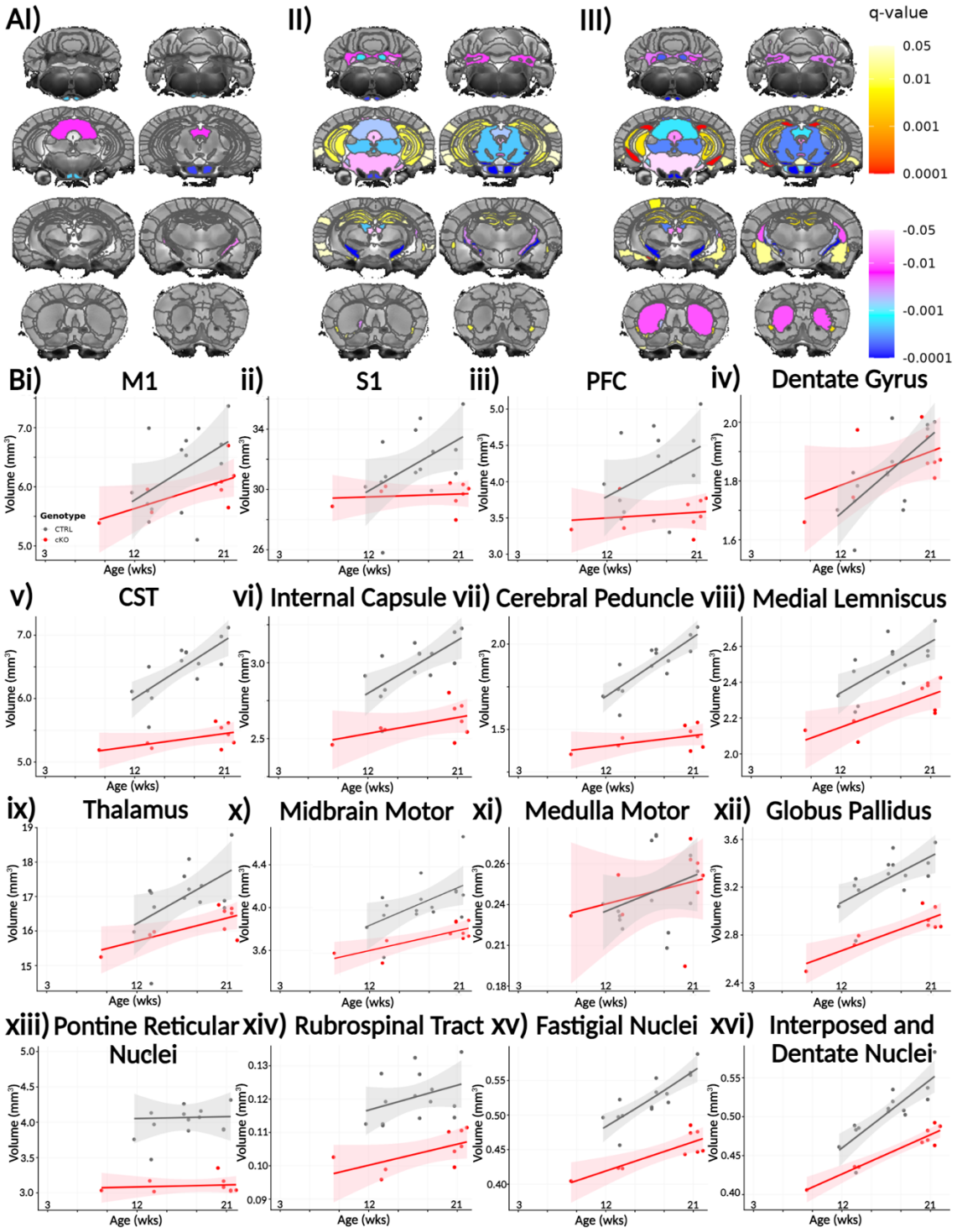


**Figure 51.** Volumetric ROI analysis following T2W *ex vivo* MRI in L5-cKO vs CTRL mice. A) Illustrates interpolated volumetric differences extrapolated at I) 4wks and interpolated at II) 12wks and III) 21wks. B) ROIs belonging to i-iv) cortical and hippocampal areas housing *Rbp4*-Cre$^{+}$ soma; v-viii) *Rbp4*-Cre$^{+}$ axon projection tracts (**5.3.1**); and ix-xvi) motor-related subcortical targets correspond to definitions in **Figure 48**. Note that, unlike **Figure 49**, points are not connected as *ex vivo* data are not repeated measures. See **Table 10** and **A.2** for replicate and statistical details.

Overall, similar trends towards decreased volumes emerge in L5-cKO mice across motor-related ROIs (the dentate gyrus remaining an exception). However, neither overall genotype nor genotype×age effects are statistically significant in cortical or hippocampal regions (**Figure 51Bi-iv**), while overall and interactive differences in white matter tracts clearly emerge and diverge over time (**Figure 51Bv-viii**). Other subcortical ROIs (**Figure 51Bix-xvi**) show the same pattern of consistently decreased L5-cKO volumes over time as indicated *in vivo* (**Figure 49Bix-xvi**). Having established overall regional effects of *Rbp4*-Cre-driven *Snap*25-cKO, *ex vivo* T2W anatomical scans provide a standard-space reference towards which more complex DWI (**5.2.4**) and QSM (**5.2.5**) data may be mapped.

### *5.2.4 Ex vivo DTI*

*Ex vivo* diffusion analyses encompass FA, MD, MK, OD, ICVF, and FISO metrics, each of which complimentarily inform tissue properties. FA describes the variance of eigenvalues ($\lambda_{1\text{-}3}$) representing water diffusion along each of three axes per voxel, where high variance indicates high diffusion directionality (e.g., in white matter tracts containing greater axon alignment relative to grey matter). I predicted that decreased FA would accompany axon degeneration in motor-related tracts upon L5-cKO[442]. Relatedly, MD denotes water diffusivity as the average of constituent eigenvalues, being typically consistent across white and grey matter regions. I expected values to increase with *Rbp4*-Cre$^{+}$ degeneration. MK–with eigenvector directionality according to eigenvalue diffusivity–is calculated as the ratio of diffusion variance to the square of mean diffusion such that higher MK indicates greater deviation from Gaussian signal decay. Normal decay is expected if voxels represent homogeneous areas of uniformly moving water. I hypothesised decreased MK in *Rbp4*-Cre$^{+}$ regions where, in the cortex where cytoarchitectural heterogeneity may prevent uniform water displacement, structural neurite barrier deterioration due to *Rbp4*-Cre$^{+}$ degeneration would intuitively result in decreased structural complexity and kurtosis. Distinctly, OD is derived from the NODDI model (**2.5.3.3**)[310] and defines the distribution

of neurite orientations within voxels as the degree of clustering about a mean orientation, thereby informing neurite dispersion rather than density. I expected increased OD in organised white matter tracts (OD=1 for perfectly orientated neurites), with decreases emerging upon *Rbp4*-Cre+ axon degeneration (OD=0 for entirely random branching)[77]. NODDI mathematically compartmentalises water across imaged voxels as being 'trapped' within neurites or 'freely moving' extracellularly or in cerebrospinal fluid. The proportion deemed restricted within neurites, encompassing axons and dendrites, is measured by the ICVF (also known as the neurite density index) where high values indicate regions of dense white matter or neurite networks. The proportion deemed to exhibit free triaxial diffusion is indicated by FISO （also termed the isotropic volume fraction) which should be high in ventricular areas and low in neurite-restricted tissue. If detectable, I initially predicted that decreased ICVF and increased FISO may emerge in regions of *Rbp4*-Cre$^{+}$ neuron degeneration; however, locally increased ICVF could provide insight into whether *in vivo* T1W volumetric increases (**5.2.1**) may be due to neuroinflammation or edema. Together, diffusion analyses inform how tissue microstructure may change upon L5-cKO.

Results of L5-cKO vs CTRL *ex vivo* diffusion analyses across each metric are summarised regionally in **Figure 52** and voxelwise in **Figure 53**. Effects in the same selection of motor-related ROIs (**5.2.1**, **5.2.3**), age-related trends, and reduced-threshold t-statistic maps are provided in **Figure 54**-**Figure 59** for exploratory appraisal (FA=**Figure 54**, MD=**Figure 55**, MK=**Figure 56**, OD=**Figure 57**, ICVF=**Figure 58**, and FISO=**Figure 59**). Given the large number of brain regions and metrics analysed, the capacity for false-negatives following FDR corrections warrants underpowered exploratory speculation. No statistically significant differences emerged following FDR corrections, save decreased FA in the internal capsule and globus pallidus (**Figure 52BI**). However, voxelwise p-value (**Figure 53**) and t-statistic maps (**Figure 54**-**Figure 59B**) reveal prominent and consistent trends which were seldom indicated regionally. Critically, across voxelwise plots, laminar distinctions emerge which appear to be localised to areas of expected

*Rbp4*-Cre-expression (**Figure 53**, **Figure 54**-**Figure 59BII,IV**). Traces of increased FA in L5 appear in **Figure 54BII,IV**, yet no consistent regional or voxelwise trends emerge elsewhere over time (**Figure 52**-**Figure 53I, Figure 54A,C**). Minimal decreases in MD are regionally indicated in prefrontal areas (**Figure 52AII**), yet this is more prominent in **Figure 53II** and **Figure 55BII** where L5-localised sub-threshold effects extend rostrocaudally (**Figure 55BIV**). Increased MD emerges through the CSTover time (**Figure 55v,vi,xv**) while no genotype or age×genotype effects appear elsewhere (**Figure 52**-**Figure 53II, Figure 55A,C**). Similarly, increased MK appears in prefrontal areas of sub-threshold p-value and t-statistic voxelwise maps, yet effects do not extend throughout L5 (**Figure 53III**, **Figure 56BII,IV**). ROI analyses indicate no significant influence of genotype over time (**Figure 52**-**Figure 53III, Figure 56A,C**). While assumptions for modelling tissue compartments via NODDI[310] are not maintained in grey matter, voxelwise maps indicate subtly increased OD and ICVF throughout L5 (**Figure 57**-**Figure 58BII,IV**), particularly in the PFC and M1 (**Figure 52**-**Figure 53IV-V**, **Figure 57**-**Figure 58BII**). As with MK, no obvious region-specific differences in OD and ICVF emerged due to genotype (**Figure 57**-**Figure 58A,C**), nor did any differences in FISO across regional or voxelwise analyses (**Figure 52**-**Figure 53VI**, **Figure 59**).

Considered jointly, diffusion findings reveal distinct patterns across 1) areas of expected *Rbp4*-Cre$^{+}$ soma expression, 2) tracts through which *Rbp4*-Cre$^{+}$ axons project, and 3) motor-related subcortical targets. I was not originally optimistic that either *in vivo* or *ex vivo* isotropic resolutions of >75μm and >60μm, respectively, could resolve changes in L5 or specific thalamic nuclei. I reasoned that voxels were too large, and that the need to qualitatively rely on voxelwise maps due to limited atlas definitions would render such insight indiscernible. While this was the case in *ex vivo* T2W maps (**5.2.3**), *ex vivo* diffusion maps proved otherwise as voxelwise bands in L5 indicated decreases in MD (**Figure 55BII,IV**) and increases in MK (**Figure 56BII,IV**), OD (**Figure 57II,IV**), and ICVF (**Figure 58BII,IV**). This warrants follow-up investigation as to whether MRI can achieve laminar resolution and, with further development, cell-specific effects (**5.5.5**).

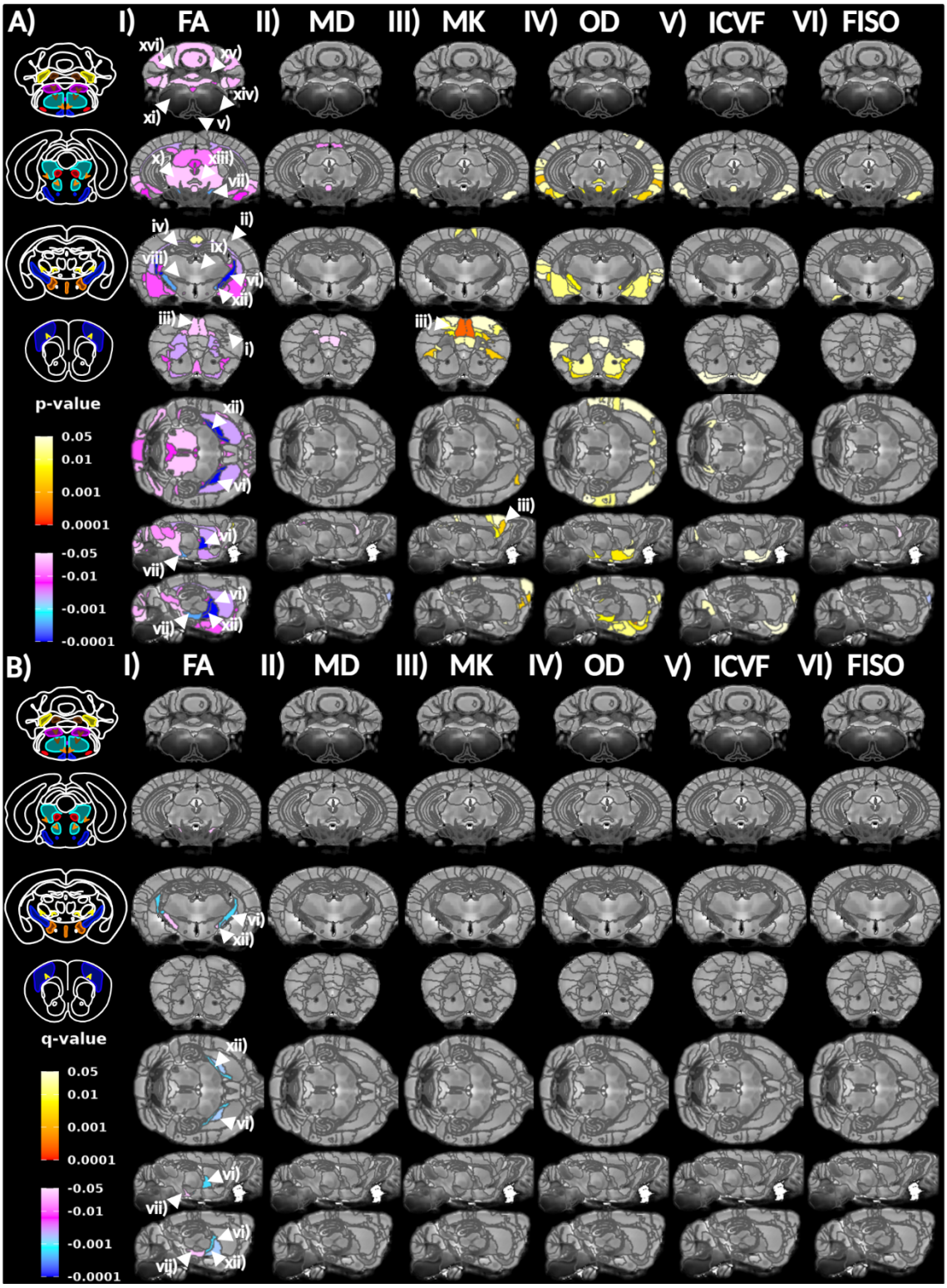


**Figure 52.** *Ex vivo* DWI regional analyses reveal brain-wide changes upon L5-cKO. Voxelwise equivalents are provided in **Figure 53**. A) p-value and B) q-value heat maps represent increases (yellow-red) and decreases (purple-blue) due to genotype at 21wks across I) FA; II) MD; III) MK; IV) OD; ICVF; and VI) FISO metrics. ROI-specific plots and features for each metric are elaborated upon in **Figure 54**-**Figure 59**, respectively. Sketches from **Figure 2** reference motor-related ROIs labelled i-xvi) as in **Figure 48**. See **Table 10** and **A.2** for replicate and statistical details.

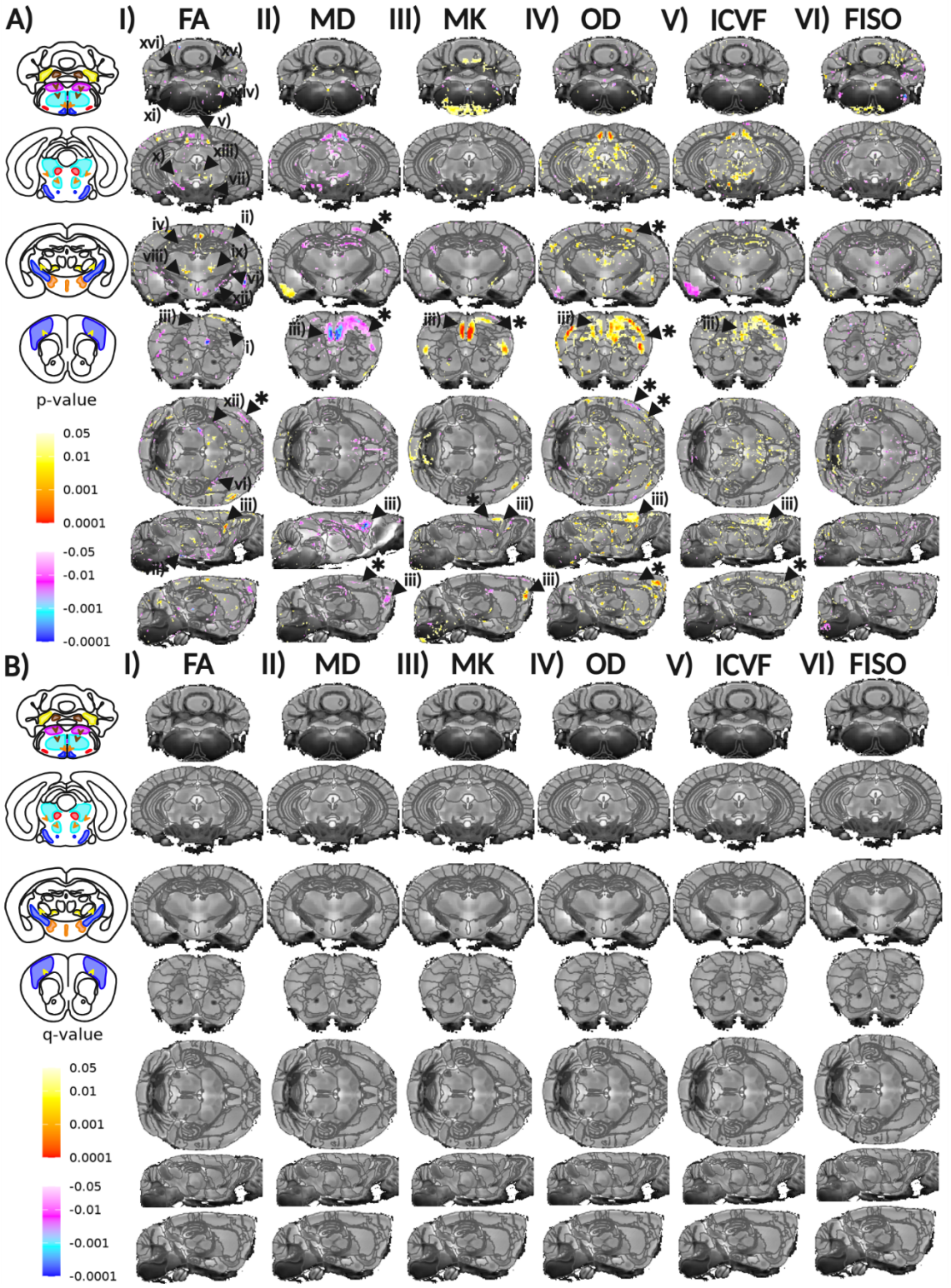


**Figure 53.** *Ex vivo* DWI voxelwise analyses. Reveals localised differences upon L5-cKO which are seldom captured regionally (**Figure 52**). A) p-value and B) q-value heat maps represent increases (yellow-red) and decreases (purple-blue) due to genotype at 21wks across I) FA; II) MD; III) MK; IV) OD; ICVF; and VI) FISO metrics. ROI-specific plots and features for each metric are elaborated upon in **Figure 54**-**Figure 59**, respectively, and sketches from **Figure 2** reference motor-related ROIs labelled i-xvi) as in **Figure 48**. *=L5-specific differences which only appear to emerge upon voxelwise dissemination. See **Table 10** and **A.2** for replicate and statistical details.

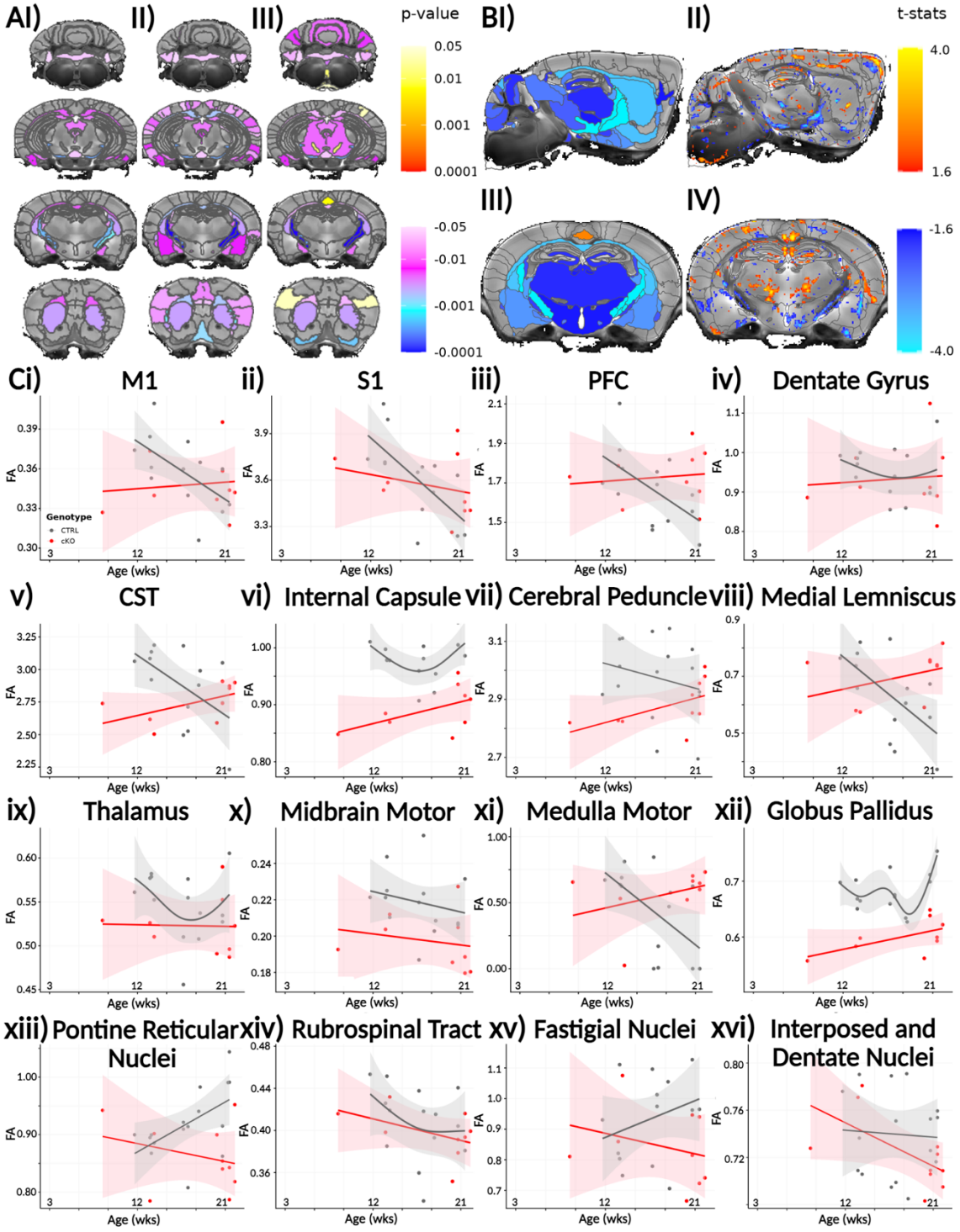


**Figure 54.** *Ex vivo* FA analyses. Reveals decreases in motor-associated tracts over time and voxelwise patterns suggesting increases in L5 upon L5-cKO. A) Illustrates regional differences in FA extrapolated at I) 4wks and interpolated at II) 12wks and III) 21wks. B) Sub-threshold t-statistic maps consider effects of L5-cKO across I,III) regional and II,IV) voxelwise I-II) sagittal and III-IV) coronal perspectives to highlight voxelwise insights (compare to **Figure 52**-**Figure 53I**). C) Analysis of ROIs belonging to i-iv) cortical and hippocampal areas housing *Rbp4*-Cre$^{+}$ soma; v-viii) *Rbp4*-Cre$^{+}$ axon projection tracts (**5.3.1**); and ix-xvi) motor-related subcortical targets (**Figure 48**). A-B) Statistical increases and decreases are indicated by yellow-red and blue-purple gradients, respectively. See **Table 10** and **A.2** for replicate and statistical details.

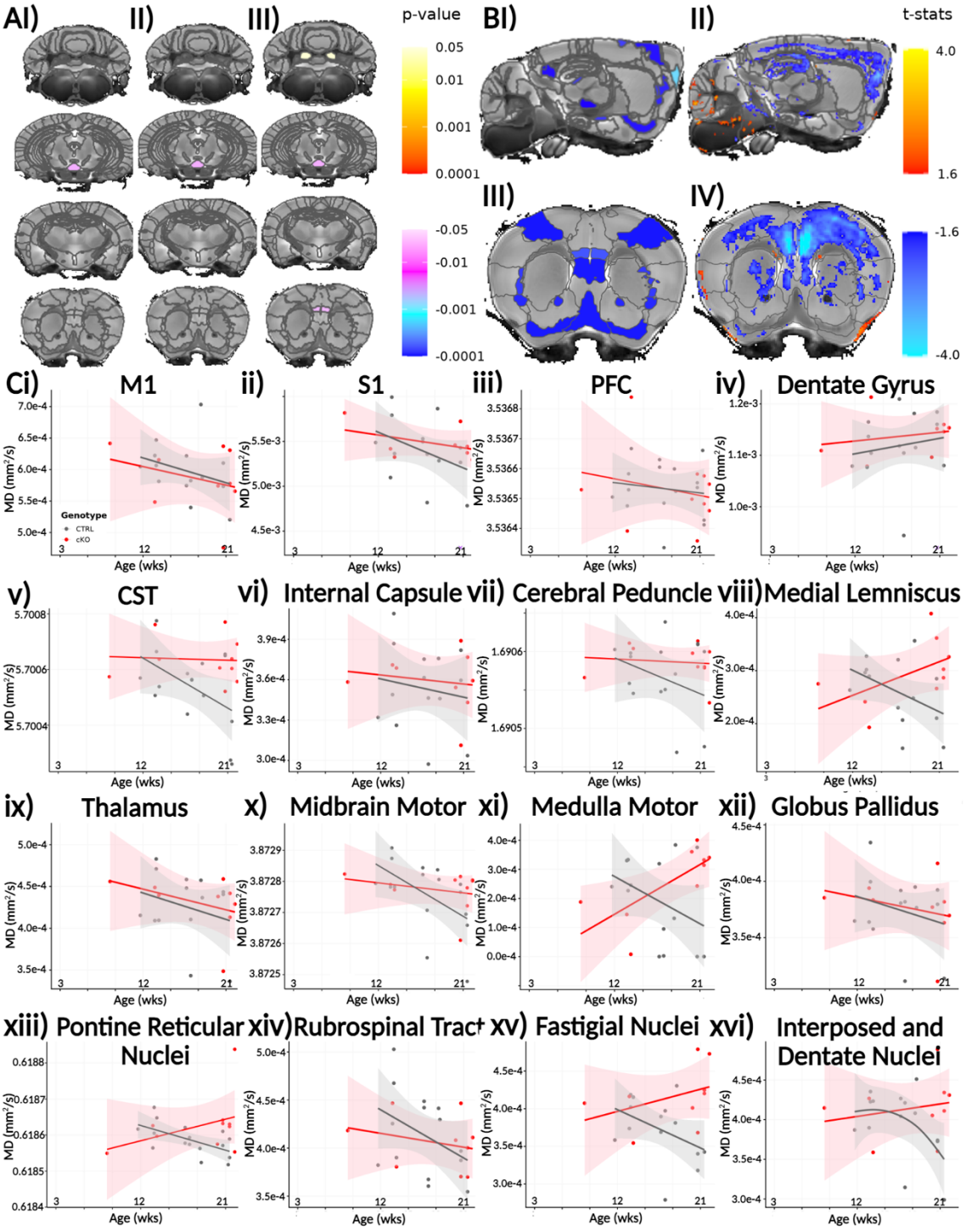


**Figure 55.** *Ex vivo* MD analyses. Reveals no regional differences in motor-associated areas over time, yet voxelwise patterns suggest decreases in L5 and PFC upon L5-cKO. A) Illustrates a lack of regional differences in MD extrapolated at I) 4wks and interpolated at II) 12wks and III) 21wks. B) Sub-threshold t-statistic maps compare effects of L5-cKO across I,III) regional and II,IV) voxelwise I-II) sagittal and III-IV) coronal maps to highlight voxelwise insights (compare to **Figure 52**-**Figure 53II**). C) Analysis of ROIs belonging to i-iv) cortical and hippocampal areas housing *Rbp4*-Cre$^{+}$ soma; v-viii) *Rbp4*-Cre$^{+}$ projection tracts (**5.3.1**); and ix-xvi) motor-related subcortical targets (**Figure 48**). A-B) Statistical increases and decreases are indicated by yellow-red and blue-purple gradients, respectively. See **Table 10** and **A.2** or replicate and statistical details.

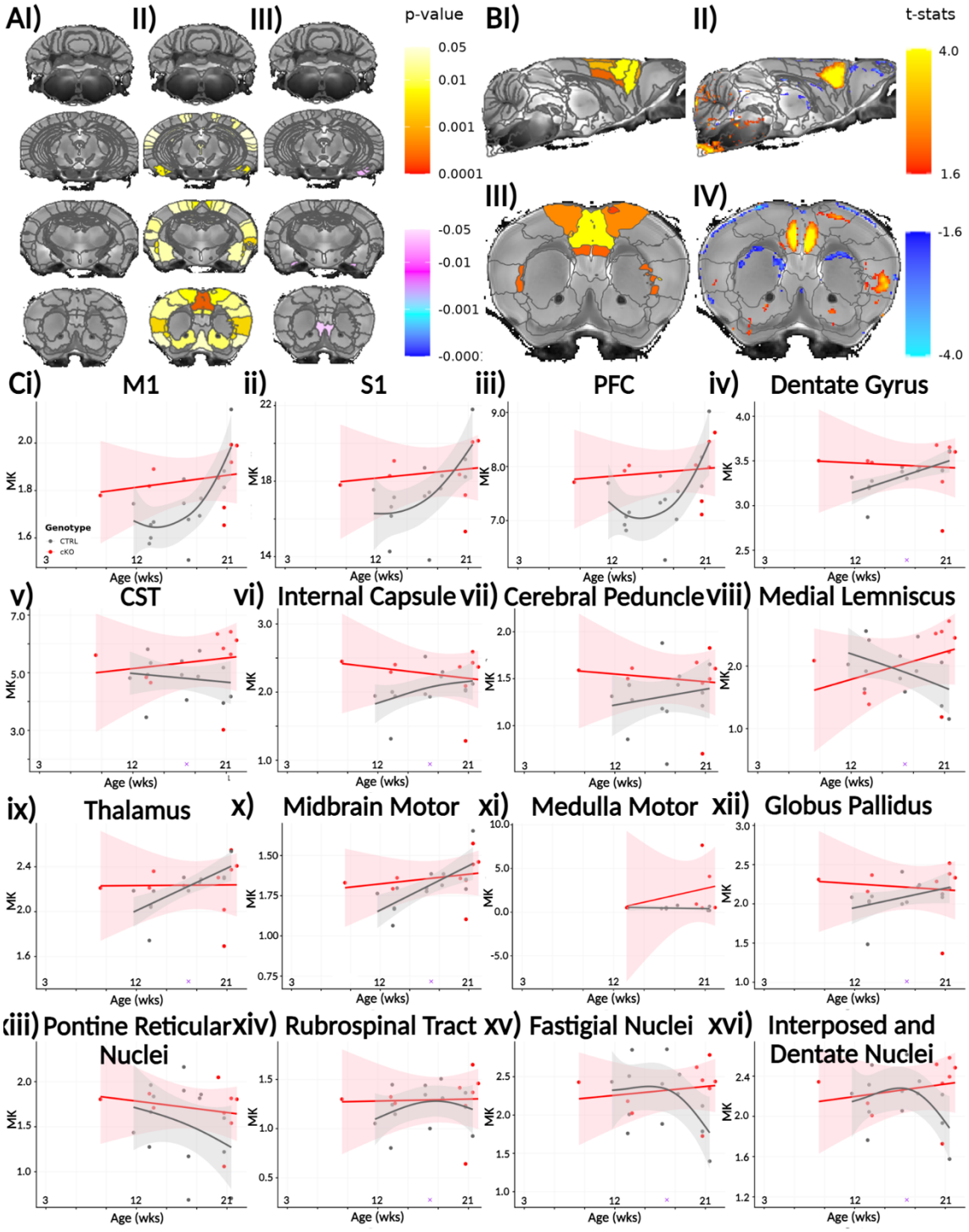


**Figure 56.** *Ex vivo* MK analyses. Reveals minimal regional differences in motor-associated areas over time, yet voxelwise patterns suggest increases in the PFC upon L5-cKO. A) Illustrates a lack of regional MK differences extrapolated at I) 4wks and interpolated at II) 12wks and III) 21wks. B) Sub-threshold t-statistic maps compare L5-cKO effects across I,III) regional and II,IV) voxelwise I-II) sagittal and III-IV) coronal maps to highlight voxelwise insights (compare to **Figure 52**-**Figure 53III**). C) Analyses of ROIs belonging to i-iv) cortical and hippocampal areas housing *Rbp4*-Cre$^{+}$ soma; v-viii) *Rbp4*-Cre$^{+}$ axon projection tracts (**5.3.1**); and ix-xvi) motor-related subcortical targets (**Figure 48**). A-B) Statistical increases and decreases are indicated by yellow-red and blue-purple gradients, respectively. See **Table 10** and **A.2** for replicate and statistical details.

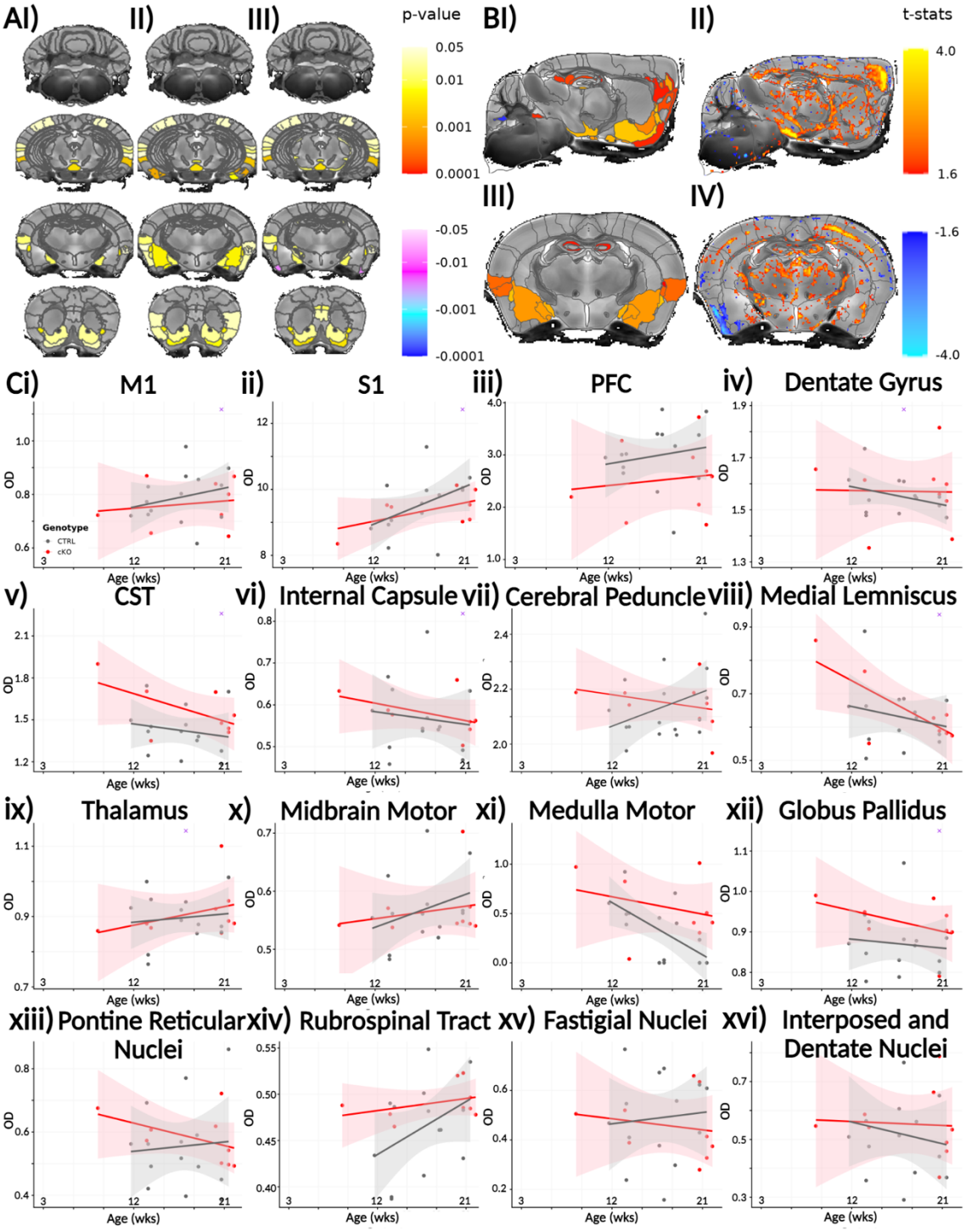


**Figure 57.** *Ex vivo* OD analyses. Reveals minimal regional differences in motor-associated areas over time, yet voxelwise patterns suggest increases in L5 and PFC upon L5-cKO. A) Illustrates a lack of regional change in OD extrapolated at I) 4wks and interpolated at II) 12wks and III) 21wks. B) Sub-threshold t-statistic maps compare L5-cKO effects across I,III) regional and II,IV) voxelwise I-II) sagittal and III-IV) coronal maps to highlight voxelwise insights (compare to **Figure 52**-**Figure 53IV**). C) Analyses in ROIs belonging to i-iv) cortical and hippocampal areas housing *Rbp4*-Cre$^{+}$ soma; v-viii) *Rbp4*-Cre$^{+}$ axon projection tracts (**5.3.1**); and ix-xvi) motor-related subcortical targets (**Figure 48**). A-B) Statistical increases and decreases are indicated by yellow-red and blue-purple gradients, respectively. See **Table 10** and **A.2** for replicate and statistical details.

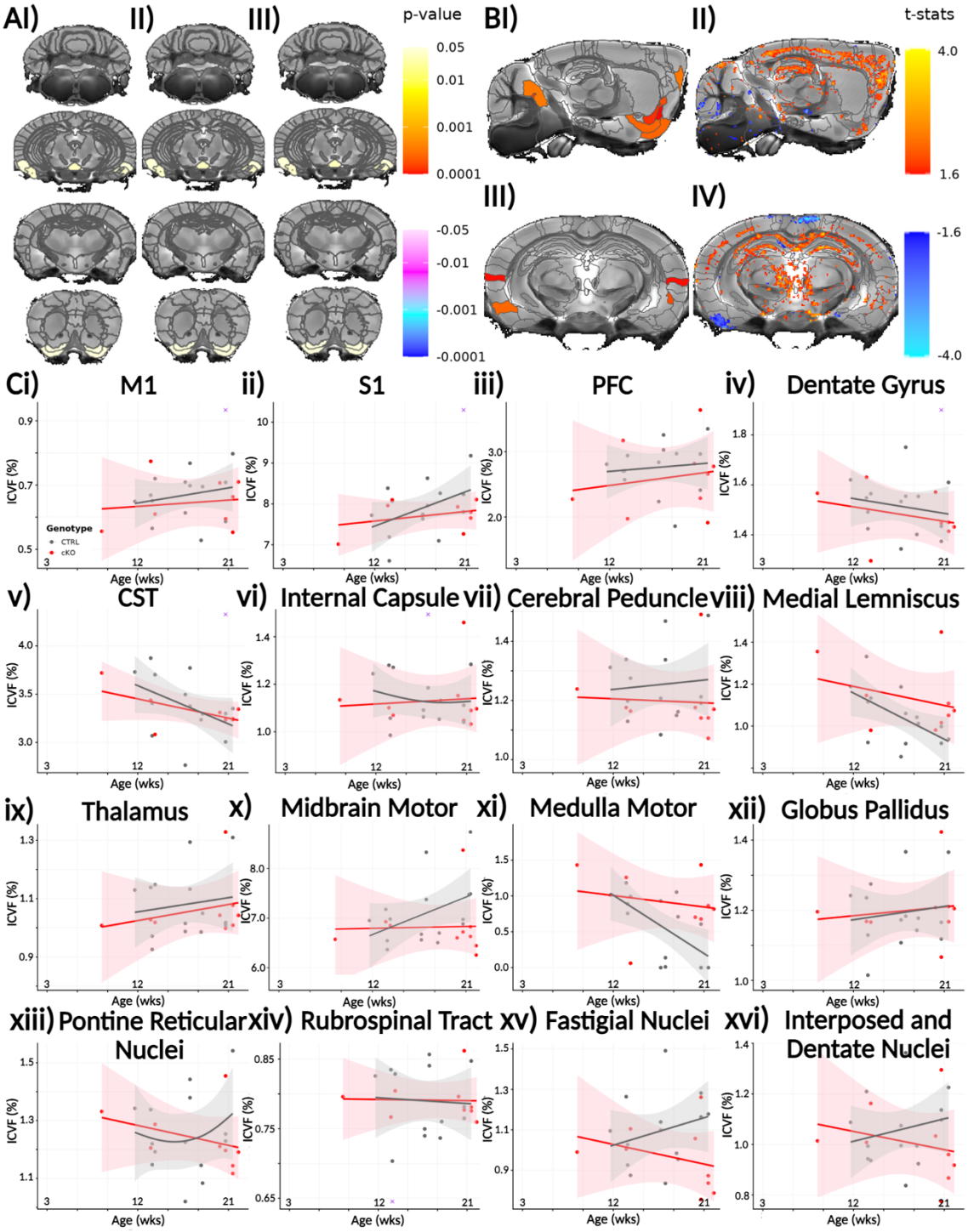


**Figure 58.** *Ex vivo* ICVF analyses. Reveals minimal regional differences in motor-associated areas over time, yet voxelwise patterns indicate increases in L5 and PFC upon L5-cKO. A) Illustrates a lack of differences extrapolated at I) 4wks and interpolated at II) 12wks and III) 21wks. B) Sub-threshold t-statistic maps compare effects of L5-cKO across I,III) regional and II,IV) voxelwise I-II) sagittal and III-IV) coronal maps to highlight voxelwise insights (compare to **Figure 52**-**Figure 53V**). C) Analyses in ROIs belonging to i-iv) cortical and hippocampal areas housing *Rbp4*-Cre$^{+}$ soma; v-viii) *Rbp4*-Cre$^{+}$ axon projection tracts (**5.3.1**); and ix-xvi) motor-related subcortical targets (**Figure 48**). A-B) Statistical increases and decreases are indicated by yellow-red and blue-purple gradients, respectively. See **Table 10** and **A.2** for replicate and statistical details.

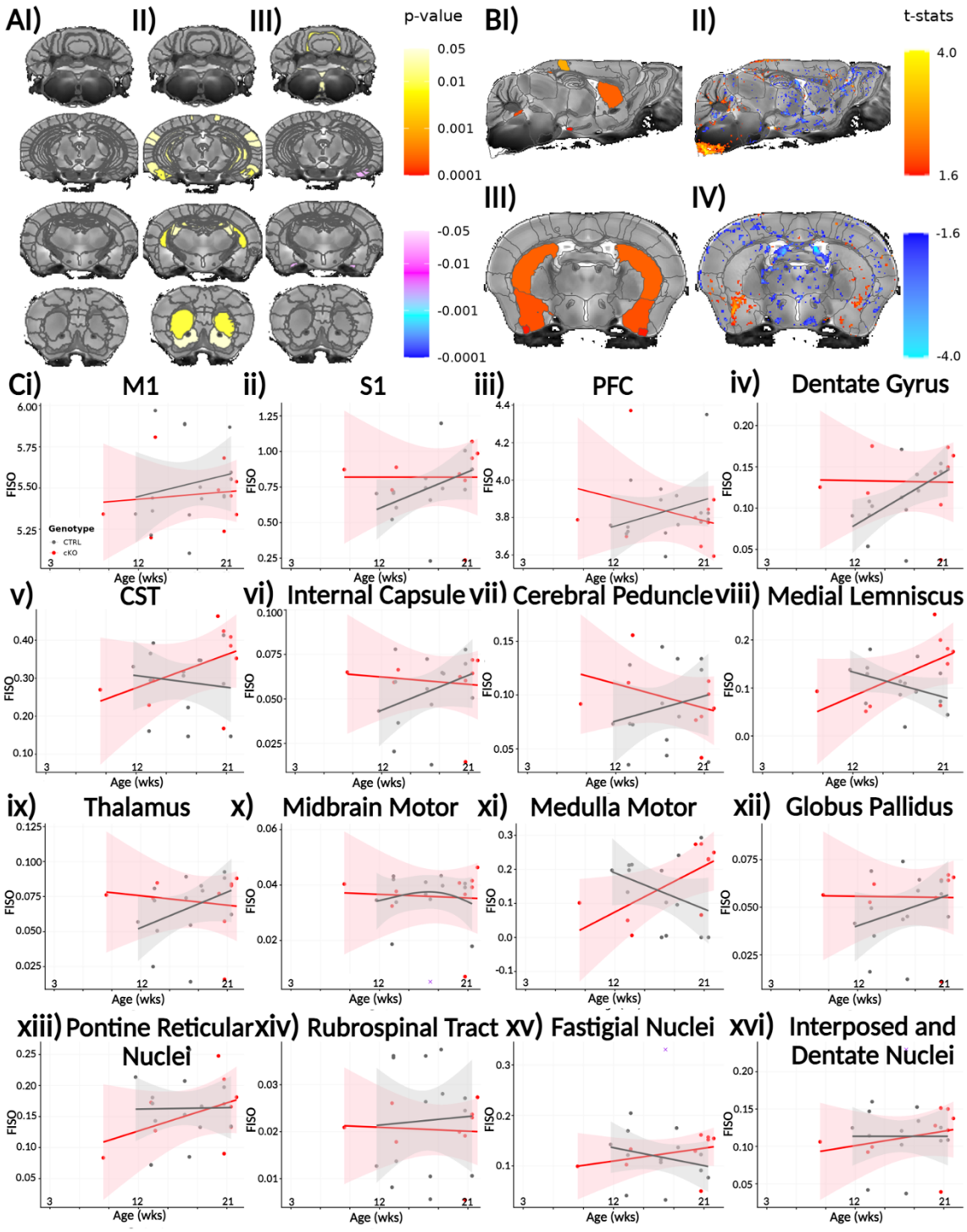


**Figure 59.** *Ex vivo* FISO analyses. Reveals minimal differences in motor-associated areas upon L5-cKO. A) Illustrates a lack of consistent regional differences in FISO extrapolated at I) 4wks and interpolated at II) 12wks and III) 21wks. B) Sub-threshold t-statistic maps compare effects of L5-cKO across I,III) regional and II,IV) voxelwise I-II) sagittal and III-IV) coronal planes (compare to **Figure 52**-**Figure 53VI**). C) Depicts analyses in ROIs belonging to i-iv) cortical and hippocampal areas housing *Rbp4*-Cre$^{+}$ soma; v-viii) *Rbp4*-Cre$^{+}$ axon projection tracts (**5.3.1**); and ix-xvi) motor-related subcortical targets (**Figure 48**). A-B) Statistical increases and decreases are indicated by yellow-red and blue-purple gradients, respectively. See **Table 10** and **A.2** for replicate and statistical details.

### *5.2.5 Ex vivo QSM*

I pre-processing and analysed of *ex vivo* MGE acquisitions to generate T2*, R2*, and X maps alongside anatomical and diffusion outputs. QSM mapping returns physical measurements rather than relative anatomical contrasts; susceptibility in ppm indicates the proportion of change in the external magnetic field due to intrinsic tissue properties upon scanning, and T2* in ms represents effective relaxation time. T2* is sensitive to tissue capable of magnetic distortion–susceptibility, or magnetisability–where the magnitude of nuclear spin dephasing decreases relative to T2 in paramagnetic tissues with high susceptibility (e.g., iron content) and increases in diamagnetic tissues with low susceptibility (e.g., high myelin content or calcium deposits, respectively) relative to T2. R2* results simply from T2* inversion (i.e., R2*=1/T2*) which, though representative of the same underlying properties, can be interpreted as the rate by which tissues induce changes in magnetic fields. R2* is therefore linearly proportional to tissue paramagnetism and presents unique advantages upon interpretation; in cases where high field distortions induce fast signal decay, low T2* values converge upon zero rendering differences more difficult to detect, while R2* rather continually increases. Therefore, considering both T2* and R2* may differentiate whether the magnitude of induced changes result due to high iron content with very short T2*, rather than variable myelin content lending to comparatively longer T2*, if changes are detectable upon R2* analyses but not T2*. In addition to magnitude discernment, additionally considering susceptibility enables classification according to phase, where imaginary signal components are either augmented by paramagnetism or opposed by diamagnetism. Biologically, this can distinguish pathological iron accumulation from calcium deposits; both induce field distortions and shorten T2*, yet by iron positively reinforcing or mineralised calcium negatively counteracting the external magnetic field, lending to increased or decreased susceptibility, respectively. If pathological iron accumulation emerges in projection tracts or subcortical nuclei associated with high baseline

iron levels (i.e., thalamus and globus pallidus) upon *Rbp4*-Cre-induced *Snap25*-cKO, QSM analyses should reveal increased R2*, potentially but not necessarily decreased T2*, and increased susceptibility. In contrast, abnormal calcium deposits would be indicated by increased R2*, likely decreased T2*, and decreased X. If present, demyelination in motor-related tracts would be indicated by increased T2*, decreased R2*, and decreased X.

**Figure 60** summarises *ex vivo* QSM analyses both regionally and voxelwise. I illustrate effects in the same selection of motor-related ROIs (**5.2.1**, **5.2.3**, **5.2.4**) only as reduced-threshold t-statistic maps due to $N_E$ being otherwise underpowered to detect statistically significant differences upon sample exclusion following quality control checks (**A.7.2**-**A.7.7**). Results here are therefore exploratory, where incorporating data from additional samples remains an active future direction (**5.5.3**). Note that T2* maps are inverted such that colour schemes match R2* for comparison; T2* and R2* genotype differences are expected to emerge to opposite effects, yet T2* inversion improves the extent to which conceivably biologically relevant differences between T2* and R2* due to T2* scaling can be visually assessed. **Figure 60** shows a trend towards increased T2* in the hippocampal dentate gyrus, and indications of decreased T2* in CST regions only voxelwise (**Figure 60AIa-b**). R2* appears to decrease in the dentate gyrus yet increase both regionally and voxelwise in the CST, internal capsule, and medial lemniscus more prominently than suggested by T2* maps (**Figure 60AIIa-b**). Susceptibility maps further reveal: decreases in hippocampal regions regionally and voxelwise (**Figure 60AIIIa-b**); signs of regional decreases in the CST and internal capsule (**Figure 60AIIIa**,**BIII**) despite voxelwise increases (**Figure 60AIIIb**); only voxelwise decreases in prefrontal regions–particularly L5 which extends at least to S1 (**Figure 60AIIIb**); and what appear to be decreases in thalamic HOTN areas only in the voxelwise sagittal plane (**Figure 60AIIIb**). I provide extended regional and voxelwise maps, ROI plots, and statistical analyses in **A.10.19** and **A.2**.

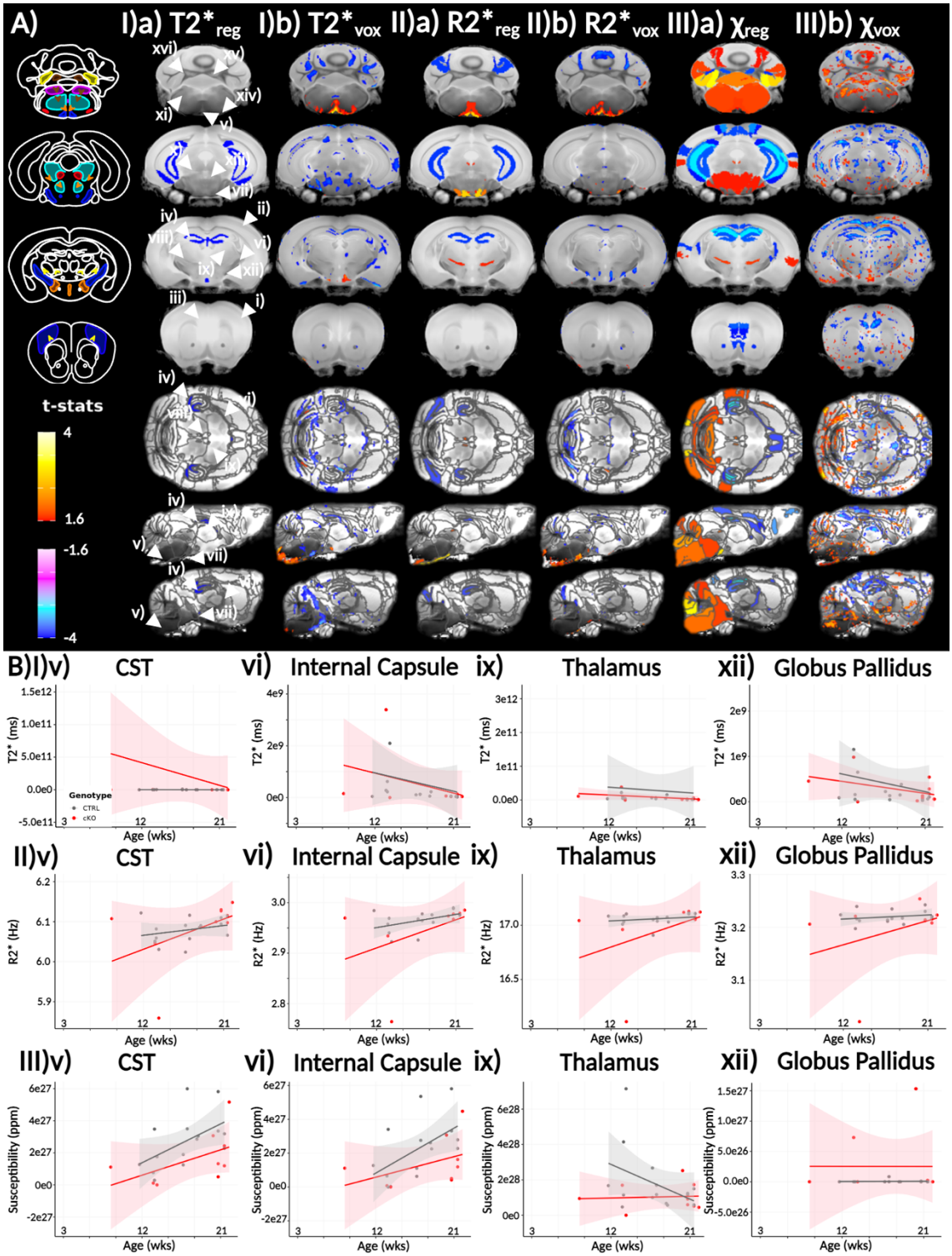


**Figure 60.** *Ex vivo* QSM analyses. Reveals sub-threshold indications of regional and voxelwise T2*, R2*, and susceptibility (X) differences in motor-associated areas upon L5-cKO. A) t-statistic maps compare effects of *Rbp4*-Cre-driven *Snap25*-cKO on I) T2*, II) R2*, and III) X across a) regional (reg) and b) voxelwise (vox) maps for comparison to sketches from **Figure 2**. Statistical increases and decreases are indicated by yellow-red and blue-purple gradients, respectively. B) Individual plots are provided for the v) CST, vi) internal capsule, ix) thalamus, and xii) globus pallidus. Further motor-related ROIs are labelled i-xvi) in A) according to previous definitions (**Figure 48**). I provide extended figures and statistics in **Table 10** and **A.2**.

## 5.3 Histology

### *5.3.1 Rbp4-Cre characterisation*

Following *ex vivo* MRI, I then sliced, stained, and imaged, and qualitatively analysed L5-cKO and CTRL brains to provide cellular-level insights at 21wks according to **Figure 2**, **Figure 4**, and **Table 13**. This first required *Rbp4*-Cre$^{+}$ characterisation throughout the central nervous system (**5.3.5** considers peripheral organs). **Figure 62** shows *Rbp4*-Cre$^{+}$ expression in the brain and spinal cord of L5-cKO and CTRL tissues. As previously characterised[77], *Rbp4*-Cre$^{+}$ cells are prominently expressed throughout L5, the dentate gyrus, and the cerebellum with trace expression in the hypothalamus[77, 114]. However, additional *Rbp4*-Cre$^{+}$ signal appears in the amygdala (also see **Figure 64**). Contrary to prior reports[77], soma also appear scattered throughout spinal grey matter (refer to **Figure 65**, **Figure 71**, and **Figure 75**). *Rbp4*-Cre$^{+}$ projections resemble prior characterisations, being clearly visible in descending major tracts including the internal capsule, cerebral peduncle, and CST throughout the brain and spinal cord. As anticipated, fibres appear to bypass FOTN, selectively target HOTN, and pass through regions corresponding to midbrain and medullar motor nuclei, reticular nuclei, and both rubrospinal and lemniscal tracts. In the spinal cord, axons most densely traverse the dorsal-CST, yet are also present in lateral and ventral regions. This is consistent with the possibility of *Rbp4*-Cre$^{+}$ neurons directly contributing to other tracts (**Figure 62VI-VII**). These patterns are consistent in both CTRL and L5-silenced tissues, yet signs of neurodegeneration clearly emerge upon *Snap25*-cKO. Profound soma loss emerges in L5 across the cortex in L5-cKOs, and axons deteriorate throughout cerebral and spinal projection tracts. Degeneration is accompanied by signs of punctation previously posited to represent lipofuscin deposits due to autofluorescent broad-spectrum emissions[77]. Interestingly, *Rbp4*-Cre$^{+}$ soma in the dentate gyrus and cerebellum do not appear to degenerate (at least at the ages presently assessed), the relevance of which I consider alongside behavioural and neuroimaging insights in **Figure 64** and **5.4**-**5.5**.

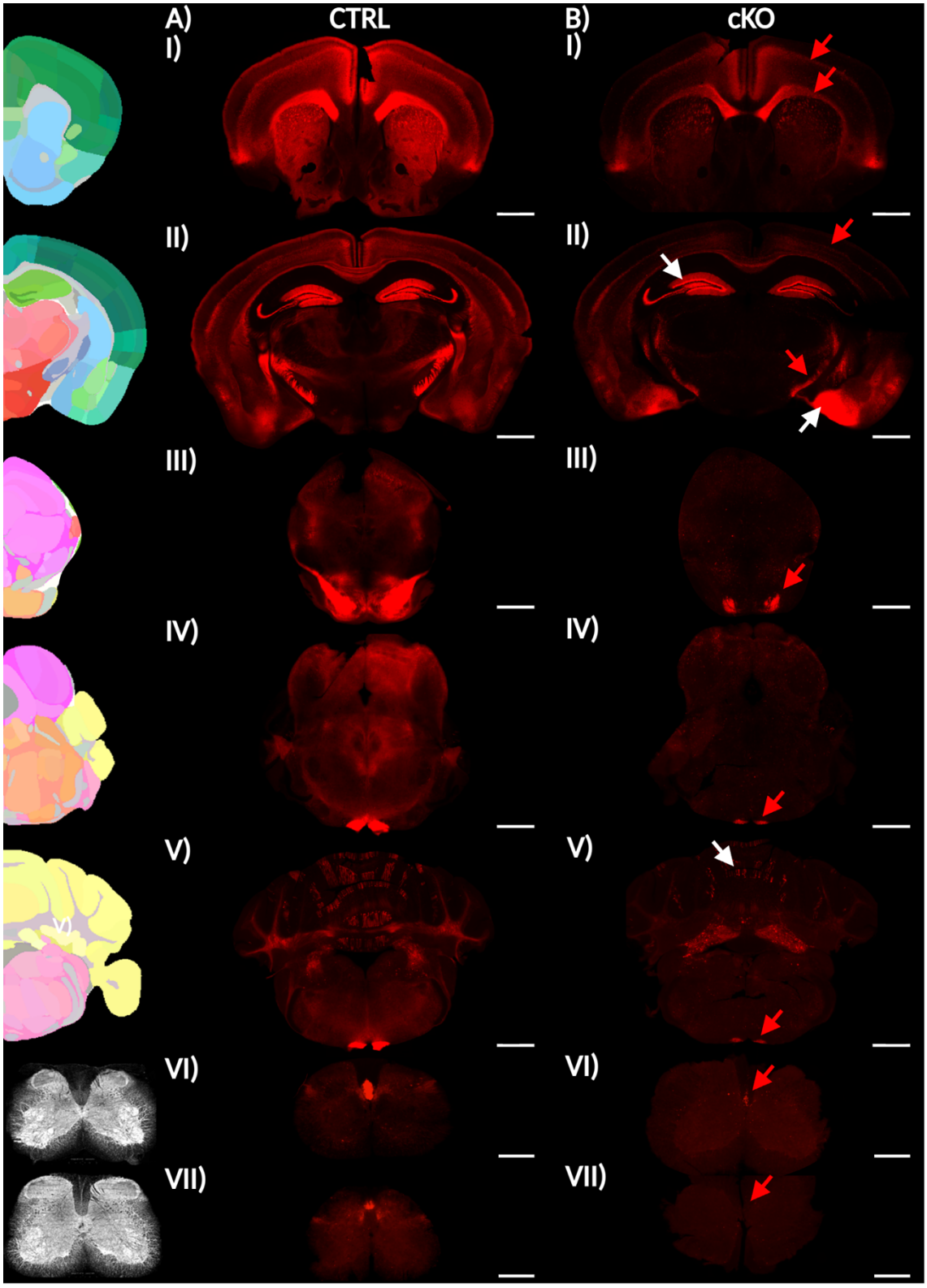


**Figure 61.** *Rbp4*-Cre$^{+}$ expression in the brain and spinal cord. Cre$^{+}$ neurons exhibit degeneration in across AP-levels upon *Snap25*-cKO. Arrows indicate areas of prominent degeneration in cKO samples compared to CTRLs (**Figure 62**, **Figure 63**), while white arrows indicate where *Rbp4*-Cre soma show comparatively little to no degeneration (**Figure 64**). A) *Rbp4*-Cre$^{+}$;*Snap25*$^{+/-}$ CTRL and B) *Rbp4*-Cre$^{+}$;*Snap25*$^{-/-}$ cKO tissues are shown in the I-V) brain, VI) cervical spinal cord, and VII) lumbar spinal cord according to **Figure 4E#1**. Scale bars: I-V) =1mm; VI-VII) =500µm.

### *5.3.2 Motor neurons*

Two stain combinations informed how *Rbp4*-Cre-driven *Snap25*-cKO may influence Cre-expressing subpopulations, putative UMNs, and LMNs (**Table 7**, **A.5.1**). NEUN/SMI32 co-staining (#1 in **Figure 4** and #3 in **Table 13**) aimed to distinguish neurons ($NEUN^+$) with or without NF-H peptide expression ($SMI32^+$) associated with large myelinated extratelencephalic neurons, including UMNs in M1[118]. I expected *Rbp4*-$Cre^+$ cells to co-express $NEUN^+$, yet this must be confirmed in regions of previously undocumented soma expression (**Figure 62**). The extent to which *Rbp4*-$Cre^+$ neurons overlap with extratelencephalic subtypes has been evaluated transcriptomically (**Figure 4B**) but not yet histologically, and whether cortical *Rbp4*-$Cre^+$ neurons exhibit subtype-selective degeneration remains unknown. If large pyramidal tract *Rbp4*-$Cre^+$ projection neurons are selectively vulnerable to effects of *Snap25*-cKO as hypothesised (**1.3.1**,**1.3.5**), signs of degeneration should arise earlier or more prominently in SMI32 co-expressing populations. Furthermore, increased $SMI32^+$/*Rbp4*-$Cre^-$ prevalence in L5-cKO brains could indicate a compensatory means by which other neurons adapt to *Rbp4*-$Cre^+$ infarct. Better intratelencephalic-extratelencephalic neuron discrimination could be theoretically achieved via CTIP2[119]/SATB2[48, 125, 126] co-staining (**A.5.1**), which I attempted (**A.5.5**) unsuccessfully (**A.5.7**). CTIP2 antibodies were incompatible with tissues from this cohort likely due to mouse age (antibodies were only optimised using younger animals in developmental studies), extended post-perfusion-fixation storage (required for *ex vivo* MRI), or the process of overnight scanning at room temperature. SMI32 therefore presented as the next-best available option following optimisation (**A.5.6**). *Rbp4*-$Cre^+$ soma co-expressed $NEUN^+$, indicating that targeted cells indeed represent neurons (**Figure 62**-**Figure 64**). *Rbp4*-$Cre^+$ soma appear to degenerate by 21wks, perhaps more prominently in SMI32 co-expressing subpopulations (**Figure 62ii-iii**), supporting the possibility of increased vulnerability (**1.3.5**). Again note that *Rbp4*$^+$ cells in the dentate gyrus, cerebellum, and amygdala do not appear to similarly degenerate (**Figure 64**).

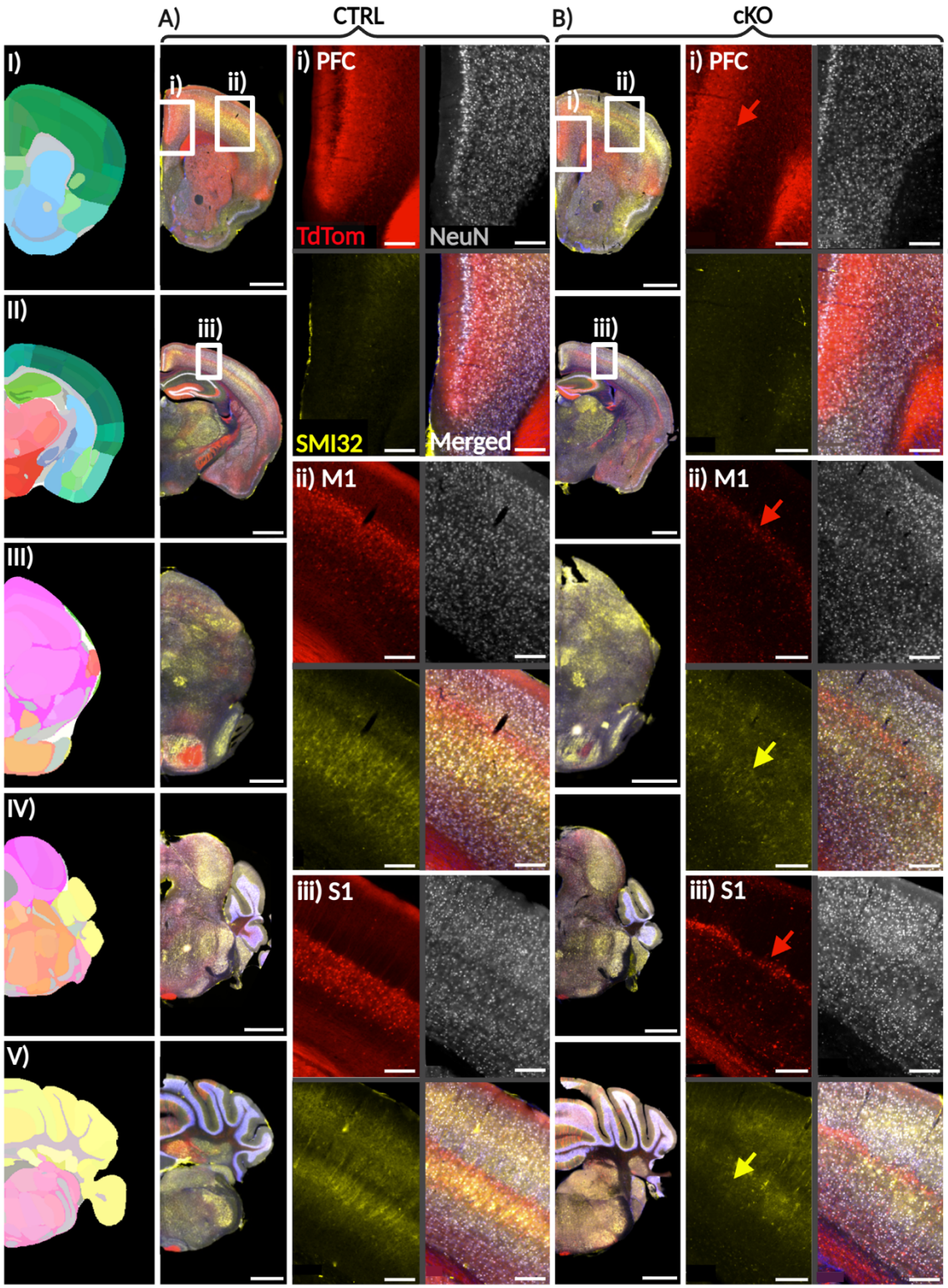


**Figure 62.** *Rbp4*-Cre/NEUN/SMI32 degeneration in cortical ROIs at 21wks. SMI32 colocalisation with L5b *Rbp4*-Cre$^{+}$ neurons appears to decrease upon *Snap25*-cKO, suggesting selective vulnerability. Arrows indicate areas of degeneration in cKO samples compared to CTRLs. A) *Rbp4*-Cre$^{+}$;*Snap25*$^{+/-}$ CTRL and B) *Rbp4*-Cre$^{+}$;*Snap25*$^{-/-}$ cKO tissues are shown at I-V) coronal AP-levels according to **Figure 4E#1**. RFP is clear in L5 of the i) PFC; ii) M1; and iii) S1, where B) cells degenerate upon *Snap25*-cKO. All *Rbp4*$^{+}$ soma appear to co-express NEUN, yet *Rbp4*-Cre$^{+}$ soma only represent a portion of NEUN$^{+}$ neurons in L5 (~15%)[77]. Scale bars: I-V) =1mm; i-iii) =200µm.

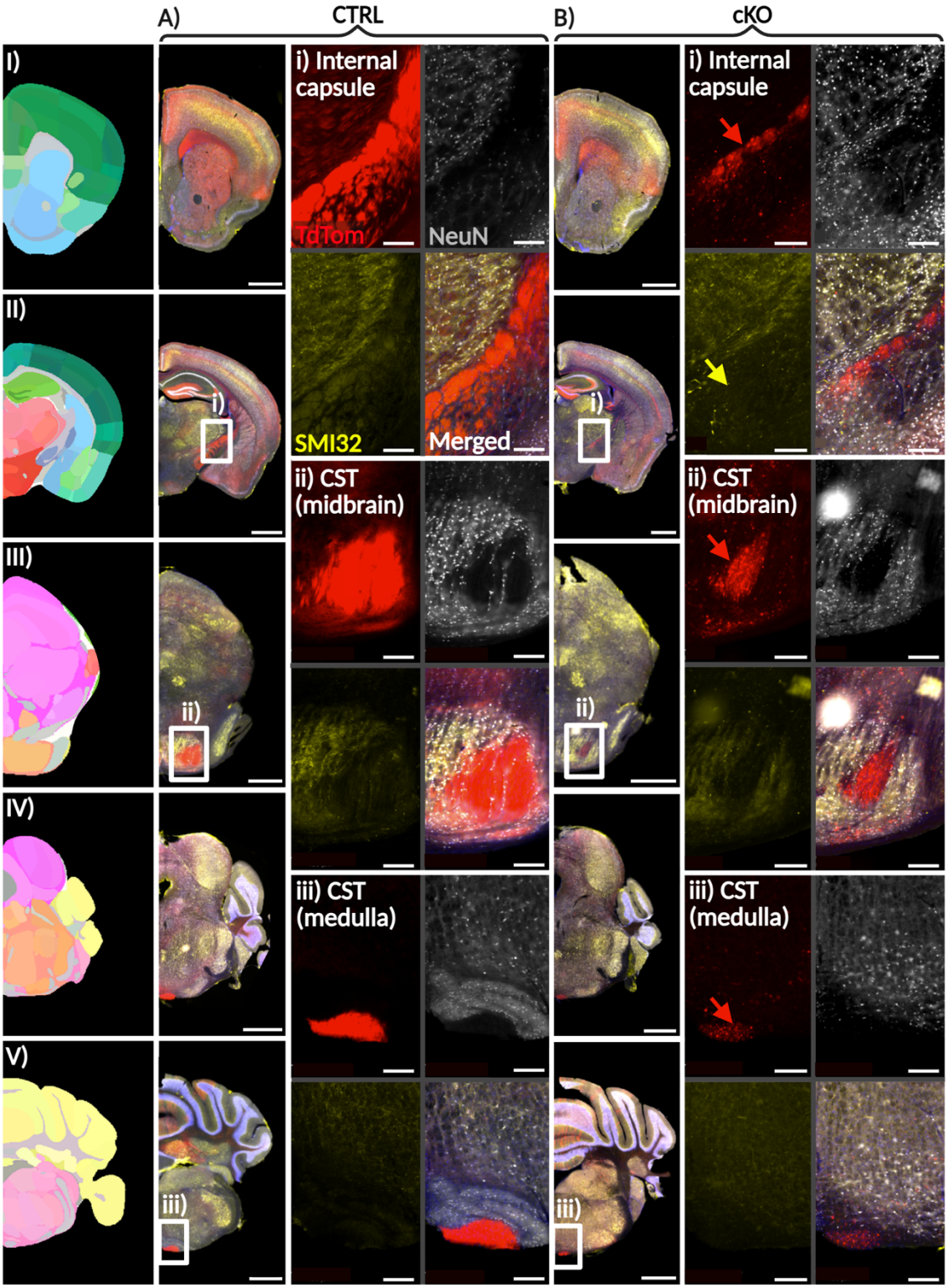


**Figure 63.** *Rbp4*-Cre/NEUN/SMI32 degeneration in motor projection tracts at 21wks. Arrows highlight where cKO samples show notable signs of degeneration compared to CTRLs. A) *Rbp4*-Cre$^{+}$;*Snap25*$^{+/-}$ CTRL and B) *Rbp4*-Cre$^{+}$;*Snap25*$^{-/-}$ cKO tissues are shown at I-V) AP-levels according to **Figure 4E#1**. RFP is clear throughout CTRL tracts including the i) internal capsule, ii) midbrain CST, and iii) medullar CST. RFP$^{+}$ debris appears scattered throughout L5-cKO tracts. Scale bars: I-V) =1mm; i-iii) =200µm.

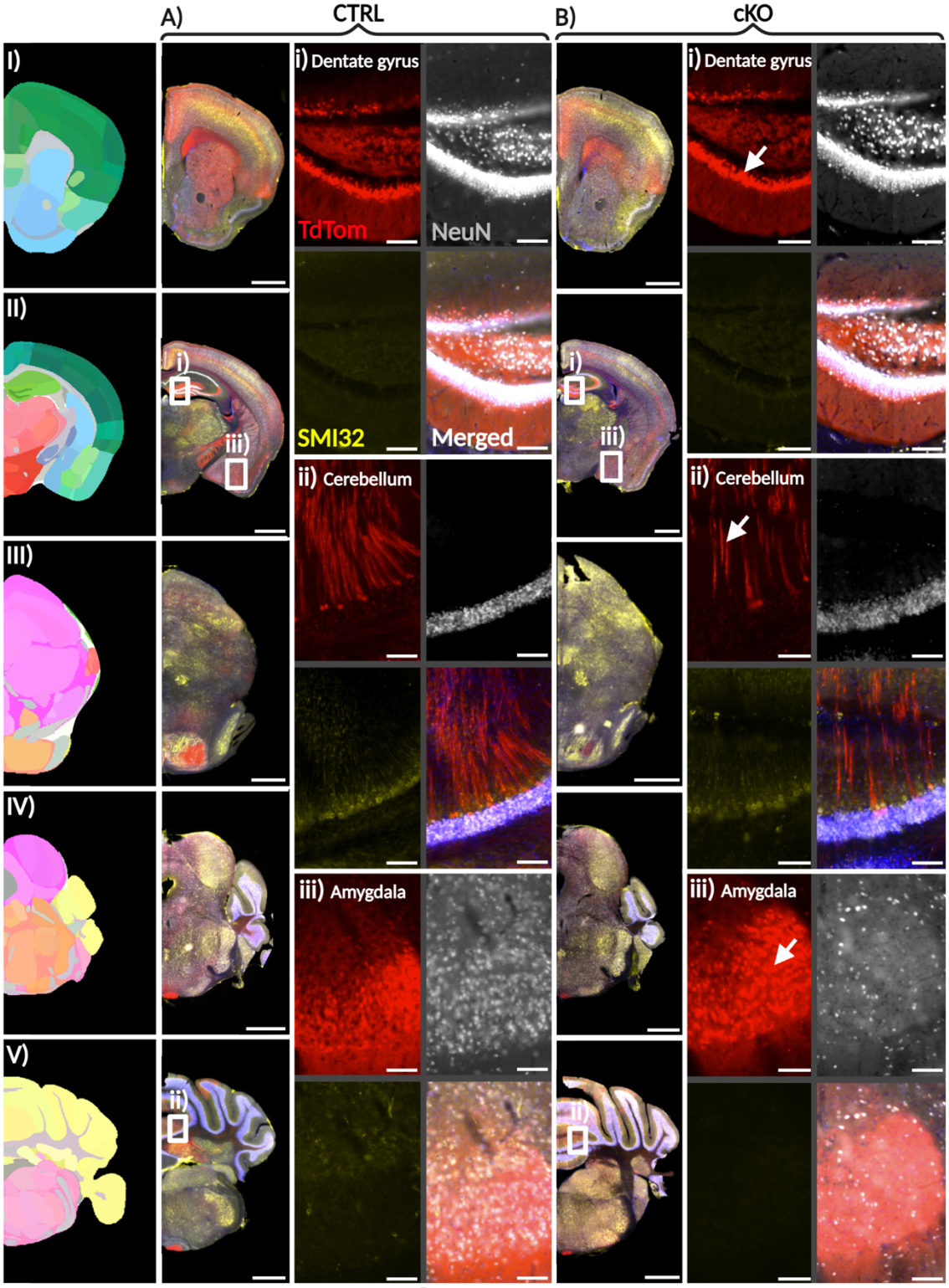


**Figure 64.** *Rbp4*-Cre/NEUN/SMI32 non-L5 expression at 21wks. A) *Rbp4*-Cre$^{+}$;*Snap25*$^{+/-}$ CTRL and B) *Rbp4*-Cre$^{+}$;*Snap25*$^{-/-}$ cKO tissues at I-V) target coronal AP-levels (**Figure 4E#1**) show off-target subcortical expression in the i) dentate gyrus, ii) cerebellum (Purkinje fibres), and iii) amygdala. Most *Rbp4*-Cre$^{+}$ cells here—but not all—co-express NEUN, and only some in the cerebellum co-express SMI32. Across i-iii), *Rbp4*-Cre$^{+}$ cells do not appear to degenerate upon *Snap25*-cKO (white arrows) compared to CTRLs, suggesting that *Rbp4*-Cre$^{+}$/SMI32$^{+}$ L5 neurons may be particularly vulnerable to effects *Snap25*-cKO. Scale bars: I-V) =1mm; i-iii) =100µm.

CHAT/SMI32 co-staining (#2 in **Figure 4** and #4 in **Table 13**) aimed to distinguish LMNs ($CHAT^+$) and prototypically large, myelinated, NF-H-expressing lower α-MNs ($CHAT^+/SMI32^+$) in the brainstem and spinal cord[118] for two reasons: firstly, to determine whether *Rbp4*-$Cre^+$ cells unexpectedly co-express CHAT in the spinal cord, which would contradict evidence supporting top-down hypotheses via direct LMN-silencing (**1.4.5**); and secondly, whether $CHAT^+/SMI32^+$ neurons degenerate as a downstream consequence *Rbp4*-Cre-driven *Snap25*-cKO, which would be consistent with the behavioural decline observed in **5.1.** In the brainstem, the oculomotor, pedunculopontine, and trigeminal motor nuclei were strategically selected for more detailed observation (**Figure 65i-iii**). Oculomotor and motor trigeminal nuclei co-express SMI32, thus may be more susceptible to degeneration upon *Snap25*-cKO, however prior work suggests that oculomotor nuclei are uniquely spared from degeneration in ALS[196, 233, 246]. Pedunculopontine nuclei do not largely co-express SMI32, therefore may be more resistant to degeneration. Pedunculopontine and motor trigeminal nuclei can conveniently be found in the same coronal plane, and therefore act as mutual within-subject controls against technical confounds (e.g., staining and imaging quality).

CHAT staining indeed labels both CTRL and L5-cKO brainstem and spinal cord LMN (**Figure 65**-**Figure 66**). *Rbp4*-$Cre^+$ expression was unexpectedly yet clearly present in the spinal cord (**Figure 66III**) where, though infrequently, some $CHAT^+$/*Rbp4*-$Cre^+$ neurons were observed (**Figure 65Ai**, **Figure 66Biv**). Signs of $CHAT^+$ membrane punctation consistently emerged—predominantly in L5-cKO mice—in the motor trigeminal nucleus (**Figure 65iii**) and spinal motor nuclei (**Figure 66D** vs **Figure 66F**), yet to a much lesser extent in pedunculopontine (**Figure 65ii**) and oculomotor nuclei (**Figure 65i**) which appeared largely indistinguishable across genotypes. However, without quantitative analyses, the extent to which the density, distribution, or morphology of $CHAT^+/SMI32^+$ and $CHAT^+/SMI32^-$ neurons changes upon L5-cKO remains unknown and is therefore an ongoing future direction (**5.5.3**).

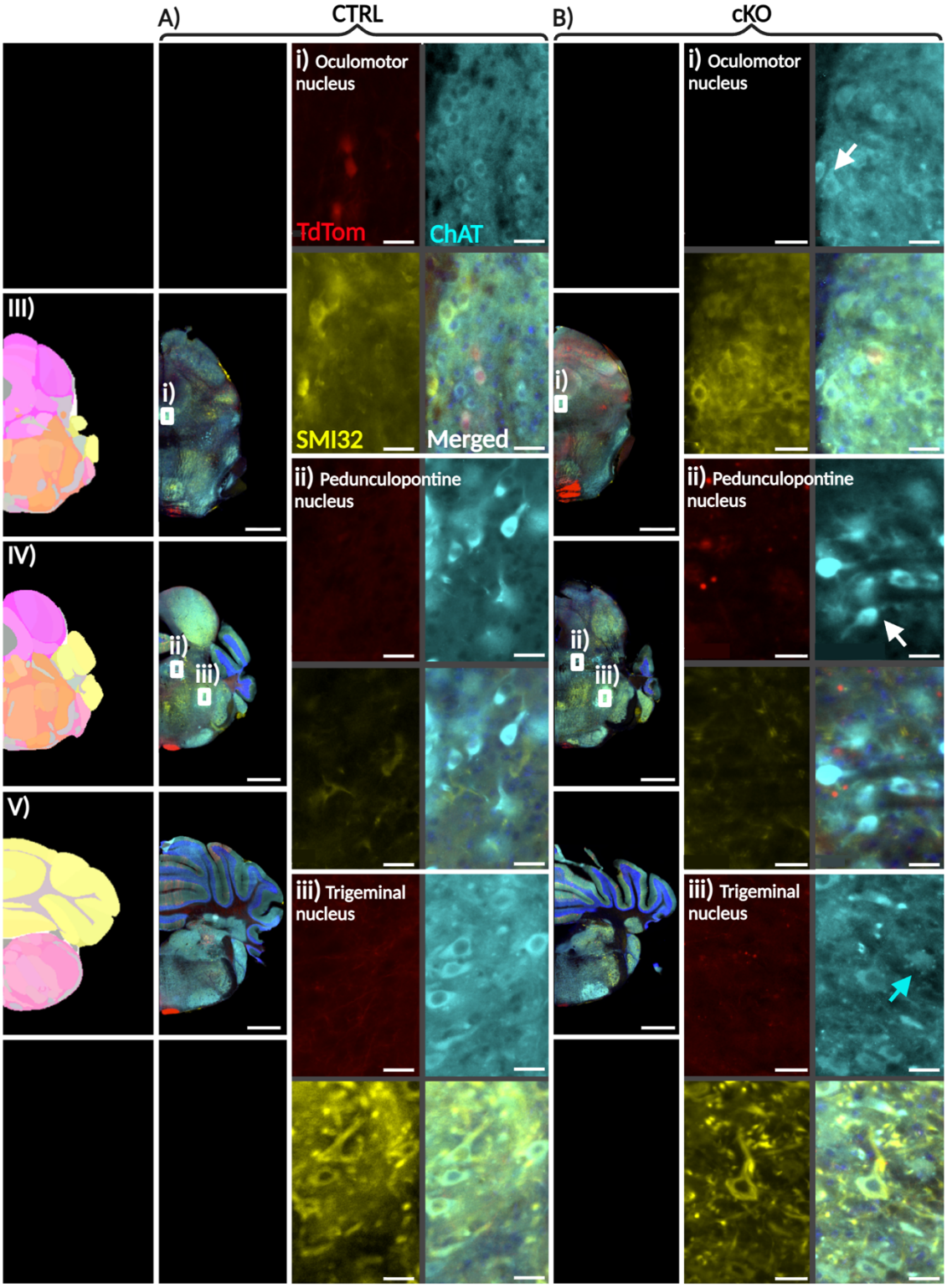


**Figure 65.** *Rbp4*-Cre/CHAT/SMI32 expression and colocalisation in the brainstem at 21wks. In A) *Rbp4*-Cre$^{+}$;*Snap25*$^{+/-}$ CTRL and B) *Rbp4*-Cre$^{+}$;*Snap25*$^{-/-}$ cKO tissues at III-V) target coronal AP-levels (**Figure 4E#2**), degeneration is clear in *Rbp4*-Cre$^{+}$ tracts. Signs of CHAT$^{+}$ LMN deterioration appear to emerge in iii) motor trigeminal nuclei (cyan arrows), but not ii) pedunculopontine or i) oculomotor nuclei (white arrows) which have previously been reported as resistant to degeneration in ALS[196, 233, 246]. Scale bars: III-V) =1mm; i-iii) =30µm.

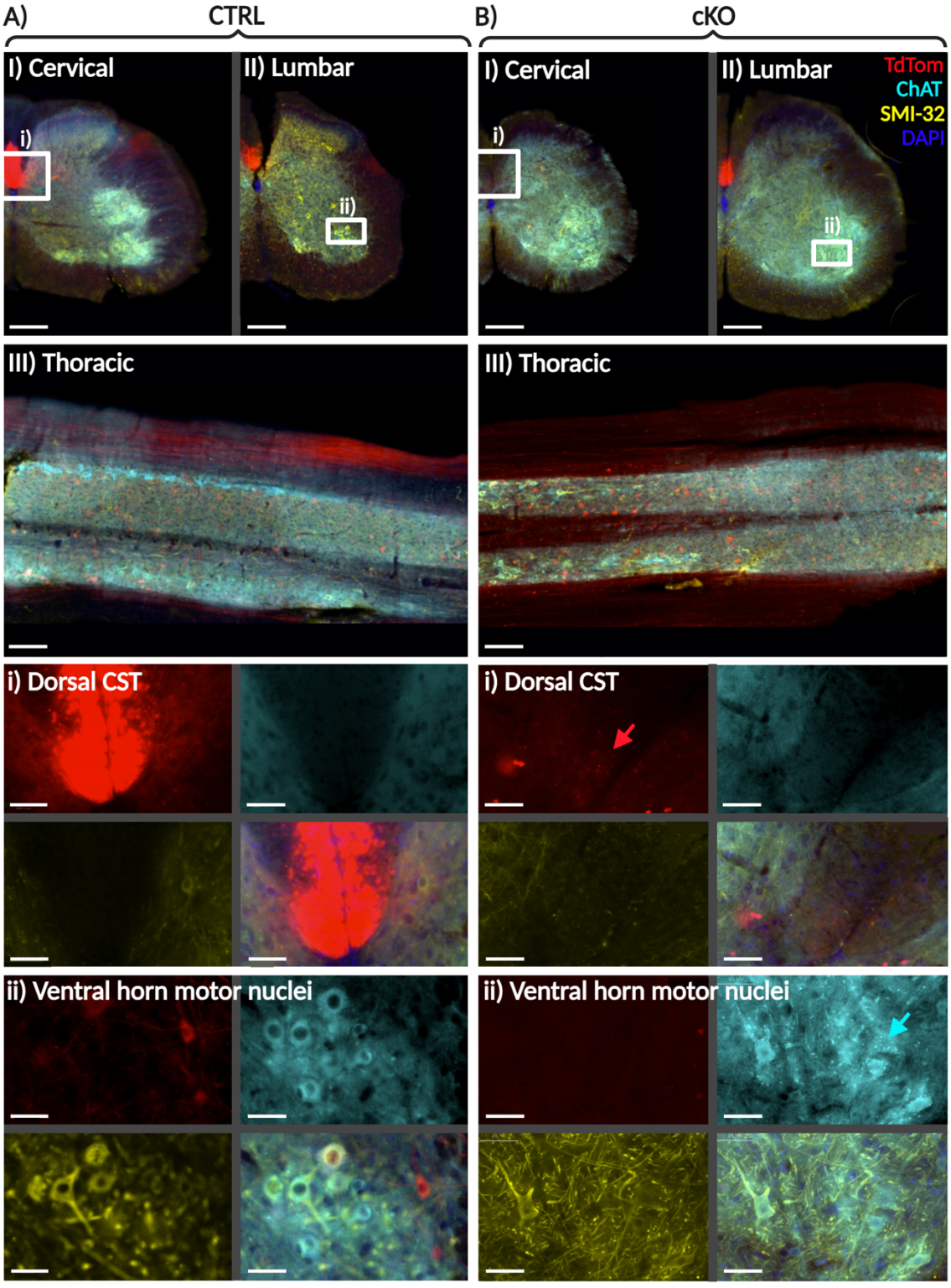


**Figure 66.** *Rbp4*-Cre/CHAT/SMI32 expression and colocalisation in the spinal cord at 21wks. Across A) *Rbp4*-Cre$^{+}$;*Snap25*$^{+/-}$ CTRL and B) *Rbp4*-Cre$^{+}$;*Snap25*$^{-/-}$ cKO I) cervical and II) lumbar spinal cord coronal sections and III) horizontal thoracic slices (**Figure 4E#2**), signs of degeneration (arrows) clearly emerge in the i) dorsal-CST or L5-cKOs compared to CTRLs. CHAT$^{+}$ LMN membrane punctation appears in ii) ventral horn motor nuclei ofL5-cKO mice. Scale bars: I-III) full spinal sections=250µm; i-ii) nuclei=50µm.

### *5.3.3 Myelination and protein aggregates*

MBP/AT8 co-staining (#3 in **Figure 4** and #5 in **Table 13, A.5.1**) served three purposes: 1) to determine whether decreased myelin degeneration is observable in older ~21wk mice upon *Rbp4*-Cre-driven *Snap25*-cKO, where a lack of genotype differences had only been previously evaluated before postnatal day 21[79]; 2) to assess whether pathological AT8 protein aggregates are detectable upon L5-silencing; and 3) if AT8 is present, to distinguish grey vs white matter distribution via MBP colocalisation (**Table 7**). AT8 is associated with neurodegeneration and motor dysfunction and may inform which brain regions are affected by L5-silencing–predictably in M1 and motor-related white matter tracts[187, 188, 191, 193]. I predicted myelin loss in *Rbp4*-Cre$^+$-projecting pathways given indications of neurodegeneration (**5.3.1**)[77] and motor deficits (**5.1**), both of which could be associated with decreased myelin due to soma and axon infarct upon *Snap25*-cKO, failed maintenance via oligodendrocytes[443], or glial-mediated phagocytosis (**5.3.4**)[444]. I strategically stained myelin to secondarily enable comparisons between histological and neuroimaging data–namely, to support or refute QSM interpretations (**5.2.5**). I expand upon the methodological relevance of this in **5.5.5**.

No changes in the expected pattern or intensity of MBP expression were qualitatively obvious between genotypes at ~21wks (**Figure 67**-**Figure 68**). However, AT8 immunoreactivity emerged in select areas through which *Rbp4*-Cre$^+$ axons project (**Figure 67**)–most notably the cerebral peduncles (**Figure 67Bii**)–indicating pathological tau phosphorylation within MBP-colocalised white matter upon *Snap25*-cKO. I did not consistently observe AT8 in the spinal cord in either CTRLs or L5-cKOs; however, some L5-cKO samples exhibited cells with AT8 expression (**Figure 68E**-**F**). This should be replicated before testing for colocalisation with microglia, astrocytes, and oligodendrocytes, which may conceivably uptake AT8 as a neuroprotective measure. I considered and optimised oligodendrocyte CC1 co-staining for this purpose (**A.5.6**) yet did not pursue its full-cohort analyses.

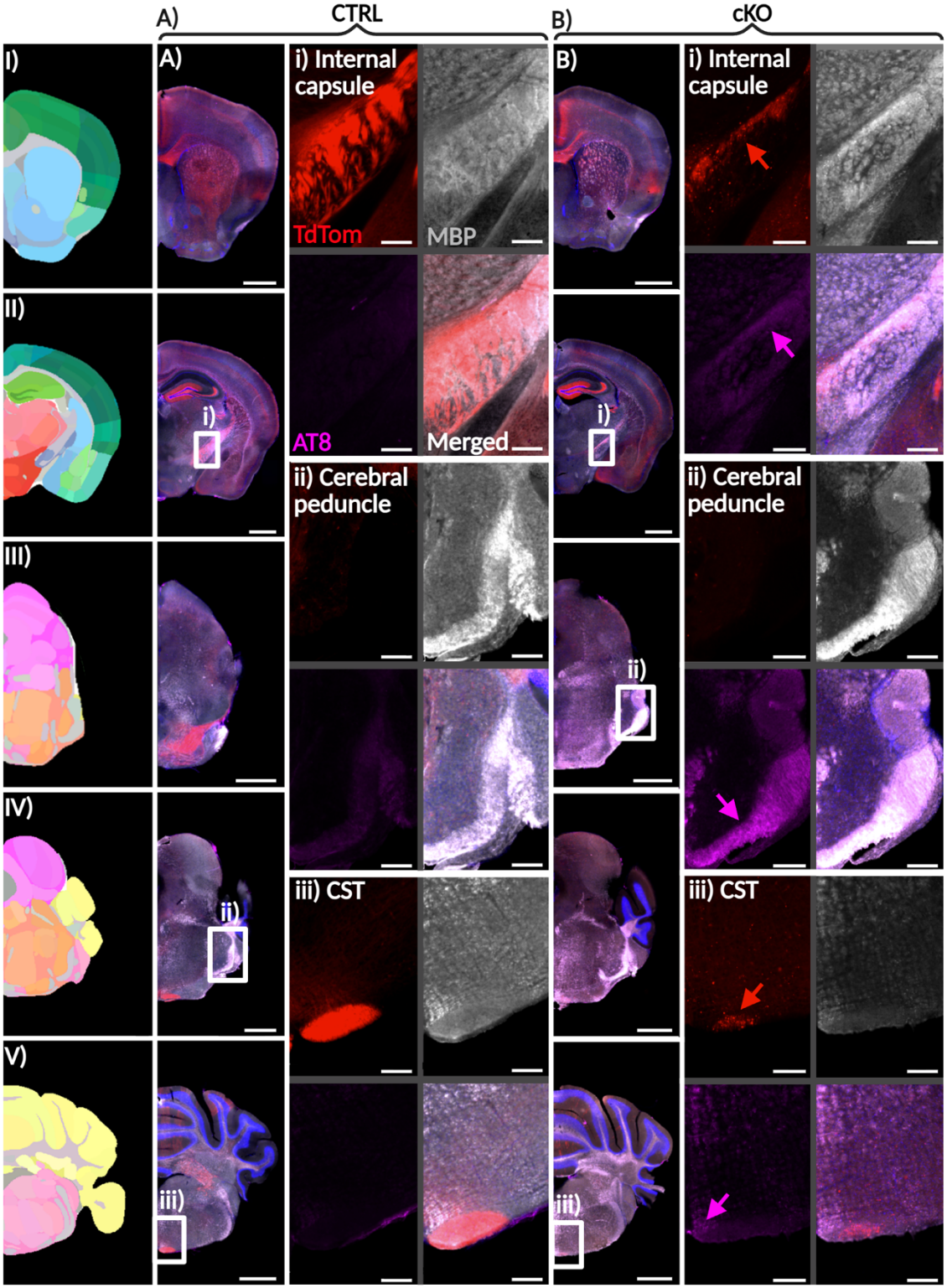


**Figure 67.** *Rbp4*-Cre$^{+}$/MBP/AT8 expression in motor-related projection tracts at 21wks. As in **Figure 4E#3**, A) *Rbp4*-Cre$^{+}$;*Snap25*$^{+/-}$ CTRL and B) *Rbp4*-Cre$^{+}$;*Snap25*$^{-/-}$ cKO tissues are shown at I-V) target AP-levels. No obvious differences in MBP expression emerge in the i) internal capsule, ii) cerebral peduncle, and iii) CST. However, AT8 appears to accumulate (magenta arrows) upon *Snap25*-cKO. Scale bars: I-V) =1mm; i-iii) =200µm.

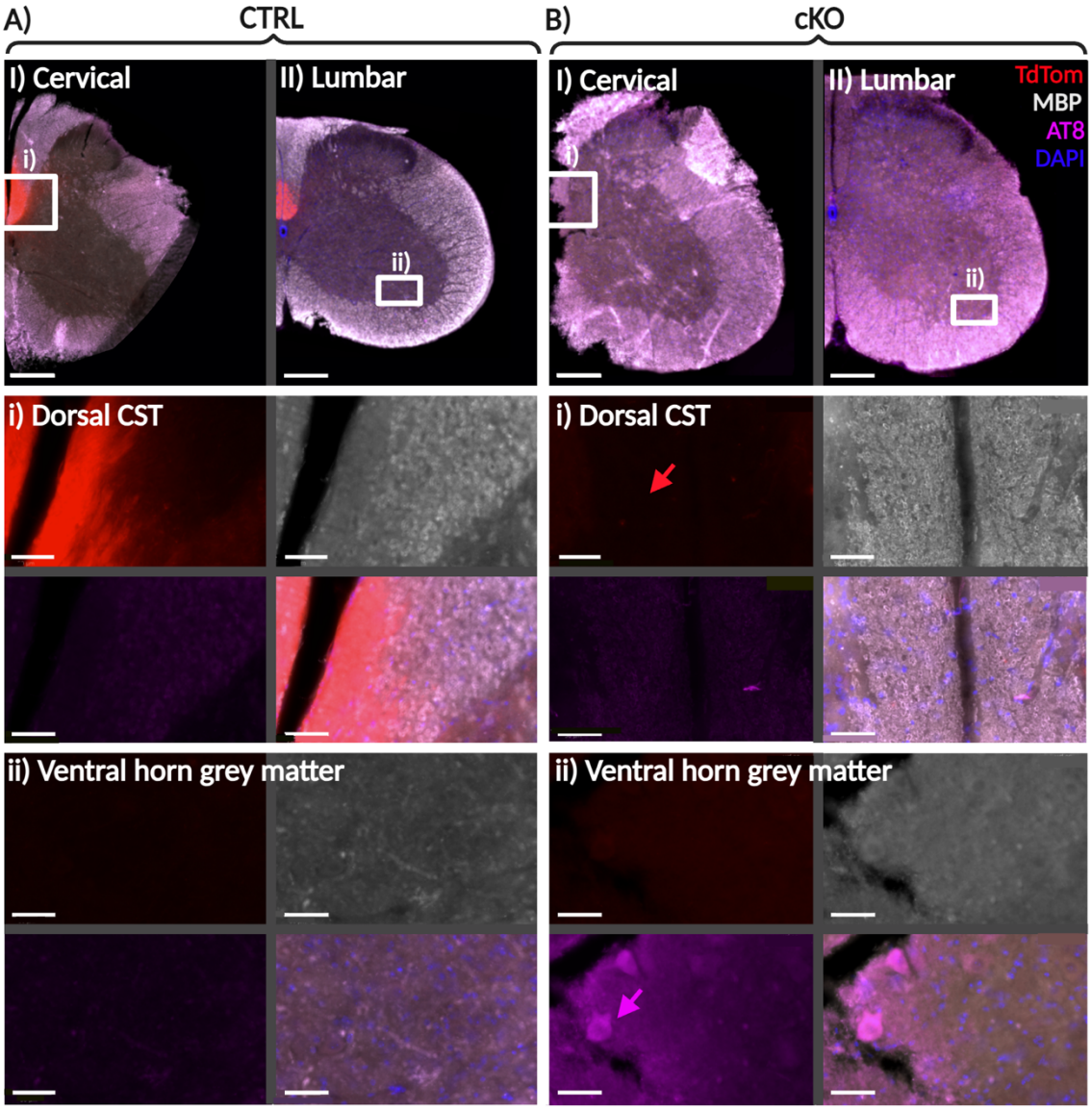


**Figure 68.** *Rbp4*-Cre/MBP/AT8 expression and colocalisation in the spinal cord at 21wks. Across A) *Rbp4*-Cre$^{+}$;*Snap25*$^{+/-}$ CTRL and B) *Rbp4*-Cre$^{+}$;*Snap25*$^{-/-}$ cKO I) cervical and II) lumbar spinal cord coronal sections (**Figure 4E#3**), no obvious differences in MBP expression emerge in the i) dorsal-CST or ii) ventral horn grey matter of L5-cKOs compared to CTRLs. However, signs of AT8 accumulation sparsely appear in cells in the ii) grey matter (magenta arrow). Scale bars: I-II) full spinal sections=250µm; i-ii) ROIs=50µm.

### *5.3.4 Glial cells and interneurons*

Stain combinations involving IBA1/GFAP (#4 in **Figure 4** and #6 in **Table 13**) and PV/VVA (#5 in **Figure 4** and #1 in **Table 13**) then considered roles of microglia, astrocytes, interneurons, and perineuronal nets in local (i.e., areas of *Rbp4*-Cre expression) and global (i.e., subcortically and in the spinal cord) network responses to effects of *Snap25*-cKO (**1.1.4, Table 7**, **A.5.1**).

Glial cells are well-known to maintain network function, stability, and plasticity where significant evidence shows neuron-to-glial and glial-to-neuron interactions under both normal conditions and following perturbation to either cell subtype[147, 405, 445, 446]. Therefore, I used IBA1/GFAP staining to assess whether microglia and astrocytes exhibit increased densities or altered distributions as a reactive consequence of *Rbp4*-Cre *Snap25*-cKO. This has been shown to occur under acute[147] and chronic conditions[405], however these studies did not consider analyses throughout the hindbrain, cerebellum, and spinal cord. Changes in glial prevalence and reactivity have been previously reported in spinal cords of genetically modified mice exhibiting motor dysfunction[447] and may conceivably corelate to phenotype progression.

Upon *Snap25*-cKO, IBA1 and GFAP staining showed strikingly increased microglial and astrocyte infiltration across cortical layers and in white matter tracts through which *Rbp4*-Cre$^+$ axons project in CTRLs and degenerate in L5-cKOs (**Figure 69**-**Figure 71**). This was especially prominent in PFC and M1 (**Figure 69**). In the spinal cord, microglia concentrated in the grey matter while astrocytes perused the white matter. Microglia densities appeared to decrease in L5-cKO tissues compared to CTRLs; however, this is likely a staining artifact due to the lack of surveillance microglia as in CTRLs (**Figure 71B**), therefore spinal cord microglial staining should be repeated (**5.5.4**). White matter astrocyte prevalence increased upon L5-cKO, yet the quality of this observation is also poor due to unfocussed SSFM rendering neurites indiscernible. Given DWI and QSM insights, I qualitatively looked for any signs of altered microglial densities and morphologies in L5 (but not astrocytes due to poor staining quality) across the PFC, M1, and S1 (**Figure 72**). Indeed, microglia interestingly appeared to adopt different forms across regions upon L5-cKO; those in the PFC were perhaps larger and more circular, while cells in S1 appeared more elongated. These findings contribute to and expanded upon more extensive morphological and functional characterisations of local and global glial effects upon *Rbp4*-Cre-driven *Snap25*-cKO, which have now been accepted for publication[405].

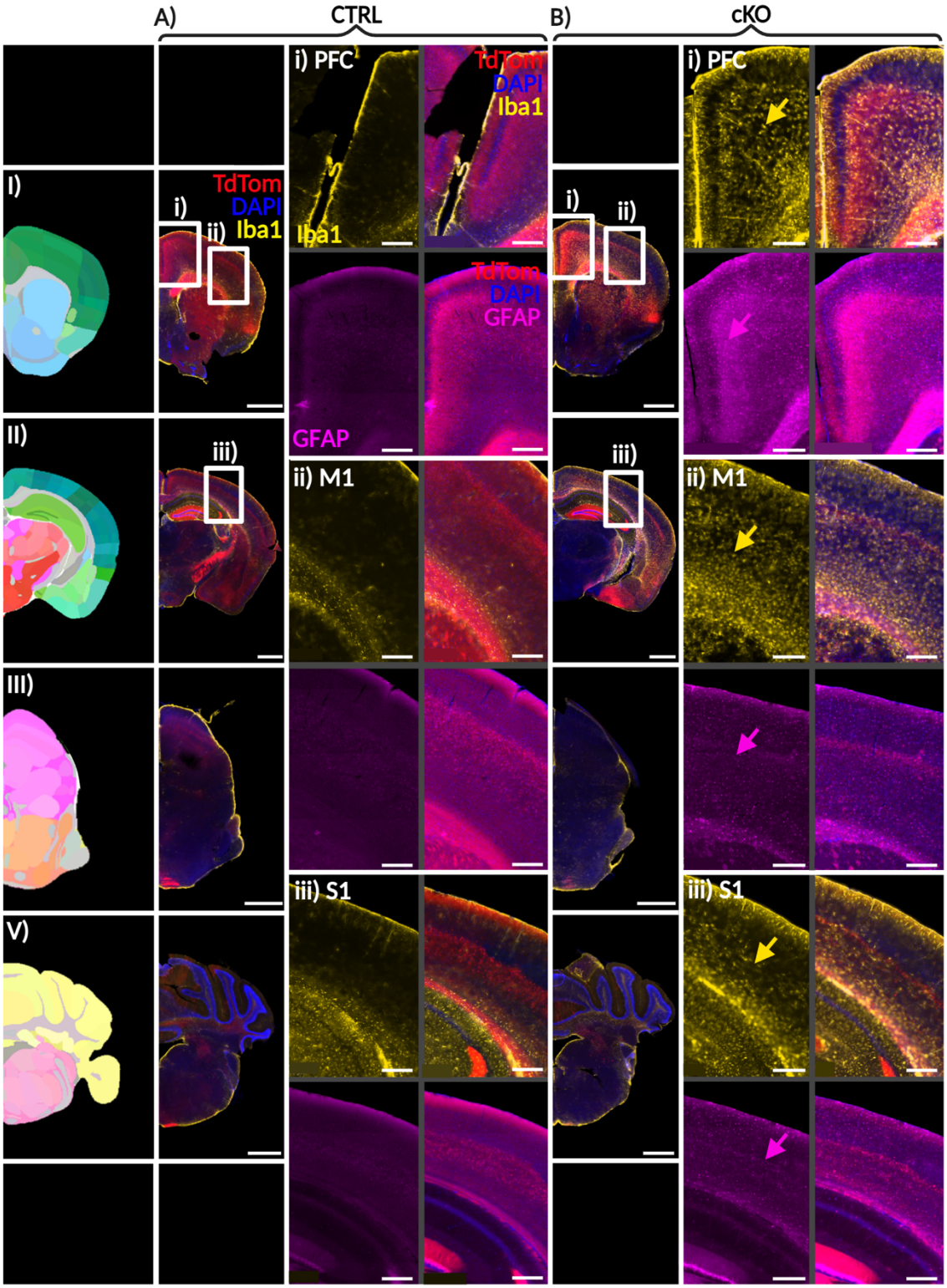


**Figure 69.** *Rbp4*-Cre$^{+}$ degeneration is accompanied by glial infiltration upon L5-cKO. A) *Rbp4*-Cre$^{+}$;*Snap25*$^{+/-}$ CTRL and B) *Rbp4*-Cre$^{+}$;*Snap25*$^{-/-}$ cKO tissues are shown at I-III, V) coronal planes according to **Figure 4E#4**. In the i) PFC, ii) M1, and iii) S1, B) both microglia and astrocytes emerge across cortical layers (highlighted with arrows), not being limited to expression in L5 where *Rbp4*-Cre$^{+}$ cells deteriorate. Scale bars: I-III, V) =1mm; i-iii) =200µm.

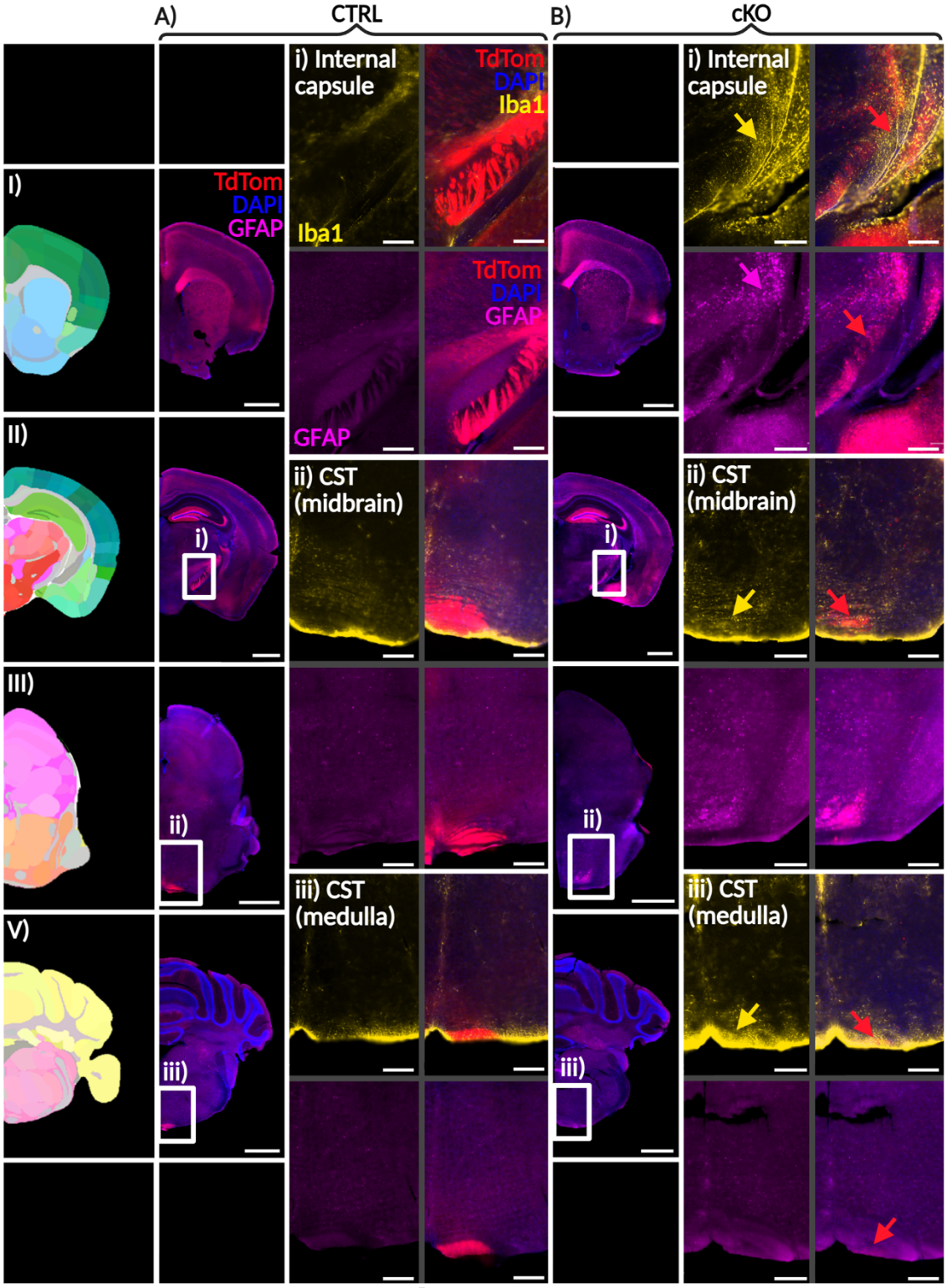


**Figure 70.** *Rbp4*-Cre$^{+}$ tract degeneration prompts microglia and astrocyte infiltration. A) *Rbp4*-Cre$^{+}$;*Snap25*$^{+/-}$ CTRL and B) *Rbp4*-Cre$^{+}$;*Snap25*$^{-/-}$ cKO tissues are shown at I-III, V) coronal AP-levels according to **Figure 4E#4**, where microglia and astrocytes invade the i) internal capsule, ii) midbrain CST, and iii) medullar CST upon *Rbp4*-Cre-driven *Snap25*-cKO (highlighted with arrows). Scale bars: I-III, V) =1mm; i-iii) =200µm.

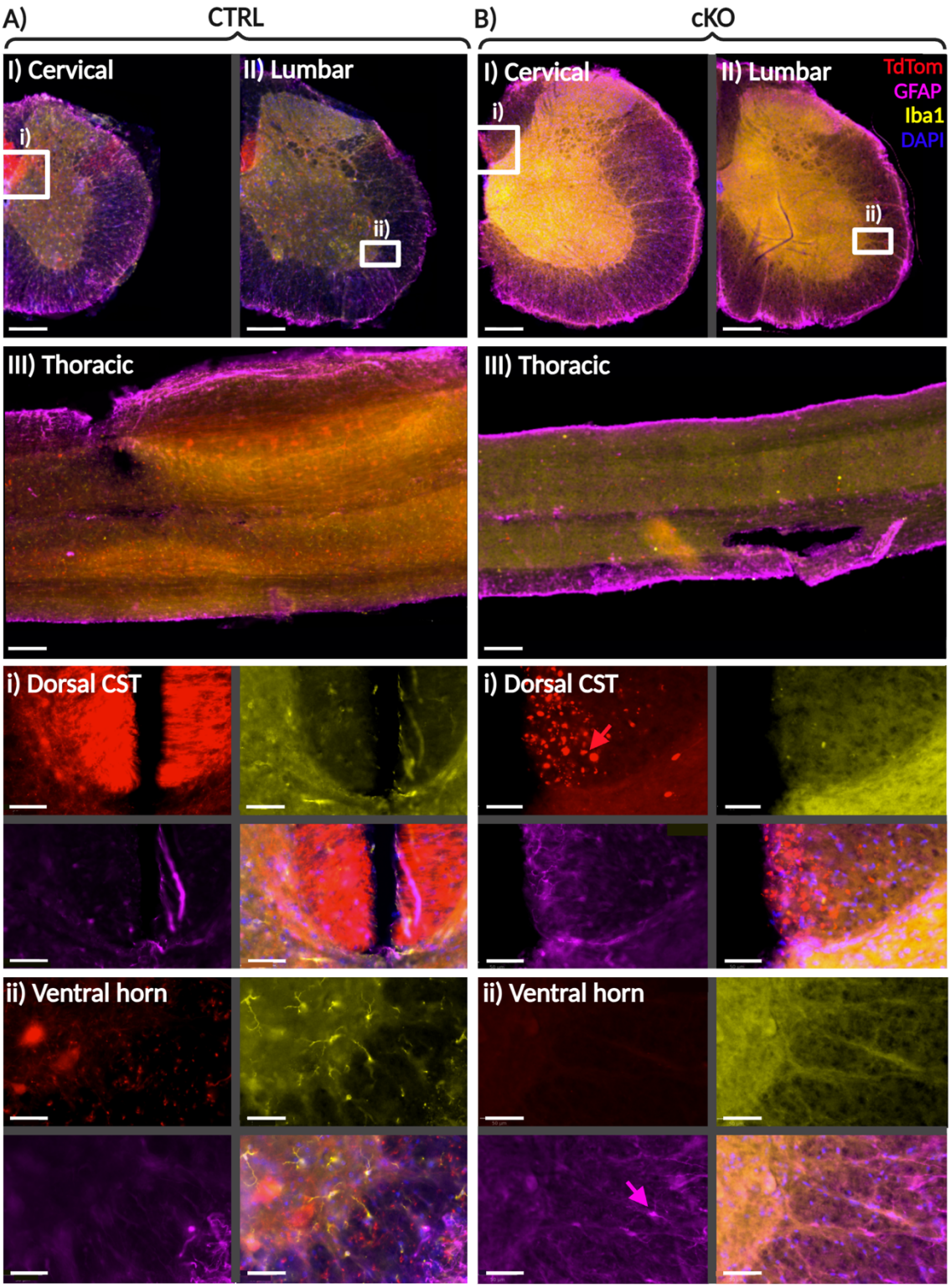


**Figure 71.** Changes in glial expression emerge in the spinal cord at 21wks. Across A) *Rbp4*-Cre$^{+}$;*Snap25*$^{+/-}$ CTRL and B) *Rbp4*-Cre$^{+}$;*Snap25*$^{-/-}$ cKO I) cervical and II) lumbar spinal cord coronal sections and III) thoracic horizontal slices (**Figure 4E#4**), no obvious differences in IBA1 or GFAP expression appear in the i) dorsal-CST or ii) ventral horn of L5-cKOs compared to CTRLs, save increased GFAP in white matter. These stains should be repeated due to what I think were unreliable IBA1 antibodies across cKO histology experiments. Scale bars: I-II) full spinal sections=250µm; i-ii) ROIs=50µm.

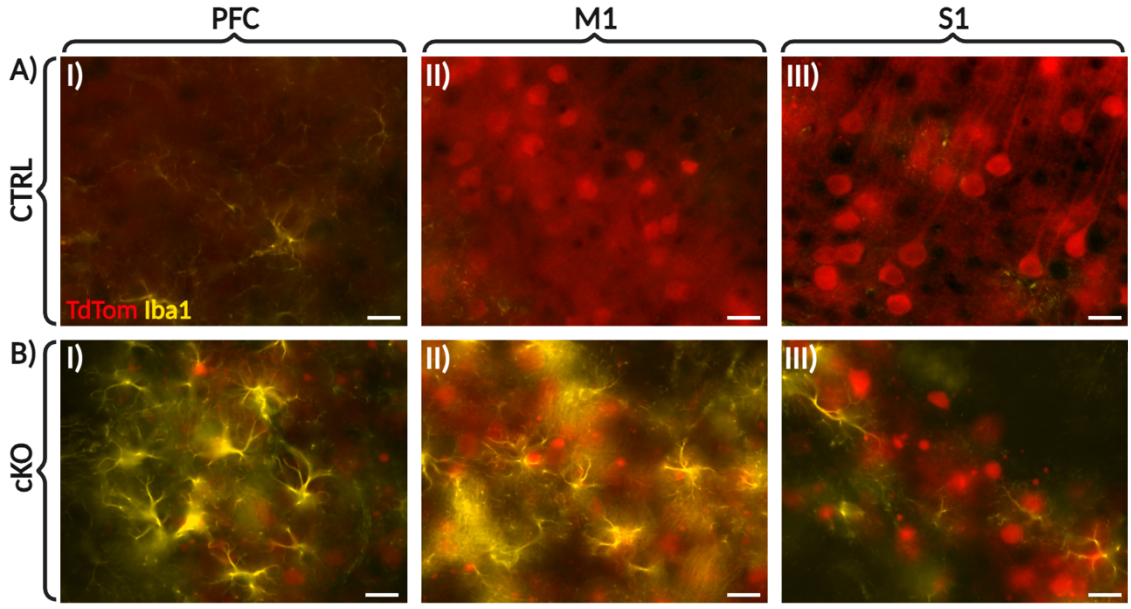


**Figure 72.** Cortical heterogeneity in microglial infiltration emerges upon L5-cKO. A) CTRL and B) L5-cKO I) PFC, II) M1, and III) S1 L5 regions of *Rbp4*-Cre expression are shown, where astrocytes appear to converge to various extents. Scale bars=20µm.

PV/VVA staining then tested whether L5-cKO influences interneuron and perineuronal net density, distribution, and integrity. Interneuron deterioration has been implicated in motor neuron disease progression, specifically in the spinal cord, as has perineural net organisation[447]. In qualitatively observing VVA expression patterns in **4.1.4**, **4.2**, and **4.3.4**, signals appeared most prominent in regions related to motor and somatosensory function. Therefore, whether signs of interneuron or perineural net deficits in these areas emerge–also in the yet-unexplored brainstem and spinal cord near degenerating LMN nuclei (**5.3.2**)—may indicate their involvement as a downstream consequence of *Rbp4*-Cre-driven *Snap25*-cKO.

PV/VVA expression patterns in the cortex and subcortical nuclei did not appear to notably differ between CTRL and L5-cKO mice (**Figure 73**), nor did changes appear in or around projection tracts (**Figure 74**). This does not preclude more subtle changes in morphologies or distributions which may only be detectable with higher-magnification imaging and quantitative analyses (**5.5.3**). This broadly aligns with more extensive published findings[146]. In the spinal cord, however, some $PV^+$ cells appear to show signs of membrane punction and potentially decreased cell densities in L5-cKO mice relative to CTRLs (**Figure 74**).

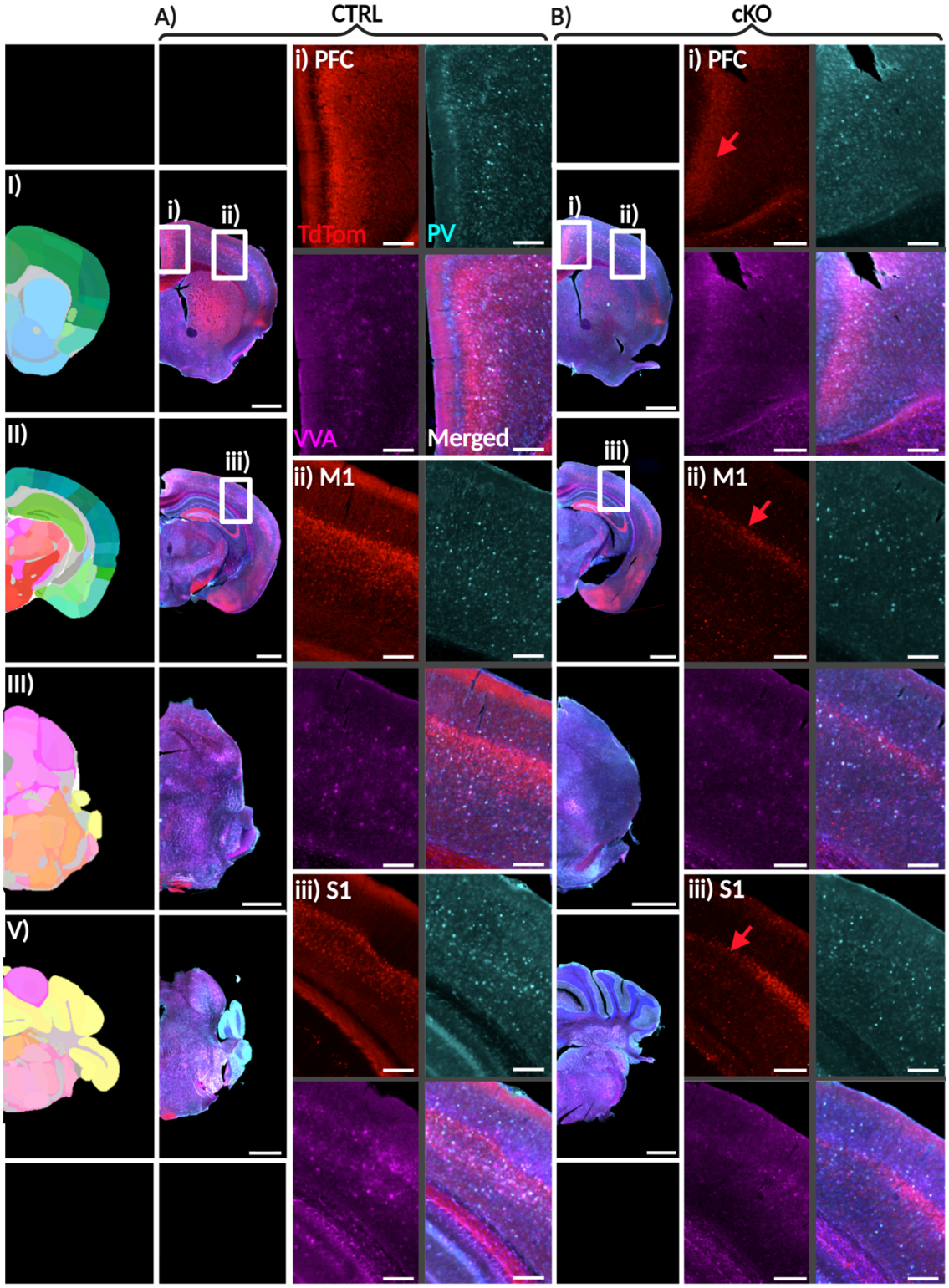


**Figure 73.** No obvious changes in cortical PV/VVA expression emerge at 21wks. Red arrows again highlight patterns of Cre$^{+}$ degeneration across cortical areas. A) *Rbp4*-Cre$^{+}$;*Snap25*$^{+/-}$ CTRL and B) *Rbp4*-Cre$^{+}$;*Snap25*$^{-/-}$ cKO tissues are shown in I-III, V) according to **Figure 4E#5** in the i) PFC, ii) M1, and iii) S1. Scale bars: I-III, V) =1mm; i-iii) =200µm.

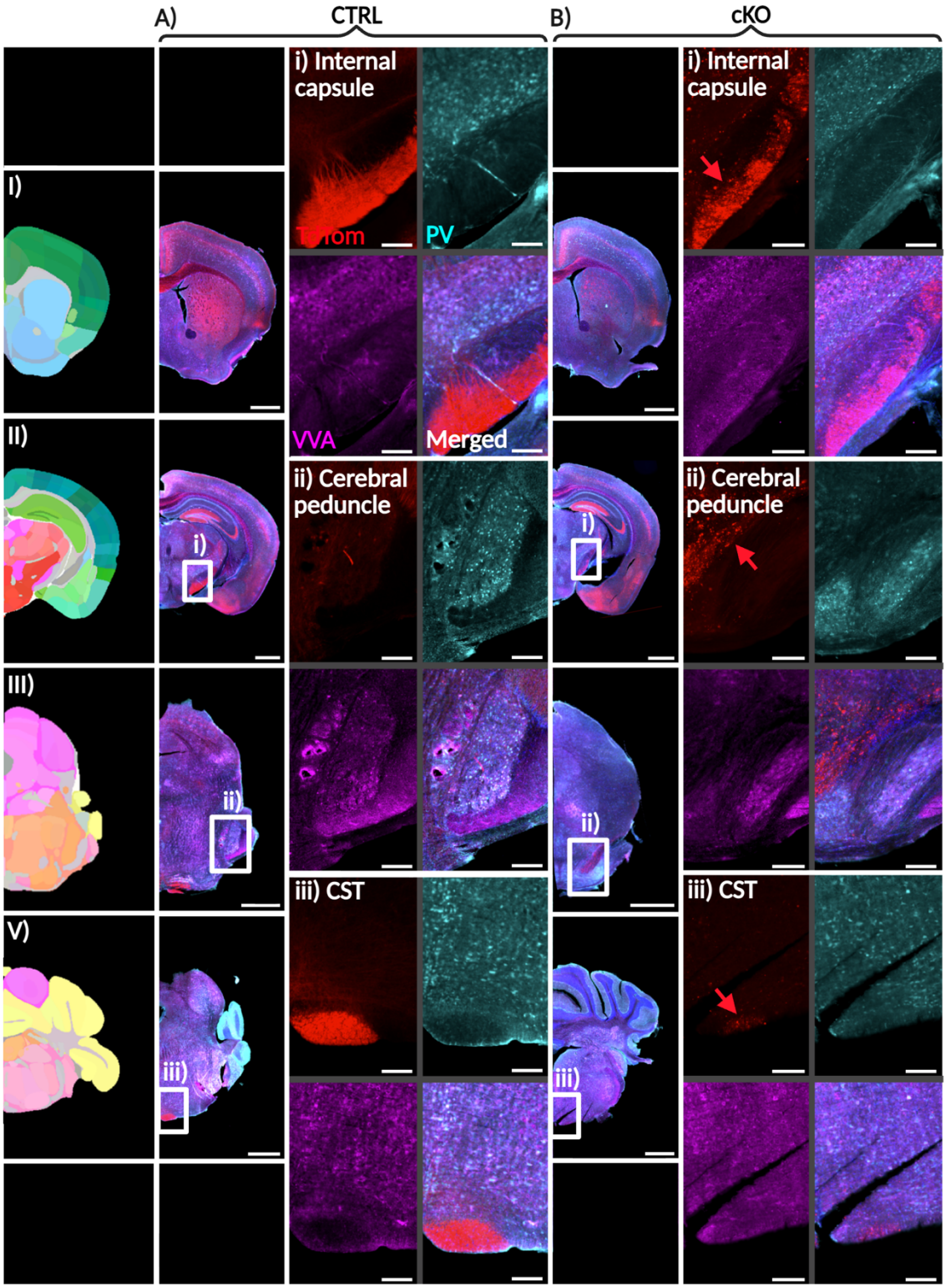


**Figure 74.** No obvious changes in PV/VVA emerge in motor tracts upon *Snap25*-cKO. Red arrows show degeneration in *Rbp4*-Cre$^{+}$ axons. A) *Rbp4*-Cre$^{+}$;*Snap25*$^{+/-}$ CTRL and B) *Rbp4*-Cre$^{+}$;*Snap25*$^{-/-}$ cKO tissues are provided in I-III, V) according to **Figure 4E#5** in the i) internal capsule, ii) cerebral peduncle, and iii) CST. Scale bars: I-III, V) =1mm; i-iii) =200µm.

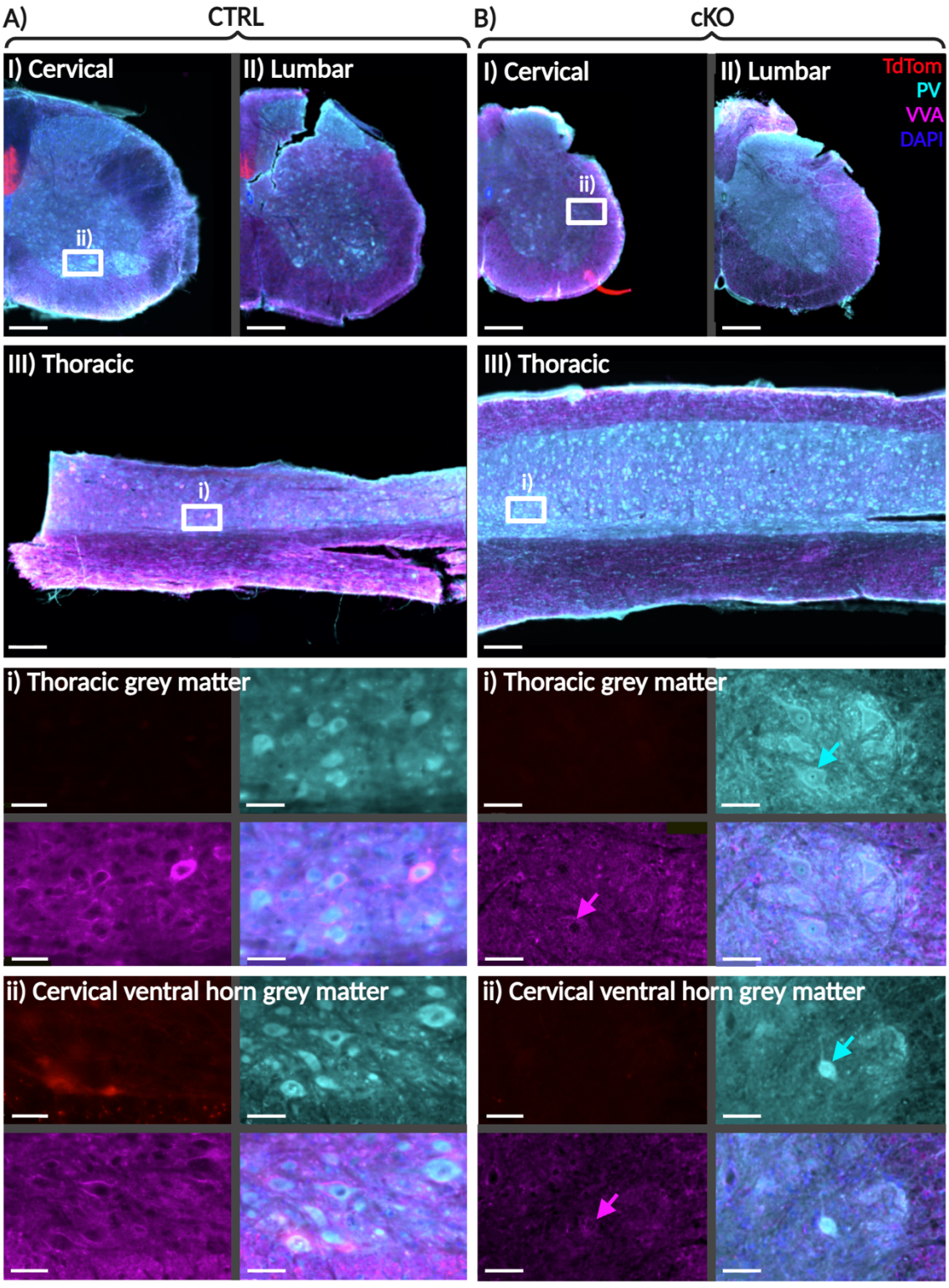


**Figure 75.** Illustrates *Rbp4*-Cre/PV/VVA expression in the spinal cord at 21wks. In grey matter regions of A) *Rbp4*-Cre$^{+}$;*Snap25*$^{+/-}$ CTRL and B) *Rbp4*-Cre$^{+}$;*Snap25*$^{-/-}$ cKO I) cervical and II) lumbar spinal cord coronal sections and III) thoracic horizontal slices (**Figure 4E#5**), PV$^{+}$ interneurons show signs of membrane punctation in L5-cKOs relative to CTRLs. This appears to be accompanied by decreased VVA expression, indicating the possibility of perineuronal net degradation. Scale bars: I-II) full spinal sections=250µm; i-ii) ROIs=50µm.

### *5.3.5 Peripheral expression*

When performing perfusions (**2.3.2**), striking differences emerged in the appearance of L5-cKO internal organs which had not been previously characterised. CTRL anatomy appeared normal, yet cKO organs were pink. **Figure 76A-B** illustrates CTRL and L5-cKO tissues including the liver (**Figure 76I**), duodenum (**Figure 76II**), and pancreas (**Figure 76III**). The presence of TdTom in peripheral organs indicates off-target Cre-expression, where functional consequences are conceivable if *Snap25* is truncated. *Snap25*-cKO can lead to liver impairment, increased insulin secretion from pancreatic beta cells, and metabolic dysfunction[438, 448]. RBP4 is produced in the liver and notably transports vitamin A to the kidney, pancreas, adipose tissue, eye, and skeletal muscles[438, 449], thus broader ramifications of *Rbp4*-Cre cKO may include phenotypes associated with vitamin A deficiency[438, 448-450]. Further experiments (**5.5.4**) should characterise the extent to which off-target expression manifests as this may drastically confound result interpretation.

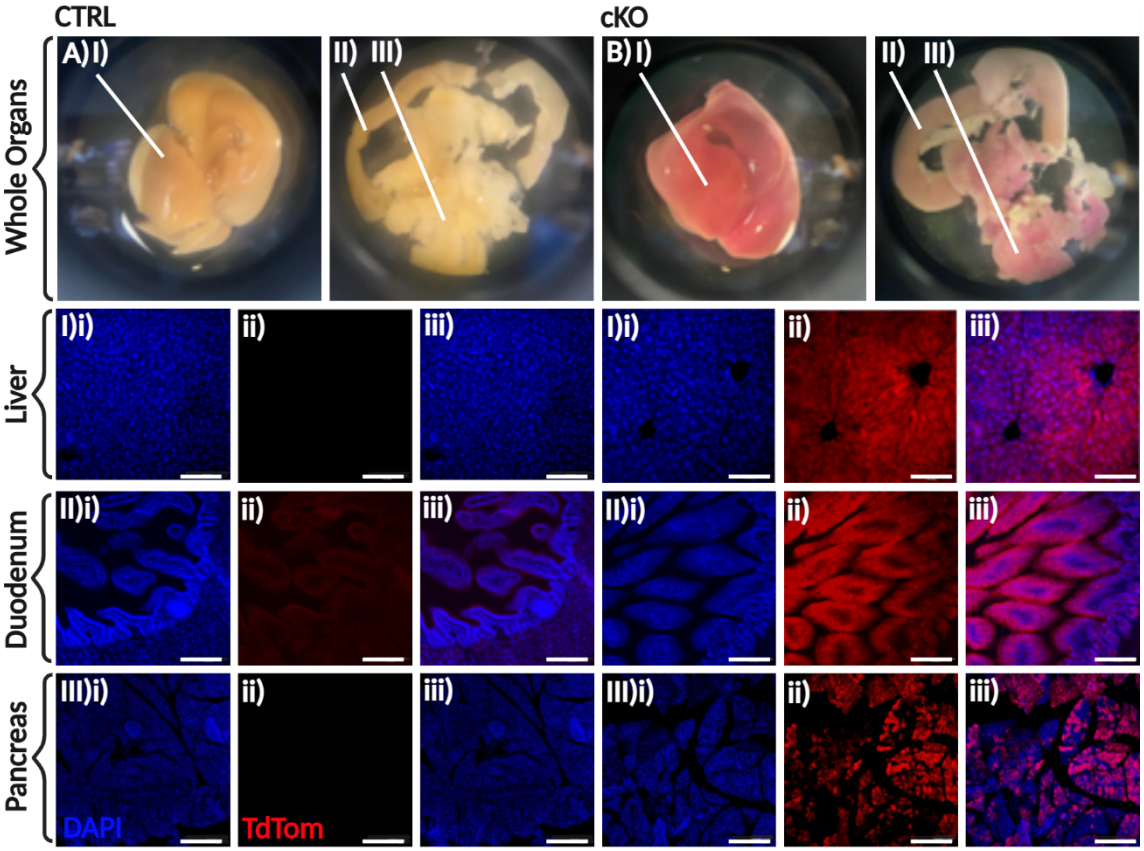


**Figure 76.** *Rbp4*-Cre$^{+}$ expression emerges in peripheral organs at ~21wks. Shows *Rbp4*- A) Cre$^{WT}$ CTRL and B) Cre$^{+}$ *Snap25*-cKO I) liver, II) duodenum, and III) pancreatic tissue. Scale bars=250µm.

## 5.4 Multimodal insight

### *5.4.1 Experimental strategy*

STAMINA combined MRI, histology, and behavioural data to characterise consequences of silencing *Rbp4*-Cre L5-projection neurons. I hypothesised that this would yield progressive behavioural changes due to underlying degeneration in both local (Cre-expressing) and global (downstream target) regions which could be detected by MRI and confirmed histologically. This multimodal framework providesmethodological cross-validation (**Figure 77**). Anatomical results informed neuroimaging, particularly as 2×MGE acquisitions were acquired to resolve cortical layers. *In vivo* and *ex vivo* results informed histology (**5.3**) by corroborating targeting areas I had initially predicted to be affected (i.e., where *Rbp4*-Cre soma and axons, **Figure 2**) and revealing additional ROIs exhibiting genotype differences. Future histology will target the striatum, FOTN vs HOTN, and indusium griseum (**5.4.5**) due to these novel unbiased neuroimaging insights. Yet, here I focus on interpreting results in ROIs selected *a priori* throughout **5.4-5.5** in the context of behavioural, MRI, and histological findings. Considered jointly, my results provide proof-of-concept that behavioural, neuroimaging, and histology data can interactively drive hypotheses and reveal convergent evidence of neuromotor phenotypes. This presents as an improved means of understanding biological underpinnings of diseases using preclinical models.

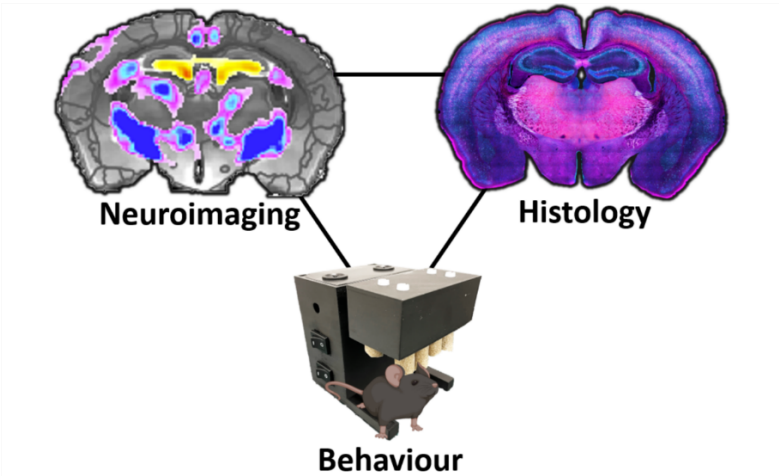


**Figure 77.** Illustrates STAMINA's multimodal experimental strategy. This encompasses complimentary behavioural, neuroimaging, and histological domains.

### *5.4.2 Model characterisation*

Behavioural, neuroimaging, and histological techniques convergently identify and collectively characterise anatomical and functional effects of chronically ablating *Snap25*-dependent cellular mechanisms (namely, regulated synaptic vesicular release) from *Rbp4*-Cre-expressing cells. I summarise known effects of L5-cKO studied to date–including both those previously published and currently presented in this thesis—in **Figure 78**.

*Rbp4*-Cre-driven *Snap25*-cKO resulted in multiple adverse motor-related functional consequences which onset along various trajectories, while some behaviours did not differ compared to CTRLs (**Figure 78A**). Body weights (**Figure 41**) and nesting scores in L5-cKO mice were consistently lower (**Figure 45**) at all ages evaluated throughout STAMINA which aligns with prior reports[77, 114]. At no age did total food intake or the diurnal pattern of food-seeking behaviour differ across genotypes (**Figure 42**), the latter of which is consistent with published findings[114]. However, total activity was slightly and consistently greater in L5-cKO mice compared to CTRLs over time (**Figure 42**), which aligns with previously reported sleep disturbances documented only at ~10-12wks[114]. In contrast, diurnal patterns of food intake in L5-cKOs began to plateau and differ from CTRLs at ~14wks (**A.9.4**), becoming more prominent by 21wks (**Figure 42**), which could be explained by the progressive deterioration of fine motor skills required for regular *SnackerTracker* feeding. Upon further CAMP evaluation, subtle signs of uncoordinated ledge-walking emerged in L5-cKO mice at ~5wks, and hindlimb-clasping at ~7wks (**Figure 43**). More sophisticated CatWalk gait assessments revealed a shift towards the alternate step pattern and decreased cadence in L5-cKO mice at ~5wks, then decreased speed at ~8wks (**Figure 46**). Decreased grip strength in L5-cKO mice only emerged later at ~13wks (**Figure 45**). These behavioural timelines can be directly compared to those which emerged upon analyses of multimodal *in vivo* and *ex vivo* neuroimaging data and histology (**Figure 78B**-**C**).

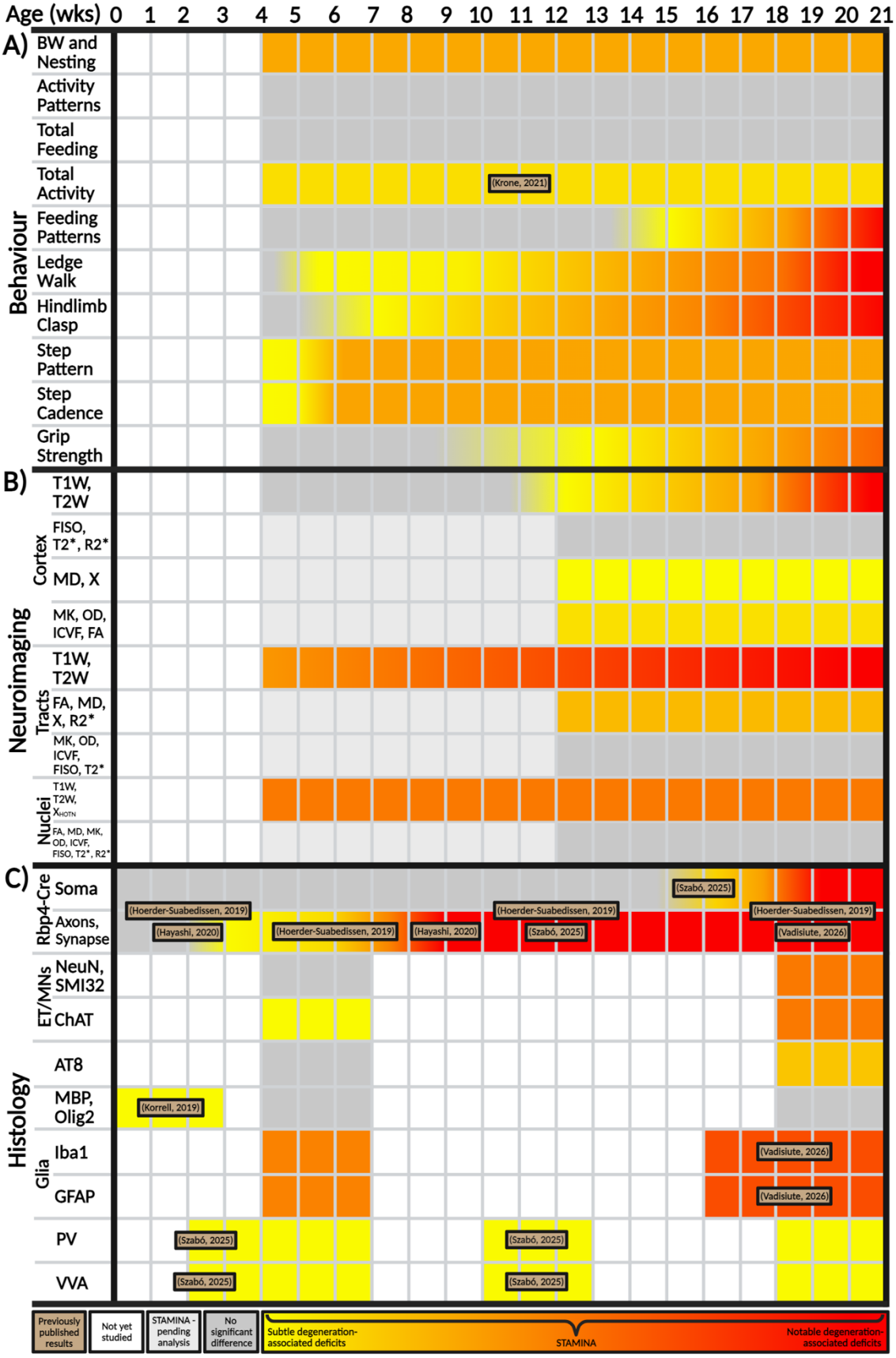


**Figure 78.** *Rbp4*-Cre$^{+}$::*Snap25*$^{fl/fl}$ model characterisation. Summarises previously published and presently reported A) behavioural, B) neuroimaging, and C) histological effects of L5-cKO.

In cortical ROIs where *Rbp4*-Cre$^{+}$ is expected in L5 (i.e., M1, PFC, and S1), T1W/T2W volumes increase over time in CTRLs yet, from ~15wks onward, to a lesser extent in L5-cKO mice (**Figure 48**-**Figure 51**). The time course of genotype differences across *ex vivo* diffusion metrics are currently only observable from 12wks onward given the limited number of samples at younger ages (**5.5.3**); nevertheless, speculations can be derived. While no change in FA or FISO is observable over time (**Figure 52**-**Figure 54**, **Figure 59**), trends towards decreased MD (**Figure 52**-**Figure 53**, **Figure 55**) and increased MK, OD, and ICVF emerge in L5 of L5-cKO mice–notably in prefrontal regions–upon visual inspection of ROI plots and voxelwise maps (**Figure 52**-**Figure 53**, **Figure 56**-**Figure 58**). In motor-related tracts through which *Rbp4*-Cre$^{+}$ axons project (**Figure 62**), T1W/T2W volumes appear smaller in L5-cKO mice as early as ~4wks; both CTRL and L5-cKO volume then increase yet to a lesser extent in L5-cKOs (**Figure 48**-**Figure 51**). L5-cKOs exhibit consistently decreased FA across ~12-21wks (**Figure 52**-**Figure 54**), with no differences emerging across other diffusion metrics (**Figure 52**-**Figure 53**, **Figure 55**-**Figure 59**). Downstream motor-related nuclei exhibit decreased volumes from ~4wks onward (**Figure 48**-**Figure 51**) and no clear changes across diffusion metrics at ~12-21wks (**Figure 52**-**Figure 53**, **Figure 55**-**Figure 59**). QSM results are underpowered for data interpretation; however, sub-threshold voxelwise patterns across T2*, R2*, and susceptibility maps at ~21wks indicate: 1) decreased susceptibility not accompanied by T2* or R2* changes in prefrontal and L5 areas of expected *Rbp4*-Cre$^{+}$ soma expression; 2) increased susceptibility in tracts through which *Rbp4*-Cre$^{+}$ axons project, accompanied by little change in T2* yet a more notable increase in R2*; and 3) decreased susceptibility not accompanied by obvious T2* or R2* differences in HOTN (**Figure 60**).

Histologically, qualitative observations corroborate and expand upon numerous prior studies (**Figure 78C**)[77, 79, 114, 145-147, 405]. Present *Rbp4*-Cre$^{+}$ characterisations indicate NEUN$^{+}$ colocalisation (with no obvious changes NEUN$^{+}$ expression otherwise) and expression across L5 and the dentate gyrus[77], yet critically reveal the presence of soma in the amygdala, cerebellum,

spinal cord, and peripheral organs (**Figure 61**-**Figure 76**). As reported previously, *Rbp4*-Cre$^+$ intratelencephalic and extratelencephalic projections appear to develop normally (**Figure 62**); however, axons begin to show signs of fragmentation at 3wks and disappear by 7wks, which is not accompanied by obvious changes in soma density[77, 145, 146, 405]. Previous work also identified that, while synaptogenesis appears normal from P8 to P14, specialised hypertrophic synapses fail to develop in the posteromedial HOTN by P18[145]. Later, from ~16-21wks, synaptic densities and puncta size in cortical, hippocampal, and colliculi ROIs increase in L5-cKOs compared to CTRLs[405]. As early as ~16wks yet profoundly by ~8mo (indicated in **Figure 78** at 21wks), *Rbp4*-Cre$^+$ soma densities decrease (**Figure 62**) and *Rbp4*-Cre$^+$ axons appear disintegrated in the spinal cord[77, 146, 405]. It remains possible that SMI32 colocalisation may confer selective vulnerability, though further quantitative analyses are needed (**5.5.3**). At ~21wks, fragmented neurites exhibit lipofuscin deposits, autophagosome-like structures, and increased microglial prevalence (**Figure 69**)[77], though more recent work indicates increased IBA1 expression as early as ~16 wks[405]. This recent publication documents changes in glial cell populations in L5-cKO mice compared to CTRLs at ~16-24wks using tissues I provided from the present STAMINA cohort. Analyses were conducted in the primary visual cortex (V1), S1, superior colliculus, and hippocampal CA1 and CA3 to compare effects in areas of *Rbp4*-Cre$^+$ expression to those in both directly- and indirectly targeted downstream ROIs. While notable heterogeneity was observed and is described in detail in the publication[405], general findings are consistent with my qualitative indications in **Figure 69**-**Figure 72**. Here, neuroinflammation emerges most prominently in frontal cortical areas and descending projection tracts (**Figure 69**-**Figure 70**) with microglial morphologies appearing heterogeneous across cortical ROIs upon *Snap25*-cKO (**Figure 72**). In the publication, L5-cKO mice exhibit decreased microglial cell volumes accompanied by increased reactivity with a significant age×genotype interaction upon CD68 co-staining (**A.5.1**)[405]. IBA1 expression was documented throughout spinal cord (**Figure 71**), where densities appeared to decrease non-

preferentially in L5-cKO mice at ~21wks[405]. Similarly, astrocyte densities were consistently greater upon L5-cKO and more reactive upon S100β co-staining over time[405]. Interestingly, astrocyte morphologies were highly variable and clustered distinctly according to genotype and circuit topology upon t-stochastic neighbour embedding analyses; heterogeneity increased over time upon *Snap25*-cKO and was most pronounced in regions of *Rbp4*-Cre$^{+}$ expression[405]. Here, increased GFAP densities emerged most profoundly in frontal cortical ROIs and descending motor tracts (**Figure 69**-**Figure 70**). Unlike microglia, astrocytes were predominantly found in the spinal cord white matter and were significantly more prevalent upon *Rbp4*-Cre-driven *Snap25*-cKO (**Figure 71**)[405]. Further analyses of spinal cord CHAT immunoreactivity revealed no changes in density[405]; however, morphological quantifications and qualitative appearances were not evaluated, nor were midbrain ROI considered, which together indicate selective LMN degeneration in locomotive-associated brainstem and spinal cord nuclei at ~21wks. Additional signs of degeneration emerged upon AT8 staining for pathological tau protein aggregates, where deposits appeared in the cerebral peduncle and sparsely in spinal cord ventral horn grey matter soma by ~21wks. Prior studies have established that myelination exhibits normal spatiotemporal developmental trajectories[451] in both CTRLs and L5-cKO mice, with no notable differences in the pattern or intensity of MBP expression across P8-P22[79]. However, a trend emerged towards decreased node of Ranvier lengths in the corpus callosum at P14, and decreased g-ratios in the dorsal-CST at P18 (**1.3.2**)[79]. No visually obvious differences in PV densities appeared to emerge upon L5-cKO (**Figure 73**-**Figure 74**); however, subtle differences have been previously reported, which present findings do not refute and may simply be unable to discern. These differences include decreased VVA+ only in L2/3 and L5 of M1; increased VVA+ only in L4 of S1; and decreased PV+/VVA- only in M1 L5[146]. Together, these insights provide immense capacity for multimodal comparisons across behavioural, neuroimaging, and histological domains (**Figure 78**).

### *5.4.3 Local degeneration*

Together, behaviour, neuroimaging, and histological insights enable spatiotemporal characterisation of patterns of degeneration in local areas of *Rbp4*-Cre$^+$ expression which may otherwise remain undetected (**Figure 78**). The multimodal strategy employed (**5.4.1**) enhances methodological confidence by revealing parallel trends across independent experiments.

Analyses of *Rbp4*-Cre$^+$ soma expression patterns–which both reflect published reports and reveal additional areas of extracortical soma expression–reflect regions indicated by both *in vivo* and *ex vivo* neuroimaging to selectively exhibit either volumetric increases or decreases upon L5-silencing (**5.2.1**-**5.2.3**) *according to both the timing and severity of histologically observed neurodegeneration* (**5.3.1**). Cortical regions (e.g., M1, PFC, and S1) where *Rbp4*-Cre$^+$ soma are expressed and degenerate by 21wks (**Figure 62**) appear to decrease in volume over time following T1W/T2W analyses (**Figure 48**, **Figure 49**), though voxelwise laminar resolution could not be achieved to discern whether regional decreases were localised to L5. Strikingly, T1W longitudinal trends indicate the emergence of volumetric decreases around ~15ws, which is only one week before the first signs of *Rbp4*-Cre$^+$ soma degeneration have been documented in present literature (**Figure 78B-C**). In white matter projection tracts, T1W/T2W show volumetric decreases even at the earliest ~4wk timepoint, which aligns with the histologically-reported first signs of axon degeneration (**Figure 78B-C**). T1W/T2W analyses also indicated volumetric increases in the dentate gyrus (**Figure 48**-**Figure 51**) where *Rbp4*-Cre$^+$ expression had been previously documented[77]. This is reflected in **Figure 62** where, notably, no degeneration is obvious at 21wks. Voxelwise maps interestingly indicated volumetric increases in the amygdala and cerebellum (**Figure 50B**), which prompted me to consider whether *Rbp4*-Cre$^+$ soma are expressed in this previously uncharted territory. I indeed found this to be the case (**Figure 62**). As in the dentate gyrus, *Rbp4*-Cre$^+$ neurons in the amygdala and cerebellum do not appear to degenerate (**Figure 62**). This critically indicates that both *ex vivo* and *in vivo* neuroimaging may

be sensitive to cell-specific genetic manipulations. Neuroimaging blindly drove the identification of extracortical *Rbp4*-Cre$^{+}$ expression in the amygdala and cerebellum and appears to indicate whether cells degenerate (i.e., volumetric decreases where soma degenerate, and volumetric increases where soma do not). Volumetric decreases were also observed in areas lacking *Rbp4*-Cre$^{+}$ soma, however these strikingly corresponded to motor-associated nuclei and projection tracts where further insight is gleaned upon *ex vivo* diffusion and quantitative analyses.

*Rbp4*-Cre-expressing cortical areas exhibit nonsignificant trends–exclusively observable in voxelwise maps–towards decreased MD and X yet increased FA, MK, OD, and ICVF (**5.2.4**-**5.2.5**). This could be due to combinations of several possible explanations. MD, FA, and X trends could suggest increased myelination in non-degenerating axons; while I saw no notable changes in MBP (**Figure 67**-**Figure 68**), subtle yet functionally significant differences would likely not be observable simply by qualitative assessment of SSFM-obtained images (rather requiring higher-resolution confocal imaging and quantitative analyses)[79]. Yet, differences in myelination would not alone explain prefrontal MK, ICVF, and OD patterns which could alternatively be attributed to neuroinflammation. Histological findings support this notion, where striking increases in microglial and astrocyte infiltration throughout the cortex emerge particularly in prefrontal regions (**Figure 69**, **Figure 72**). Astrocytes may specifically contribute to these MRI signatures given their markedly increased prevalence upon L5-silencing, capacity to adopt highly complex and heterogeneous morphologies upon *Rbp4*-Cre-driven *Snap25*-cKO, and capacity for heterogeneity to spatiotemporally amplify (**Figure 71**-**Figure 72**)[405]. This is relatable to MK, OD, and ICVF, which were initially hypothesised to decrease due to *Rbp4*-Cre degeneration (**5.2.4**). Increased MK suggests greater tissue complexity, cellularity (corroborated by ICVF), and heterogeneity driving non-Gaussian signal decay. Increased OD indicates higher degrees of randomly orientated neurite branching. All the above is consistent with astrocyte histology (**Figure 71**-**Figure 72**)[405]. More prominent differences in microglial in older L5-silenced mice

could be due to immune cells exhibiting increased sensitivity to effects of *Snap25*-cKO with age[405], or reacting proportionally to infarct severity over time. Volumetric increases in *Rbp4*-Cre-expressing regions lacking degeneration (e.g., the dentate gyrus) appear to be accompanied by similar patterns in MD, OD, and ICVF. Neuroinflammation could similarly explain this trend. Initially, I hypothesised that conceivable volumetric increases could be explained at least in part by extracellular edema; however, a lack of decrease in FISO supports glial explanations.

The most prominent effect across diffusion metrics presented in the major descending motor tracts through which *Rbp4*-Cre$^+$ axons project—notably, the CST and internal capsule—where FA decreased significantly (**Figure 52**-**Figure 54**). Decreased anisotropy, or increased isotropy, indicates white matter disorganisation in L5-cKOs relative to CTRLs which may directly correspond with *Rbp4*-Cre$^+$ axon degeneration (**Figure 62**). In these same tracts, alongside volumetric decreases, subtle nonsignificant trends indicated decreased X and R2*, but only slightly increased T2* (**Figure 60**). This suggests the possibility of pathological iron accumulation over alternative explanations of decreased calcium deposition or demyelination due to the inverted and skewed nature of T2* signal, where paramagnetic tissues show fast susceptibility-induced signal decay; differences reported by T2* maps are proportionally smaller than R2* maps (**5.2.5**). Interestingly, iron accumulation has been linked to AT8 aggregation as a cofactor promoting protein hyperphosphorylation, neurofibrillary tangle formation, and pathological accumulation[452]. Indeed, qualitative histological finding indicate AT8 expression prominently in the cerebral peduncles, and more subtly in the dorsal-CST (**Figure 67**-**Figure 68**).

Together, these motor-degenerative indications are relevant in determining 1) the human disorders which the phenotypes presented by this mouse model may resemble (**5.5.1**), 2) the underlying cell populations deemed responsible via targeted *Rbp4*-Cre *Snap25*-cKO, and 3) the multimodal methodological ramifications which indicate that MRI can uncover subtle histologically-confirmed biological insights (**Figure 78**).

### *5.4.4 Downstream degeneration*

While no regional or voxelwise DWI metrics reveal changes in motor-related subcortical nuclei (**Figure 52**-**Figure 53**, **Figure 2**), T1W/T2W signatures identify interesting thalamic distinctions (**Figure 48**, **Figure 50**). In the thalamus, volumetric decreases emerge across HOTN only upon voxelwise T1W analyses; however, following FDR corrections both in T1W and T2W maps, differences appear to further converge in the ventromedial nucleus (**Figure 48C,F** and **Figure 50C,F**). Critically, the ventromedial nucleus is commonly termed the 'motor thalamus'; it is responsible for relaying information from basal ganglia to M1, enabling sensorimotor integration and mediating feed-forward inhibition from the PFC[453]. Further signs of increased FA in the ventromedial thalamus are shown in **Figure 53AI** and **Figure 54BIV**. Decreased T1W/T2W yet increased FA may seem paradoxical yet can be explained by selective axon degeneration (i.e., if smaller or less-myelinated fibres degenerate, resulting in volume loss yet consolidated anisotropy) or crossing tracts (i.e., if white matter pathways cross, yet one degenerates selectively, volume would decrease and FA would increase)[454]. I will revisit the potential disease relevance of this in **5.5.1**.

### *5.4.5 A note out of interest*

This STAMINA dataset now serves as a resource for future follow-up investigations. I have now imaged and archived all histology slides (**2.3.2**) if higher-resolution images and analyses are to be conducted in the future. Additional brain, spinal cord, and peripheral tissues remain available in storge for both exploratory and targeted follow-up analyses. One such follow-up experiment relates to my prior observation of VVA expression in the insudeum griseum and fasciola cinerea in **4.5.3**. **Figure 79** illustrates regionally overlapping VVA expression patterns, *OrxR*-in situ hybridisation (**A.5.9**)[93], and MRI-derived metrics which question historical opinions deeming the insudeum griseum and fasciola cinerea vestigial structures[428].

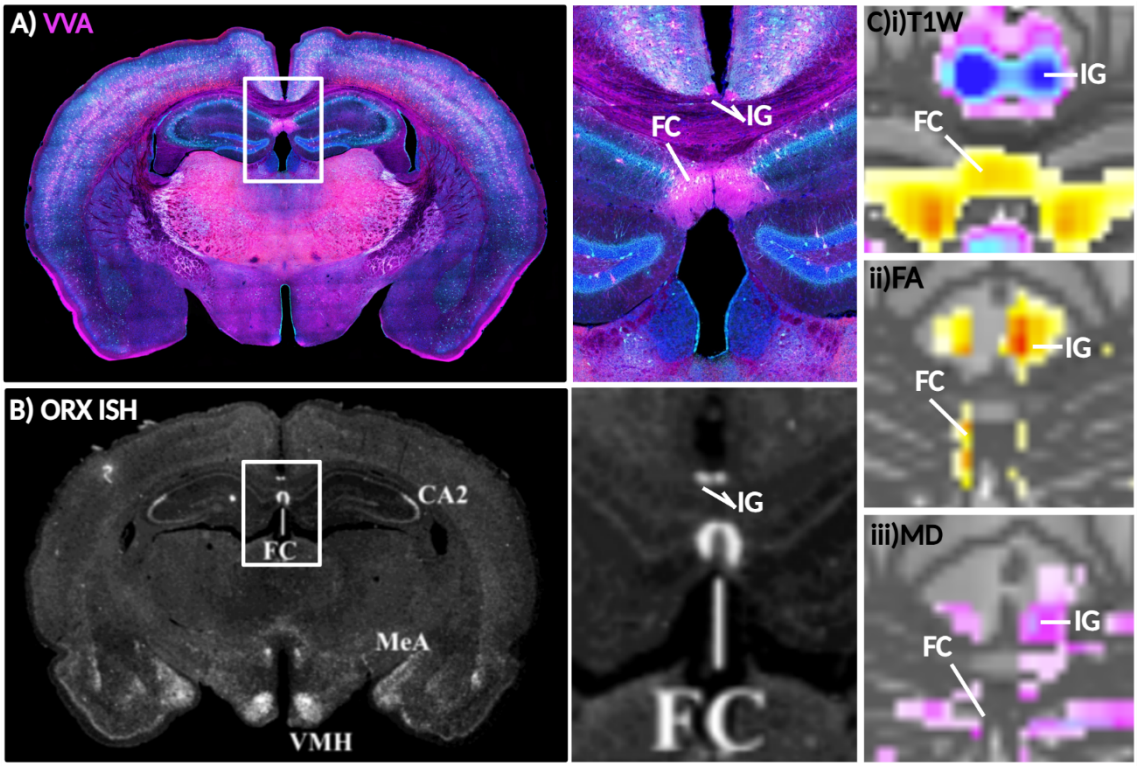


**Figure 79.** Exploratory insudeum griseum (IG) and fasciola cinerea (FC) illustration. A) VVA express appears localised to both the IG and FC, as does B) *OrxR1* in situ hybridisation[93]. C) Using cropped images from the STAMINA dataset, differences in i) T1W, ii) FA, and iii) MD appear to emerge in regions aligning with the FC and IG.

## 5.5 Indications and future directions

### *5.5.1 Motor neuron degeneration*

Results strongly suggest that chronically silencing L5 neurons induces a cascade of progressive degenerative changes affecting both cortical and L5-projection regions–including motor-associated projection tracts and nuclei (**Figure 2**)–corroborating a top-down cortical contribution to motor system integrity. In the context of human degenerative conditions associated with motor neuron dysfunction (**1.3.4**-**1.3.5**), the phenotypes revealed upon *Rbp4*-Cre-driven *Snap25*-cKO across multiple experimental modalities resemble comorbid features of FTD and ALS, or ALS-FTD as a distinctly defined disease[162, 187, 190-194, 455-458]. Similarities between findings in this thesis and clinical presentations of ALS-FTD include: L5b extratelencephalic-pyramidal tract neuron deterioration particularly in the frontal cortex (**5.3.1**)[187, 188, 455-457]; a

putatively cortical origin, then conceivably accompanied by peripheral influences (**5.4.2**)[77, 160-162, 190-192, 196, 232-236]; degeneration in both LMNs and UMNs (**5.3.1**-**5.3.2**)[190-194]; highly specific degeneration in only a subset of lower motor nuclei, excluding extraocular and pelvic sphincter nuclei (**5.3.2**)[196, 233, 246]; pathological protein aggregates including TDP-43 and hyperphosphorylated tau (AT8) in the axons of spinal cord MNs (**5.3.3**)[187, 188, 191, 193]; increased neuron progenitor proliferation and differentiation in the subventricular zone accompanied by volumetric increases (**5.2.1**)[459, 460]; neuroinflammation (**5.3.4**), including astrocyte complexity[244, 247, 405, 461]; increased microglial activation[191, 245, 405, 461, 462]; perineuronal net plasticity and reorganisation[146, 461]; $PV^{+}/VVA^{-}$ neuron deterioration and reorganisation (**5.3.4**)[146, 462]; prefrontal cortical volumetric reductions (**5.2.1**, **5.2.3**)[462, 463]; signs of thalamic atrophy (**5.2.1**, **5.2.3**)[464]; motor decline with age (**5.1**)[77, 160, 162, 191-194, 247, 248, 458]; activity and sleep disturbance (**5.1.1**)[114, 465, 466]; decreased FA in motor-associated corticospinal projection tracts reflecting functional deficits, which has been indicated as capable of clinically evaluating degrees of UMN impairment in ALS (**5.2**, **5.3.1**)[442, 463, 467]; and susceptibility-R2*-indicated and histologically-corroborated indications of iron accumulation in motor-associated tracts, which is also posited as a potential future biomarker and clinical indicate of early disease presentation (**5.2.5**, **5.3.3**)[315, 468]; and–notably–globus pallidus, thalamic, and striatal atrophy identified by both neuroimaging and histological techniques which is suggested to differentiate ALS-FTD from 1) FTD without motor decline, 2) behavioural-variant FTD, and 3) ALS lacking cognitive impairment (**5.2**-**5.4**)[457, 467]. Collectively, while anatomical regions corresponding to major motor tracts (**Figure 2**) appear to show signs of degeneration upon *Rbp4*-Cre-driven *Snap25*-cKO (**5.2**-**5.3**), present multimodal findings considered in the context of this literature are perhaps more anatomically and functionally consistent with the degeneration of a broader integrative network involving prefrontal corticothalamic-thalamocortical loops, basal ganglia, and descending motor pathways. Critically, my results do not definitively suggest that this *Rbp4*-Cre line may be

deemed a mouse model of ALS-FTD: rather, I argue that behavioural phenotypes which emerge upon *Rbp4*-Cre-driven *Snap25*-cKO resemble aspects of human disease presentations; that present neuroimaging and histological signatures are consistent with preclinical, clinical, and postmortem indications in present literature; and that further research is warranted.

### *5.5.2 The seemingly contradictory notion of hyperexcitability*

A flaw in comparing *Rbp4*-Cre-driven *Snap25*-cKO to ALS models emerges in that L5 glutamatergic *hyperexcitability* is typically associated with degeneration in ALS-FTD—not *silencing/hypoexcitability*[160, 187, 190-192, 196, 232, 244]. However, an alternative perspective may reconcile this contradiction. *Snap25*-cKO only abolishes neurotransmission induced by *regulated* presynaptic vesicle release; cells maintain capacity for neurotransmission via *spontaneous* miniature excitatory postsynaptic currents (mEPSCs)[77, 80, 145]. While prior work has operationally deemed *Rbp4*-Cre *Snap25*-cKO mice functionally 'silenced' (therefore I maintained this term throughout this thesis), this may not be fully true. *Rbp4*-Cre *Snap25*-cKO does not preclude the possibility that, due to abolished regulated neurotransmission, compensatory increases in mEPSCs render neurons *hyperexcitatory*. Consistent with this, previous work has suggested that "excessive spontaneous synaptic excitatory neurotransmission in [M1] is correlated with dendritic regression of [L5 pyramidal neurons] before neuronal death and other ALS-like symptoms"[192]. This may be relevant to the first study[79] to follow the initial characterisation of the *Rbp4*-Cre$^{+}$;*Snap25*$^{fl/fl}$;Ai14$^{fl/fl}$ line[77], which reported decreased callosal node of Ranvier lengths. The authors reason that whether counteracts L5-cKO axon hypoexcitability by reducing action potential firing thresholds, or provokes failure where nodes are excessively close, remains indiscernible[148, 149]. However, both phenomena are plausible: perhaps node of Ranvier lengths initially decrease and lower firing thresholds; neurons then become increasingly capable of eliciting mEPSCs; hyperexcitability thereafter leads to excitatory neurotoxicity; neurites then disintegrate, and soma degeneration follows. mEPSCs-induced excitatory neurotoxicity is a

documented phenomenon where, in cases of chronic action potential abolition following injury, mEPSCs can increase in amplitude and trigger NMDA-receptor-mediated apoptotic pathways (prototypically linked to ALS-FTD)[469-471]. Excitotoxic mEPSCs have been specifically shown to trigger neuroinflammatory astrocyte responses[470], which then accelerate neurodegenerative processes; this is consistent with present histological and MRI findings (**5.2.4**-**5.2.5**, **5.3.4**, **5.4**). My alternative hypothesis is merely speculative and I think would be interesting to test (**5.5.4**).

### *5.5.3 Limitations and ongoing analyses*

Several notable limitations limit the interpretation of STAMINA results and analyses. While data from behavioural experiments were blinded and assessed by another researcher whenever possible (i.e., for nesting scores, all CAMP assessments, and CatWalk analyses) (**2.4**, **5.1**), I was not blinded while collecting the data itself. Unintentional bias is therefore possible. Particularly across histological and neuroimaging domains, $N_E$ is insufficient to spatiotemporally resolve trajectories of changes in cellular densities (i.e., *Rbp4*-Cre+ soma, CHAT, AT8, IBA1, and GFAP) or MRI signatures (i.e., *ex vivo* T2W, DWI, and QSM) which entirely lack data of sufficient quality <8wks (**5.2.3**-**5.2.5**, **A.2**). While it would have been ideal to simply collect more *in vivo* and *ex vivo* data, prohibitive ethical (i.e., minding the 3Rs)[276, 472], financial (i.e., high associated experimental costs), and time considerations (i.e., both in breeding new mice and my physical capacity to conduct experiments in ≤24 simultaneously, **A.4.4**) prevented higher *in vivo* and *ex vivo* $N_E$ throughout the STAMINA timeline (**Figure 4**). I strategically selected MRI timepoints according to expected neuroanatomical and functional genotype differences (**Figure 4**, **Figure 78**)[77, 79, 114, 145-147, 405]; however, these foundational studies are themselves spatiotemporally limited. Further investigations to improve temporal resolution would prove insightful particularly in relating the timing of the emergence of changes in MRI-derived metrics to the those of behavioural and cellular characteristics. Analyses are presently underpowered to ascertain the statistical significance of changes at younger timepoints and age×genotype

interactions, despite the clear emergence of trends towards both. Histologically, I acquired data from each of two cohorts–4-7wks and 18-21wks–yet only present the latter here due to time constraints. I intended to analyse all histology data using r-QUINT as in **4.1** and **4.3**, however this proved overly ambitious due to the large number of sections stained (i.e., ≈3280 for STAMINA alone). MBP and AT8 analyses will require special handling as r-QUINT is currently optimised for soma detection and regionalisation; this could involve intensity-based MBP thresholding, AT8 particle-counting (whether obtained via QuPath detections or intensity-based thresholding), and AT8 white matter vs grey matter allocation according to MBP masking. Therefore, while I only include qualitative observations from ~21wk mice in **5.3**, such future quantitative analyses will enable correlations between the histological, behavioural, and neuroimaging-derived ramifications of *Rbp4*-Cre-driven *Snap25*-cKO. Additional future analyses include that of resting-state fMRI data (e.g., via RABIES, **2.5.3.5**)[317] and tractography (e.g., via *probtrackx*[301, 473] using outputs of *bedpostx*[311] preprocessing, **2.5.3.3**), which will be particularly useful in discerning progressive deterioration in motor-related pathways (**5.5.1**). Analysis discrepancy presents in the use of Akaike vs Bayesian statistical model selection (**2.5.5.3**) as voxelwise analyses cannot accommodate GAMs. Therefore, where Akaike/Bayesian information criteria dictate regional GAM analyses, voxelwise processing remains linear rendering comparisons between voxelwise and regional maps–which are currently attributed to voxel-averaging across atlas-defined regions (**5.2.1**)–potentially confounded by statistical model selection (**Figure 54**-**Figure 59**). Both factors likely contribute to differences observed. Nevertheless, considering both regional and voxelwise maps proved useful throughout **5.2**. T1W, T2W, and DWI analyses employed an updated .Rmd script which removes outliers and integrates Akaike/Bayesian model selection (**2.5.5.2**), yet I have not yet used this to re-run QSM analyses. Regional QSM results therefore appear highly skewed, particularly given the small $N_E$ at younger ages due to data exclusion upon quality control checks (**A.7.2-A.7.7**). Despite this, voxelwise signs of susceptibility-induced

differences nevertheless emerge and are discussed for exploratory merits (**5.2.5**). To address limitations due to $N_E$, I recently perfused an additional $N_E$=6 *Rbp4*-Cre$^{WT}$ CTRL and $N_E$=6 *Rbp4*-Cre$^{+}$ *Snap25*-cKO mice aged ~4-6wks for *ex vivo* scanning and histology. All experiments are now complete, yet analyses remain an active future direction such that this <7wk dataset can be integrated with present STAMINA results.

### *5.5.4 Future experiments*

Additional electrophysiological, histological, morphological, metabolic, and spatial transcriptomic experiments would provide further insight into the results presently observed. Electrophysiologically, obtaining single-cell patch-clamp recordings from *Rbp4*-Cre$^{+}$ neurons could discern whether mEPSCs indeed increase upon *Snap25*-cKO (**5.5.2**). This could involve a whole-cell voltage-clamp setup, fresh cortical tissue (i.e., the PFC, where neuroimaging results indicated the greatest differences), and tetrodotoxin application to block regulated inputs. Resulting recordings could be observed and analysed to evaluate conceivable genotype differences in the frequency (proportional to the number of functional synapses) or amplitude (proportional to postsynaptic cell receptor prevalence or neurotransmitter sensitivity) of mEPSCs, expectedly around ~7-30pA[474]. Further histological investigations should involve higher-resolution imaging and analyses of astrocytes and microglia specifically in the PFC and M1–including multidimensional assessments of glial complexity resembling that which was conducted in V1 and S1[405]–for targeted comparison to regional neuroimaging signatures (**5.2.4**, **5.2.5**, **5.3.4**, **5.4.3**, **5.5.2**). Simply out of interest, DiI crystals should be inserted into the area of the insudeum griseum and fasciola cinerea to determine projection patterns and inform possible future directions (**A.8.6**). Future research should explore the underlying mechanisms by which cortical silencing initiates degeneration, and test whether restoring cortical activity can mitigate motor decline. Phenotype rescue could theoretically be attempted via viral delivery of *Snap25* genes with functional exons a-b into L5-cKO neurons, which has been shown to restore stimulus-

evoked neurotransmitter release and prevent axon degeneration[475, 476]. Other silencing modalities could be tested (e.g., Kir2.1 electroporation, *Munc13*-cKO, or tamoxifen-inducible *Fezf2*-Cre$^{ER}$) to evaluate whether similar phenotypes emerge. Electrophysiological and behavioural *Fezf2*-Cre$^{ER}$ studies are currently underway to characterise this alternative L5-cKO model, which lacks off-target dentate gyrus expression and is notably inducible. Parallel to *Rbp4*-Cre histology, I conducted the same combination of immunohistochemistry experiments using a complete cohort of Fezf2-Cre$^{ER}$ tissues, yet have only partially analysed the results (**A.8.5**). More extensive characterisations should be conducted across models to systematically evaluate off-target expression–particularly in skeletal muscles, which have been previously documented in some *Rbp4*-Cre lines[438, 449]–which could mislead present interpretations (**5.3.5**). Physiological consequences of off-target expression could be tested by measuring average blood glucose and blood insulin levels in CRTL and L5-cKO animals, which may indicate regarding whether *Rbp4*-Cre$^{+}$ expression results in functional impairment more directly associated with *Snap25*-cKO in the liver or pancreas. Conceivably, *Rbp4*-Cre-driven *Snap25* truncation in the pancreas could lead to increased insulin secretion[438, 448], which alone may explain increased food-seeking behaviour (**5.1.1**) and sleep disruptions[114]. Spatial transcriptomic experiments have been conducted using coronal sections from both *Drd1a*-Cre and *Rbp4*-Cre lines, in collaboration with Dr. Chiaki Ohtaka-Maruyama at the Tokyo Metropolitan Institute of Medical Science, using sections at the level of HOTN (Xenium, with the standard 300+ genes). Analyses will compliment histological and neuroimaging datasets yet are beyond the scope of this present thesis. This may provide further insight into the single-cell properties of *Rbp4*-Cre$^{+}$ neurons[455, 456] (e.g., in the PFC compared to other cortical regions, then to non-degenerating dentate gyrus, cerebellar, and amygdalar *Rbp4*-Cre-expressing cells) and downstream projection targets (e.g., LMN subpopulations) and conceivable differences between CTRL and L5-cKO cells. However, incorporating spatial transcriptomics holds greater methodological relevance.

### *5.5.5 MRI-histology insights*

My findings throughout STAMINA contributed to a Wellcome Bioimaging grant application, which proposed developing *in vivo* MRI technology to achieve cell-specificity. A major component of this project involves "combining high resolution diffusion and quantitative MRI with 2D and 3D microscopy and spatial transcriptomics to generate models that can predict cell distribution". By characterising the behavioural, neuroimaging, and histological effects of *Rbp4*-Cre-driven *Snap25*-cKO, my results in this chapter provide proof-of-concept that MRI can detect network-level differences which emerge due to targeted cell manipulations. In then presenting a model in which we know when and where specific and highly diverse cellular differences are expected to emerge, and how behaviour deteriorates accordingly, newly developed MRI sequences can be tested to evaluate the accuracy and specificity of cell density and morphology predictions. The ability to distinguish cell-subtypes *in vivo* would have tremendous experimental relevance in enabling whole-brain anatomical investigations over time at a level currently only obtainable via histological processing, which obviously lacks capacity for repeated measures. Eventually, these sequences will be tested in postmortem human tissues to determine translatability to clinical applications with immense potential: consider the capacity to detect cancerous masses in the brain or elsewhere without the need for biopsy; to monitor glial-subtype-specific responses to therapies; to diagnose autoimmune conditions solely via *in vivo* cellular signatures; to cellularly track degrees of graft integration with host tissue; to identify early brain changes associated with neurodegenerative diseases, enabling earlier therapeutic interventions; and to offer all the above without the need for radiation. This project grant was awarded in March. I greatly anticipate joining the team, having accepted a postdoctoral position, and to contributing to this work in the years to come.

# Conclusions

## Behavioural home-cage monitoring

Chapter 3 introduces the *SnackerTracker-TracKIT* platform and tests its capacity to continuously measure and analyse mouse food intake, feeding behaviour, and ambient cage lighting (**3.1**). Operational and processing software accommodate a range of data collection and filtering options according to user-specifications (**3.2**). Validations indicate *SnackerTracker* precision over time across benchtop (**3.1.5**) and *in vivo* applications (**3.3**). Experiments using mice with known circadian differences demonstrate the *SnackerTracker's* ability to record and reveal biologically relevant behaviours, identifying light suppression of food intake in CTRL but not arrhythmic mice and detecting ultradian rhythms in the control of feeding behaviour (**3.3.1**-**3.3.3**). Advantages of using *SnackerTrackers* with parallel DVC, PIR, and video-based systems are demonstrated (**3.3.1**-**3.3.4**), which further reveal phase-delayed behavioural patterns under DLE conditions (**3.3.4**) and compatibility in HCs of other laboratory rodents (e.g., hamsters) (**3.3.5**). Inherent limitations and design considerations stress the importance of thorough methodological documentation and continued platform improvement (**3.4**) for use across a range of future HCM applications (**3.5**). All material information, 3D-printable files, electronics schematics, construction details, and operational/analysis software are provided on open-access platforms such that researchers can download, customise, and build *SnackerTrackers* according to future experiment-specific requirements (**A.3**). The ability of the *SnackerTracker* to reveal subtle biological differences, alongside its low-cost and ease-of-operation, demonstrates its usefulness as a methodological contribution to the field of animal HCM.

## Layer 6b: Characterising subplate remnant neuroanatomy

Chapter 4 proposes refinements to the QUINT image analysis pipeline, uses this method to characterise cellular densities and distributions of cortical L6b neuron subtypes upon *Drd1a*-

Cre-driven genetic augmentation (i.e., PTEN-cKO) and silencing (i.e., *Snap25*-cKO), and provides morphological comparisons supporting the analogy of mouse L6b cells and human WMIN subplate remnants. After introducing QUINT pipeline modifications enabling fluorophore multiplexing and morphometric tagging (**4.1.1**-**4.1.3**), the resulting workflow is tested against prior datasets to support detection and regionalisation validity (**4.1.4**-**4.1.5, 4.3.4**). Pilot experimental applications using excitatory and inhibitory DREADD mouse lines identify subtle changes in PV/VVA densities and distributions, suggesting capacity for rapid activity-dependent interactions between neuron networks, interneurons, and perineuronal nets (**4.2**). Upon confirming expected laminar cell expression patterns (**4.3.1**), the r-QUINT pipeline demonstrates only subtle differences upon *Drd1a*-Cre-driven *Snap25*-cKO. However, PTEN-cKO results in profoundly increased soma areas, more prominent apical dendrites, and notably altered *Drd1a*$^{+}$ densities and distributions specifically in CPLX3 co-expressing subpopulations (**4.3.2**,**4.3.3**). These differences compound across regions and layers, emphasising the importance of accounting for cortical heterogeneity when conducting experiment and interpreting results. Morphometric similarity between mouse *Drd1a*-Cre neurons and human WMINs supports their presumed homology. PTEN manipulation may be relevant to conditions of mTOR pathway dysfunction, diseases of cortical hyperexcitability, and corresponding avenues of pharmacological interest. More broadly, subpopulations of subplate remnants exhibiting unique signal responsivity and projection selectivity may serve as a neurodevelopmentally-persistent and evolutionarily preserved network node capable of integrating and potentiating wake- and attention-promoting ORX-gated CT-TC loops driving brain state control[91]. Subplate remnants are likely to influence adult cortical circuitry and neurodevelopmental origins of brain disease.

## Layer 5: Multimodal methods reveal progressive neuromotor degeneration

Chapter 5 characterises trajectories of neuromotor degeneration resulting from genetically silencing a subpopulation of cortical L5 neurons (i.e., *Rbp4*-Cre) using complimentary

behavioural, histological, and multimodal neuroimaging techniques, which both provides biological insights into networks putatively associated with motor neuron degeneration and demonstrates the capacity of advanced MRI to detect nuanced anatomical genotype differences. Ultimately, from what began as a subtle observation of abnormal *SnackerTracker* feeding behaviour and a hindlimb clap (**5.1.1**), STAMINA evolved as a comprehensive longitudinal multimodal investigation (**1.5.5)** having both biological and methodological relevance. Here, this previously reported[77] yet uncharacterised phenotype drove biological questions regarding 1) the features and trajectories of motor decline (**5.1**), 2) whether neuroimaging may be able to detect corresponding anatomical, structural, and functional change over time (**5.2**), and 3) which underlying cell populations exhibit signs of neurodegeneration, directed migration, or otherwise altered expression patterns (**5.3**). The trajectory of neuroimaging-determined volumetric changes over time largely reflects and even precedes the extensive motor decline observed behaviourally across HCM, CAMP, VCT, grip strength, and CatWalk assessments (**5.4**). Together alongside diffusion- and QSM-derived microstructural changes detected *ex vivo*–which reflect patterns of histologically observed *Rbp4*-Cre$^{+/+}$:*Snap25*$^{fl/fl}$ neuron degeneration, LMN punctation, pathological protein aggregation, glial infiltration, and signs of interneuron and perineuronal net degeneration–this suggests that neuroimaging may be used in the future to identify structural or microstructural changes *before* behavioural effects materialise and *prior* to histological confirmation (**5.4**). Together, the data collected across these three distinct domains complimentarily provided more comprehensive insight into the underlying networks associated with observed neuromotor degeneration than any modality would have in isolation (**5.4**). Thus, while our findings corroborate that L5 neuron degeneration can precipitate progressive functional deficits, supporting top-down theories of motor degeneration[160], this experimental strategy holds greater implications for the scope of advanced MRI techniques in preclinical studies and future clinical applications (**5.5**).

# Appendices

## A.1 Genetic strategies and mechanisms

### *A.1.1 PTEN mechanisms*

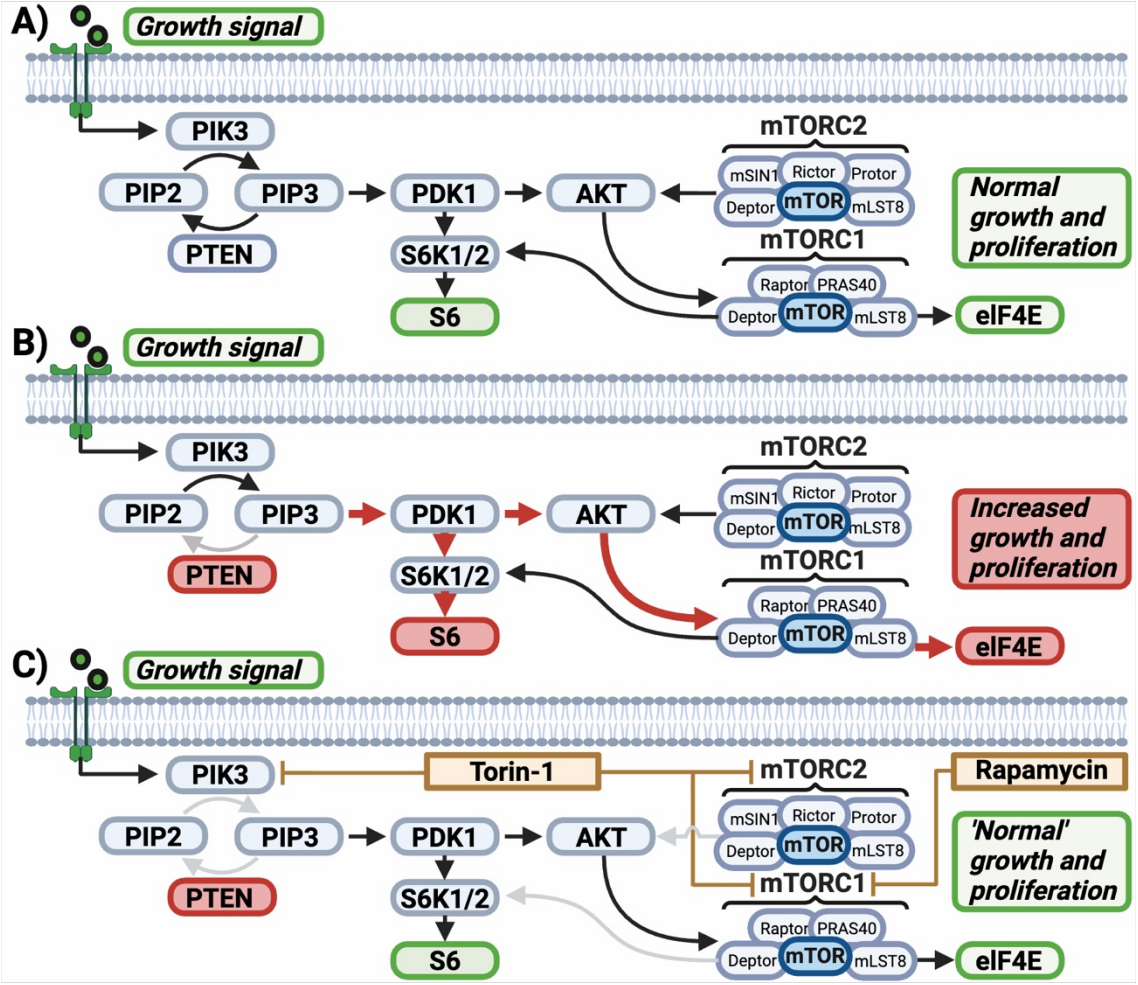


**Appx-Figure 1.** Schematic representation of mTOR pathway functionality under A) normal, B) PTEN-deficient, and C) pharmacologically rescued conditions. Products eukaryotic translation initiation factor 4E (eIF4E) and ribosomal protein S6 promote translation and cell survival/replication, respectively. Green=proliferative states; red=inhibited states; and yellow= drugs (e.g., first-generation mTORC1 inhibitors rapamycin/rapalogs and second-generation mTORC1/mTORC2/phosphatidylinositol 3-kinase (PI3K) inhibitors torin-1/vistusertib)[61, 436, 477]. PIP2=phosphatidylinositol 4,5-bisphosphate; PIP3=phosphatidylinositol (3,4,5)-trisphosphate; PDK1=3-phosphoinositide-dependent protein kinase 1; S6K1/2=S6 kinase 1/2; AKT=protein kinase B; mSIN1=mammalian stress-activated protein kinase-interacting protein 1; Rictor=rapamycin-insensitive companion of mTOR; Proctor=protein observed with Rictor; Deptor=DEP domain-containing mTOR-interacting protein; mSLT8=mammalian lethal with SEC13 protein 8; Raptor=regulatory-associated protein of mTOR; PRAS40=proline-rich AKT substrate of 40kDa.

### *A.1.2 Snap25 mechanisms*

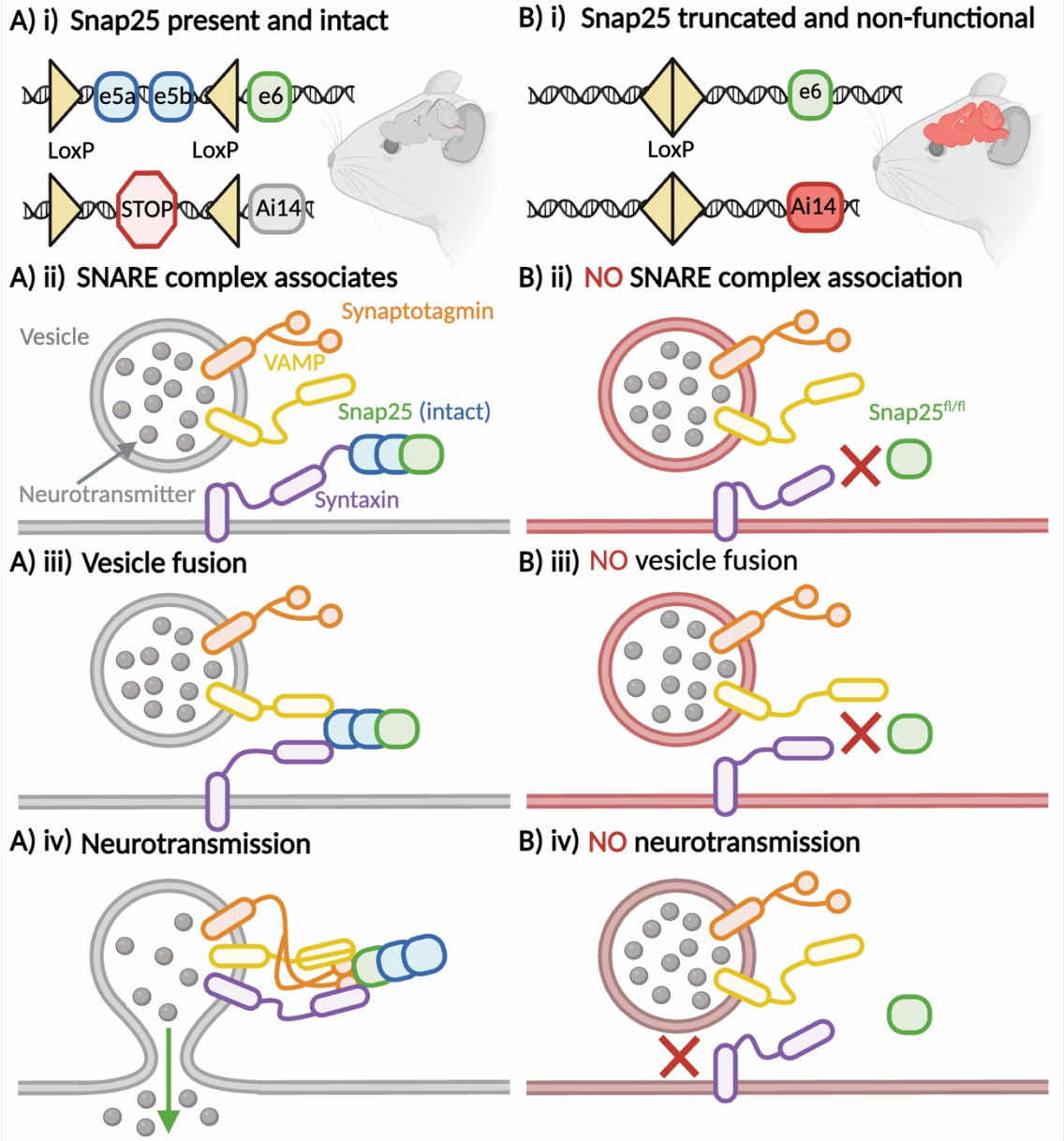


**Appx-Figure 2.** Illustrates Cre-mediated *Snap25* truncation resulting in cell 'silencing'[77]. A) i-iv) shows normal synaptic physiology as expected in CTRLs, and B) i-iv) shows thwarted synaptic transmission in Cre$^{+}$ *Snap25*-cKOs. In CTRLs, A) i) all *Snap25* exons are transcribed, and a stop codon blocks Ai14 expression. A) ii) and functional SNARE proteins A) iii) associate to facilitate A) iv) presynaptic vesicle fusion Synaptic components and neurotransmission. B) i) In cKOs, B) i) Cre excises LoxP-flanked *Snap25* exons 5a-b and the stop codon such that the Ai14 RFP is expressed and cells glow red. B) ii) The truncated SNAP25 protein is nonfunctional and B) iii) cannot facilitate SNARE assembly. B) iv) Membrane fusion and SNARE-mediated neurotransmission cannot occur, resulting in cells which cannot communicate with afferent targets. Note that some CTRLs are Cre$^{+}$ heterozygotes possessing one functional SNAP25 domain (**Table 9**); these animals exhibit normal neurotransmission as in A) ii-iv) yet transcribe Ai14 and glow red (i.e., necessary for IHC controls).

### *A.1.3 DREADD mechanisms*

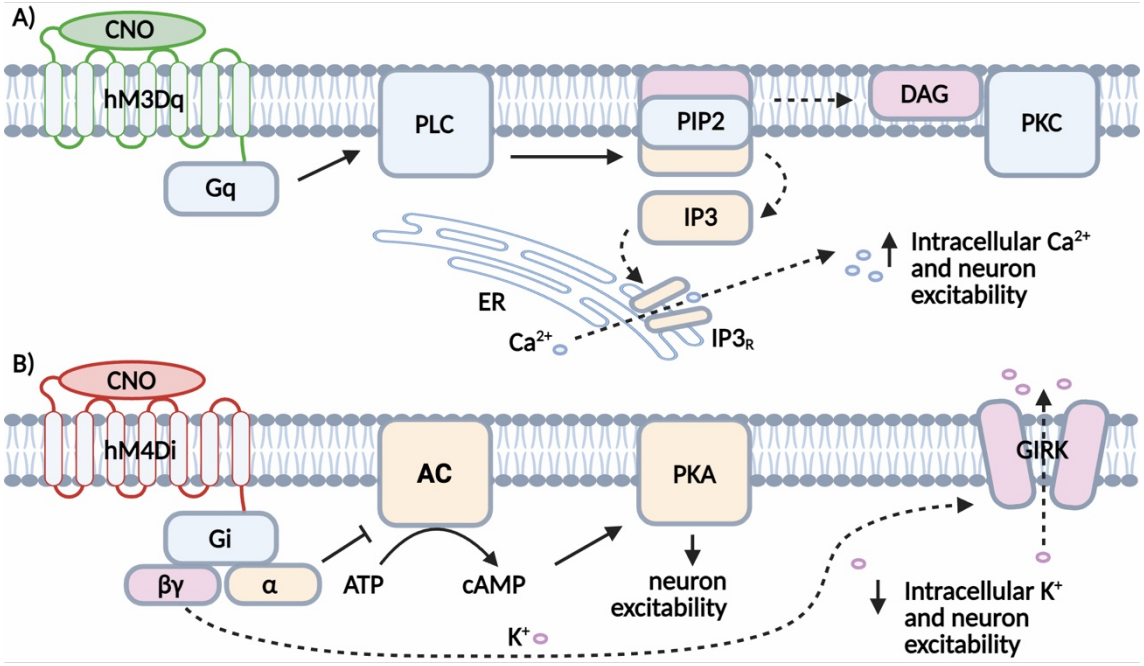


**Appx-Figure 3.** DREADD mechanisms of action underlying acute cell A) excitation and B) inhibition. A) CNO is a synthetic ligand which, when administered, binds to the extracellular domain of hM3Dq—a designer G-protein-coupled receptor which mimics the human muscarinic acetylcholine receptor M3. CNO-bound hM3Dq undergoes a confirmational change which activates the Gq protein, which in turn activates phospholipase C (PLC). PLC hydrolyses phosphatidylinositol 4,5-bisphosphate (PIP2) into inositol 1,4,5-trisphosphate (IP3) and diacylglycerol (DAG). IP3 binds to the IP3 receptor ($IP3_R$), which is a $Ca^{2+}$ channel enabling the release of ions from endoplasmic reticulum (ER) stores into the cytosol. DAG associates with protein kinase C (PKC) which increases intracellular $Ca^{2+}$ levels. This results in membrane hypopolarisation, decreasing the threshold required to fire an action potential, thereby increasing neuron excitability. B) CNO binds to the extracellular domain of hM4Di—another designer g-protein coupled receptor mimicking human muscarinic acetylcholine receptor M4—which activates the Gi protein. The Gi protein α-subunit inhibits adenylyl cyclase (AC), which otherwise converts ATP to cAMP. Decreased intracellular cAMP leads to reduced activation of protein kinase A (PKA) and correspondingly reduced activation of its downstream targets which otherwise promote neuron excitability. Gi protein βγ-subunits activate G protein-gated inwardly rectifying potassium channels (GIRKs), which allows $K^+$ to exit the cell. Decreased intracellular $K^+$ results in membrane hyperpolarisation, increasing the threshold required to fire an action potential, thereby decreasing neuron excitability[265, 268, 478].

## A.2 Statistics

The details and results of all statistical tests in this thesis, including power calculations, have been deposited to Figshare[479, 480].

## A.3 SnackerTracker development

### *A.3.1 Bill of materials*

**Appx-Table 1.** Lists active components (green), mounting/accessory elements (blue), and construction equipment (yellow) needed to build one *SnackerTracker* (V10). The number/amount of each item required is provided with linked supplier websites. N/A=components which can be re-used in constructing other devices and are therefore excluded from price calculations. At the time of writing, the total material cost for one device was £104.77 (VAT included).

| Category | Shorthand Name | # per Device | Category | Shorthand Name | # per Device |
|---|---|---|---|---|---|
| **Chassis** | 3D Printing Material - ABS Black | 222g | **Fasteners** | Hex Standoff F-F - LDR Mount | 1 |
| **Electronics Agents** | Arduino MKR WiFi 1010 | 1 | | Screws - LDR Mount | 1 |
| | Arduino MKR MEM Shield | 1 | | Hex Nut - Food Mount Plate | 6 |
| | Load Cell and Amplifier | 1 | | Screws - Food Mount Plate | 6 |
| | Load Cell | 1 | | Hex Standoff M-F - Microchip | 4 |
| | HX711 Amplifier | 1 | | Hex Nut - Microchip | 4 |
| | Protoboard - LDR Mount | 1 | | Hex Nut - Load Cell Interior | 2 |
| | LDR | 1 | | Washers - Load Cell Interior | 2 |
| | Resistor | 1 | | Screws - Load Cell Interior | 2 |
| | Toggle Switches | 2 | | Velcro - Loop Tape | 1 |
| | LiPo Battery | 1 | | Velcro - Hook Tape | 1 |
| | Micro SD Card and Adapter | 1 | **Accessories** | Glass Cover Slides | 1 |
| **Wires** | Peripheral Connector Wires | 10 | | Grommet - Cable Retention | 2 |
| | Push Crimp Connector | 4 | | Grommet - Closed | 2 |
| | Pin Headers M-F | 5 | | USB Cable | 1 |
| | Pin Headers M-M | 8 | | Micro SD Card and Reader | 1 |
| | Heat Shrink Wrap | 8 | | 10-Port USB Hub | N/A |
| | JST Connector Housing | 1 | | Microchip PCB Solder Wire Kit | 1 |
| | JST Wire Crimp Connector | 2 | | USB Flash Drive | N/A |
| **Assembly - Wiring** | Wire Cutter | N/A | **Assembly-Operation** | 3D Printer | N/A |
| | Wire Stripper | N/A | | 3D Printing Glass Care - Glue | N/A |
| | Solder | N/A | | Chassis Care - Acetone | N/A |
| | Solder Station | N/A | | USB Flash Drive | N/A |
| | Crimper - JST | N/A | | Super Glue | N/A |
| | Crimper - Push Plugs | N/A | | Screw Driver | N/A |
| | Multimeter | N/A | | Scale | N/A |
| | Heat Gun | N/A | | USB-UK Adapter | N/A |

## *A.3.2 Ultimaker Cura print settings*

**Appx-Table 2.** Lists custom Ultimaker Cura settings for *SnackerTracker* chassis 3D-printing as determined by iterative testing. Automatically assigned values were maintained for parameters not listed here. Parameters are grouped by those influencing chassis body quality and composition (green); overhang and build plate supports, which are later removed (blue); and the mesh, which is an immaterial computational construct (yellow).

| Classification | Specification | Value | Classification | Specification | Value | Classification | Specification | Value |
|---|---|---|---|---|---|---|---|---|
| Quality | Layer Height | 0.2 mm | Material | Printing Temp | 250 °C | Support | Join Distance | 2.0 mm |
| | Initial Layer Height | 0.27 mm | | Build Plate Temp | 85 °C | | Horizontal Expansion | 1.0 mm |
| | Line Width (All) | 0.4 mm | Speed | Print Speed | 60.0 mm/s | | Infill Layer Thickness | 0.2 mm |
| Walls | Wall Thickness | 0.8 mm | Travel | Enable Retraction | Yes | | Gradual Infill Steps | 0 |
| | Wall Line Count | 2 | | Combing Mode | Not Out | | Min Area | 9.0 $mm^2$ |
| | Optimize Printing Order | Yes | | Z Hop When Retracted | Yes | | Enable Interface | Yes |
| | Wall Ordering | Out to In | Cooling | Enable | Yes | | Enable Roof/Floor | Yes |
| | Alternate Extra Wall | No | | Fan Speed | 2.00% | | Interface Thickness (All) | 0.4 mm |
| | Min Line Width (All) | 0.34 mm | Support | Generate Support | Yes | | Interface Resolution | 0.2 mm |
| | Print Thin Walls | Yes | | Structure | Normal | | Interface Density (All) | 80.00% |
| | Min Feature Size | 0.1 mm | | Placement | All | | Line Distance (All) | 0.5 mm |
| | Horizontal Expansion | -0.02 mm | | Overhang Angle | 60 ° | | Interface Pattern (All) | Concentric |
| | Initial Layer Expansion | -0.02 mm | | Support Pattern | Lines | | Min Interface Area (All) | 1.0 $mm^2$ |
| | Hole Horizontal Expansion | 0.00 mm | | Wall Line Count | 0 | | Interface Horizontal Expand (All) | 1.0 mm |
| Top/Bottom | Thickness (All) | 1.2 mm | | Connect Lines | Yes | | Fan Speed Override | No |
| | Layers | 6 | | Density | 15.00% | | Use Towers | No |
| | Ironing Pattern | Concentric | | Line Distance (All) | 2.66 mm | Build Plate Adhesion | Enable Prime Blob | No |
| | Enable Ironing, Highest Only | Yes | | Enable Brim | Yes | | Build Plate Adhesion Type | Brim |
| Infill | Density | 20.00% | | Brim Width | 8.0 mm | Mesh Fixes | Union Overlapping Volumes | Yes |
| | Line Distance | 6.0 mm | | Z/Top/XY Distance | 0.3 mm | | Remove All Holes | No |
| | Pattern | Triangles | | Bottom Distance | 0.15 mm | | Extensive Stitching | No |
| | Layer Thickness | 0.2 mm | | Distance Priority | Z over XY | | Disconnected Faces | No |
| | Gradual Steps | 1 | | Stair Step Height | 0.3 mm | | Meshes Overlap | 0.0 mm |
| | Gradual Step Height | 1.0 mm | | Stair Max Width | 5.0 mm | | Remove Intersection | Yes |
| | | | | Stair Min Angle | 10.0 ° | | Alternate Removal | Yes |

## *A.3.3 Chassis schematics*

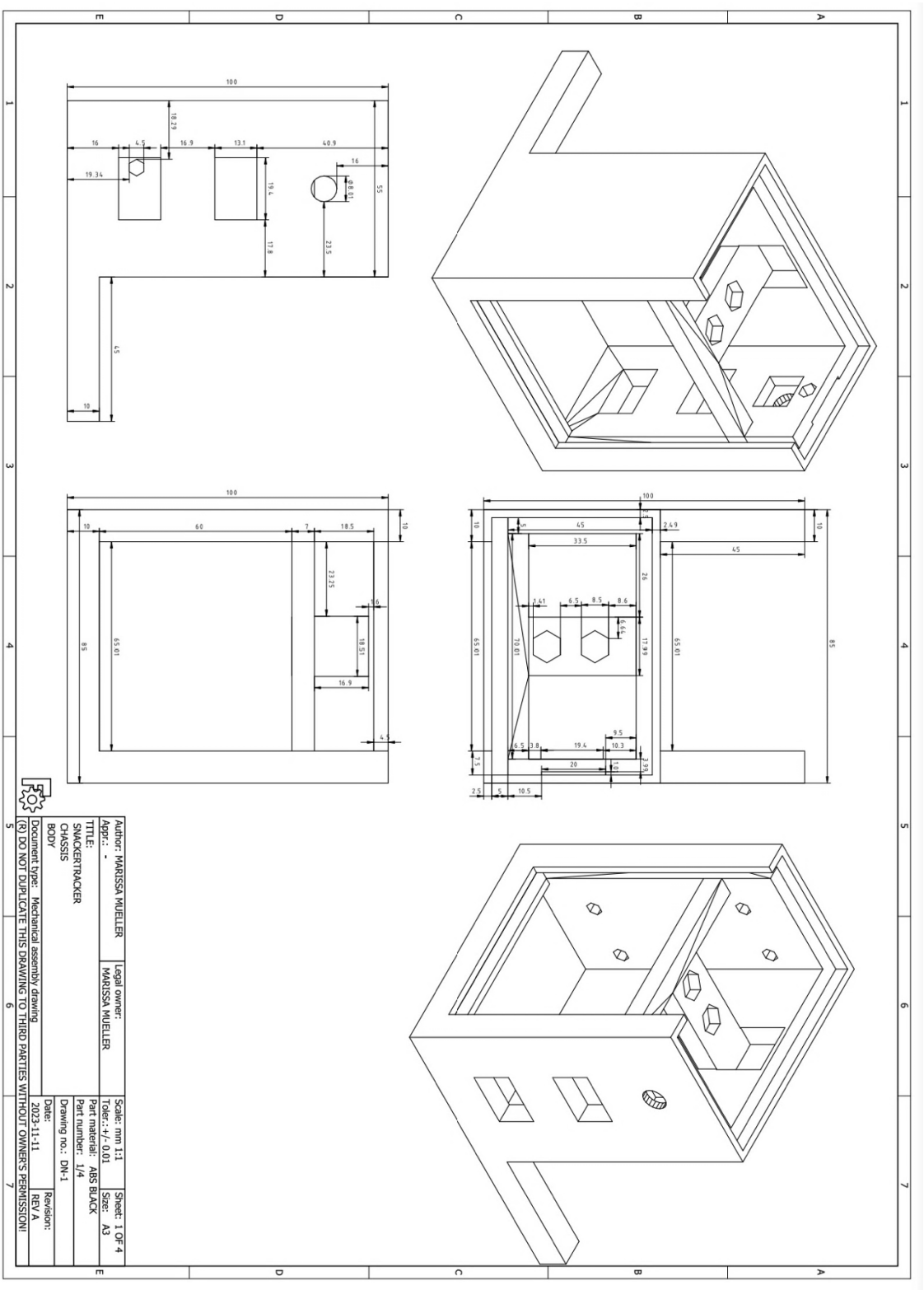


**Appx-Figure 4.** *SnackerTracker* chassis schematics for the I=body.

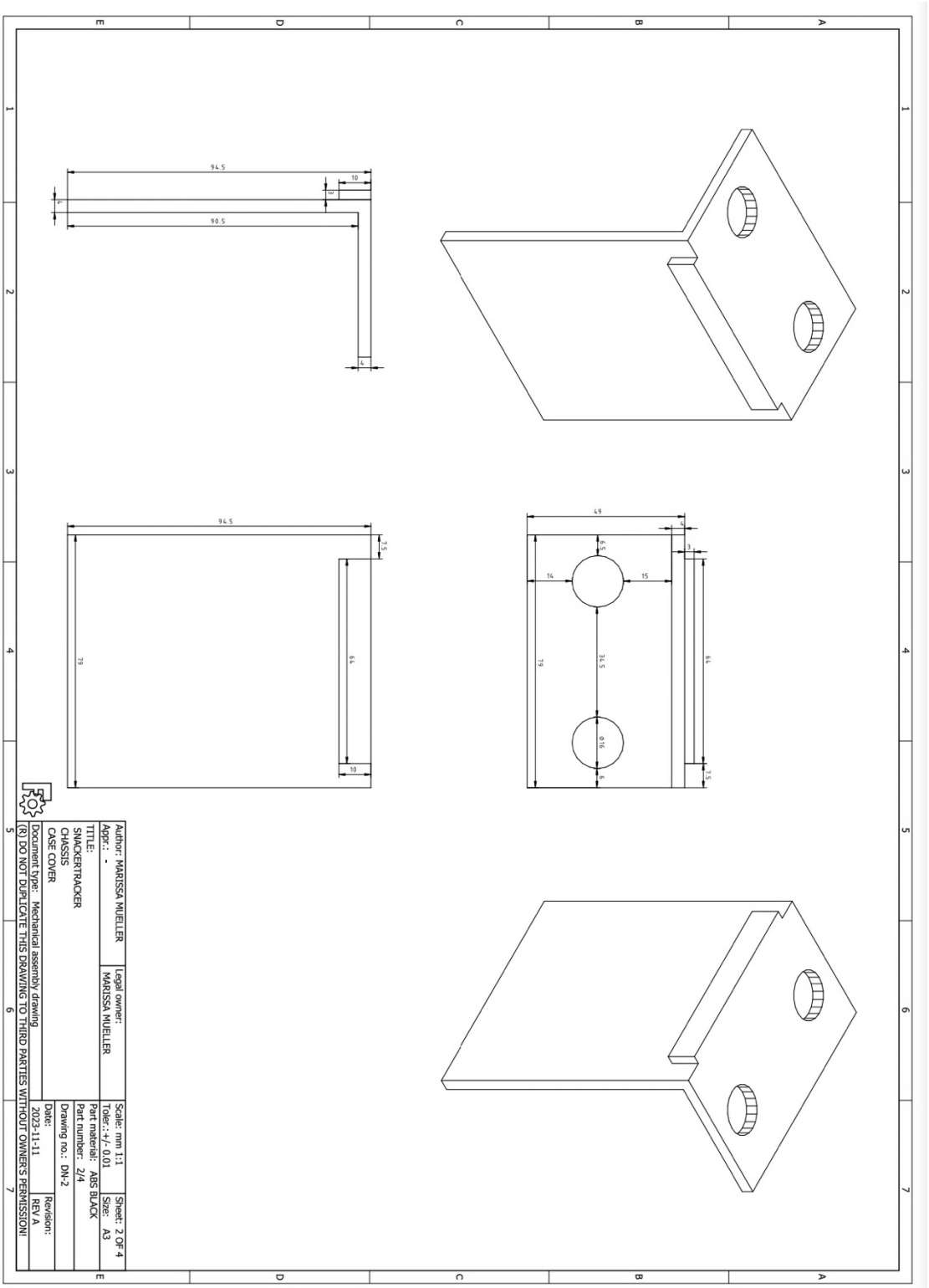


**Appx-Figure 5.** *SnackerTracker* chassis schematics for the II=case cover.

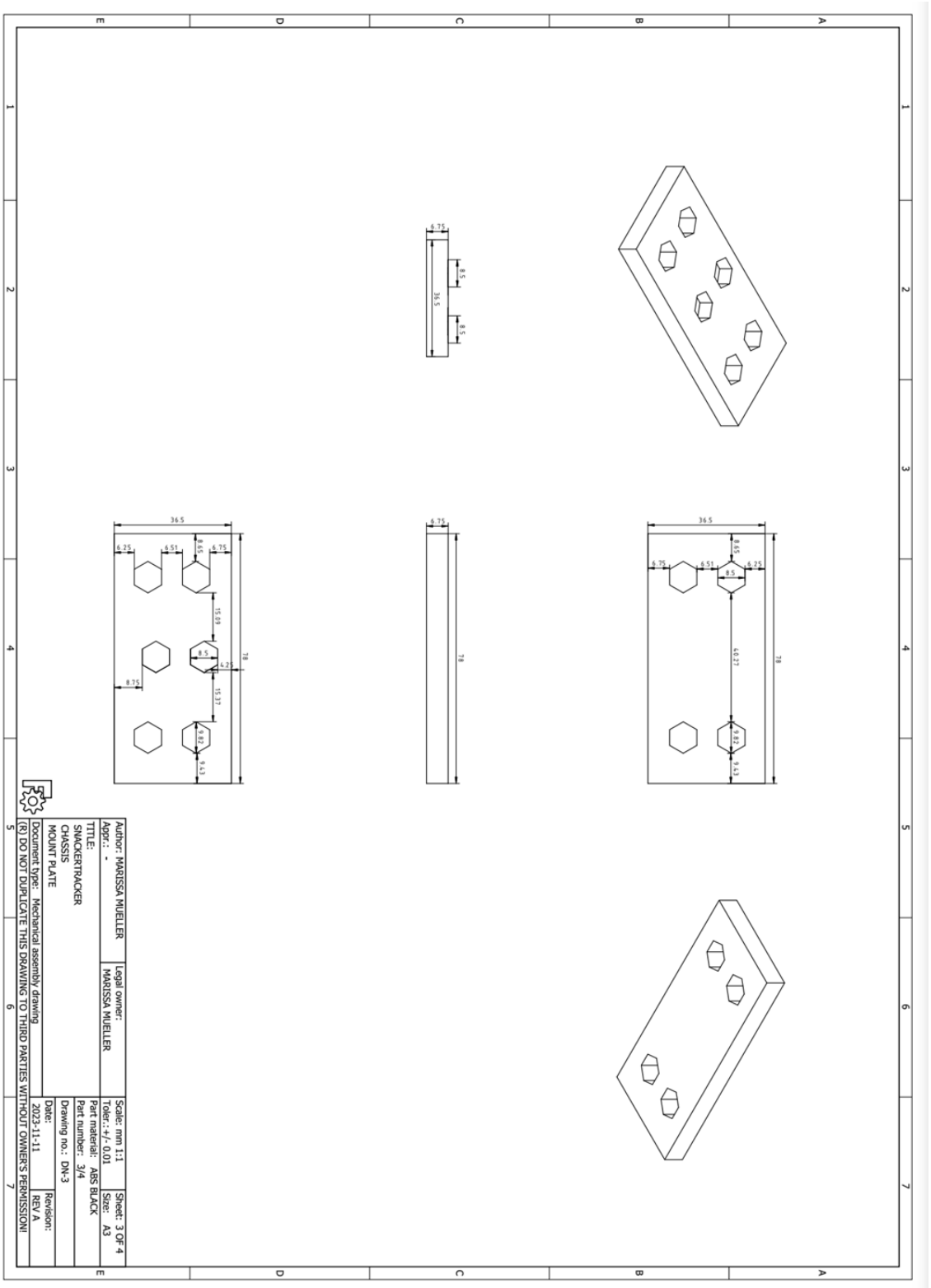


**Appx-Figure 6.** *SnackerTracker* chassis schematics for the III=mount plate.

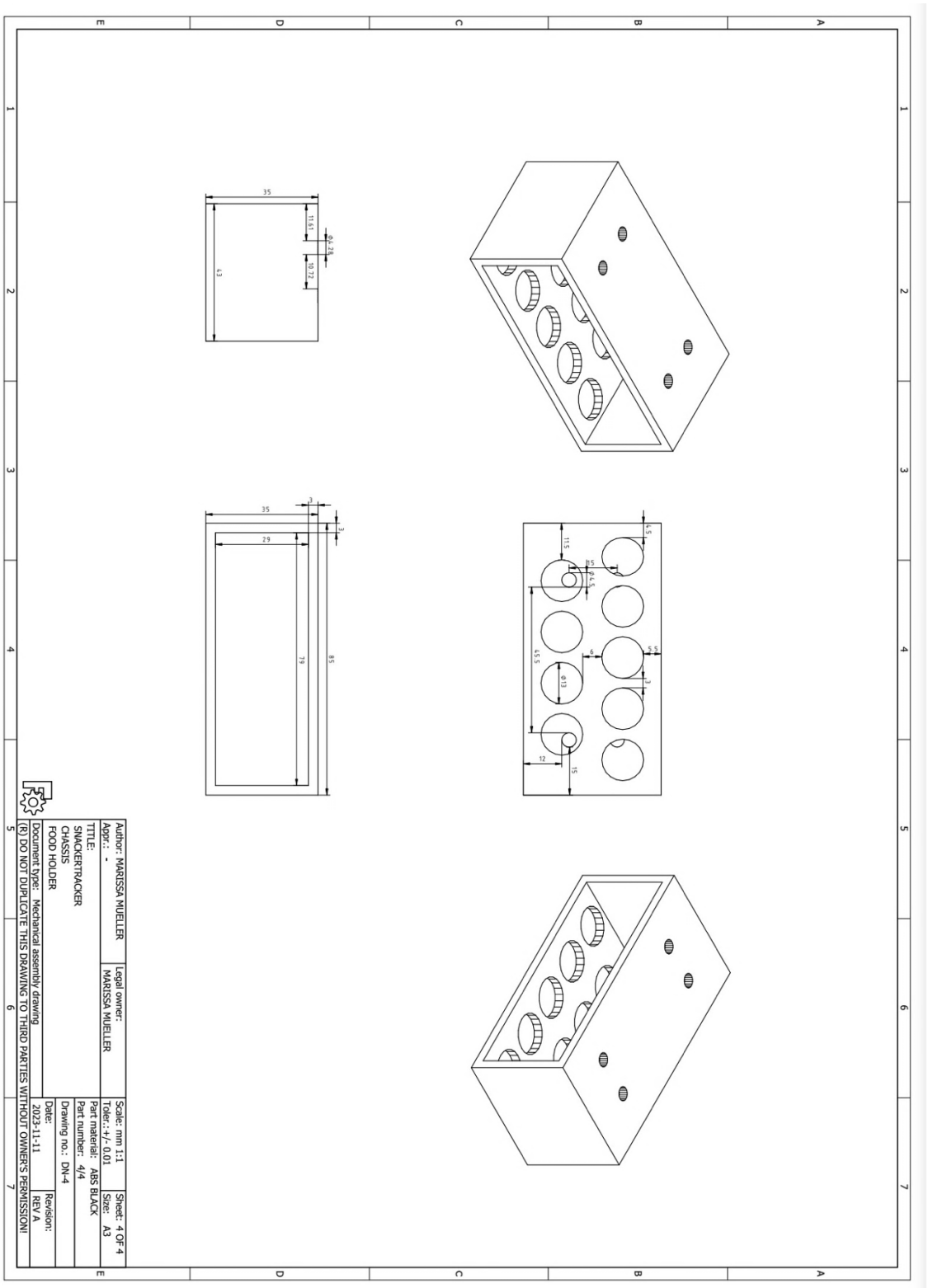


**Appx-Figure 7.** *SnackerTracker* chassis schematics for the IV=food holder.

### *A.3.4 Electronics schematics*

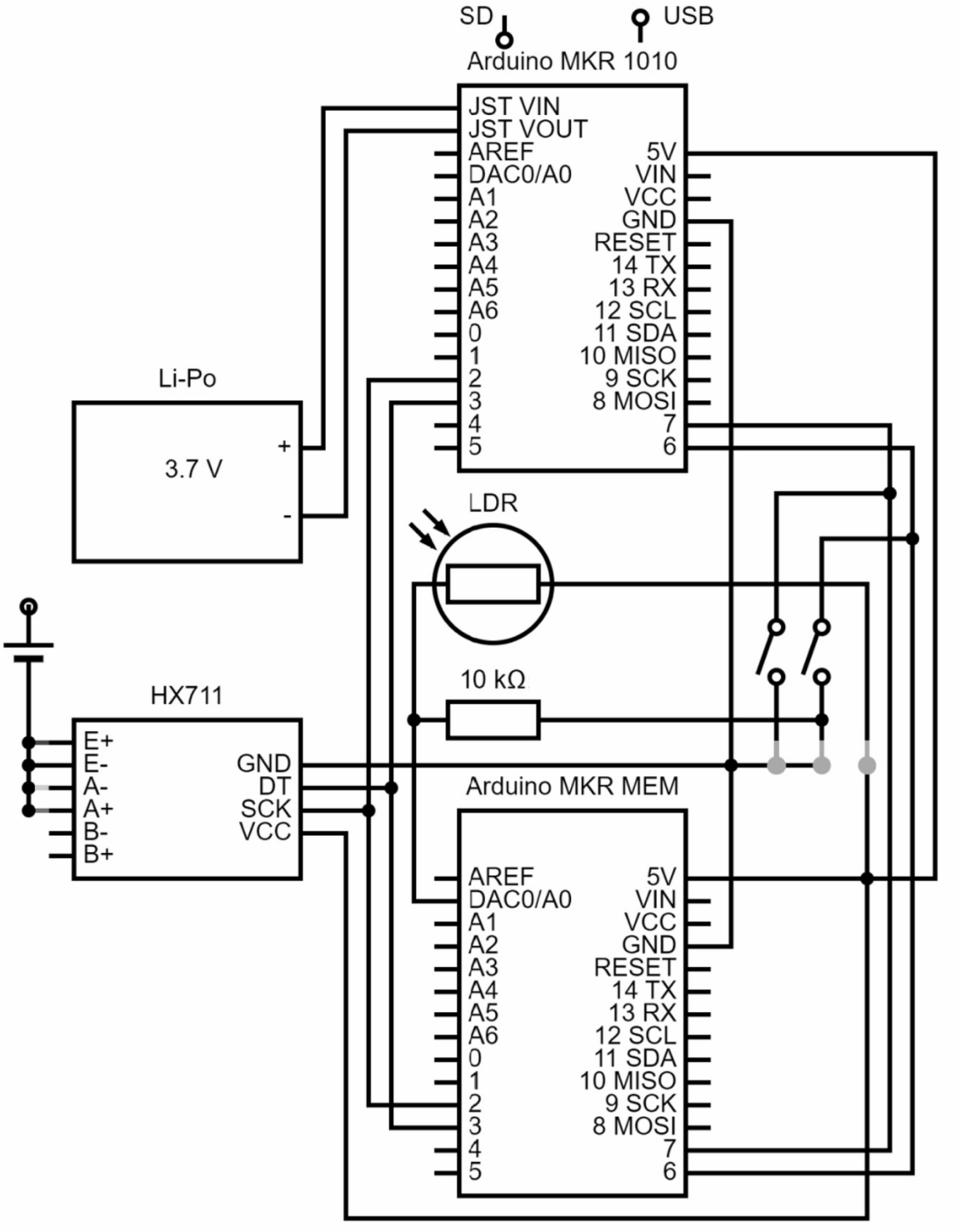


**Appx-Figure 8.** *SnackerTracker* electronics schematics. This is freely available via Figshare[376] and can be used for contracted construction.

### *A.3.5 Component assembly*

*Microchips and major inputs:* Videos below depict *SnackerTracker* assembly as follows. Electronics were sourced (see **A.3.1** for the BOM), soldered, and mounted to the chassis. 2 rows of 4-per-row 2.54mm pitch M-M pin headers (PH) (Molex, Lisle, USA) were inserted into E+/E-/A-/A+ and GND/DT/SCK/VCC through-holes on a HX711 signal amplifier (Radwell, Newcastle-under-Lyme, UK) and soldered with load cell (LC)(Adafruit, New York, NY, USA) wires (red/E+, black/E-, white/A-, and green/A+). HX711 headers were soldered to the Arduino MKR MEM protoboard (Arduino, Redmond, USA), with three 2.54mm pitch M-F PHs (Harwin, Portsmouth, UK) and a 10kΩ resistor (RS PRO, Corby, UK). The protoboard underside was soldered to facilitate circuitry detailed in **A.3.4** using u-shaped jumper wires (3M). The MEM shield stacked atop an Arduino MKR Wi-Fi 1010 microcontroller (Arduino) with an on-chip RTC such that MKR 1010 I/O pins operate through MEM proxies.

*Wire connections:* Four 0.2mm$^2$ 7/0.2mm connective wires (RS PRO) were cut to 10cm and stripped at each end. One bare end was crimped to a vinyl-insulated female receptacle spade connector (6.3×0.8mm tab size) (RS PRO) which joined to one of the two contacts on 'on'/'off' SPST 19.4×13mm panel-mount toggle switches (E-SWITCH, Minneapolis, USA). The other bare end was soldered to single M-M PHs. Two connective wires were cut and stripped at both ends for soldering to M-M PHs. 3mm diameter (3:1) heat shrink wrap (RS PRO) was cut into 1cm segments and bonded around all wire-PH junctions. Two M-F PHs were soldered to a 1in$^2$ accessory protoboard (SparkFun, Boulder, USA) with each end of a LDR (LPRS, Witney, UK) affixed in each M-pin through-hole. Bare lithium-polymer battery (RS PRO) wires were crimped to 30-24 AWG JST-PH female crimp terminals (JST, Doshomachi, JP) and inserted into JST-PH housing (2mm pitch, 2 way, 1 row) (JST) such that, upon inserting into the Arduino MKR 1010's JST-PH port, the black battery wire was closest to (and red furthest from) the AREF PH. The most updated version of the *SnackerTracker* employs pre-crimped JST-PH leads, which is highly recommended for future applications.

*Microchip inserts and mounting:* A U3 micro-SDXC card (Integral, Bristol, UK) was inserted into the MEM shield after being re-formatted from exFAT to FAT-32 format using MiniTool Partition Wizard (v12.7, MiniTool, Vancouver, CA) for system compatibility. Cyanoacrylate glue (RS PRO) affixed the following standoffs and nuts to the chassis for electronics mounting: four 10+5mm M2 F-M hex standoffs (Mac 8, Canoga Park, USA) to the chassis body wall; one 10mm (cut in half to 5mm) M2.5 F-F hex standoff (The Pi Hut, Haverhill, UK) to the opposite chassis body wall above the LDR opening (pushed in, but not so far as to obstruct the vertical slot above the opening); two M5 hex nuts (7.8mm width, 4mm height) (RS PRO) to the interior chassis body bridge for LC attachment; and six 6mm M4 standoffs (Essentra Components, UK) to the mount plate. The MKR 1010 was vertically mounted to the four M-F standoffs with M2 hex nuts (RS PRO) with the stacked MEM configuration.

*Input mounting and configuration:* The LC was inserted through the chassis body and secured to the bridge using two trimmed 20mm M5 screws (MultiComp Pro, London, UK) and two M5 washers per screw (RS PRO) between the LC and bridge. 20mm hook and loop Velcro tape (RS PRO) were trimmed to 3cm segments and adhered to the base of the chassis interior and lithium-polymer battery, respectively. This secured the battery such that wire leads emerged directly underneath the MKR 1010's JST port. An 18×18mm glass cover slide (Scientific Laboratory Supplies, Nottingham, UK) was placed into the vertical slot above the LDR opening in the chassis wall. The LDR-mounted protoboard attached to chassis interior, with the sensor

visible from the exterior through the glass cover, using trimmed 10mm M2.5 screws (TR Fastenings, Uckfield, UK). Toggle switches and wires pushed through each of the two rectangular through-holes from the outside-in below the LDR. One M-pin lead extending from each switch connected to a F-pin header soldered nearest the HX711 on the MEM protoboard. The other lead from the top toggle switch was plugged into pin 7 on the MEM shield, and from the bottom toggle switch to pin 6. One end from each of the two remaining wires (M-pins at both extremities) plugged into F-pin headers on the LDR-mounted protoboard. The opposite end of one was plugged into the third F-pin header on the MEM protoboard, and the other into the MEM's DAC0/A0 pin. Two trimmed 10mm M4 screws (TR Fastenings) extended through the LC holes protruding under the chassis and affixed to the hex nuts along the mount plate midline.

*Usage:* Food pellets press through the food holder (inside-out) with tape affixed to secure the top of each pellet tip to the chassis interior (Thorlabs, Newton, USA). The food holder was tightened to the upper side of the mount plate using four 10mm M4 screws (TR Fastenings). Two 15.9mm diameter cable retention grommets (Essentra Components) were pushed into the case cover, which inserted into the chassis body after plugging the lithium battery into the MKR 1010's JST port.




**Appx-Figure 9.** Videos depict *SnackerTracker* assembly and *in vivo* function. A) A 10-minute video illustrates *SnackerTracker* construction. The device is then shown in a mouse cage operating both B) wirelessly and C) wired through open-top cages.

### *A.3.6 SnackerTracker calibration*

*SnackerTracker* initialisation first involves removing the case cover and ensuring that a charged battery is connected to the JST power port. The food holder should be empty and placed on the mount plate. The weight of pellets which are to be added should be recorded. After opening the Arduino Editor script and running the Arduino Create Agent, code can be uploaded via USB (only in the first instance). The setup() function first connects to the HX711 and RTC, then prompts the user to enter the mass of food which is to be added in the Editor's serial monitor. After providing this calibration mass, the user has 3 minutes to add taped pellets to the food holder to then screw to the mount plate. This 3-minute timeframe can be adjusted within the script if needed. setup() then tares and calibrates the device, connects to on-board LED lights, checks that an SD card is present, creates an output .csv file on the SD card, then passes control to the loop() function for data recording. Loop() reads and writes input load cell, LDR, and RTC data to the output .csv file. The program continually checks that the SD card is present and indicates connectivity or data logging errors flashing the red on-board LED light.

### *A.3.7 Preliminary test details*

Preliminary *SnackerTracker* validation tests assessed 1) device calibration accuracy, 2) measurement consistency, 3) time-sensitivity, 4) LDR function, 5) combined operation, and 6) correlation to manual measurements of daily food intake upon *in vivo* introduction:

1) Calibration testing involved initialising *SnackerTracker* using pellet-masses roughly equivalent to that of a i) empty (28g), ii) half-full (55g), and iii) full (82g) food holder, then sequentially removing and manually weighing pellets for comparison to *SnackerTracker* recordings. This assessed both the accuracy of SnackerTracker measurements and whether this accuracy depends on the calibration mass selected (which it should not).
2) Measurement consistency was tested by assessing drift and tap recovery. Drift is a phenomenon wherein device performance deteriorates after calibration. This presents as erroneously fluctuating measurements over time[281]. To evaluate drift, a known mass was placed on the food holder. Data was collected without interference to determine whether measurements ideally remain constant or incorrectly shift over time. Applied forces (herein termed a 'tap') can also induce a form of drift, wherein strain gauges deviate during mechanical deformation but may not reliably return to the pre-load state. A post-hoc recording was extracted wherein the food holder was loaded with pellets as with in vivo recordings, subjected to 'taps' (i.e., lightly pushing or pulling upwards or downwards on pellets without any pellet removal/consumption), and analysed for post-tap recovery to pre-tap values.
3) Time-sensitivity tests assessed the accuracy of *SnackerTracker* timestamps compared to manual recordings. The SnackerTracker's Arduino MKR 1010 microchip features two means by which time can be registered in operational code: via script-based frequency loops, or by extracting information directly from the on-chip RTC. Loop() records data at a user-defined frequency (e.g., 1Hz), however hardware and processor burden may cause software lag. This can result in mass/light measurements being erroneously reported as occurring earlier in time. Alternatively, RTCs register time independent of peripheral mass/light measurements and should prevent lag. To test this and confirm RTC performance over looped LC timestamps, SnackerTracker data was collected, using both RTC and load cell recordings, during the sequential removal of 12 food pellets (one every 30 minutes). Pellets were manually weighed and removal times were documented for comparison to SnackerTracker load cell/RTC data.
4) LDR recordings are intended to confirm scheduled light-dark cycles, which is important when assessing or controlling for circadian and homeostatic functions (e.g., sleep). To test LDR function, a researcher first lowered an opaque box overtop the SnackerTracker, then then repeatedly flipped the room's light switch to test the ability of the SnackerTracker to identify 'ramping' and absolute periods of lights being 'on' or 'off', respectively.
5) The combined test simulated cage light conditions (i.e., turning lights 'on' and 'off'), animal food consumption over time (i.e., manually removing pellets from the food holder), and switch functionality (as switches can be used for event-marking and data-filtering during post-processing). Lights were scheduled at two cycles of 30s 'off' and 60s 'on', followed by a final 30s 'off'. Pellets were removed during the light-phase, and switches 1 (top) and 2 (bottom) were flipped directly before lights turned 'on' or 'off', respectively. This was repeated with and without IoT connectivity. The test mimicked *in vivo* patterns (i.e., pellet removal occurring in the dark phase for nocturnal animals) and evaluated SnackerTracker function before exposing the device to animals.

6) Three experiments then evaluated *in vivo* compatibility and performance following at least one day of habituation. i) Devices were loaded with pellets, weighed, placed in cages with singly housed WT mice for 24h, then weighed afterwards. The difference between the mass of the *SnackerTracker* with food before and after recordings was documented and compared to values returned by the *SnackerTracker* itself to assess *in vivo* accuracy. ii) Food intake was measured manually by weighing pellets, adding them to cages with singly housed WT mice, then removing and weighing the remaining pellets after 24h. Manual cage-floor vs *SnackerTracker*-obtained data were paired and compared to evaluate whether the method of food presentation and measurement altered daily food intake. iii) 47-92h *SnackerTracker* recordings were obtained using surplus *Rbp4*-Cre mice (see **Preface**), which were singly housed with fresh alpha-dry bedding, to test device performance with extended recording durations and to evaluate conceivable effects of pellet crumbling. After recordings terminated, bedding was sieved to isolate crumbs (having been removed from the food holder but not eaten) which could erroneously inflate *SnackerTracker*-documented food consumption. Crumb masses were normalised by time to determine average crumbling per day, and all mice were weighed before and after recordings.

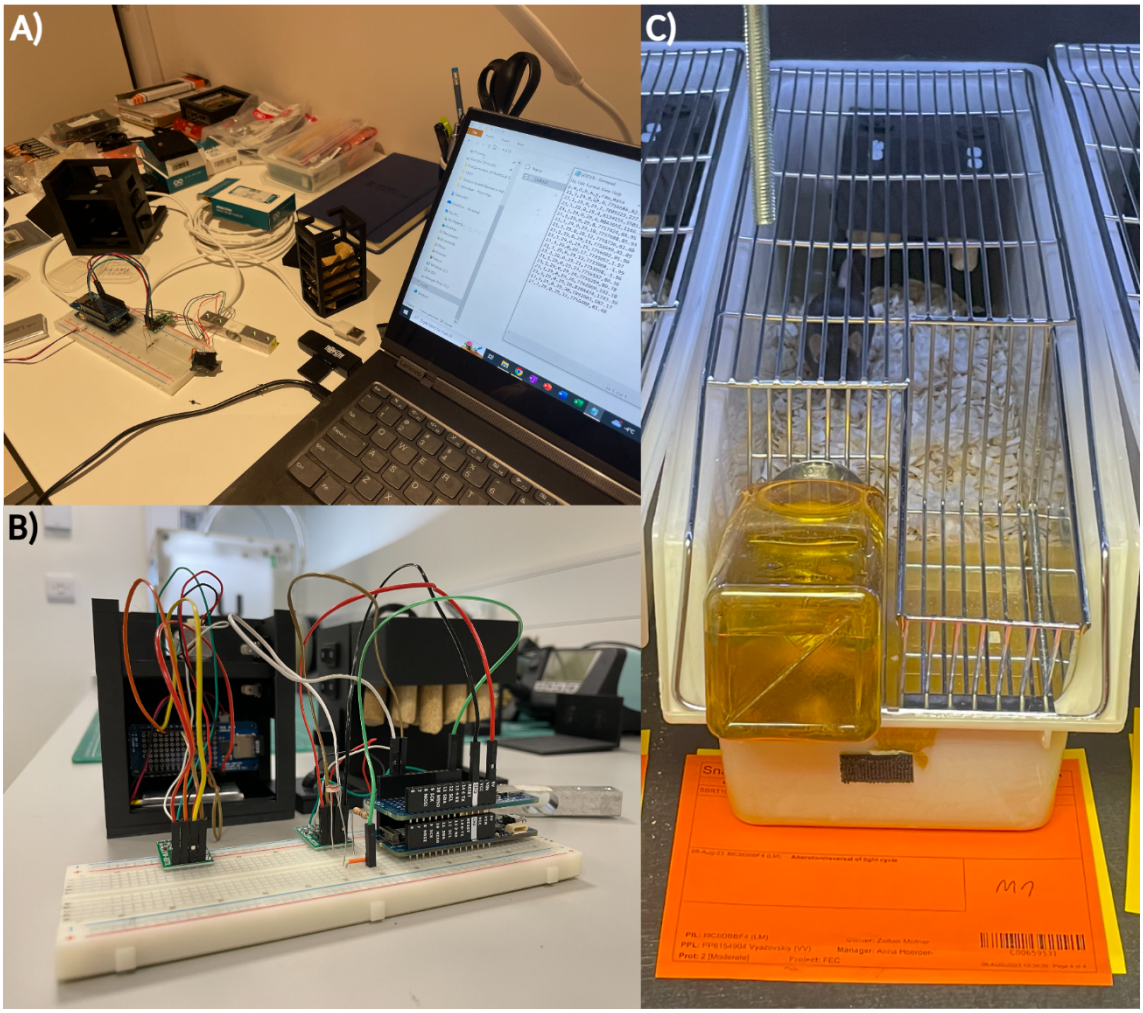


**Appx-Figure 10.** Preliminary benchtop test configurations. Setups are shown for: A) device calibration accuracy, measurement consistency, and time-sensitivity (1-3 above); B) LDR function and combined operation (4-5 above), and 6) correlation to manual measurements of daily food intake upon *in vivo* introduction (6i-iii above).

### *A.3.8 Preliminary test results*

Results from the six sets of preliminary validation tests are shown below. Collectively, test outcomes support *SnackerTracker* measurement validity as follows:

1) The calibration test (A) shows good alignment between *SnackerTracker*-recorded masses and known values, irrespective of the initial mass used for calibration. That is, expected masses correlate well with *SnackerTracker*-obtained values and corresponding trendline slopes do not differ significantly from an expected value of 1 (i.e., y = x) across all calibration masses ($r^2$=0.9987, F(1,14)=3.286, p=0.0913 for 28g; $r^2$=0.9987, F(1,14)=0.01674, p=0.9990 for 55g; and $r^2$=0.9996, F(1,14)=0.05310, p=0.8211 for 82g). This indicates that the *SnackerTracker* precisely returns the mass expected irrespective of the calibration mass selected.
2) No notable deviance from the initial values or random fluctuation was observed in the drift test (B). This suggests that simply performing regular device calibrations should suffice for reliable device performance (e.g., at the start of each *SnackerTracker* recording). Mean random fluctuations were functionally negligible (±0.045g) and informed the value to which the band-pass filter (*bufferHere*) should be initialised (i.e., 2×0.045≈0.1g).
3) In the step test (C), the *SnackerTracker* recordings closely matched those of known mass values upon sequential load removal ($r^2$=0.9999). However, while masses plotted against RTC-time precisely reflected the manually documented times at which food was removed (final time difference≈2s), LC-time differed notably (time difference≈54min). This shows that frequency-based timestamps do not reliably correlate with real-time. Operational code was modified solely to extract RTC timestamps.
4) In the LDR test (D), both lights 'dimming' light and absolute periods of lights being 'on' and 'off' can be identified in *SnackerTracker* outputs.
5) In the combined test (E), and as expected, mass measurements decreased during the light-phase with pellet removal. LDR recordings reflected light-status in the room, and switches are accurately shown as flipping either just before (switch 1) or after (switch 2) a change in lighting. When outside the recording room, the researcher successfully connected to the Arduino IoT and monitored recordings both from a networked laptop and mobile phone.
6) Then progressing to *in vivo* testing, Fi) shows very high correlation between *SnackerTracker* daily food intake (X) and the manually-obtained mass of the *SnackerTracker* (including food, Y) before and after 24h in a mouse cage (not differing significantly from a direct 1:1 relationship; Y=1.000X vs Y=X, $r^2$=0.9925, F(1,23)=0.004299, p=0.9483). This indicates good device accuracy *in vivo*. Fii) shows data comparing *SnackerTracker* outputs (Y) to manual mass recordings from cage-feeding (Y) from the same mouse over independent 24h periods. These do not significantly differ from an ideal direct relationship and demonstrate moderate correlation (i.e., Y=0.9736X vs Y=X, $r^2$=0.6291, F(1,23)=2.158, p=0.1554), suggesting that the method of food presentation does not consistently alter animal food intake in wild-type animals (i.e., in the *SnackerTracker* food holder as opposed to from the cage food-hopper or cage floor, notwithstanding likely error due to practical difficulties in recovering food manually). Iii) In the separate animal cohort, daily crumbling a manually measured at $\bar{x}$=0.219±0.016g/d. Animals did not show any signs of weight loss during recordings.

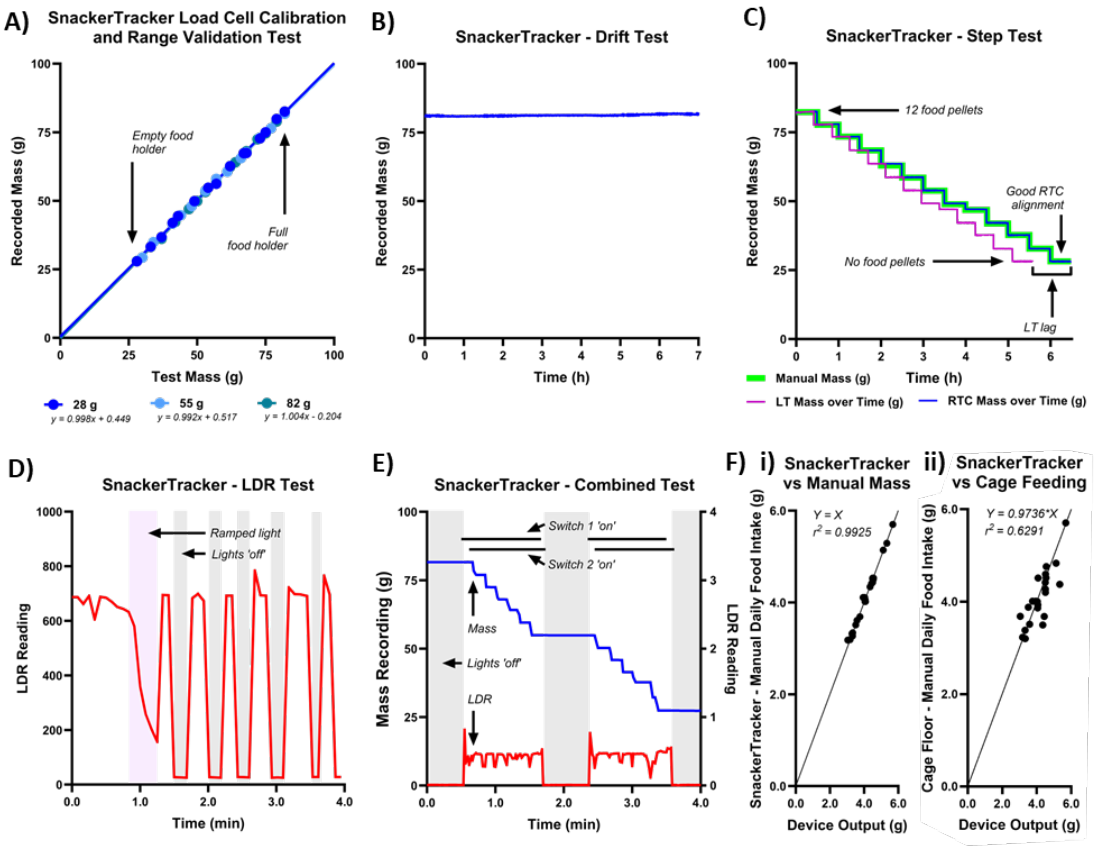


**Appx-Figure 11.** Shows the results of *SnackerTracker* benchtop validations and preliminary *in vivo* testing. A) The load cell calibration and range validation test shows near-perfect agreement between *SnackerTracker recordings* and manually obtained measurements, regardless as to which calibration mass was used (here tested at 28g, 55g, and 82g corresponding to a food holder which is near-empty, half-full, and full respectively). B) The drift test shows insignificant measurement fluctuation when subjected to a load for 7h without further perturbation, which indicates good system performance. C) The step test demonstrates close agreement between manually obtained expected mass-time values and those resulting with use of the RTC. LC timestamps appear inaccurate and temporally compressed, therefore indicating the RTC as the superior time-measurement method. D) The LDR test shows that the *SnackerTracker* can both report dimming light and absolute periods of lights being 'on' or 'off'. E) The combined test indicates that all outputs function as expected. Switch data is accurately returned to reflect switches 1 and 2 changing status directly before and after each time the lights are turned 'on' or 'off'. Reported masses align with 6 pellets being sequentially removed during each light phase, during which LDR recordings increase as expected. F) *SnackerTracker* data correlates i) very closely with the manually-weighed difference in the mass of the device with food before and after a 24h period, indicating good *in vivo* measurement accuracy; and ii) moderately with manual measurements obtained without the *SnackerTracker* during an independent 24h period in the same mouse cage (i.e., paired *SnackerTracker* vs non-*SnackerTracker* daily food intake, where manual data was obtained the traditional way by simply adding, removing, and weighing pellets). Daily measurements are not consistently increased or decreased with cage floor vs *SnackerTracker* food presentation.

## *A.3.9 Software variables*

**Appx-Table 3.** Lists and describes *TracKIT* processing variables employed across steps I-V) (**3.2.2**). Effects of increasing or decreasing each are described with sample values where applicable.

| Step | Variable ID | Variable Name | Description | Effect of Increasing | Effect of Decreasing | Input Details |
|---|---|---|---|---|---|---|
| | alignLight | Light alignment | Enables users to shift and align 24-hour outputs to begin at light/dark onset | N/A (yes or no input) | N/A (yes or no input) | Y/N |
| | do24HStart | Manual 24-h crop onset | If 24-hour cropping is not applied, indicate the index of the first data point to be retained | N/A (yes or no input) | N/A (yes or no input) | Y/N |
| | do24H/ Truncation | 24-hour cropping | Indicates whether raw data should be cropped to 24-hour timeframe(s) | N/A (yes or no input) | N/A (yes or no input) | Y/N |
| | endPoint | End data exclusion | Specifies the number of indexed datapoints which are to be truncated from the end of recordings | Retains more data by ending recordings later | Retains less data by ending recordings earlier | Index |
| | howMany24H | 24-hour duration | If 24-hour cropping is applied, indicates how many to keep | Increases total duration in 24-hour blocks | Decreases total dataset duration in 24-hour blocks | Integer |
| | lightFor24H/ Crop | Light cropping | If any cropping is to be applied, this allows data retention to begin when lights turn ‘on’ or ‘off’ | N/A (yes or no input) | N/A (yes or no input) | Y/N |
| | lightFor24H/ CropONOFF | Light cropping specification | If light cropping is applied, this indicates whether data retention should begin when lights turn 'on' or 'off' | N/A (yes or no input) | N/A (yes or no input) | Y/N |
| | massUnit | Mass unit | The unit of mass for inputs and outputs | N/A (constant) | N/A (constant) | g |
| | skrtkrFile/ Location | File folder location | Directs the program to the folder containing raw *SnackerTracker data files* | N/A (constant) | N/A (constant) | N/A |
| | startDate | Start date | The date on which data recording began | N/A (constant) | N/A (constant) | N/A |
| | startPoint | Initial data exclusion | Specifies the number of indexed datapoints to be truncated from the start | Retains less data beginning later in time | Retains more data beginning earlier in time | Index |
| | timeFormat | Time format | The unit of time for final outputs | N/A (constant) | N/A (constant) | w/d/h/min/s |
| | timeLightOff | Lights ‘off’ | Defines when lights turn ‘off’ | Shifts dark regions later in time (to the right) relative to mass data | Shifts dark regions earlier in time (to the left) relative to mass data | 24-h time |
| | timeLightOn | Lights ‘on’ | Defines when lights turn ‘on’ | Shifts light-regions later in time (to the right) relative to mass data | Shifts light-regions earlier in time (to the left) relative to mass recordings | 24-h time |
| | timeStart | Start time | Defines the time at which recordings began | Shifts data to the right (later in time) relative | Shifts data recordings to the left (earlier in time) relative to | 24-h time |

| | | | | | | |
|---|---|---|---|---|---|---|
| | | | | to unaltered light- regions | unaltered light regions | |
| | truncateEnd | Final cropping | If applied, the user can exclude measurements at the end of recordings | N/A (yes or no input) | N/A (yes or no input) | Y/N |
| | truncateStart | Initial cropping | If applied, the user can exclude measurements from recording onset | N/A (yes or no input) | N/A (yes or no input) | Y/N |
| **II)** | bufferHere | Band-pass filter | Removes datapoints greater or less than the prior value by that which is specified | Yields a less-restrictive filter (removes fewer data) | Results in a restrictive filter (removes more datapoints) | e.g., 0.1g |
| | chipEndTime | Chip end index | Defines the end-point defining the flanked region for chip filter application | N/A (identifying index) | N/A (identifying index) | Index |
| | chipMass | Chip mass | For each chip filter, the user must specify the mass cutoff which the difference between initial and final flanking values must exceed | Results in a more-restrictive filter (i.e., a greater mass difference is required for filter application) | Results in a less-restrictive filter (i.e., the chip filter can be applied upon smaller mass differences) | e.g., 0.5 |
| | chipStartTime | Chip start index | Defines the start-point defining the flanked region for chip filter application | N/A (identifying index) | N/A (identifying index) | Index |
| | crudeMass | Crude mass | The expected mass difference obtained from manual measurements | N/A (identifying index) | N/A (identifying index) | e.g., 19.43 |
| | doChipFilter | Chip filter | Determines whether chip filters will be applied. If the difference between start and end values (chipStartTime and chipEndTime) exceeds chipMass, subsequent data will be shifted to the value directly preceeding chipStartTime | N/A (yes or no input) | N/A (yes or no input) | Y/N |
| | doScaleFilter | Scale filter | Determines whether scale filters will be applied to confirm whether the expected mass difference obtained from manual measurements is reflected in *SnackerTracker* data outputs. | Increases the total amount of food reportedly consumed by up-scaling according to the value defined by crudeMass | Decreases the total amount of food reportedly consumed by down-scaling according to the value defined by crudeMass | Y/N |
| | measureSpan | Time-pass filter | The span over which measurement values will be checked for whether they fall within the band-pass filter | Results in a restrictive filter which applies band-pass criteria over a greater range | Results in a less-restrictive filter which applies band-pass criteria across fewer data | e.g., 30 |
| | setTime | Baseline establishment | Determines the number of data points which should be incorporated into baseline establishment, which will be used as a start-buffer for data filtering | Enables a longer band-pass filtering baseline and window. High values may result in over-conservative filtering. | Shortens the baseline and windows for band-pass filtering. Low values cannot facilitate sufficient truncations | e.g., 32 |

| | | | | | | |
|---|---|---|---|---|---|---|
| | shiftFilter | Shift filter | Loops through data points to check whether each corresponds to food being consumed | Results in a more-restrictive filter as more data can be shifted | Results in a less-restrictive filter as fewer data can be shifted | e.g., 1000 |
| | shiftTolerance | Shift tolerance | Defines shift tolerance. shiftTolerance*100 represents the percentage of data within a shiftFilter loop which must be less than the indexed value. | The shift filter can be more readily applied; fewer 'outlier' values are required for shift correction | The shift filter is not as easily applied; fewer 'outlier' values are permitted | e.g., 0.99 |
| | window | Smoothing filter | Defines the number of data points which can be incorporated into a moving-mean filter | Increases preliminary smoothing. Data appears more clean yet information may be lost | Decreases preliminary data-smoothing. Data appears less-clean, however more information is retained | e.g., 60 |
| **III)** | fooddervBuffer | Feeding derivative | Determines the number of data points across which the derivative of the cumulative food intake plot will be calculated | Rates are calculated across a longer timeframe. Feeding patterns may be easier to visualise, yet details may be lost | Rates are calculated across a shorter timeframe. Feeding patterns may be more difficult to visualise, yet detailed insights may be retained | e.g., 6000 |
| | intdervBuffer | Interactions derivative | Determines the number of data points across which the derivative of the cumulative animal-device interactions plot will be calculated | Rates are calculated across a longer timeframe. Interaction patterns may be easier to visualise, yet detailed data may be lost | Rates are calculated across a shorter timeframe. Data may be more difficult to visualise (i.e., 'noisier'), yet information is retained | e.g., 6000 |
| | lightCutoff | Light cutoff | For binary light filtering, this specifies the threshold wherein greater values = 1 and lesser-values = 0 | Brighter lighting is needed. Results in a more strict filter | Dimmer lighting is sufficient for representation by a '1'. Results in a less-strict filter | e.g., 15 |
| | lightFilterType | Light filter type | If light filtering is to be applied, the user must indicate whether continuous (i.e., smoothing) or binary (i.e., assigned by thresholding) | N/A (0 for binary, or 1 for continuous) | N/A (0 for binary, or 1 for continuous) | 1/0 |
| | smoothLight/ Window | Continuous smoothing | Apply data smoothing to continuous light measurements | Increases smoothing. | Decreases smoothing | e.g., 200 |
| **IV)** | binDuration | Data compression bin size | Defines binned timeframes | Outputs arrays are smaller for processing yet may conceal data insights | Outputs arrays are larger and more difficult to handle during processing | e.g., 60 |
| | Compress/ Seconds/ Factor | Compression format | If compression is applied, whether as a factor of file or bin size | N/A (0 for bin size, 1 as a factor) | N/A (0 for bin size, 1 as a factor) | Y/N |
| | doFile/ Compression | Data compression | Enables the user to 'bin' and thus compress data | N/A (yes or no input) | N/A (yes or no input) | Y/N |
| **V)** | finaliseOutput | Summary confirmation | Confirms the user is satisfied with all data filtering | N/A (yes or no input) | N/A (yes or no input) | Y/N |

## *A.3.10 Representative output file*

**Appx-Figure 12.** Depicts a representative *SnackerTracker* output/metadata file following data processing. Green = summary information as obtained from the entire recording sample, blue = processing specifications, and yellow = sample timeline outputs. Timeline outputs are produced in a separate file, with an additional compressed file if specified, and are shown transposed here for brevity.

| SnackerTracker Data: Summative and Processing Information | | | | |
|---|---|---|---|---|
| | | | | |
| Data Summary: | | | | |
| | | | | |
| Total Mass Consumed: | 4.0615 | | | |
| Total Mass Consumed in the Dark: | 3.7045 | | | |
| Total Mass Consumed in the Light: | 0.35698 | | | |
| Total Mass Consumed at Darkness Onset: | 1.0348 | | | |
| Total Mass Consumed at Light Onset: | 0.2815 | | | |
| Total Interactions: | 5586 | | | |
| Total Interactions in the Dark: | 4486 | | | |
| Total Interactions in the Light: | 1100 | | | |
| Total Interactions at Darkness Onset: | 1455 | | | |
| Total Interactions at Light Onset: | 213 | | | |
| | | | | |
| Data Processing Information: | | | | |
| | | | | |
| Start Date and Time \|\| End Date and Time: | 2023-09-23 12:26:18 \|\| 2023-09-24 12:26:16 | | | |
| Lights On: | 6:00 | | | |
| Lights Off: | 18:00 | | | |
| Crop at Start (Yes-No/# Cropped): | Yes/1000 | | | |
| Crop at End (Yes-No/# Cropped): | Yes/300 | | | |
| 24-Hour Truncation (Yes-No for Truncation/# Days/Start Index/Yes-No for Light Alignment/0-1 for at Lights Off-On/Yes-No for Light Shifting): | Yes/1/4000/N/NA/Y | | | |
| Output Time Units: | h | | | |
| Switch 1 Filter (Inversion/Yes-No for Mass/Yes-No for Light): | Original/No/No | | | |
| Switch 2 Filter (Inversion/Yes-No for Mass/Yes-No for Light): | Original/No/No | | | |
| Baseline Mass: | 15.2194 | | | |
| Mass Units: | g | | | |
| Data Points Set to Baseline: | 32 | | | |
| Mass Buffer: | 0.1 | | | |
| Time Buffer: | 30 | | | |
| Mean Filter Window: | 60 | | | |
| Mass Filter Option: | 6 | | | |
| Shift Filter: | 1000 | | | |
| Shift Tolerance: | 0.99 | | | |
| Plateau-Only Filter Applicaiton (Yes-No): | Yes | | | |
| Shift-Only Filter Applicaiton (Yes-No): | No | | | |
| Plateau and Shift Filter Applicaiton (Yes-No): | No | | | |
| Chip Filter Application (Yes-No (Start Time/End Time/Mass Threshold): | No | | | |
| Food Derivative Buffer: | 6000 | | | |
| Interactions Derivative Buffer: | 6000 | | | |
| Short Derivative Correction (Yes-No): | No | | | |
| Light Filter (Yes-No Overall/Binary-Continuous/Mean Filter Window/Light Cutoff): | Yes/Binary/200/15 | | | |
| File Compression (Binned-Condensed/Factor): | Binned/60 | | | |
| | | | | |
| Sample Output: | | | | |
| | | | | |
| time_h | 0.008333333 | 0.025 | 0.041666667 | 0.058333333 |
| mass_g | 12.03182522 | 12.02582522 | 12.02247038 | 12.02182522 |
| filtered_mass_g | 12.00845376 | 12.00845376 | 12.00845376 | 12.00845376 |
| filtered_food_intake_g | 0 | 0 | 0 | 0 |
| filtered_food_intake_derv | 3.695170386 | 3.711297522 | 3.712272541 | 3.712272541 |
| interactions_amplitude_mass_g | 0 | 0 | 0 | 0 |
| interactions_binary | 0 | 0 | 0 | 0 |
| interactions_cumulative | 0 | 0 | 0 | 0 |
| interactions_derv | 3012.810077 | 3012.810077 | 3012.810077 | 3012.810077 |
| fft_raw | -20.46824380 | 4.689658394 | -9.730748289 | 8.383889931 |
| fft_interactions_derv | -395.4996813 | -446.4090401 | -386.3101642 | -368.1971011 |
| light_reading | 1 | 1 | 1 | 1 |
| light_reading_filtered | 0 | 0 | 0 | 0 |
| switch1_status | 1 | 1 | 1 | 1 |
| switch2_status | 0 | 0 | 0 | 0 |
| scheduled_light | 1 | 1 | 1 | 1 |

## A.4 SnackerTracker setups

### *A.4.1 SnackerTrackers in digitally ventilated cages*




**Appx-Figure 13.** *SnackerTracker* setup in DVCs (**1.5.1**, **2.2.3**). Opaque LED-equipped cages are shown (A) with and (B-D) without the lid. DVC monitoring areas are shown for (C) whole-cage (pink) and (D) mid-cage (purple) measurements (i.e., where the *SnackerTracker* was placed). D) DVCs were placed within the same rack for CRY experiments (N=12 total).

### *A.4.2 SnackerTrackers and passive infrared monitoring*

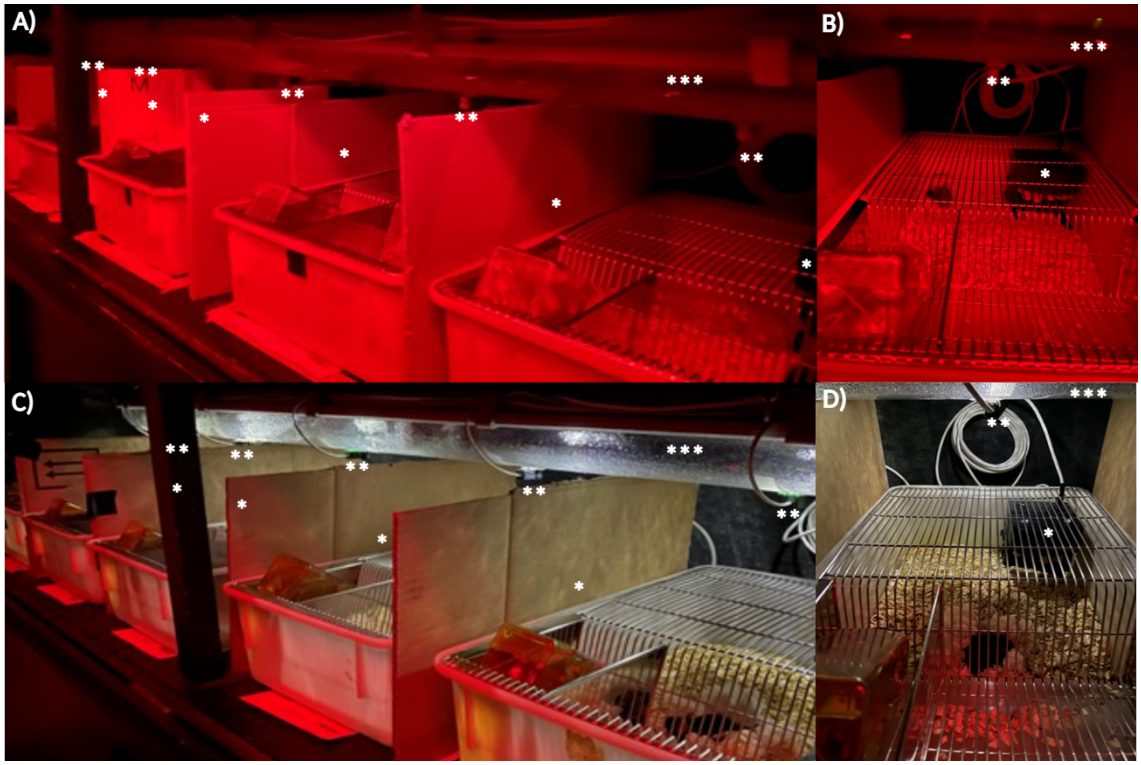


**Appx-Figure 14.** Illustrates the DLE experiment setup (**1.5.1**, **2.2.4**). Open-top-cages within LTCs are shown A-B) under regular light-dark conditions just after dark onset and C-D) with DLE before dark onset. Within LTCs, views of A,C) all cages and B,D) a single cage are provided to depict **SnackerTrackers*, **PIRs, and ***DLE lighting systems.

### *A.4.3 SnackerTrackers in Faraday LTCs with hamsters*

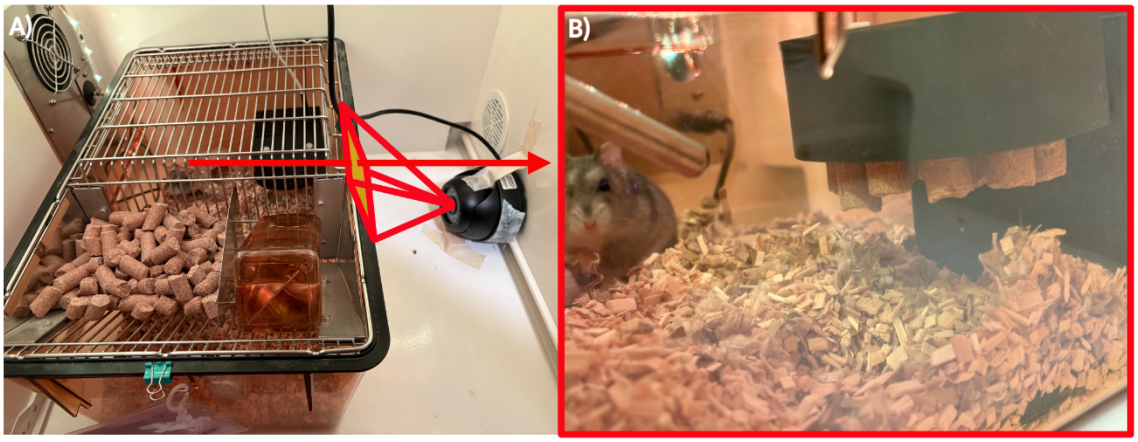


**Appx-Figure 15.** Shows the hamster *SnackerTracker* recording setup. Note the wall-mounted camera in A) through which the image in B) was acquired (the field of view illustrated in red). The hamster is visible to the left in B) next to the *SnackerTracker* with fresh pellets suspended.

### *A.4.4 SnackerTracker feeding behaviour*

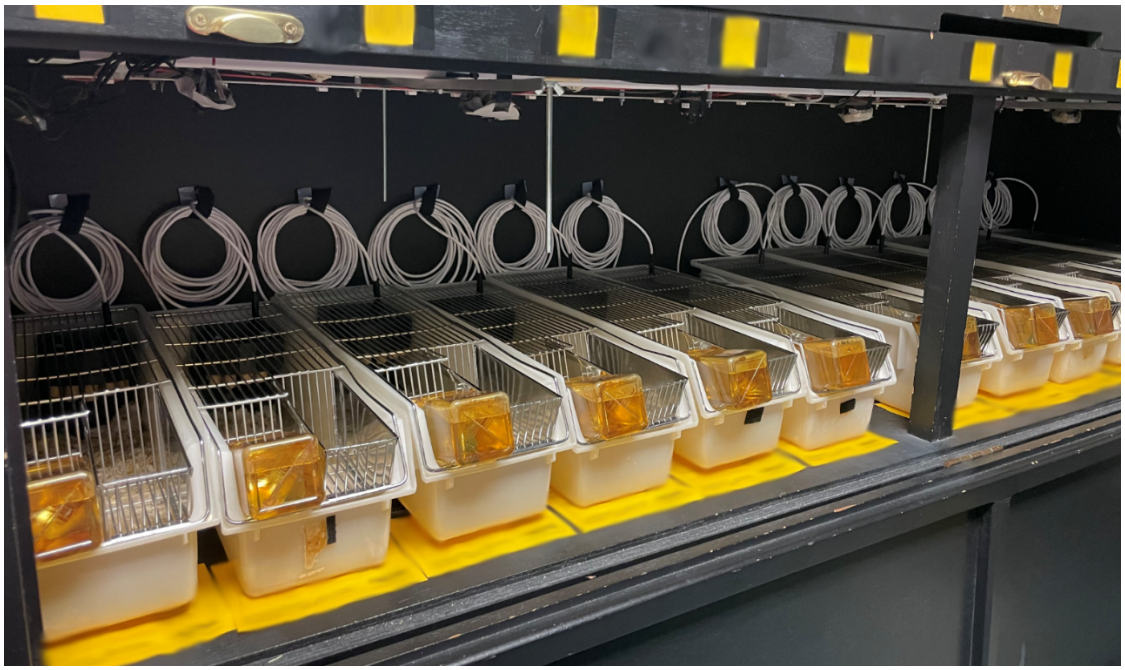

**Appx-Figure 16.** Shows wired *SnackerTrackers* within a single LTC (12 per chamber).

### *A.4.5 SnackerTracker feeding behaviour*




**Appx-Figure 17.** Illustrates the *SnackerTrackers* assembled within LTCs on the first day of full-cohort STAMINA experiments (12 mice per coffin). AnyMaze is configured on the computer monitor, and the VCT is set up next to the step stool (just lacking containment walls).

## A.5 Tissue processing

### *A.5.1 Protein targets*

**Appx-Table 4.** Details the genes, proteins, and antibodies which were employed, optimised, or comparatively considered in IHC experiments throughout this thesis. Information is provided for each regarding expected anatomical locations in the central nervous system, subcellular expression patterns, and relevance to present work.

| **Name (Abbreviation, GENE[283])** | **Anatomical Location** | **Subcellular Location (Uniprot #).** | **Present Relevance** |
|---|---|---|---|
| **Dopamine receptor 1a (*Drd1a*, DRD1A)** | L6a-b, to a lesser extent in CA1, and occasionally in the striatum as animals age[4, 35, 40, 77]. | Membranous (Uniprot #Q61616). | DRD1A is a g-protein coupled receptor which enables cell responsivity to dopaminergic signalling, being found both on and within neurons (e.g., endoplasmic reticula, cilium, dendrites, and dendritic spines). Its Cre-driver line is used for L6 investigations (see **1.2**). |
| **Retinol binding protein 4 (*Rbp4*, RBP4)** | L5, hippocampal CA3 and dentate gyrus, and in the cerebellum[40, 77, 481]. | Cytoplasmic (Uniprot #Q00724). | RBP4 is a secreted transport protein which delivers retinol to tissues and facilitates transport across the cell membrane. Its Cre driver line is used for L5 investigations (see **1.3**). |
| **FEZ family zinc finger 2 (*Fezf2*, FEZF2)** | Predominantly L5, and to a lesser extend in L6[399]. | Nuclear (Uniprot #Q9ESP5). | FEZF2 is a transcription repressor which influences cortical L5b extratelencephalic development[119, 127, 482]. Its driver line was employed (see **1.3.1**), for histological comparison to *Rbp4*-Cre findings. |
| **Complexin 3 (*Cplx3*, CPLX3)** | Predominantly L6b[35, 46, 482]. | Membranous, synaptic concentration (Uniprot #Q8R1B5). | CPLX3 is a protein which positively regulates SNARE-mediated synaptic vesicle fusion. It represents a subset of *Drd1a*-Cre cells in L6b, conceivably corresponding to L1-projecting subcircuits (see **1.2**)[35, 46, 48, 483]. |
| **Connective tissue growth factor (*Ctgf*, CTGF)** | Predominantly L6b[482]. | Extracellular matrix (Uniprot #P29268). | Ctgf is a secreted protein which is associated with promoting dendrite branching and modulating nearby oligodendrocyte activity. It is expressed in a subset of subplate remnants and has been used to identify *Drd1a*-Cre L6b subpopulations[47, 48, 482, 484]. |
| **T-box brain 1 (*Tbr1*, TBR1)** | Expressed through L2-6b[44, 45]. | Nuclear (Uniprot #Q64336). | TBR1 is a transcriptional repressor associated with neuronal migration, regionalisation, lamination, and axon pathfinding during cortical development. It's repression of *Fezf2* restricts CST projections such that mature tracts consist of L5b axons. TBR1 can be used to visually discriminate the L5-6 boundary (being more highly expressed in L6 than in L5)[45]. |
| **Neuronal nuclei (*NeuN*¸*Rbfox 3,* NEUN, RBFOX3)** | Throughout L2-6, in subcortical nuclei, and throughout the peripheral nervous system[482]. | Binds to RNA transcripts (RBFOX3 N-terminal) in postmitotic neuronal nuclei (Uniprot #Q8BIF2). | RBFOX3 is an RNA binding protein which regulates pre-mRNA alternative splicing, particularly of strands containing premature stop codons designated for degradation. NEUN can be used as a pan-neuronal mask to enable quantifications of the proportions of neurons labelled by Cre-drivers and co-expression patterns therein (e.g., *Drd1a*/CPLX3, *Rbp4*/SMI-32, and *Rbp4*/CHAT). |
| **SMI32, targeting neuro-filament heavy** | Labels large projection neurons, including L5b extratelencephalic pyramidal neurons | Cytoplasmic expression; binds to non-phosphorylated epitopes of NF-H chains | NF-H is a major element of the neuronal cytoskeleton. Reduced SMI-32 expression may indicate cytoskeletal degeneration due to NF-H dysfunction, and commonly indicates MN decline in ALS research[485-487]. SMI-32 colocalisation with *Rbp4*/*Fezf2* is predicted, yet the proportion of SMI- |

| | | | |
|---|---|---|---|
| **peptide (*Nf-H*, NF-H, NEFH)** | and spinal cord ventral horn α-motor neurons. | (Uniprot #P19246). | 32$^{+}$/*Rbp4*\|\|*Fezf2*-Cre$^{+}$ and SMI-32$^{+}$/*Rbp4*-Cre$^{-}$ cells across cortical regions under normal and silenced states remains unknown. |
| **Choline acetyl-transferase (*ChAT*, CHAT)** | Expressed in cholinergic LMNs located in the spinal cord (i.e., anterior horn) and brainstem. | Cytoplasmic, particularly at the synapse (Uniprot #Q03059). | CHAT catalyses the reversible synthesis of Ach from acetyl CoA and choline. UMNs do not express high levels of CHAT, thus CHAT should not colocalise with *Rbp4* or *Fezf2*. Notable colocalisation with SMI-32 is predicted, yet the extent to which this is the case and whether CHAT$^{+}$/SMI-32$^{+}$ or CHAT$^{+}$/SMI-32$^{-}$ neurons degenerate upon *Rbp4*/*Fezf2* cKO remains unknown. |
| **Myelin binding protein (*Mbp*, MBP)** | Throughout myelinated axons in the central and peripheral nervous system. | Extracellular adhesive protein (Uniprot #P04370). | Mbp contributes to the formation and structural integrity of myelin by enabling compact membrane stacking, lending to enhanced axon insulation and conductance. Myelin loss may accompany motor neuron dysfunction in *Rbp4*/*Fezf2 Snap25*-cKOs, which can be qualitatively evaluated and quantitatively investigated via intensity-based thresholding. Thresholds can detect and mask white matter tracts for AT8 analyses. |
| **AT8 (*Mapt*, AT8)** | Primarily found in degenerating axons within the central nervous system; however, in diseased states, AT8 can also be engulfed by astrocytes or oligodendrocytes. | Cytosolic, wherein AT8 binds to abnormally phosphorylated tau proteins at sites S202 and T205 (Uniprot #P10637). | Tau proteins promote microtubule assembly, stability, and membrane-anchoring. AT8 is a monoclonal antibody which targets phosphorylated tau, including pathological aggregates. In motor degenerative models (e.g., ALS-FTD), AT8 has been shown to accompany or precede TDP-43 aggregation after motor deficits emerge[488, 489]. This may occur upon *Rbp4*/*Fezf2 Snap25*-cKO and will be studied alongside whether aggregation (if present) occurs within myelinated axons or elsewhere. |
| **Ionized calcium binding adaptor molecule 1 (*Iba1,* IBA1, AIF1)** | Mature microglia throughout the central nervous system. | Binds to cytoskeletal F-actin within microglial cytosol (Uniprot #O70200). | IBA1 calcium-binding proteins enable microglial actin bundle formation, which facilitates membrane ruffling for cell motility and phagocytosis. *Rbp4*/*Fezf2 Snap25*-cKO may increase IBA1 expression near Cre-expressing cells or projection targets, which may exacerbate with age and as motor deficits emerge. |
| **Cluster of differentiation 68 (*Cd68*, CD68)** | Mature reactive microglia throughout the central nervous system. | Cytosol (lysosomes and endosomes) and membranes (Uniprot #P31996). | CD68 is expressed in reactive microglia, playing a role in cell-antigen interactions and metabolism upon phagocytosis. Co-staining with IBA1 may reveal an increased prevalence of reactive microglia upon *Rbp4*/*Fezf2 Snap25*-cKO both in Cre-expressing and projection regions. |
| **Glial fibrillary acid protein (*Gfap*, GFAP)** | Mature astrocytes throughout the central nervous system. | Cytoplasmic, particularly near intermediate filaments (Uniprot #P03995). | GFAP is associated with various inflammation-related processes including cell proliferation, differentiation, enzyme regulation, calcium homeostasis, and cytoskeletal function[184]. As with IBA1/CD68, *Rbp4*/*Fezf2 Snap25*-cKO may lead to increased GFAP expression, which may exacerbate with age and as motor deficits emerge. |
| **S100 calcium-binding protein β (*S100β*, S100β)** | Mature reactive astrocytes throughout the central nervous system[490, 491]. | Expressed in the nucleus, cytoplasm, and as a secreted protein (Uniprot #P50114). | S100β is a zinc- and calcium-binding protein which promotes astrocytosis and axon proliferation. It is associated with reactive astrocytes[490, 491]. As with IBA1/CD68, GFAP co-staining may reveal an increased prevalence of reactive astrocytes upon *Rbp4*/*Fezf2 Snap25*-cKO both in Cre-expressing and projection regions. |

| | | | |
|---|---|---|---|
| **Parvalbumin (*Pvalb*, PV, PVALB)** | Expressed subcortically and cortically (save L1) throughout the central nervous system[262, 484, 492]. | Cytoplasmic calcium binding protein, particularly at synaptic terminals (Uniprot #P32848). | PV is a reliable marker for a subset of fast-spiking GABAergic interneurons. PV regulates intracellular environments by rapidly buffering $Ca^{2+}$ in nerve terminals to prevent over-accumulation $^{+}$ during high-frequency firing. Interneuron dysfunction has been implicated in motor neuron disease progression[261, 487, 493-495]. Expression may decrease in L5 or the spinal cord upon *Rbp4*/*Fezf2 Snap25*-cKO. |
| **Vicia villosa agglutinin (VVA, N/A)** | Targets both cortical and subcortical perineural nets throughout the central nervous system[262]. | Binds to specialised proteoglycans of the extracellular matrix (Uniprot #P56625). | VVA is a plant-derived protein which binds to mouse perineural nets. $VVA^{+}$ is associated with neuron maturity and capacity for plasticity[262]. Perineural nets are responsible for: structurally supporting synapses; restricting synaptic remodelling; limiting or selectively re-opening plasticity; shielding cells from oxidative stress; and controlling cell surface access[386]. Perineural net deficits have been implicated in ALS[461, 493], thus IHC experiments will test whether *Rbp4*/*Fezf2 Snap25*-cKO influences VVA density, distribution, and PV colocalisation (or lack thereof). |
| **COUP TF1-interacting protein 2 (*Ctip2*, *Bcl11B*, CTIP2, BCL11B)** | Throughout cortical layers, particularly in extratelencephalic L5b projections[118, 119] and a subset of corticothalamic L6 neurons[45, 119, 482]. | Nuclear (Uniprot #Q99PV8). | CTIP2 is a transcriptional repressor influencing CST motor neuron neurodevelopment (e.g., facilitiating L5 extratelencephalic projections)[119]. CTIP2 and SATB2 co-staining can distinguish extratelencephalic- and intratelencephalic *Rbp4*/*Fezf2* Cre-expressing subsets respectively, and whether either is more susceptible to effects of *Snap25*-cKO. |
| **Special AT-rich sequence-binding protein (*Satb2*, SATB2)** | Throughout cortical layers, save L1[482]. | Nucleus (Uniprot #Q8VI24). | SATB2 is a transcriptional repressor (including of CTIP2) which regulates intratelencephalic connections during neurodevelopment (particularly L5)[48, 125, 126]. CTIP2/SATB2 co-staining can distinguish extratelencephalic- and intratelencephalic *Rbp4*/*Fezf2* Cre-expressing subsets respectively, and whether either is more susceptible to effects of *Snap25*-cKO. |
| **CC1 (*Qki-7*, QKI-7, CC1)** | Mature oligodendrocytes throughout the central nervous system. | Binds to proteins found primarily in the nucleus and in the cytoplasm (Uniprot #Q9QYS9). | CC1 is an antibody which targets quaking 7 (QKI-7)—an RNA-binding protein which regulates splicing during oligodendrocyte differentiation. It may detect changes in densities upon *Rbp4*/*Fezf2 Snap25*-cKO; previous studies only studied oligodendrocytes <P21, and the OLIG2 antibody used is only compatible with younger and freshly perfused tissues[79]. |
| **Orexin receptor 1 (*OrxR1*, *Hcrtr1*, ORXR1, HCRTR1)** | Subcortically and in deep cortical layers (L6b)[93, 96, 427]. | Membranous (Uniprot #P58307). | ORXR1 is a g-protein coupled receptor which exhibits greater affinity for ORXA and promotes wakefulness and feeding (**1.2.4**). |
| **Orexin receptor 2 (*OrxR2*, *Hcrtr2,* ORXR2, HCRTR2)** | Subcortically, and cortically in L5-6b and sparsely in L2-4[44, 93, 96]. | Membranous (Uniprot #P58308). | ORXR2 is a g-protein coupled receptor which exhibits near-equal affinity for ORXA and ORXB . It is known to promote wakefulness and feeding (see **1.2.4**). |

### *A.5.2 Expected protein expression*

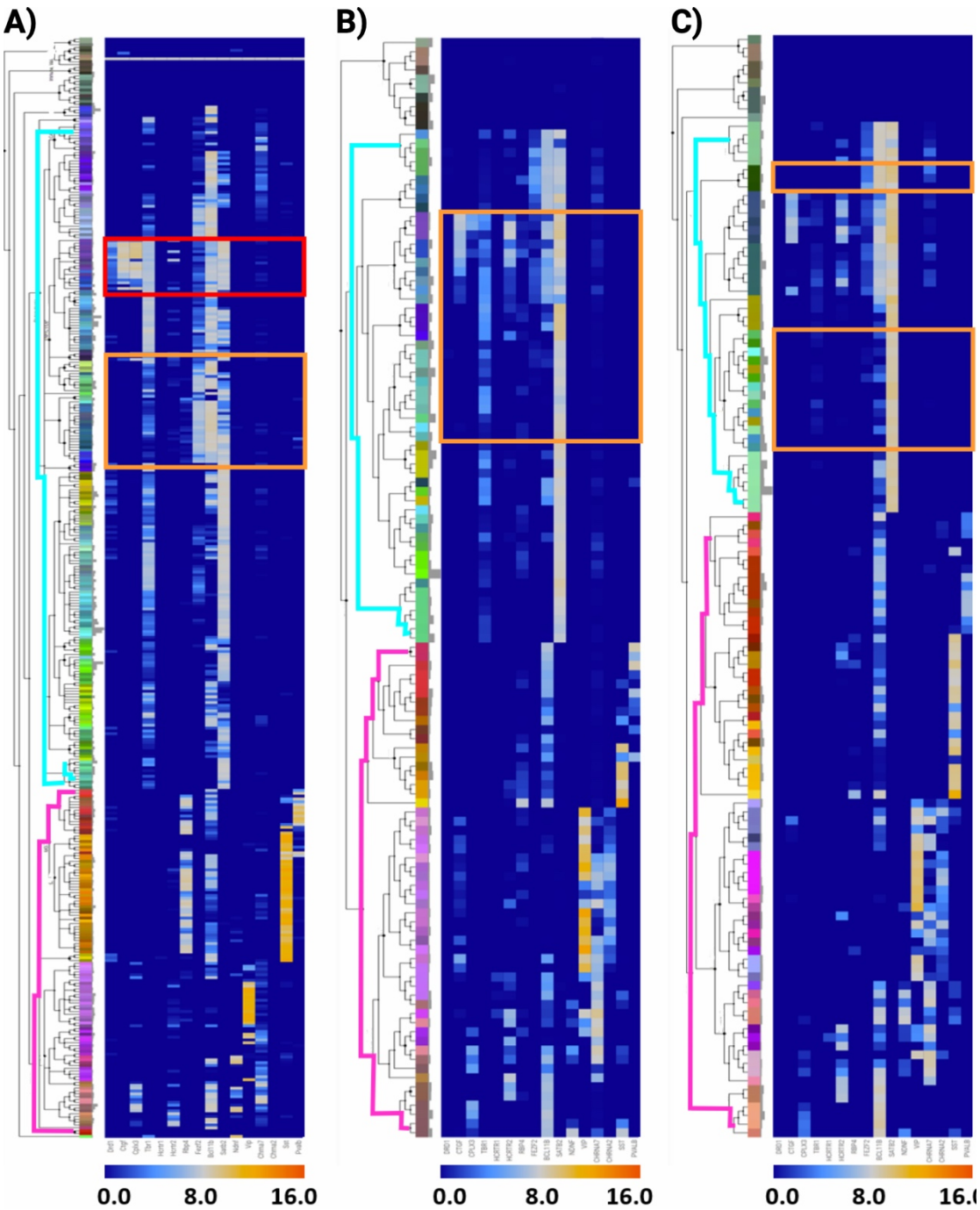


**Appx-Figure 18.** Transcriptomic RNA-sequencing heat maps of the A) mouse cortex and hippocampus, B) multiple human cortical areas, and C) human primary motor cortex compare protein mRNA expression in cell populations and cortical layers of interest. Cyan = excitatory neurons, magenta = inhibitory neurons, orange = L5 *Rbp4*-Cre targets (L5 for humans), and red= L6b *Drd1a*-Cre targets (N/A for humans; WMINs are not included). Colour legend units represent trimmed means, where higher numbers indicate greater expression. Data were acquired and adapted from the Allen Brain Institute where cell hierarchy details are freely available[81].

### *A.5.3 Vibratome slicing*

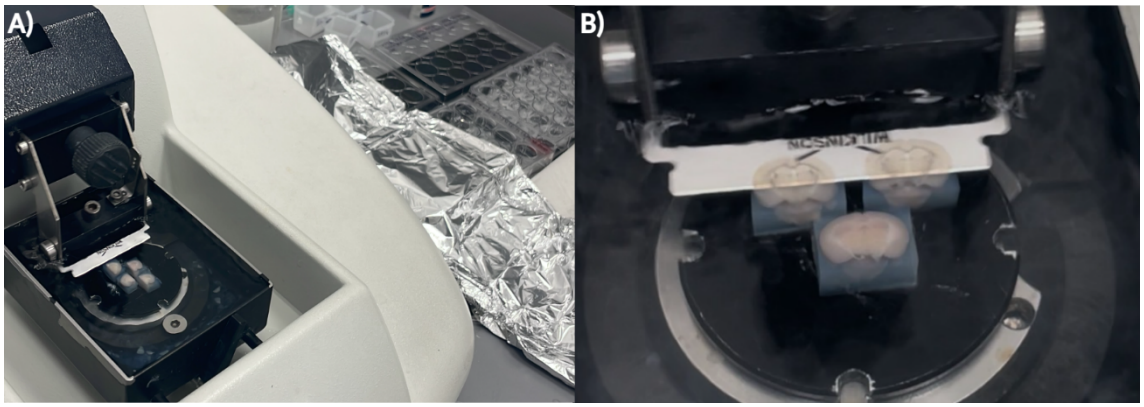


**Appx-Figure 19.** Depicts vibratome slicing of multiple coronal sections simultaneously.

### *A.5.4 Spinal scaffolds*

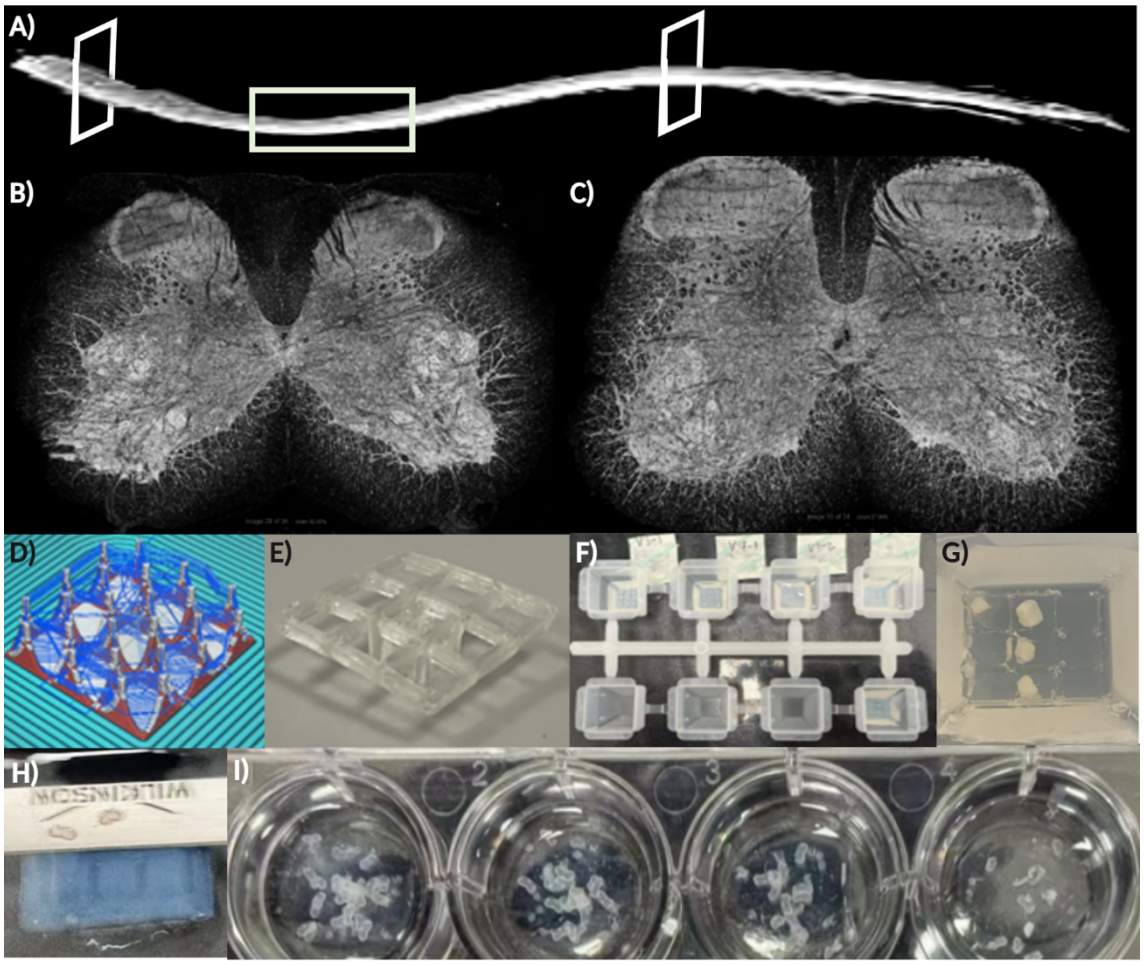


**Appx-Figure 20.** Spinal sectioning using a novel system. A) Spinal cord sections at the B) cervical, thoracic, and C) lumbar level were targeted for immunohistochemistry. I designed custom spinal scaffolds as shown D) rendered in Ultimaker Cura for E) 3D printing. The scaffold was printed using combinations of various parameters and optimised to F) evaluate which settings optimally resulted in G) dissolution upon agarose embedding and gelatinisation. H) gel structures with dissolved scaffolds were then sliced with a vibratome, expediting processing I) 9-fold.

## *A.5.5 Immunohistochemistry specifications*

**Appx-Table 5.** Lists product information and optimised stain specifications. As detailed in **Table 13**, experiments per driver involved: *Rbp4*-Cre DREADDs → 1; *Drd1a*-Cre-PTEN → 1-2; *Drd1a*-Cre-*Snap25* → 2; *Rbp4*-Cre-*Snap25* → 1, 3-6; and *Fezf2*-Cre$^{ER}$-*Snap25* → 1, 3-6. See **A.5.1** for protein targets and **A.5.6** for optimisations. All secondary antibody dilutions=1:500. *Protocols involving IBA1, GFAP, or CC1 required aldehyde-quenching, and CC1 required heat-induced epitope retrieval. All blocking solutions were diluted in PBS, save †stain sets involving VVA which included 0.15M NaCl and 0.1mM $CaCl_2$. Targets are coloured according to their appearance in this thesis, and secondary antibodies according to emission wavelengths (λ, nm). NDS=normal donkey serum; NGS=normal goat serum; Rb=rabbit; Ms=mouse; Rt=rat; Ck=chicken; TX=Triton-X; N/A=not applicable; Bt=biotinylated; Cy5=cyanine-5; and SAV=streptavidin.

| Stain Set & Targets | | *†Block Solution #1 | | Primary Antibody | | | | †Block Solution #2 | | Secondary Antibody | | |
|---|---|---|---|---|---|---|---|---|---|---|---|---|
| | | TX | Serum | Name | Supplier | Product # | Dilution | TX | Serum | Name | Supplier | Product # |
| 1 | PV | 0.2% | 2% NDS | RbαPV | **Swant** | PV27 | 1:500 | 0.2% | 2% NDS | DkαRb (488) | **Invitrogen** | A21206 |
| | VVA | | | Bt-VVA | **Vector Labs** | B-1235-2 | 2µg/mL | | | Cy5 (650) | **Invitrogen** | SA1011 |
| | DAPI | | | N/A | **Invitrogen** | D1306 | 1:1000 | | | N/A (358) | N/A | N/A |
| | Driver | | | N/A | N/A | N/A | N/A | | | N/A (581) | N/A | N/A |
| 2 | CPLX3 | 0.1% | 2% NDS | RbαCPLX3 | **SySy** | 122 302 | 1:1000 | 0.1% | 2% NDS | DkαRb (488) | **Invitrogen** | A21206 |
| | TBR1 | | | MsαTBR1 | **ProteinTech** | 66564-1-LG | 1:500 | | | DkαMs (647) | **Invitrogen** | A32787 |
| | DAPI | | | N/A | **Invitrogen** | D1306 | 1:1000 | | | N/A (358) | N/A | N/A |
| | Driver | | | N/A | N/A | N/A | N/A | | | N/A (581) | N/A | N/A |
| 3 | NEUN | 0.3% | 10% NDS | RbαNEUN | **Bio-techne** | NBP1-92716 | 1:500 | 0.3% | 5% NDS | DkαRb (488) | **Invitrogen** | A21206 |
| | SMI-32 | | | MsαSMI-32 | **BioLegend** | 801701 | 1:500 | | | DkαMs (647) | **Invitrogen** | A32787 |
| | DAPI | | | N/A | **Invitrogen** | D1306 | 1:1000 | | | N/A (358) | N/A | N/A |
| | Driver | | | N/A | N/A | N/A | N/A | | | N/A (581) | N/A | N/A |
| 4 | CHAT | 0.3% | 10% NDS | RbαCHAT | **Abcam** | ab178850 | 1:500 | 0.3% | 5% NDS | DkαRb (488) | **Invitrogen** | A21206 |
| | SMI-32 | | | MsαSMI-32 | **BioLegend** | 801701 | 1:500 | | | DkαMs (647) | **Invitrogen** | A32787 |
| | DAPI | | | N/A | **Invitrogen** | D1306 | 1:1000 | | | N/A (358) | N/A | N/A |
| | Driver | | | N/A | N/A | N/A | N/A | | | N/A (581) | N/A | N/A |
| 5 | MBP | 0.3% | 10% NGS | RtαMbp | **Abcam** | ab7349 | 1:500 | 0.3% | 5% NGS | GtαRt (488) | **Invitrogen** | A11006 |
| | AT8 | | | MsαAT8 | **ThermoFisher** | MN1020 | 1:500 | | | GtαMs (633) | **Abcam** | ab150115 |
| | DAPI | | | N/A | **Invitrogen** | D1306 | 1:1000 | | | N/A (358) | N/A | N/A |
| | Driver | | | N/A | N/A | N/A | N/A | | | N/A (581) | N/A | N/A |
| 6 | IBA1 | 0.3% | 10% NGS | RbαIBA1 | **FUJIFILM** | 019-19741 | 1:500 | 0.3% | 5% NGS | GtαRb (488) | **Invitrogen** | A11034 |
| | GFAP | | | CkαGFAP | **Abcam** | ab4674 | 1:500 | | | GtαCk (647) | **Abcam** | ab150171 |
| | DAPI | | | N/A | **Invitrogen** | D1306 | 1:1000 | | | N/A (358) | N/A | N/A |
| | Driver | | | N/A | N/A | N/A | N/A | | | N/A (581) | N/A | N/A |
| 7 | CTIP2 | 0.3% | 10% NGS | RtαCTIP2 | **Abcam** | ab18465 | 1:200 | 0.3% | 5% NGS | GtαRt (488) | **Invitrogen** | A11006 |
| | SATB2 | | | MsαSATB2 | **Abcam** | ab51502 | 1:1000 | | | GtαMs (633) | **Invitrogen** | A21052 |
| | DAPI | | | N/A | **Invitrogen** | D1306 | 1:1000 | | | N/A (358) | N/A | N/A |
| | Driver | | | N/A | N/A | N/A | N/A | | | N/A (581) | N/A | N/A |
| 8 | IBA1 | 0.3% | 10% NGS | RbαIBA1 | **FUJIFILM** | 019-19741 | 1:500 | 0.3% | 5% NGS | GtαRb (647) | **Invitrogen** | A21245 |
| | CD68 | | | MsαCD68 | **Abcam** | ab955 | 1:500 | | | GtαMs (488) | **Invitrogen** | A11001 |
| | DAPI | | | N/A | **Invitrogen** | D1306 | 1:1000 | | | N/A (358) | N/A | N/A |
| | Driver | | | N/A | N/A | N/A | N/A | | | N/A (581) | N/A | N/A |
| 9 | S100β | 0.3% | 10% NGS | MsαS100β | **Sigma-Aldrich** | 287 004 | 1:200 | 0.3% | 5% NGS | GtαMs (488) | **Invitrogen** | A11001 |
| | GFAP | | | RbαGFAP | **Dako** | Z0334 | 1:500 | | | GtαRb (647) | **Invitrogen** | A21245 |
| | DAPI | | | N/A | **Invitrogen** | D1306 | 1:1000 | | | N/A (358) | N/A | N/A |
| | Driver | | | N/A | N/A | N/A | N/A | | | N/A (581) | N/A | N/A |
| 10 | MBP | 0.3% | 10% NGS | RtαMbp | **Abcam** | ab7349 | 1:500 | 0.3% | 5% NGS | GtαRt (488) | **Invitrogen** | A11006 |
| | CC1 | | | MsαCC1 | **Abcam** | ab16794 | 1:200 | | | GtαMs (633) | **Invitrogen** | A21052 |
| | DAPI | | | N/A | Invitrogen | D1306 | 1:1000 | | | N/A (358) | N/A | N/A |
| | Driver | | | N/A | N/A | N/A | N/A | | | N/A (581) | N/A | N/A |
| 11 | TDP43 | 0.3% | 10% NDS | RbαTdp43 | **Proteintech** | 10782-2-AP | 1:500 | 0.3% | 5% NDS | DkαRb (488) | **Invitrogen** | A21206 |
| | SMI-32 | | | MsαSMI-32 | **BioLegend** | 801701 | 1:500 | | | DkαMs (647) | **Invitrogen** | A32787 |
| | DAPI | | | N/A | Invitrogen | D1306 | 1:1000 | | | N/A (358) | N/A | N/A |
| | Driver | | | N/A | N/A | N/A | N/A | | | N/A (581) | N/A | N/A |

## *A.5.6 Sample immunohistochemistry optimisations*

**Appx-Table 6**. Depicts sample antibody optimisations for SMI32. Tests were conducted with and without glycine aldehyde-quenching, with and without heat-induced epitope retrieval (HIER), at each of three primary dilutions, and with an incubation time (inc.) of 18hrs or 30hrs. Black boxes indicate untested conditions, and the condition deemed optimal for subsequent experiments is highlighted with a coloured box.

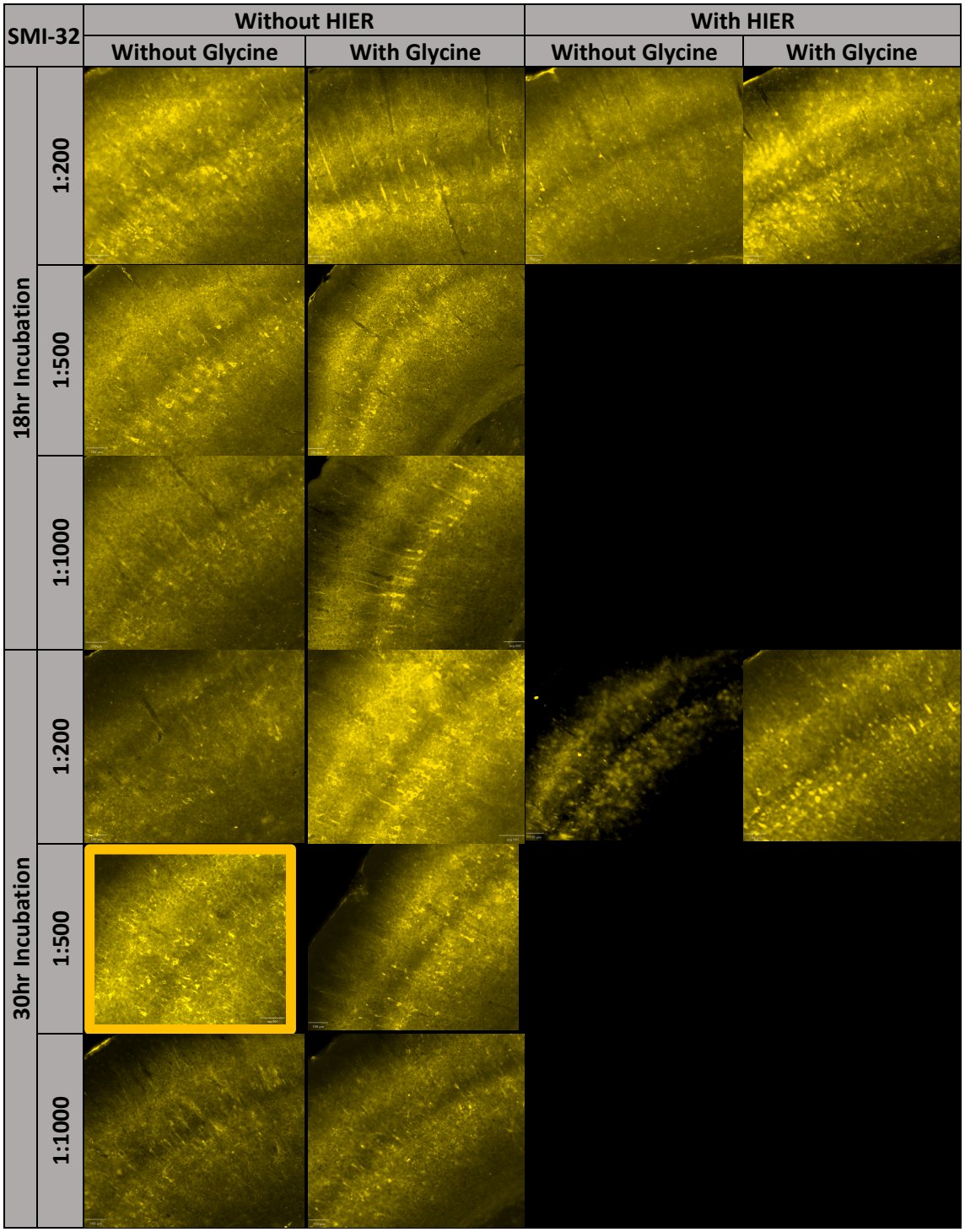

**Appx-Table 7**. Depicts sample antibody optimisations for Mbp. Tests were conducted with and without glycine aldehyde-quenching, with and without heat-induced epitope retrieval (HIER), at each of three primary dilutions, and with an incubation time (inc.) of 18hrs or 30hrs. Black boxes indicate untested conditions, and the condition deemed optimal for subsequent experiments is highlighted with a coloured box.

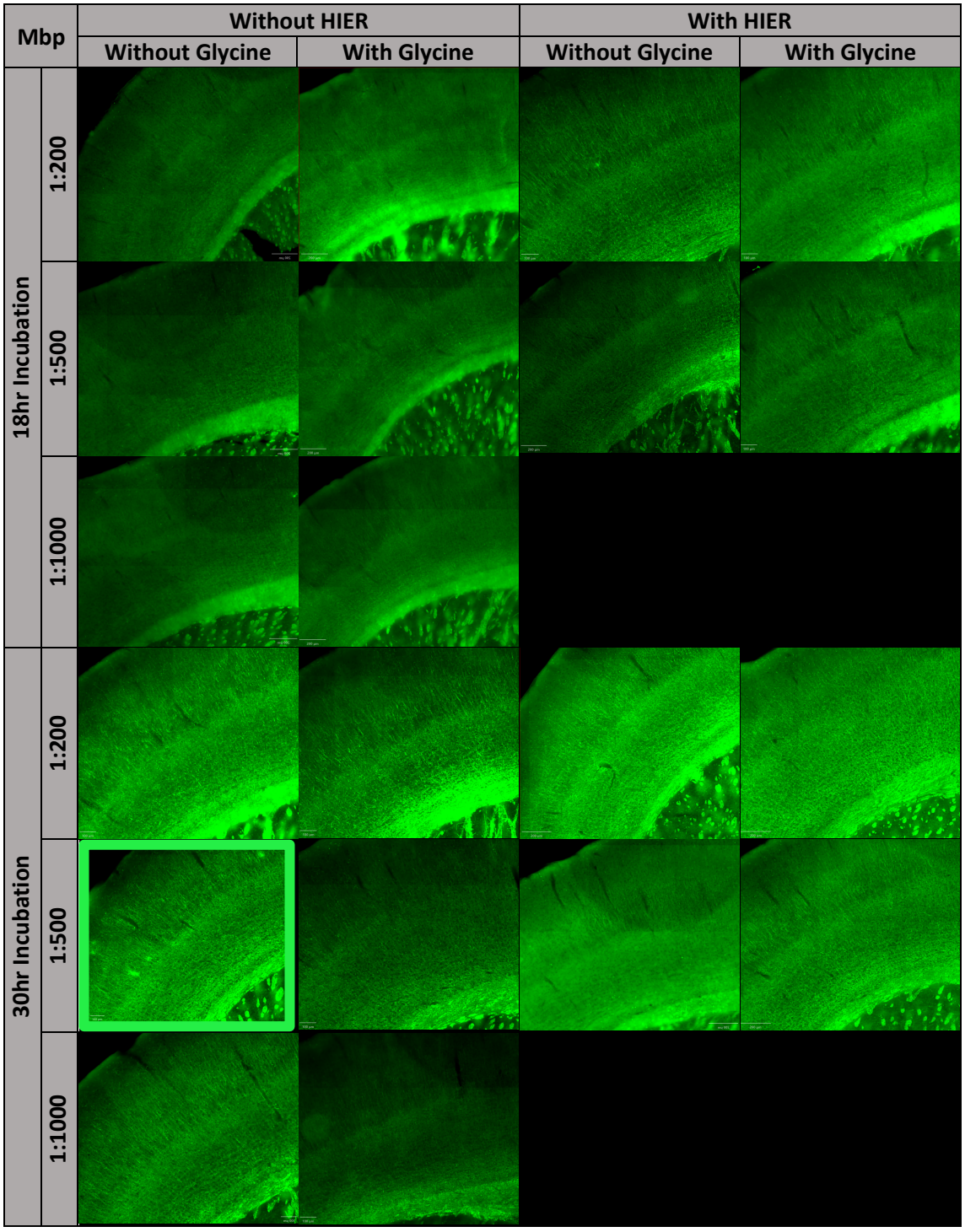

**Appx-Table 8**. Depicts sample antibody optimisations for CC1. Tests were conducted with and without glycine aldehyde-quenching, with and without heat-induced epitope retrieval (HIER), at each of three primary dilutions, and with an incubation time (inc.) of 18hrs or 30hrs. Black boxes indicate untested conditions, and the condition deemed optimal for subsequent experiments is highlighted with a coloured box. CC1 staining was ultimately not pursued further due to cost-benefit assessments and prior work suggesting that age- and genotype-differences may not be detectable[79].

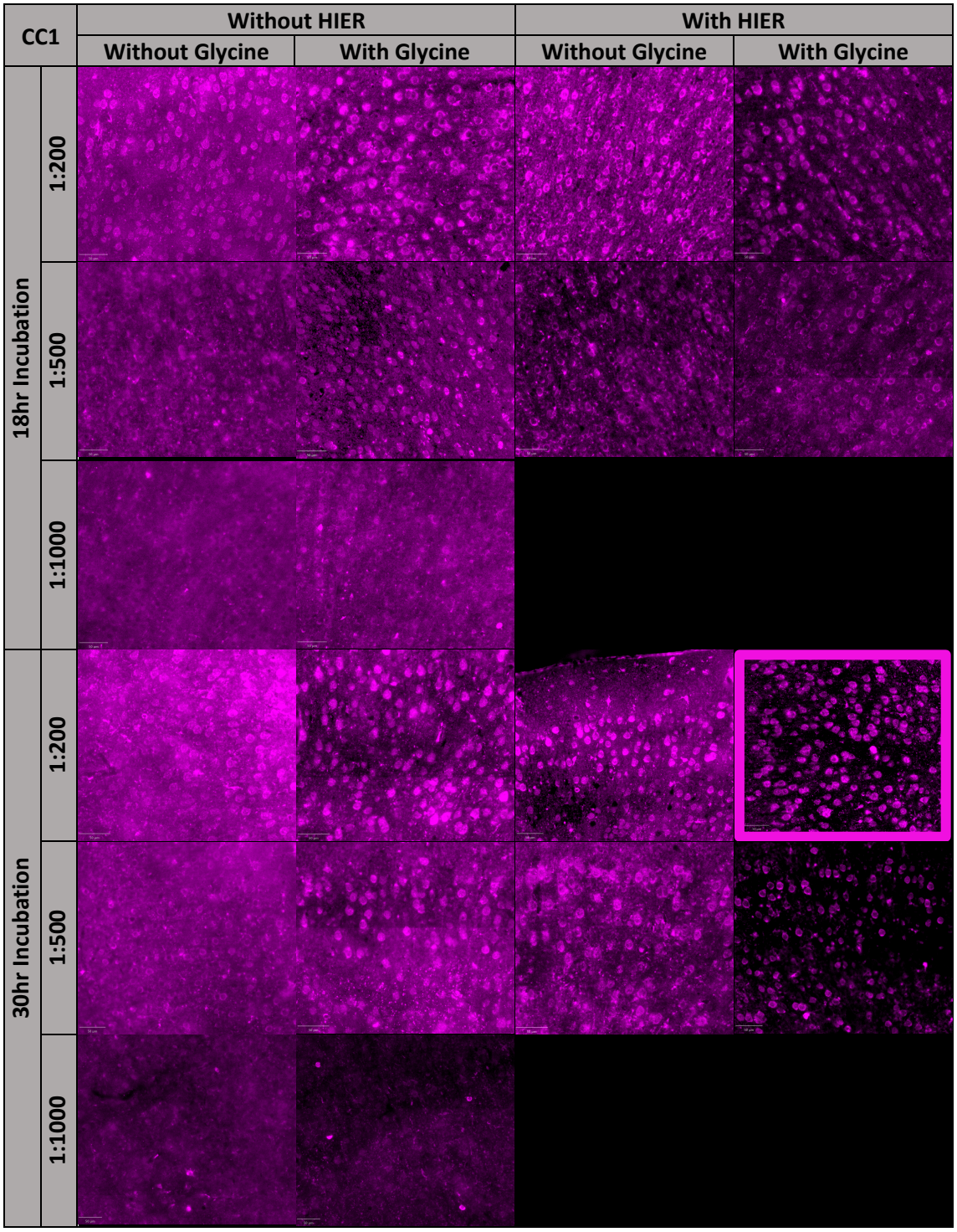

## *A.5.7 Sample initial immunohistochemistry combinations*

**Appx-Table 9.** Optimised IHC for preliminary L5-6b driver lines and subtype classifications, as described in **A.5.5**. Rows distinguish animal genotypes as A) L6-augmented, B) L6-silenced, and C-D) L5-silenced (*Rbp4*-Cre). Columns distinguish fluorophore channels and/or protein targets as: i) DAPI nuclei; ii) A,B) PV interneurons (**A.5.5 #1**), C) CPLX3 L6b cells (**A.5.5 #2**), and D) CTIP2 L5 extratelencephalic neurons (**A.5.5 #7**); iii) TdTomato A-B) *Drd1a*-Cre L6 subtype and C-D) *Rbp4*-Cre L5 subtype; iv) A,B) VVA perineural nets (**A.5.5 #1**), C) TBR1 cells (**A.5.5 #2**), and D) SATB2 L5 intratelencephalic neurons (**A.5.5 #7**); and v) merged channels. The upper-right box in each panel indicates the location of higher-resolution images in the coronal plane. Note that CTIP2 staining failed and was not pursued further. Scale bars = 250µm.

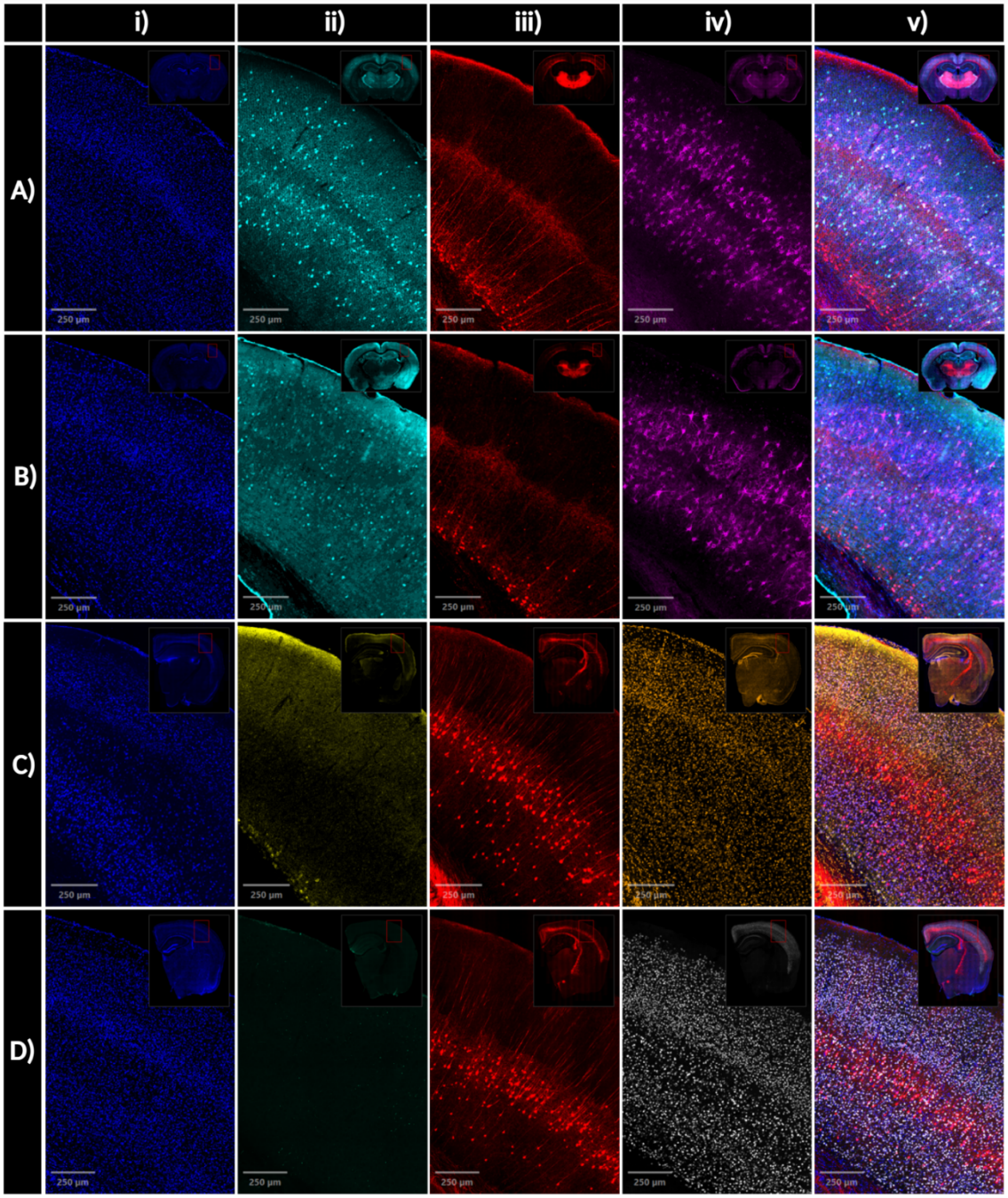

## *A.5.8 r-QUINT of regions of interest*

**Appx-Table 10.** Lists brain regions of interests included for classification and sub-classification in the modified QUINT pipeline. Areas of distinct neurodevelopmental origin are indicated by green = mesencephalic, blue = diencephalic, and yellow = telencephalic (continued on the next page). Light grey indicates regions which have not yet been incorporated into the pipeline.

| Brain Region | Sub-Region(s) | Sub-Region(s) | Abbreviation(s) |
|---|---|---|---|
| **Cortex** | **Cortex** | N/A | CTX |
| | | Cortical layers 1-6b | CL1-6b-All |
| | **Frontal Pole** | Cortical layers 1-6b | FP_All/CL1-6b |
| | **Primary motor** | Cortical layers 1-6b | M1_All/CL1-6b |
| | **Secondary motor** | Cortical layers 1-6b | M2_All/CL1-6b |
| | **Primary somatosensory** | Cortical layers 1-6b | S1_All/CL1-6b |
| | **Secondary somatosensory** | Cortical layers 1-6b | S2_All/CL1-6b |
| | **Gustatory and visceral areas** | Cortical layers 1-6b | GVA_All/CL1-6b |
| | **Auditory** | Cortical layers 1-6b | Aud_All/CL1-6b |
| | **Visual areas** | Cortical layers 1-6b | Vis_All/CL1-6b |
| | **Prefrontal cortex** | Cortical layers 1-6b | PFC_All/CL1-6b |
| | | Prelimbic cortical areas (layers 1-6b) | PFC_Pla_CL1-6b |
| | | Infralimbic cortical areas (layers 1-6b) | PFC_Ila_CL1-6b |
| | | Anterior cingulate cortex (layers 1-6b) | PFC_Acc_CL1-6b |
| | **Orbital areas** | Cortical layers 1-6b | Orb_All/CL1-6b |
| | **Agranular insular area** | Cortical layers 1-6b | Ins_All/CL1-6b |
| | **Retrosplenial** | Cortical layers 1-6b | Rsa_CL1-6b |
| | **Posterior parietal association areas** | Cortical layers 1-6b | Ppa_All/CL1-6b |
| | **Temporal association areas** | Cortical layers 1-6b | Taa_All/CL1-6b |
| | **Rhinal areas** | Cortical layers 1-6b | Rhi_All/CL1-6b |
| | **Olfactory areas** | Tenia tecta | OLF_TT |
| | | Piriform area | OLF_PA |
| | | Nucleus of the lateral olfactory tract | OLF_NLOT |
| | | Cortical amygdalar areas | OLF_CAA |
| | | Piriform-amygdalar area | OLF_PAA |
| | **Cortical subplate (atlas-defined, including CL6b)** | N/A | CSP |
| | | Amygdalar nuclei | CSP_AN |
| | | Amygdalar nuclei (lateral) | CSP_ANl |
| | | Amygdalar nuclei (basolateral) | CSP_ANbl |
| | | Amygdalar nuclei (basomedial) | CSP_ANbm |
| | | Amygdalar nuclei (posterior) | CSP_ANp |
| **Hippocampus** | **Hippocampal body** | N/A (excludes entorhinal areas and amygdalar transition regions) | Hip |
| | **Cornu Ammonis divisions** | CA1 | Hip_CA1 |
| | | CA2 | Hip_CA2 |
| | | CA3 | Hip_CA3 |
| | **Dentate divisions** | Dentate gyrus areas | Hip_DG |
| | | Dentate gyrus molecular area | Hip_DGm |
| | | Dentate gyrus polymorph layer | Hip_DGp |
| | | Dentate gyrus granule cell layer | Hip_DGg |
| | | Dentate gyrus subgranular zone | Hip_DGsg |
| | **Fasciola cinerea** | N/A | Hip_FC |
| | **Insudeum griseum** | N/A | Hip_IG |
| | **Retrohippocampal areas** | Cortical layers 1-6b | Hip_Era_All/CL1-6b |
| | **Subiculum areas** | N/A | Hip_Sub |

| | | | |
|---|---|---|---|
| **Cortical subplate** | **Atlas-defined, including CL6b** | N/A | CSP |
| | | Amygdalar nuclei | CSP_AN |
| | | Amygdalar nuclei (lateral) | CSP_ANl |
| | | Amygdalar nuclei (basolateral) | CSP_ANbl |
| | | Amygdalar nuclei (basomedial) | CSP_ANbm |
| | | Amygdalar nuclei (posterior) | CSP_ANp |
| **Cerebral nuclei** | **Striatum** | N/A | STR |
| | | Caudoputamen | STR_CP |
| | | Striatum-like amygdalar nuclei | STR_SLAN |
| | **Pallidum** | N/A | PLD |
| | | Dorsal region (globus pallidus internal) | PLD_d_Gpi |
| | | Dorsal region (globus pallidus external) | PLD_d_Gpe |
| | | Ventral region | PLD_v |
| | | Medial region (nucleus of the diagonal band and medial septal nucleus) | PLD_m |
| | | Caudal region (bed nucleus of the stria terminalis and anterior commissure) | PLD_c |
| **Amygdala** | **Subregions scattered elsewhere** | N/A | A |
| **Midbrain** | **Superior colliculus** | Sensory related | Mid_SCs |
| | | Motor related | Mid_SCm |
| | **Inferior colliculus** | N/A | Mid_IC |
| | **Substantia nigra** | Reticular | Mid_SNr |
| | | Lateral | Mid_SNl |
| | | Compact | Mid_SNc |
| | **Ventral tegmental area** | N/A | Mid_VTA |
| | **Periaqueductal gray** | N/A | Mid_PAG |
| | **Anterior pretectal nucleus** | N/A | Mid_APTN |
| **Pons** | **Locus ceruleus** | N/A | PONS_LC |
| **Thalamus** | **Thalamus** | N/A | Th |
| | **Thalamic higher-order nuclei** | N/A | Th_HOTN |
| | | Ventral group of the dorsal thalamus | Th_HOTN_VGDT |
| | | Geniculate nucleus | Th_HOTN_GN |
| | | Dorso-lateral thalamus | Th_HOTN_DLT |
| | | Ventral anterior nucleus | Th_HOTN_DLT_VA |
| | | Midline nuclei | Th_HOTN_DLT_MLN |
| | | Intralaminar nuclei | Th_HOTN_DLT_ILN |
| | **Reticular nucleus of the thalamus** | N/A | Th_RNT |
| **Hypothalamus** | **Periventricular zone** | N/A | HT_PVZ |
| | **Periventricular region** | N/A | HT_PVR |
| | | Dorsomedial nucleus of the hypothalamus | HT_PVR_DMH |
| | | Medial preoptic area and nucleus | HT_PVR_MPO |
| | | Suprachiasmatic nucleus | HT_PVR_SCN |
| | | Suprachiasmatic preoptic nucleus | HT_PVR_SCNpo |
| | **Anterior hypothalamic areas** | N/A | HT_AHA |
| | **Hypothalamic medial zone** | N/A | HT_HMZ |
| | | Tuberomamillary nucleus | HT_HMZ_TMN |
| | | Medial preoptic nucleus | HT_HMZ_mPON |
| | | Ventromedial hypothalamic nucleus | HT_HMZ_VMH |
| | | Posterior hypothalamic nucleus | HT_HMZ_PHN |
| | **Hypothalamic lateral zone** | N/A | HT_HLZ |
| | | Lateral hypothalamic area | HT_HLZ_LHA |
| | | Lateral preoptic area | HT_HLZ_LPOA |
| | | Subthalamic nucleus | HT_HLZ_STN |
| | | Zona incerta | HT_HLZ_ZI |

### *A.5.9 Orexin receptor in situ hybridisation*

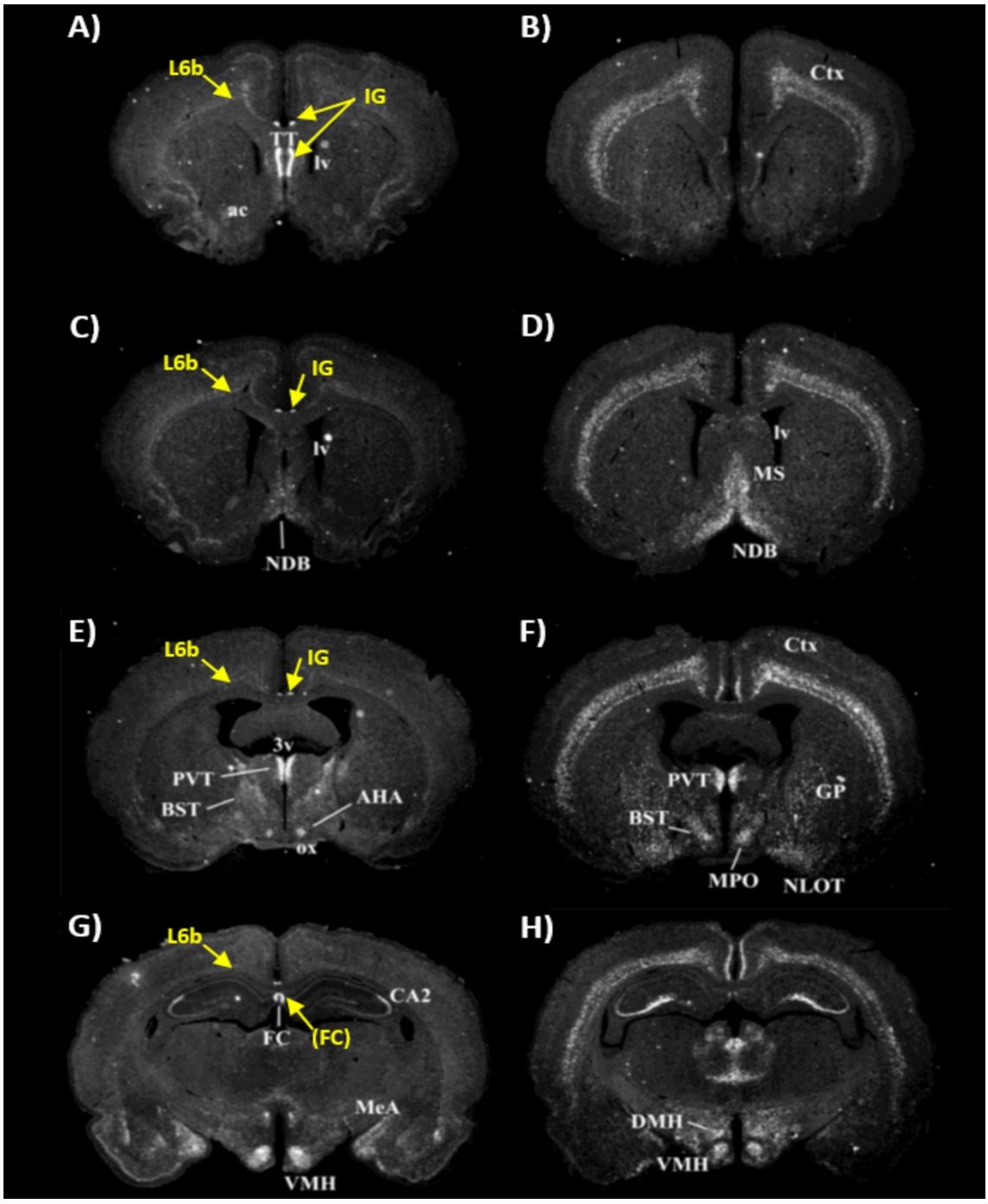


**Appx-Figure 21.** Previously published *in situ* hybridisation illustrates A,C,E,G) *OrxR1* and B,D,F,G) *OrxR2* expression in the rat brain[38]. This includes *OrxR1* expression (yellow) in deep frontal cortical layers (i.e., L6b), in the insudeum griseum (IG), and in the fasciola cinerea (FC). TT = tenia tecta (which I believe is incorrectly labelled and should be the IG); ac = anterior commissure; lv = lateral ventricle; Ctx = cortex; NDB = nucleus of the diagonal band; MS = medial septal nucleus; 3v = third ventricle; PVT = paraventricular thalamic nucleus; BST = bed nucleus of the stria terminalis; AHA = anterior hypothalamic area; ox = optic chiasm; GP = globus pallidus; MPO = medial preoptic nucleus; NLOT = nucleus of the lateral olfactory tract; MeA = medial amygdala; VMH = ventromedial hypothalamic nucleus; and DMH = dorsomedial hypothalamic nucleus.

## A.6 Imaging and analyses

### *A.6.1 Microscopy cost estimation*

The equations below estimated requisite imaging time (**Equation 4**), cost-recovery charges (**Equation 5**), and data storage requirements (**Equation 6**) to assess imaging feasibility across QUINT analyses. Formulae were added into an Excel sheet for SDCM and SSFM comparison.

**Equation 4.** Estimates the total time required to image one brain.

$$T_b = T_s F_{xt} S_b A_f A_c N_{fc}$$

$$T_s = \frac{N_{st}}{T_{st}}$$

$$F_{xt} = \left(\frac{x_t}{x_x}\right)^2 \left(\frac{c_x}{c_t}\right)\left(\frac{z_x}{z_t}\right)\left(\frac{\bar{e}_x}{\bar{e}_t}\right)$$

**Equation 5.** Estimates the total cost per brain.

$$C_b = T_b C_r$$

**Equation 6.** Estimates the data storage capacity required for one brain.

$$D_b = d_t \left(\frac{T_b}{T_s S_t}\right)\left(\frac{x_t}{x_x}\right)^2$$

*$T_b$ = Estimated image acquisition time per brain*
*$T_s$ = Estimated time per brain section based on the trial image reconstruction test set*
*$F_{xt}$ = Fractional relator for queried versus test set key image acquisition parameters*
*$S_b$ = Sections per brain*
*$A_f$ = Area per image; one for a full section, and fractional for sub-section assessments*
*$A_c$ = Area count; one for a full section, and an integer count for sub-section assessments*
*$N_{fc}$ = Number of fluorophore combinations to be used in the queried set*
*$N_{st}$ = Number of sections in the trial reconstruction test set*
*$T_{st}$ = Time to image all sections in the trial reconstruction test set*
*$x_t$ = Magnification parameter for the test set*
*$x_x$ = Magnification parameter for the queried set*
*$c_t$ = Number of channels in the test set*
*$c_x$ = Number of channels in the queried set*
*$z_t$ = Number of z-stacks in the test set*
*$z_x$ = Number of z-stacks in the queried set*
*$\bar{e}_t$ = Exposure time (mean across channels) in the test set*
*$\bar{e}_x$ = Exposure time (mean across channels) in the queried set*
*$C_b$ = Total cost per brain*
*$C_r$ = Cost recovery for imaging*
*$D_b$ = Data storage space required per brain*
*$d_t$ = Data storage space required for the test set*
*$S_t$ = Number of sections in the test set*

## *A.6.2 Microscopy specifications*

**Appx-Table 11.** Lists optimised SDCM microscope and image acquisition specifications.

| SDCM Settings | Imaging specifications |
|---|---|
| Objective | 20X/0.8 air |
| Pixel resolution | 0.325µm |
| Lamp (voltage) | Halogen IX3 (3V) |
| Laser wavelength (name, power, exposure time) | 405nm (DAPI, 10%, 50ms) |
| | 488nm (FITC, 40%, 100ms) |
| | 565nm (Cy3, 40%, 150ms) |
| | 640nm (Cy5, 40%, 100ms) |
| Number of z-stacks (step size) | 3 (7.49µm) |
| Pixel clock | 480MHz |
| Tile pixel resolution (sub-array) | 2304×2304 (1500×1500) |
| Pinhole disk | B525/50um |
| Disk rotation speed | 1600rpm |
| Aperture stop | 75% |
| DIC slider | 2950 |

**Appx-Table 12.** Lists optimised SSFM microscope and image acquisition specifications.

| SSFM Settings | Imaging specifications |
|---|---|
| Objective | UPLXAPO 20X/0.8 air |
| Pixel resolution | 0.325µm |
| Lamp (max.) | LED IX3 (1000) |
| Laser wavelength (name, intensity, exposure time) | 455nm (DAPI, 100, 3.2ms) |
| | 518nm (FITC, 1000, 20ms) |
| | 565nm (Cy3, 300, 20ms) |
| | 670nm (Cy5, 200, 50ms) |
| Number of z-stacks (step size) | 1 (0µm) |
| Pixel clock | 120MHz |
| Microscope camera maximum frame | 2016×2016 |

## *A.6.3 QuPath cell detection parameters*

**Appx-Table 13.** QuPath cell detection parameters.

| QuPath Parameters | Primary detection | Secondary detection) |
|---|---|---|
| Requested Pixel Size (µm) | 0.5 | 0.5 |
| Background Radius (µm) | 8.6 | 6 |
| Median Radius (µm) | 2.3 | 3 |
| Sigma (µm) | 1.5 | 3 |
| Minimum Area (µm) | 25 | 60 |
| Maximum Area (µm) | 400 | 600 |
| Detection Threshold | 5000 | 200 |
| Split by Shape | Yes | Yes |
| Cell Expansion (µm) | 4 | 2 |
| Include Nuclei | No | No |
| Smooth Boundaries | Yes | Yes |
| Make Measurements | Yes | Yes |
| Positive Detection Threshold 1 | 800 | N/A |
| Positive Detection Threshold 2 | 800 | N/A |
| Positive Detection Threshold 3 | 800 | N/A |
| Single Threshold | Yes | N/A |
| Area | < 200.0 | >20 |
| Circularity | > 0.8 | N/A |
| Signal intensity standard deviation | > 200.0 | > 354.9 |

## *A.6.4 Nutil brain region definitions*

| B | C | D | E | F | G | H | I |
|---|---|---|---|---|---|---|---|
| CTX | CL1_All | CL2_All | CL3_All | CL4_All | CL5_All | CL6a_All | CL6b_All |
| 119;21;21 | 251;229;229 | 248;212;212 | 239;161;161 | 229;101;101 | 218;42;42 | 188;32;32 | 119;21;21 |
| fig | pearl | sorbet | morganite | brick | quondong | barberry | fig |
| 8 | 68 | 667 | 667 | 12995 | 526157192 | 526157196 | 16 |
| 567 | 264 | 492 | 492 | 865 | 352 | 476 | 526322264 |
| 688 | 448 | 412 | 412 | 654 | 630 | 440 | 516 |
| 695 | 484 | 524 | 582 | 1047 | 620 | 910 | 488 |
| 315 | 969 | 582 | 288 | 1094 | 1125 | 608 | 527696977 |
| 184 | 107 | 288 | 219 | 950 | 299 | 644 | 680 |
| 68 | 12993 | 219 | 12994 | 577 | 12996 | 12997 | 947 |
| 667 | 793 | 12994 | 346 | 1086 | 921 | 686 | 12998 |
| 500 | 558 | 346 | 838 | 182305701 | 702 | 889 | 719 |
| 107 | 981 | 838 | 201 | 1035 | 1070 | 1038 | 929 |
| 219 | 1030 | 201 | 113 | 678 | 1128 | 478 | 1062 |
| 299 | 878 | 113 | 657 | 816 | 974 | 1102 | 510 |
| 644 | 450 | 657 | 854 | 759 | 625 | 945 | 2 |
| 947 | 1006 | 854 | 670 | 990 | 1111 | 9 | 1026 |
| 985 | 182305693 | 670 | 182305697 | 480149214 | 182305705 | 182305709 | 461 |
| 320 | 873 | 182305697 | 806 | 480149242 | 1090 | 862 | 182305713 |
| 943 | 320 | 806 | 943 | 913 | 648 | 844 | 893 |
| 648 | 656 | 943 | 962 | 1114 | 767 | 1021 | 882 |
| 844 | 527 | 962 | 600 | 401 | 252 | 156 | 1085 |
| 882 | 735 | 600 | 251 | 573 | 847 | 954 | 243 |
| 993 | 696 | 251 | 643 | 721 | 791 | 249 | 1005 |
| 656 | 959 | 643 | 755 | 869 | 1023 | 520 | 456 |
| 962 | 480149206 | 755 | 480149210 | 501 | 480149218 | 480149222 | 598 |
| 767 | 480149234 | 480149210 | 480149238 | 312782586 | 480149246 | 480149250 | 480149226 |
| 1021 | 801 | 480149238 | 561 | 312782640 | 937 | 457 | 480149254 |
| 1085 | 1074 | 561 | 905 | 480149270 | 233 | 601 | 497 |
| 453 | 281 | 905 | 1066 | 480149298 | 433 | 1046 | 649 |
| 12993 | 421 | 1066 | 973 | 480149326 | 613 | 74 | 441 |
| 12994 | 593 | 973 | 821 | 545 | 778 | 33 | 121 |
| 12995 | 750 | 821 | 269 | 635 | 902 | 377 | 305 |
| 12996 | 805 | 269 | 41 | 312782558 | 565 | 257 | 393 |
| 12997 | 312782578 | 41 | 312782582 | 312782612 | 312782590 | 312782594 | 469 |
| 12998 | 312782632 | 312782582 | 312782636 | 148 | 312782644 | 312782648 | 312782598 |
| 322 | 480149262 | 312782636 | 480149266 | 1010 | 683 | 308 | 312782652 |
| 793 | 480149290 | 480149266 | 480149294 | 92 | 312782562 | 312782566 | 340 |
| 346 | 480149318 | 480149294 | 480149322 | 312 | 312782616 | 312782620 | 312782570 |
| 865 | 572 | 480149322 | 1053 | 712 | 739 | 179 | 312782624 |
| 921 | 935 | 1053 | 211 | 419 | 1015 | 919 | 227 |
| 686 | 588 | 211 | 296 | 234 | 772 | 810 | 927 |
| 719 | 171 | 296 | 304 | | 363 | 84 | 819 |
| 353 | 707 | 304 | 556 | | 827 | 1054 | 132 |
| 558 | 671 | 195 | 965 | | 774 | 906 | 1081 |
| 838 | 442 | 747 | 434 | | 480149274 | 480149278 | 279 |
| 654 | 606 | 556 | 430 | | 480149302 | 480149306 | 480149282 |
| 702 | 532 | 965 | 241 | | 480149330 | 480149334 | 480149310 |
| 889 | 312782550 | 434 | 312782554 | | 610 | 274 | 480149338 |
| 929 | 312782604 | 430 | 312782608 | | 687 | 590 | 330 |
| 329 | 996 | 241 | 328 | | 683 | 308 | 622 |
| 981 | 120 | 312782554 | 163 | | 312782562 | 312782566 | 340 |
| 201 | 704 | 312782608 | 694 | | 312782616 | 312782620 | 312782570 |
| 1047 | 36 | 328 | 180 | | 1101 | 783 | 312782624 |
| 1070 | 897 | 163 | 1106 | | 344 | 314 | 831 |
| 1038 | 540 | 694 | 888 | | 800 | 675 | 355 |
| 1062 | 836 | 180 | 427 | | 187 | 638 | 699 |
| 480149202 | 1121 | 1106 | 999 | | 1058 | 857 | 662 |
| 480149206 | 526 | 888 | 664 | | 692 | 335 | 849 |
| 480149210 | 259 | 427 | 371 | | 988 | 977 | 368 |
| 480149214 | 97 | 20 | 1127 | | 312 | 387 | 1045 |
| 480149218 | | 999 | | | 139 | 28 | 60 |

**Appx-Figure 22.** Depicts a screenshotted excerpt of a data table I made to customise Nutil ROIs. Column headers correspond to newly specified areal definitions constructed using numbers and colours (green/blue cells below) linked to Allen Brain atlas codes. This spreadsheet uniquely defines the 214 ROIs employed throughout r-QUINT analyses in this thesis. I deposited this file to Figshare—titled *CustomRegionTemplate_MM_DPhil.xlsx*—for future users to download and adapt for future applications[260].

### *A.6.5 Ex vivo MRI sample preparation*

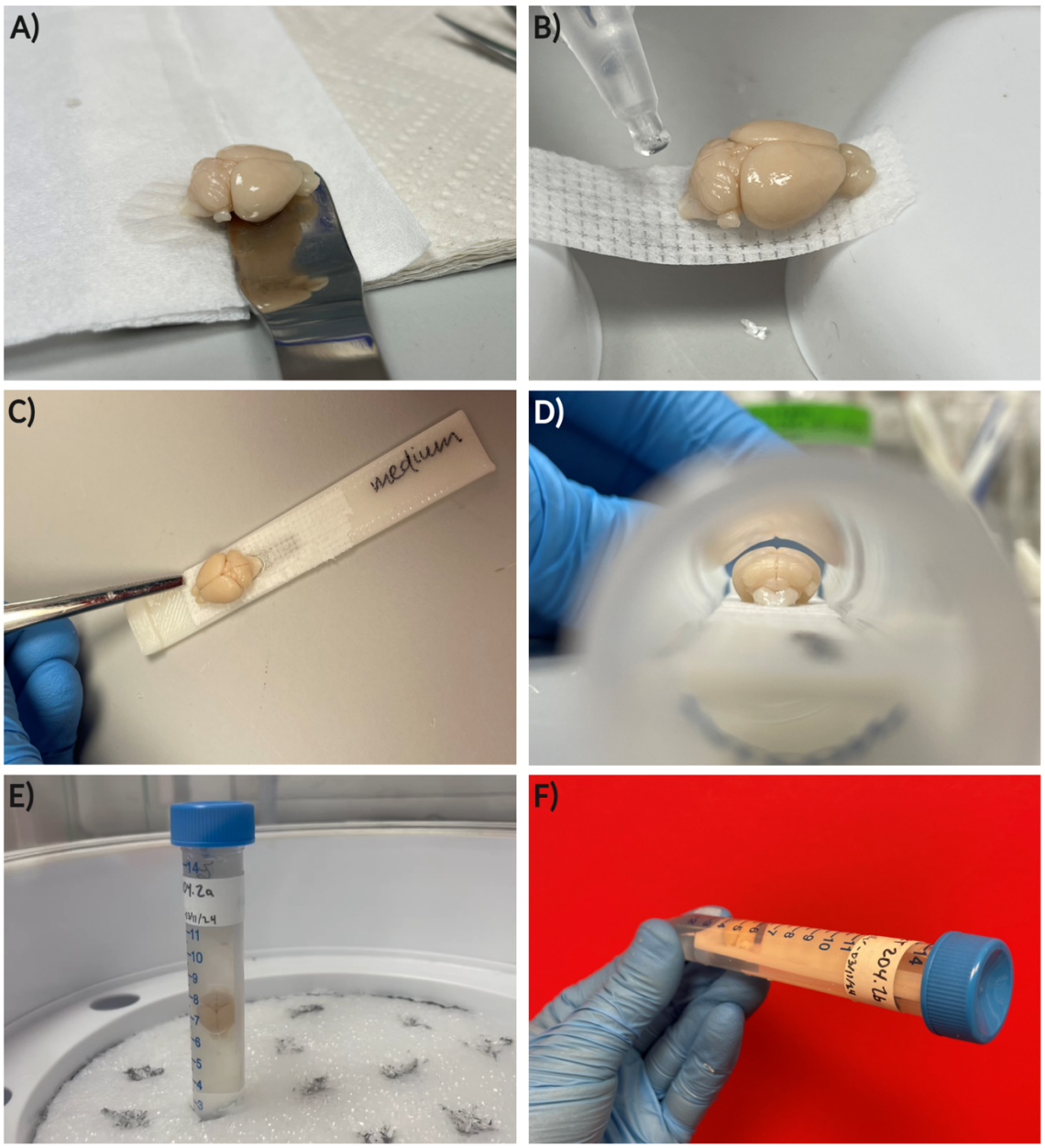


Appx-Figure 23. *Ex vivo* MRI setup for an out-of-skull brain. A) A dissected brain is B) glued to surgical tape at the base of the medulla. C) The surgical tape is placed atop a custom 3D-printed plinth, which is then D) inserted into a Falcon tube while ensuring that there is a visible gab between the dorsal surface of the brain and the inner surface of the Falcon tube. E) Samples are then de-bubbled via vacuum-pumping before F) a plastic bubble-trap is inserted into the tube and a lid is affixed. The sample can then undergo bubble-check scans, which ensure adequate sample quality before proceeding to overnight imaging. De-bubbling is important as trapped air in or around the brain (when skulls are present) can cause susceptibility artifacts, induce geometric distortions, and corrupt scan data. Note that, while the above images feature a brain without the skull, solely within-skull images were ultimately kept for analyses following QC checks (i.e., out-of-skull samples compromised registrations) (2.5.2.2**,** 2.5.3.3**,** 2.5.3.4**,** A.7.2).

## A.7 Quality control

### *A.7.1 Morphometrics – trace projections*

**Appx-Table 14.** Provides examples of human and mouse single neuron images and traces[394].

| Neuron type | Human | | Mouse | |
|---|---|---|---|---|
| | Image stack | Resulting trace | Image stack | Resulting trace |
| Pyramidal Orexin-sensitive |  |  | 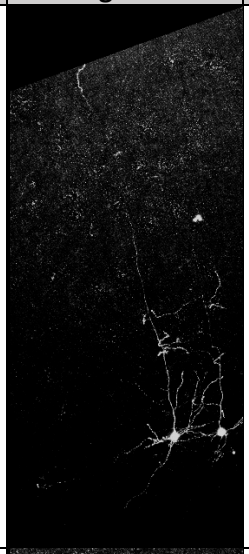 |  |
| Pyramidal Orexin-insensitive | 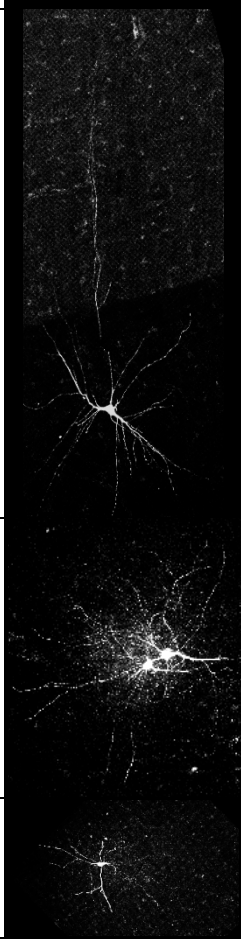 | 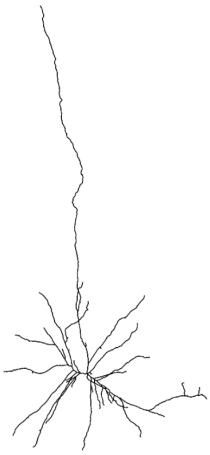 | 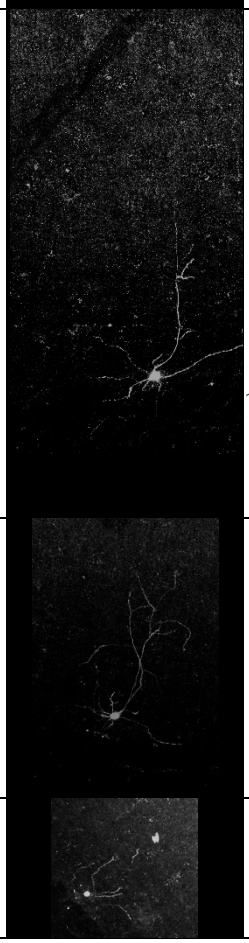 | 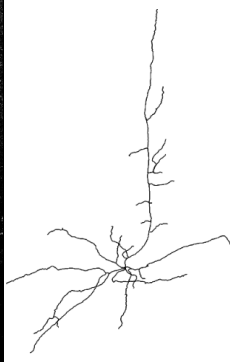 |
| Non-Pyramidal Orexin-sensitive | |  |  | 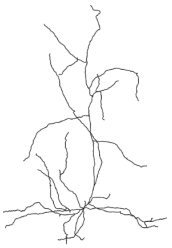 |
| Non-Pyramidal Orexin-insensitive | | 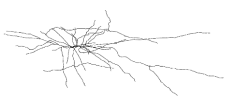 | |  |

### *A.7.2 Effects of out-of-skull sample inclusion*

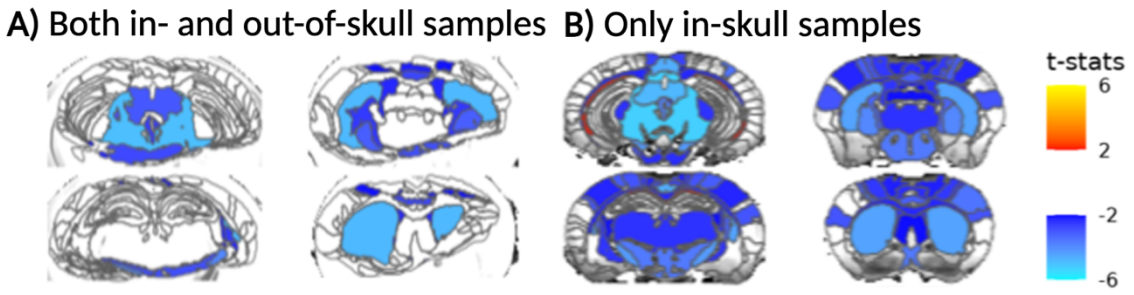


**Appx-Figure 24.** Out-of-skull *ex vivo* samples compromise the quality of T2W MRI analyses. A) Genotype differences were calculated using both in-skull and out-of-skull samples, followed by B) solely in-skull samples which improved mapping fidelity.

### *A.7.3 T2W nonuniformity corrections*

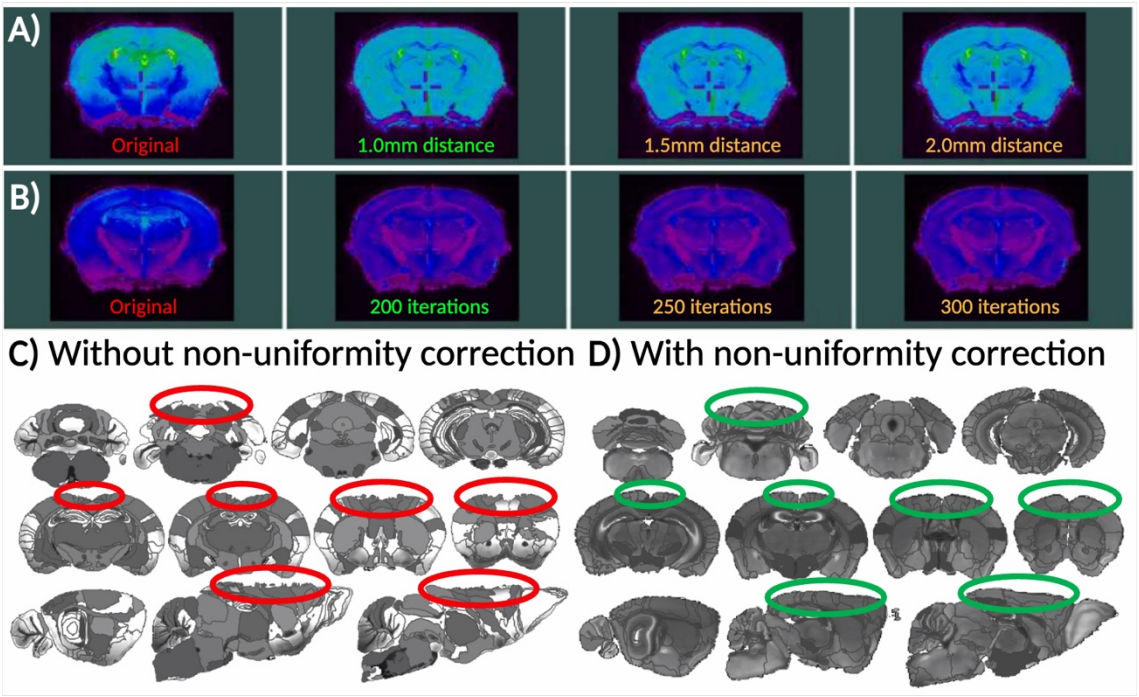


**Appx-Figure 25.** The non-uniformity correction improves registration quality. Dorso-ventral gradient artifacts are optimally reduced by setting A) distance parameter to 2.0mm and B) number of iterations to 200. *Ex vivo* T2W maps illustrate dorsal signal loss C) without the non-uniformity correction (red) which is D) remedied with the correction applied (green).

### *A.7.4 Ex vivo DWI pre-processing*

Quality control checks are detailed in Figshare as 'dwi_preprocessing.pdf'[479, 496]. Samples kept or discarded for analyses are marked with a ✓ and ✗, respectively. The following snapshots are provided for each sample: 1) b0 volumes following Gibbs and Eddy corrections; 2) topup maps to identify distortions; 3) b0 masks generated from the diffusion pre-processing pipeline (**2.5.3.3**) before improvements were implemented (**2.5.4.1**-**2.5.4.3**), 4) vector maps to confirm fibre orientations; 5) FA maps, and 6) MD maps. Further 1) anatomical, 2) FA, and 3) MD maps are then provided with standardised rendering to identify differences in absolute values or the signal-to-noise ratio. Quality control notes are included in the subject header for each sample.

### *A.7.5 Ex vivo QSM pre-processing*

Quality checks performed during QSM pre-processing are detailed in the Figshare collection[479, 496] as 'qsm_preprocessing.pdf'. For each sample, images detail: 1) signal decay curves for both MGE acquisitions; 2) magnitude data; 3) T2* maps; 4) R2* maps; and 5) susceptibility maps.

### *A.7.6 MGE masking*

Individual masks for MGE data (equivalent for T2W and DWI following **2.5.4.1**-**2.5.4.3**) are illustrated within Figshare[479, 496] as 'mge_masking.pdf'. 'd' and 'e' represent successive dilation and erosion steps, respectively, which were manually conducted to optimise brain coverage. Text colours indicate which sequence of attempted dilations/erosions was deemed to produce the optimal mask, which is shown rendered atop anatomical maps in the column to the right.

### *A.7.7 MGE-T2W co-registration*

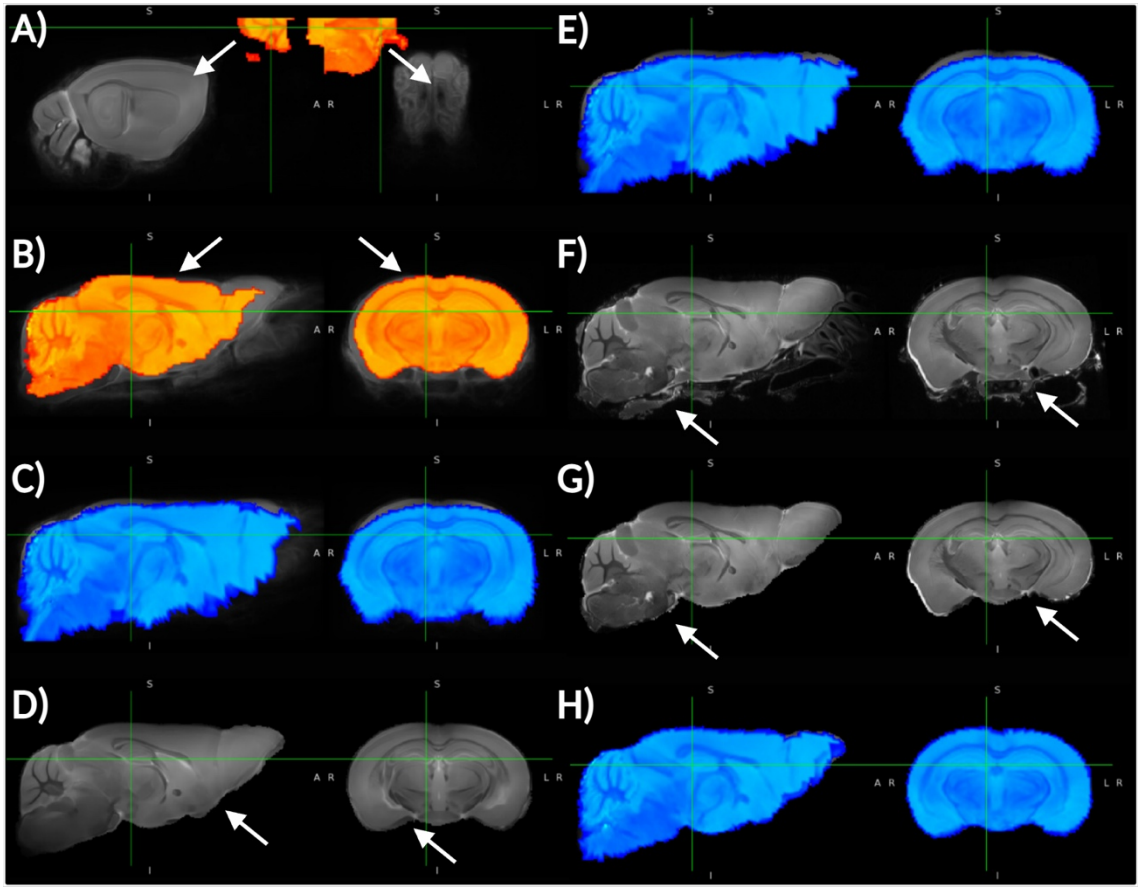


**Appx-Figure 26.** Troubleshooting MGE-to-T2W image coregistration. A) AntsQuick registrations initially failed, where I observed that source (MGE) and target (T2W) volumes did not overlap in 3D space due to corrupted .mnc headers. B) I manually modified headers to at least partially align source/target volumes via x/y/z translations. C) The pipeline then generated outputs, yet these were significantly warped. D) I masked the nonlinear T2W target file, reasoning that out-of-skull signal may skew registrations. E) Registrations did not improve significantly. F) In then examining pipeline inputs, outputs, and intermediaries, it appeared that the MGE image rather registers to the lsq-6 (not the nonlinear) transform. G) I then also masked this lsq-6 T2W image. H) Re-running AntsQuick then generated the best registrations obtained to date.

## A.8 Histology supplements

### *A.8.1 Excitatory DREADD subcortical PV/VVA co-expression and densities*

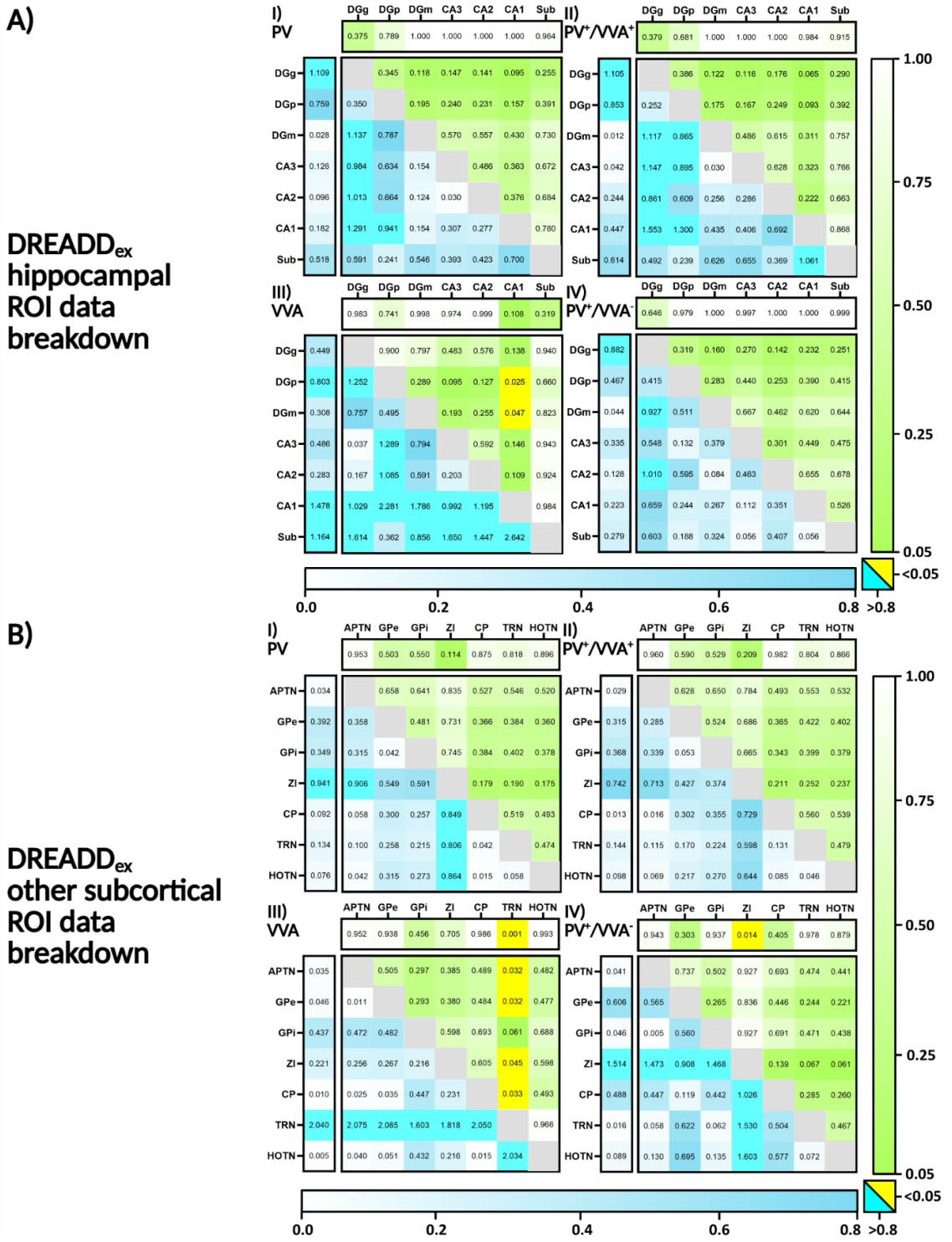


**Appx-Figure 27.** Subcortical changes in PV/VVA expression patterns upon Rbp4-Cre-driven CNO activation of excitatory DREADDs. Depicts individual p/d-values for A) hippocampal and B) other subcortical ROIs, distinguished by cells which are I) $PV^+$, II) $PV^+/VVA^+$, III) $VVA^+$, or $PV^+/VVA^-$.

### *A.8.2 Inhibitory DREADD subcortical PV/VVA co-expression and densities*

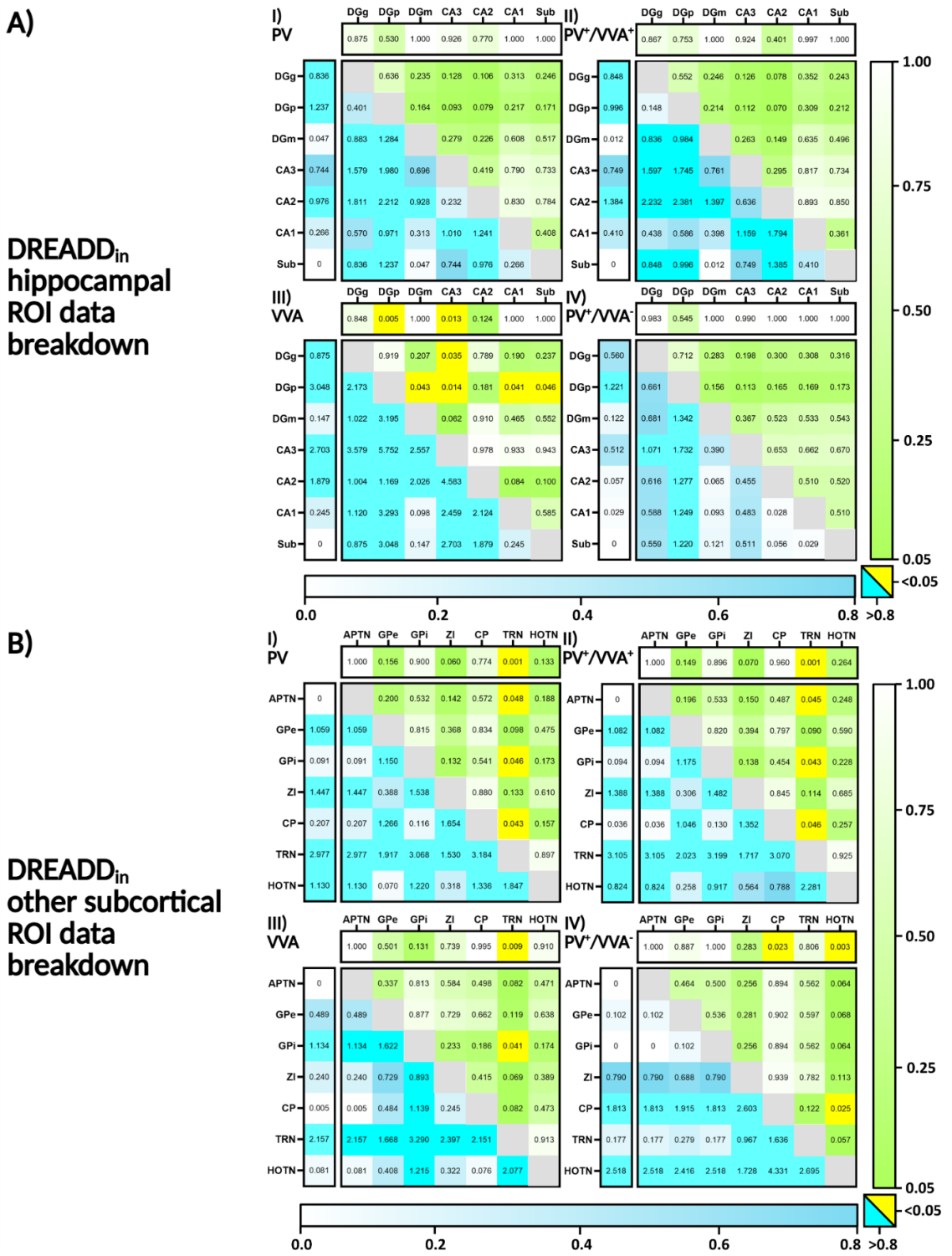


**Appx-Figure 28.** Subcortical changes in PV/VVA expression patterns upon Rbp4-Cre-driven CNO activation of inhibitory DREADDs. Depicts p/d-values for A) hippocampal and B) other subcortical ROIs, distinctly for cells which are I) $PV^+$, II) $PV^+/VVA^+$, III) $VVA^+$, or $PV^+/VVA^-$.

## *A.8.3 Excitatory DREADD cortical PV/VVA co-expression and VVA densities*

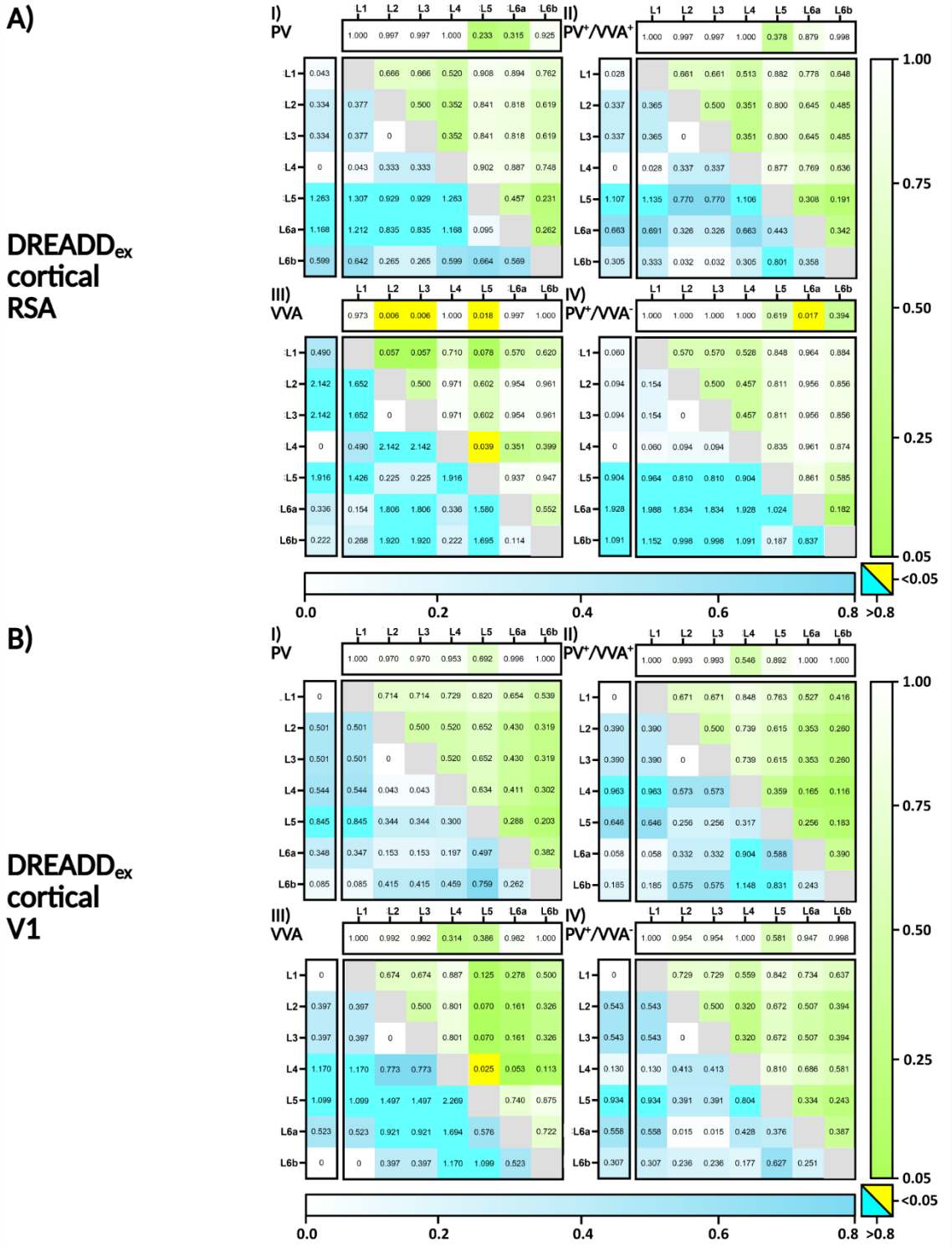

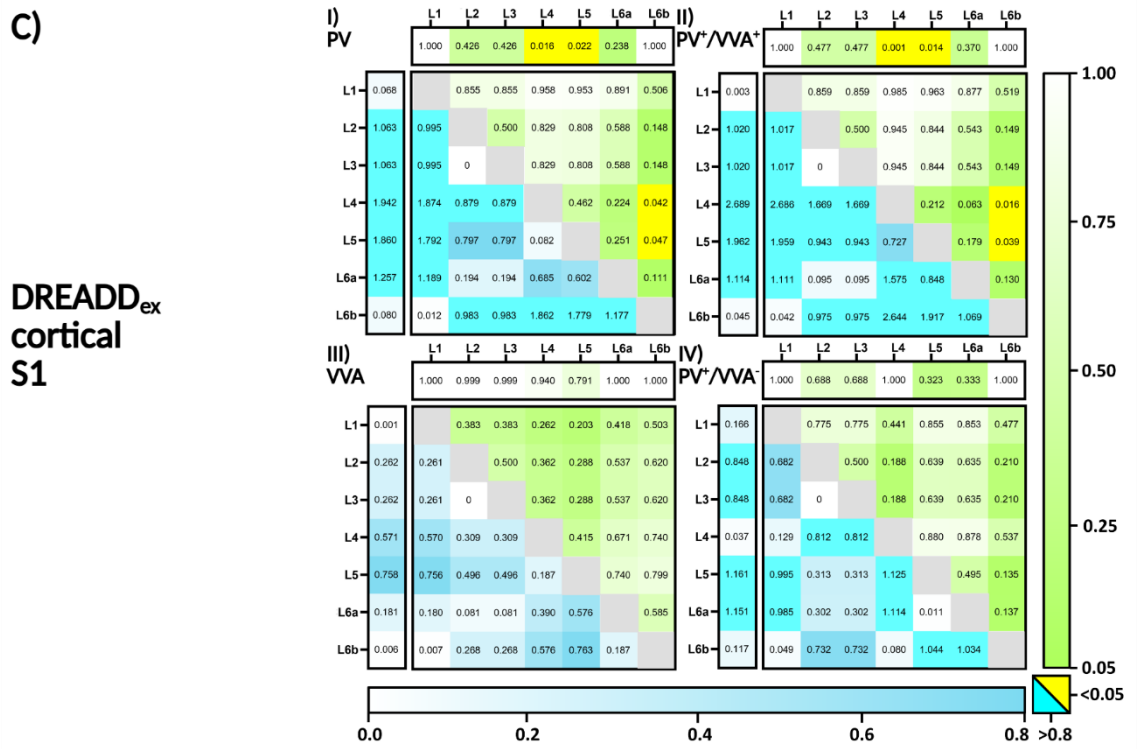


**Appx-Figure 29.** Cortical changes in PV/VVA expression patterns upon Rbp4-Cre-driven CNO activation of excitatory DREADDs. Depicts p/d-values for cortical A) RSA, B) V1, and C) S1 ROIs, distinctly for cells which are I) $PV^+$, II) $PV^+/VVA^+$, III) $VVA^+$, or $PV^+/VVA^-$.

### *A.8.4 Inhibitory DREADD cortical PV/VVA co-expression and VVA densities*

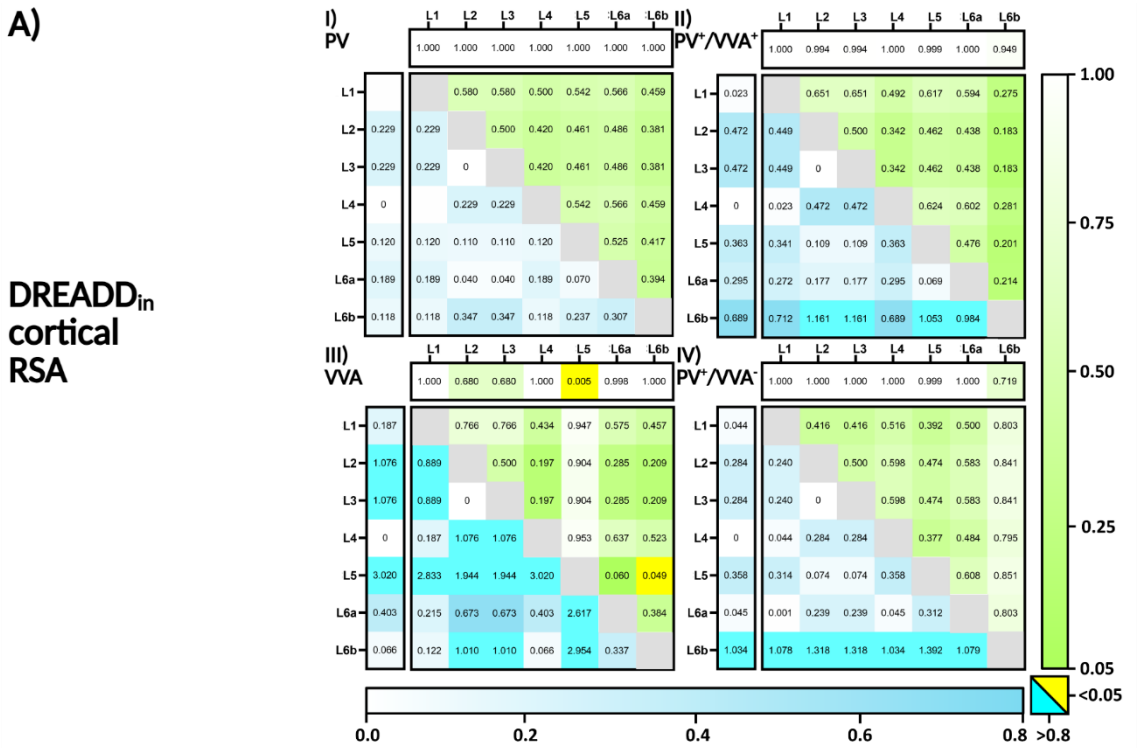

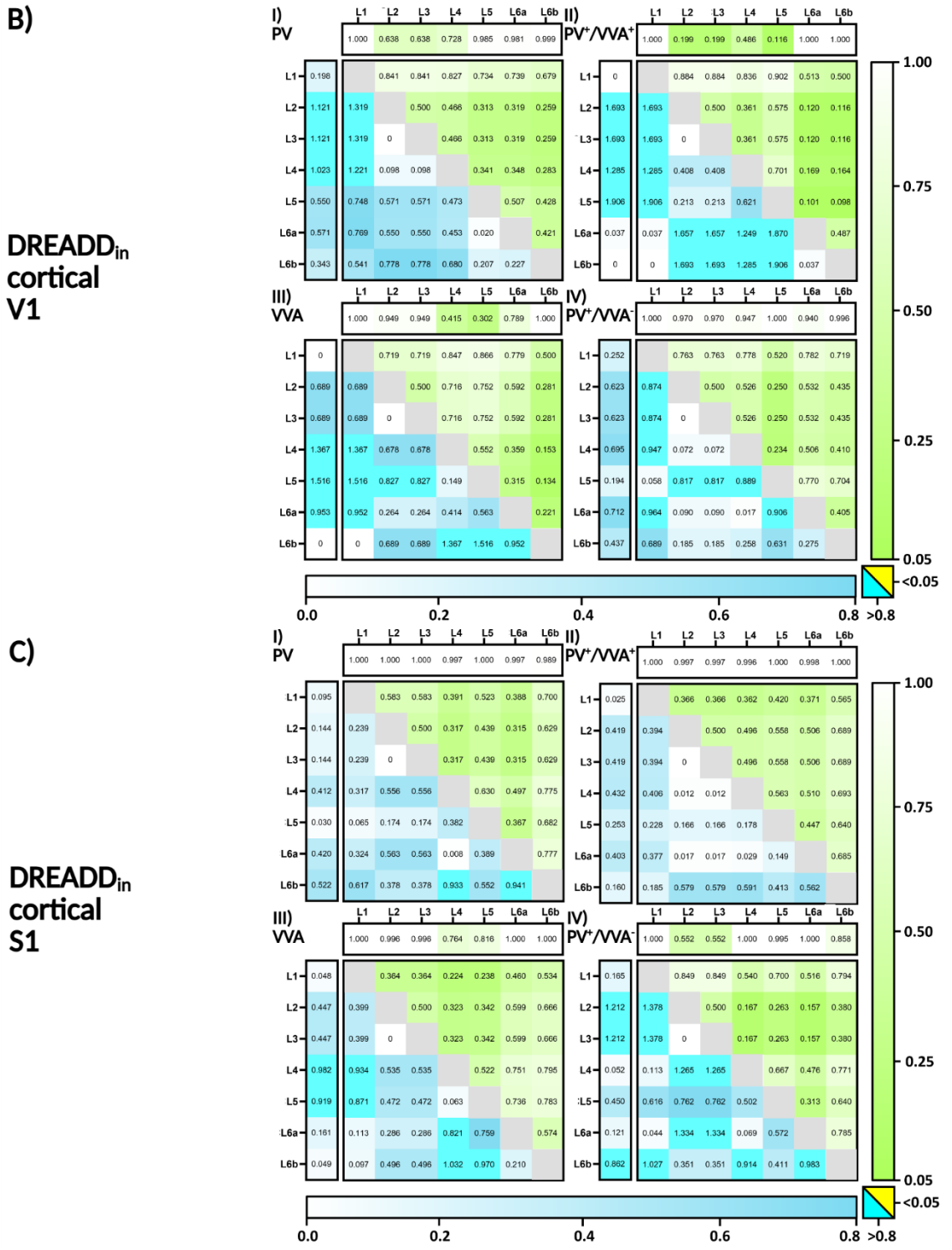


**Appx-Figure 30.** Cortical changes in PV/VVA expression patterns upon Rbp4-Cre-driven CNO activation of inhibitory DREADDs. Depicts p/d-values for cortical A) RSA, B) V1, and C) S1 ROIs, distinctly for cells which are I) $PV^+$, II) $PV^+/VVA^+$, III) $VVA^+$, or $PV^+/VVA^-$.

### *A.8.5 Fezf2 Histology*

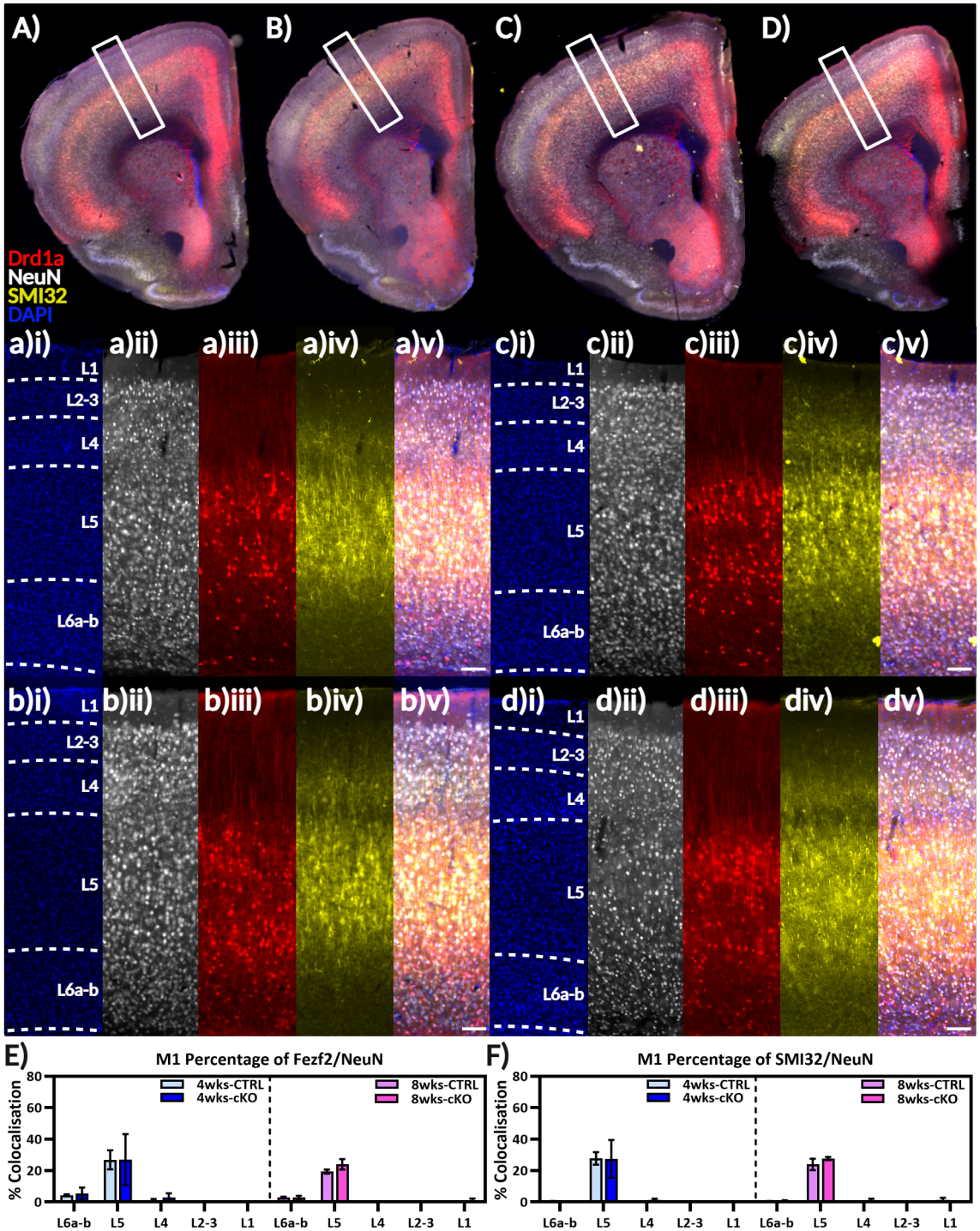


**Appx-Figure 31.** Densities of *Fezf2*-Cre neurons and subcortically-projecting SMI-32 subtypes do not change upon Cre$^{ER}$-induction of *Snap25*-cKO. This contrasts *Rbp4*-Cre-driven *Snap25*-cKO. Hemisections for A,C) CTRL (Cre$^{WT}$) and B,D) cKO (Cre$^{ER}$) samples A-B) 4wks and C-D) 8wks post-tamoxifen feature M1 cortical ROIs in a-d). Across time (i.e., 4wks vs 8wks) and genotype (i.e., Cre$^{WT}$ vs Cre$^{ER}$) conditions, no differences emerge in the proportion of neurons which are E) FEZF2$^{+}$ and F) SMI32$^{+}$. Similarly, proportions of neurons doubly-labelled for FEZF2$^{+}$/SMI32$^{+}$ and SMI32$^{+}$/FEZF2$^{+}$ remain constant (data not shown). The panels below indicate additional *Fezf2* histology conducted (yet only one representative replicate per animal and stain combination).

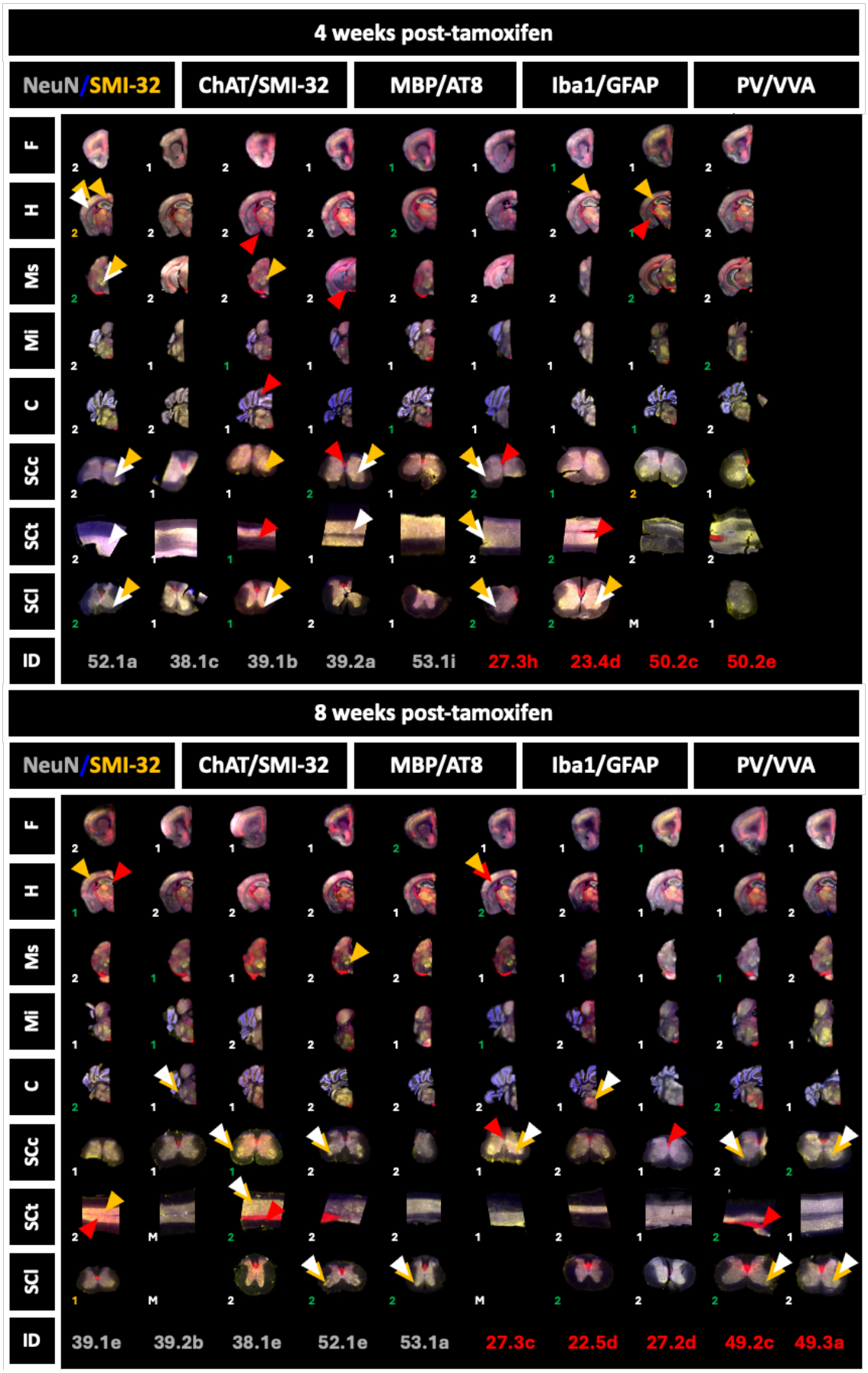
4 weeks post-tamoxifen
NeuN/SMI-32
ChAT/SMI-32
MBP/AT8
Iba1/GFAP
PV/VVA
F
H
Ms
Mi
C
SCc
SCt
SCl
ID
52.1a
38.1c
39.1b
39.2a
53.1i
27.3h
23.4d
50.2c
50.2e
8 weeks post-tamoxifen
NeuN/SMI-32
ChAT/SMI-32
MBP/AT8
Iba1/GFAP
PV/VVA
F
H
Ms
Mi
C
SCc
SCt
SCl
ID
39.1e
39.2b
38.1e
52.1e
53.1a
27.3c
22.5d
27.2d
49.2c
49.3a

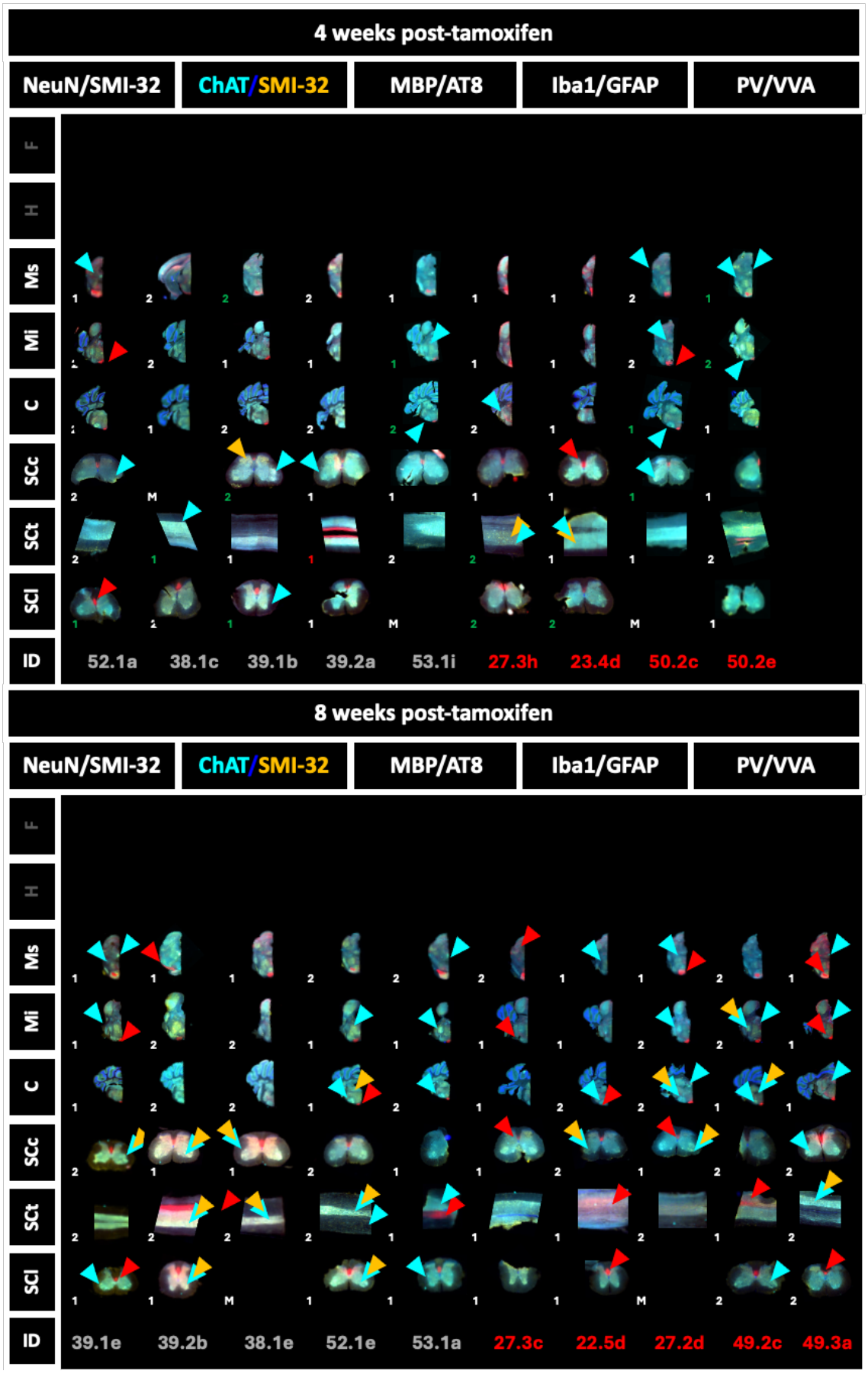
4 weeks post-tamoxifen
NeuN/SMI-32
ChAT/SMI-32
MBP/AT8
Iba1/GFAP
PV/VVA
F
H
Ms
Mi
C
SCc
SCt
SCl
ID
52.1a
38.1c
39.1b
39.2a
53.1i
27.3h
23.4d
50.2c
50.2e
8 weeks post-tamoxifen
NeuN/SMI-32
ChAT/SMI-32
MBP/AT8
Iba1/GFAP
PV/VVA
F
H
Ms
Mi
C
SCc
SCt
SCl
ID
39.1e
39.2b
38.1e
52.1e
53.1a
27.3c
22.5d
27.2d
49.2c
49.3a

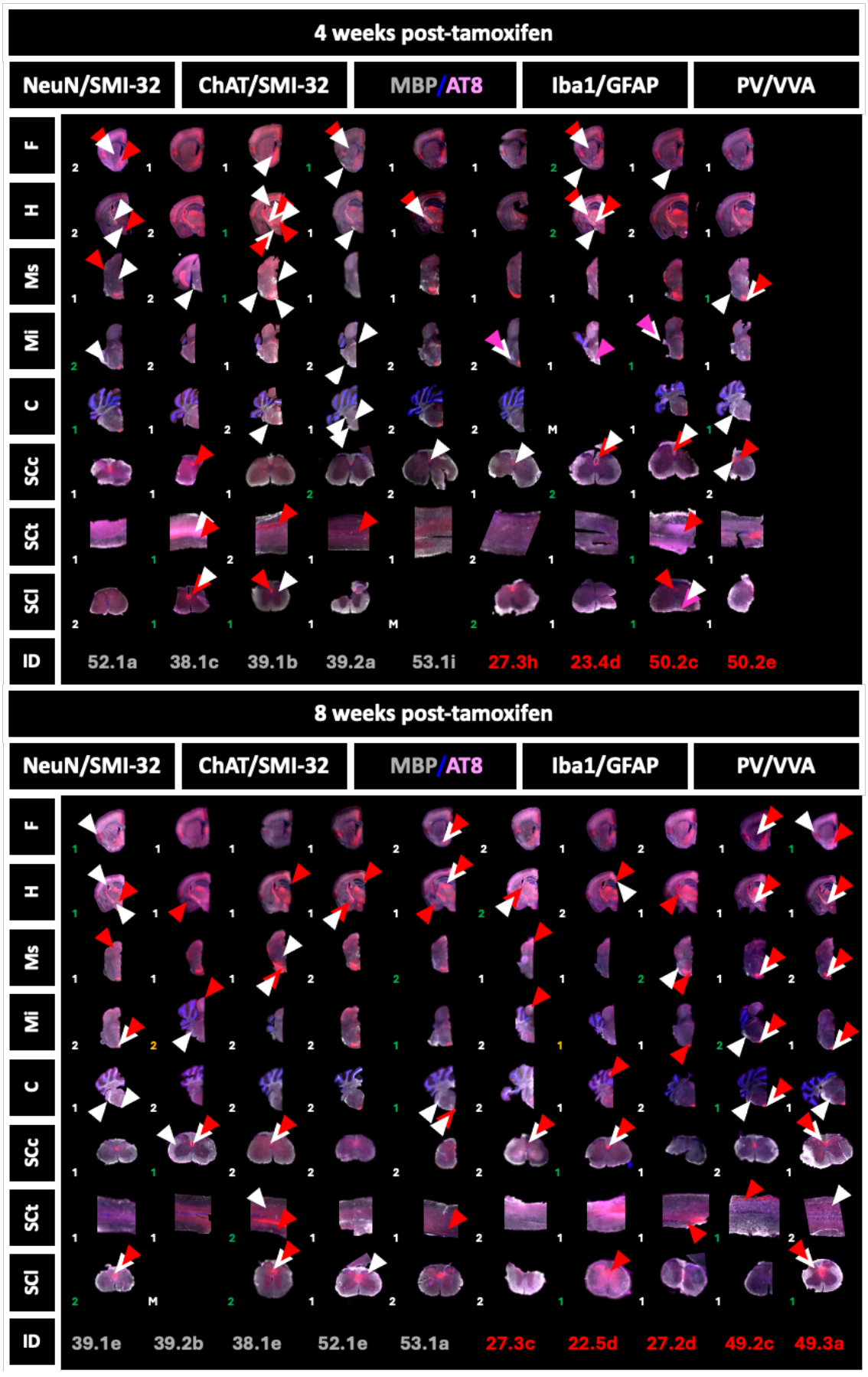
4 weeks post-tamoxifen
NeuN/SMI-32
ChAT/SMI-32
MBP/AT8
Iba1/GFAP
PV/VVA
F
H
Ms
Mi
C
SCc
SCt
SCl
ID
52.1a
38.1c
39.1b
39.2a
53.1i
27.3h
23.4d
50.2c
50.2e
8 weeks post-tamoxifen
NeuN/SMI-32
ChAT/SMI-32
MBP/AT8
Iba1/GFAP
PV/VVA
F
H
Ms
Mi
C
SCc
SCt
SCl
ID
39.1e
39.2b
38.1e
52.1e
53.1a
27.3c
22.5d
27.2d
49.2c
49.3a

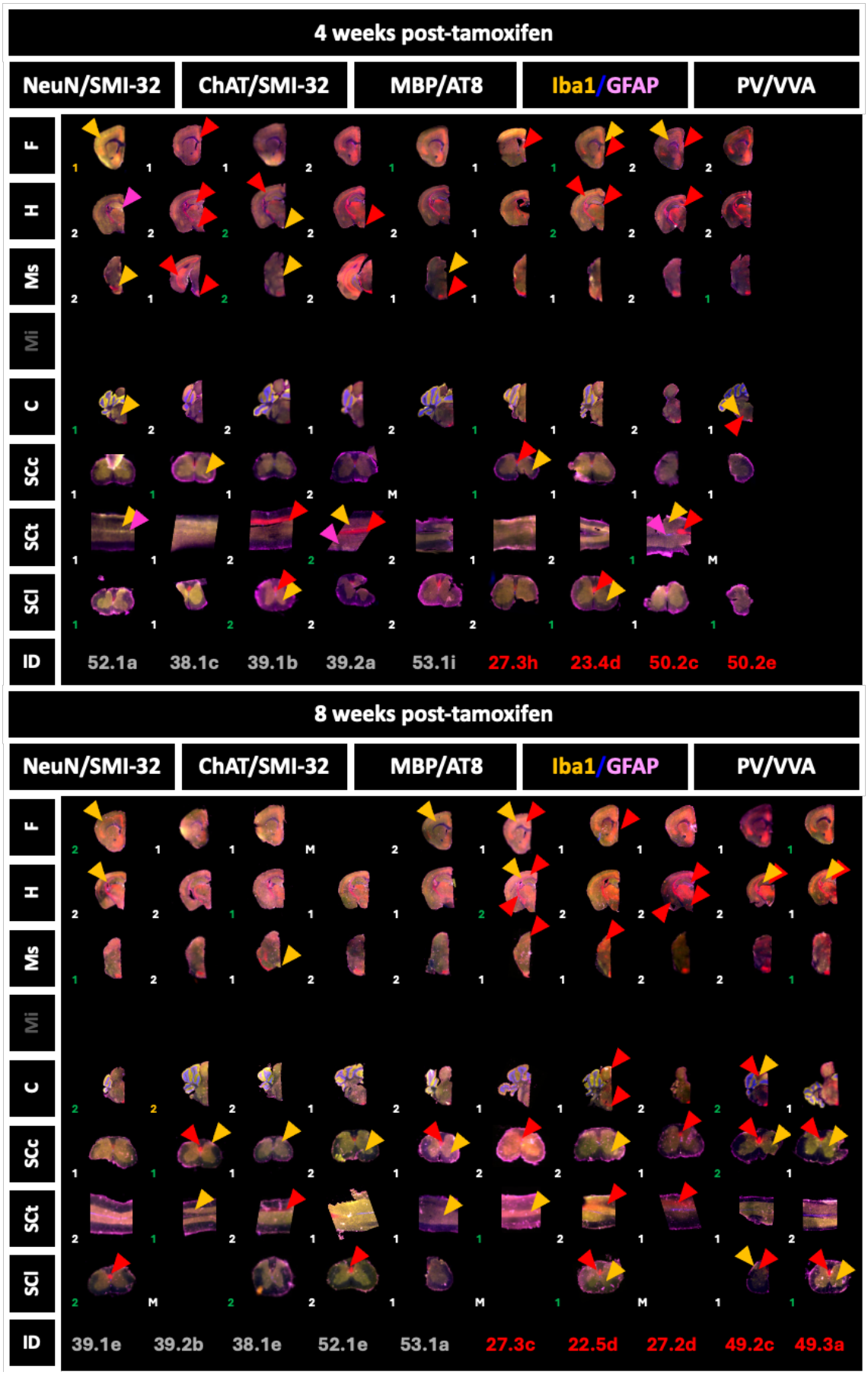
4 weeks post-tamoxifen
NeuN/SMI-32
ChAT/SMI-32
MBP/AT8
Iba1/GFAP
PV/VVA
F
H
Ms
Mi
C
SCc
SCt
SCl
ID
52.1a
38.1c
39.1b
39.2a
53.1i
27.3h
23.4d
50.2c
50.2e
8 weeks post-tamoxifen
NeuN/SMI-32
ChAT/SMI-32
MBP/AT8
Iba1/GFAP
PV/VVA
F
H
Ms
Mi
C
SCc
SCt
SCl
ID
39.1e
39.2b
38.1e
52.1e
53.1a
27.3c
22.5d
27.2d
49.2c
49.3a

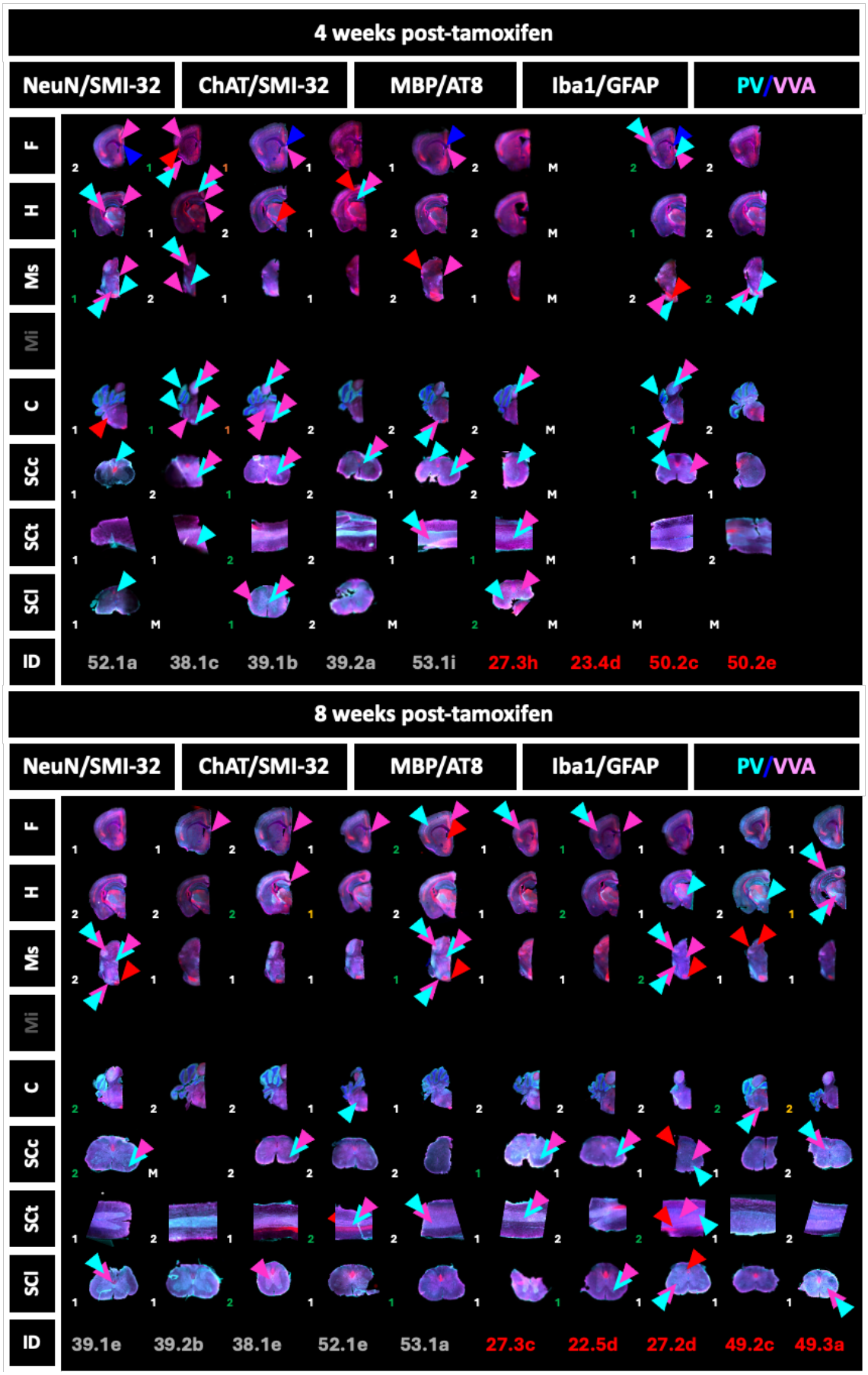
4 weeks post-tamoxifen
NeuN/SMI-32
ChAT/SMI-32
MBP/AT8
Iba1/GFAP
PV/VVA
F
H
Ms
Mi
C
SCc
SCt
SCl
ID
52.1a
38.1c
39.1b
39.2a
53.1i
27.3h
23.4d
50.2c
50.2e
8 weeks post-tamoxifen
NeuN/SMI-32
ChAT/SMI-32
MBP/AT8
Iba1/GFAP
PV/VVA
F
H
Ms
Mi
C
SCc
SCt
SCl
ID
39.1e
39.2b
38.1e
52.1e
53.1a
27.3c
22.5d
27.2d
49.2c
49.3a

### *A.8.6 Exploratory DiI tracing setup*

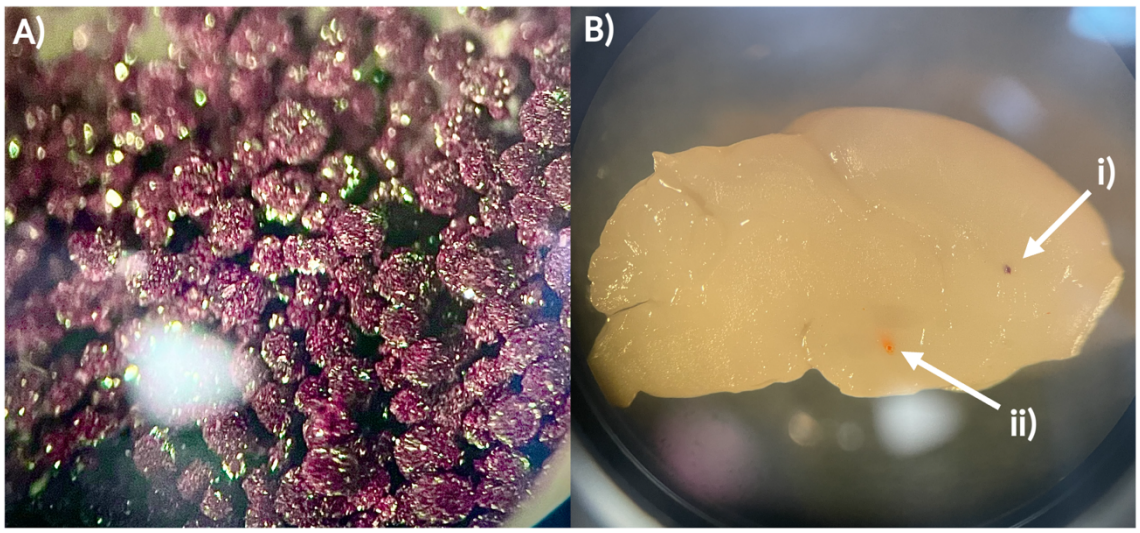


**Appx-Figure 32.** Illustrates DiI/DiA crystal placements. A) Small portions of individual crystals (DiI shown here) were extracted and manually inserted into a B) 2wk-old WT brain hemisection. Arrows indicate of i) DiI in the indusium griseum, and ii) DiA in the lateral hypothalamus.

## A.9 Behaviour supplements

### *A.9.1 CRY-deficiency: disaggregated by sex*

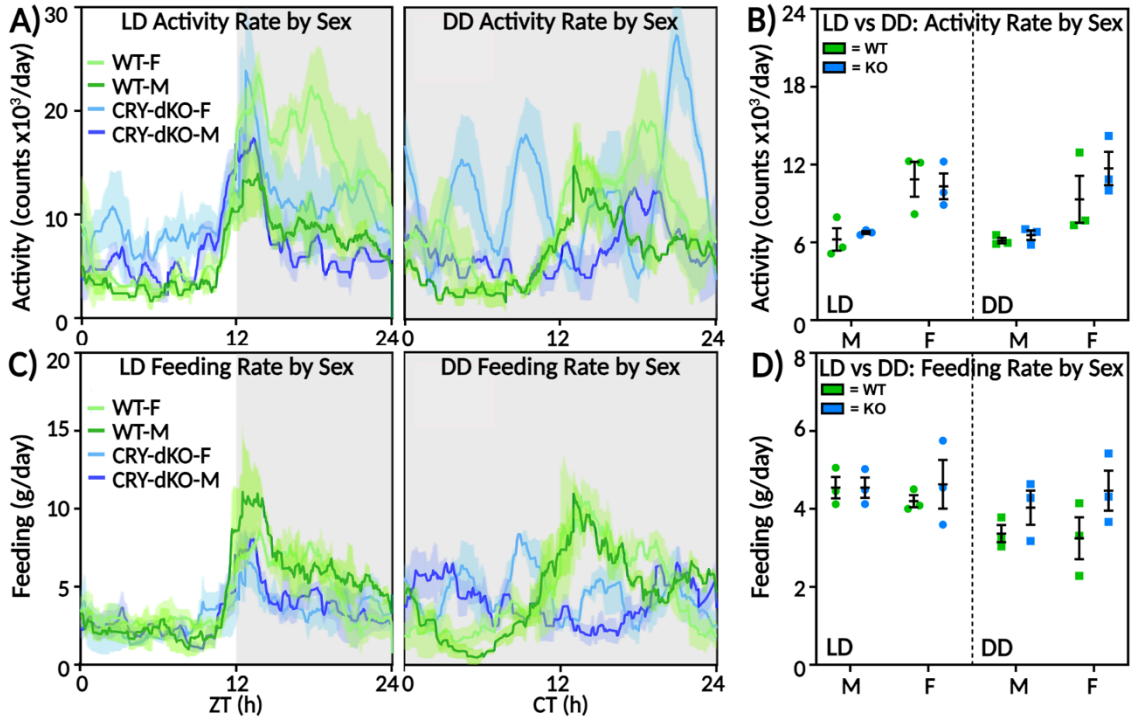


**Appx-Figure 33.** When housed under 12:12hr conditions or constant darkness, sex differences emerge in CTRL and CRY-deficient behaviour. A) rates of animal-device interactions are disaggregated for both males and females in conditions of 12:12hr light cycles and constant-darkness. B) Female activity and food-seeking behaviour is notably greater than that of males. C) Feeding rate traces are similarly separated by sex, where D) totals do not significantly.

### *A.9.2 CRY-deficiency: individual SnackerTracker recordings*

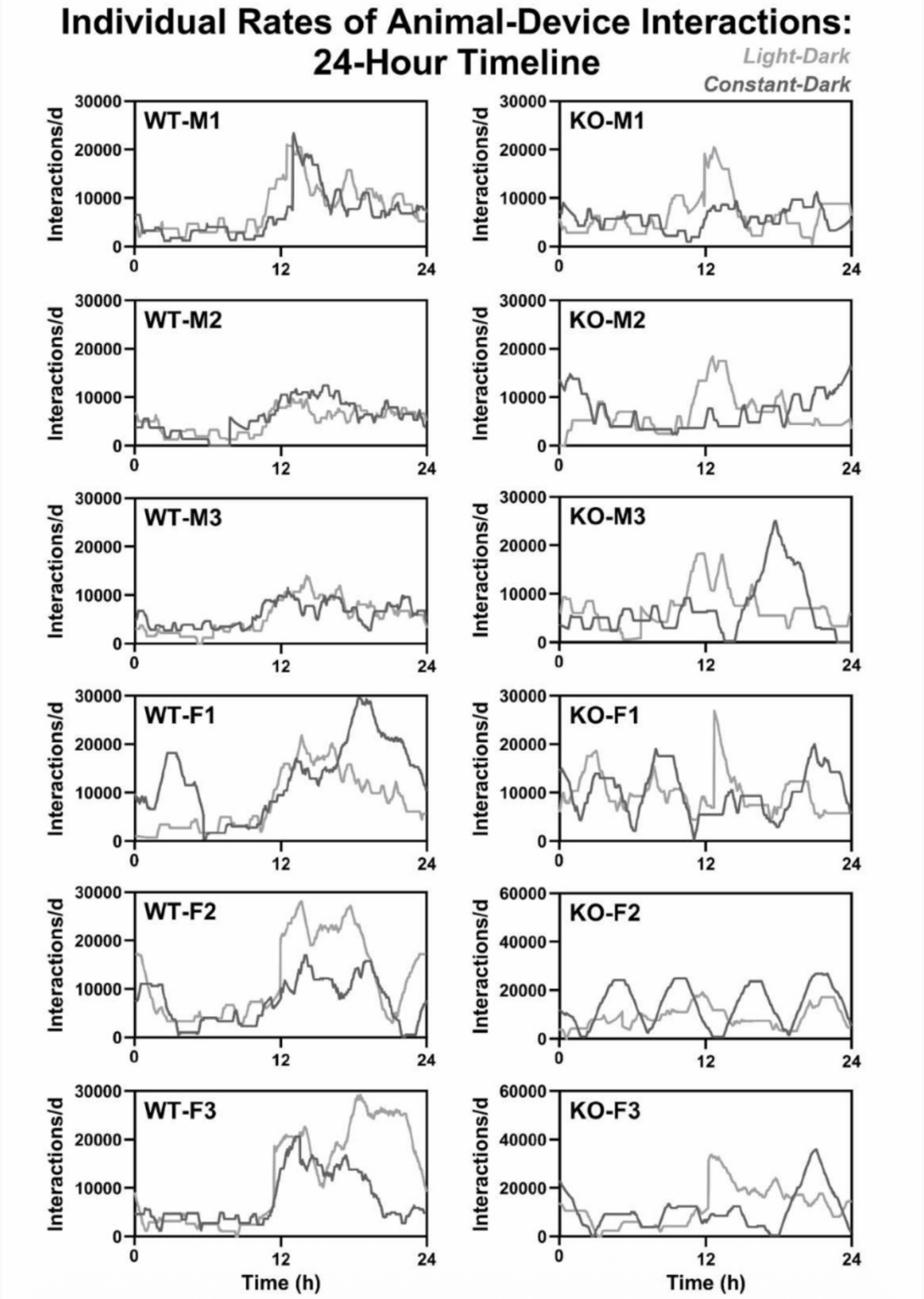


**Appx-Figure 34.** Individual behavioural traces of animal-device interactions from male and female WT and CRY-deficient (KO) mice under 12:12hr light cycles and constant-darkness.

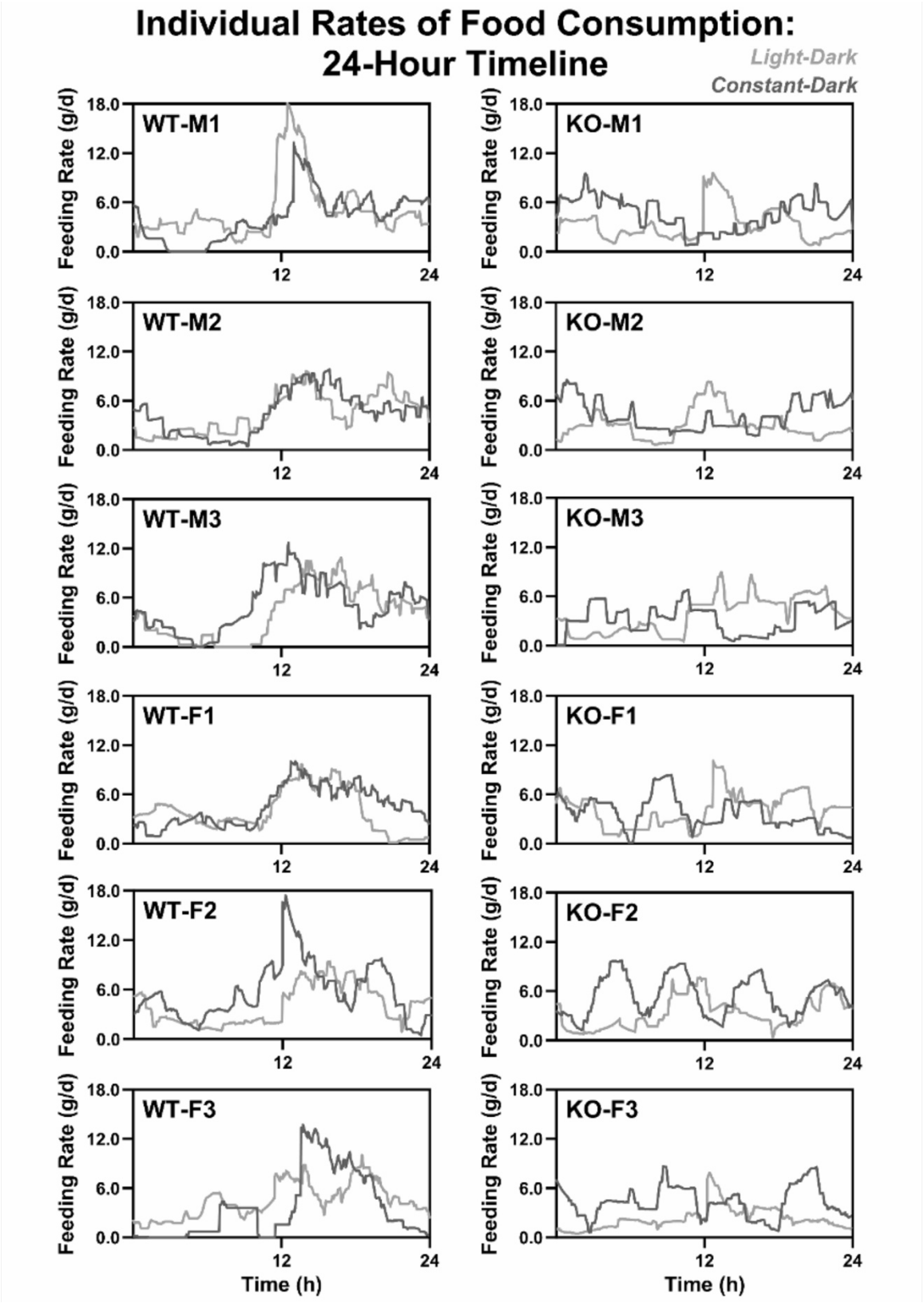


**Appx-Figure 35.** Individual behavioural traces of animal food-intake from male and female WT and CRY-deficient (KO) mice under 12:12hr light cycles and constant-darkness.

### *A.9.3 DLE: PIR data*

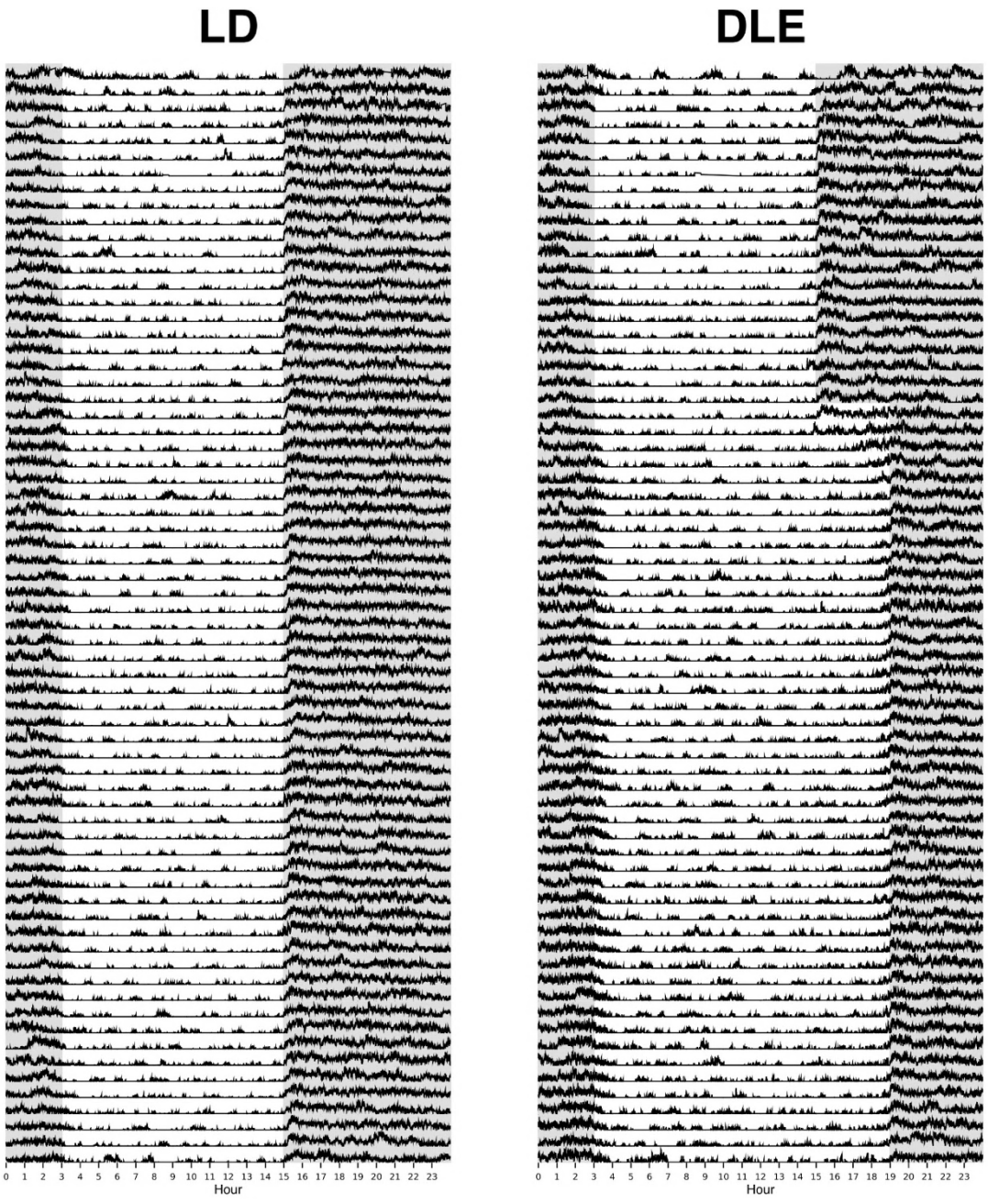


**Appx-Figure 36.** Illustrates sample PIR data plotted as an actogram from one animal housed under 12:12hr conditions and one animal housed with DLE. These recordings immediately preceded those conducted in this thesis which examined the effect of DLE on animal food-intake and feeding behaviour.

## *A.9.4 STAMINA: SnackerTracker results disaggregated by sex*

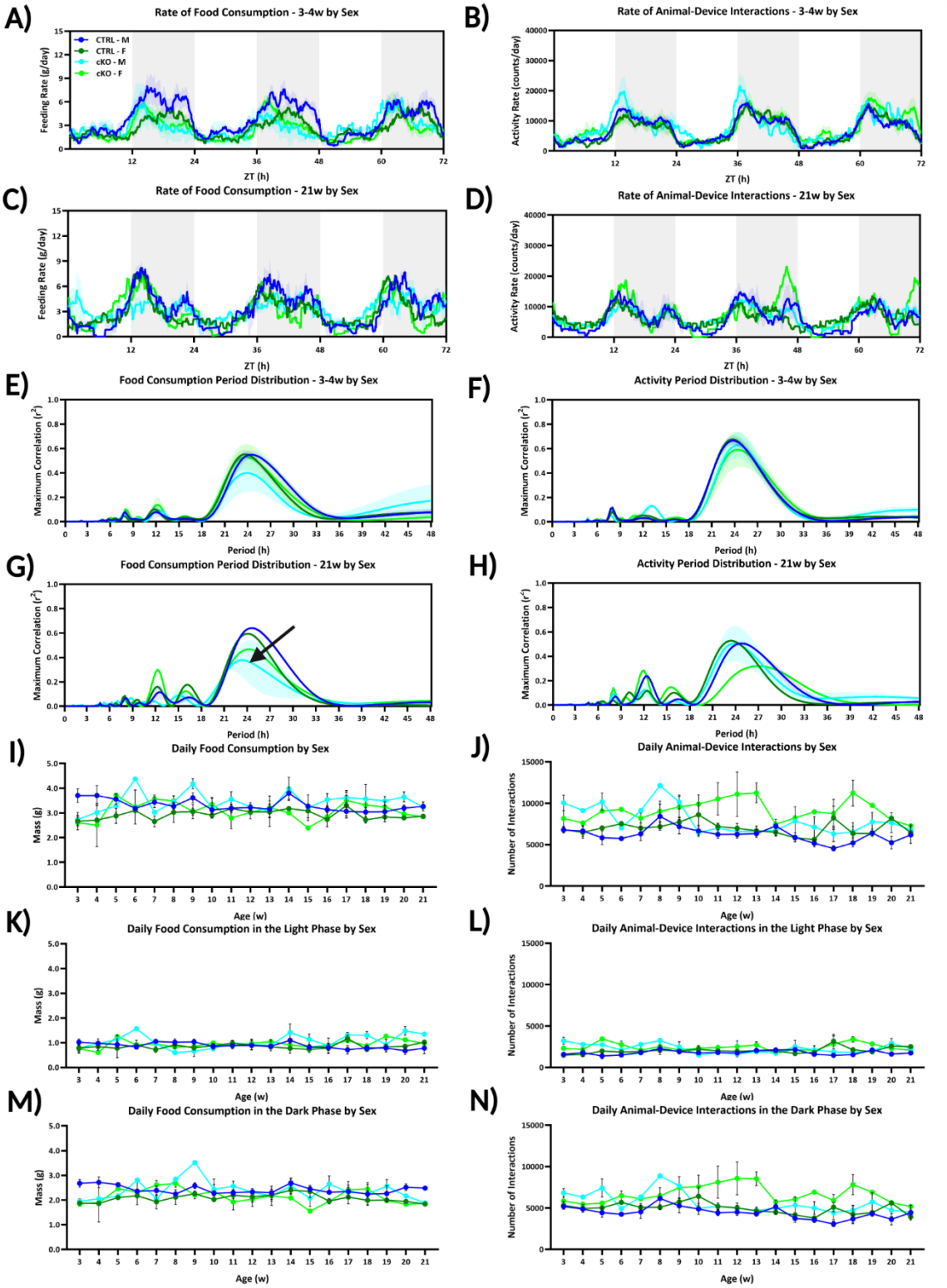


**Appx-Figure 37.** Summary of sex-disaggregated STAMINA *SnackerTracker* results. Patterns of A,C) food intake and B,D) feeding behaviour in L5-cKO vs CTRL mice are shown for A-B) 3-4wk and C-D) 21wk mice, with period decompositions in E-H). The arrow in G) indicates a decreased amplitude at τ=24h in L5-cKO mice. Daily totals over time are shown for I) food intake in the K) light-phase and M) dark-phase, as is J) feeding behaviour in the L) light-phase and N) dark-phase.

### *A.9.5 STAMINA: CAMP results disaggregated by sex*

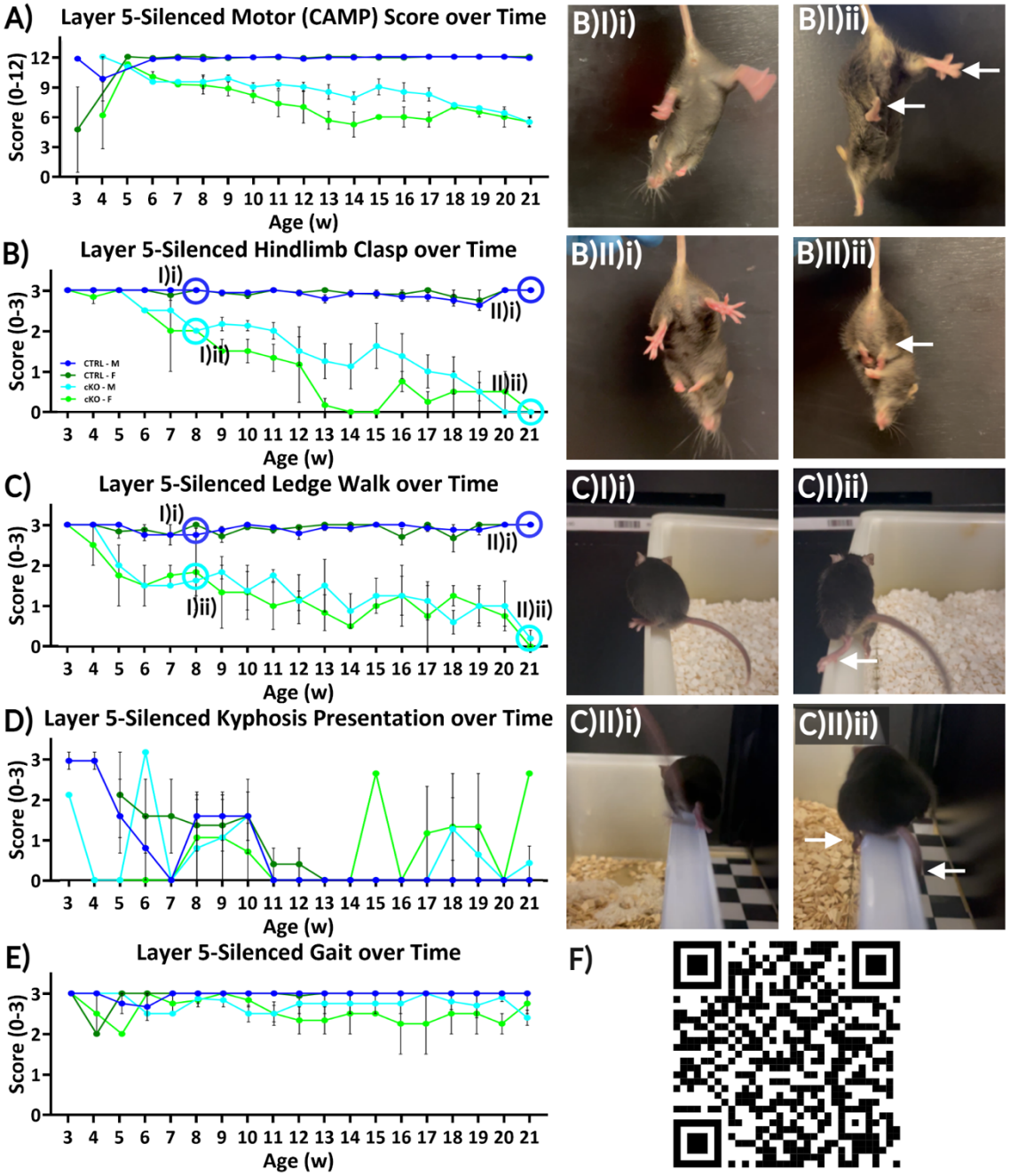


**Appx-Figure 38.** STAMINA sex-disaggregated CAMP results reveal motor deterioration in L5-cKO mice. A) CAMP scores encompass motor-associated assessments of B) the hindlimb clasp, C) the ledge-walk, D) kyphosis, and E) gait. Representative images of i) CTRL and ii) L5-cKO mice at I) 8wks and II) 21wks are provided for the B) hindlimb clasp and C) ledge-walk. Corresponding videos can be accessed using the F) QR code provided[437].

### *A.9.6 STAMINA: VCT results disaggregated by sex*

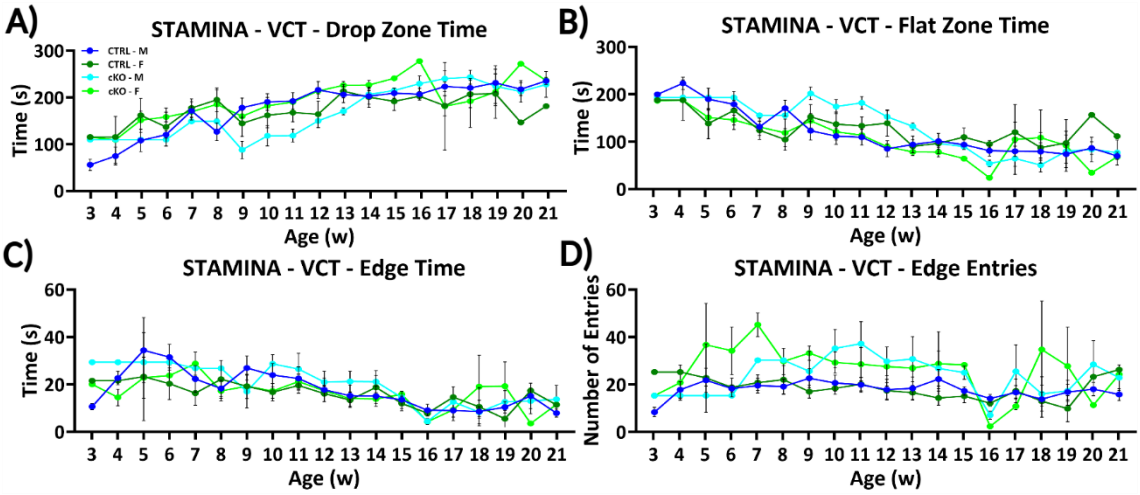


**Appx-Figure 39.** Summarises sex-disaggregated STAMINA VCT results. No obvious differences between L5-cKO and CTRL mice emerge in time spent in the A) drop-zone, B) flat-zone, or C) edge-zone, though L5-cKO mice appear to generally exhibit D) a greater number of edge entries.

### *A.9.7 STAMINA: Grip strength and nesting disaggregated by sex*

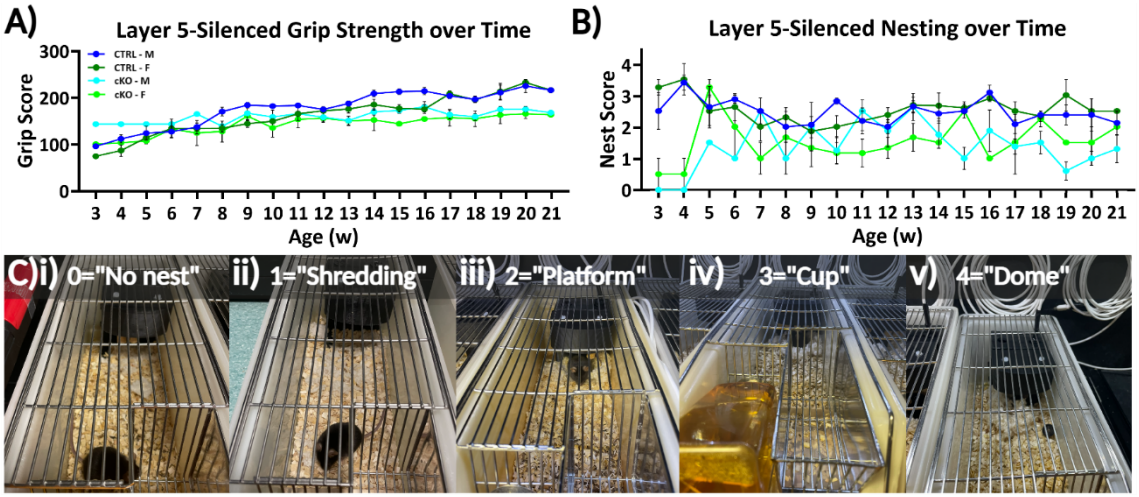


**Appx-Figure 40.** Sex-disaggregated STAMINA grip and home-cage nesting data. A) Initially indiscernible, the grip strength of L5-cKO mice increases to a lesser extent than that of CTRL mice with age. B) L5-cKO mice exhibit poor nesting behaviour compared to CTRLs across time.

### *A.9.8 STAMINA: CatWalk results disaggregated by sex*

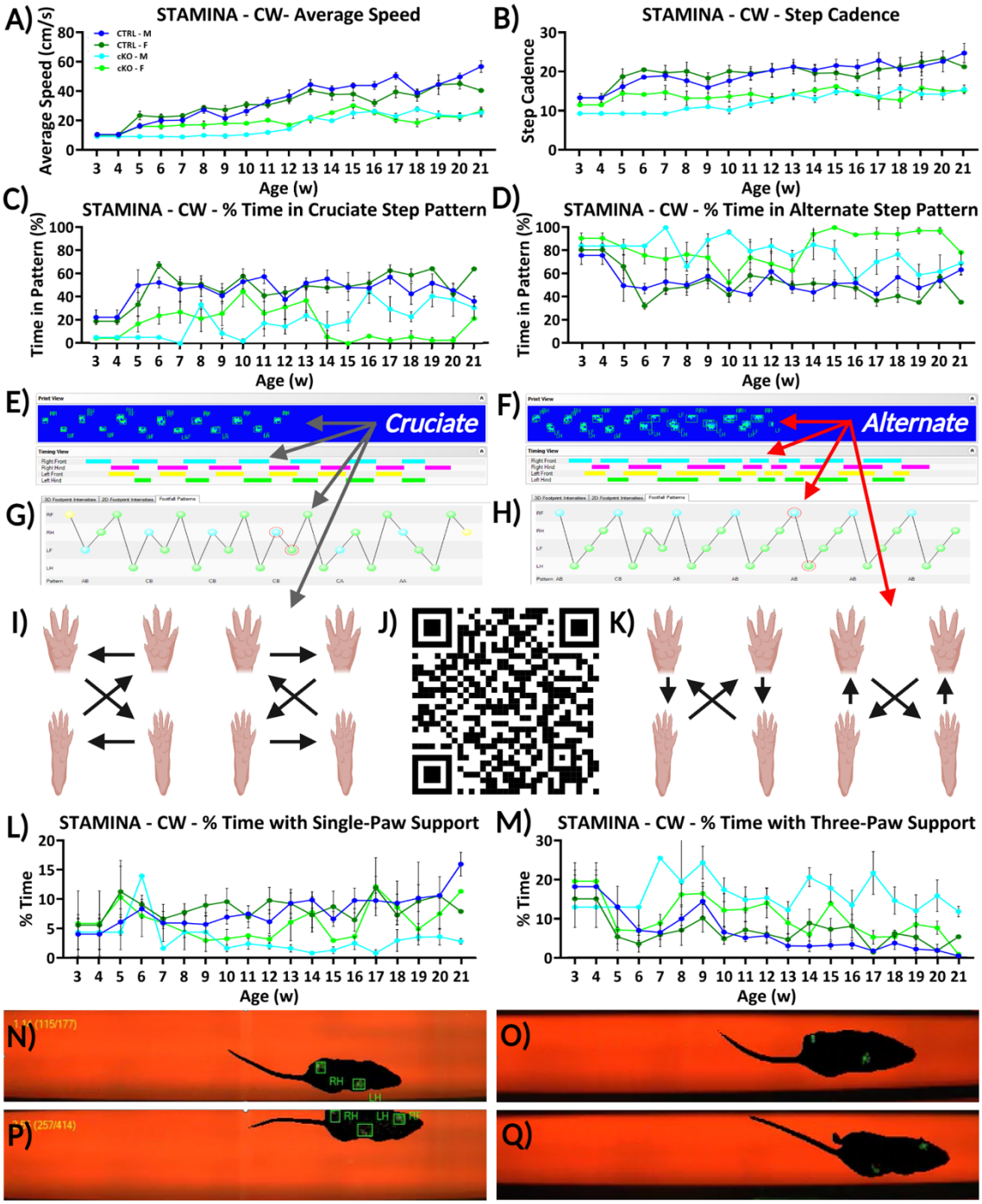


**Appx-Figure 41.** Sex-disaggregated STAMINA CatWalk gait evaluations reveal motor deficits in L5-cKO mice. Summary metrics comparing L5-cKO vs CTRL gait features include A) average speed, B) step cadence, C) time in the cruciate step pattern, D) time in the alternate step pattern, L) time with single-paw support, and M) time spent with three-paw support. E,G,I) Cruciate and F,H,K) alternate step sequences are illustrated, where a greater percentage of CTRL and L5-cKO strides are of the cruciate and alternate patterns, respectively. Images of representative CatWalk runs are shown for N) 8wk CTRL, O) 21wk CTRL, P) 8wk L5-cKO, and Q) 21wk L5-cKO mice. J) Corresponding videos are provided via the QR code[437].

## A.10 Original software

Software I created as a part of this work are listed below. References are provided where scripts have been already published. I uploaded all others to Figshare[479, 497].

### *A.10.1 Arduino software development – Editor and IoT*

- `SnackerTracker_V11.ino`[211, 280]
- `SnackerTracker_V10-IoT.ino`[211, 280]

### *A.10.2 MATLAB – TracKIT*

- `TracKIT_v1.mlapp`, with `dataCompressionBin.m` and `dataCompression.m`[258]

### *A.10.3 ImageJ – r-QUINT pre-processing*

- `quint_preprocessing.ijm`[497]

### *A.10.4 Groovy – r-QUINT downsampling and segmentation*

- `quint_detections_TdTom.groovy`[497]
- `quint_detections_VVA.groovy`[497]
- `quint_project_PTEN_Cplx3-Tbr1.groovy`[497]
- `quint_project_PTEN_PV-VVA.groovy`[497]
- `quint_project_DCST_Cplx3-Tbr1.groovy`[497]
- `quint_project_DCST_PV-VVA.groovy`[497]
- `quint_project_DCST_DREADDs.groovy`[497]

### *A.10.5 Groovy – r-QUINT object classifiers*

- `Drd1a-TdTom_Circularity_0.7.json`[497]
- `PV_Circularity_0.7.json`[497]
- `PV-VVA_composite.json`[497]
- `PV-VVA_PTEN-VVAposneg.json`[497]
- `PV-VVA_PTEN-VVAstdev.json`[497]
- `VVA_area.json`[497]
- `VVA_mean.json`[497]
- `VVA_stdev.json`[497]

### *A.10.6 ImageJ – conversions*

- comp_to_png_and_rgbtif.ijm[497]
- quint_svgtopng.ijm[497]

### *A.10.7 MATLAB – r-QUINT reformatting and soma integration*

- `ImARef_Core_v1.m`[260]
- `ImARef_HeatMaps_v1.m`[260]

### *A.10.8 ImageJ – Z-stack modification*

- `z-stack-add-imj-macro.ijm`[497]
- `z-stack-remove-imj-macro.ijm`[497]

### *A.10.9 ImageJ – Trace rotation*

- `trace-rotation-imj-macro.ijm`[497]

### *A.10.10 MATLAB – Neurite morphometrics*

- `morphometrics_l6b_mm_v2.m`[497]
- `polar_plotting_v1.m`[269]

### *A.10.11 Bash – File conversions*

- `convert-from-dicom.sh`[497]
- `nifti-to-minc.sh`[497]

### *A.10.12 CLI – pydpiper pipelines*

- `pydpiper_stamina_t1w_mm.txt`[497]
- `pydpiper_stamina_t2w_mm.txt`[497]
- `pydpiper_stamina_b0avg_mm.txt`[497]
- `pydpiper_stamina_mge_mm.txt`[497]

### *A.10.13 Bash – T2W pre-processing*

- `remove_min_v2.sh`[497]

### *A.10.14 Bash – QSM orientation corrections*

- `orient_corr.sh`[497]

### *A.10.15 Bash – Mask generation*

- `make_lsq6_masks.sh`[497]
- `make_b0avg_masks.sh`[497]

### *A.10.16 Bash – Registrations*

- `register_dwi-all_to_t2w_mm.sh`[497]
- `register_qsm-all_to_t2w_mm.sh`[497]

### *A.10.17 Python – kurtosis filtering*

- `cleanMNCS.py`[497]

### *A.10.18 Bash – MGE filtering*

- cleanMncsT2SBulk.sh[497]
- cleanMncsR2SBulk.sh[497]
- cleanMncsSUSBulk.sh[497]

### *A.10.19 R – MRI analyses*

I deposited extended neuroimaging results as a separate item[498] within Figshare[479]. Files include:

- MK analyses: MMueller_DPhilThesis_5-2-4_MAIN_Figure52-53-56_ExVi-DWI-MK
- OD analyses: MMueller_DPhilThesis_5-2-4_MAIN_Figure52-53-57_ExVi-DWI-OD
- RD analyses: MMueller_DPhilThesis_5-2-4_ExVi-DWI-RD
- RK analyses: MMueller_DPhilThesis_5-2-4_ExVi-DWI-RK
- T2W analyses: MMueller_DPhilThesis_5-2-3_MAIN_Figure50-51_ExVi-T2W
- Initial T1W analyses: MMueller_DPhilThesis_5-2-1_MAIN_Figure47_InVi-T1W-S
- T1W analyses: MMueller_DPhilThesis_5-2-1_MAIN_Figure47-48-49-79_InVi-T1W-B
- AD analyses: MMueller_DPhilThesis_5-2-4_MAIN_ExVi-DWI-AD
- AK analyses: MMueller_DPhilThesis_5-2-4_ExVi-DWI-AK
- FA analyses: MMueller_DPhilThesis_5-2-4_MAIN_Figure52-53-54-79_ExVi-DWI-FA
- FN analyses: MMueller_DPhilThesis_5-2-4_MAIN_Figure52-53-58_ExVi-DWI-ICVF
- FS analyses: MMueller_DPhilThesis_5-2-4_MAIN_Figure52-53-59_ExVi-DWI-FISO
- MD analyses: MMueller_DPhilThesis_5-2-4_MAIN_Figure52-53-55-79_ExVi-DWI-MD
- T2S analyses: MMueller_DPhilThesis_5-2-5_MAIN_Figure60_ExVi-QSM-T2S
- R2S analyses: MMueller_DPhilThesis_5-2-5_MAIN_Figure60_ExVi-QSM-R2S
- SUS analyses: MMueller_DPhilThesis_5-2-5_MAIN_Figure60_ExVi-QSM-SUS

# Bibliography


(1) Qian, X.; Su, Y.; Adam, C.; Lu, L.; Jacob, F.; Nguyen, P.; Huh, S.; Hoke, A.; Swinford-Jackson, S.; Wu, H.; et al. Sliced human cortical organoids for modeling distinct cortical layer formation. *Cell Stem Cell* **2020**, *26* (5), 766–781. DOI: 10.1016/j.stem.2020.02.002.

(2) Cruz, E.; Soares, L.; Greene, G.; Messore, F.; Abuelem, M.; Li, M.; Andersen, C.; Domocos, M.; Vitiello, E.; Abdul Razak, R.; et al. Astrocyte enrichment of 3D cortical constructs enhances brain repair. *Adv Sci* **2026**, *13* (20). DOI: 10.1002/advs.202507423.

(3) Molnár, Z.; Kim, Y.; Kronman, F. N.; Mueller, M. H.; Price, D. J. Chapter 23 - brain development. In *Kaufman's atlas of mouse development supplement*, Morriss-Kay, G., Srinivas, S. Eds.; Academic Press, **2025**; pp 371–390. DOI: 10.1016/B978-0-443-23739-3.00003-1.

(4) Hoerder-Suabedissen, A.; Hayashi, S.; Upton, L.; Nolan, Z.; Casas-Torremocha, D.; Grant, E.; Viswanathan, S.; Kanold, P. O.; Clasca, F.; Kim, Y.; et al. Subset of cortical layer 6b neurons selectively innervates higher order thalamic nuclei in mice. *Cereb Cortex* **2018**, *28* (5), 1882–1897. DOI: 10.1093/cercor/bhy036.

(5) Hoerder-Suabedissen, A.; Molnár, Z. Development, evolution and pathology of neocortical subplate neurons. *Nat Rev Neurosci* **2015**, *16* (3), 133–146. DOI: 10.1038/nrn3915.

(6) Rakic, P. Molecular and cellular mechanisms of neuronal migration: relevance to cortical epilepsies. *Adv Neurol* **2000**, *84*, 1–14. PMID: 11091853.

(7) Molnár, Z.; Garel, S.; López-Bendito, G.; Maness, P.; Price, D. J. Mechanisms controlling the guidance of thalamocortical axons through the embryonic forebrain. *Eur J Neurosci* **2012**, *35* (10), 1573–1585. DOI: 10.1111/j.1460-9568.2012.08119.x.

(8) Guillemot, F.; Molnár, Z.; Tarabykin, V.; Stoykova, A. Molecular mechanisms of cortical differentiation. *Eur J Neurosci* **2006**, *23* (4), 857–868. DOI: 10.1111/j.1460-9568.2006.04626.x

(9) Hevner, R. F.; Hodge, R. D.; Daza, R. A. M.; Englund, C. Transcription factors in glutamatergic neurogenesis: conserved programs in neocortex, cerebellum, and adult hippocampus. *Neurosci Res* **2006**, *55* (3), 223–233. DOI: https://doi.org/10.1016/j.neures.2006.03.004.

(10) Molyneaux, B. J.; Arlotta, P.; Menezes, J. R. L.; Macklis, J. D. Neuronal subtype specification in the cerebral cortex. *Nat Rev Neurosci* **2007**, *8* (6), 427–437. DOI: 10.1038/nrn2151.

(11) Price, D. J.; Kennedy, H.; Dehay, C.; Zhou, L.; Mercier, M.; Jossin, Y.; Goffinet, A. M.; Tissir, F.; Blakey, D.; Molnár, Z. The development of cortical connections. *Eur J Neurosci* **2006**, *23* (4), 910–920. DOI: 10.1111/j.1460-9568.2006.04620.x.

(12) López-Bendito, G.; Molnár, Z. Thalamocortical development: how are we going to get there? *Nat Rev Neurosci* **2003**, *4* (4), 276–289. DOI: 10.1038/nrn1075.

(13) Dehay, C.; Kennedy, H. Cell-cycle control and cortical development. *Nature Rev Neurosci* **2007**, *8* (6), 438–450. DOI: 10.1038/nrn2097.

(14) Bakken, T.; Miller, J.; Ding, S.; Sunkin, S.; Smith, K.; Ng, L.; Szafer, A.; Dalley, R.; Royall, J.; Lemon, T.; et al. A comprehensive transcriptional map of primate brain development. *Nature* **2016**, *535* (7612), 367–375. DOI: 10.1038/nature18637.

(15) Molnár, Z. Cortical layer with no known function. In *Eur J Neurosci*, Vol. 49; **2019**; pp 957–963.

(16) Kanold, P.; Kara, P.; Reid, R.; Shatz, C. Role of subplate neurons in functional maturation of visual cortical columns. *Science* **2003**, *301* (5632), 521–525. DOI: 10.1126/science.1084152.

(17) Shatz, C. J.; Luskin, M. B. The relationship between the geniculocortical afferents and their cortical target cells during development of the cat's primary visual cortex. *J Neurosci* **1986**, *6* (12), 3655–3668. DOI: 10.1523/jneurosci.06-12-03655.1986.

(18) Friauf, E.; McConnell, S.; Shatz, C. Functional synaptic circuits in the subplate during fetal and early postnatal development of cat visual cortex. *J Neurosci* **1990**, *10* (8), 2601–2613. DOI: 10.1523/jneurosci.10-08-02601.1990.

(19) Ghosh, A.; Antonini, A.; McConnell, S.; Shatz, C. Requirement for subplate neurons in the formation of thalamocortical connections. *Nature* **1990**, *347* (6289), 179–181. DOI: 10.1038/347179a0.

(20) Yamamoto, N.; López-Bendito, G. Shaping brain connections through spontaneous neural activity. *Eur J Neurosci* **2012**, *35* (10), 1595–1604. DOI: 10.1111/j.1460-9568.2012.08101.x.

(21) Piñon, M. C.; Jethwa, A.; Jacobs, E.; Campagnoni, A.; Molnár, Z. Dynamic integration of subplate neurons into the cortical barrel field circuitry during postnatal development in the golli-tau-eGFP (GTE) mouse. *J Physiol* **2009**, *587* (Pt 9), 1903–1915. DOI: 10.1113/jphysiol.2008.167767.

(22) Innocenti, G. M.; Price, D. J. Exuberance in the development of cortical networks. *Nat Rev Neurosci* **2005**, *6* (12), 955–965. DOI: 10.1038/nrn1790.

(23) Friedlander, M. J.; Torres-Reveron, J. The changing roles of neurons in the cortical subplate. *Front Neuroanat* **2009**, *3*, 15. DOI: 10.3389/neuro.05.015.2009.

(24) Krubitzer, L.; Kaas, J. The evolution of the neocortex in mammals: how is phenotypic diversity generated? *Curr Opin Neurobiol* **2005**, *15* (4), 444–453. DOI: 10.1016/j.conb.2005.07.003.

(25) Marín, O.; Rubenstein, J. L. Cell migration in the forebrain. *Ann Rev Neurosci* **2003**, *26*, 441–483. DOI: 10.1146/annurev.neuro.26.041002.131058.

(26) Tasic, B.; Yao, Z.; Graybuck, L. T.; Smith, K. A.; Nguyen, T. N.; Bertagnolli, D.; Goldy, J.; Garren, E.; Economo, M. N.; Viswanathan, S.; et al. Shared and distinct transcriptomic cell types across neocortical areas. *Nature* **2018**, *563* (7729), 72–78. DOI: 10.1038/s41586-018-0654-5.

(27) Molnár, Z.; Clowry, G. J.; Šestan, N.; Alzu'bi, A.; Bakken, T.; Hevner, R. F.; Hüppi, P. S.; Kostović, I.; Rakic, P.; Anton, E. S.; et al. New insights into the development of the human cerebral cortex. *J Anat* **2019**, *235* (3), 432–451. DOI: 10.1111/joa.13055.

(28) Letinic, K.; Rakic, P. Telencephalic origin of human thalamic GABAergic neurons. *Nat Neurosci* **2001**, *4* (9), 931–936. DOI: 10.1038/nn0901-931.

(29) Markram, H.; Toledo-Rodriguez, M.; Wang, Y.; Gupta, A.; Silberberg, G.; Wu, C. Interneurons of the neocortical inhibitory system. *Nat Rev Neurosci* **2004**, *5* (10), 793–807. DOI: 10.1038/nrn1519.

(30) Nadarajah, B.; Parnavelas, J. G. Modes of neuronal migration in the developing cerebral cortex. *Nat Rev Neurosci* **2002**, *3* (6), 423–432. DOI: 10.1038/nrn845.

(31) Walsh, C. A.; Goffinet, A. M. Potential mechanisms of mutations that affect neuronal migration in man and mouse. *Curr Opin Genet Dev* **2000**, *10* (3), 270–274. DOI: 10.1016/s0959-437x(00)00076-9.

(32) Allen reference atlas - mouse brain. Allen Institute for Brain Science: **2026**.

(33) Sedmak, G.; Judaš, M. White matter interstitial neurons in the adult human brain: 3% of cortical neurons in quest for recognition. *Cells* **2021**, *10* (1), 190.

(34) Akbarian, S.; Kim, J.; Potkin, S.; Hetrick, W.; Bunney, W.; Jones, E. Maldistribution of interstitial neurons in prefrontal white matter of the brains of schizophrenic patients. *Arch Gen Psychiatry* **1996**, *53* (5), 425–436. DOI: 10.1001/archpsyc.1996.01830050061010.

(35) Hoerder-Suabedissen, A.; Oeschger, F. M.; Krishnan, M. L.; Belgard, T. G.; Wang, W. Z.; Lee, S.; Webber, C.; Petretto, E.; Edwards, A. D.; Molnár, Z. Expression profiling of mouse subplate reveals a dynamic gene network and disease association with autism and schizophrenia. *Proc Natl Acad Sci USA* **2013**, *110* (9), 3555–3560. DOI: doi:10.1073/pnas.1218510110.

(36) Judaš, M.; Sedmak, G.; Pletikos, M. Early history of subplate and interstitial neurons: from Theodor Meynert (1867) to the discovery of the subplate zone (1974). *J Anat* **2010**, *217* (4), 344–367. DOI: 10.1111/j.1469-7580.2010.01283.x.

(37) Judaš, M.; Sedmak, G.; Kostović, I. The significance of the subplate for evolution and developmental plasticity of the human brain. *Front Hum Neurosci* **2013**, *7*, 423–423. DOI: 10.3389/fnhum.2013.00423.

(38) Sauer, B.; Henderson, N. Site-specific DNA recombination in mammalian cells by the Cre recombinase of bacteriophage P1. *Proc Natl Acad Sci USA* **1988**, *85* (14), 5166–5170. DOI: 10.1073/pnas.85.14.5166.

(39) Gong, S.; Doughty, M.; Harbaugh, C. R.; Cummins, A.; Hatten, M. E.; Heintz, N.; Gerfen, C. R. Targeting Cre recombinase to specific neuron populations with bacterial artificial chromosome constructs. *J Neurosci* **2007**, *27* (37), 9817. DOI: 10.1523/JNEUROSCI.2707-07.2007.

(40) Gerfen, C. R.; Paletzki, R.; Heintz, N. GENSAT BAC Cre-recombinase driver lines to study the functional organization of cerebral cortical and basal ganglia circuits. *Neuron* **2013**, *80* (6), 1368–1383. DOI: 10.1016/j.neuron.2013.10.016.

(41) Feldmeyer, D. Structure and function of neocortical layer 6b. *Front Cell Neurosci* **2023**, *17*, Review. DOI: 10.3389/fncel.2023.1257803.

(42) Marx, M.; Feldmeyer, D. Morphology and physiology of excitatory neurons in layer 6b of the somatosensory rat barrel cortex. *Cereb Cortex* **2013**, *23* (12), 2803–2817. DOI: 10.1093/cercor/bhs254.

(43) Briggs, F. Organizing principles of cortical layer 6. *Front Neural Circuits* **2010**, *4*, 3. DOI: 10.3389/neuro.04.003.2010.

(44) Yao, Z.; van Velthoven, C. T. J.; Nguyen, T. N.; Goldy, J.; Sedeno-Cortes, A. E.; Baftizadeh, F.; Bertagnolli, D.; Casper, T.; Chiang, M.; Crichton, K.; et al. A taxonomy of transcriptomic cell types across the isocortex and hippocampal formation. *Cell* **2021**, *184* (12), 3222–3241.e3226. DOI: https://doi.org/10.1016/j.cell.2021.04.021.

(45) Hevner, R. F. Layer-specific markers as probes for neuron type identity in human neocortex and malformations of cortical development. *J Neuropathol Exp Neurol* **2007**, *66* (2), 101–109. DOI: 10.1097/nen.0b013e3180301c06.

(46) Hoerder-Suabedissen, A.; Wang, W.; Lee, S.; Davies, K.; Goffinet, A.; Rakić, S.; Reim, K.; Nicolić, M.; Paulsen, O.; et al. Novel markers reveal subpopulations of subplate neurons in the murine cerebral cortex. *Cereb Cortex* **2008**, *19* (8), 1738–1750. DOI: 10.1093/cercor/bhn195.

(47) Hoerder-Suabedissen, A.; Molnár, Z. Molecular diversity of early-born subplate neurons. *Cereb Cortex* **2012**, *23* (6), 1473–1483. DOI: 10.1093/cercor/bhs137.

(48) Zolnik, T.; Bronec, A.; Ross, A.; Staab, M.; Sachdev, R.; Molnár, Z.; Eickholt, B.; Larkum, M. Layer 6b controls brain state via apical dendrites and the higher-order thalamocortical system. *Neuron* **2024**, *112* (5), 805–820.e804. DOI: 10.1016/j.neuron.2023.11.021.

(49/91) Zolnik, T. A.; Larkum, M. The layer 6b theory of attention. In *Preprints*, Preprints: **2025**. URL: https://www.preprints.org/manuscript/202506.2342

(50) Zolnik, T.; Ledderose, J.; Toumazou, M.; Trimbuch, T.; Oram, T.; Rosenmund, C.; Eickholt, B.; Sachdev, R.; Larkum, M. Layer 6b is driven by intracortical long-range projection neurons. *Cell Rep* **2020**, *30* (10), 3492–3505.e3495. DOI: 10.1016/j.celrep.2020.02.044.

(51) Sateia, M. J. International classification of sleep disorders. *Chest* **2014**, *146* (5), 1387–1394. DOI: https://doi.org/10.1378/chest.14-0970.

(52) Connor, C.; Crawford, B.; Akbarian, S. White matter neuron alterations in schizophrenia and related disorders. *Int J Dev Neurosci* **2011**, *29* (3), 325–334. DOI: 10.1016/j.ijdevneu.2010.07.236.

(53) Bailey, A.; Luthert, P.; Dean, A.; Harding, B.; Janota, I.; Montgomery, M.; Rutter, M.; Lantos, P. A clinicopathological study of autism. *Brain* **1998**, *121*, 889–905. DOI: 10.1093/brain/121.5.889.

(54) Blatt, G. J. The neuropathology of autism. *Scientifica* **2012**, *2012*, 703675. DOI: 10.6064/2012/703675.

(55) Richter, Z.; Janszky, J.; Sétáló, G., Jr.; Horváth, R.; Horváth, Z.; Dóczi, T.; Seress, L.; Ábrahám, H. Characterization of neurons in the cortical white matter in human temporal lobe epilepsy. *Neuroscience* **2016**, *333*, 140–150. DOI: 10.1016/j.neuroscience.2016.07.011.

(56) Canitano, R. Epilepsy in autism spectrum disorders. *Eur Child Adolesc Psychiatry* **2007**, *16* (1), 61–66. DOI: 10.1007/s00787-006-0563-2.

(57) Amiet, C.; Gourfinkel-An, I.; Laurent, C.; Carayol, J.; Génin, B.; Leguern, E.; Tordjman, S.; Cohen, D. Epilepsy in simplex autism pedigrees is much lower than the rate in multiplex autism pedigrees. *Biol Psychiatry* **2013**, *74* (3), e3–e4. DOI: 10.1016/j.biopsych.2013.01.037 (accessed 2026/01/25).

(58) Takarae, Y.; Sweeney, J. Neural hyperexcitability in autism spectrum disorders. *Brain Sci* **2017**, *7* (10). DOI: 10.3390/brainsci7100129.

(59) Bozzi, Y.; Provenzano, G.; Casarosa, S. Neurobiological bases of autism–epilepsy comorbidity: a focus on excitation/inhibition imbalance. *Eur J Neurosci* **2018**, *47* (6), 534–548. DOI: https://doi.org/10.1111/ejn.13595.

(60) Clarke, D. F.; Roberts, W.; Daraksan, M.; Dupuis, A.; McCabe, J.; Wood, H.; Snead, O. C., 3rd; Weiss, S. K. The prevalence of autistic spectrum disorder in children surveyed in a tertiary care epilepsy clinic. *Epilepsia* **2005**, *46* (12), 1970–1977. DOI: 10.1111/j.1528-1167.2005.00343.x.

(61) Steelman, L. S.; Chappell, W. H.; Abrams, S. L.; Kempf, R. C.; Long, J.; Laidler, P.; Mijatovic, S.; Maksimovic-Ivanic, D.; Stivala, F.; Mazzarino, M. C.; et al. Roles of the Raf/MEK/ERK and PI3K/PTEN/Akt/mTOR pathways in controlling growth and sensitivity to therapy-implications for cancer and aging. *Aging* **2011**, *3* (3), 192–222. DOI: 10.18632/aging.100296.

(62) Ronzano, N.; Scala, M.; Abiusi, E.; Contaldo, I.; Leoni, C.; Vari, M. S.; Pisano, T.; Battaglia, D.; Genuardi, M.; Elia, M.; et al. Phosphatase and tensin homolog (PTEN) variants and epilepsy: a multicenter case series. *Seizure-Eur J Epilep* **2022**, *100*, 82–86. DOI: https://doi.org/10.1016/j.seizure.2022.06.013**.**

(63) Valverde, F.; López-Mascaraque, L.; Santacana, M.; De Carlos, J. A. Persistence of early-generated neurons in the rodent subplate: assessment of cell death in neocortex during the early postnatal period. *J Neurosci* **1995**, *15* (7 Pt 1), 5014–5024. DOI: 10.1523/jneurosci.15-07-05014.1995.

(64) Munz, M.; Bharioke, A.; Kosche, G.; Moreno-Juan, V.; Brignall, A.; Rodrigues, T. M.; Graff-Meyer, A.; Ulmer, T.; Haeuselmann, S.; Pavlinic, D.; et al. Pyramidal neurons form active, transient, multilayered circuits perturbed by autism-associated mutations at the inception of neocortex. *Cell* **2023**, *186* (9), 1930–1949.e1931. DOI: https://doi.org/10.1016/j.cell.2023.03.025.

(65) Andrews, M. G.; Subramanian, L.; Kriegstein, A. R. mTOR signaling regulates the morphology and migration of outer radial glia in developing human cortex. *Elife* **2020**, *9*. DOI: 10.7554/eLife.58737.

(66) van Campen, J. S.; Jansen, F. E.; Pet, M. A.; Otte, W. M.; Hillegers, M. H.; Joels, M.; Braun, K. P. Relation between stress-precipitated seizures and the stress response in childhood epilepsy. *Brain* **2015**, *138* (Pt 8), 2234–2248. DOI: 10.1093/brain/awv157.

(67) Rademacher, S.; Eickholt, B. J. PTEN in autism and neurodevelopmental disorders. *Cold Spring Harb Perspect Med* **2019**, *9* (11). DOI: 10.1101/cshperspect.a036780.

(68) Williams, M. R.; DeSpenza, T., Jr.; Li, M.; Gulledge, A. T.; Luikart, B. W. Hyperactivity of newborn Pten knock-out neurons results from increased excitatory synaptic drive. *J Neurosci* **2015**, *35* (3), 943–959. DOI: 10.1523/jneurosci.3144-14.2015.

(69) Kwon, C. H.; Luikart, B. W.; Powell, C. M.; Zhou, J.; Matheny, S. A.; Zhang, W.; Li, Y.; Baker, S. J.; Parada, L. F. Pten regulates neuronal arborization and social interaction in mice. *Neuron* **2006**, *50* (3), 377–388. DOI: 10.1016/j.neuron.2006.03.023.

(70) Kwon, C. H.; Zhu, X.; Zhang, J.; Knoop, L. L.; Tharp, R.; Smeyne, R. J.; Eberhart, C. G.; Burger, P. C.; Baker, S. J. Pten regulates neuronal soma size: a mouse model of Lhermitte-Duclos disease. *Nat Genet* **2001**, *29* (4), 404–411. DOI: 10.1038/ng781.

(71) Pun, R. Y. K.; Rolle, I. J.; LaSarge, C. L.; Hosford, B. E.; Rosen, J. M.; Uhl, J. D.; Schmeltzer, S. N.; Faulkner, C.; Bronson, S. L.; Murphy, B. L.; et al. Excessive activation of mTOR in postnatally generated granule cells is sufficient to cause epilepsy. *Neuron* **2012**, *75* (6), 1022–1034. DOI: https://doi.org/10.1016/j.neuron.2012.08.002.

(72) Avino, T.; Hutsler, J. J. Supernumerary neurons within the cerebral cortical subplate in autism spectrum disorders. *Brain Res* **2021**, *1760*, 147350. DOI: https://doi.org/10.1016/j.brainres.2021.147350.

(73) Liu, J. Y.; Ellis, M.; Brooke-Ball, H.; de Tisi, J.; Sisodiya, S. M.; Thom, M. High-throughput, automated quantification of white matter neurons in mild malformation of cortical development in epilepsy. *Acta Neuropathol Commun* **2014**, *2*, 72. DOI: 10.1186/2051-5960-2-72.

(74) Hay, Y.; Andjelic, S.; Badr, S.; Lambolez, B. Orexin-dependent activation of layer vib enhances cortical network activity and integration of non-specific thalamocortical inputs. *Brain Struct Funct* **2015**, *220* (6), 3497–3512. DOI: 10.1007/s00429-014-0869-7.

(75) Meijer, E. J.; Mueller, M.; Krone, L. B.; Yamagata, T.; Hoerder-Suabedissen, A.; Wilcox, S.; Alfonsa, H.; Chakrabarty, A.; Guidi, L.; Oliver, P. L.; et al. Cortical layer 6b mediates state-dependent changes in brain activity and effects of orexin on waking and sleep. *eLife* **2025**. DOI: 10.7554/eLife.106992.2.

(76) Kirchgessner, M. A.; Franklin, A. D.; Callaway, E. M. Distinct “driving” versus “modulatory” influences of different visual corticothalamic pathways. *Curr Biol* **2021**, *31* (23), 5121–5137.e5127. DOI: https://doi.org/10.1016/j.cub.2021.09.025.

(77) Hoerder-Suabedissen, A.; Korrell, K. V.; Hayashi, S.; Jeans, A.; Ramirez, D. M. O.; Grant, E.; Christian, H. C.; Kavalali, E. T.; Wilson, M. C.; Molnár, Z. Cell-specific loss of SNAP25 from cortical projection neurons allows normal development but causes subsequent neurodegeneration. *Cereb Cortex* **2019**, *29* (5), 2148–2159. DOI: 10.1093/cercor/bhy127.

(78/426) Messore, F.; Narayanan Therpurakal, R.; Dufour, J.; Hoerder-Suabedissen, A.; Guidi, L.; Korrell, K.; Mueller, M.; Abuelem, M.; Lak, A.; Bannerman, D.; et al. An orexin-sensitive subpopulation of layer 6 neurons regulates cortical excitability and anxiety behaviour. *Transl Psychiatry* **2025**, *15* (1), 147. DOI: 10.1038/s41398-025-03350-2.

(79) Korrell, K. V.; Disser, J.; Parley, K.; Vadisiute, A.; Knott, G.; Molnár, Z.; Hoerder-Suabedissen, A. Differential effect on myelination through abolition of activity-dependent synaptic vesicle release or reduction of overall electrical activity of selected cortical projections in the mouse. *J Anat* **2019**, *235* (3), 452–467. DOI: https://doi.org/10.1111/joa.12974.

(80) Washbourne, P.; Thompson, P. M.; Carta, M.; Costa, E. T.; Mathews, J. R.; Lopez-Benditó, G.; Molnár, Z.; Becher, M. W.; Valenzuela, C. F.; Partridge, L. D.; et al. Genetic ablation of the t-SNARE SNAP-25 distinguishes mechanisms of neuroexocytosis. *Nat Neurosci* **2002**, *5* (1), 19–26. DOI: 10.1038/nn783.

(81) Rizo, J.; Südhof, T. C. The membrane fusion enigma: SNAREs, Sec1/Munc18 proteins, and their accomplices - guilty as charged? *Annu Rev Cell Dev Biol* **2012**, *28*, 279–308. DOI: 10.1146/annurev-cellbio-101011-155818.

(82) Kapustina, M.; Bristow, B. N.; Cembrowski, M. S. Distinct Layer 6b transcriptomic subtypes parcellate the cortical mantle. *Prog Neurobiol* **2025**, *254*, 102841. DOI: https://doi.org/10.1016/j.pneurobio.2025.102841.

(83) Molnár, Z.; López-Bendito, G.; Small, J.; Partridge, L. D.; Blakemore, C.; Wilson, M. C. Normal development of embryonic thalamocortical connectivity in the absence of evoked synaptic activity. *J Neurosci* **2002**, *22* (23), 10313–10323. DOI: 10.1523/jneurosci.22-23-10313.2002.

(84) Blakey, D.; Wilson, M. C.; Molnár, Z. Termination and initial branch formation of SNAP-25-deficient thalamocortical fibres in heterochronic organotypic co-cultures. *Eur J Neurosci* **2012**, *35* (10), 1586–1594. DOI: 10.1111/j.1460-9568.2012.08120.x.

(85) Ayalew, M.; Le-Niculescu, H.; Levey, D. F.; Jain, N.; Changala, B.; Patel, S. D.; Winiger, E.; Breier, A.; Shekhar, A.; Amdur, R.; et al. Convergent functional genomics of schizophrenia: from comprehensive understanding to genetic risk prediction. *Mol Psychiatry* **2012**, *17* (9), 887–905. DOI: 10.1038/mp.2012.37.

(86) Dai, D.; Wang, Y.; Yuan, J.; Zhou, X.; Yin, H.; Duan, S. Meta-analyses of 10 polymorphisms associated with the risk of schizophrenia. *Biomed Rep* **2014**, *2* (5), 729–736. DOI: 10.3892/br.2014.308.

(87) Micoulaud-Franchi, J. A.; Vaillant, F.; Lopez, R.; Peri, P.; Baillif, A.; Brandejsky, L.; Steffen, M. L.; Boyer, L.; Richieri, R.; Cermolacce, M.; et al. Sensory gating in adult with attention-deficit/hyperactivity disorder: Event-evoked potential and perceptual experience reports comparisons with schizophrenia. *Biol Psychol* **2015**, *107*, 16–23. DOI: https://doi.org/10.1016/j.biopsycho.2015.03.002.

(88) Hasan, A.; Schneider, M.; Schneider-Axmann, T.; Ruge, D.; Retz, W.; Rösler, M.; Falkai, P.; Wobrock, T. A similar but distinctive pattern of impaired cortical excitability in first-episode schizophrenia and ADHD. *Neuropsychobiology* **2013**, *67* (2), 74–83. DOI: 10.1159/000343912.

(89) Alexander-Bloch, A. F.; Reiss, P. T.; Rapoport, J.; McAdams, H.; Giedd, J. N.; Bullmore, E. T.; Gogtay, N. Abnormal cortical growth in schizophrenia targets normative modules of synchronized development. *Biol Psychiatry* **2014**, *76* (6), 438–446. DOI: 10.1016/j.biopsych.2014.02.010.

(90) Shaw, P.; Malek, M.; Watson, B.; Sharp, W.; Evans, A.; Greenstein, D. Development of cortical surface area and gyrification in attention-deficit/hyperactivity disorder. *Biol Psychiatry* **2012**, *72* (3), 191–197. DOI: 10.1016/j.biopsych.2012.01.031.

(91/49) Zolnik, T.; Eickholt, B.; Molnár, Z.; Larkum, M. The layer 6b theory of attention. *Neuron* **2026**, *114* (4), 565–582. DOI: 10.1016/j.neuron.2025.11.024 (accessed 2026/03/26).

(92) Messore, L. F.; Vadisiute, A.; Edmead, H.; Durmaz, A.; Abuelem, M.; Chedotal, F.; Hoerder-Suabedissen, A.; Mann, E. O.; Molnár, Z. Chronic silencing of Drd1a-Cre+ neurons impairs dopaminergic-driven cortical activation. *Front Neuroanat* **2025**, *19*, 1548545. DOI: 10.3389/fnana.2025.1548545.

(93) Marcus, J. N.; Aschkenasi, C. J.; Lee, C. E.; Chemelli, R. M.; Saper, C. B.; Yanagisawa, M.; Elmquist, J. K. Differential expression of orexin receptors 1 and 2 in the rat brain. *J Comp Neurol* **2001**, *435* (1), 6–25. DOI: 10.1002/cne.1190.

(94) Peyron, C.; Tighe, D. K.; van den Pol, A. N.; de Lecea, L.; Heller, H. C.; Sutcliffe, J. G.; Kilduff, T. S. Neurons containing hypocretin (orexin) project to multiple neuronal systems. *J Neurosci* **1998**, *18* (23), 9996–10015. DOI: 10.1523/JNEUROSCI.18-23-09996.1998..

(95) de Lecea, L. Optogenetic control of hypocretin (orexin) neurons and arousal circuits. *Curr Top Behav Neurosci* **2015**, *25*, 367–378. DOI: 10.1007/7854_2014_364.

(96) Sakurai, T.; Amemiya, A.; Ishii, M.; Matsuzaki, I.; Chemelli, R. M.; Tanaka, H.; Williams, S. C.; Richarson, J. A.; Kozlowski, G. P.; Wilson, S.; et al. Orexins and orexin receptors: a family of hypothalamic neuropeptides and G protein-coupled receptors that regulate feeding behavior. *Cell* **1998**, *92* (5), 1 page following 696. DOI: 10.1016/s0092-8674(02)09256-5.

(97) de Lecea, L.; Kilduff, T. S.; Peyron, C.; Gao, X.; Foye, P. E.; Danielson, P. E.; Fukuhara, C.; Battenberg, E. L.; Gautvik, V. T.; Bartlett, F. S., 2nd; et al. The hypocretins: hypothalamus-specific peptides with neuroexcitatory activity. *Proc Natl Acad Sci USA* **1998**, *95* (1), 322–327. DOI: 10.1073/pnas.95.1.322.

(98) Bayer, L.; Serafin, M.; Eggermann, E.; Saint-Mleux, B.; Machard, D.; Jones, B.; Mühlethaler, M. Exclusive postsynaptic action of hypocretin-orexin on sublayer 6b cortical neurons. *J Neurosci* **2004**, *24* (30), 6760–6764. DOI: 10.1523/jneurosci.1783-04.2004.

(99) Willie, J. T.; Chemelli, R. M.; Sinton, C. M.; Yanagisawa, M. To eat or to sleep? Orexin in the regulation of feeding and wakefulness. *Annu Rev Neurosci* **2001**, *24*, 429–458. DOI: 10.1146/annurev.neuro.24.1.429.

(100) Wenger Combremont, A. L.; Bayer, L.; Dupré, A.; Mühlethaler, M.; Serafin, M. Effects of hypocretin/orexin and major transmitters of arousal on fast spiking neurons in mouse cortical layer 6b. *Cereb Cortex* **2016**, *26* (8), 3553–3562. DOI: 10.1093/cercor/bhw158.

(101) Willie, J. T.; Chemelli, R. M.; Kohlmeier, K. A.; et al. Distinct narcolepsy syndromes in orexin receptor-2 and orexin null mice: molecular genetic dissection of non-REM and REM sleep regulatory processes. *Neuron* **2003**, *38* (5), 715–730. DOI: 10.1016/s0896-6273(03)00330-1.

(102) Mishima, K.; Fujiki, N.; Yoshida, Y.; Sakurai, T.; Honda, M.; Mignot, E.; Nishino, S. Hypocretin receptor expression in canine and murine narcolepsy models and in hypocretin-ligand deficient human narcolepsy. *Sleep* **2008**, *31* (8), 1119–1126.

(103) Tsujino, N.; Sakurai, T. Role of orexin in modulating arousal, feeding, and motivation. *Front Behav Neurosci* **2013**, *7*, Review. DOI: 10.3389/fnbeh.2013.00028.

(104) Inutsuka, A.; Yamanaka, A. The physiological role of orexin/hypocretin neurons in the regulation of sleep/wakefulness and neuroendocrine functions. *Front Endocrinol (Lausanne)* **2013**, *4*, 18–18. DOI: 10.3389/fendo.2013.00018.

(105) Adamantidis, A.; de Lecea, L. The hypocretins as sensors for metabolism and arousal. *J Physiol* **2009**, *587* (1), 33–40. DOI: 10.1113/jphysiol.2008.164400.

(106) Berner, L. A.; Brown, T. A.; Lopez, E.; Wierenga, C. E.; Kaye, W. H. Neuroendocrinology of reward in anorexia nervosa and bulimia nervosa: beyond leptin and ghrelin. *Mol Cell Endocrinol* **2019**, *497*, 110320. DOI: https://doi.org/10.1016/j.mce.2018.10.018.

(107) Morales-Mulia, M.; Morales-Mulia, S. Possible dysregulation of orexin and dopamine systems in anorexia nervosa. In *Anorexia and bulimia nervosa*, Hubertus, H., Ignacio Jáuregui, L. Eds.; IntechOpen, 2019; p Ch. 5. DOI: 10.5772/intechopen.83843.

(108) Steward, T.; Mestre-Bach, G.; Fernández-García, J. C.; et al. Reduced plasma orexin-a concentrations are associated with cognitive deficits in anorexia nervosa. *Sci Rep* **2019**, *9* (1), 7910. DOI: 10.1038/s41598-019-44450-6.

(109) Nagahara, T.; Saitoh, T.; Yanagisawa, M.; et al. Design and synthesis of non-peptide, selective orexin receptor 2 agonists. *J Med Chem* **2015**, *58* (20), 7931–7937. DOI: 10.1021/acs.jmedchem.5b00988.

(110) Iio, K.; Hashimoto, K.; Nagumo, Y.; Amezawa, M.; Hasegawa, T.; Yamamoto, N.; Kutsumura, N.; Takeuchi, K.; Ishikawa, Y.; Yamamoto, H.; et al. Design and synthesis of orexin 1 receptor-selective agonists. *J Med Chem* **2023**, *66* (8), 5453–5464. DOI: 10.1021/acs.jmedchem.2c01773.

(111) Fujimoto, T.; Rikimaru, K.; Fukuda, K.; Sugimoto, H.; Masuda, K.; Ohyabu, N.; Banno, Y.; Tokunaga, N.; Kawamoto, T.; Tomata, Y.; et al. Discovery of TAK-925 as a potent, selective, and brain-penetrant orexin 2 receptor agonist. *ACS Med Chem Lett* **2022**, *13* (3), 457–462. DOI: 10.1021/acsmedchemlett.1c00626.

(112) Sakurai, T.; Nagata, R.; Yamanaka, A.; Kawamura, H.; Tsujino, N.; Muraki, Y.; Kageyama, H.; Kunita, S.; Takahashi, S.; Goto, K.; et al. Input of orexin/hypocretin neurons revealed by a genetically encoded tracer in mice. *Neuron* **2005**, *46* (2), 297–308. DOI: 10.1016/j.neuron.2005.03.010.

(113) Yoshida, K.; McCormack, S.; España, R. A.; Crocker, A.; Scammell, T. E. Afferents to the orexin neurons of the rat brain. *Journal of Comparative Neurology* **2006**, *494* (5), 845–861. DOI: 10.1002/cne.20859.

(114) Krone, L. B.; Yamagata, T.; Blanco-Duque, C.; Guillaumin, M. C. C.; Kahn, M. C.; van der Vinne, V.; McKillop, L. E.; Tam, S. K. E.; Peirson, S. N.; Akerman, C. J.; et al. A role for the cortex in sleep-wake regulation. *Nat Neurosci* **2021**, *24* (9), 1210–1215. DOI: 10.1038/s41593-021-00894-6.

(115) Nishijo, H.; Ono, T. Neural mechanisms of feeding behavior and its disorders. In *New insights into metabolic syndrome*, IntechOpen, **2020**; p Ch. 2. DOI: 10.5772/intechopen.92723.

(116) Woolley, J. D.; Gorno-Tempini, M. L.; Miller, B. L. Binge eating is associated with right orbitofrontal-insular-striatal atrophy in frontotemporal dementia. *Neurology* **2007**, *69* (14), 1424–1433. DOI: 10.1212/01.wnl.0000277461.06713.23.

(117) Kim, E. J.; Juavinett, A. L.; Kyubwa, E. M.; Jacobs, M. W.; Callaway, E. M. Three types of cortical layer 5 neurons that differ in brain-wide connectivity and function. *Neuron* **2015**, *88* (6), 1253–1267. DOI: 10.1016/j.neuron.2015.11.002.

(118) Voelker, C. C. J.; Garin, N.; Taylor, J. S. H.; Molnár, Z. Selective neurofilament (SMI-32, FNP-7 and N200) expression in subpopulations of layer v pyramidal neurons in vivo and in vitro. *Cereb Cortex* **2004**, *14* (11), 1276–1286. DOI: 10.1093/cercor/bhh089.

(119) Arlotta, P.; Molyneaux, B. J.; Chen, J.; Inoue, J.; Kominami, R.; Macklis, J. D. Neuronal subtype-specific genes that control corticospinal motor neuron development in vivo. *Neuron* **2005**, *45* (2), 207–221. DOI: https://doi.org/10.1016/j.neuron.2004.12.036.

(120) Moberg, S.; Takahashi, N. Neocortical layer 5 subclasses: from cellular properties to roles in behavior. *Front Synaptic Neurosci* **2022**, *14*, Review. DOI: 10.3389/fnsyn.2022.1006773.

(121) Winter, C. C.; Jacobi, A.; Su, J.; Chung, L.; van Velthoven, C. T. J.; Yao, Z.; Lee, C.; Zhang, Z.; Yu, S.; Gao, K.; et al. A transcriptomic taxonomy of mouse brain-wide spinal projecting neurons. *Nature* **2023**, *624* (7991), 403–414. DOI: 10.1038/s41586-023-06817-8.

(122) Beine, Z.; Wang, Z.; Tsoulfas, P.; Blackmore, M. G. Single nuclei analyses reveal transcriptional profiles and marker genes for diverse supraspinal populations. *J Neurosci* **2022**, *42* (47), 8780. DOI: 10.1523/JNEUROSCI.1197-22.2022.

(123) Wang, Z.; Maunze, B.; Wang, Y.; Tsoulfas, P.; Blackmore, M. G. Global connectivity and function of descending spinal input revealed by 3D microscopy and retrograde transduction. *J Neurosci* **2018**, *38* (49), 10566. DOI: 10.1523/JNEUROSCI.1196-18.2018.

(124) Kasper, E. M.; Larkman, A. U.; Lübke, J.; Blakemore, C. Pyramidal neurons in layer 5 of the rat visual cortex. I. Correlation among cell morphology, intrinsic electrophysiological properties, and axon targets. *J Comp Neurol* **1994**, *339* (4), 459–474. DOI: 10.1002/cne.903390402.

(125) McKenna, W. L.; Ortiz-Londono, C. F.; Katzman, S.; Chen, B. Mutual regulation between Satb2 and Fezf2 promotes subcerebral projection neuron identity in the developing cerebral cortex. *Proc Natl Acad Sci* **2015**, *112* (37), 11702–11707. DOI: doi:10.1073/pnas.1504144112.

(126) Leone, D. P.; Heavner, W. E.; Ferenczi, E. A.; Dobreva, G.; Huguenard, J. R.; Grosschedl, R.; McConnell, S. K. Satb2 regulates the differentiation of both callosal and subcerebral projection neurons in the developing cerebral cortex. *Cereb Cortex* **2015**, *25* (10), 3406–3419. DOI: 10.1093/cercor/bhu156.

(127) Chen, B.; Schaevitz, L. R.; McConnell, S. K. Fezl regulates the differentiation and axon targeting of layer 5 subcortical projection neurons in cerebral cortex. *Proc Natl Acad Sci USA* **2005**, *102* (47), 17184–17189. DOI: 10.1073/pnas.0508732102.

(128) Hattox, A. M.; Nelson, S. B. Layer V neurons in mouse cortex projecting to different targets have distinct physiological properties. *J Neurophysiol* **2007**, *98* (6), 3330–3340. DOI: 10.1152/jn.00397.2007.

(129) Groh, A.; Meyer, H. S.; Schmidt, E. F.; Heintz, N.; Sakmann, B.; Krieger, P. Cell-type specific properties of pyramidal neurons in neocortex underlying a layout that is modifiable depending on the cortical area. *Cereb Cortex* **2010**, *20* (4), 826–836. DOI: 10.1093/cercor/bhp152.

(130) Mason, A.; Larkman, A. Correlations between morphology and electrophysiology of pyramidal neurons in slices of rat visual cortex. II. electrophysiology. *J Neurosci* **1990**, *10* (5), 1415–1428. DOI: 10.1523/jneurosci.10-05-01415.1990.

(131) Constantinople, C. M.; Bruno, R. M. Deep cortical layers are activated directly by thalamus. *Science* **2013**, *340* (6140), 1591–1594. DOI: 10.1126/science.1236425.

(132) Petreanu, L.; Mao, T.; Sternson, S. M.; Svoboda, K. The subcellular organization of neocortical excitatory connections. *Nature* **2009**, *457* (7233), 1142–1145. DOI: 10.1038/nature07709.

(133) Mao, T.; Kusefoglu, D.; Hooks, B. M.; Huber, D.; Petreanu, L.; Svoboda, K. Long-range neuronal circuits underlying the interaction between sensory and motor cortex. *Neuron* **2011**, *72* (1), 111–123. DOI: 10.1016/j.neuron.2011.07.029.

(134) Takahashi, N.; Ebner, C.; Sigl-Glöckner, J.; Moberg, S.; Larkum, M. E. Active dendritic currents gate descending cortical outputs in perception. In *Nat Neurosci*, Vol. 23; **2020**; pp 1277–1285.

(135) Chagnac-Amitai, Y.; Luhmann, H. J.; Prince, D. A. Burst generating and regular spiking layer 5 pyramidal neurons of rat neocortex have different morphological features. *J Comp Neurol* **1990**, *296* (4), 598–613. DOI: 10.1002/cne.902960407.

(136) Guan, D.; Armstrong, W. E.; Foehring, R. C. Electrophysiological properties of genetically identified subtypes of layer 5 neocortical pyramidal neurons: $Ca^{2+}$ dependence and differential modulation by norepinephrine. *J Neurophysiol* **2015**, *113* (7), 2014–2032. DOI: 10.1152/jn.00524.2014.

(137) Harris, K. D.; Shepherd, G. M. G. The neocortical circuit: themes and variations. *Nat Neurosci* **2015**, *18* (2), 170–181. DOI: 10.1038/nn.3917.

(138) Young, H.; Belbut, B.; Baeta, M.; Petreanu, L. Laminar-specific cortico-cortical loops in mouse visual cortex. *Elife* **2021**, *10*. DOI: 10.7554/eLife.59551.

(139) Brown, S. P.; Hestrin, S. Intracortical circuits of pyramidal neurons reflect their long-range axonal targets. *Nature* **2009**, *457* (7233), 1133–1136. DOI: 10.1038/nature07658.

(140) Kiritani, T.; Wickersham, I. R.; Seung, H. S.; Shepherd, G. M. Hierarchical connectivity and connection-specific dynamics in the corticospinal-corticostriatal microcircuit in mouse motor cortex. *J Neurosci* **2012**, *32* (14), 4992–5001. DOI: 10.1523/jneurosci.4759-11.2012.

(141) Schwarz, L. A.; Miyamichi, K.; Gao, X. J.; Beier, K. T.; Weissbourd, B.; DeLoach, K. E.; Ren, J.; Ibanes, S.; Malenka, R. C.; Kremer, E. J.; et al. Viral-genetic tracing of the input-output organization of a central noradrenaline circuit. *Nature* **2015**, (1476-4687). DOI: 10.1038/nature14600.

(142) Hao, Y.; Hao, S.; Andersen-Nissen, E.; Mauck, W. M., 3rd; Zheng, S.; Butler, A.; Lee, M. J.; Wilk, A. J.; Darby, C.; Zager, M.; et al. Integrated analysis of multimodal single-cell data. *Cell* **2021**, *184* (13), 3573–3587.e3529. DOI: 10.1016/j.cell.2021.04.048.

(143) Mouse whole cortex and hippocampus SMART-seq transcriptomic dataset. Science, A.I.f.B., **2021**.

(144) Hoogland, P. V.; Van der Loos, H. Ultrastructure of giant and small thalamic terminals of cortical origin: a study of the projections from the barrel cortex in mice using Phaseolus vulgaris leuco-agglutinin (PHA-L). *Exp Brain Res* **1991**, *87* (1), 159–172. DOI: 10.1007/bf00228517.

(145) Hayashi, S.; Hoerder-Suabedissen, A.; Kiyokage, E.; Maclachlan, C.; Toida, K.; Knott, G.; Molnár, Z. Maturation of complex synaptic connections of layer 5 cortical axons in the posterior thalamic nucleus requires SNAP25. *Cereb Cortex* **2020**, *31* (5), 2625–2638. DOI: 10.1093/cercor/bhaa379.

(146) Szabó, F. P.; Sigutova, V.; Schneider, A. M.; Hoerder-Suabedissen, A.; Molnár, Z. Chronic silencing of subsets of cortical layer 5 pyramidal neurons has a long-term influence on the laminar distribution of parvalbumin interneurons and the perineuronal nets. *J Anat* **2025**, *246* (4), 479–504. DOI: https://doi.org/10.1111/joa.14181.

(147) Vadisiute, A.; Meijer, E.; Therpurakal, R. N.; Mueller, M.; Szabó, F.; Messore, F.; Jursenas, A.; Bredemeyer, O.; Krone, L. B.; Mann, E.; et al. Glial cells undergo rapid changes following acute chemogenetic manipulation of cortical layer 5 projection neurons. *Commun Biol* **2024**, *7* (1), 1286, Research article. DOI: 10.1038/s42003-024-06994-w.

(148) Etxeberria, A.; Hokanson, K. C.; Dao, D. Q.; Mayoral, S. R.; Mei, F.; Redmond, S. A.; Chan, J. R. Dynamic modulation of myelination in response to visual stimuli alters optic nerve conduction velocity. *J Neurosci* **2016**, *36* (26), 6937-6948. DOI: 10.1523/jneurosci.0908-16.2016.

(149) Arancibia-Cárcamo, I. L.; Ford, M. C.; Cossell, L.; Ishida, K.; Tohyama, K.; Attwell, D. Node of Ranvier length as a potential regulator of myelinated axon conduction speed. *Elife* **2017**, *6*. DOI: 10.7554/eLife.23329.

(150) Howell, O. W.; Palser, A.; Polito, A.; Melrose, S.; Zonta, B.; Scheiermann, C.; Vora, A. J.; Brophy, P. J.; Reynolds, R. Disruption of neurofascin localization reveals early changes preceding demyelination and remyelination in multiple sclerosis. *Brain* **2006**, *129* (12), 3173–3185. DOI: 10.1093/brain/awl290.

(151) Lonigro, A.; Devaux, J. J. Disruption of neurofascin and gliomedin at nodes of Ranvier precedes demyelination in experimental allergic neuritis. *Brain* **2008**, *132* (1), 260–273. DOI: 10.1093/brain/awn281.

(152) Vyazovskiy, V. V.; Olcese, U.; Hanlon, E. C.; Nir, Y.; Cirelli, C.; Tononi, G. Local sleep in awake rats. *Nature* **2011**, *472* (7344), 443–447. DOI: 10.1038/nature10009.

(153) Hinard, V.; Mikhail, C.; Pradervand, S.; Curie, T.; Houtkooper, R. H.; Auwerx, J.; Franken, P.; Tafti, M. Key electrophysiological, molecular, and metabolic signatures of sleep and wakefulness revealed in primary cortical cultures. *J Neurosci* **2012**, *32* (36), 12506–12517. DOI: 10.1523/jneurosci.2306-12.2012.

(154) Borbély, A. A.; Daan, S.; Wirz-Justice, A.; Deboer, T. The two-process model of sleep regulation: a reappraisal. *J Sleep Res* **2016**, *25* (2), 131–143. DOI: 10.1111/jsr.12371.

(155) Economo, M. N.; Viswanathan, S.; Tasic, B.; Bas, E.; Winnubst, J.; Menon, V.; Graybuck, L. T.; Nguyen, T. N.; Smith, K. A.; Yao, Z.; et al. Distinct descending motor cortex pathways and their roles in movement. *Nature* **2018**, *563* (7729), 79–84. DOI: 10.1038/s41586-018-0642-9.

(156) Mohan, H.; An, X.; Xu, X. H.; Kondo, H.; Zhao, S.; Matho, K. S.; Wang, B.; Musall, S.; Mitra, P.; Huang, Z. J. Cortical glutamatergic projection neuron types contribute to distinct functional subnetworks. *Nat Neurosci* **2023**, *26* (3), 481–494. DOI: 10.1038/s41593-022-01244-w.

(157) Arber, S.; Costa, R. M. Networking brainstem and basal ganglia circuits for movement. *Nat Rev Neurosci* **2022**, *23* (6), 342–360. DOI: 10.1038/s41583-022-00581-w.

(158) Inoue, T.; Ueno, M. The diversity and plasticity of descending motor pathways rewired after stroke and trauma in rodents. *Front Neural Circuits* **2025**, *19*, Review. DOI: 10.3389/fncir.2025.1566562.

(159) Welniarz, Q.; Dusart, I.; Roze, E. The corticospinal tract: evolution, development, and human disorders. *Dev Neurobiol* **2017**, *77* (7), 810–829. DOI: https://doi.org/10.1002/dneu.22455.

(160) van den Bos, M. A. J.; Geevasinga, N.; Higashihara, M.; Menon, P.; Vucic, S. Pathophysiology and diagnosis of ALS: insights from advances in neurophysiological techniques. *Int J Mol Sci* **2019**, *20* (11). DOI: 10.3390/ijms20112818.

(161) Chou, S. M.; Norris, F. H. Amyotrophic lateral sclerosis: lower motor neuron disease spreading to upper motor neurons. *Muscle Nerve* **1993**, *16* (8), 864–869. DOI: 10.1002/mus.880160810.

(162) Eisen, A. The dying forward hypothesis of ALS: tracing its history. *Brain Sci* **2021**, *11* (3), 300. DOI: 10.3390/brainsci11030300.

(163) Murray, A. J.; Croce, K.; Belton, T.; Akay, T.; Jessell, T. M. Balance control mediated by vestibular circuits directing limb extension or antagonist muscle co-activation. *Cell Rep* **2018**, *22* (5), 1325–1338. DOI: https://doi.org/10.1016/j.celrep.2018.01.009.

(164) Klein, A.; Sacrey, L. R.; Whishaw, I. Q.; Dunnett, S. B. The use of rodent skilled reaching as a translational model for investigating brain damage and disease. *Neurosci Biobehav Rev* **2012**, *36* (3), 1030–1042. DOI: https://doi.org/10.1016/j.neubiorev.2011.12.010.

(165) Wang, Z.; Romanski, A.; Mehra, V.; Wang, Y.; Tsoulfas, P.; Blackmore, M. G. Brain-wide analysis of the supraspinal connectome reveals anatomical correlates to functional recovery after spinal injury. *eLife* **2022**, *11*, e76254. DOI: 10.7554/eLife.76254.

(166) Liang, H.; Paxinos, G.; Watson, C. Projections from the brain to the spinal cord in the mouse. *Brain Struct Funct* **2011**, *215* (3), 159–186. DOI: 10.1007/s00429-010-0281-x.

(167) Lemon, R. N. Descending pathways in motor control. *Ann Rev Neurosci* **2008**, *31*, 195–218. DOI: https://doi.org/10.1146/annurev.neuro.31.060407.125547.

(168) Carmona, L. M.; Thomas, E. D.; Smith, K.; Tasic, B.; Costa, R. M.; Nelson, A. Topographical and cell type-specific connectivity of rostral and caudal forelimb corticospinal neuron populations. *Cell Rep* **2024**, *43* (4), 113993. DOI: 10.1016/j.celrep.2024.113993.

(169) Muir, G. D.; Whishaw, I. Q. Red nucleus lesions impair overground locomotion in rats: a kinetic analysis. *Eur J Neurosci* **2000**, *12* (3), 1113–1122. DOI: https://doi.org/10.1046/j.1460-9568.2000.00987.x.

(170) Küchler, M.; Fouad, K.; Weinmann, O.; Schwab, M. E.; Raineteau, O. Red nucleus projections to distinct motor neuron pools in the rat spinal cord. *J Comp Neurol* **2002**, *448* (4), 349–359. DOI: https://doi.org/10.1002/cne.10259.

(171) Ferreira-Pinto, M. J.; Kanodia, H.; Falasconi, A.; Sigrist, M.; Esposito, M. S.; Arber, S. Functional diversity for body actions in the mesencephalic locomotor region. *Cell* **2021**, *184* (17), 4564–4578.e4518. DOI: 10.1016/j.cell.2021.07.002.

(172) Matsuyama, K.; Drew, T. Vestibulospinal and reticulospinal neuronal activity during locomotion in the intact cat. I. walking on a level surface. *J Neurophysiol* **2000**, *84* (5), 2237–2256. DOI: 10.1152/jn.2000.84.5.2237.

(173) Matsuyama, K.; Takakusaki, K.; Nakajima, K.; Mori, S. Multi-segmental innervation of single pontine reticulospinal axons in the cervico-thoracic region of the cat: anterograde PHA-L tracing study. *J Comp Neurol* **1997**, *377* (2), 234–250. DOI: https://doi.org/10.1002/(SICI)1096-9861(19970113)377:2.

(174) Brocard, F.; Dubuc, R. Differential contribution of reticulospinal cells to the control of locomotion induced by the mesencephalic locomotor region. *J Neurophysiol* **2003**, *90* (3), 1714–1727. DOI: 10.1152/jn.00202.2003.

(175) Basaldella, E.; Takeoka, A.; Sigrist, M.; Arber, S. Multisensory signaling shapes vestibulo-motor circuit specificity. *Cell* **2015**, *163* (2), 301–312. DOI: 10.1016/j.cell.2015.09.023.

(176) Ji, C.; Zhang, Y.; Lin, Z.; Zhao, Z.; Jiao, Z.; Zheng, Z.; Shi, X.; Yu, S.; et al. Activation of hypothalamic-pontine-spinal pathway promotes locomotor initiation and functional recovery after spinal cord injury in mice. *Nat Comm* **2025**, *17* (1), 446. DOI: 10.1038/s41467-025-67133-5.

(177) Sathyamurthy, A.; Barik, A.; Dobrott, C. I.; Matson, K. J. E.; Stoica, S.; Pursley, R.; Chesler, A. T.; Levine, A. J. Cerebellospinal neurons regulate motor performance and motor learning. *Cell Rep* **2020**, *31* (6). DOI: 10.1016/j.celrep.2020.107595.

(178) Low, A. Y. T.; Thanawalla, A. R.; Yip, A. K. K.; Kim, J.; Wong, K. L. L.; Tantra, M.; Augustine, G. J.; Chen, A. I. Precision of discrete and rhythmic forelimb movements requires a distinct neuronal subpopulation in the interposed anterior nucleus. *Cell Rep* **2018**, *22* (9), 2322–2333. DOI: 10.1016/j.celrep.2018.02.017.

(179) Allen reference atlas - mouse spinal cord [annotated adult]. Allen Institute for Brain Science: **2026**.

(180) Rosas, D. H.; Salat, D. H.; Lee, S. Y.; Zaleta, A. K.; Pappu, V.; Fischl, B.; Greve, D.; Hevelone, N.; Hersch, S. M. Cerebral cortex and the clinical expression of Huntington's disease: complexity and heterogeneity. *Brain* **2008**, *131* (4), 1057–1068. DOI: 10.1093/brain/awn025.

(181) Pressl, C.; Mätlik, K.; Kus, L.; Darnell, P.; Paul, M. R.; Weiss, A. R.; Liguore, W.; Carroll, T. S.; Davis, D. A.; et al. Selective vulnerability of layer 5a corticostriatal neurons in Huntington's disease. *Neuron* **2024**, *112* (6), 924–941.e910. DOI: https://doi.org/10.1016/j.neuron.2023.12.009.

(182) Malkus, K. A.; Tsika, E.; Ischiropoulos, H. Oxidative modifications, mitochondrial dysfunction, and impaired protein degradation in Parkinson's disease: how neurons are lost in the Bermuda triangle. *Mol Neurodegener* **2009**, *4*, 24. DOI: 10.1186/1750-1326-4-24.

(183) Chen, L.; Daniels, S.; Kim, Y.; Chu, H. Y. Cell type-specific decrease of the intrinsic excitability of motor cortical pyramidal neurons in Parkinsonism. *J Neurosci* **2021**, *41* (25), 5553. DOI: 10.1523/JNEUROSCI.2694-20.2021.

(184) Escartin, C.; Galea, E.; Lakatos, A.; O'Callaghan, J. P.; Petzold, G. C.; Serrano-Pozo, A.; Steinhäuser, C.; Volterra, A.; Carmignoto, G.; Agarwal, A.; et al. Reactive astrocyte nomenclature, definitions, and future directions. *Nat Neurosci* **2021**, *24* (3), 312–325. DOI: 10.1038/s41593-020-00783-4.

(185) Goralski, T. M.; Meyerdirk, L.; Breton, L.; Brasseur, L.; Kurgat, K.; Turner, L.; Becker, K.; Adams, M.; Newhouse, D. J.; et al. Spatial transcriptomics reveals molecular dysfunction associated with cortical Lewy pathology. *Nat Comm* **2024**, *15* (1), 2642. DOI: 10.1038/s41467-024-47027-8.

(186) Swanson, O. K.; Yevoo, P. E.; Maffei, A. Altered thalamocortical signaling in a mouse model of Parkinson's disease. *J Neurosci* **2023**, *43* (34), 6021. DOI: 10.1523/JNEUROSCI.2871-20.2023.

(187) Nana, A. L.; Sidhu, M.; Gaus, S. E.; Hwang, J. L.; Li, L.; Kim, E. J.; Pasquini, L.; Allen, I. E.; Rankin, K. P.; et al. Neurons selectively targeted in frontotemporal dementia reveal early stage TDP-43 pathobiology. *Acta Neuropathol* **2019**, *137* (1), 27–46. DOI: 10.1007/s00401-018-1942-8.

(188) Seeley, W. W.; Carlin, D. A.; Allman, J. M.; Macedo, M. N.; Bush, C.; Miller, B. L.; DeArmond, S. J. Early frontotemporal dementia targets neurons unique to apes and humans. *Ann Neurol* **2006**, *60* (6), 660–667. DOI: https://doi.org/10.1002/ana.21055.

(189) Ozdinler, P. H.; Gautam, M.; Gozutok, O.; Konrad, C.; Manfredi, G.; Area Gomez, E.; Mitsumoto, H.; Erb, M. L.; Tian, Z.; Haase, G. Better understanding the neurobiology of primary lateral sclerosis. *Amyotroph Lateral Scler Frontotemporal Degener* **2020**, *21* (sup1), 35–46. DOI: 10.1080/21678421.2020.1837175.

(190) Genç, B.; Jara, J. H.; Lagrimas, A. K.; Pytel, P.; Roos, R. P.; Mesulam, M. M.; Geula, C.; Bigio, E. H.; Özdinler, P. H. Apical dendrite degeneration, a novel cellular pathology for Betz cells in ALS. *Sci Rep* **2017**, *7*, 41765. DOI: 10.1038/srep41765.

(191) Kiernan, M. C.; Vucic, S.; Cheah, B. C.; Turner, M. R.; Eisen, A.; Zoing, M. C. Amyotrophic lateral sclerosis. *Lancet* **2011**, *377* (9769), 942–955. DOI: 10.1016/S0140-6736(10)61156-7.

(192) Fogarty, M. J.; Noakes, P. G.; Bellingham, M. C. Motor cortex layer V pyramidal neurons exhibit dendritic regression, spine loss, and increased synaptic excitation in the presymptomatic hSOD1(G93A) mouse model of amyotrophic lateral sclerosis. *J Neurosci* **2015**, *35* (2), 643–647. DOI: 10.1523/jneurosci.3483-14.2015.

(193) De Cock, L.; Bercier, V.; Van Den Bosch, L. New developments in pre-clinical models of ALS to guide translation. In *International Review of Neurobiology*, Shaw, P. J., Kirby, J. Eds.; Vol. 176; Academic Press, **2024**; pp 477–524. DOI: 10.1016/bs.irn.2024.04.008.

(194) Moya, M. V.; Kim, R. D.; Rao, M. N.; Cotto, B. A.; Pickett, S. B.; Sferrazza, C. E.; Heintz, N.; Schmidt, E. F. Unique molecular features and cellular responses differentiate two populations of motor cortical layer 5b neurons in a preclinical model of ALS. *bioRxiv* **2021**, 2021.2005.2020.445032. DOI: 10.1101/2021.05.20.445032.

(195) Wang, X.; Michaelis, E. K. Selective neuronal vulnerability to oxidative stress in the brain. *Front Aging Neurosci* **2010**, *2*, Review. DOI: 10.3389/fnagi.2010.00012.

(196) Eisen, A.; Braak, H.; Del Tredici, K.; Lemon, R.; Ludolph, A. C.; Kiernan, M. C. Cortical influences drive amyotrophic lateral sclerosis. *J Neurol Neurosurg Psychiatry* **2017**, *88* (11), 917. DOI: 10.1136/jnnp-2017-315573.

(197) Grieco, F.; Bernstein, B. J.; Biemans, B.; Bikovski, L.; Burnett, C. J.; Cushman, J. D.; van Dam, E. A.; Fry, S. A.; Richmond-Hacham, B.; Homberg, J. R.; et al. Measuring behavior in the home cage: study design, applications, challenges, and perspectives. *Front Behav Neurosci* **2021**, *15*, 735387. DOI: 10.3389/fnbeh.2021.735387.

(198) Voikar, V.; Gaburro, S. Three pillars of automated home-cage phenotyping of mice: novel findings, refinement, and reproducibility based on literature and experience. *Front Behav Neurosci* **2020**, *14*, 575434. DOI: 10.3389/fnbeh.2020.575434.

(199) Chen, Z.; Raj, A.; Prateek, G. V.; Di Francesco, A.; Liu, J.; Keyes, B. E.; Kolumam, G.; Jojic, V.; Freund, A. Automated, high-dimensional evaluation of physiological aging and resilience in outbred mice. *eLife* **2022**, *11*, e72664, Research article. DOI: 10.7554/eLife.72664.

(200) Geiger, S. S.; Traba, J.; Richoz, N.; Farley, T. K.; Brooks, S. R.; Petermann, F.; Wang, L.; Gonzalez, F. J.; Sack, M. N.; Siegel, R. M. Feeding-induced resistance to acute lethal sepsis is dependent on hepatic BMAL1 and FXR signalling. *Nat Commun* **2021**, *12* (1), 2745, Research article. DOI: 10.1038/s41467-021-22961-z.

(201) Nguyen, K. P.; O'Neal, T. J.; Bolonduro, O. A.; White, E.; Kravitz, A. V. Feeding experimentation device (FED): a flexible open-source device for measuring feeding behavior. *J Neurosci Methods* **2016**, *267*, 108–114, Tools and resources article. DOI: 10.1016/j.jneumeth.2016.04.003.

(202) Golding, D. M.; Rees, D. J.; Davies, J. R.; Relkovic, D.; Furby, H. V.; Guschina, I. A.; Hopkins, A. L.; Davies, J. S.; Resnick, J. L.; Isles, A. R.; et al. Paradoxical leanness in the imprinting-centre deletion mouse model for Prader-Willi syndrome. *J Endocrinol* **2017**, *232* (1), 123–135, Research article. DOI: 10.1530/joe-16-0367.

(203) Saeedi, M.; Maddahi, A.; Nassiri, A. M.; Jackson, M.; Zareinia, K. CageView: a smart food control and monitoring system for phenotypical research in vivo. *Appl Sci* **2022**, *12* (10), Article. DOI: 10.3390/app12104966.

(204) Mathis, A.; Mamidanna, P.; Cury, K. M.; Abe, T.; Murthy, V. N.; Mathis, M. W.; Bethge, M. DeepLabCut: markerless pose estimation of user-defined body parts with deep learning. *Nat Neurosci* **2018**, *21* (9), 1281–1289, Technical report. DOI: 10.1038/s41593-018-0209-y.

(205) Brown, L. A.; Hasan, S.; Foster, R. G.; Peirson, S. N. COMPASS: continuous open mouse phenotyping of activity and sleep status. *Wellcome Open Res* **2016**, *1*, 2, Method article. DOI: 10.12688/wellcomeopenres.9892.2.

(206) Hut, R. A.; Pilorz, V.; Boerema, A. S.; Strijkstra, A. M.; Daan, S. Working for food shifts nocturnal mouse activity into the day. *PLoS One* **2011**, *6* (3), e17527, Research article. DOI: 10.1371/journal.pone.0017527.

(207) Zielinski, T.; Moore, A. M.; Troup, E.; Halliday, K. J.; Millar, A. J. Strengths and limitations of period estimation methods for circadian data. *PLoS One* **2014**, *9* (5), e96462. DOI: 10.1371/journal.pone.0096462.

(208) Kane, G. A.; Lopes, G.; Saunders, J. L.; Mathis, A.; Mathis, M. W. Real-time, low-latency closed-loop feedback using markerless posture tracking. *eLife* **2020**, *9*. DOI: 10.7554/eLife.61909.

(209) Brown, L. A.; Banks, G. T.; Horner, N.; Wilcox, S. L.; Nolan, P. M.; Peirson, S. N. Simultaneous assessment of circadian rhythms and sleep in mice using passive infrared sensors: a user's guide. *Curr Protoc Mouse Biol* **2020**, *10* (3), e81. DOI: 10.1002/cpmo.81.

(210) Steel, L. C. E.; Tam, S. K. E.; Brown, L. A.; Foster, R. G.; Peirson, S. N. Light sampling behaviour regulates circadian entrainment in mice. *BMC Biol* **2024**, *22* (1), 208. DOI: 10.1186/s12915-024-01995-x.

(211) Mueller, M. H.; Tir, S.; Pothecary, C.; Meijer, E.; Brown, L.; Foster, K.; Vyazovskiy, V.; Peirson, S.; Molnár, Z. The SnackerTracker: A novel home-cage monitoring device for measuring food-intake and food-seeking behaviour in mice. *Wellcome Open Res* **2025**, *10* (172). DOI: 10.12688/wellcomeopenres.23850.1.

(212) Tir, S.; Foster, R. G.; Peirson, S. N. Evaluation of the Digital Ventilated Cage® system for circadian phenotyping. *Sci Rep* **2025**, *15* (1), 3674, Research article. DOI: 10.1038/s41598-025-87530-6.

(213) Mueller, M.; Chimenti, R.; Merkle, S.; Frey–Law, L. Accelerometry analysis options produce large differences in lifestyle physical activity measurement. *Physiol Meas* **2020**, *41* (6), 065006. DOI: 10.1088/1361-6579/ab94d4.

(214) Schmid, B.; Helfrich-Förster, C.; Yoshii, T. A new ImageJ plug-in "ActogramJ" for chronobiological analyses. *J Biol Rhythms* **2011**, *26* (5), 464–467. DOI: 10.1177/0748730411414264.

(215) Wu, B.; Ja, W. W. easyClock: a user-friendly desktop application for circadian rhythm analysis and visualization. *bioRxiv* **2025**. DOI: 10.1101/2025.07.08.663749.

(216) Bastiaanssen, T. F. S.; Leigh, S. J.; Tofani, G. S. S.; Gheorghe, C. E.; Clarke, G.; Cryan, J. F. Kronos: a computational tool to facilitate biological rhythmicity analysis. *bioRxiv* **2023**, 2023.2004.2021.537503. DOI: 10.1101/2023.04.21.537503.

(217) Salem, G.; Cope, N.; Garmendia, M.; Pu, A.; Somenhalli, A.; Krynitsky, J.; Cubert, N.; Jones, T.; Dold, G.; Fletcher, A.; et al. MouseVUER: video based open-source system for laboratory mouse home-cage monitoring. *Sci Rep* **2024**, *14* (1), 2662. DOI: 10.1038/s41598-024-52788-9.

(218) de Chaumont, F.; Ey, E.; Torquet, N.; Lagache, T.; Dallongeville, S.; Imbert, A.; Legou, T.; Le Sourd, A. M.; Faure, P.; Bourgeron, T.; et al. Real-time analysis of the behaviour of groups of mice via a depth-sensing camera and machine learning. *Nat Biomed Eng* **2019**, *3* (11), 930–942. DOI: 10.1038/s41551-019-0396-1.

(219) Goodwin, N. L.; Choong, J. J.; Hwang, S.; Pitts, K.; Bloom, L.; Islam, A.; Zhang, Y. Y.; Szelenyi, E. R.; Tong, X.; Newman, E. L.; et al. Simple Behavioral Analysis (SimBA) as a platform for explainable machine learning in behavioral neuroscience. *Nat Neurosci* **2024**, *27* (7), 1411–1424. DOI: 10.1038/s41593-024-01649-9.

(220) Yates, S. C.; Groeneboom, N. E.; Coello, C.; Kreshuk, A.; et al. QUINT: workflow for quantification and spatial analysis of features in histological images from rodent brain. *Front Neuroinform* **2019**, *13*, Methods. DOI: 10.3389/fninf.2019.00075.

(221) Puchades, M. A.; Csucs, G.; Ledergerber, D.; Leergaard, T. B.; Bjaalie, J. G. Spatial registration of serial microscopic brain images to three-dimensional reference atlases with the QuickNII tool. *PLOS ONE* **2019**, *14* (5), e0216796. DOI: 10.1371/journal.pone.0216796.

(222) Berg, S.; Kutra, D.; Kroeger, T.; Straehle, C. N.; Kausler, B. X.; Haubold, C.; Schiegg, M.; Ales, J.; Beier, T.; Rudy, M.; et al. ilastik: interactive machine learning for (bio)image analysis. *Nat Methods* **2019**, *16* (12), 1226–1232. DOI: 10.1038/s41592-019-0582-9.

(223) Schneider, C. A.; Rasband, W. S.; Eliceiri, K. W. NIH image to ImageJ: 25 years of image analysis. *Nat Methods* **2012**, *9* (7), 671–675. DOI: 10.1038/nmeth.2089.

(224) Groeneboom, N. E.; Bjaalie, J. G. Nutil: a pre- and post-processing toolbox for histological rodent brain section images. *Front Neuroinform* **2020**, *14*, 37. DOI: 10.3389/fninf.2020.00037.

(225) Kim, S. J.; Babola, T. A.; Lee, K.; Spiegel, A. C.; Matney, C. J.; Liew, M. H.; Schulteis, E. M.; Coye, A. E.; Proskurin, M.; Kang, H.; et al. A consensus definition for deep layer 6 excitatory neurons in mouse somatosensory, visual, and motor cortex. *Cell Rep* **2025**, *44* (9), 116167. DOI: 10.1016/j.celrep.2025.116167.

(226) Bureau, I.; von Saint Paul, F.; Svoboda, K. Interdigitated paralemniscal and lemniscal pathways in the mouse barrel cortex. *PLoS Biol* **2006**, *4* (12), e382. DOI: 10.1371/journal.pbio.0040382

(227) Kostovic, I.; Rakic, P. Cytology and time of origin of interstitial neurons in the white matter in infant and adult human and monkey telencephalon. *J Neurocytol* **1980**, *9* (2), 219–242. DOI: 10.1007/BF01205159.

(228) García-Marín, V.; Blazquez-Llorca, L.; Rodriguez, J. R.; Gonzalez-Soriano, J.; DeFelipe, J. Differential distribution of neurons in the gyral white matter of the human cerebral cortex. *J Comp Neurol* **2010**, *518* (23), 4740–4759. DOI: https://doi.org/10.1002/cne.22485.

(229) Hoerder-Suabedissen, A.; Molnár, Z. Morphology of mouse subplate cells with identified projection targets changes with age. *J Comp Neurol* **2012**, *520* (1), 174–185. DOI: https://doi.org/10.1002/cne.22725.

(230) Zeng, H.; Shen, E. H.; Hohmann, J. G.; Oh, S. W.; Bernard, A.; Royall, J. J.; Glattfelder, K. J.; Sunkin, S. M.; Morris, J. A.; Guillozet-Bongaarts, A. L.; et al. Large-scale cellular-resolution gene profiling in human neocortex reveals species-specific molecular signatures. *Cell* **2012**, *149* (2), 483–496. DOI: 10.1016/j.cell.2012.02.052.

(231) Viswanathan, S.; Sheikh, A.; Looger, L. L.; Kanold, P. O. Molecularly defined subplate neurons project both to thalamocortical recipient layers and thalamus. *Cereb Cortex* **2017**, *27* (10), 4759–4768. DOI: 10.1093/cercor/bhw271.

(232) Turner, M. R.; Kiernan, M. C.; Leigh, P. N.; Talbot, K. Biomarkers in amyotrophic lateral sclerosis. *Lancet Neurol* **2009**, *8* (1), 94–109. DOI: 10.1016/S1474-4422(08)70293-X.

(233) Eisen, A.; Kim, S.; Pant, B. Amyotrophic lateral sclerosis (ALS): a phylogenetic disease of the corticomotoneuron? *Muscle Nerve* **1992**, *15* (2), 219–224. DOI: 10.1002/mus.880150215.

(234) Khabibrakhmanov, A. N.; Akhmadieva, L. A.; Nagiev, K. K.; Mukhamedyarov, M. A. Mechanisms of neuromuscular junction dysfunction in amyotrophic lateral sclerosis. *ACEN* **2025**, *19* (1), 53–61. DOI: 10.17816/acen.1070.

(235) Campanari, M. L.; García-Ayllón, M. S.; Ciura, S.; Sáez-Valero, J.; Kabashi, E. Neuromuscular junction impairment in amyotrophic lateral sclerosis: reassessing the role of acetylcholinesterase. *Front Mol Neurosci* **2016**, *9*, 160. DOI: 10.3389/fnmol.2016.00160.

(236) Hu, Y.; Chen, W.; Wei, C.; Jiang, S.; Li, S.; Wang, X.; Xu, R. Pathological mechanisms of amyotrophic lateral sclerosis. *Neural Regen Res* **2024**, *19* (5), 1036–1044. DOI: 10.4103/1673-5374.382985.

(237) Williamson, T. L.; Cleveland, D. W. Slowing of axonal transport is a very early event in the toxicity of ALS-linked SOD1 mutants to motor neurons. *Nat Neurosci* **1999**, *2* (1), 50–56. DOI: 10.1038/4553.

(238) Fallini, C.; Bassell, G. J.; Rossoll, W. The ALS disease protein TDP-43 is actively transported in motor neuron axons and regulates axon outgrowth. *Hum Mol Genet* **2012**, *21* (16), 3703–3718. DOI: 10.1093/hmg/dds205.

(239) Wong, M.; Martin, L. J. Skeletal muscle-restricted expression of human SOD1 causes motor neuron degeneration in transgenic mice. *Hum Mol Genet* **2010**, *19* (11), 2284–2302. DOI: 10.1093/hmg/ddq106.

(240) Burden, S. J. Building the vertebrate neuromuscular synapse. *J Neurobiol* **2002**, *53* (4), 501–511. DOI: https://doi.org/10.1002/neu.10137.

(241) Baudet, C.; Pozas, E.; Adameyko, I.; Andersson, E.; Ericson, J.; Ernfors, P. Retrograde signaling onto Ret during motor nerve terminal maturation. *J Neurosci* **2008**, *28* (4), 963. DOI: 10.1523/JNEUROSCI.4489-07.2008.

(242) Sanes, J. R.; Lichtman, J. W. Induction, assembly, maturation and maintenance of a postsynaptic apparatus. *Nat Rev Neurosci* **2001**, *2* (11), 791–805. DOI: 10.1038/35097557.

(243) Pokrishevsky, E.; Grad, L. I.; Cashman, N. R. TDP-43 or FUS-induced misfolded human wild-type SOD1 can propagate intercellularly in a prion-like fashion. *Sci Rep* **2016**, *6*, 22155. DOI: 10.1038/srep22155.

(244) Bogaert, E.; d'Ydewalle, C.; Van Den Bosch, L. Amyotrophic lateral sclerosis and excitotoxicity: from pathological mechanism to therapeutic target. *CNS Neurol Disord Drug Targets* **2010**, *9* (3), 297–304. DOI: 10.2174/187152710791292576.

(245) Magrané, J.; Cortez, C.; Gan, W. B.; Manfredi, G. Abnormal mitochondrial transport and morphology are common pathological denominators in SOD1 and TDP43 ALS mouse models. *Hum Mol Genet* **2014**, *23* (6), 1413–1424. DOI: 10.1093/hmg/ddt528.

(246) Hudson, A. J.; Kiernan, J. N. Preservation of certain voluntary muscles in motoneurone disease. *Lancet* **1988**, *331* (8586), 652–653. DOI: https://doi.org/10.1016/S0140-6736(88)91455-9.

(247) Jara, J. H.; Villa, S. R.; Khan, N. A.; Bohn, M. C.; Ozdinler, P. H. AAV2 mediated retrograde transduction of corticospinal motor neurons reveals initial and selective apical dendrite degeneration in ALS. *Neurobiol Dis* **2012**, *47* (2), 174–183. DOI: 10.1016/j.nbd.2012.03.036.

(248) Sharma, A.; Lyashchenko, A. K.; Lu, L.; Nasrabady, S. E.; Elmaleh, M.; Mendelsohn, M.; Nemes, A.; Tapia, J. C.; Mentis, G. Z.; Shneider, N. A. ALS-associated mutant FUS induces selective motor neuron degeneration through toxic gain of function. *Nat Commun* **2016**, *7*, 10465. DOI: 10.1038/ncomms10465.

(249) van der Horst, G. T. J.; Muijtjens, M.; Kobayashi, K.; Takano, R.; Kanno, S.; Takao, M.; de Wit, J.; Verkerk, A.; Eker, A. P. M.; van Leenen, D.; et al. Mammalian Cry1 and Cry2 are essential for maintenance of circadian rhythms. *Nature* **1999**, *398* (6728), 627–630, Research article. DOI: 10.1038/19323.

(250) Tir, S.; Steel, L. C. E.; Tam, S. K. E.; Semo, M.; Pothecary, C. A.; Vyazovskiy, V. V.; Foster, R. G.; Peirson, S. N. Rodent models in translational circadian photobiology. *Prog Brain Res* **2022**, *273* (1), 97–116, Textbook chapter. DOI: 10.1016/bs.pbr.2022.02.015.

(251) Reppert, S. M.; Weaver, D. R. Coordination of circadian timing in mammals. *Nature* **2002**, *418* (6901), 935–941, Review. DOI: 10.1038/nature00965.

(252) Börding, T.; Abdo, A. N.; Maier, B.; Gabriel, C.; Kramer, A. Generation of human CRY1 and CRY2 knockout cells using duplex CRISPR/Cas9 technology. *Front Physiol* **2019**, *10*, Research article. DOI: 10.3389/fphys.2019.00577.

(253) Tam, S. K. E.; Brown, L. A.; Wilson, T. S.; Tir, S.; Fisk, A. S.; Pothecary, C. A.; van der Vinne, V.; Foster, R. G.; Vyazovskiy, V. V.; Bannerman, D. M.; et al. Dim light in the evening causes coordinated realignment of circadian rhythms, sleep, and short-term memory. *Proc Natl Acad Sci* **2021**, *118* (39), e2101591118. DOI: doi:10.1073/pnas.2101591118.

(254) Viljoen, A.; Oosthuizen, M. K. Dim light at night affects the locomotor activity of nocturnal African pygmy mice (Mus minutoides) in an intensity-dependent manner. *Proc R Soc B* **2023**, *290* (1997). DOI: 10.1098/rspb.2023.0526.

(255) Fonken, L. K.; Workman, J. L.; Walton, J. C.; Weil, Z. M.; Morris, J. S.; Haim, A.; Nelson, R. J. Light at night increases body mass by shifting the time of food intake. *Proc Natl Acad Sci* **2010**, *107* (43), 18664–18669. DOI: doi:10.1073/pnas.1008734107.

(256) Haugg, E.; Herwig, A.; Diedrich, V. Body temperature and activity adaptation of short photoperiod-exposed Djungarian hamsters (Phodopus sungorus): timing, traits, and torpor. *Front Physiol* **2021**, *12*, 626779. DOI: 10.3389/fphys.2021.626779.

(257) Hauffmann, K. The influence of photoperiod and melatonin on testis size, body weight, and pelage colour in the Djungarian hamster (Phodopus sungorus). J Comp Physiol: **1973**; Vol. 3, pp 267–282. DOI: 10.1007/BF00694233.

(258) Mueller, M.; Vyazovskiy, V.; Molnar, Z.; Peirson, S. TracKIT. 2 ed.; Zenodo: **2025**. DOI: 10.5281/zenodo.20286841.

(259) Blume, C.; Santhi, N.; Schabus, M. nparACT' package for R: a free software tool for the non-parametric analysis of actigraphy data. *MethodsX* **2016**, *3*, 430–435. DOI: 10.1016/j.mex.2016.05.006.

(260) Mueller, M.; Vadisiute, A.; Molnar, Z. ImARef. 2 ed.; Zenodo, **2024**.

(261) Kim, Y.; Yang, G. R.; Pradhan, K.; Venkataraju, K. U.; Bota, M.; García Del Molino, L. C.; Fitzgerald, G.; Ram, K.; He, M.; Levine, J. M.; et al. Brain-wide maps reveal stereotyped cell-type-based cortical architecture and subcortical sexual dimorphism. *Cell* **2017**, *171* (2), 456–469.e422. DOI: 10.1016/j.cell.2017.09.020.

(262) Lupori, L.; Totaro, V.; Cornuti, S.; Ciampi, L.; Carrara, F.; Grilli, E.; Viglione, A.; Tozzi, F.; Putignano, E.; Mazziotti, R.; et al. A comprehensive atlas of perineuronal net distribution and colocalization with parvalbumin in the adult mouse brain. *Cell Rep* **2023**, *42* (7), 112788. DOI: 10.1016/j.celrep.2023.112788.

(263) Redfern, C. H.; Degtyarev, M. Y.; Kwa, A. T.; Salomonis, N.; Cotte, N.; Nanevicz, T.; Fidelman, N.; Desai, K.; Vranizan, K.; Lee, E. K.; et al. Conditional expression of a Gi-coupled receptor causes ventricular conduction delay and a lethal cardiomyopathy. *Proc Natl Acad Sci USA* **2000**, *97* (9), 4826–4831. DOI: 10.1073/pnas.97.9.4826.

(264) Sternson, S. M.; Roth, B. L. Chemogenetic tools to interrogate brain functions. *Annu Rev Neurosci* **2014**, *37* (Volume 37, 2014), 387–407. DOI: https://doi.org/10.1146/annurev-neuro-071013-014048.

(265) Armbruster, B. N.; Li, X.; Pausch, M. H.; Herlitze, S.; Roth, B. L. Evolving the lock to fit the key to create a family of G protein-coupled receptors potently activated by an inert ligand. *Proc Natl Acad Sci USA* **2007**, *104* (12), 5163–5168. DOI: 10.1073/pnas.0700293104.

(266) Guettier, J. M.; Gautam, D.; Scarselli, M.; de Azua, I. R.; Li, J. H.; Rosemond, E.; Ma, X.; Gonzalez, F. J.; Armbruster, B. N.; Lu, H.; et al. A chemical-genetic approach to study G protein regulation of β cell function in vivo. *Proc Natl Acad Sci* **2009**, *106* (45), 19197–19202. DOI: doi:10.1073/pnas.0906593106.

(267) Vardy, E.; Robinson, J. E.; Li, C.; Olsen, R. H. J.; DiBerto, J. F.; Giguere, P. M.; Sassano, F. M.; Huang, X. P.; Zhu, H.; Urban, D. J.; et al. A new DREADD facilitates the multiplexed chemogenetic interrogation of behavior. *Neuron* **2015**, *86* (4), 936–946. DOI: 10.1016/j.neuron.2015.03.065.

(268) Alexander, G. M.; Rogan, S. C.; Abbas, A. I.; Armbruster, B. N.; Pei, Y.; Allen, J. A.; Nonneman, R. J.; Hartmann, J.; Moy, S. S.; Nicolelis, M. A.; et al. Remote control of neuronal activity in transgenic mice expressing evolved G protein-coupled receptors. *Neuron* **2009**, *63* (1), 27–39. DOI: 10.1016/j.neuron.2009.06.014.

(269) Mueller, M.; Zolnik, T.; Molnar, Z. Polar Plotting. 1 ed.; Zenodo: **2026**. DOI: 10.5281/zenodo.20287398.

(270) Molnár, Z.; Clowry, G.; Bandiera, S.; Messore, F.; Achiwa, H.; Hoerder-Suabedissen, A.; Pattabiraman, K.; Zolnik, T. A.; Larkum, M. E.; Eickholt, B. J.; et al. Subcortical plate: a transient structure with lasting impact on evolution, circuit assembly and cognitive functions. J Anat **2026**. DOI: pending.

(271) Kreis, P.; Leondaritis, G.; Lieberam, I.; Eickholt, B. J. Subcellular targeting and dynamic regulation of PTEN: implications for neuronal cells and neurological disorders. *Front Mol Neurosci* **2014**, *7*, 23. DOI: 10.3389/fnmol.2014.00023.

(272) Mueller, M. H.; Greene, G.; Mellor-Davis, E.; Yuan, R.; Kyne, R. S.; Lavda, M.; Oh, J.; Ho, T. T. B.; Blachowiak, K.; Platt, M.; et al. MRI, histology, and behaviour data reveals neuromotor degeneration upon cortical layer 5 silencing. *Hum Brain Mapp*, **2026**. DOI: 10.5281/zenodo.20817055.

(273) Guyenet, S. J.; Furrer, S. A.; Damian, V. M.; Baughan, T. D.; La Spada, A. R.; Garden, G. A. A simple composite phenotype scoring system for evaluating mouse models of cerebellar ataxia. *J Vis Exp* **2010**, (39). DOI: 10.3791/1787.

(274) Garrick, J. M.; Costa, L. G.; Cole, T. B.; Marsillach, J. Evaluating gait and locomotion in rodents with the CatWalk. *Curr Protoc* **2021**, *1* (8), e220. DOI: 10.1002/cpz1.220.

(275) Timotius, I. K.; Roelofs, R. F.; Richmond-Hacham, B.; Noldus, L. P. J. J.; von Hörsten, S.; Bikovski, L. CatWalk XT gait parameters: a review of reported parameters in pre-clinical studies of multiple central nervous system and peripheral nervous system disease models. *Front Behav Neurosci* **2023**, *17-2023*, Review. DOI: 10.3389/fnbeh.2023.1147784.

(276) Percie du Sert, N.; Ahluwalia, A.; Alam, S.; Avey, M. T.; Baker, M.; Browne, W. J.; Clark, A.; Cuthill, I. C.; Dirnagl, U.; Emerson, M.; et al. Reporting animal research: explanation and elaboration for the ARRIVE guidelines 2.0. *PLoS Biol* **2020**, *18* (7), e3000411, Community page. DOI: 10.1371/journal.pbio.3000411.

(277) Mueller, M.; Tir, S.; Pothecary, C.; Meijer, E.; Brown, L.; Foster, K.; Vyazovskiy, V.; Peirson, S.; Molnar, Z. Video resources - SnackerTracker overview and user guidance. *Figshare* **2025**, Supplementary resource. DOI: 10.6084/m9.figshare.28189793.

(278) The Gene Expression Nervous System Atlas (GENSAT) project. NINDS Contracts N01NS02331 & HHSN271200723701C to The Rockefeller University (New York, NY). **2026**.

(279) Erdfelder, E.; Faul, F.; Buchner, A. GPOWER: A general power analysis program. *Behavior Research Methods, Instruments & Computers* **1996**, *28* (1), 1–11. DOI: 10.3758/BF03203630.

(280) Mueller, M.; Tir, S.; Pothecary, C.; Meijer, E.; Brown, L.; Foster, K.; Vyazovskiy, V.; Peirson, S.; Molnar, Z. SnackerTracker. *protocols.io* **2025**, Workflow. DOI: 10.17504/protocols.io.rm7vzke8rvx1/v1.

(281) Morris, A. S.; Langari, R. Chapter 2 - instrument types and performance characteristics. *IEEE Trans Instrum Meas* **2012**, 11–37, Textbook chapter. DOI: 10.1016/B978-0-12-381960-4.00002-4.

(282) Fisher, S. P.; Godinho, S. I.; Pothecary, C. A.; Hankins, M. W.; Foster, R. G.; Peirson, S. N. Rapid assessment of sleep-wake behavior in mice. *J Biol Rhythms* **2012**, *27* (1), 48–58. DOI: 10.1177/0748730411431550.

(283) Stelzer, G.; Rosen, N.; Plaschkes, I.; Zimmerman, S.; Twik, M.; Fishilevich, S.; Stein, T. I.; Nudel, R.; Lieder, I.; Mazor, Y.; et al. The GeneCards suite: from gene data mining to disease genome sequence analyses. *Curr Protoc Bioinform* **2016**, *54* (1), 1.30.31–31.30.33. DOI: https://doi.org/10.1002/cpbi.5.

(284) Rappaport, N.; Nativ, N.; Stelzer, G.; Twik, M.; Guan-Golan, Y.; Stein, T. I.; Bahir, I.; Belinky, F.; Morrey, C. P.; Safran, M.; et al. MalaCards: an integrated compendium for diseases and their annotation. *Oxford Database* **2013**, *2013*, bat018. DOI: 10.1093/database/bat018.

(285) UniProt: a worldwide hub of protein knowledge. *Nucleic Acids Res* **2018**, *47* (D1), D506–D515. DOI: 10.1093/nar/gky1049.

(286) Shen, J.; Shi, D.; Suzuki, T.; Xia, Z.; Zhang, H.; Araki, K.; Wakana, S.; Takeda, N.; Yamamura, K.; Jin, S.; et al. Severe ocular phenotypes in Rbp4-deficient mice in the C57BL/6 genetic background. *Lab Invest* **2016**, *96* (6), 680–691. DOI: 10.1038/labinvest.2016.39.

(287) Bankhead, P.; Loughrey, M. B.; Fernández, J. A.; Dombrowski, Y.; McArt, D. G.; Dunne, P. D.; McQuaid, S.; Gray, R. T.; Murray, L. J.; Coleman, H. G.; et al. QuPath: open source software for digital pathology image analysis. *Sci Rep* **2017**, *7* (1), 16878. DOI: 10.1038/s41598-017-17204-5.

(288) Wang, Q.; Ding, S. L.; Li, Y.; Royall, J.; Feng, D.; Lesnar, P.; Graddis, N.; Naeemi, M.; Facer, B.; Ho, A.; et al. The Allen mouse brain common coordinate framework: a 3D reference atlas. *Cell* **2020**, *181* (4), 936–953.e920. DOI: 10.1016/j.cell.2020.04.007.

(289) Cohen, J. *Statistical power analysis for the behavioral sciences*; Hillsdale, N.J. : L. Erlbaum Associates, **1998**. DOI: 10.4324/9780203771587.

(290) Longair, M. H.; Baker, D. A.; Armstrong, J. D. Simple Neurite Tracer: open source software for reconstruction, visualization and analysis of neuronal processes. *Bioinformatics* **2011**, *27* (17), 2453–2454. DOI: 10.1093/bioinformatics/btr390.

(291) Lewarch, C. L.; Hoekstra, H. E. The evolution of nesting behaviour in Peromyscus mice. *Anim Behav* **2018**, *139*, 103–115. DOI: https://doi.org/10.1016/j.anbehav.2018.03.008.

(292) Schindelin, J.; Arganda-Carreras, I.; Frise, E.; Kaynig, V.; Longair, M.; Pietzsch, T.; Preibisch, S.; Rueden, C.; Saalfeld, S.; Schmid, B.; et al. Fiji: an open-source platform for biological-image analysis. *Nat Methods* **2012**, *9* (7), 676–682. DOI: 10.1038/nmeth.2019.

(293) Fox, M. W. The visual cliff test for the study of visual depth perception in the mouse. *Anim Behav* **1965**, *13* (2), 232–IN233. DOI: 10.1016/0003-3472(65)90040-0.

(294) Hamers, F. P.; Lankhorst, A. J.; van Laar, T. J.; Veldhuis, W. B.; Gispen, W. H. Automated quantitative gait analysis during overground locomotion in the rat: its application to spinal cord contusion and transection injuries. *J Neurotrauma* **2001**, *18* (2), 187–201. DOI: 10.1089/08977150150502613.

(295) Bonetto, A.; Andersson, D. C.; Waning, D. L. Assessment of muscle mass and strength in mice. *BoneKEy Rep* **2015**, *4*, 732. DOI: 10.1038/bonekey.2015.101.

(296) Lerch, J. P.; Yiu, A. P.; Martinez-Canabal, A.; Pekar, T.; Bohbot, V. D.; Frankland, P. W.; Henkelman, R. M.; Josselyn, S. A.; Sled, J. G. Maze training in mice induces MRI-detectable brain shape changes specific to the type of learning. *Neuroimage* **2011**, *54* (3), 2086–2095. DOI: 10.1016/j.neuroimage.2010.09.086.

(297) Adamczak, J. M.; Farr, T. D.; Seehafer, J. U.; Kalthoff, D.; Hoehn, M. High field BOLD response to forepaw stimulation in the mouse. *NeuroImage* **2010**, *51* (2), 704–712. DOI: https://doi.org/10.1016/j.neuroimage.2010.02.083.

(298) Baker, N. J.; Schofield, J. C.; Caswell, M. D.; McLellan, A. D. Effects of early atipamezole reversal of medetomidine-ketamine anesthesia in mice. *J Am Assoc Lab Anim Sci* **2011**, *50* (6), 916–920.

(299) Cahill, L. S.; Laliberté, C. L.; Ellegood, J.; Spring, S.; Gleave, J. A.; Eede, M. C.; Lerch, J. P.; Henkelman, R. M. Preparation of fixed mouse brains for MRI. *Neuroimage* **2012**, *60* (2), 933–939. DOI: 10.1016/j.neuroimage.2012.01.100.

(300) Tisca, C.; Tachrount, M.; Lange, F.; Wang, C.; Qiu, L. R.; Barallobre-Barreiro, J.; Fava, M.; Mayr, M.; Lerch, J. P.; Martins-Bach, A. B.; et al. Vcan mutation leads to sex-specific changes in white matter microstructure in mice. ISMRM & SMRT: **2021**.

(301) Jenkinson, M.; Beckmann, C. F.; Behrens, T. E.; Woolrich, M. W.; Smith, S. M. FSL. *Neuroimage* **2012**, *62* (2), 782–790. DOI: 10.1016/j.neuroimage.2011.09.015.

(302) Dorr, A. E.; Lerch, J. P.; Spring, S.; Kabani, N.; Henkelman, R. M. High resolution three-dimensional brain atlas using an average magnetic resonance image of 40 adult C57Bl/6J mice. *NeuroImage* **2008**, *42* (1), 60–69. DOI: https://doi.org/10.1016/j.neuroimage.2008.03.037.

(303) Lerch, J. P.; Carroll, J. B.; Spring, S.; Bertram, L. N.; Schwab, C.; Hayden, M. R.; Henkelman, R. M. Automated deformation analysis in the YAC128 Huntington disease mouse model. *NeuroImage* **2008**, *39* (1), 32–39. DOI: 10.1016/j.neuroimage.2007.08.033.

(304) Chakravarty, M. M.; Steadman, P.; van Eede, M. C.; Calcott, R. D.; Gu, V.; Shaw, P.; Raznahan, A.; Collins, D. L.; Lerch, J. P. Performing label-fusion-based segmentation using multiple automatically generated templates. *Hum Brain Mapp* **2013**, *34* (10), 2635–2654. DOI: https://doi.org/10.1002/hbm.22092.

(305) Friedel, M.; van Eede, M. C.; Pipitone, J.; Chakravarty, M. M.; Lerch, J. P. Pydpiper: a flexible toolkit for constructing novel registration pipelines. *Front Neuroinform* **2014**, *8*, 67. DOI: 10.3389/fninf.2014.00067.

(306) Kellner, E.; Dhital, B.; Kiselev, V. G.; Reisert, M. Gibbs-ringing artifact removal based on local subvoxel-shifts. *Magn Reson Med* **2016**, *76* (5), 1574–1581. DOI: https://doi.org/10.1002/mrm.26054.

(307) Bautista, T.; O'Muircheartaigh, J.; Hajnal, J. V.; Tournier, J. D. Removal of Gibbs ringing artefacts for 3D acquisitions using subvoxel shifts. In *ISMRM*, **2021**; Proc Intl Soc Mag Reson Med: p 3535.

(308) Andersson, J. L. R.; Skare, S.; Ashburner, J. How to correct susceptibility distortions in spin-echo echo-planar images: application to diffusion tensor imaging. *Neuroimage* **2003**, *20* (2), 870–888. DOI: 10.1016/s1053-8119(03)00336-7.

(309) Andersson, J. L. R.; Sotiropoulos, S. N. An integrated approach to correction for off-resonance effects and subject movement in diffusion MR imaging. *Neuroimage* **2016**, *125*, 1063–1078. DOI: 10.1016/j.neuroimage.2015.10.019.

(310) Zhang, H.; Schneider, T.; Wheeler-Kingshott, C. A.; Alexander, D. C. NODDI: practical in vivo neurite orientation dispersion and density imaging of the human brain. *Neuroimage* **2012**, *61* (4), 1000–1016. DOI: 10.1016/j.neuroimage.2012.03.072.

(311) Hernandez-Fernandez, M.; Reguly, I.; Jbabdi, S.; Giles, M.; Smith, S.; Sotiropoulos, S. N. Using GPUs to accelerate computational diffusion MRI: from microstructure estimation to tractography and connectomes. *Neuroimage* **2019**, *188*, 598–615. DOI: 10.1016/j.neuroimage.2018.12.015.

(312) Tisca, C.; Tachrount, M.; Lange, F. J.; Howard, A. F. D.; Lerch, J. P.; Martins-Bach, A. B.; Miller, K. L. A diffusion-weighted MRI post-processing pipeline for ex vivo rodent brains to extract DTI, DKI and NODDI metrics (1.0.0). Zenodo: **2023**. DOI: 10.5281/zenodo.8129321.

(313) Tisca, C.; Tachrount, M.; Lange, F. J.; Wang, C.; Tendler, B. C.; Lerch, J. P.; Martins-Bach, A. B.; Miller, K. L. R2*- and quantitative susceptibility mapping (QSM) post-processing pipelines for ex vivo rodent brains (1.0.0). Zenodo: **2023**. DOI: 0.5281/zenodo.8130910.

(314) Eckstein, K.; Dymerska, B.; Bachrata, B.; Bogner, W.; Poljanc, K.; Trattnig, S.; Robinson, S. D. Computationally efficient combination of multi-channel phase data from multi-echo acquisitions (ASPIRE). *Magn Reson Med* **2018**, *79* (6), 2996–3006. DOI: 10.1002/mrm.26963.

(315) Wang, C.; Foxley, S.; Ansorge, O.; Bangerter-Christensen, S.; Chiew, M.; Leonte, A.; Menke, R. A.; Mollink, J.; Pallebage-Gamarallage, M.; Turner, M. R.; et al. Methods for quantitative susceptibility and R2* mapping in whole post-mortem brains at 7T applied to amyotrophic lateral sclerosis. *Neuroimage* **2020**, *222*, 117216. DOI: 10.1016/j.neuroimage.2020.117216.

(316) Wang, C.; Martins-Bach, A. B.; Alfaro-Almagro, F.; Douaud, G.; Klein, J. C.; Llera, A.; Fiscone, C.; Bowtell, R.; Elliott, L. T.; Smith, S. M.; et al. Phenotypic and genetic associations of quantitative magnetic susceptibility in UK Biobank brain imaging. *Nat Neurosci* **2022**, *25* (6), 818–831. DOI: 10.1038/s41593-022-01074-w.

(317) Desrosiers-Grégoire, G.; Devenyi, G. A.; Grandjean, J.; Chakravarty, M. M. A standardized image processing and data quality platform for rodent fMRI. *Nat Commun* **2024**, *15* (1), 6708. DOI: 10.1038/s41467-024-50826-8

(318) Steadman, P. E.; Ellegood, J.; Szulc, K. U.; Turnbull, D. H.; Joyner, A. L.; Henkelman, R. M.; Lerch, J. P. Genetic effects on cerebellar structure across mouse models of autism using a magnetic resonance imaging atlas. *Autism Res* **2014**, *7* (1), 124–137. DOI: 10.1002/aur.1344.

(319) Ullmann, J. F.; Watson, C.; Janke, A. L.; Kurniawan, N. D.; Reutens, D. C. A segmentation protocol and MRI atlas of the C57BL/6J mouse neocortex. *Neuroimage* **2013**, *78*, 196–203. DOI: 10.1016/j.neuroimage.2013.04.008.

(320) Richards, K.; Watson, C.; Buckley, R. F.; Kurniawan, N. D.; Yang, Z.; Keller, M. D.; Beare, R.; Bartlett, P. F.; Egan, G. F.; Galloway, G. J.; et al. Segmentation of the mouse hippocampal formation in magnetic resonance images. *Neuroimage* **2011**, *58* (3), 732–740. DOI: 10.1016/j.neuroimage.2011.06.025.

(321) Qiu, L. R.; Fernandes, D. J.; Szulc-Lerch, K. U.; Dazai, J.; Turnbull, D. H.; Foster, J. A.; Palmert, M. R.; Lerch, J. P. Mouse MRI shows brain areas relatively larger in males emerge before those larger in females. *Nat Comm* **2018**, *9* (1), 2615. DOI: 10.1038/s41467-018-04921-2.

(322) Mueller, M.; Tir, S.; Pothecary, C.; Meijer, E.; Brown, L.; Foster, K.; Vyazovskiy, V.; Peirson, S.; Molnar, Z. SnackerTracker - construction components, supplies, tools, and machines. *Figshare* **2025**, Supplemental resource. DOI: 10.6084/m9.figshare.28464317.

(323) Mueller, M.; Tir, S.; Pothecary, C.; Meijer, E.; Brown, L.; Foster, K.; Vyazovskiy, V.; Peirson, S.; Molnar, Z. Extended data - the SnackerTracker: a novel home-cage monitoring device for measuring food-intake and food-seeking behaviour in mice. *Figshare* **2025**, Extended data. DOI: 10.6084/m9.figshare.28407689.

(324) Mueller, M.; Tir, S.; Pothecary, C.; Meijer, E.; Brown, L.; Foster, K.; Vyazovskiy, V.; Peirson, S.; Molnar, Z. SnackerTracker. *NIH 3D* **2025**, 3D Model. DOI: 10.60705/3dpx/21724.1.

(325) Witting, W.; Kwa, I. H.; Eikelenboom, P.; Mirmiran, M.; Swaab, D. F. Alterations in the circadian rest-activity rhythm in aging and Alzheimer's disease. *Biol Psychiatry* **1990**, *27* (6), 563–572. DOI: 10.1016/0006-3223(90)90523-5.

(326) Bur, I. M.; Cohen-Solal, A. M.; Carmignac, D.; Abecassis, P. Y.; Chauvet, N.; Martin, A. O.; van der Horst, G. T. J.; Robinson, I. C. A. F.; Maurel, P.; Mollard, P.; et al. The circadian clock components CRY1 and CRY2 are necessary to sustain sex dimorphism in mouse liver metabolism. *J Biol Chem* **2009**, *284* (14), 9066–9073, Research article. DOI: 10.1074/jbc.M808360200.

(327) Barclay, J. L.; Shostak, A.; Leliavski, A.; Tsang, A. H.; Jöhren, O.; Müller-Fielitz, H.; Landgraf, D.; Naujokat, N.; van der Horst, G. T. J.; Oster, H. High-fat diet-induced hyperinsulinemia and tissue-specific insulin resistance in Cry-deficient mice. *Am J Physiol Endocrinol* **2013**, *304* (10), E1053–E1063, Research article. DOI: 10.1152/ajpendo.00512.2012.

(328) Cretenet, G.; Le Clech, M.; Gachon, F. Circadian clock-coordinated 12 hr period rhythmic activation of the IRE1α pathway controls lipid metabolism in mouse liver. *Cell Metab* **2010**, *11* (1), 47–57, Research article. DOI: 10.1016/j.cmet.2009.11.002.

(329) Antunes, L. C.; Levandovski, R.; Dantas, G.; Caumo, W.; Hidalgo, M. P. Obesity and shift work: chronobiological aspects. *Nutr Res Rev* **2010**, *23* (1), 155–168, Review. DOI: 10.1017/s0954422410000016.

(330) Arendt, J. Shift work: coping with the biological clock. *Occup Med* **2010**, *60* (1), 10–20, Review. DOI: 10.1093/occmed/kqp162.

(331) Griebel, G.; Ravinet-Trillou, C.; Beeské, S.; Avenet, P.; Pichat, P. Mice deficient in cryptochrome 1 (Cry1 (-/-)) exhibit resistance to obesity induced by a high-fat diet. *Front Endocrinol (Lausanne)* **2014**, *5*, 49, Research article. DOI: 10.3389/fendo.2014.00049.

(332) Kohsaka, A.; Laposky, A. D.; Ramsey, K. M.; Estrada, C.; Joshu, C.; Kobayashi, Y.; Turek, F. W.; Bass, J. High-fat diet disrupts behavioral and molecular circadian rhythms in mice. *Cell Metab* **2007**, *6* (5), 414–421, Research article. DOI: 10.1016/j.cmet.2007.09.006.

(333) Sherman, H.; Genzer, Y.; Cohen, R.; Chapnik, N.; Madar, Z.; Froy, O. Timed high-fat diet resets circadian metabolism and prevents obesity. *FASEB J* **2012**, *26* (8), 3493–3502, Research article. DOI: 10.1096/fj.12-208868.

(334) Yagi, M.; Miller, S.; Nagai, Y.; Inuki, S.; Sato, A.; Hirota, T. A methylbenzimidazole derivative regulates mammalian circadian rhythms by targeting cryptochrome proteins. *F1000Res* **2022**, *11*, 1016, Research article. DOI: 10.12688/f1000research.124658.2.

(335) Doruk, Y. U.; Yarparvar, D.; Akyel, Y. K.; Gul, S.; Taskin, A. C.; Yilmaz, F.; Baris, I.; Ozturk, N.; Türkay, M.; Okyar, A.; et al. A CLOCK-binding small molecule disrupts the interaction between CLOCK and BMAL1 and enhances circadian rhythm amplitude. *J Biol Chem* **2020**, *295* (11), 3518–3531, Research article. DOI: 10.1074/jbc.RA119.011332.

(336) Hirota, T.; Lee, J. W.; St John, P. C.; Sawa, M.; Iwaisako, K.; Noguchi, T.; Pongsawakul, P. Y.; Sonntag, T.; Welsh, D. K.; Brenner, D. A.; et al. Identification of small molecule activators of cryptochrome. *Science* **2012**, *337* (6098), 1094–1097, Research article. DOI: 10.1126/science.1223710.

(337) Putker, M.; Wong, D. C. S.; Seinkmane, E.; Rzechorzek, N. M.; Zeng, A.; Hoyle, N. P.; Chesham, J. E.; Edwards, M. D.; Feeney, K. A.; Fischer, R.; et al. Cryptochromes confer robustness, not rhythmicity, to circadian timekeeping. *EMBO J* **2021**, *40* (7), e106745, Research article. DOI: 10.15252/embj.2020106745.

(338) Iijima, M.; Yamaguchi, S.; van der Horst, G. T. J.; Bonnefont, X.; Okamura, H.; Shibata, S. Altered food-anticipatory activity rhythm in cryptochrome-deficient mice. *J Neurosci Res* **2005**, *52* (2), 166–173, Research article. DOI: 10.1016/j.neures.2005.03.003.

(339) Pendergast, J. S.; Wendroth, R. H.; Stenner, R. C.; Keil, C. D.; Yamazaki, S. mPeriod2$^{Brdm1}$ and other single period mutant mice have normal food anticipatory activity. *Sci Rep* **2017**, *7* (1), 15510, Research article. DOI: 10.1038/s41598-017-15332-6.

(340) Liu, Z.; Huang, M.; Wu, X.; Shi, G.; Xing, L.; Dong, Z.; Qu, Z.; Yan, J.; Yang, L.; Panda, S.; et al. PER1 phosphorylation specifies feeding rhythm in mice. *Cell Rep* **2014**, *7* (5), 1509–1520, Research article. DOI: 10.1016/j.celrep.2014.04.032.

(341) Bae, K.; Jin, X.; Maywood, E. S.; Hastings, M. H.; Reppert, S. M.; Weaver, D. R. Differential functions of mPer1, mPer2, and mPer3 in the SCN circadian clock. *Neuron* **2001**, *30* (2), 525–536, Research article. DOI: 10.1016/S0896-6273(01)00302-6.

(342) Pendergast, J. S.; Nakamura, W.; Friday, R. C.; Hatanaka, F.; Takumi, T.; Yamazaki, S. Robust food anticipatory activity in BMAL1-deficient mice. *PLoS One* **2009**, *4* (3), e4860, Research article. DOI: 10.1371/journal.pone.0004860.

(343) Takasu, N. N.; Kurosawa, G.; Tokuda, I. T.; Mochizuki, A.; Todo, T.; Nakamura, W. Circadian regulation of food-anticipatory activity in molecular clock-deficient mice. *PLoS One* **2012**, *7* (11), e48892, Research article. DOI: 10.1371/journal.pone.0048892.

(344) Bunger, M. K.; Wilsbacher, L. D.; Moran, S. M.; Clendenin, C.; Radcliffe, L. A.; Hogenesch, J. B.; Simon, M. C.; Takahashi, J. S.; Bradfield, C. A. Mop3 is an essential component of the master circadian pacemaker in mammals. *Cell* **2000**, *103* (7), 1009–1017, Research article. DOI: 10.1016/s0092-8674(00)00205-1.

(345) Vitaterna, M. H.; King, D. P.; Chang, A. M.; Kornhauser, J. M.; Lowrey, P. L.; McDonald, J. D.; Dove, W. F.; Pinto, L. H.; Turek, F. W.; Takahashi, J. S. Mutagenesis and mapping of a mouse gene, clock, essential for circadian behavior. *Science* **1994**, *264* (5159), 719–725, Research article. DOI: 10.1126/science.8171325.

(346) Lowrey, P. L.; Takahashi, J. S. Mammalian circadian biology: elucidating genome-wide levels of temporal organization. *Annu Rev Genomics Hum Genet* **2004**, *5*, 407–441, Review. DOI: 10.1146/annurev.genom.5.061903.175925.

(347) Pitts, S.; Perone, E.; Silver, R. Food-entrained circadian rhythms are sustained in arrhythmic Clk/Clk mutant mice. *Am J Physiol Regul Integr Comp Physiol* **2003**, *285* (1), R57–67, Research article. DOI: 10.1152/ajpregu.00023.2003.

(348) Vollmers, C.; Gill, S.; DiTacchio, L.; Pulivarthy, S. R.; Le, H. D.; Panda, S. Time of feeding and the intrinsic circadian clock drive rhythms in hepatic gene expression. *Proc Natl Acad Sci USA* **2009**, *106* (50), 21453–21458, Research article. DOI: doi:10.1073/pnas.0909591106.

(349) Kornmann, B.; Schaad, O.; Bujard, H.; Takahashi, J. S.; Schibler, U. System-driven and oscillator-dependent circadian transcription in mice with a conditionally active liver clock. *PLoS Biol* **2007**, *5* (2), e34, Research article. DOI: 10.1371/journal.pbio.0050034.

(350) Lamia, K. A.; Storch, K. F.; Weitz, C. J. Physiological significance of a peripheral tissue circadian clock. *Proc Natl Acad Sci USA* **2008**, *105* (39), 15172–15177, Research article. DOI: 10.1073/pnas.0806717105.

(351) Blum, I. D.; Zhu, L.; Moquin, L.; Kokoeva, M. V.; Gratton, A.; Giros, B.; Storch, K. F. A highly tunable dopaminergic oscillator generates ultradian rhythms of behavioral arousal. *Elife* **2014**, *3*, Research article. DOI: 10.7554/eLife.05105.

(352) Gerkema, M. P.; Groos, G. A.; Daan, S. Differential elimination of circadian and ultradian rhythmicity by hypothalamic lesions in the common vole, microtus arvalis. *J Biol Rhythms* **1990**, *5* (2), 81–95, Research article. DOI: 10.1177/074873049000500201.

(353) Stowie, A. C.; Glass, J. D. Longitudinal study of changes in daily activity rhythms over the lifespan in individual male and female C57BL/6J mice. *J Biol Rhythms* **2015**, *30* (6), 563–568, Research article. DOI: 10.1177/0748730415598023.

(354) Smarr, B.; Kriegsfeld, L. J. Female mice exhibit less overall variance, with a higher proportion of structured variance, than males at multiple timescales of continuous body temperature and locomotive activity records. *Biol Sex Differ* **2022**, *13* (1), 41, Research article. DOI: 10.1186/s13293-022-00451-1.

(355) Alvord, V. M.; Pendergast, J. S. The estrous cycle coordinates the circadian rhythm of eating behavior in mice. *J Biol Rhythms* **2024**, *39* (5), 413–422, Research article. DOI: 10.1177/07487304241262356.

(356) Joye, D. A. M.; Evans, J. A. Sex differences in daily timekeeping and circadian clock circuits. *Semin Cell Dev Biol* **2022**, *126*, 45–55, Review. DOI: 10.1016/j.semcdb.2021.04.026.

(357) Storch, K. F.; Weitz, C. J. Daily rhythms of food-anticipatory behavioral activity do not require the known circadian clock. *Proc Natl Acad Sci USA* **2009**, *106* (16), 6808–6813, Research article. DOI: doi:10.1073/pnas.0902063106.

(358) Dowse, H.; Umemori, J.; Koide, T. Ultradian components in the locomotor activity rhythms of the genetically normal mouse, mus musculus. *J Exp Biol* **2010**, *213* (10), 1788–1795, Research article. DOI: 10.1242/jeb.038877.

(359) Mong, J. A.; Baker, F. C.; Mahoney, M. M.; Paul, K. N.; Schwartz, M. D.; Semba, K.; Silver, R. Sleep, rhythms, and the endocrine brain: influence of sex and gonadal hormones. *J Neurosci* **2011**, *31* (45), 16107–16116, Review. DOI: 10.1523/jneurosci.4175-11.2011.

(360) Almey, A.; Milner, T. A.; Brake, W. G. Estrogen receptors in the central nervous system and their implication for dopamine-dependent cognition in females. *Horm Behav* **2015**, *74*, 125–138, Review. DOI: 10.1016/j.yhbeh.2015.06.010.

(361) Hughes, R. B.; Bano-Otalora, B.; Davey, M.; Martial, F. P.; Babu, A.; Wynne, J.; Brown, T. M.; Lucas, R. J. The impact of self-selected light on activity rhythms in the diurnal striped mouse. *Curr Biol* **2026**, *36* (8), 2078–2089.e2075. DOI: 10.1016/j.cub.2026.03.036.

(362) Pritchett, D.; Jagannath, A.; Brown, L. A.; Tam, S. K.; Hasan, S.; Gatti, S.; Harrison, P. J.; Bannerman, D. M.; Foster, R. G.; Peirson, S. N. Deletion of metabotropic glutamate receptors 2 and 3 (mGlu2 & mGlu3) in mice disrupts sleep and wheel-running activity, and increases the sensitivity of the circadian system to light. *PLoS One* **2015**, *10* (5), e0125523. DOI: 10.1371/journal.pone.0125523.

(363) Vyazovskiy, V. V.; Ruijgrok, G.; Deboer, T.; Tobler, I. Running wheel accessibility affects the regional electroencephalogram during sleep in mice. *Cereb Cortex* **2006**, *16* (3), 328–336. DOI: 10.1093/cercor/bhi110.

(364) Vyazovskiy, V. V.; Tobler, I. The temporal structure of behaviour and sleep homeostasis. *PLoS One* **2012**, *7* (12), e50677. DOI: 10.1371/journal.pone.0050677.

(365) Tizard, I. Sickness behavior, its mechanisms and significance. *Anim Health Res Rev* **2008**, *9* (1), 87–99, Review. DOI: 10.1017/S1466252308001448.

(366) González, M. M. C. Dim light at night and constant darkness: two frequently used lighting conditions that jeopardize the health and well-being of laboratory rodents. *Front Neurol* **2018**, *9*, 609. DOI: 10.3389/fneur.2018.00609.

(367) Emmer, K. M.; Russart, K. L. G.; Walker, W. H.; Nelson, R. J.; DeVries, A. C. Effects of light at night on laboratory animals and research outcomes. *Behav Neurosci* **2018**, *132* (4), 302–314. DOI: 10.1037/bne0000252.

(368) Donocoff, R. S.; Teteloshvili, N.; Chung, H.; Shoulson, R.; Creusot, R. J. Optimization of tamoxifen-induced Cre activity and its effect on immune cell populations. *Sci Rep* **2020**, *10* (1), 15244, Research article. DOI: 10.1038/s41598-020-72179-0.

(369) Chassaing, B.; Aitken, J. D.; Malleshappa, M.; Vijay-Kumar, M. Dextran sulfate sodium (DSS)-induced colitis in mice. *Curr Protoc Immunol* **2014**, *104*, 15.25.11–15.25.14, Protocol. DOI: 10.1002/0471142735.im1525s104.

(370) Fang, Y.; Jo, S. K.; Park, S. J.; Yang, J.; Ko, Y. S.; Lee, H. Y.; Oh, S. W.; Cho, W. Y.; Kim, K.; Son, G. H.; et al. Role of the circadian clock and effect of time-restricted feeding in adenine-induced chronic kidney disease. *Lab Invest* **2023**, *103* (1), 100008, Research article. DOI: 10.1016/j.labinv.2022.100008.

(371) Damiola, F.; Le Minh, N.; Preitner, N.; Kornmann, B.; Fleury-Olela, F.; Schibler, U. Restricted feeding uncouples circadian oscillators in peripheral tissues from the central pacemaker in the suprachiasmatic nucleus. *Genes Dev* **2000**, *14* (23), 2950–2961, Research article. DOI: 10.1101/gad.183500.

(372) Garaulet, M.; Gómez-Abellán, P. Timing of food intake and obesity: a novel association. *Physiol Behav* **2014**, *134*, 44–50, Research article. DOI: 10.1016/j.physbeh.2014.01.001.

(373) Pickel, L.; Sung, H. K. Feeding rhythms and the circadian regulation of metabolism. *Front Nutr* **2020**, *7*, 39, Review. DOI: 10.3389/fnut.2020.00039.

(374) Hoces, D.; Lan, J.; Sun, W.; Geiser, T.; Stäubli, M. L.; Cappio Barazzone, E.; Arnoldini, M.; Challa, T. D.; Klug, M.; Kellenberger, A.; et al. Metabolic reconstitution of germ-free mice by a gnotobiotic microbiota varies over the circadian cycle. *PLoS Biol* **2022**, *20* (9), e3001743, Research article. DOI: 10.1371/journal.pbio.3001743.

(375) van der Vinne, V.; Pothecary, C. A.; Wilcox, S. L.; McKillop, L. E.; Benson, L. A.; Kolpakova, J.; Tam, S. K. E.; Krone, L. B.; Fisk, A. S.; Wilson, T. S.; et al. Continuous and non-invasive thermography of mouse skin accurately describes core body temperature patterns, but not absolute core temperature. *Sci Rep* **2020**, *10* (1), 20680, Research article. DOI: 10.1038/s41598-020-77786-5.

(376) Mueller, M.; Tir, S.; Pothecary, C.; Meijer, E.; Brown, L.; Foster, K.; Vyazovskiy, V.; Peirson, S.; Molnar, Z. SnackerTracker. *Figshare* **2025**, Collection. DOI: 10.6084/m9.figshare.c.7622126.v2.

(377) Mueller, M. MMueller DPhil Thesis - Supplemental Cell Segmentation-Registration-Reconstruction. Figshare: **2026**. DOI: 10.6084/m9.figshare.31988403.

(378) Szabo, F. The short-and long-term effects of genetically silencing deep-layer cortical glutamatergic projection neurons on GABAergic neurons. University of Oxford Oxford University Research Archive, **2025**. DOI: 10.5287/ora-bmzorwzvk.

(379) Kumar, P.; Goettemoeller, A. M.; Espinosa-Garcia, C.; Tobin, B. R.; Tfaily, A.; Nelson, R. S.; Natu, A.; Dammer, E. B.; Santiago, J. V.; Malepati, S.; et al. Native-state proteomics of parvalbumin interneurons identifies unique molecular signatures and vulnerabilities to early Alzheimer's pathology. *Nat Comm* **2024**, *15* (1), 2823. DOI: 10.1038/s41467-024-47028-7.

(380) Donato, F.; Rompani, S. B.; Caroni, P. Parvalbumin-expressing basket-cell network plasticity induced by experience regulates adult learning. *Nature* **2013**, *504* (7479), 272–276. DOI: 10.1038/nature12866.

(381) Fawcett, J. W.; Fyhn, M.; Jendelova, P.; Kwok, J. C. F.; Ruzicka, J.; Sorg, B. A. The extracellular matrix and perineuronal nets in memory. *Mol Psychiatry* **2022**, *27* (8), 3192–3203. DOI: 10.1038/s41380-022-01634-3.

(382) Lensjø, K. K.; Lepperød, M. E.; Dick, G.; Hafting, T.; Fyhn, M. Removal of perineuronal nets unlocks juvenile plasticity through network mechanisms of decreased inhibition and increased gamma activity. *J Neurosci* **2017**, *37* (5), 1269–1283. DOI: 10.1523/jneurosci.2504-16.2016.

(383) Devienne, G.; Picaud, S.; Cohen, I.; Piquet, J.; Tricoire, L.; Testa, D.; Di Nardo, A. A.; Rossier, J.; Cauli, B.; Lambolez, B. Regulation of perineuronal nets in the adult cortex by the activity of the cortical network. *J Neurosci* **2021**, *41* (27), 5779–5790. DOI: 10.1523/jneurosci.0434-21.2021.

(384) Fornasiero, E. F.; Mandad, S.; Wildhagen, H.; Alevra, M.; Rammner, B.; Keihani, S.; Opazo, F.; Urban, I.; Ischebeck, T.; Sakib, M. S.; et al. Precisely measured protein lifetimes in the mouse brain reveal differences across tissues and subcellular fractions. *Nat Comm* **2018**, *9* (1), 4230. DOI: 10.1038/s41467-018-06519-0.

(385) Schwaller, B. Cytosolic Ca2+ buffers. *Cold Spring Harb Perspect Biol* **2010**, *2* (11), a004051. DOI: 10.1101/cshperspect.a004051.

(386) Fawcett, J. W.; Oohashi, T.; Pizzorusso, T. The roles of perineuronal nets and the perinodal extracellular matrix in neuronal function. *Nat Rev Neurosci* **2019**, *20* (8), 451–465. DOI: 10.1038/s41583-019-0196-3.

(387) Kuramoto, E.; Tanaka, Y. R.; Hioki, H.; Goto, T.; Kaneko, T. Local connections of pyramidal neurons to parvalbumin-producing interneurons in motor-associated cortical areas of mice. *eNeuro* **2022**, *9* (1). DOI: 10.1523/eneuro.0567-20.2021.

(388) Gallent, E. A.; Steward, O. Neuronal PTEN deletion in adult cortical neurons triggers progressive growth of cell bodies, dendrites, and axons. *Exp Neurol* **2018**, *303*, 12–28. DOI: 10.1016/j.expneurol.2018.01.005.

(389) Gutilla, E. A.; Buyukozturk, M. M.; Steward, O. Long-term consequences of conditional genetic deletion of PTEN in the sensorimotor cortex of neonatal mice. *Exp Neurol* **2016**, *279*, 27–39. DOI: 10.1016/j.expneurol.2016.02.013.

(390) Sperow, M.; Berry, R. B.; Bayazitov, I. T.; Zhu, G.; Baker, S. J.; Zakharenko, S. S. Phosphatase and tensin homologue (PTEN) regulates synaptic plasticity independently of its effect on neuronal morphology and migration. *J Physiol* **2012**, *590* (4), 777–792. DOI: 10.1113/jphysiol.2011.220236.

(391) Xiong, Q.; Oviedo, H. V.; Trotman, L. C.; Zador, A. M. PTEN regulation of local and long-range connections in mouse auditory cortex. *J Neurosci* **2012**, *32* (5), 1643–1652. DOI: 10.1523/jneurosci.4480-11.2012.

(392) Tikhonova, T.; Miyamae, T.; Gulchina, Y.; Lewis, D.; Gonzalez Burgos, G. Cell type- and layer-specific muscarinic potentiation of excitatory synaptic drive onto parvalbumin neurons in mouse prefrontal cortex. *eNeuro* **2018**, *5*, ENEURO.0208–0218.2018. DOI: 10.1523/ENEURO.0208-18.2018.

(393) Wicke, K. D.; Oppe, L.; Geese, C.; Sternberg, A. K.; Felmy, F. Neuronal morphology and synaptic input patterns of neurons in the intermediate nucleus of the lateral lemniscus of gerbils. *Sci Rep* **2023**, *13* (1), 14182. DOI: 10.1038/s41598-023-41180-8.

(394) Mueller, M. MMueller DPhil Thesis - Supplemental Morphometrics. Figshare: **2026**. DOI: 10.6084/m9.figshare.32217474.

(395) Henning, T.; Bandiera, S.; Molnár, Z. Towards the transcriptionally based classification of L6b in the adult mouse brain. In *Neocortical Neurogenesis in Development and Evolution*, **2023**; pp 317–330. DOI: 10.1002/9781119860914.ch16.

(396) Clancy, B.; Cauller, L. J. Widespread projections from subgriseal neurons (layer VII) to layer I in adult rat cortex. *J Comp Neurol* **1999**, *407* (2), 275–286. DOI: 10.1002/(SICI)1096-9861(19990503)407:2<275::AID-CNE8>3.0.CO;2-0.

(397) Liu, J. J.; Mirabella, V. R.; Pang, Z. P. Cell type- and pathway-specific synaptic regulation of orexin neurocircuitry. *Brain Res* **2020**, *1731*, 145974. DOI: 10.1016/j.brainres.2018.10.003.

(398) Sorensen, S. A.; Rubel, E. W. The level and integrity of synaptic input regulates dendrite structure. *J Neurosci* **2006**, *26* (5), 1539–1550. DOI: 10.1523/jneurosci.3807-05.2006.

(399) Callaway, E. M.; Dong, H.-W.; Ecker, J. R.; Hawrylycz, M. J.; Huang, Z. J.; Lein, E. S.; Ngai, J.; Osten, P.; Ren, B.; Tolias, A. S.; et al. A multimodal cell census and atlas of the mammalian primary motor cortex. *Nature* **2021**, *598* (7879), 86–102. DOI: 10.1038/s41586-021-03950-0.

(400) Richardson, D. S.; Guan, W.; Matsumoto, K.; Pan, C.; Chung, K.; Ertürk, A.; Ueda, H. R.; Lichtman, J. W. Tissue clearing. *Nat Rev Methods Primers* **2021**, *1* (1). DOI: 10.1038/s43586-021-00080-9.

(401) Susaki, E. A.; Tainaka, K.; Perrin, D.; Kishino, F.; Tawara, T.; Watanabe, T. M.; Yokoyama, C.; Onoe, H.; Eguchi, M.; Yamaguchi, S.; et al. Whole-brain imaging with single-cell resolution using chemical cocktails and computational analysis. *Cell* **2014**, *157* (3), 726–739. DOI: 10.1016/j.cell.2014.03.042.

(402) Tainaka, K.; Kubota, S. I.; Suyama, T. Q.; Susaki, E. A.; Perrin, D.; Ukai-Tadenuma, M.; Ukai, H.; Ueda, H. R. Whole-body imaging with single-cell resolution by tissue decolorization. *Cell* **2014**, *159* (4), 911–924. DOI: 10.1016/j.cell.2014.10.034.

(403) Stringer, C.; Wang, T.; Michaelos, M.; Pachitariu, M. Cellpose: a generalist algorithm for cellular segmentation. *Nat Methods* **2021**, *18* (1), 100–106. DOI: 10.1038/s41592-020-01018-x.

(404) Cutler, K. J.; Stringer, C.; Lo, T. W.; Rappez, L.; Stroustrup, N.; Brook Peterson, S.; Wiggins, P. A.; Mougous, J. D. Omnipose: a high-precision morphology-independent solution for bacterial cell segmentation. *Nat Methods* **2022**, *19* (11), 1438–1448. DOI: 10.1038/s41592-022-01639-4.

(405) Vadisiute, A.; Szabo, F.; Luchanskaya, S.; Drevenakova, V.; Messore, F.; Ugwudike, A.; Greene, G.; Mueller, M.; Morse, S. V.; Hoerder-Suabedissen, A.; et al. Deletion of Snap25 disrupts glial remodelling in aging mouse brain. iScience: **2026**. DOI: 10.1016/j.isci.2026.116478.

(406) Le, D.; Kaplan, D. I.; Trigos, A. S. 2D spatial tissue analysis often misrepresents true biological patterns of 3D tissues. *bioRxiv* **2026**, 2026.2001.2021.700966. DOI: 10.64898/2026.01.21.700966.

(407) Retho, A.; Govindan, A. D.; Bonnet, M. L.; Brot, S.; Gaillard, A. Contribution of tissue clearing and 3D image analysis to in vitro modeling of human cortical development. *Sci Rep* **2026**, *16* (1). DOI: 10.1038/s41598-026-41741-7.

(408) Ruusuvuori, P.; Valkonen, M.; Kartasalo, K.; Visakorpi, T.; Nykter, M.; Latonen, L. Spatial analysis of histology in 3D: quantification and visualization of organ and tumor level tissue environment. *Heliyon* **2022**, *8* (1), e08762. DOI: 10.1016/j.heliyon.2022.e08762.

(409) Jouvet, M.; Michel, F.; Courjon, J. EEG study of physiological sleep in the intact, decorticated and chronic mesencephalic cat. *Rev Neurol* **1960**, *102*, 309–310. PMID: 13790850.

(410) Saper, C. B.; Fuller, P. M. Wake-sleep circuitry: an overview. *Curr Opin Neurobiol* **2017**, *44*, 186–192. DOI: 10.1016/j.conb.2017.03.021.

(411) Piccoli, L.; Micioni Di Bonaventura, M. V.; Cifani, C.; Costantini, V. J.; Massagrande, M.; Montanari, D.; Martinelli, P.; Antolini, M.; Ciccocioppo, R.; Massi, M.; et al. Role of orexin-1 receptor mechanisms on compulsive food consumption in a model of binge eating in female rats. *Neuropsychopharmacology* **2012**, *37* (9), 1999–2011. DOI: 10.1038/npp.2012.48.

(412) Coleman, P. J.; Gotter, A. L.; Herring, W. J.; Winrow, C. J.; Renger, J. J. The discovery of suvorexant, the first orexin receptor drug for insomnia. *Annu Rev Pharmacol Toxicol* **2017**, *57* (1), 509–533. DOI: 10.1146/annurev-pharmtox-010716-104837.

(413) Beuckmann, C. T.; Ueno, T.; Nakagawa, M.; Suzuki, M.; Akasofu, S. Preclinical in vivo characterization of lemborexant (E2006), a novel dual orexin receptor antagonist for sleep/wake regulation. *Sleep* **2019**, *42* (6). DOI: 10.1093/sleep/zsz076.

(414) Mignot, E.; Mayleben, D.; Fietze, I.; Leger, D.; Zammit, G.; Bassetti, C. L. A.; Pain, S.; Kinter, D. S.; Roth, T. Safety and efficacy of daridorexant in patients with insomnia disorder: results from two multicentre, randomised, double-blind, placebo-controlled, phase 3 trials. *Lancet Neurol* **2022**, *21* (2), 125–139. DOI: 10.1016/S1474-4422(21)00436-1.

(415) Hartman, D.; Kong, J.; Ratti, E.; Accardi, M.; Saha, S.; Im, E. Phase 1 clinical data with orexin receptor 2 (OX2R) agonist, ORX750, in acutely sleep-deprived healthy participants. *Neurology* **2025**, *104* (7_Supplement_1), 2277. DOI: 10.1212/WNL.0000000000209036.

(416) Ishikawa, T.; Hara, H.; Kawano, A.; Tohyama, K.; Kajita, Y.; Miyanohana, Y.; Koike, T.; Kimura, H. TAK-994, a novel orally available brain-penetrant orexin 2 rReceptor-selective agonist, suppresses fragmentation of wakefulness and cataplexy-like episodes in mouse models of narcolepsy. *J Pharmacol Exp Ther* **2023**, *385* (3), 193–204. DOI: 10.1124/jpet.122.001449.

(417) Plante, D.; Grunstein, R.; Plazzi, G.; Maski, K.; Ramos, J.; Du, Y.; Lovett, A.; Yountz, M.; Rege, B. P033 vibrance-3: safety and efficacy of Alixorexton (ALKS 2680) in idiopathic hypersomnia. In *Sleep Adv*, **2025**. DOI: 10.1093/sleepadvances/zpaf053.093.

(418) Mitsukawa, K.; Terada, M.; Yamada, R.; Monjo, T.; Hiyoshi, T.; Nakakariya, M.; Kajita, Y.; Ando, T.; Koike, T.; Kimura, H. TAK-861, a potent, orally available orexin receptor 2-selective agonist, produces wakefulness in monkeys and improves narcolepsy-like phenotypes in mouse models. *Sci Rep* **2024**, *14* (1), 20838. DOI: 10.1038/s41598-024-70594-1.

(419) Bonaventure, P.; Shelton, J.; Yun, S.; Nepomuceno, D.; Sutton, S.; Aluisio, L.; Fraser, I.; Lord, B.; Shoblock, J.; Welty, N.; et al. Characterization of JNJ-42847922, a selective orexin-2 receptor antagonist, as a clinical candidate for the treatment of insomnia. *J Pharmacol Exp Ther* **2015**, *354* (3), 471–482. DOI: https://doi.org/10.1124/jpet.115.225466.

(420) Malherbe, P.; Borroni, E.; Gobbi, L.; Knust, H.; Nettekoven, M.; Pinard, E.; Roche, O.; Rogers-Evans, M.; Wettstein, J. G.; Moreau, J. L. Biochemical and behavioural characterization of EMPA, a novel high-affinity, selective antagonist for the OX(2) receptor. *Br J Pharmacol* **2009**, *156* (8), 1326–1341. DOI: 10.1111/j.1476-5381.2009.00127.x.

(421) Smart, D.; Sabido-David, C.; Brough, S. J.; Jewitt, F.; Johns, A.; Porter, R. A.; Jerman, J. C. SB-334867-A: the first selective orexin-1 receptor antagonist. *Br J Pharmacol* **2001**, *132* (6), 1179–1182. DOI: https://doi.org/10.1038/sj.bjp.0703953.

(422) Steiner, M. A.; Gatfield, J.; Brisbare-Roch, C.; Dietrich, H.; Treiber, A.; Jenck, F.; Boss, C. Discovery and characterization of ACT-335827, an orally available, brain penetrant orexin receptor type 1 selective antagonist. *ChemMedChem* **2013**, *8* (6), 898–903. DOI: 10.1002/cmdc.201300003.

(423) Chung, H. S.; Kim, J. G.; Kim, J. W.; Kim, H. W.; Yoon, B. J. Orexin administration to mice that underwent chronic stress produces bimodal effects on emotion-related behaviors. *Regul Pept* **2014**, *194-195*, 16–22. DOI: https://doi.org/10.1016/j.regpep.2014.11.003.

(424) Li, S.; Franken, P.; Vassalli, A. Bidirectional and context-dependent changes in theta and gamma oscillatory brain activity in noradrenergic cell-specific hypocretin/orexin receptor 1-KO mice. *Sci Rep* **2018**, *8* (1), 15474. DOI: 10.1038/s41598-018-33069-8.

(425) Mochizuki, T.; Arrigoni, E.; Marcus, J. N.; Clark, E. L.; Yamamoto, M.; Honer, M.; Borroni, E.; Lowell, B. B.; Elmquist, J. K.; Scammell, T. E. Orexin receptor 2 expression in the posterior hypothalamus rescues sleepiness in narcoleptic mice. *Proc Natl Acad Sci USA* **2011**, *108* (11), 4471–4476. DOI: 10.1073/pnas.1012456108.

(426/78) Messore, F. Cortical Layer 6b Silencing Blocks PFC Response to Orexin. **2023**. DOI: 10.1038/s41398-025-03350-2.

(427) Jin, J.; Chen, Q.; Qiao, Q.; Yang, L.; Xiong, J.; Xia, J.; Hu, Z.; Chen, F. Orexin neurons in the lateral hypothalamus project to the medial prefrontal cortex with a rostro-caudal gradient. *Neurosci Lett* **2016**, *621*, 9–14. DOI: https://doi.org/10.1016/j.neulet.2016.04.002.

(428) Sanders, M.; Petrasch-Parwez, E.; Habbes, H. W.; Düring, M. V.; Förster, E. Postnatal developmental expression profile classifies the indusium griseum as a distinct subfield of the hippocampal formation. In *Front Cell Dev Biol*, **2020**; Vol. 8, p 615571. DOI: 10.3389/fcell.2020.615571.

(429) Shu, T.; Richards, L. J. Cortical axon guidance by the glial wedge during the development of the corpus callosum. *J Neurosci* **2001**, *21* (8). DOI: 10.1523/jneurosci.21-08-02749.2001.

(430) Fuzik, J.; Rehman, S.; Girach, F.; Miklosi, A. G.; Korchynska, S.; Arque, G.; Romanov, R. A.; Hanics, J.; Wagner, L.; Meletis, K.; et al. Brain-wide genetic mapping identifies the indusium griseum as a prenatal and shared target of pharmacologically-unrelated psychostimulants. *bioRxiv* **2019**, 759423. DOI: 10.1101/759423.

(431) Rollins, N. K. Diffusion imaging of the congenitally thickened corpus callosum. *Am J Neuroradiol* **2013**, *34* (3), 660–665. DOI: 10.3174/ajnr.A3245.

(432) Pogledic, I.; Bobić-Rasonja, M.; Mitter, C.; Štajduhar, A.; Schwartz, E.; Milković-Periša, M.; Baltzer, P. A.; Lequin, M.; Krampl-Bettelheim, E.; Kasprian, G.; et al. Fetal indusium griseum is a possible biomarker of the regularity of brain midline development in 3T MR imaging: a retrospective observational study. *Acta Obstet Gynecol Scand* **2024**, *103* (5), 897–906. DOI: 10.1111/aogs.14781.

(433) Nakada, T. High-field, high-resolution MR imaging of the human indusium griseum. *AJNR Am J Neuroradiol* **1999**, *20* (3), 524–525. PMCID: PMC7056066.

(434) Chéreau, R.; Holtmaat, A. New recipes with CaMPARI for 'snapshots' of synaptic circuit activity. *J Physiol* **2017**, *595* (5), 1435–1436. DOI: 10.1113/jp273733.

(435) Zolnik, T. A.; Sha, F.; Johenning, F. W.; Schreiter, E. R.; Looger, L. L.; Larkum, M. E.; Sachdev, R. N. All-optical functional synaptic connectivity mapping in acute brain slices using the calcium integrator CaMPARI. *J Physiol* **2017**, *595* (5), 1465–1477. DOI: 10.1113/jp273116.

(436) Liu, Q.; Chang, J. W.; Wang, J.; Kang, S. A.; Thoreen, C. C.; Markhard, A.; Hur, W.; Zhang, J.; Sim, T.; Sabatini, D. M.; et al. Discovery of 1-(4-(4-propionylpiperazin-1-yl)-3-(trifluoromethyl)phenyl)-9-(quinolin-3-yl)benzo[h][1,6]naphthyridin-2(1H)-one as a highly potent, selective mammalian rarget of rapamycin (mTOR) inhibitor for the treatment of cancer. *J Med Chem* **2010**, *53* (19), 7146–7155. DOI: 10.1021/jm101144f.

(437) Mueller, M. MMueller DPhil Thesis - Supplemental Behavioural Media. Figshare: **2026**. DOI: 10.6084/m9.figshare.32228571.

(438) Steinhoff, J. S.; Lass, A.; Schupp, M. Biological functions of RBP4 and its relevance for human diseases. *Front Physiol* **2021**, *12*, 659977. DOI: 10.3389/fphys.2021.659977.

(439) Sabbah, S.; Berg, D.; Papendorp, C.; Briggman, K. L.; Berson, D. M. A Cre mouse line for probing irradiance- and direction-encoding retinal networks. *eNeuro* **2017**, *4* (2). DOI: 10.1523/eneuro.0065-17.2017.

(440) Pardillo-Díaz, R.; Pérez-García, P.; Ortego-Domínguez, M.; Gómez-Oliva, R.; Martínez-Gómez, N.; Domínguez-García, S.; García-Cózar, F.; Muñoz-Miranda, J. P.; Hernández-Galán, R.; Carrascal, L.; et al. The subventricular zone neurogenic niche provides adult born functional neurons to repair cortical brain injuries in response to diterpenoid therapy. *Stem Cell Res Ther* **2025**, *16* (1), 1. DOI: 10.1186/s13287-024-04105-4.

(441) David-Bercholz, J.; Kuo, C.; Deneen, B. Astrocyte and oligodendrocyte responses from the subventricular zone after injury. *Front Cell Neurosci* **2021**, *15*, Review. DOI: 10.3389/fncel.2021.797553.

(442) Iwata, N. K.; Aoki, S.; Okabe, S.; Arai, N.; Terao, Y.; Kwak, S.; Abe, O.; Kanazawa, I.; Tsuji, S.; Ugawa, Y. Evaluation of corticospinal tracts in ALS with diffusion tensor MRI and brainstem stimulation. *Neurology* **2008**, *70* (7), 528–532. DOI: 10.1212/01.wnl.0000299186.72374.19.

(443) Kang, S. H.; Li, Y.; Fukaya, M.; Lorenzini, I.; Cleveland, D. W.; Ostrow, L. W.; Rothstein, J. D.; Bergles, D. E. Degeneration and impaired regeneration of gray matter oligodendrocytes in amyotrophic lateral sclerosis. *Nat Neurosci* **2013**, *16* (5), 571–579. DOI: 10.1038/nn.3357.

(444) Yu, F.; Wang, Y.; Stetler, A. R.; Leak, R. K.; Hu, X.; Chen, J. Phagocytic microglia and macrophages in brain injury and repair. *CNS Neurosci Ther* **2022**, *28* (9), 1279–1293. DOI: 10.1111/cns.13899.

(445) Schafer, D. P.; Lehrman, E. K.; Kautzman, A. G.; Ransohoff, R. M.; Greenberg, M. E.; Barres, B. A.; Stevens, B. Microglia sculpt postnatal neural circuits in an activity and complement-dependent manner. *Neuron* **2012**, *74* (4), 691–705. DOI: 10.1016/j.neuron.2012.03.026.

(446) Theodosis, D. T.; Poulain, D. A.; Oliet, S. H. Activity-dependent structural and functional plasticity of astrocyte-neuron interactions. *Physiol Rev* **2008**, *88* (3), 983–1008. DOI: 10.1152/physrev.00036.2007.

(447) Crabé, R.; Aimond, F.; Raoul, C. How degeneration of cells surrounding motoneurons Contributes to amyotrophic lateral sclerosis. *Cells* **2020**, *9* (12). DOI: 10.3390/cells9122550.

(448) Hao, X.; Zhu, B.; Yang, P.; Dong, D.; Sahbaie, P.; Oliver, P. L.; Shen, W. J.; Azhar, S.; Kraemer, F. B. SNAP25 mutation disrupts metabolic homeostasis, steroid hormone production and central neurobehavior. *Biochim Biophys Acta Mol Basis Dis* **2022**, *1868* (2), 166304. DOI: 10.1016/j.bbadis.2021.166304.

(449) Liu, L.; Gudas, L. J. Disruption of the lecithin: retinol acyltransferase gene makes mice more susceptible to vitamin a deficiency. *J Biol Chem* **2005**, *280* (48), 40226–40234. DOI: 10.1074/jbc.M509643200.

(450) Hodge, C.; Taylor, C. Vitamin A deficiency. In *StatPearls*, **2026**. PMID: 33620821.

(451) Foran, D. R.; Peterson, A. C. Myelin acquisition in the central nervous system of the mouse revealed by an MBP-Lac Z transgene. *J Neurosci* **1992**, *12* (12), 4890–4897. DOI: 10.1523/jneurosci.12-12-04890.1992.

(452) Rao, S. S.; Adlard, P. A. Untangling tau and iron: exploring the interaction between iron and tau in neurodegeneration. *Front Mol Neurosci* **2018**, *Volume 11 - 2018*, Mini Review. DOI: 10.3389/fnmol.2018.00276.

(453) Sieveritz, B.; García-Muñoz, M.; Arbuthnott, G. W. Thalamic afferents to prefrontal cortices from ventral motor nuclei in decision-making. *Eur J Neurosci* **2019**, *49* (5), 646–657. DOI: 10.1111/ejn.14215.

(454) Figley, C. R.; Uddin, M. N.; Wong, K.; Kornelsen, J.; Puig, J.; Figley, T. D. Potential pitfalls of using fractional anisotropy, axial diffusivity, and radial diffusivity as biomarkers of cerebral w hite matter microstructure. *Front Neurosci* **2021**, *15*, 799576. DOI: 10.3389/fnins.2021.799576.

(455) Pineda, S. S.; Lee, H.; Ulloa-Navas, M. J.; Linville, R. M.; Garcia, F. J.; Galani, K.; Engelberg-Cook, E.; Castanedes, M. C.; Fitzwalter, B. E.; Pregent, L. J.; et al. Single-cell dissection of the human motor and prefrontal cortices in ALS and FTLD. *Cell* **2024**, *187* (8), 1971–1989.e1916. DOI: 10.1016/j.cell.2024.02.031.

(456) Hodge, R. D.; Miller, J. A.; Novotny, M.; Kalmbach, B. E.; Ting, J. T.; Bakken, T. E.; Aevermann, B. D.; Barkan, E. R.; Berkowitz-Cerasano, M. L.; Cobbs, C.; et al. Transcriptomic evidence that von Economo neurons are regionally specialized extratelencephalic-projecting excitatory neurons. *Nat Commun* **2020**, *11* (1), 1172. DOI: 10.1038/s41467-020-14952-3.

(457) Cividini, C.; Basaia, S.; Spinelli, E. G.; Canu, E.; Castelnovo, V.; Riva, N.; Cecchetti, G.; Caso, F.; Magnani, G.; Falini, A.; et al. Amyotrophic lateral sclerosis-frontotemporal dementia: shared and divergent neural correlates across the clinical spectrum. *Neurology* **2022**, *98* (4), e402–e415. DOI: 10.1212/wnl.0000000000013123.

(458) Strong, M. J.; Abrahams, S.; Goldstein, L. H.; Woolley, S.; McLaughlin, P.; Snowden, J.; Mioshi, E.; Roberts-South, A.; Benatar, M.; HortobáGyi, T.; et al. Amyotrophic lateral sclerosis - frontotemporal spectrum disorder (ALS-FTSD): Revised diagnostic criteria. *Amyotroph Lateral Scler Frontotemporal Degener* **2017**, *18* (3-4), 153–174. DOI: 10.1080/21678421.2016.1267768.

(459) Galan, L.; Gomez-Pinedo, U.; Guerrero, A.; Garcia-Verdugo, J.; Matías-Guiu, J. Amyotrophic lateral sclerosis modifies progenitor neural proliferation in adult classic neurogenic brain niches. *BMC Neurol* **2017**, *17*, 163. DOI: 10.1186/s12883-017-0956-5.

(460) Galan, L.; Gomez-Pinedo, U.; Vela-Souto, A.; García-Verdugo, J. M.; Matias-Guiu, J. Subventricular zone in motor neuron disease with frontotemporal dementia. *Neurosci Lett* **2011**, *499* (1), 9–13. DOI: https://doi.org/10.1016/j.neulet.2011.05.019.

(461) Cheung, S. W.; Bhavnani, E.; Simmons, D. G.; Bellingham, M. C.; Noakes, P. G. Perineuronal nets are phagocytosed by MMP-9 expressing microglia and astrocytes in the SOD1G93A ALS mouse model. *Neuropathol Appl Neurobiol* **2024**, *50* (3), e12982. DOI: https://doi.org/10.1111/nan.12982.

(462) Lin, Z.; Kim, E.; Ahmed, M.; Han, G.; Simmons, C.; Redhead, Y.; Bartlett, J.; Pena-Altamira, L. E.; Callaghan, I.; White, M. A.; et al. MRI-guided histology of TDP-43 knock-in mice implicates parvalbumin interneuron loss, impaired neurogenesis and aberrant neurodevelopment in amyotrophic lateral sclerosis-frontotemporal dementia. *Brain Commun* **2021**, *3* (2). DOI: 10.1093/braincomms/fcab114.

(463) Iuzzolino, V. V.; Scaravilli, A.; Carignani, G.; Senerchia, G.; Pontillo, G.; Dubbioso, R.; Cocozza, S. Mapping motor and extra-motor gray and white matter changes in ALS: a comprehensive review of MRI insights. *Neuroradiology* **2025**, *67* (7), 1683–1696. DOI: 10.1007/s00234-025-03629-7.

(464) Schönecker, S.; Neuhofer, C.; Otto, M.; Ludolph, A.; Kassubek, J.; Landwehrmeyer, B.; Anderl-Straub, S.; Semler, E.; Diehl-Schmid, J.; Prix, C.; et al. Atrophy in the thalamus but not cerebellum is specific for C9orf72 FTD and ALS patients - an atlas-based volumetric MRI study. *Front Aging Neurosci* **2018**, *10*, 45. DOI: 10.3389/fnagi.2018.00045.

(465) Filardi, M.; Gnoni, V.; Nigro, S.; Urso, D.; Vilella, D.; Tafuri, B.; Giugno, A.; De Blasi, R.; Zoccolella, S.; et al. Sleep and circadian rhythm disruptions in behavioral variant frontotemporal dementia. *Alzheimers Dement* **2024**, *20* (3), 1966–1977. DOI: 10.1002/alz.13570.

(466) Yang, T.; Pang, D.; Huang, J.; Xiao, Y.; Li, C.; Wei, Q.; Ou, R.; Cheng, Y.; Lin, J.; Che, N.; et al. Association between sleep and ALS-FTSD: a prospective cohort study based on 396,918 UK biobank participants. *Transl Psychiatry* **2025**, *15* (1), 123. DOI: 10.1038/s41398-025-03328-0.

(467) Castelnovo, V.; Canu, E.; Agosta, F. Basal ganglia alterations in amyotrophic lateral sclerosis. *Front Neurosci* **2023**, *17*, 1133758. DOI: 10.3389/fnins.2023.1133758.

(468) Mohammadi, S.; Ghaderi, S.; Fatehi, F. Quantitative susceptibility mapping as an early neuroimaging biomarker for amyotrophic lateral sclerosis: A review. *iRADIOLOGY* **2024**, *2* (4), 387–395. DOI: https://doi.org/10.1002/ird3.88.

(469) Verma, M.; Lizama, B. N.; Chu, C. T. Excitotoxicity, calcium and mitochondria: a triad in synaptic neurodegeneration. *Transl Neurodegener* **2022**, *11* (1), 3. DOI: 10.1186/s40035-021-00278-7.

(470) Armada-Moreira, A.; Gomes, J. I.; Pina, C. C.; Savchak, O. K.; Gonçalves-Ribeiro, J.; Rei, N.; Pinto, S.; Morais, T. P.; Martins, R. S.; Ribeiro, F. F.; et al. Going the extra (synaptic) mile: excitotoxicity as the road toward neurodegenerative diseases. *Front Cell Neurosci* **2020**, *14*, 90. DOI: 10.3389/fncel.2020.00090.

(471) Fishbein, I.; Segal, M. Miniature synaptic currents become neurotoxic to chronically silenced neurons. *Cereb Cortex* **2007**, *17* (6), 1292–1306. DOI: 10.1093/cercor/bhl037.

(472) Burden, N.; Chapman, K.; Sewell, F.; Robinson, V. Pioneering better science through the 3Rs: an introduction to the national centre for the replacement, refinement, and reduction of animals in research (NC3Rs). *J Am Assoc Lab Anim Sci* **2015**, *54* (2), 198–208. PMID: 25836967.

(473) Behrens, T. E.; Berg, H. J.; Jbabdi, S.; Rushworth, M. F.; Woolrich, M. W. Probabilistic diffusion tractography with multiple fibre orientations: what can we gain? *Neuroimage* **2007**, *34* (1), 144–155. DOI: 10.1016/j.neuroimage.2006.09.018.

(474) Gordleeva, S.; Dembitskaya, Y.; Kazantsev, V.; Postnikov, E. B. Estimation of cumulative amplitude distributions of miniature postsynaptic currents allows characterising their multimodality, quantal size and variability. *Sci Rep* **2023**, *13* (1), 15660. DOI: 10.1038/s41598-023-42882-9.

(475) Sharma, M.; Burré, J.; Bronk, P.; Zhang, Y.; Xu, W.; Südhof, T. C. CSPα knockout causes neurodegeneration by impairing SNAP-25 function. *Embo J* **2012**, *31* (4), 829–841. DOI: 10.1038/emboj.2011.467

(476) Delgado-Martínez, I.; Nehring, R. B.; Sørensen, J. B. Differential abilities of SNAP-25 homologs to support neuronal function. *J Neurosci* **2007**, *27* (35), 9380–9391. DOI: 10.1523/jneurosci.5092-06.2007.

(477) Heitman, J.; Movva, N. R.; Hall, M. N. Targets for cell cycle arrest by the immunosuppressant rapamycin in yeast. *Science* **1991**, *253* (5022), 905–909. DOI: doi:10.1126/science.1715094.

(478) Roth, B. L. DREADDs for neuroscientists. *Neuron* **2016**, (1097-4199 (Electronic)). DOI: 10.1016/j.neuron.2016.01.040.

(479) Mueller, M. MMueller DPhil Thesis - Supplemental Materials. Figshare: **2026**. DOI: 10.6084/m9.figshare.c.8491800.

(480) Mueller, M. MMueller DPhil Thesis - Supplemental Statistics. Figshare: **2026**. DOI: 10.6084/m9.figshare.32352261.

(481) Borgland, S. L.; Chang, S. J.; Bowers, M. S.; Thompson, J. L.; Vittoz, N.; Floresco, S. B.; Chou, J.; Chen, B. T.; Bonci, A. Orexin A/Hypocretin-1 Selectively Promotes Motivation for Positive Reinforcers. *Journal of Neuroscience* **2009**, *29* (36), 11215–11225. DOI: 10.1523/jneurosci.6096-08.2009.

(482) Yao, Z.; van Velthoven, C. T. J.; Kunst, M.; Zhang, M.; McMillen, D.; Lee, C.; Jung, W.; Goldy, J.; Abdelhak, A.; Aitken, M.; et al. A high-resolution transcriptomic and spatial atlas of cell types in the whole mouse brain. *Nature* **2023**, *624* (7991), 317–332. DOI: 10.1038/s41586-023-06812-z.

(483) Reim, K.; Wegmeyer, H.; Brandstätter, J. H.; Xue, M.; Rosenmund, C.; Dresbach, T.; Hofmann, K.; Brose, N. Structurally and functionally unique complexins at retinal ribbon synapses. *J Cell Biol* **2005**, *169* (4), 669–680. DOI: 10.1083/jcb.200502115.

(484) Yao, Z.; van Velthoven, C. T. J.; Nguyen, T. N.; Goldy, J.; Sedeno-Cortes, A. E.; Baftizadeh, F.; Bertagnolli, D.; Casper, T.; Chiang, M.; Crichton, K.; et al. A taxonomy of transcriptomic cell types across the isocortex and hippocampal formation. *Cell* **2021**, *184* (12), 3222–3241.e3226. DOI: https://doi.org/10.1016/j.cell.2021.04.021.

(485) Rojas, F.; Gonzalez, D.; Cortes, N.; Ampuero, E.; Hernández, D. E.; Fritz, E.; Abarzua, S.; Martinez, A.; Elorza, A. A.; Alvarez, A.; et al. Reactive oxygen species trigger motoneuron death in non-cell-autonomous models of ALS through activation of c-Abl signaling. *Front Cell Neurosci* **2015**, *9*, 203. DOI: 10.3389/fncel.2015.00203.

(486) Nishitoh, H.; Kadowaki, H.; Nagai, A.; Maruyama, T.; Yokota, T.; Fukutomi, H.; Noguchi, T.; Matsuzawa, A.; Takeda, K.; Ichijo, H. ALS-linked mutant SOD1 induces ER stress- and ASK1-dependent motor neuron death by targeting Derlin-1. *Genes Dev* **2008**, *22* (11), 1451–1464. DOI: 10.1101/gad.1640108.

(487) Maekawa, S.; Al-Sarraj, S.; Kibble, M.; Landau, S.; Parnavelas, J.; Cotter, D.; Everall, I.; Leigh, P. N. Cortical selective vulnerability in motor neuron disease: a morphometric study. *Brain* **2004**, *127* (Pt 6), 1237–1251. DOI: 10.1093/brain/awh132.

(488) Clippinger, A. K.; D'Alton, S.; Lin, W. L.; Gendron, T. F.; Howard, J.; Borchelt, D. R.; Cannon, A.; Carlomagno, Y.; Chakrabarty, P.; Cook, C.; et al. Robust cytoplasmic accumulation of phosphorylated TDP-43 in transgenic models of tauopathy. *Acta Neuropathol* **2013**, *126* (1), 39–50. DOI: 10.1007/s00401-013-1123-8.

(489) Latimer, C. S.; Stair, J. G.; Hincks, J. C.; Currey, H. N.; Bird, T. D.; Keene, C. D.; Kraemer, B. C.; Liachko, N. F. TDP-43 promotes tau accumulation and selective neurotoxicity in bigenic Caenorhabditis elegans. *Dis Model Mech* **2022**, *15* (4). DOI: 10.1242/dmm.049323.

(490) Michetti, F.; Clementi, M. E.; Di Liddo, R.; Valeriani, F.; Ria, F.; Rende, M.; Di Sante, G.; Romano Spica, V. The S100B protein: a multifaceted pathogenic factor more than a biomarker. *Int J Mol Sci* **2023**, *24* (11). DOI: 10.3390/ijms24119605.

(491) Escartin, C.; Galea, E.; Lakatos, A.; O'Callaghan, J. P.; Petzold, G. C.; Serrano-Pozo, A.; Steinhäuser, C.; Volterra, A.; Carmignoto, G.; Agarwal, A.; et al. Reactive astrocyte nomenclature, definitions, and future directions. *Nat Neurosci* **2021**, *24* (3), 312–325. DOI: 10.1038/s41593-020-00783-4.

(492) Schuman, B.; Machold, R. P.; Hashikawa, Y.; Fuzik, J.; Fishell, G. J.; Rudy, B. Four unique interneuron populations reside in neocortical layer 1. *J Neurosci* **2019**, *39* (1), 125–139. DOI: 10.1523/jneurosci.1613-18.2018.

(493) Khademullah, C. S.; Aqrabawi, A. J.; Place, K. M.; Dargaei, Z.; Liang, X.; Pressey, J. C.; Bedard, S.; Yang, J. W.; Garand, D.; Keramidis, I.; et al. Cortical interneuron-mediated inhibition delays the onset of amyotrophic lateral sclerosis. *Brain* **2020**, *143* (3), 800–810. DOI: 10.1093/brain/awaa034.

(494) Kang, Q.; Jiang, S.; Min, J.; Hu, F.; Xu, R. Parvalbumin interneurons dysfunction is potentially associated with FαMNs decrease and NRG1-ErbB4 signaling inhibition in spinal cord in amyotrophic lateral sclerosis. *Aging* **2023**, *15* (24), 15324–15339. DOI: 10.18632/aging.205351.

(495) van den Bos, M. A. J.; Menon, P.; Pavey, N.; Higashihara, M.; Kiernan, M. C.; Vucic, S. Direct interrogation of cortical interneuron circuits in amyotrophic lateral sclerosis. *Brain* **2025**, *148* (4), 1169–1179. DOI: 10.1093/brain/awae317.

(496) Mueller, M. MMueller DPhil Thesis - Supplemental Quality Control. Figshare: **2026**. DOI: 10.6084/m9.figshare.32373807.

(497) Mueller, M. MMueller DPhil Thesis - Supplemental Software. Figshare: **2026**. DOI: 10.6084/m9.figshare.32351481.

(498) Mueller, M. MMueller DPhil Thesis - Supplemental Neuroimaging Results. Figshare: **2026**. DOI: 10.6084/m9.figshare.32352162.